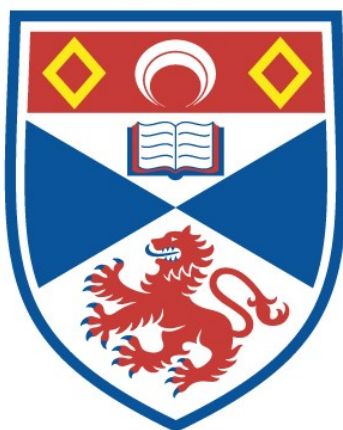


Design and synthesis of red thermally activated delayed fluorescence emitters for OLEDs, sensors and bioimaging

Changfeng Si

A thesis submitted for the degree of PhD
at the
University of St Andrews



2023

Full metadata for this thesis is available in
St Andrews Research Repository
at:

<https://research-repository.st-andrews.ac.uk/>

Identifier to use to cite or link to this thesis:

DOI: <https://doi.org/10.17630/sta/650>

This item is protected by original copyright

This item is licensed under a
Creative Commons Licence

<https://creativecommons.org/licenses/by/4.0>

Candidate's declaration

I, Changfeng Si, do hereby certify that this thesis, submitted for the degree of PhD, which is approximately 70,000 words in length, has been written by me, and that it is the record of work carried out by me, or principally by myself in collaboration with others as acknowledged, and that it has not been submitted in any previous application for any degree. I confirm that any appendices included in my thesis contain only material permitted by the 'Assessment of Postgraduate Research Students' policy.

I was admitted as a research student at the University of St Andrews in August 2018.

I received funding from an organisation or institution and have acknowledged the funder(s) in the full text of my thesis.

Date 28/10/2023

Signature of candidate

Supervisor's declaration

I hereby certify that the candidate has fulfilled the conditions of the Resolution and Regulations appropriate for the degree of PhD in the University of St Andrews and that the candidate is qualified to submit this thesis in application for that degree. I confirm that any appendices included in the thesis contain only material permitted by the 'Assessment of Postgraduate Research Students' policy.

Date 28/10/2023

Signature of supervisor

Permission for publication

In submitting this thesis to the University of St Andrews we understand that we are giving permission for it to be made available for use in accordance with the regulations of the University Library for the time being in force, subject to any copyright vested in the work not being affected thereby. We also understand, unless exempt by an award of an embargo as requested below, that the title and the abstract will be published, and that a copy of the work may be made and supplied to any bona fide library or research worker, that this thesis will be electronically accessible for personal or research use and that the library has the right to migrate this thesis into new electronic forms as required to ensure continued access to the thesis.

I, Changfeng Si, confirm that my thesis does not contain any third-party material that requires copyright clearance.

The following is an agreed request by candidate and supervisor regarding the publication of this thesis:

Printed copy

Embargo on all of print copy for a period of 1 year on the following ground(s):

- Publication would preclude future publication

Supporting statement for printed embargo request

Not all the material in this thesis has been published at the current stage.

Electronic copy

Embargo on all of electronic copy for a period of 1 year on the following ground(s):

- Publication would preclude future publication

Supporting statement for electronic embargo request

Not all the material in this thesis has been published at the current stage.

Title and Abstract

- I agree to the title and abstract being published.

Date 28/10/2023

Signature of candidate

Date 28/10/2023

Signature of supervisor

Underpinning Research Data or Digital Outputs

Candidate's declaration

I, Changfeng Si, understand that by declaring that I have original research data or digital outputs, I should make every effort in meeting the University's and research funders' requirements on the deposit and sharing of research data or research digital outputs.

Date 28/10/2023

Signature of candidate

Permission for publication of underpinning research data or digital outputs

We understand that for any original research data or digital outputs which are deposited, we are giving permission for them to be made available for use in accordance with the requirements of the University and research funders, for the time being in force.

We also understand that the title and the description will be published, and that the underpinning research data or digital outputs will be electronically accessible for use in accordance with the license specified at the point of deposit, unless exempt by award of an embargo as requested below.

The following is an agreed request by candidate and supervisor regarding the publication of underpinning research data or digital outputs:

Embargo on all of electronic files for a period of 1 year on the following ground(s):

- Publication would preclude future publication

Supporting statement for embargo request

Not all the material in this thesis has been published at the current stage.

Date 28/10/2023

Signature of candidate

Date 28/10/2023

Signature of supervisor

Abstract

Developing efficient red thermally activated delayed fluorescence (TADF) emitters remains a formidable challenge due to their low photoluminescence quantum yield governed by the energy-gap law. This thesis concerns the study of orange-to-red TADF materials, focusing on their molecular design, synthesis and photophysics. In addition to OLEDs, these materials were employed as sensors and bioimaging reagents.

Chapter 1 introduces fundamental principles of photoluminescence, electroluminescence, and provides a review of red TADF emitters for OLEDs and TADF emitters for bioimaging.

Chapter 2 documents the relationship between different N-doped polycyclic aromatic hydrocarbons (PAH)-acceptor compounds (**DMACBP**, **DMACPyBP**, **DMACBPN** and **DMACPyBPN**), their photophysics and OLED performance.

Chapter 3 focuses on a molecular design strategy that combines a π -conjugated acceptors with a TPA donor. By modulating the solid-state solvatochromism and adjusting the π - π stacking interactions, a deep red emission was obtained from both the **TPAPyBPN**-doped films and its OLED. Furthermore, we demonstrated the first TADF optical sensor for ZnCl_2 based on **TPAPyBP**.

Chapter 4 explores four new yellow-to-red TADF dendrimer emitters, which were designed to be solution processable. We systematically investigated the effect of substitution position and the strength of the donors on the optoelectronic properties of these four dendrimers. Finally, we employed these emitters in solution-processed OLEDs.

Chapter 5 continues the work on TADF dendrimer emitters by investigating the effect of extending the π -conjugation of the acceptor on the photophysics of the compound. **2GCzBPPZ**, with a much larger planarity and π -conjugation acceptor, shows unusual dual emission that is both concentration-dependent and temperature-dependent in solution. **2GCzBPPZ** is the first small molecule TADF compound used for colorimetric temperature sensing.

Chapter 6 presents three tetra(donor)-acceptor compounds **TCzPhCor**, **TDMACPhCor**, and **TPXZPhCor** employing corannulene, a curved PAH, as the acceptor. These three emitters exhibit room-temperature phosphorescence from different excited triplet states. While

TPXZPhCor doped film can act as an optical temperature sensor in the range from 77 K to 298 K. We also fabricated solution-processed afterglow OLEDs using **TPXZPhCor**.

Chapter 7 explores the use of D-A TADF emitters in bioimaging. We discussed two types of water-soluble materials: nanoparticles and water-soluble sodium-salt emitters. We also document our first attempt to study these compounds in vitro.

Acknowledgement

Firstly, I would like to thank my supervisor Prof. Eli Zysman-Colman for offering me the position in the EZ-C group and continued guidance and support. I am very grateful for his invaluable guidance and advice on my research. Especially, his patience, enthusiasm, and optimism, which I profoundly admire, are poised to influence my life in its entirety. Great thanks to Eli.

I would like to thank all the St Andrews Chemistry staffs. I want to express particular appreciation for Dr. David B. Cordes and Prof. Alexandra M. Z. Slawin for their work on the X-ray crystallography.

I would like to thank Dr. Subeesh Madayanad Suresh, Dr. Dianming Sun, Dr. Tao Wang and Dr. Chenfei Li for sharing knowledge and kind help in my daily life. I am deeply grateful for the opportunity to collaborate with such wonderful colleagues during my time spent in EZ-C group. Dr. Dongyang Chen, Dr. David Hall, Dr. Biju Basumatary, Dr. Joydip De, Dr. Zhaoning Li, Dr. Wenbo Li, Dr. Tomas Matulaitis, Dr. Campbell Mackenzie, Dr. Sudhakar Pagidi, Dr. Abhishek Kumar Gupta, Dr. Ettore Crovini, Dr. Callum Prentice, Dr. Pachaiyappan Rajamalli, Dr. John Marques Dos Santos, Sen Wu, Yan Xu, Thomas Comerford, Stefan Diesing, Jingxiang Wang, Megan Bryden, Oliver Lee, Lea Hämmerling, Quan Qi, Falak Naz.

I also wanted to thank all my collaborators: Prof. Ifor Samuel; Prof. Jay S. Siegel; Will Primrose, Prof. Zac Hudson; Ya-Nan Hu, Prof. Xiaohong Zhang; Dr. Gloria Hong, Prof. Stefan Bräse; Dr. Kang Yuan, Prof. Michael Ingleson; Dr. Felix Leon, Prof. Han Sen Soo; Felicity Noakes, Prof. Jim A Thomas; Dr. Tariq Sajjad.

Finally, from the deepest recesses of my heart, I must extend my profound gratitude to my remarkable wife, Dr. Ceng Han. She has been my rock, my confidante, and my greatest supporter through every challenge and triumph we have navigated together. Living in the enchanting town of St Andrews for these past four years has been a transformative journey, made infinitely richer by her presence by my side. I am eternally grateful to have shared these formative experiences with her. Together, we have built a life and a narrative in this town that is as beautiful and enduring as the love we share. And also, I am enormously grateful to my

parents, three sisters and nieces (Lufei Luo, Yuhan Meng) and nephews (Yixuan Luo, Yuhao Meng), for their continued support, love and encouragement. In the end, I extend heartfelt thanks to my motherland, China, for her nurturing and unwavering support.

Funding

This work was supported by China Scholarship Council (CSC) (grant number: 201806890001) and the School of Chemistry at the University of St Andrews.

Research Data/Digital Outputs access statement

Research data underpinning this thesis are available at <https://doi.org/10.17630/54b79926-d8ae-4019-ad10-d2bbf1777816>

Abbreviations

Abbreviations	Expansion
2-MeTHF	2-methyltetrahydrofuran
[ⁿ Bu ₄ N]PF ₆	Tetrabutylammonium hexafluorophosphate
A	Acceptor
a.u.	Arbitrary units
Abs	Absorption of photons
ACQ	Aggregation-caused quenching
AIE	Aggregation-induced emission
Alq ₃	Tris(8-hydroxyquinoline)aluminum(III)
BP	Dibenzo[a,c]phenazine
Bphen	4,7-diphenyl-1,10-phenanthroline
BPN	1,10-phenanthroline-5,6-dione
CBP	4,4'-Bis(carbazol-9-yl)biphenyl
CE	Current efficiency
CIE	Commision Internationale de L'Éclairage
CT	Charge transfer
CV	Cyclic voltammetry
D	Donor
DCM	Dichloromethane
DET	Dexter energy transfer
DF	Delayed Fluorescence
DFT	Density functional theory
DMAC	9,9-dimethyl-9,10-dihydroacridine
DMF	Dimethylformamide
<i>D_n</i>	Stokes shift
DPEPO	bis[2-(diphenylphosphino)phenyl]ether oxide
DPV	Differential pulse voltammetry
EBL	Electron blocking layer
<i>E_g</i>	The optical bandgap
EIL	Electron injection layer

EL	Electroluminescence spectra
EML	Emissive layer
E^{ox}	Anodic peak potential
EQE	External quantum efficiency
EQE ₁₀₀	External quantum efficiency at 100 cd m ⁻²
EQE ₁₀₀₀	External quantum efficiency at 1,000 cd m ⁻²
E^{red}	Cathodic peak potential
ESIPT	Excited-state intramolecular proton transfer
ETL	Electron transport layer
EtOAc	Ethyl acetate
f	Oscillator Strength
Fc/Fc ⁺	Ferrocene/Ferrocenium couple
FRET	Förster resonant energy transfer
FWHM	Full width at half maximum
HAT-CN	1,4,5,8,9,11-hexaazatriphenylenehexacarbonitrile
HBL	Hole blocking layer
Hex	<i>n</i> -Hexane
HF	Hyperfluorescence
HIL	Hole injection layer
HLCT	Hybridized local and intramolecular charge transfer
HOMO	Highest occupied molecular orbital
HPLC	high-performance liquid chromatography
HRMS	High resolution mass spectrometry
HTL	Hole transporting layer
IC	Internal conversion
ICT	Intramolecular charge transfer
INVEST	Inverted singlet-triplet energy gap
IQE	Internal quantum efficiency
IRF	Instrument response function
ISC	Intersystem crossing
ITO	Indium tin oxide
k_{ISC}	Intersystem crossing rate constant
k_{nr}	Non-radiative rate constant

k_{nr}^S	Singlet non-radiative rate constant
k_{nr}^T	Triplet non-radiative rate constant
k_{RISC}	Reverse intersystem crossing rate constant
k_r^S	Fluorescence radiative rate constant
k_r^T	Phosphorescence radiative rate constant
LE	Locally excited
L_{max}	Maximum luminance
LUMO	Lowest unoccupied molecular orbital
mCBP	3,3'-di(9 <i>H</i> -carbazol-9-yl)bi-phenyl
mCP	1,3-bis(N-carbazolyl)benzene
MeCN	Acetonitrile
MR	Multi-resonant
NIR	Near-infrared
NMR	Nuclear magnetic resonance
N-PAH	Nitrogen-doped polycyclic aromatic hydrocarbons
NPB	N,N'-bis(naphthalen-1-yl)-N,N'-bis(phenyl)benzidine
NTO	Natural transition orbital
OLED	Organic light-emitting diode
PAH	Polycyclic aromatic hydrocarbons
PE	Power efficiency
PEDOT:PSS	Poly(3,4-ethylenedioxythiophene):Poly(styrenesulfonate)
PhMe	Toluene
Phos	Phosphorescence
PL	Photoluminescence
PMMA	Polymethyl methacrylate
PPT	Dibenzo[b,d]thiophene-2,8-diylbis-(diphenylphosphine oxide)
Py	Pyridine
RIC	Reverse internal conversion
RISC	Reverse intersystem crossing
RMSD	Root mean square deviation
RTP	Room temperature phosphorescence
S_0	Singlet ground state

S_1	Lowest singlet excited state
S_2	Second lowest singlet excited state
SCE	Saturated calomel electrode
S_{n+1}	Higher lying singlet states
SOC	Spin orbit coupling
SSPs	Surface plasmon polaritons
T_1	Lowest triplet excited state
T_2	Second lowest triplet excited state
T2T	2,4,6-tris(biphenyl-3-yl)-1,3,5-triazine
TADF	Thermally activated delayed fluorescence
TAPC	4,4'-cyclohexylidenebis[<i>N,N</i> -bis(4-methylphenyl)benzenamine]
TCSPC	Time-correlated single-photon counting
TCTA	Tris(4-carbazoyl-9-ylphenyl)amine
TDA-DFT	Tamm-Dancoff approximation to TD-DFT
TD-DFT	Time dependent density functional theory
TDM	Transition dipole moment
T_g	Glass temperature
THF	Tetrahydrofuran
T_m	Melting temperature
TmPyPB	1,3,5-tri(m-pyrid-3-yl-phenyl)benzene
T_{n+1}	Higher lying triplet states
TPA	Triplet polaron annihilation
TPBI	1,3,5-tris(<i>N</i> -phenyl-benzimidazole-2-yl)benzene
TSCT	Through-space charge transfer
TTA	Triplet-triplet annihilation
UV	Ultraviolet
Vis	Visible
V_{on}	Turn on voltage
VR	Vibrational relaxation
ΔE_{H-L}	Energy gap between HOMO and LUMO
ΔE_{ST}	Energy difference between lowest singlet and triplet excited state

ε	Molar absorptivity coefficient
λ_{abs}	Absorption maximum
λ_{EL}	Electroluminescence maximum
λ_{exc}	Excitation wavelength
λ_{PL}	Photoluminescence maximum
μ_{e}	Dipole moment of the excited state
μ_{g}	Dipole moment of the ground state
σ	Standard deviation
τ_{d}	Delayed fluorescence lifetime
τ_{p}	Prompt fluorescence lifetime
τ_{ph}	Phosphorescence lifetime
Φ_{PL}	Photoluminescence quantum yield

Table of Contents

Abstract.....	IV
Acknowledgement	VI
Abbreviations.....	VIII
Chapter 1: Fundamental Principles of Thermally Activated Delayed Fluorescence and its Applications	1
1.1 Introduction of Photoluminescence.....	1
1.1.1 Photoluminescence of Organic Materials.....	2
1.2 Parameters for Photoluminescence	4
1.2.1 Emission Spectra	4
1.2.2 Excited-state Lifetimes	7
1.2.3 Photoluminescence Quantum Yields.....	10
1.2.4 Stokes Shift.....	12
1.2.5 Solvatochromism	14
1.2.6 Aggregates	16
1.2.7 Aggregation-induced TADF.....	17
1.3 Mechanism of Electroluminescence - OLEDs.....	18
1.3.1 Structure and Operation of OLEDs	18
1.3.2 Singlet and Triplet Excited States in OLEDs	20
1.3.3 Parameters that Affect the Performance of an OLED Device.....	22
1.3.4 Exciton Harvesting in OLEDs	26
1.4 The Development of TADF and its Applications	28
1.4.1 The Mechanism of TADF.....	28
1.4.2 The History of TADF and its Applications	32
1.5 The Development of Red TADF Emitters for OLEDs	35
1.5.1 Pyridine-3,5-dicarbonitrile Acceptors	37
1.5.2 Quinoxaline Acceptor.....	38
1.5.3 Acenaphtho[1,2-b]pyrazine Acceptors	41

1.5.4 Pyrazino- or Quinoxalino- Expanded Phenanthrene Acceptors	44
1.5.5 Phenanthro[4,5-abc]phenazine-11,12-dicarbonitrile Acceptor	54
1.5.6 Conclusion	56
1.6 The Development of TADF Emitters for Bioimaging	58
1.6.1 TADF Emitters Capped with Bovine/Human Serum Albumin.....	59
1.6.2 Organic Dots.....	61
1.6.3 Silica Nanoparticles	70
1.6.4 Self-Assembled Nanoparticles	71
1.6.5 Aggregation-induced Delayed Fluorescence.....	74
1.6.6 Others TADF Bioimaging Reagents.....	78
1.6.7 Conclusions	81
1.7 Aims for the Thesis	83
Chapter 2: The Influence of Nitrogen Doping of the Acceptor in Orange–Red Thermally	
Activated Delayed Fluorescence Emitters and OLEDs.....	86
2.1 Introduction	88
2.2 Synthesis.....	91
2.3 Theoretical Calculations.....	92
2.4 Electrochemistry.....	95
2.5 Photophysics in Solution.....	97
2.6 TADF Properties in the Solid State.....	101
2.7 OLED Device Characterization	106
2.8 Conclusions	109
2.9 Experimental Section	111
Chapter 3: Multi-Responsive Thermally Activated Delayed Fluorescence: ZnCl₂ Sensor	
and Efficient Green to Deep-red OLEDs.....	133
3.1 Introduction	135
3.2 Synthesis.....	139
3.3 X-Ray Diffraction Analysis of TPAPyBP and TPAPyBPN	139
3.4 Theoretical Calculations.....	141

3.5 Electrochemistry.....	143
3.6 Photophysical Properties in Solution	144
3.7 Fluorescence Sensing toward Lewis Acids	147
3.8 TADF Properties in the Solid State.....	153
3.9 OLED Device Characterization	158
3.10 Conclusions	160
3.11 Experimental Section	161

Chapter 4: Rational Molecular Design of Efficient Yellow-Red Dendrimer TADF for Solution Processed OLED: A Combined Effect of Substitution Position and Strength of Donors174

4.1 Introduction	176
4.2 Synthesis.....	179
4.3 X-Ray Diffraction Analysis of 2DPACzBP.....	179
4.4 Theoretical Calculations.....	180
4.5 Electrochemistry.....	183
4.6 Photophysics in Solution.....	184
4.7 Photophysics in the Solid State	188
4.8 Device Characterization	192
4.9 Conclusions	196
4.10 Experimental Section	199

Chapter 5: A Sensitive Temperature Sensor with a Large Dynamic Spectral Range Based on a Dual-emissive Thermally Activated Delayed Fluorescence Dendrimer Material .227

5.1 Introduction	229
5.2 Synthesis.....	233
5.3 Theoretical Calculations.....	234
5.4 Electrochemistry.....	237
5.5 Photophysics in Solution.....	238
5.6 Aggregate Modulation.....	241
5.7 Colorimetric Temperature Sensing	244

5.8 TADF Properties in the Solid State.....	248
5.9 Solution-processed OLED Device Characterization.....	251
5.10 Conclusions	252
5.11 Experimental Section	254
Chapter 6: Room-Temperature Multiple Phosphorescence from Functionalized Corannulenes: Temperature Sensing and Afterglow Organic Light-Emitting Diode ..	272
6.1 Introduction	274
6.2 Synthesis.....	278
6.3 Single-crystal Analysis.....	279
6.4 Theoretical Modelling	280
6.5 Electrochemistry.....	284
6.6 Photophysics in Solution.....	285
6.7 RTP from Solid States.....	289
6.8 Temperature Sensing and Afterglow OLEDs	299
6.9 Conclusions	301
6.10 Experimental Section	303
Chapter 7: Exploration of Water-soluble D-A TADF Emitters for Bioimaging	333
7.1 Introduction	335
7.2 Preparation of NPs and its Characterization	336
7.2.1 Preparation of NPs.....	336
7.2.2 Characterization of NPs.....	337
7.3 Preparation of g-NPs and its Characterization	338
7.3.1 Preparation of g-NPs	338
7.3.2 Characterization of g-NPs	339
7.4 Synthesis of TNaBPPXZ.....	341
7.5 Characterization of TDIBPPXZ and TNaBPPXZ.....	342
7.6 Bioimaging Exploration of TNaBPPXZ	346
7.6.1 Cytotoxicity Studies (MTT Assay).....	346
7.6.2 Live Cell Microscopy	347
7.6.3 Fixed Cell Microscopy – Staining After Fixation and Permeabilization	347

7.7 Conclusions	348
7.8 Experimental Section	350
Chapter 8: Conclusions and Future Outlooks	354
Chapter 9: Experimental Methods	360
9.1 General Synthetic Procedures	360
9.2 Theoretical Calculations.....	360
9.3 Electrochemistry Measurements	361
9.4 X-ray Crystallography.....	361
9.5 Photophysical Measurements	362
9.6 OLED Fabrication and Characterization	363
Chapter 10: Appendix	365
10.1 Characterization Data	365
10.2 Publications Arising from my Work	365
10.2.1 Published Manuscripts.....	365
10.2.2 Unpublished Manuscripts	366
10.3 Conference Contributions	367
References.....	368

Chapter 1: Fundamental Principles of Thermally Activated Delayed Fluorescence and its Applications

1.1 Introduction of Photoluminescence

Luminescence is often considered as "cold light" because it does not involve the emission of heat, as opposed to incandescence, referred to as "hot light", which involves the emission of heat along with light.¹ More specifically, luminescence is normally a kind of spontaneous emission referring to the process by which a system in an excited state emits radiation and is not in thermal equilibrium with its environment. Based on the mode of excitation, luminescence can be classified into various types. For photoluminescence (PL), the mode of excitation is the absorption of light, which makes the material undergo a transition to an electronic excited state.^{2,3} The unstable excited state relaxes back to its ground state by emitting light. For electroluminescence (EL), the mode of excitation is the presence of an electric field, where a voltage is applied across a material causing electrons and holes to be injected into the material and move toward a region of opposite charge, as the electrons meet the holes in the emitting layer they form excited electron-hole pairs, which are called excitons.^{4,5} When the excitons recombine light is emitted. For bioluminescence, the mode of excitation is a biochemical reaction, such as that occurs with luciferase, which involves the oxidation of luciferin by this enzyme.^{6,7} The oxidation reaction releases energy, which is absorbed by a photoprotein that emits light, like how fireflies light up. Similar to bioluminescence, chemiluminescence is a type of luminescence that is a byproduct of a chemical reaction, which produces an electronically excited state and subsequently emits a photon of light as it relaxes back to its ground state.^{8,9} The modes of excitation for cathodoluminescence and sonoluminescence are from high-energy electrons and ultrasound waves, respectively. As discussed above, these are just some of the many examples of mechanisms to produce light. In this Thesis, I will focus on two types of luminescence, PL and EL from organic emitting materials.

1.1.1 Photoluminescence of Organic Materials

Photoluminescence in organic molecules can be categorized into three main types from the nature of the excited states: fluorescence, phosphorescence, and delayed fluorescence. The Perrin–Jablonski diagram shown in Figure 1.1 illustrates the electronic excited states, and radiative and non-radiative transitions in a molecule after excitation.

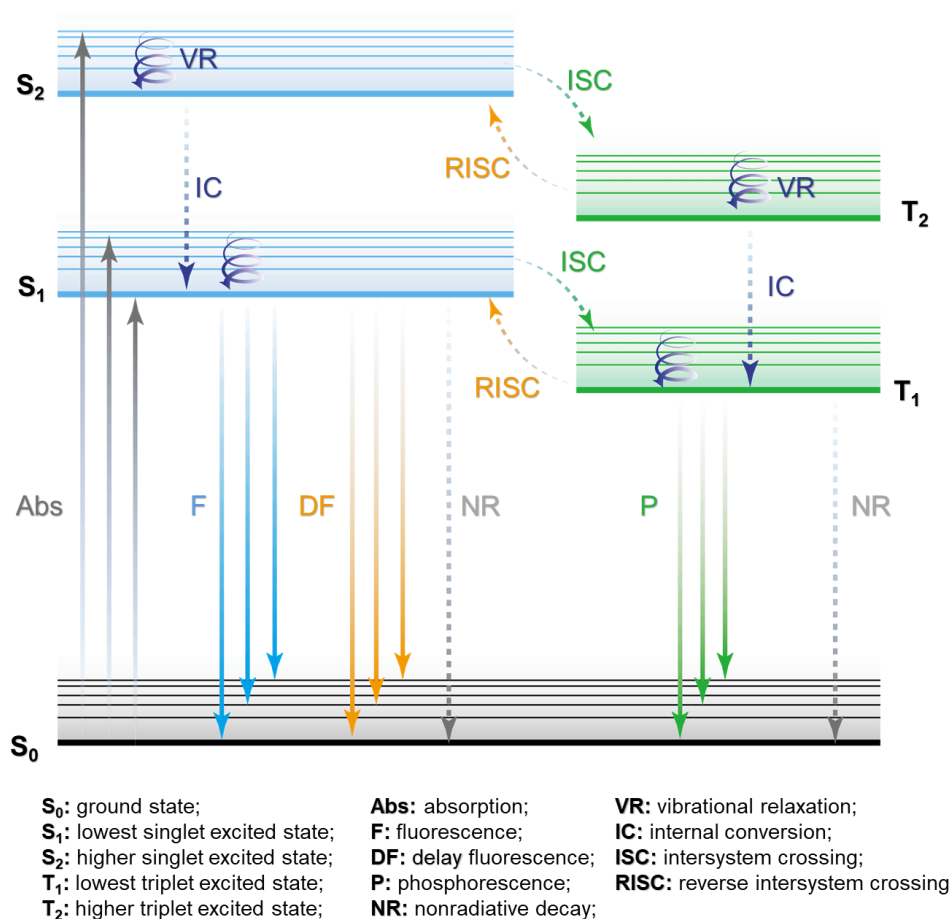


Figure 1.1. Perrin–Jablonski diagram for single molecule.

Fluorescence (F): The initial stage of photoluminescence involves a molecular electronic transition that is triggered by the absorption of photons (Abs). This transition involves the molecule moving from a lower-energy electronic state, typically the ground state (S_0), to higher-energy states, i.e., excited states. While the excited molecules at high-energy levels are typically unstable, both vibrational relaxation (VR) and internal conversion (IC), which is a nonradiative transition between two electronic states of the same spin multiplicity, relax excited molecule toward the 0th vibrational level of the lowest singlet excited state (S_1) on a time scale

of 10^{-13} - 10^{-11} s. Fluorescence (F) is defined as the emission of photons that occurs when the excited molecule relaxes from S_1 to S_0 . This process is typically very rapid and occurs on a time scale of 10^{-10} - 10^{-7} s.

Phosphorescence (P): In addition to emitting a photon, excited molecules in the S_1 state also undergo other de-excitation processes, like IC and intersystem crossing (ISC). ISC refers to a nonradiative transition that occurs between two vibrational levels belonging to electronic states of different multiplicities, like crossing from S_1 to T_1 , or crossing between higher level singlet and triplet excited states. In general, transitions between electronic states of different multiplicities (e.g., singlet to triplet or triplet to singlet) are formally forbidden; however, spin-orbit coupling (SOC) provides a weak interaction between the wavefunctions of different multiplicities, allowing for some probability of intersystem crossing to occur between them, meaning that the radiative rate constant for this transition is very slow. Phosphorescence is defined as the radiative de-excitation from any triplet excited state to S_0 state.¹⁰ During such a slow process, the excited T_1 state may undergo various nonradiative relaxation processes, such as vibrational relaxation (NR), internal conversion (IC), reverse intersystem crossing (RISC) to singlet excited states, or reaction with triplet quenchers such as O_2 . These nonradiative relaxation processes make the phosphorescence hard to observe unless at low temperatures and/or in a rigid medium or in oxygen-free environment. The lifetime of the T_1 is typically much longer than that of the S_1 state, on the order of 10^{-6} - 10^1 s.

Delayed Fluorescence (DF): Delayed fluorescence is of one of two types: E-type and P-type. E-type delayed fluorescence, which was identified for the first time with eosin Y,¹¹ is also well known as thermally activated delayed fluorescence (TADF), where RISC from triplet to singlet states occurs promoted by latent environmental thermal energy. TADF has received a lot of attention in recent years as a potential mechanism for highly efficient organic light-emitting diodes (OLEDs) and other optoelectronic devices.¹²⁻¹⁷ The TADF mechanism is explained in Section 1.5. P-type delayed fluorescence or triplet-triplet annihilation (TTA) was first described explicitly for pyrene.^{18,19} As shown in Figure 1.2, in this process, two molecules in the T_1 state collide with each other and transfer their energy to one of the molecules, while the other molecule reverts back to the ground state. To make sure TTA occurs, the combined energy of the two triplet excited states ($2T_1$) of the molecule needs to be larger than to the energy of S_1

($2T_1 \geq S_1$). These two triplets combine to form a singlet exciton and then leads to a delayed emission. The decay time constant of the delayed fluorescence process is related to the lifetime of the triplet state. The probability of TTA occurrence increases with the concentration of triplet excitons, which itself is dependent on the intensity of the excitation source.

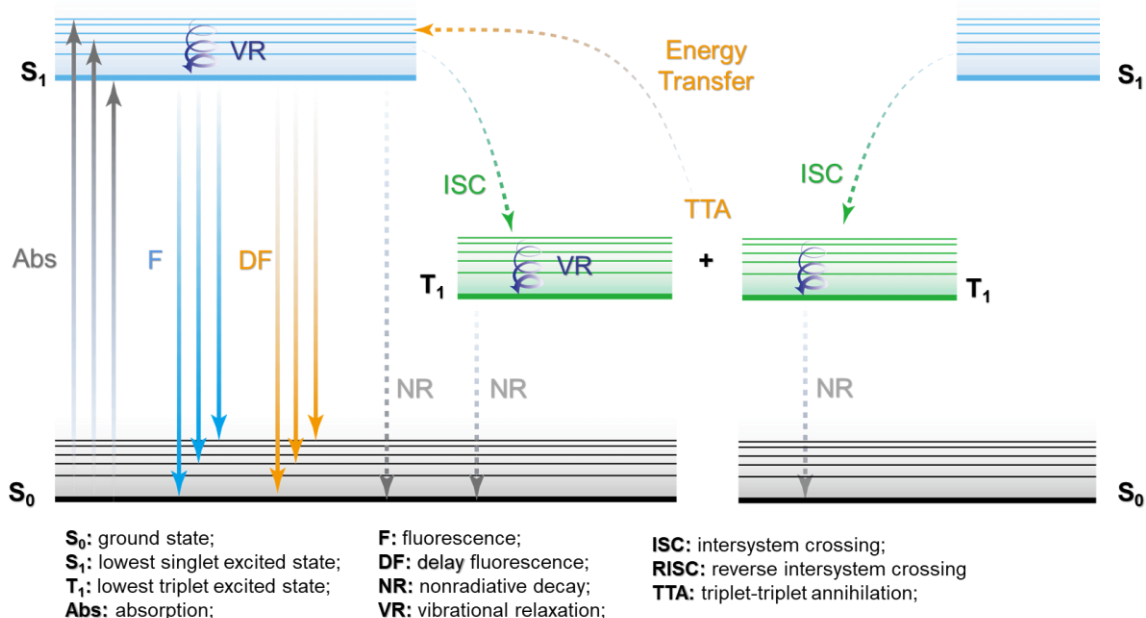


Figure 1.2. Perrin–Jablonski diagram for TTA process.

1.2 Parameters for Photoluminescence

1.2.1 Emission Spectra

Emission spectra are the distribution of energies of electromagnetic radiation emitted by a material, usually plotted as a function of wavelength, which are recorded by a spectrofluorometer. According to the type of excitation light source and the measurement method used, emission spectra can be classified into two categories: steady-state fluorescence and time-resolved emission. For steady-state fluorescence, a sample is excited with a constant intensity light source. The light source is a broadband light source, such as a Xenon lamp, which produces a continuous spectrum of light from the UV to the visible and near-IR regions. The light from the Xenon lamp is then passed through an excitation monochromator, generating a particular wavelength of the excitation light that is then directed incident on the sample. The light emitted from the sample is collected and passed through an emission monochromator, and

further directed towards a detector (photomultiplier tube, PMT). Then the fluorescence spectrum plots the intensity of fluorescence as a function of the emission wavelength. On the other hand, time-resolved emission (TRPL) is measured as a function of time after the excitation pulse, rather than as a function of wavelength. In this method, a short pulse of light is used to excite the sample, and the resulting emission is measured at different time intervals using a time-correlated single photon counting (TCSPC) system.²⁰

TCSPC is a technique to record fast decays, typically from picoseconds to microseconds. As shown in Figure **1.3a**, the function generator delivers a reference pulse to the time-to-digital converter (TDC) while simultaneously sending another pulse to trigger the laser. The sample is excited by the laser and a single photon from the sample can reach the detector, followed by the photomultiplier tube (PMT). This single photon gets converted by the PMT into an electrical signal, which is then sent to the TDC. The TDC then measures the time difference between this electrical pulse and the initial reference pulse. These time differences are recorded. After accumulating data from many cycles, a histogram is generated showing the frequency of these time differences, representing the sample's decay kinetics. It is crucial that only a single photon is detected by the PMT during each cycle to ensure the histogram accurately mirrors the decay characteristics of the sample. Overall, the TCSPC technique is a statistical method. It does not measure decay directly but gathers a large number of single-photon measurements and compiles them into a decay histogram.

Multichannel scaling (MCS) is another technique to record relatively slow decays (millisecond and second timescales). As shown in Figure **1.3b**, the working principle of an MCS measurement is based on a time sweep that sorts the detected photons into different arrival time channels. Different from TCSPC, the PMT is set to count many photons in each cycle and converts them into electrical signals. These electronic signals are categorized into bins within the memory (MEM), shaping a histogram that plots time versus intensity. More specially, the measurement time window is divided into channels (bins). After the samples are excited, the sweep initiates at bin 1, and all photons arriving in this window are logged into memory. The process progresses to bin 2, recording corresponding photon arrivals, and this continues until the entire time frame is covered. Time-resolved emission spectroscopy is a good method for studying the dynamics of excited states.

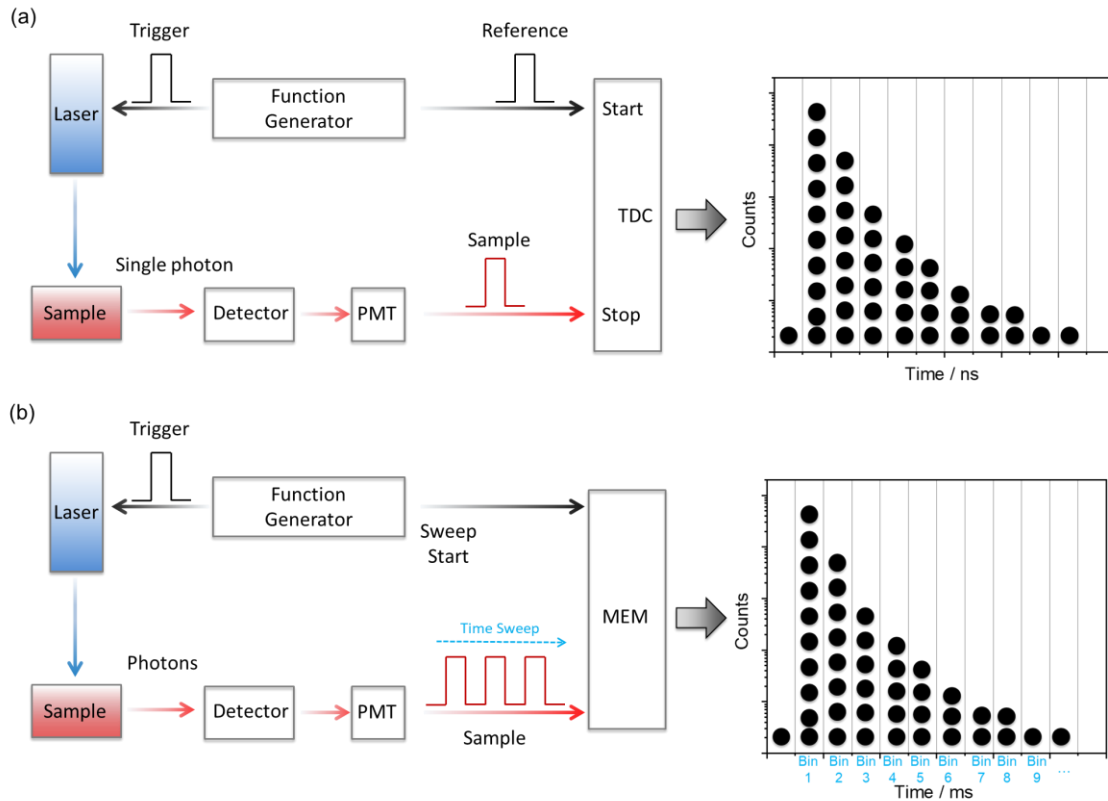


Figure 1.3. Simplified overview of the working principle of (a) TCSPC and (b) MCS. These figures have been adapted from the literature.^{21,22}

Based on the emission energy of the emitted light, emission spectra can be classified into three main categories: ultraviolet (UV) emission, visible (Vis) emission and near-infrared (NIR) emission spectra:

UV emission: these are emission spectra in the UV typically < 400 nm.

Visible emission: The visible region of the electromagnetic spectrum is typically defined as the emission spectra peak (λ_{PL}) at between 380 and 780 nm.²³ As shown in Figure 1.4, blue light normally has a λ_{PL} between approximately 380-490 nm, green light has a λ_{PL} of approximately 500-570 nm, and red light has a λ_{PL} of approximately 600-750 nm. Furthermore, these colors can be characterized using a graphical tool known as a Commission International de l'Éclairage (CIE) 1931 coordinate chromaticity diagram, where colors are mapped as points on the diagram, corresponding to the range of colors perceivable by the human eye.²⁴ The current industry standard for ultra HD-TVs, known as BT. 2020, defines the colors for blue, green, and red as (0.13, 0.05), (0.17, 0.80) and (0.71, 0.29), respectively, as shown in Figure 1.4b. By blending the colors at various points within the triangle formed between these three

sets of coordinates, all the colors that correspond to the points enclosed can be displayed.

Near-infrared (NIR) emission: these are emission spectra in the near-infrared range, typically between 750 and 2500 nm.

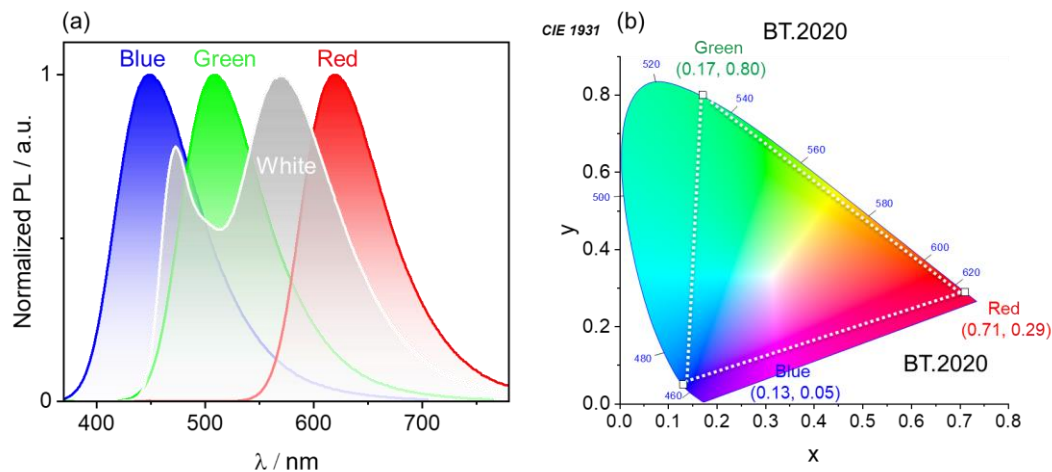


Figure 1.4. (a) Blue, green, red and white emission spectra and (b) CIE diagram where RGB colour points are highlighted as squares for BT.2020.

1.2.2 Excited-state Lifetimes

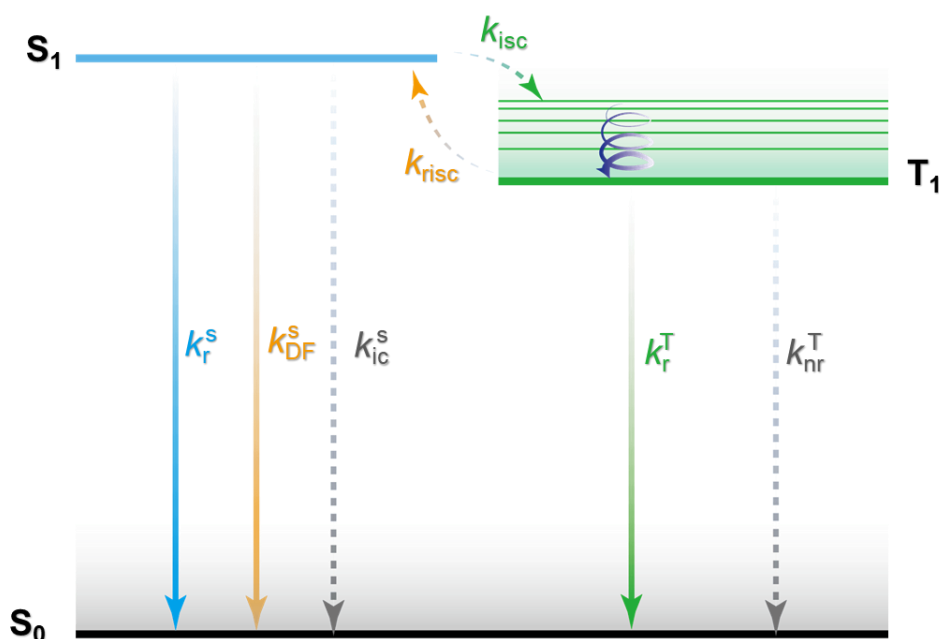
The rate constants for the deactivation processes are shown in Figure 1.5, assuming single molecule conditions, without intermolecular interactions. According to classical chemical kinetics, the rate of disappearance of excited molecules in a dilute solution of an emitter can be expressed by the following differential equation:

$$\frac{d[N(t)]}{dt} = -k[N(t)] \quad (1-1)$$

where $N(t)$ is the number of excited molecules at time t , k is the rate constant for the decay of the excited state, here for singlet state $k = k_r^S + k_{ic}^S + k_{isc}$, and the negative sign indicates that the number of excited molecules decreases with time. The solution to this differential equation is given by:

$$N[t] = N[0]\exp(-kt) \quad (1-2)$$

where $N(0)$ is the initial number of excited molecules at time $t = 0$.



- S_0 : ground state; S_1 : lowest singlet excited state; T_1 : lowest triplet excited state;
 k_r^S : rate constant for radiative deactivation from S_1 to S_0 ;
 k_{DF}^S : rate constant for radiative deactivation from S_1 to S_0 with delay fluorescence;
 k_{ic}^S : rate constant for internal conversion from S_1 to S_0 ;
 k_{isc} : rate constant for intersystem crossing;
 k_{risc} : rate constant for reverse intersystem crossing;
 k_r^T : rate constant for radiative deactivation from T_1 to S_0 ;
 k_{nr}^T : rate constant for nonradiative deactivation from T_1 to S_0 ;

Figure 1.5. The rate constants for the deactivation processes of excited states.

The lifetime of the excited state, τ , is related to the rate constant by the equation:

$$\tau = \frac{1}{k} = \frac{1}{k_r^S + k_{ic}^S + k_{isc}} = \frac{1}{k_r^S + k_{nr}^T} \quad (1-3)$$

Therefore, the lifetime of the excited state can be calculated from the slope of a plot of $\ln(N(t)/N(0))$ versus time t . If the decay of the excited state is monoexponential, the slope of the plot will be equal to $-k$, and the lifetime can be obtained by taking the inverse of the slope.

The fluorescence decay time, also known as the fluorescence lifetime, can be measured using time-resolved fluorescence spectroscopy. In this technique, a short pulse of excitation light ($t = 0$) is used to excite the fluorescent molecules, corresponding to the fluorescence intensity (I_0). The fluorescence intensity (I_t) at time t :

$$I_t = k_r^S I_0 \exp(-t/\tau) \quad (1-4)$$

The fluorescence decay curve typically shows an exponential decay of the fluorescence

intensity over time. The time required for the intensity to decrease to 1/e of its original value is called the fluorescence lifetime, as illustrated in Figure **1.6a** and **b**. To get the values of lifetime, time-resolved PL decays were fitted to a sum of exponential decays, with chi-squared (χ^2) values between 1 and 2; the quality of this fitting process is often evaluated using χ^2 , which assesses how well the fitted curve matches the experimental data, a χ^2 value close to 1 normally indicates a good fit. Normally, the fluorescence decay monoexponentially decreases, which means that the fluorescence intensity decreases exponentially over time with a single decay time constant. The corresponding fluorescence lifetime τ_F scale is around 10^{-7} - 10^{-9} s. Similarly, phosphorescence decay also monoexponentially decreases but with a long lifetime as shown in Figure **1.6d**. Different from fluorescence and phosphorescence, the emission decay for TADF is biexponential, where a prompt fluorescence resulting from direct emission from S_1 and a delayed fluorescence resulting from ISC/RISC cycling before fluorescence from the same S_1 state as shown in Figure **1.6c**. Unlike single emitters in solution where the environment is homogeneous and isotropic, the decay for the TADF emitters in the solid state could become multiexponential due to multiple emitting species, like different conformers. For multiexponential decay, the average lifetime can be a useful tool to gauge the properties of the emitter; however, the average lifetime generally has no real physical meaning as it captures multiple decay processes, sometimes from multiple species. The average lifetime is calculated using the following:

Two exponential decay model:

$$\tau_{AVG} = \tau_1 w_1 + \tau_2 w_2 \quad (1-5)$$

with weights defined as $w_1 = \frac{A_1 \tau_1}{A_1 \tau_1 + A_2 \tau_2}$ and $w_2 = \frac{A_2 \tau_2}{A_1 \tau_1 + A_2 \tau_2}$ where A_1 and A_2 are the preexponential-factors of each component.

Three exponential decay model:

$$\tau_{AVG} = \tau_1 w_1 + \tau_2 w_2 + \tau_3 w_3 \quad (1-6)$$

with weights defined as $w_1 = \frac{A_1 \tau_1}{A_1 \tau_1 + A_2 \tau_2 + A_3 \tau_3}$, $w_2 = \frac{A_2 \tau_2}{A_1 \tau_1 + A_2 \tau_2 + A_3 \tau_3}$ and $w_3 = \frac{A_3 \tau_3}{A_1 \tau_1 + A_2 \tau_2 + A_3 \tau_3}$ where A_1 , A_2 and A_3 are the preexponential-factors of each component. Each component of the decay is assigned a weight, (w_i), which is the contribution of the emission

from each component to the total emission.

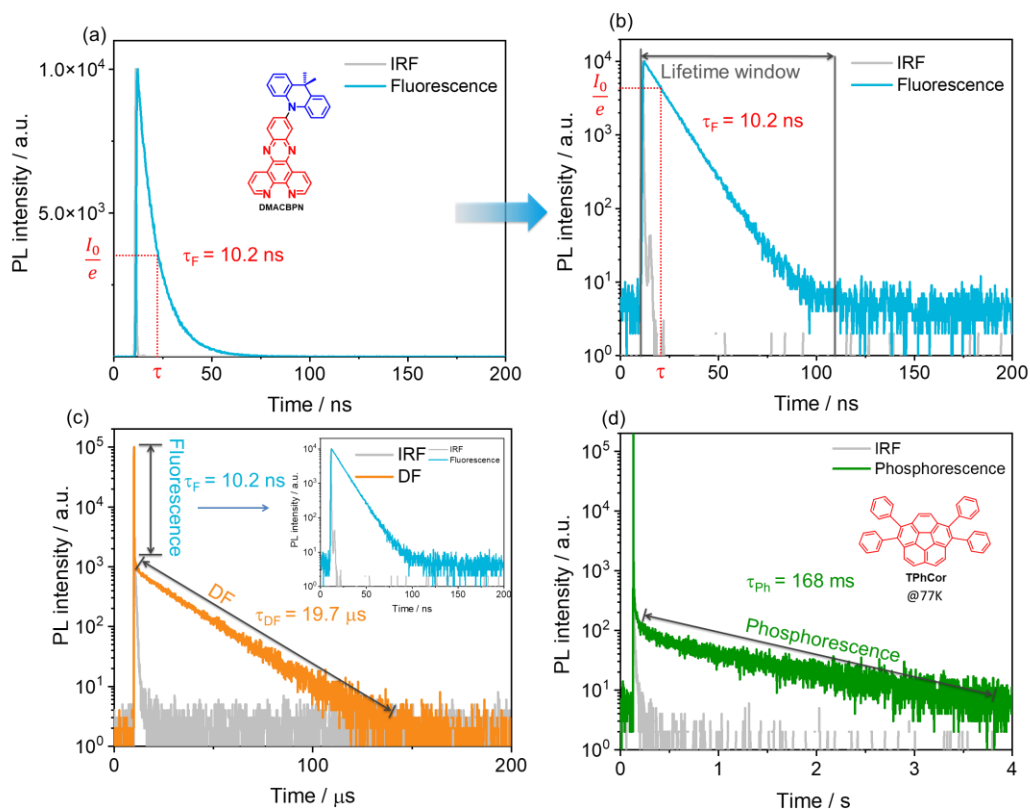


Figure 1.6. Decay of (a) fluorescence of **DMACBP** in aerated toluene at 298 K with linear scale for y-axis and (b) corresponding fluorescence decay with log scale for y-axis (TCSPC mode); (c) DF of **DMACBP** in degassed toluene (MCS mode). (d) Phosphorescence of **TPhCor** in toluene at 77 K (MCS mode).

1.2.3 Photoluminescence Quantum Yields

Photoluminescence quantum yield (Φ_{PL}) is defined as the ratio of the number of photons emitted (N_{em}) by the sample to the number of photons absorbed (N_{abs}) by the sample.²⁵ In other words, Φ_{PL} is the fraction of excited molecules that return to the ground state S_0 as a result of radiative decay.

$$\Phi_{\text{PL}} = \frac{N_{\text{em}}}{N_{\text{abs}}} = \frac{k_r}{k_r + k_{nr}} \quad (1-7)$$

Φ_{PL} is a useful parameter for characterizing the fluorescence or phosphorescence capabilities of a material, as it provides a quantitative measure of the efficiency of the luminescence process. Moreover, there are a variety of factors that affect the Φ_{PL} , including:

k_r : The radiative decay rate, often denoted as k_r , is a description of how fast a material undergoes radiative decay, transitioning from the excited states back to its ground state by emitting photons. Oscillator strength (f) expresses the probability of a particular electronic transition like absorption/emission, which is determined by the overlap of the wavefunctions of between the excited and ground state. The f is directly proportional to the square of the magnitude of the transition dipole moment (TDM, μ_{if}).

$$f \propto |\mu_{if}|^2 \quad (1-8)$$

TDM (μ_{if}) is a quantum mechanical parameter that provides a measure of the likelihood of a transition between two states, i.e., the initial state (i) and the final state (f). It's defined as:

$$\mu_{if} = \int \psi \hat{\mu} \psi^* d\tau \quad (1-9)$$

Where:

ψ is the wavefunction of the initial state;

$\hat{\mu}$ is the electric dipole moment operator;

ψ^* is the wavefunction of the final state;

The integral essentially measures the overlap between the initial and final state wavefunctions, weighted by the dipole moment operator. When there is a significant overlap between these wavefunctions, and the transition is allowed, the TDM is large. The greater this overlap and the stronger f , and thus the higher k_r . However, when the overlap is poor, k_r becomes slow. In such situations, k_{nr} pathways can become more competitive. In addition, k_r will increase with the cube of the energy gap (E_g) according to Einstein's A coefficient.²⁶

k_{nr} : 1) As mentioned before, less wavefunction overlap leads to lower k_r , and non-radiative pathways become more predominant; 2) According to the energy gap law, k_{nr} increases exponentially as the energy gap decreases. This is because smaller energy gaps allow for more efficient coupling to vibrational relaxation modes leading to energy loss. It is well documented that as the energy gap (E_g) decreases, non-radiative decay will increase as represented as:

$$k_{nr} \propto \exp\left(\frac{-E_g}{\omega}\right) \quad (1-10)$$

Where k_{nr} is the rate constant for non-radiative relaxation, E_g is the energy gap between the relevant states, and ω is a constant that depends on the specific molecular system and its environment. In other words, as the E_g decreases, the rate of non-radiative processes increases

exponentially, leading to a lower overall Φ_{PL} . 3) Interactions with neighboring molecules such as solvents, or oxygen, aggregates, or π - π stacking could also increase k_{nr} . In particular, aggregation-caused quenching (ACQ) is a common phenomenon that can lead to a reduction in Φ_{PL} . In high concentration, a material can aggregate, and these aggregates typically always lead to non-radiative decay processes, decreasing the efficiency of the radiative decay process. The ACQ effect can be caused by various factors, including π - π stacking, energy transfer between aggregated chromophores, excited-state reactions.²⁷⁻²⁹ Aggregation-induced emission (AIE) is a phenomenon that is the opposite of ACQ, where a material shows enhanced luminescence upon aggregation.³⁰ In AIE, the aggregation of chromophores leads to arrested vibrational/rotational motions in the solid state, which suppresses non-radiative decay and results in an increase in Φ_{PL} .³¹

1.2.4 Stokes Shift

The Stokes shift is the difference between the positions of the band maximum of the lowest energy absorption band (λ_{Abs} , ν_{Abs}) and the maximum of the fluorescence (λ_{PL} , ν_{PL}) spectrum. The Stokes shift, $\Delta\nu$, is typically expressed in wavenumbers.

$$\Delta\nu = \nu_{\text{Abs}} - \nu_{\text{PL}} \quad (1-11)$$

The larger the structural changes and geometric reorganization in the excited state, the larger the Stokes shift that is observed.³² As shown in Figure 1.7, Two different classes of TADF emitters in toluene exhibit large difference in Stokes shift. For the donor-acceptor (D-A) TADF emitters, exemplified in **TPAPyBP**, have larger $\Delta\nu$ of 3748 cm^{-1} than that ($\Delta\nu = 1100 \text{ cm}^{-1}$) of multiresonance TADF (MR-TADF) emitters, exemplified in **tBuDPA-Dikta**. This is because **TPAPyBP** emits from a charge transfer (CT) S_1 state, where the donor and acceptor moieties are separated, leading to a large geometry reorganization in the excited state reflected in the larger Stokes shift. Here, a CT state involves an electron transition between molecular orbitals on different moieties in one molecule, whereas a locally excited (LE) state is characterized by an electron transition within the same molecular moiety. Further, when the dipole moment of an emitter is higher in the excited state than in the ground state, the Stokes shift will increase in high polarity solvents. In contrast, **tBuDPA-DiKta** possesses much more rigid molecular

structure, which means that there is smaller geometry reorganization in the excited state leading to a smaller Stokes shift. In addition to the molecular structure. The nature of the excited state in this compound is short-range charge transfer, and as such the stabilization of the excited state will be less sensitive to solvent polarity as the strength of the CT state is weaker. The Stokes shift can be influenced by a variety of factors like solvent polarity (for molecules that emit from CT states), temperature, and PH.^{33,34}

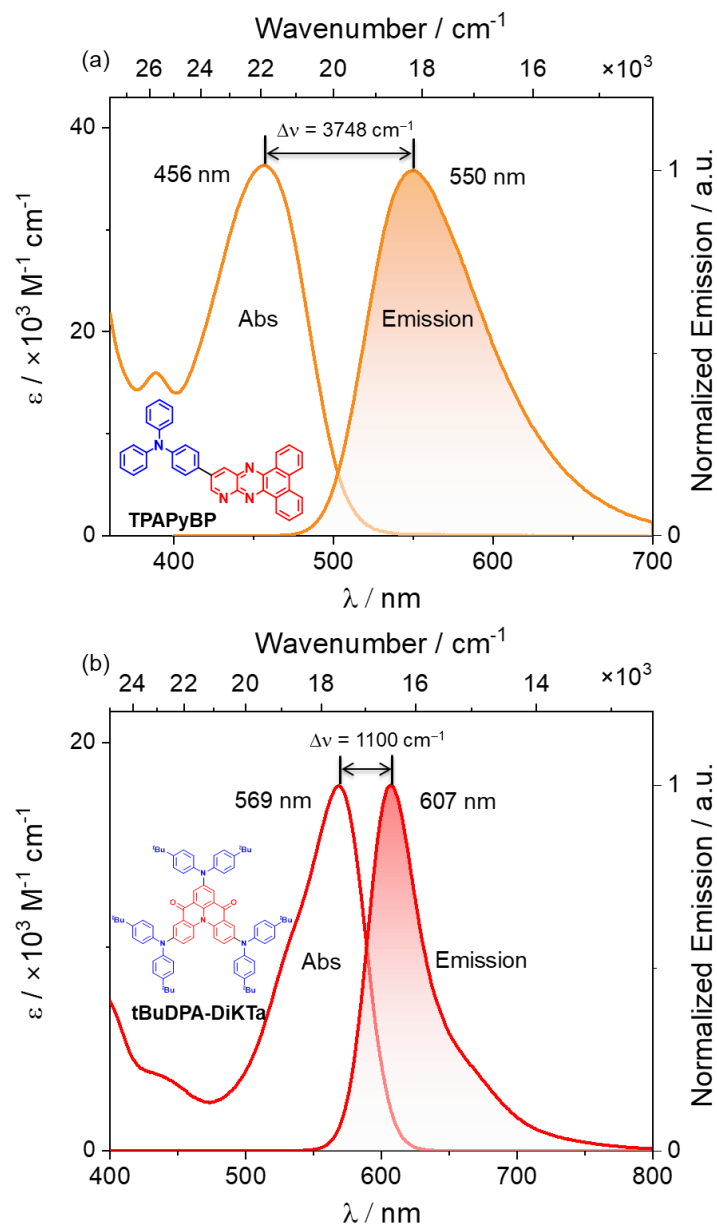


Figure 1.7. Definition of the Stokes shift. Different types of TADF examples for Stokes shift (a) TPAPyBP and (b) tBuDPA-DiKTa.

1.2.5 Solvatochromism

Solvatochromism refers to the phenomenon where the absorption or emission spectrum of a molecule changes in response to changes in the polarity of the solvent. In other words, when a solute is dissolved in a solvent, the interactions between the solute and solvent molecules can affect the energy levels of the solute's ground and excited states, leading to changes in absorption or emission spectrum of solute. The majority of solvatochromic effects can be attributed to electrostatic interactions. For the emitter, especially for D-A molecules, an electronic transition from the ground state to the excited state can be associated with a change in the dipole moment. Solvents with large permanent dipoles can stabilize the charge distribution of the solute in both its ground and excited states. The larger the dipole moment of the emitter, the greater its stabilization in high polarity solvents.

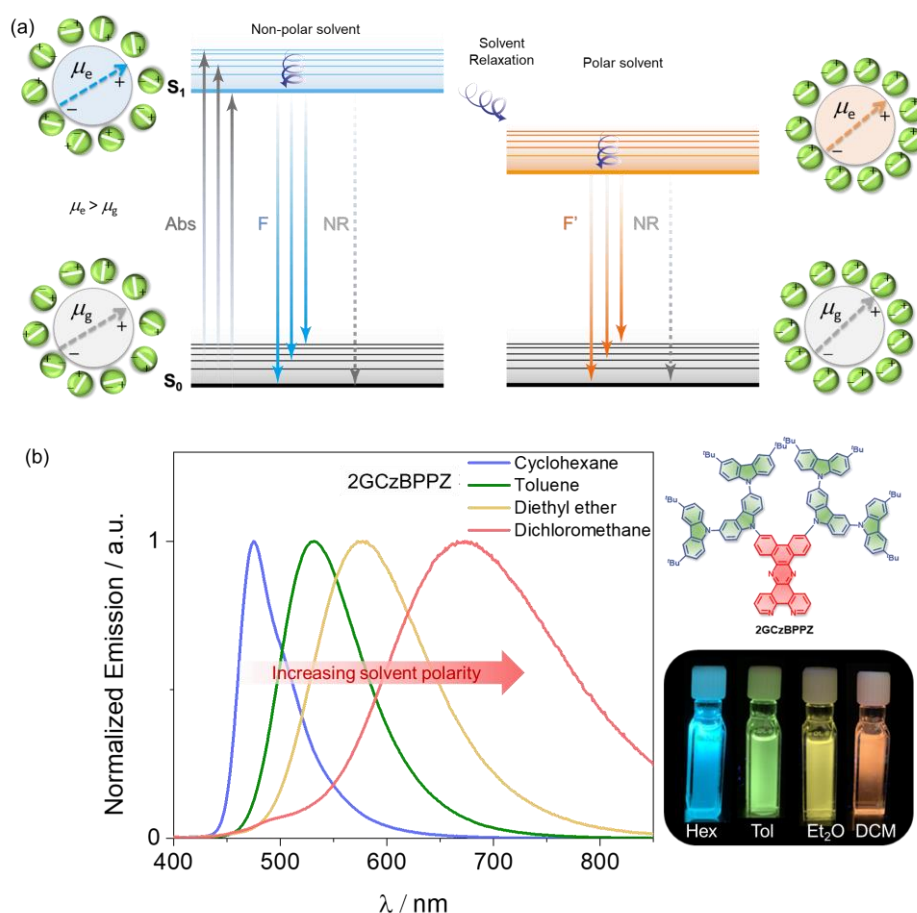


Figure 1.8. (a) Perrin–Jablonski diagram for luminescence with solvent relaxation. (b) Positive solvatochromism for the **2GCzBPPZ**;

A permanent dipole moment (μ_g) arises in a molecule when there is a net separation of positive and negative electric charges. The transition dipole moment (μ_e) is a vector quantity associated with the transition between the ground state and an excited state in a molecule. The μ_g of an aromatic molecule often differs its μ_e . After excitation of a solute molecule in a solvent, the solvent molecules surrounding the solute undergo a relaxation process or reorganization to reach a state of minimum free energy. The relaxation process involves changes in the orientation and position of the solvent molecules surrounding the solute in a way that the positive end of the solvent dipole is near the negative end of the solute dipole and vice versa to accommodate the new electronic configuration of the excited solute molecule (Figure 1.8a). In general, if there is an increase in the dipole moment like $\mu_e > \mu_g$, the more polar the solvent (Figure 1.9), the more favorable the solute-solvent interactions, and the lower the energy of the relaxed excited state, resulting in a larger red shift of the emission spectrum (Figure 1.8b). In general, the effect of solvent polarity on the absorption spectrum is often less pronounced than its effect on the emission spectrum. This is because the absorption process is very fast (around 10^{-15} s), and the solvent molecules do not have sufficient time to fully reorganize (10^{-10} – 10^{-11} s) around the excited solute molecule during the absorption process.

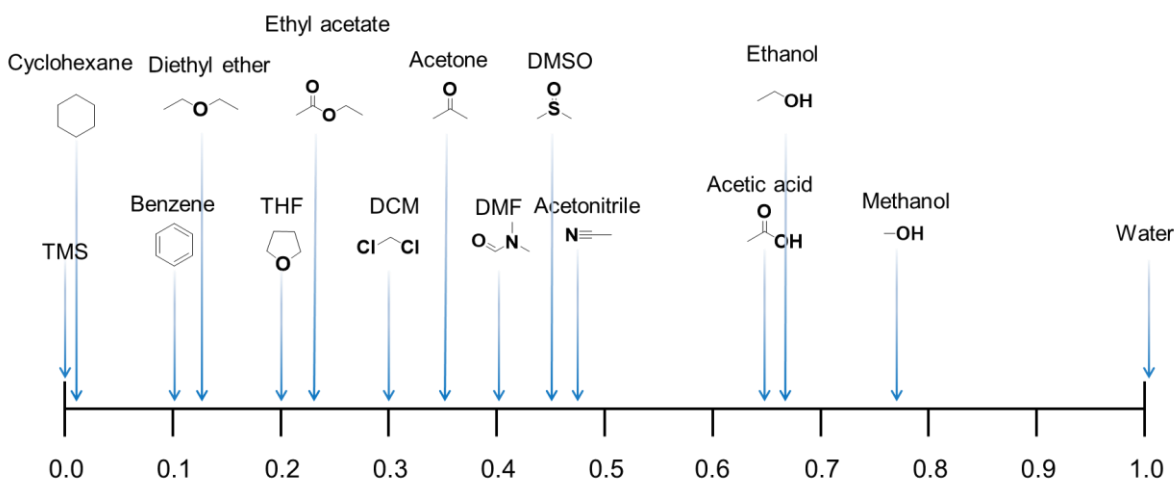


Figure 1.9. Normalized solvent polarity scale E_T^N with $E_T^N = 0.0$ for tetramethylsilane (TMS) and $E_T^N = 1.0$ for water as arbitrarily fixed points.³⁵

1.2.6 Aggregates

Beyond single organic molecules (monomers) as discussed earlier, ordered self-assembly of monomers into aggregates via non-covalent interactions such as hydrogen bonding, π - π stacking, van der Waals forces, and electrostatic interactions, are quite common in aromatic luminogens.³⁶ The properties of these aggregates, including their Φ_{PL} , emission colour, and lifetime, can be significantly different from the properties of the individual monomers due to the effects of changes in the local environment and new molecular orbitals formed within the aggregates.³⁶⁻³⁸ In 1963, Kasha and co-workers developed the theoretical conception of molecular exciton theory, indicating the emission properties of π -conjugated materials in aggregates could be greatly affected by the interactions between molecular transition dipoles.^{39,40} According to the Frenkel exciton (FE) model, the Coulomb coupling between molecules “1” and “2,” can be described as:

$$J_C^{pd} = \frac{\mu_1 \cdot \mu_2 - 3(\mu_1 \cdot \hat{R})(\mu_2 \cdot \hat{R})}{4\pi\epsilon R^3} \quad (1-12)$$

where μ_1 and μ_2 represent the dipole moments associated with the transition from $S_0 \rightarrow S_1$ for molecules “1” and “2”, respectively. $\vec{R} = R\hat{R}$ is the displacement vector connecting the molecular mass centers, and ϵ represents the dielectric constant of the medium. The situation involving parallel transition dipole moments defines packing geometries where each unit cell contains one molecule. The equation 1-12 could be simplified to

$$J_C^{pd} = \frac{\mu^2(1 - 3\cos^2\theta)}{4\pi\epsilon R^3} \quad (1-13)$$

Where two aggregation species are determined by the relative orientation of μ_1 and μ_2 , which is quantified by the angle θ as shown in Figure 1.10. In an H-aggregate (side by side orientation), where molecules are arranged in a parallel configuration with a sliding pitch angle greater than 54.7° ,⁴¹ the absorption spectra typically show a blue shift compared to those in solution. This shift is a result of strong dipole-dipole interactions, which lead to a significant energy splitting in the excited state. The lower energy level within this split state is optically dark. The absence of optical coupling between this lower excited state and the ground state suggests that the fluorescence efficiency in an H-aggregate is usually lower compared to that in an isolated state. In J-aggregates (head-to-tail orientation), molecules are arranged in a staggered configuration

with a pitch angle of less than 54.7° (Figure 1.10), where the lower energy excited state is optically allowed while the higher one is forbidden. Thus, there is a distinct red shift in the absorption and emission spectra compared to that of the monomer. Therefore, to achieve red emission, employing the formation of J-aggregates could also be an effective strategy.

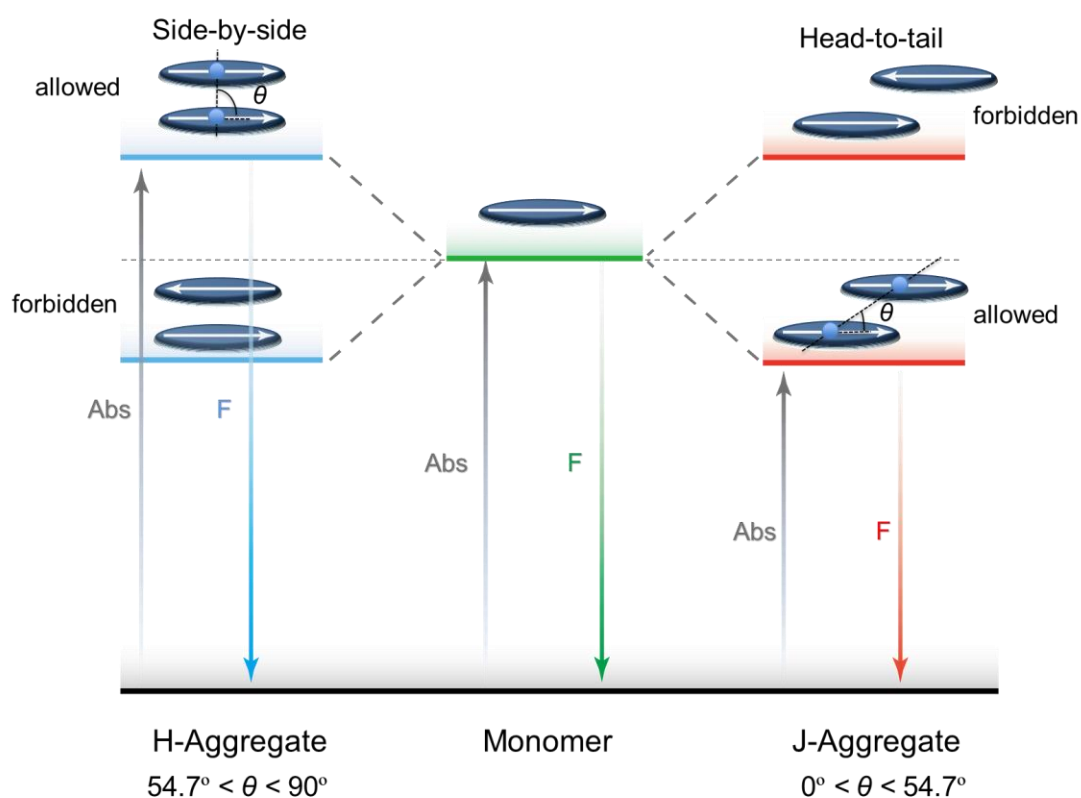


Figure 1.10. Excited states energy splitting diagram for molecular aggregates with J-aggregate, H-aggregate configurations.

1.2.7 Aggregation-induced TADF

In 2001, Tang and his colleagues introduced a novel mechanism to counteract ACQ.⁴² They demonstrated that molecules with flexible functional groups, which displayed weak emission in solution due to non-radiative decay from molecular movements (like rotations and vibrations), exhibited strong emission in a solid state where such movements were constrained. The aggregation of these emitters restricts these motions, reducing non-radiative decay, leading to enhanced emission in the aggregate – a direct contrast to ACQ. This observed effect is termed as AIE. In the subsequent years, this phenomenon has been integrated into TADF emitter design, paving the way for high-efficiency non-doped OLEDs and bypassing the technical hurdles and

constraints tied to hosts.

At the aggregate level, both fluorescence and phosphorescence can be modulated by reducing non-radiative decay and adjusting the ISC mechanism. Furthermore, harnessing both singlet and triplet excitons to produce delayed fluorescence can be accomplished by encouraging reversed intersystem crossing.⁴³ In addition, some aggregates with strong π - π interaction significantly enhance the excited-state energy splitting and substantially decreases the ΔE_{ST} , resulting in the red-shifted TADF emission by RISC. So, AIDF can be observed in the aggregate state owing to the suppressed non-radiation through limiting intramolecular motions, making ISC and RISC more competitive than nonradiative decay of S_1 .⁴⁴

1.3 Mechanism of Electroluminescence - OLEDs

Organic light-emitting diodes (OLEDs) are regarded as one of the most promising technologies for displays and lighting owing to their thinness, high contrast, flexibility, low energy consumption, light weight and fast response.⁴⁵⁻⁴⁹ OLEDs are a solid state technology that consist of a series of organic thin films sandwiched between two conductive electrodes: the anode and cathode.⁵⁰ In a working OLED, charge carriers are injected into the thin film under an external electric field, where the electrons from the cathode and holes from the anode are injected into the device, respectively. These injected charge carriers travel to the emissive layer to form a weakly bonding electron-hole pair (also called an exciton). This weakly bound electron-hole pair relax back to the ground state by giving off light. This technology has been commercialized and can be found in the latest smartphones and televisions, amongst other consumer electronic devices.^{51,52}

1.3.1 Structure and Operation of OLEDs

Most of the cases indium tin oxide (ITO) is selected as the transparent anode and some metals with low work function like aluminum (Al), silver (Ag) or magnesium and silver (Mg:Ag) alloys were employed as the cathode. A typical OLED device stack consists of a hole transport layer (HTL), an electron blocking layer (EBL), the emitting layer (EML), and an electron transport layer (ETL) or hole blocking layer (HBL) as shown in Figure **1.11a**. This

kind of multi-layer structure is designed to facilitate injection and transport of the charge carriers and to confine excitons within the EML.

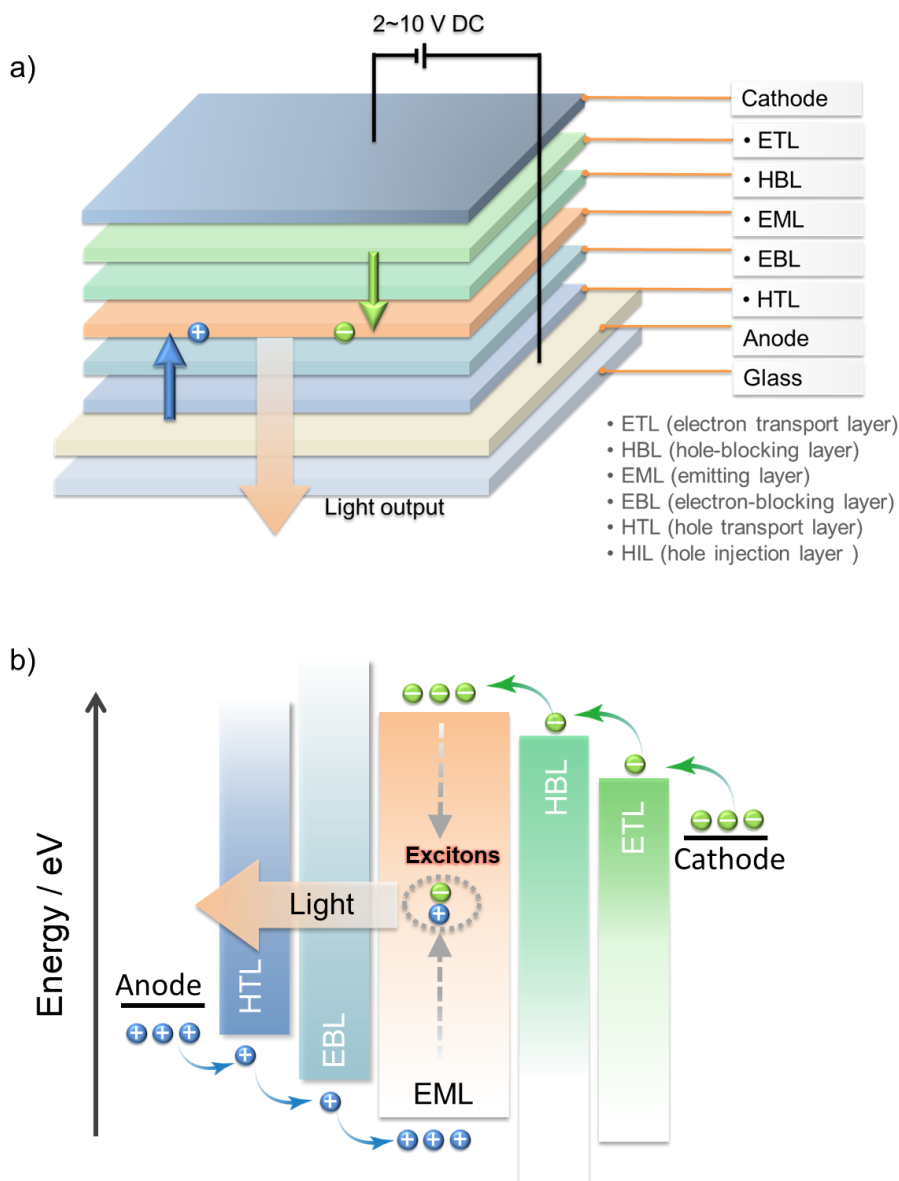


Figure 1.11. (a) OLED typical structure; (b) Energy-level diagram of a multilayer OLED; (c) Exciton generation in EML and the four spin states.

Figure 1.11b shows carrier flow in an operating OLED. Holes are injected into the highest occupied molecular orbital (HOMO) of the hole-transporting material and electrons are injected into the lowest unoccupied molecular orbital (LUMO) of the electron-transporting material from the anode and cathode, respectively. Holes and electrons are subsequently transported through HTL and ETL, respectively by a charge hopping electron transfer mechanism.⁵³ In OLEDs, the electrons do not move continuously as they would in a metal

conductor due to the discrete energy levels, but rather, they "hop" from one molecule to the next. As holes and electrons have different mobilities, electron- and hole-blocking layers (EBL and HBL) are used in OLEDs to control the charge balance such that the holes and electrons recombine within the EML to form excitons (Figure 11b). Subsequent light emission occurs as a result of radiative decay from the excited state to the ground state.

1.3.2 Singlet and Triplet Excited States in OLEDs

The Pauli exclusion principle states that no two electrons in an atom can have the same set of four identical quantum numbers (principal quantum number, n ; azimuthal quantum number, l ; magnetic quantum number, m_l ; spin quantum number, m_s).⁵⁴ So, two electrons can occupy the same orbital only if they have opposite spin states, which is known as spin pairing (Figure 1.12a). When an electron from a closed shell system is excited to a higher energy level in an atom or molecule, it can form either a singlet or a triplet state. In an excited singlet state, the promoted electron has an unpaired spin orientation that retains its original spin orientation in the ground state. In a triplet excited state, there is a change of the spin orientation of one of the electrons and the two highest energy electrons adopt the same spin (i.e., becomes parallel) (Figure 1.12a). The terms singlet and triplet are derived from the equation:

$$\text{Total spin} = 2S + 1 \quad (1-14)$$

Where S is the spin angular momentum of the multi-electron system. In quantum mechanics, the spin of an electron, is denoted as either spin up or spin down, and is represented by the spin quantum number m_s , which has a value of $+1/2$ or $-1/2$, respectively. For the singlet excited state, the spin-multiplicity value = $2(+1/2 - 1/2) + 1 = 1$; where for the triplet excited state, the spin-multiplicity value = $2(+1/2 + 1/2) + 1 = 3$.

As shown in Figure 1.12b, a vector model for electron spins is a way of visualizing the properties of electrons in terms of vectors in three-dimensional space. The magnitude of the intrinsic spin angular momentum S of an electron is:

$$S = \sqrt{m_s(m_s + 1)}\hbar \quad (1-15)$$

where \hbar is the reduced Planck constant. The spin projection quantum number m_s is associated with the z-components of spin.

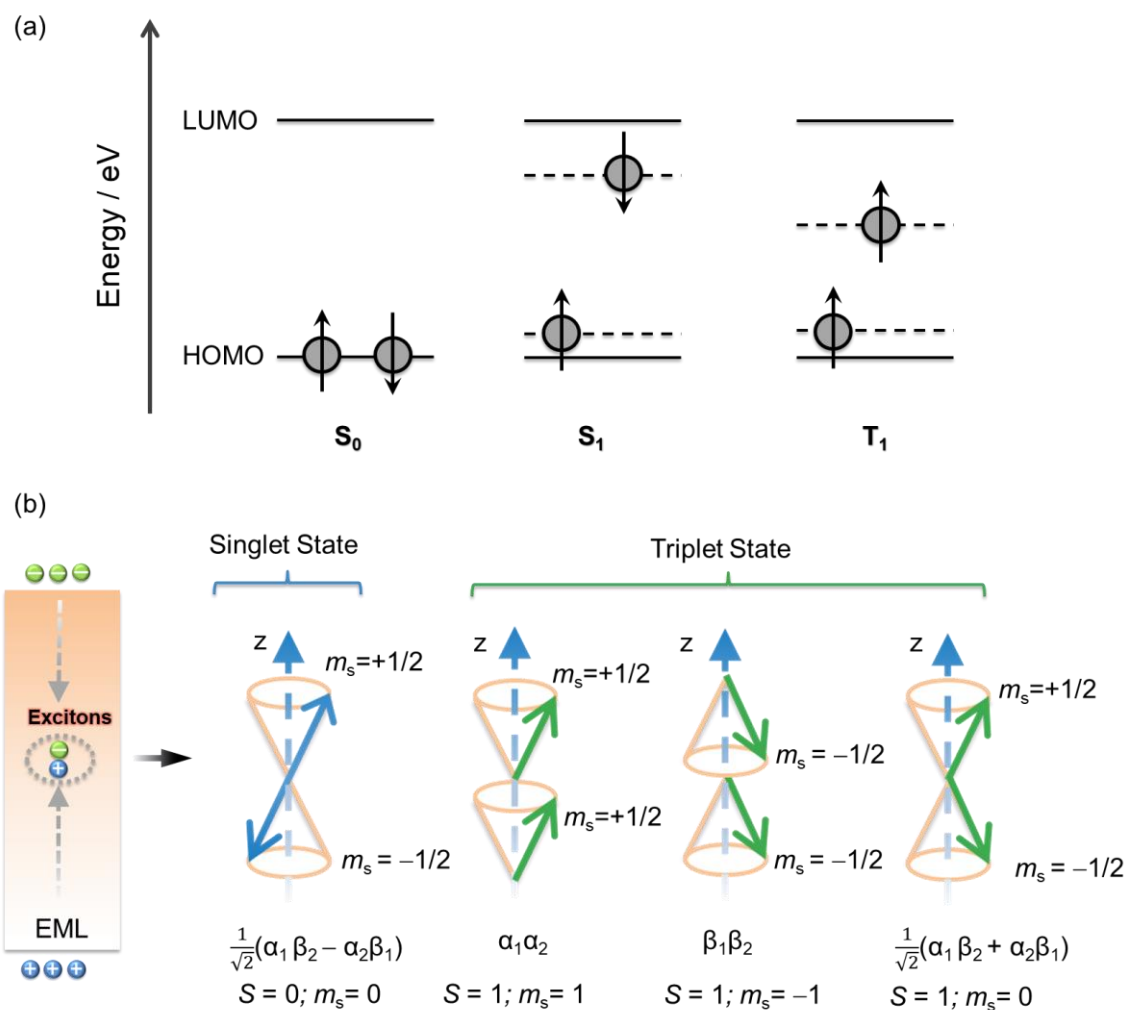


Figure 1.12. (a) Vectoral illustration of the relative orientation of the electron spins for singlet and triplet states for a two-electron system along with the corresponding spin wavefunctions; (b) Orbital configurations of ground state, singlet and triplet excited state (“+” stands for “spin up state” and “-” stands for “spin down state”).

There are two possible eigenstates, denoted by spin wavefunctions α and β with corresponding eigenvalues of $s=1/2; m_s=+1/2$ (spin up state); and $s=1/2; m_s=-1/2$ (spin down state), respectively. The spin wavefunctions of two electrons in a two-electron system can be combined to form four different eigenstates (Figure 1.12b). The spin wavefunction of $\frac{1}{\sqrt{2}}(\alpha_1\beta_2 - \alpha_2\beta_1)$ has a total spin angular momentum $S=0$ with a single value of z-component

($m_s = 0$), the corresponding quantum state is singlet state. The other three wavefunctions, $\alpha_1\alpha_2$, $\beta_1\beta_2$ and $\frac{1}{\sqrt{2}}(\alpha_1\beta_2 + \alpha_2\beta_1)$, possess a total spin $S = 1$, and different z-component ($m_s = +1, -1, 0$). Thus, the corresponding quantum state possesses three possible arrangements referred as a triplet state.⁵⁵ In OLEDs, the electrons and holes are completely uncorrelated before recombination, which means that the pairing of the two charge carrier spins (fermions with spin-half) to form a bosonic exciton is a statistical process.⁵⁴ Because the triplet states of organic molecules are threefold degenerate, there are three possible triplet states for each singlet state. As a result, the excitons formed in OLEDs exist in a ratio of 75% triplets to 25% singlets.

1.3.3 Parameters that Affect the Performance of an OLED Device

There are several important parameters to consider when evaluating the performance of an OLED device:

- Turn-on voltage (V_{on}): the turn-on voltage refers to the minimum external voltage required to achieve a specific brightness level, typically defined as 1 cd m^{-2} , in the OLED device. Generally, the V_{on} falls within the range of 2 to 4 V, which depends for instance on the emitting material, the device structure, and the thickness of layers. Achieving a low turn-on voltage is desirable, as it leads to lower power consumption and improved energy efficiency.
- Luminance: luminance (or brightness) is expressed in units of candela per square meter (cd m^{-2}) or nits. The brightness of the OLED device is dependent on the applied voltage. As the voltage increases, the brightness generally increases up to a certain point whereby efficiency may start to decrease due to exciton-exciton annihilation, an unbalance between electrons and holes that places the recombination zone near an interface promoting non-radiative exciton energy/electron transfer processes, or heat generation at high voltages.⁵¹ OLED devices can achieve a wide range of luminance levels, from tens nits (suitable for low-light environments) to several thousand nits [ideal for outdoor visibility and high-dynamic range (HDR) displays].⁵⁶ For example, a smartphone display may require a

luminance of around 500 to 1000 cd m⁻², while an HDR TV might require over 1000 cd m⁻² for optimal performance.^{56,57}

- Power efficiency (PE) and current Efficiency (CE): PE measures the amount of light output produced per unit of electrical power consumed by an OLED device. In lighting applications, it is usually expressed in lumens per watt (lm W⁻¹), while for display applications, it is often expressed in candelas per watt (cd W⁻¹). A higher power efficiency indicates that the OLED device is more effective at converting electrical energy into visible light, leading to lower energy consumption and potentially longer battery life for portable devices. CE measures the amount of light output produced per unit of electrical current flowing through an OLED device. It is expressed in candelas per ampere (cd A⁻¹). Higher CE indicates that the OLED device generates more light for the same amount of current, which implies better utilization of the electrical current supplied to the device. The relationship between PE and CE is as followed (V is voltage):

$$PE = \frac{\pi \cdot CE}{V} \quad (1-16)$$

- External quantum efficiency (EQE): EQE is a key performance parameter for OLEDs that quantifies how effectively the device converts electrical energy into light that is observed, which is defined as the ratio of the number of photons emitted by the OLED that escape the device and can be detected to the number of electrons injected. The relationship between CE and EQE can be described as the following equation.⁵⁸

$$EQE = \frac{CE \cdot 683 \text{ lm/W}}{q \cdot V} \quad (1-17)$$

Where q is the elementary charge (charge of an electron); the factor of 683 lm/W is the maximum luminous efficacy of monochromatic radiation at a wavelength of 555 nm, which is around the peak sensitivity of the human eye under bright lighting conditions; V is the operating voltage across the device, in volts.

Additionally, the EQE is also calculated using the following formula:

$$EQE = \gamma \cdot \eta_r \cdot \Phi_{PL} \cdot \eta_{out} \quad (1-18)$$

Where γ represents charge carrier injection efficiency, which represents the efficiency with which electrons and holes that are injected from the electrodes subsequently recombine in to generate an exciton. Ideally, equal numbers of electrons and holes are injected, and they all will eventually pair, so γ is usually taken to be 1. η_r is the radiative exciton fraction, which follows the quantum-mechanics spin selection rules as discussed in Section **1.4.2**. The formation of singlet and triplet excitons follows a statistical ratio of 1:3. The η_r of fluorescent materials is limited to 25%, 62.5% for the TTA emitters, while phosphorescent and TADF OLED materials can harvest both singlet and triplet excitons, leading to η_r of 100%. The internal quantum efficiency (IQE) is defined as

$$IQE = \gamma \cdot \eta_r \cdot \Phi_{PL} \quad (1-19)$$

The outcoupling efficiency (η_{out}) is calculated as the ratio of the number of photons that exit the OLED to the total number of photons generated within EML,⁵⁹ which is influenced by several factors, such as the thicknesses and refractive indices of the functional material layers as well as the direction of the photon generated during exciton relaxation.⁶⁰ The direction of the photon is contingent upon the orientation of the transition dipole moment of the emitters as the photons are predominantly emitted in a direction that's perpendicular to each emitter's transition dipole moment (TDM). The probability of this emission gradually diminishes as the angles converge towards the TDM's axis.⁶¹ In an OLED, the light generated by the radiative recombination of excitons can be trapped or lost due to several factors, like surface plasmons (~40%), waveguided modes (~10%) and substrate modes (~30%) as shown in Figure **1.13**. Surface plasmon polaritons (SPPs) are electromagnetic waves that propagate along the interface between a metal electrode and the organic layers.⁶² When the excitons recombine and generate light, some photons can couple with the free electrons in the metal layer, generating SPPs, which are trapped at the metal-organic layers interface and do not contribute to the emitted light. Waveguided modes are optical modes in which light is trapped within the layers of an OLED, which is a result of the refractive index differences between the organic layers, the transparent

electrode, and the surrounding materials. Substrate modes are also optical modes that are confined within the substrate of the OLED due to the refractive index differences between the substrate and air.

There are several strategies to improve the light outcoupling efficiency: 1) Introducing microstructures or nanostructures like micro lenses or scattering layers on the device surfaces can help disrupt total internal reflection and extract the trapped light. 2) Adjusting the thickness and refractive indices of the organic layers and transparent electrode can minimize waveguided mode losses and improve the outcoupling efficiency. 3) Controlling the orientation of the TDM of the emitter molecules in OLED devices is another approach to improve the light outcoupling efficiency.⁶¹ More specifically, compared to a random orientation (the outcoupling efficiency is around 20%), a horizontal orientation of the TDM can lead to an improvement in outcoupling efficiency by as much as 50%.⁶¹

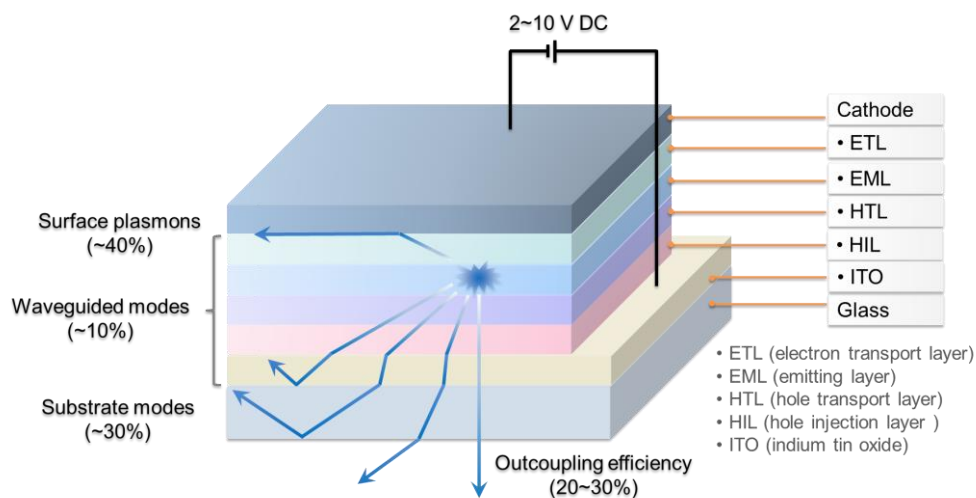


Figure 1.13. Illustration of the light extraction from OLEDs.

- Lifetime of OLEDs: The lifetime is defined as the time it takes for the brightness of the device to decrease to a specific percentage (95%, LT95 or 90%, LT90; or 50%, LT50) of its initial brightness (usually taken as 1000 cd/m² but this is not standardized and so other values like 500 cd/m² can be used). There are two types of methods to measure the lifetime: one is operating the OLED device continuously, the other is following a predefined on-off

cycling pattern. Both these methods need to maintain a constant operating conditions like voltage or current. However, it is not always practical to measure the complete lifetime of a device due to the long timescales involved. So, researchers often extrapolate the lifetime based on a mathematical model from shorter-term tests.⁶³

1.3.4 Exciton Harvesting in OLEDs

In 1987, CW Tang and S Van Slyke firstly reported a functional fluorescent OLED employing 4,4',4''-tri(N-carbazolyl)triphenylamine (TCTA) as HTL, tris(8-hydroxyquinolino)aluminum(III) (Alq3) as an emitter, which showed an EQE_{max} of ~1%.⁴⁵ As Alq3 emits only from the singlet excited state and is fluorescent, in this first-generation of OLEDs (Figure 1.14) radiative decay of triplet excitons is a spin-forbidden process, and there is no light contribution from triplet excitons.⁶⁴ So, the η_r of these fluorescent OLEDs is 0.25 and the maximum IQE (IQE_{max}) is limited to 25%. Assuming that outcoupling efficiency is 20%, the EQE_{max} of these first-generation OLEDs is capped at around 5%.

The second-generation OLEDs, called PhOLEDs, are capable of eclipsing this 5% EQE_{max} barrier by using phosphorescent emitters. First reported by Baldo *et al.*, in 1998,⁶⁵ due to the SOC mediated by a heavy metal ion (e.g., Pt(II), Ir(III)) in the compound, organometallic phosphorescent emitters can harvest both singlet and triplet excitons to generate light. As a result, PhOLEDs can achieve up to 100% IQE.⁶⁶

TTA OLEDs, sometimes called generation 2.5 devices, discussed in Section 1.2, exploit a bimolecular energy transfer process that takes place between two triplet excitons, resulting in the formation of a new singlet exciton at twice the energy of the triplets. In the TTA OLED, up to 75% of electrically excited triplet excitons will then undergo TTA, leading to half of them being upconverted to singlet excitons, leading to a maximum of 37.5% of radiative singlet excitons that originate from the TTA. So, the maximum IQE will be up to 62.5%, which is sum of 37.5% and the 25% of directly formed singlet excitons.

The third generation of OLEDs use TADF emitters, and has gained increasing attention since Adachi reported the first examples of efficient TADF OLED with EQE_{max} of 19.3% (for the green devices) in 2012.¹² TADF OLEDs can achieve 100% IQE through the up-conversion

of triplet excitons to singlets via thermally activated RISC. Along with phosphorescence, TADF is considered to be one of the most promising approaches to efficiently harvest triplet excitons in OLEDs.

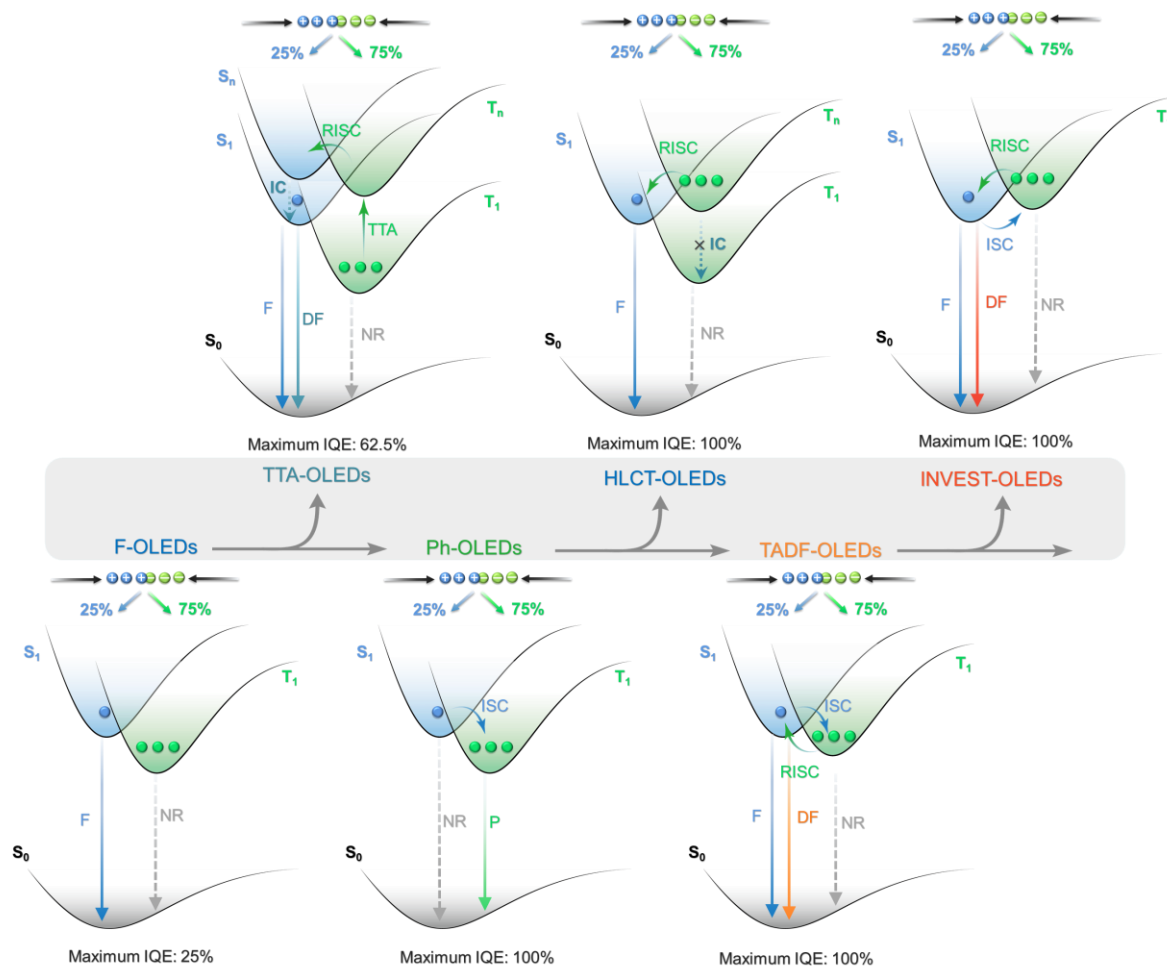


Figure 1.14 Mechanism and evolution of exciton formation and light generation in different classes of OLEDs.

Hybridized local and intramolecular charge transfer (HLCT) OLEDs are known as ‘hot exciton’ OLEDs, which involves the conversion of higher energy triplet states ($T_{n>1}$) into singlets via RISC, followed by radiative decay from the singlet excited states.^{67–69} Despite an IQE_{max} of up to 100%, such a RISC process from T_n must compete with typically rapid internal conversion to T_1 , and the device must also efficiently produce the higher-energy T_n triplet excitons. The mechanism behind the RISC processes in HLCT type emitters are still not clearly understood as it is difficult to directly detect these higher-level triplet excited states.

Materials that emit with an inverted singlet-triplet gap (INVEST) mechanism have

recently garnered much excitement in the organic semiconductor community. Initial frameworks for INVEST materials design have been proposed through computational studies,^{70,71} and the first report of an INVEST OLED has recently been published.⁷² The INVEST mechanism involves a fundamental violation of Hund's rule, where the S_1 state is lower in energy than the T_1 state, rendering RISC a formally exothermic process that should thus be accelerated.

1.4 The Development of TADF and its Applications

1.4.1 The Mechanism of TADF

As mentioned in Sections 1.1 and 1.3.4, TADF involves the upconversion of triplet excitons to singlet excitons via a RISC process, which can be evidenced by a biexponential decay profile, prompt fluorescence (with lifetime of ns) and delayed fluorescence (with lifetime typically of μ s) in the transient PL (Figure 1.6c). As shown in Figure 1.15a, in the photoexcitation process, singlet excited states are first populated, which relax to S_1 by rapid IC and VR processes. There are generally two productive different processes for the S_1 excitons, which can either decay radiatively to the ground state as prompt fluorescence or undergo ISC to form T_1 or T_n triplet excitons. A small energy difference between S_1 and T_1 (ΔE_{ST}) facilitates thermal up-conversion of the formed triplet excitons back to the singlet state, and if the rate of RISC is relative high compared to that of ISC, which allows for multiple cycles of ISC and RISC, radiative decay from S_1 as delayed fluorescence can occur.^{73,74} The delayed fluorescence spectrum overlaps with the prompt fluorescence spectrum as emission is from the same singlet excited state, but with longer lifetime, τ_d , of $10^{-8} - 10^{-2}$ s. In the electrical excitation process in the OLED (Figure 1.15b), singlet and triplet excitons are formed in a ratio of 1:3 as discussed in Section 1.4.2. The EL originates from singlet excited states, which are populated from singlet excitons and RISC acting on triplet excitons. A fast rate constant for RISC (k_{RISC}) is desirable for the efficient thermal up-conversion of triplet excitons to singlet excitons, enabling efficient harvesting of both singlet and triplet excitons for light emission.

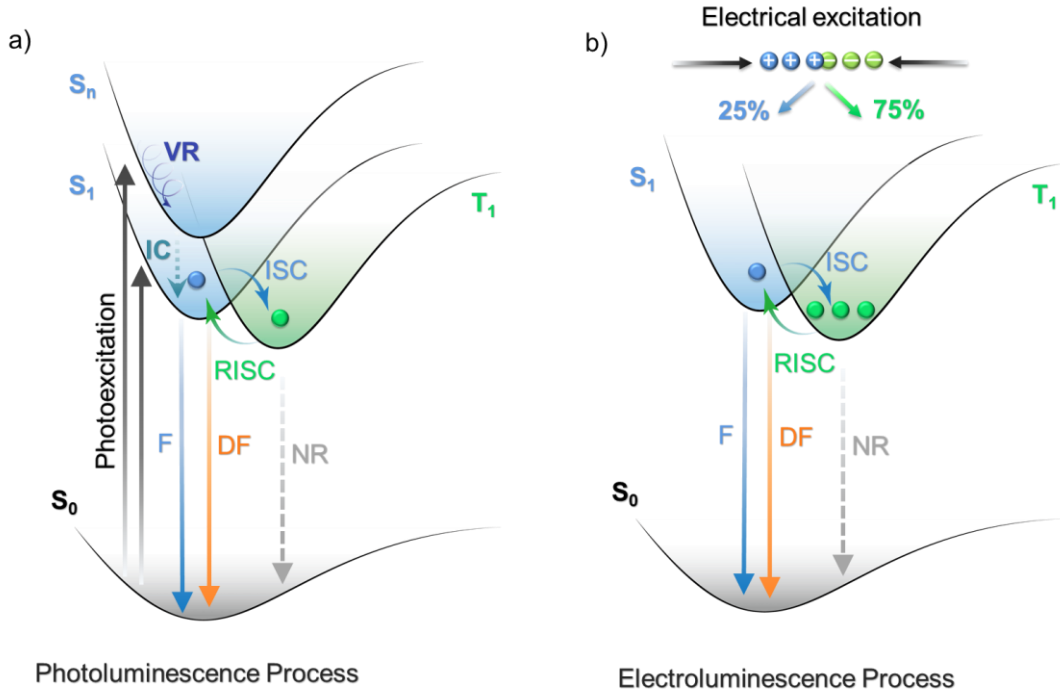


Figure 1.15. TADF mechanism from (a) photoluminescence and (b) electroluminescence pathways.

Using the first-order perturbation theory, specifically Fermi's golden rule formulation, k_{RISC} can be expressed as follows:

$$k_{RISC} = \frac{2\pi}{\hbar} |\langle T_n | \hat{H}_{SO} | S_n \rangle|^2 \times \rho_{FCWD} \quad (1-20)$$

Where: $|\langle T_n | \hat{H}_{SO} | S_n \rangle|$ is the matrix element of the SOC Hamiltonian between the any triplet state (T_n) and any singlet state (S_n) states, representing the probability amplitude for the transition between these states due to SOC. ρ_{FCWD} is the Franck-Condon-weighted density of states, which can be expressed as:⁷⁵

$$\rho_{FCWD} = \frac{1}{\sqrt{4\pi\lambda k_B T}} \exp\left(-\frac{(\Delta E_{ST} + \lambda)^2}{4\lambda k_B T}\right) \quad (1-21)$$

where λ is the Marcus reorganization energy associated with the intermolecular and intramolecular low-frequency vibrations; k_B is Boltzmann's constant; and T is temperature.

According to equations (1-20) and (1-21), k_{RISC} is proportional to $|\langle T_n | \hat{H}_{SO} | S_n \rangle|^2 \times \exp(-(\Delta E_{ST})^2)$:

$$k_{RISC} \propto |\langle T_n | \hat{H}_{SO} | S_n \rangle|^2 \times \exp(-(\Delta E_{ST})^2) \quad (1-22)$$

So, both a large SOC and a small ΔE_{ST} are critical for an efficient k_{RISC} . The ΔE_{ST} is related to the orbital energy (E), Coulomb repulsion energy (K), and electron exchange energy (J) of the molecular system. When an electron is excited from the highest occupied molecular orbital (HOMO) to the lowest unoccupied molecular orbital (LUMO), the energy levels of lowest singlet (E_S) and triplet (E_T) excited states can be expressed as:

$$E_S = E(\text{LUMO}) - E(\text{HOMO}) + K + J \quad (1-23)$$

$$E_T = E(\text{LUMO}) - E(\text{HOMO}) + K - J \quad (1-24)$$

In the excited state, both unpaired electrons possess the same charge, leading to positive values for the K and increasing the energy of both the E_S and E_T compared to the ground state. ΔE_{ST} is equal to twice that of J .

$$\Delta E_{ST} = E_S - E_T = 2J \quad (1-25)$$

The exchange energy (J) depends on the spatial overlap of the orbitals involved in the transition from the emissive excited state, where the distribution can be approximated to the LUMO and HOMO, respectively:

$$J = \frac{e^2}{4\pi\epsilon_0} \iint \phi_{\text{HOMO}}^*(r_1) \phi_{\text{LUMO}}^*(r_2) \left(\frac{1}{r_1 - r_2} \right) \phi_{\text{HOMO}}(r_2) \phi_{\text{LUMO}}(r_1) dr_1 dr_2 \quad (1-26)$$

where, $\phi_{\text{HOMO}}^*(r_1)$ and $\phi_{\text{LUMO}}(r_1)$ represent the wavefunctions of the HOMO and LUMO orbitals for electron 1 at position r_1 , respectively. Likewise, $\phi_{\text{LUMO}}^*(r_2)$ and $\phi_{\text{HOMO}}(r_2)$ represent the wavefunctions of the HOMO and LUMO orbitals for electron 2 at position r_2 , respectively. e is the electronic charge, ϵ_0 is the vacuum permittivity, and r_1 and r_2 are the positions of electron 1 and electron 2, respectively. Based on equation 1-26, one

straightforward strategy to reduce J is to minimize the overlap of the electron density in the HOMO and LUMO. So, a small ΔE_{ST} can be realized by separating the HOMO and LUMO of the TADF emitters using donor and acceptor moieties that are poorly electronically coupled, which can occur when there is only a small degree of conjugation such as when there are large dihedral angles between the two fragments, inducing a charge transfer character in the S_1 and T_1 excited states.

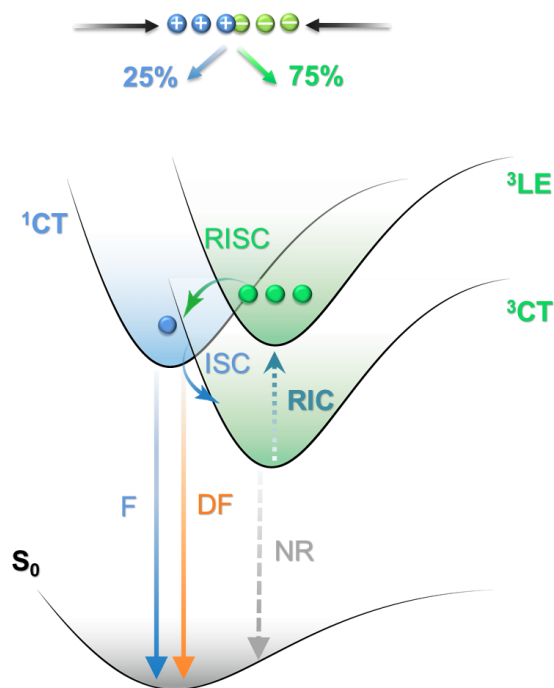


Figure 1.16. Perrin–Jablonski diagram of TADF via an intermediate 3LE triplet state.

According to Equation 1-20, there's a general trend observed where a smaller ΔE_{ST} leads to a faster k_{RISC} , but the relationship is not always straightforward or linear.⁷⁶ So, the efficiency of TADF cannot be only accounted by the first-order mixing of states. In other words, RISC doesn't always transition directly from T_1 to S_1 , especially when this transition is not allowed by symmetry according to *EI-Sayed's* rule.^{77,78} But it also involves other excited states made accessible through spin-vibronic coupling. According to *EI-Sayed's* rule, there is no spin-orbit coupling between singlet and triplet states of the same configuration. Thus, the k_{ISC} of $S_1(n, \pi^*) \rightarrow T_1(n, \pi^*)$ or $S_1(\pi, \pi^*) \rightarrow T_2(n, \pi^*) \rightarrow T_1(\pi, \pi^*)$ should be much faster than that of $S_1(n, \pi^*) \rightarrow T_1(n, \pi^*)$.⁷⁹ As shown in Figure 1.16, up-conversion from the 3CT (T_1) to the 1CT (S_1) can occur through intermediary, higher-energy triplet states (3LE), due to strong vibrational coupling between 3CT and 3LE which also described as reverse internal conversion (RIC). Then,

second order coupling occurs between the ^3CT and the ^1CT , employing the ^3LE as an intermediate state. The high efficiency of second-order coupling stems from the rapid spin-vibronic interaction between the ^3CT and ^3LE , along with effective SOC between the ^3LE and ^1CT .^{79,80}

1.4.2 The History of TADF and its Applications

Dating back to 1929, microsecond-to-millisecond TADF was already observed in Eosin Y (Figure 1.17), but it was called as “fluorescence with long duration” or room-temperature phosphorescence (RTP).¹¹ In 1961, this photophysical phenomenon in Eosin Y in solution was demonstrated as TADF, which is why TADF is also called as E-type delayed fluorescence in early publications.⁸¹ Until 1970s and 1980s, researchers explored the cause of the delayed emission in benzophenone and thiones which were identified as TADF.^{82,83} In 1980s, McMillin and Crosby also observed TADF in Cu(I) complexes.⁸⁴ In 2009, the first reported example of a TADF emitter (tin(IV) porphyrin-based complex) used in OLEDs was introduced. However, these devices exhibited a low efficiency.⁸⁵ Until 2010, the TADF copper(I) complex, **{Cu(PNP-*t*Bu)}**, based OLED exhibit high EQE_{max} of 16.1%, which is the first example of a TADF OLED showing an EQE_{max} far surpassing the 5% fluorescence limit.⁸⁶ In 2011, Adachi and co-workers developed the first all-organic TADF OLEDs, featuring the D-A emitter **PIC-TRZ**; however, the device EQE_{max} was low at 5.3%.⁸⁷ One year later, the same group succeeded in synthesizing a series of TADF emitters derived from carbazoyl dicyanobenzenes, representing a significant breakthrough in the development of TADF OLED emitters. The OLED based on **4CzIPN** showed an outstanding EQE_{max} of 19.3%, which demonstrated the pure organic TADF would be the next generation emitter for OLEDs.⁸⁸ Following that breakthrough, There have now been thousands of reported TADF materials, all of which are based on a twisted D-A structure.

Other hallmarks in TADF emitter development include that in 2014, Wang *et al.* reported the first AIE TADF OLEDs using **TXO-PhCz** with an EQE_{max} over 21%.⁸⁹ In 2016, Lin *et al.* designed a family of spiroacridine-triazine based TADF molecules whose EQE_{max} of the OLEDs was over 35%.⁹⁰ Chen *et al.* realized a champion EQE_{max} of 39.1% by using an

extended linear D–A–D structure molecule, where the orientation of TDM was manipulated by controlling the molecular orientation and a high horizontal dipole ratio of 92% was achieved.⁹¹ Beyond organic twisted D-A systems TADF,^{13,16} researchers extended the types of TADF, like MR-TADF (like **BNSeSe** in Figure 1.17) that show narrowband emission,^{92,93} through-space charge transfer (TSCT) TADF (**TpAT-tFFO**),^{94,95} excited-state intramolecular proton transfer (ESIPT) TADF (**TQB-TA**),^{96,97} circularly polarized luminescence (CPL) TADF (**DPHN**),^{98,99} TADF polymers¹⁰⁰ and dendrimers (**tBuCz2m2pTRZ**),^{101,102} and other types of TADF materials. There are also several applications of TADF emitters beyond their use as emitters in OLEDs. TADF compounds also can be employed in, for instance, bioimaging,¹⁰³ sensors,¹⁰⁴ photocatalysis,¹⁰⁵ solar cells,¹⁰⁶ photodynamic therapy^{107,108} and lasers.^{109,110}

In this thesis, I will focus on red-emissive D-A TADF and employ them as emitters in OLEDs, as sensors and as bioimaging reagents.

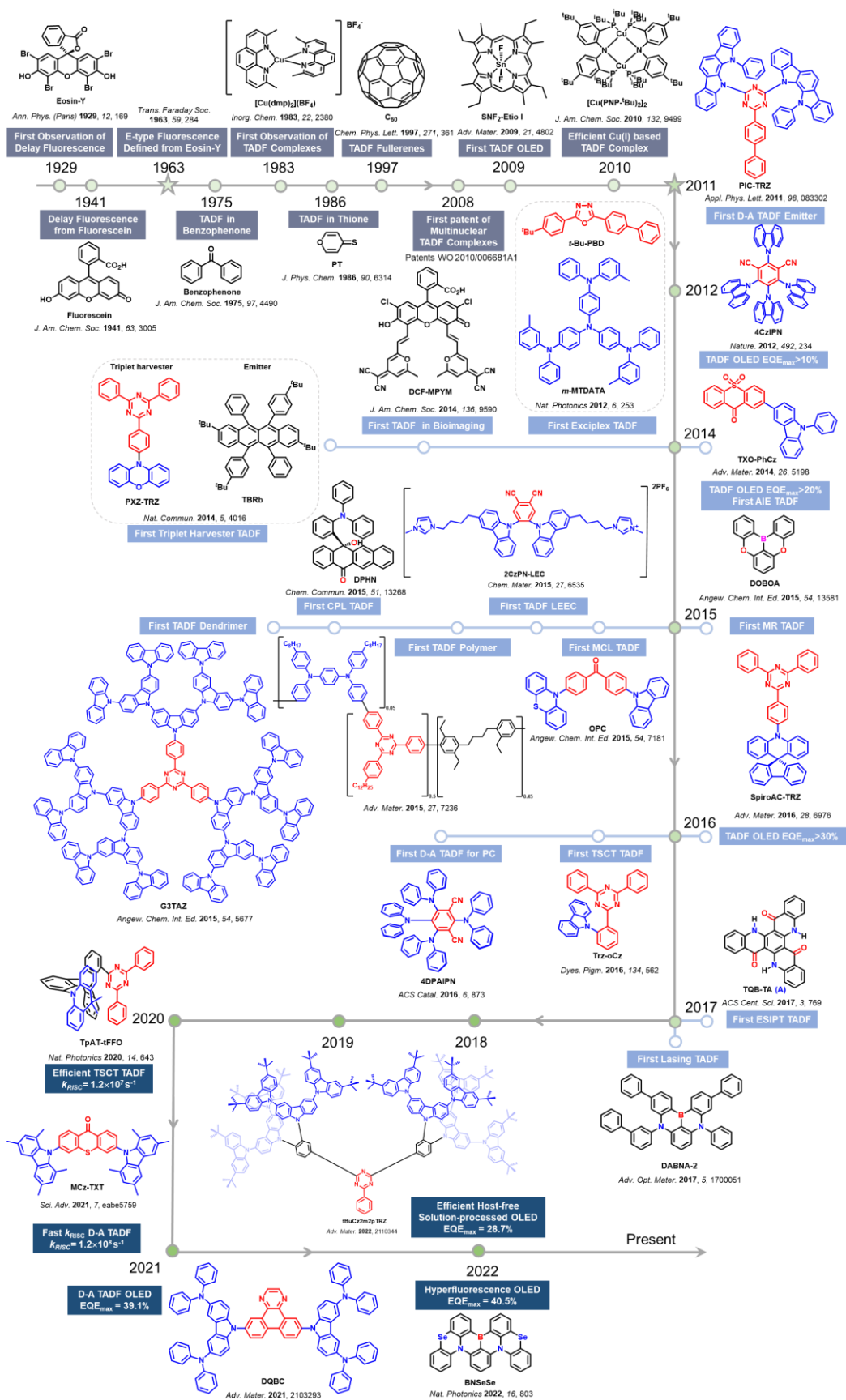


Figure 1.17. Overview of milestones TADF active materials.

1.5 The Development of Red TADF Emitters for OLEDs

Red emitters represent an underdeveloped area of TADF research owing to fundamental difficulties in engineering high Φ_{PL} in the red color region. This is primarily a consequence of the energy gap law, which states that as the ΔE_{g} decreases between the excited and ground states, the density of vibronic states in both the ground and excited states will increase.¹¹¹ Such an increased density of states (and smaller energy gaps between the S_1 and S_0 sublevels) leads to increased internal conversion rates for S_1 to S_0 , and accelerated overall non-radiative decay. As well, the rate of radiative decay is proportional to the cube of the frequency of the transition, therefore a decreased S_1 - S_0 energy gap leads to a decrease in k_r . Thus, the inherent photophysics of small bandgap emitters make it fundamentally more difficult to engineer high Φ_{PL} in materials that emit at longer wavelengths and is particularly challenging for deep red and NIR emitting materials. Additionally, the low-energy S_1 states that are associated with red emission typically require significantly expanded π -conjugation systems, making π - π stacking interactions more likely and resulting in significant ACQ for red emitters. As a result, the design of efficient red TADF materials (and red emitters in general) has not progressed as rapidly as that of blue and green counterparts.^{112–116}

For the general molecular design principles, red TADF emitters typically incorporate strong electron D and A linked in a strongly twisted D-A geometry. This choice of molecular fragments affords a shallow HOMO for D and a deep LUMO for A, which together induces a narrow bandgap and therefore a low ^1CT emission energy.¹¹⁷ Examples of chemical structures used as acceptors along with their acceptor strength (informed by experimental inferred LUMO energies) and the extent of π -conjugation are shown in Figure **1.18a**. To help suppress non-radiative decay pathways, rigid and/or planar fused donors or acceptors are favored, resulting in simultaneously higher EQE and a narrowing of the emission spectrum. Some of representative donors are shown in Figure **1.18b**. This can in turn increase the λ_{PL} of these emitters and ultimately the device EQE_{max} , reaching above 30% for vacuum-deposited OLEDs despite intrinsic challenges for this color.¹¹⁸ However, increased the planarity of the emitter increases the likelihood of $\pi - \pi$ stacking, worsening aggregation and potentially leading to increased ACQ. Therefore, rationally controlling molecular packing with appropriate intra- and

inter-molecular interactions is important for the control of TADF-activity, λ_{PL} , and effective carrier transport.^{112,116}

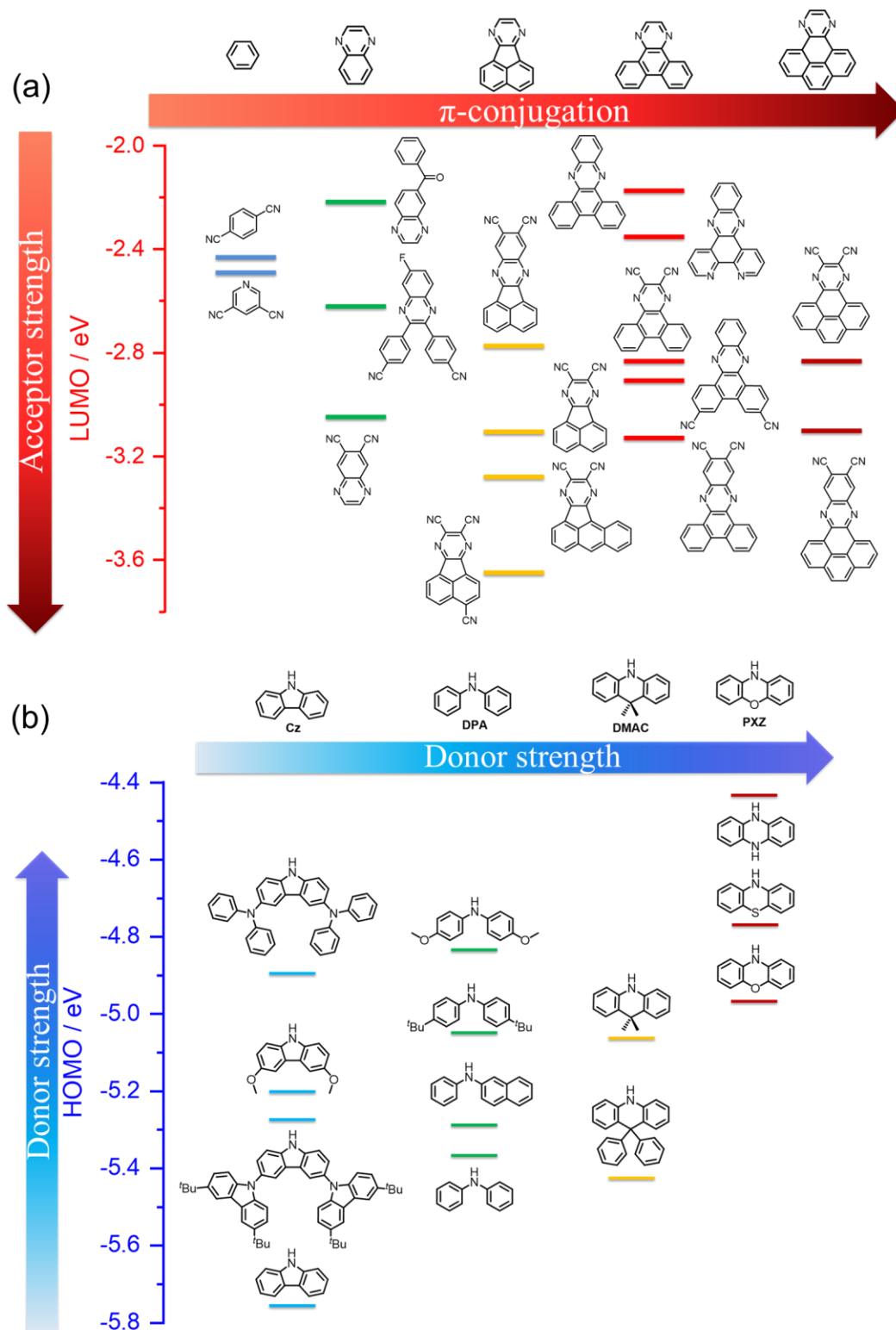


Figure 1.18. Acceptors and donors used to design red TADF emitters according to the acceptor π conjugation, acceptor, and donor strength.

In this section, I will review five types of TADF red emitters, differing according to the magnitude of the π conjugation in the acceptor, mainly focusing on N-doped polycyclic aromatic hydrocarbons (PAH) as acceptors. For the purpose of this section, we consider only those red/NIR emitters where the device emits at $\lambda_{\text{EL}} > 580$ nm and/or has an EQE_{max} greater than 9%.

1.5.1 Pyridine-3,5-dicarbonitrile Acceptors

The first red TADF emitter, 1,4-dicyano-2,3,5,6-tetrakis(3,6-diphenylcarbazol-9-yl)benzene (**4CzTPN-Ph**), was reported by Adachi and co-workers group in 2012.⁸⁸ Composed of a strongly electron-deficient terphthalonitrile acceptor unit and four carbazole derivative donors, **4CzTPN-Ph** has a small τ_{d} of 1.1 μs and a Φ_{PL} of 26.3% in toluene, emitting at $\lambda_{\text{PL}} = 577$ nm. The device showed an EQE_{max} of 11.2% at electroluminescence peaking ($\lambda_{\text{EL}} \approx 580$ nm, corresponding to CIE coordinates of (0.52, 0.45) and efficiency roll-off of $\sim 20\%$ at 100 cd m^{-2} and $\sim 70\%$ at 1000 cd m^{-2} . Chen *et al.* reported three emitters **PXZ-PCN**, **bis-PXZ-PCN**, and **tri-PXZ-PCN** (Figure 1.19) that contain one to three PXZ donors with a pyridine-3,5-dicarbonitrile (PCN) acceptor.¹¹⁹ The emission of **bis-** and **tri-PXZ-PCN** peaks narrowly between λ_{PL} of 601 and 606 nm in 10 wt% doped films in CBP while **PXZ-PCN** emits at 565 nm. **Bis-PXZ-PCN**, and **tri-PXZ-PCN** have low Φ_{PL} of 36 and 34%, respectively, yet short τ_{d} of 1.40 and 1.48 μs and fast k_{RISC} of 9.8 and $8.8 \times 10^5 \text{ s}^{-1}$, respectively. Whilst the devices with **bis-PXZ-PCN**, and **tri-PXZ-PCN** showed EQE_{max} of only 9.8 ($\lambda_{\text{EL}} = 600$ nm) and 9.7% ($\lambda_{\text{EL}} = 608$ nm), respectively, their EQE_{1000} remained at 8.3 and 8.0%, representing a low efficiency roll-off.

Liu *et al.* subsequently reported two red-emitters, **NP** and **TP** (Figure 1.19), with the same PCN acceptor substituted with either naphthyl or thienyl donor groups.¹²⁰ **NP** and **TP** emit at 622 and 619 nm in toluene, though emit at 560 and 555 nm, respectively, in 10 wt% doped films in CBP. They have Φ_{PL} of 50 and 40% and ΔE_{ST} of 0.14 and 0.15 eV, and very short τ_{d} of 0.65 and 0.80 μs , in 10 wt% doped films in CBP, respectively. The devices with **TP** showed an EQE_{max} of 12.4% at λ_{EL} at 591 nm and with **NP** showed an EQE_{max} of 17.1% at λ_{EL} at 590 nm.

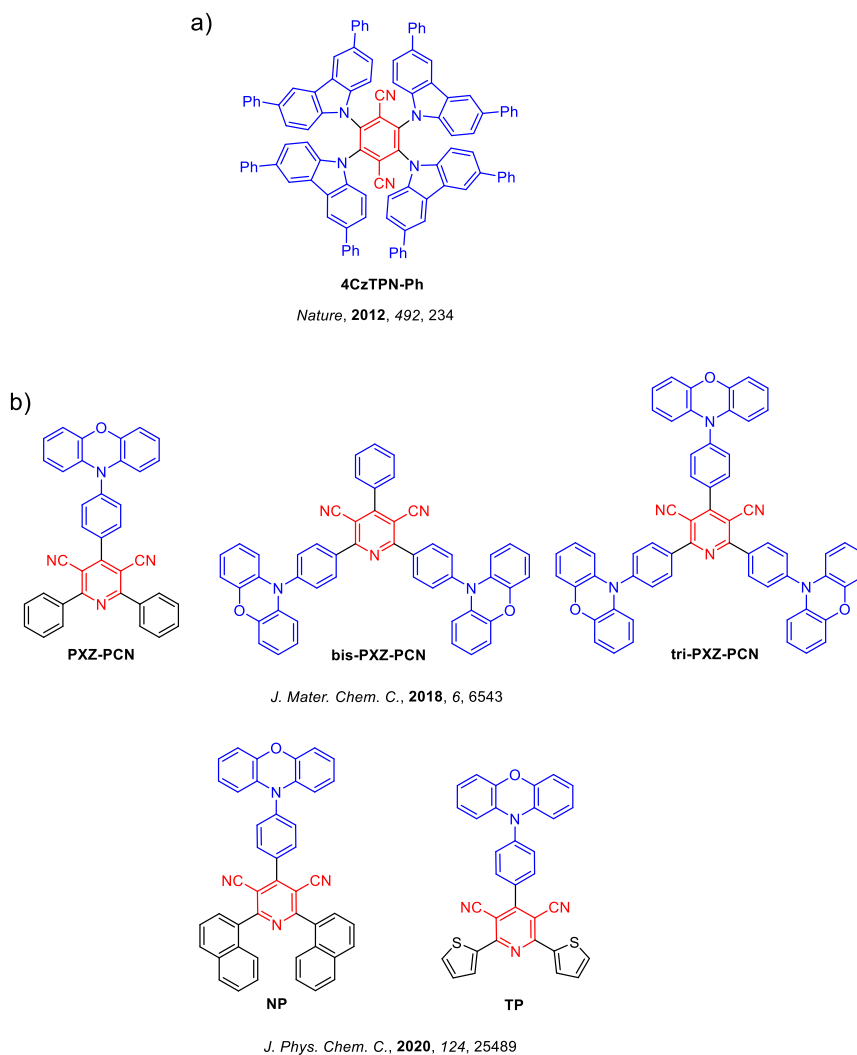


Figure 1.19. Molecular structures and corresponding CIE coordinates of red TADF emitters using a) terephthalonitrile and b) pyridine-3,5-dicarbonitrile as acceptor.

1.5.2 Quinoxaline Acceptor

Quinoxalines are another strong electron-acceptor that has been used in red TADF emitter design. Li *et al.* reported an asymmetric D-A emitter, **TPA-QCN** (Figure 1.20).¹²¹ Varying the concentration in doped **TPA-QCN**: TPBi films from 15 to 30 wt% shifted the λ_{PL} from 649 to 700 nm (with the neat film emitting at $\lambda_{\text{PL}} = 733$ nm). Their Φ_{PL} remained at a higher level (47–70%) although dropped considerably in the neat film ($\Phi_{\text{PL}} = 21\%$). **TPA-QCN** has a rather large ΔE_{ST} of 0.23 eV in toluene at 77 K and a long τ_{d} of 943 μs . The OLEDs showed an EQE_{max} of 14.5% at 644 nm (15 wt% doped in TPBi); however, this was accompanied by a large efficiency roll-off of $\sim 72\%$ at 100 cd m^{-2} . A much lower EQE_{max} of 3.9% was obtained for the

non-doped NIR device ($\lambda_{\text{EL}} = 728 \text{ nm}$).

Using a bis-cyano substituted quinoxaline unit as the acceptor substituted with two DMAC donors Kothavale *et al* reported the emitters **5,8-DCQx-Ac** and **6,7-DCQx-Ac**.¹²² Compound **5,8-DCQx-Ac** displayed a much deeper LUMO, leading to a red-shift in emission from 620 nm (**6,7-DCQx-Ac**) to 663 nm (**5,8-DCQx-Ac**) in toluene. **5,8-DCQx-Ac** has a moderate Φ_{PL} of 72%, a ΔE_{ST} of 0.11 eV and short τ_{d} of 3.12 μs . The OLEDs with this emitter doped in the bipolar host (1 wt% mCP-PFP) showed an EQE_{max} of 16.4% at λ_{EL} of 602 nm and CIE coordinates of (0.55, 0.44). Despite the **6,7-DCQx-Ac** device showing an EQE_{max} of 21.1%, the λ_{EL} was 578 nm. In a subsequent paper by the same group, analogue emitters **6,7-DCQx-DICz** and **5,8-DCQx-DICz** (Figure 1.20) were reported, with a diindolocarbazole donor in lieu of an acridan.¹²³ Changing the position of the two cyano groups from the *ortho* to the *meta* positions with respect to the pyrazine ring resulted in a significant increase in Φ_{PL} from 40 (**5,8-DCQx-DICz**) to 73% (**6,7-DCNQx-DICz**). However, this improvement is accompanied by a blue-shift of almost 50 nm in the emission λ_{PL} from 651 (**5,8-DCQx-DICz**) to 603 nm (**6,7-DCQx-DICz**). The device with **6,7-DCQx-DICz** (1 wt% doped in PBICT) showed a higher EQE_{max} of 23.9% at λ_{EL} of 578 nm than the device with **6,7-DCQx-Ac** at 21.1% at λ_{EL} of 578 nm. The **5,8-DCQx-DICz** device, on the other hand, showed an EQE_{max} of 12.5% at λ_{EL} of 603 nm. Analogous to **5,8-DCQx-Ac** and **6,7-DCQx-Ac**, **5,8-DCQx-DICz** has a redder emission than **6,7-DCQx-DICz**, where the cyano groups are *ortho* to the pyrazine ring.

The strong donor, phenoxazine, was combined with similar acceptors 6-(trifluoromethyl)quinoxaline or 6-(cyano)quinoxaline to form compounds **TFM-QP** and **CN-QP** (Figure 1.20).¹²⁴ **TFM-QP** and **CN-QP** emit at λ_{PL} of 613 and 611 nm in toluene solutions and have Φ_{PL} of 61% in both cases in 5 wt% doped films in CBP. The compounds showed delayed fluorescence with rather long τ_{d} of 5.0 ms (**TFM-QP**) and 1.6 ms (**CN-QP**) despite their small ΔE_{ST} of 0.04 and 0.03 eV, all respectively. The yellow OLEDs fabricated with **TFM-QP** and **CN-QP** exhibited EQE_{max} of 14.1 and 9.7%, both with λ_{EL} of 584 nm, illustrating that the red emission achieved in solution measurements is not always straightforward to translate into devices.

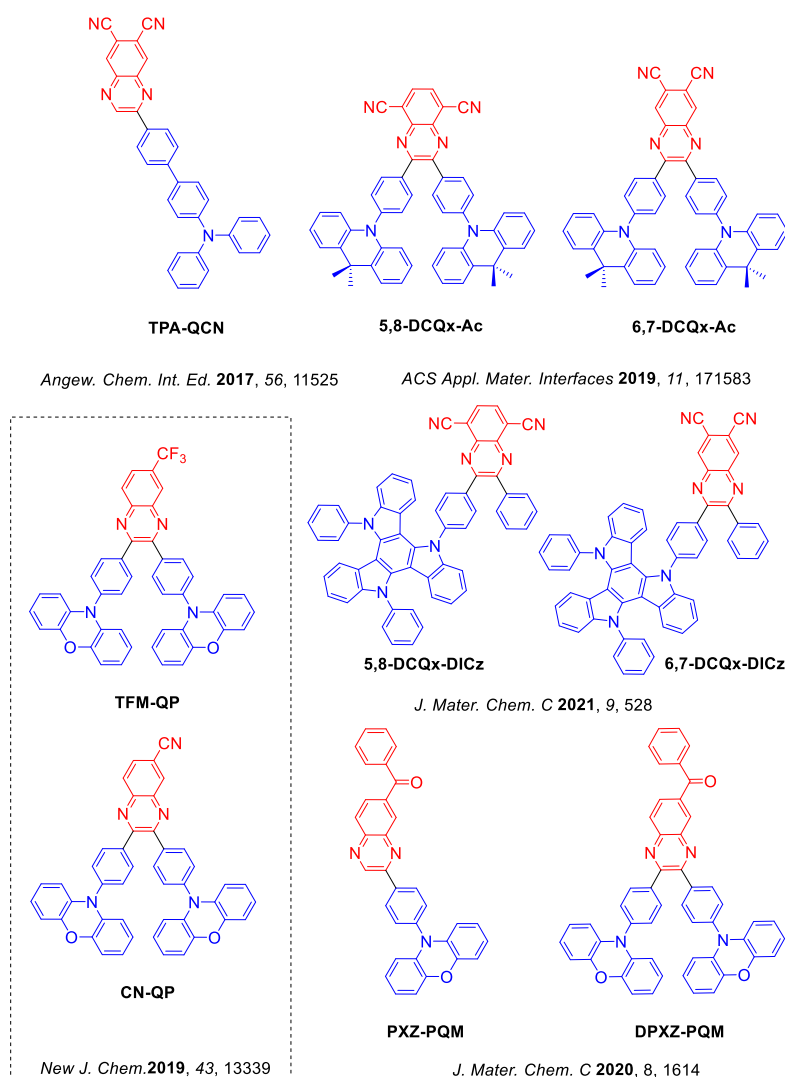


Figure 1.20. Molecular structure of red TADF emitters featuring quinoxaline acceptors.

PXZ-PQM and **DPXZ-PQM** (Figure 1.20) combine benzoyl and quinoxaline units with differing numbers of donor units from one (**PXZ-PQM**) to two (**DPXZ-PQM**).¹²⁵ The PL spectra of **PXZ-PQM** (ΔE_{ST} of 0.03 eV) and **DPXZ-PQM** (ΔE_{ST} of 0.02 eV) in 5 wt% doped films in DCzDPy gave broad orange-to-red emission at λ_{PL} of 588 and 586 nm, demonstrating little impact of the number of donor groups in this case. The device with **DPXZ-PQM** exhibited the best EL performance with an EQE_{max} of 26.0%, displaying orange-red emission at λ_{EL} of 590 nm, corresponding to CIE coordinates of (0.51, 0.48). This performance was attributed to the high Φ_{PL} (88%), relatively small ΔE_{ST} (0.02 eV) and fast RISC rate ($k_{RISC} = 2.05 \times 10^5 \text{ s}^{-1}$). The OLED with **PXZ-PQM** showed a somewhat lower EQE_{max} of 20.4% attributed to the Φ_{PL} of 70% of the emitter. The efficiency roll-off at 100 and 1000 cd m^{-2} were 14 and 45% for the **PXZ-PQM**-based device and, 23 and 47% for the **DPXZ-PQM**-based device, respectively.

1.5.3 Acenaphtho[1,2-b]pyrazine Acceptors

Acenaphtho[1,2-b]pyrazine-8,9-dicarbonitrile (**APDC**), a stronger acceptor than quinoxaline, was used in conjunction with two TPA donors to produce the deep-red emitter **APDC-DTPA** (Figure 1.21).¹²⁶ Doped at 10 wt% in TPBi, **APDC-DTPA** emits at λ_{PL} of 687 nm and has a Φ_{PL} of 63% and a ΔE_{ST} of 0.14 eV. As neat films the emission is red-shifted to $\lambda_{\text{PL}} = 756$ nm, which was accompanied by a drop in Φ_{PL} to 17% due to ACQ. The OLEDs with **APDC-DTPA** showed an EQE_{max} of 10.2% at λ_{EL} of 693 nm. Non-doped OLEDs produced NIR λ_{EL} of 777 nm although with a lower EQE_{max} of 2.2%. While both devices represent some of the deepest red TADF OLEDs reported to date, they also suffer from severe efficiency roll-off; the EQE_{100} for the doped device being $\sim 0.8\%$, while the non-doped device did not reach this level of luminance. This low efficiency was attributed to triplet-triplet or singlet-triplet annihilation arising from the relatively long triplet lifetime, along with low Φ_{PL} in the solid state..^{127,128}

Xue *et al.* reported two D-A type TADF emitters (**TPAAP** and **TPAAQ**, Figure 1.21), containing the strong electron-drawing acceptors acenaphtho[1,2-b]pyrazine-8,9-dicarbonitrile (AP) and acenaphtho[1,2-b]quinoxaline-8,9-dicarbonitrile (AQ), respectively.³⁸ Compared to **APDC-DTPA**, **TPAAP** possesses only one TPA moiety. both compounds contain only one TPA moiety. In toluene **TPAAP** emits at λ_{PL} of 609 nm, has a high Φ_{PL} of 97% and a ΔE_{ST} of 0.19 eV, while **TPAAQ** has a Φ_{PL} value of 93% but with a larger ΔE_{ST} of 0.33 eV. Notably, both molecules exhibited significantly red-shifted PL spectra in their aggregated forms, falling into the NIR region with λ_{PL} at 777 nm for **TPAAP** and 716 nm for **TPAAQ** due to the formation of J-aggregates that possess strong intermolecular CT excited states. OLEDs with 5 or 10 wt% **TPAAP**:TPBi showed EQE_{max} of 15.8 and 14.1% with λ_{EL} of 630 and 657 nm, respectively. The non-doped devices with **TPAAQ** ($\Phi_{\text{PL}} = 16.3\%$) and **TPAAP** ($\Phi_{\text{PL}} = 20.3\%$) exhibited NIR emission with EQE_{max} of 3.5% at 711 nm and 5.1% at 765 nm, respectively.

Congrave *et al.* reported a NIR TADF emitter, **CAT-1** (3-triphenylamine-4-cyano-acenaphtho[1,2-b]-pyrazine-8,9-dicarbonitrile), which is structurally similar to **TPAAP**. **CAT-1** incorporates triphenylamine as the donor and acenaphtho[1,2-b]-pyrazine as the acceptor, enabling NIR TADF emission (Figure 1.21).¹²⁹ Compared to **APDC-DTPA** (neat, $\lambda_{\text{PL}} = 756$

nm), **CAT-1** in 10 wt% doped films in CBP has a red-shifted emission ($\lambda_{\text{PL}} = 763$ nm) at modest Φ_{PL} of 8.8% and a rather long τ_{d} of 80 μs considering a ΔE_{ST} of ca. 0.04 eV. Increasing the doping ratio of **CAT-1** in the evaporated films led to significant red-shift of the emission and a corresponding decrease in Φ_{PL} ; for example, the 40 wt% doped CBP film emission was recorded at $\lambda_{\text{PL}} = 820$ nm with low Φ_{PL} of 2%. Evaporated neat films of **CAT-1** emit at λ_{PL} of 887 nm, while neat films dropcasted from chlorobenzene solution were further red-shifted to $\lambda_{\text{PL}} = 950$ nm. The non-doped OLEDs showed an EQE_{max} of 0.019% at an λ_{EL} at 904 nm. Computational studies of this material revealed the potential for intramolecular hydrogen bonding (CH-CN) between the donor (TPA) and CN acceptor group as assisting in the overall performance compared to **TPAAP**.¹³⁰

Gong *et al.* reported the emitters **ANQDC-DMAC** and **ANQDC-MeFAC** (Figure 1.21) using the same acceptor as **TPAAQ** but coupled with either DMAC or MeFAC as the donor unit.¹³¹ This combination of donor and acceptor resulted in λ_{PL} at 596 and 604 nm in 1.5 wt% CBP:TPBi co-host and high Φ_{PL} of 95% for **ANQDC-DMAC** and 77% for **ANQDC-MeFAC**, along with a small ΔE_{ST} values of 0.06 eV for **ANQDC-DMAC** and 0.05 eV for **ANQDC-MeFAC**. Both compounds displayed preferential horizontal TD alignments of $\sim 80\%$, attributed by the authors to the linear and planar acceptor motif and rod-like molecular configuration. The OLEDs with **ANQDC-DMAC** and **ANQDC-MeFAC** achieved EQE_{max} of 27.5% and 26.3% at λ_{EL} at 615 and 614 nm, respectively, corresponding to CIE coordinates of (0.58, 0.41) and (0.60, 0.40).

Cheng *et al.* reported a NIR TADF emitter containing an auxiliary electron-withdrawing group attached to the AQ acceptor, **AQTC-DTPA** (Figure 1.21).¹³² **AQTC-DTPA** emits at λ_{PL} of 718 nm, has a Φ_{PL} of 19.1% in 10 wt% doped film in CBP and at λ_{PL} of 878 nm and has Φ_{PL} of 1.1% as a neat film. The large red-shift (82 nm) observed in the emission spectrum of **AQTC-DTPA** in the 10 wt% doped film relative to that in toluene (636 nm) is suggestive of strong interaction between **AQTC-DTPA** molecules in the solid state. The EL spectra showed a significant bathochromic shift from 694 to 894 nm when the doping ratio increased in CBP film from 10 to 100 wt% (neat). The red-shifting of the emission was attributed to strong intermolecular interactions in the emissive layer, growing in strength as the doping concentration increased. The large and coplanar AQ unit in **AQTC-DTPA** favoured π - π

stacking interactions in thin films, which was supported by single-crystal X-ray analysis. The solid-state structure of amorphous **AQTC-DTPA** obtained by cluster analysis indeed showed a tight packing pattern, aggregated in a head-to-head mode with π - π distances below 3.6 Å. A device with **AQTC-DTPA** (10 wt% doped CBP film) showed an EQE_{max} of 9.3% at λ_{EL} of 694 nm. The EQE_{max} decreased significantly to 0.51/0.41/0.30/0.23% as the doping concentration increased from 60/70/80/100 wt% at λ_{EL} of 810/828/852/894 nm, respectively.

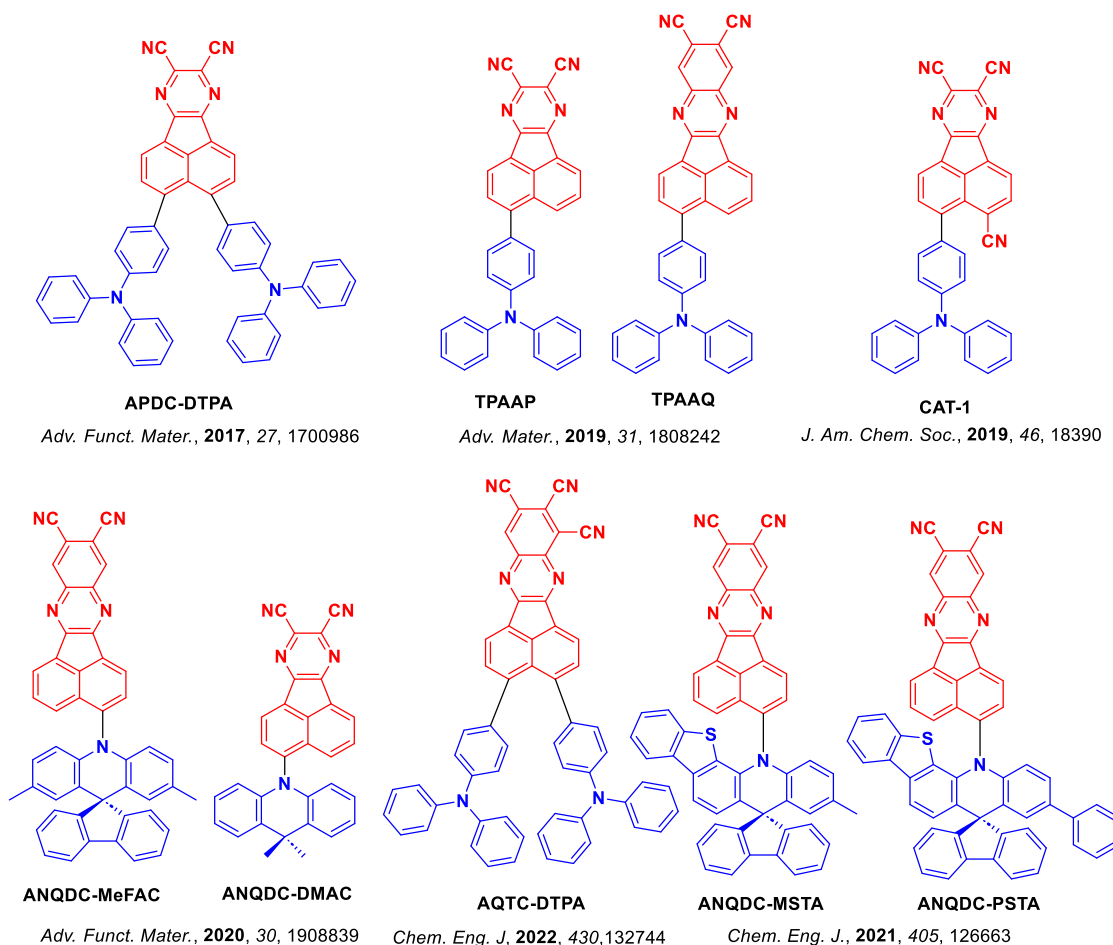


Figure 1.21. Molecular structures of red TADF emitters featuring acenaphtho[1,2-b]pyrazine acceptors.

Recently, Gong *et al.* reported the two red emitters **ANQDC-MSTA** and **ANQDC-PSTA** (Figure 1.21) using with a rigid, linear, and planar ANQDC as the acceptor coupled with thienocarbazole-fused acridine donors MSTA and PSTA.¹³³ The compounds emit at λ_{PL} of 623 and 618 nm and have Φ_{PL} of 65 and 72%, respectively, in 1.5 wt% doped films in a 1:1 CBP:TPBi co-host. The **ANQDC-MSTA**-based OLED (1.5 wt% emitter doped in CBP:TPBi co-host) exhibited an EQE_{max} of 21.8%, while the **ANQDC-PSTA**-based OLEDs displaying

slightly higher EQE_{max} of 24.7%. Both OLEDs displayed λ_{EL} of 622 nm and CIE coordinates of (0.61, 0.38).

1.5.4 Pyrazino- or Quinoxalino- Expanded Phenanthrene Acceptors

Pyrazine-fused phenanthrene is a rigid, π -conjugated structure that has been widely used as an acceptor of red TADF emitters. For example, Wang *et al.* employed dicyano-substituted pyrazino-phenanthrene (DCPP) as the acceptor and DPA or DMAC as the donor in a series red and deep-red TADF emitters.¹³⁴ emit at 618 and 594 nm, have Φ_{PL} of 33 and 65%, small ΔE_{ST} of 0.08 eV and 0.05 eV and short τ_{d} of 2.4 and 3.2 μs , respectively. The OLEDs with **DMAC-DCPP** and **DMAC-Ph-DCPP** showed EQE_{max} of 10.1 and 16.5%, with CIE coordinates of (0.60, 0.40) and (0.53,0.46), respectively. However, large efficiency roll-off was observed with EQE_{500} of just 4.2% for the device with **DMAC-DCPP** and 6.3% for the device with **DMAC-Ph-DCPP**. Replacing DMAC with DPA resulted in red-shifted emission at $\lambda_{\text{PL}} = 606$ and 628 nm for **DPA-DCPP** and **DPA-Ph-DCPP**, respectively, along with Φ_{PL} of 64 and 65%. The devices with these two emitters also experienced severe efficiency roll-off (EQE_{max} of 10.4 and 15.1%, EQE_{500} of 0.9 and 1.6%), due to their larger ΔE_{ST} (0.28 and 0.10 eV) and much longer delayed lifetimes ($\tau_{\text{d}} = 579$ and 82 μs). The same DCPP acceptor unit was also reported by Wang *et al.* coupled with stronger phenoxazine and phenothiazine donors, **PXZ-DCPP** and **PTZ-DCPP**, respectively (Figure 1.22).¹³⁵ In toluene, **PXZ-DCPP** and **PTZ-DCPP** emit at 564 and 580 nm, have λ_{PL} of 11.9 and 17.4% and ΔE_{ST} of 0.09 and 0.18 eV, respectively. The devices with **PXZ-DCPP** and **PTZ-DCPP** showed EQE_{max} of 17.4 and 12.3% at λ_{EL} of 608 and 640 nm associated with CIE coordinates of (0.56, 0.43) and (0.62, 0.36), respectively. Importantly, these devices exhibited only modest efficiency roll-off with the EQE_{1000} of 12.9% and 6.1%. A similar red emitter ($\lambda_{\text{PL}} = 663$ nm in 10 wt% doped film in CBP) with bulky carbazole derivatives that are decorated with two TPA units as solubilizing donors **DDTPACz-DCPP** (Figure 1.22) was reported by Wang *et al.*¹³⁶ This compound has a Φ_{PL} of 53% in 10 wt% doped films in CBP films, a ΔE_{ST} of 0.16 eV and a τ_{d} of 9.7 μs . The solution-processed devices with **DDTPACz-DCPP** showed an EQE_{max} of 13.6% at λ_{EL} of 646 nm and CIE coordinates of (0.63, 0.37). The rigid, large π -conjugated structure and strong

electron-withdrawing nature of DCPD are responsible for the long-wavelength emission of the emitters. The devices with DCPD-based emitters with DMAC, PXZ, and PTZ as donors, demonstrated moderate EQE_{max} ranging from 9.8 to 17.4% and λ_{EL} ranging from 596 to 640 nm. Among the the devices with DCPD-based emitters, those with **DDPhCz-DCPD** and **DDTPACz-DCPD** are particularly noteworthy as these devices are solution-processable and exhibited EQE_{max} values of 20.6 and 13.6%, respectively.

Furue *et al.* reported two asymmetric D- π -A emitters **Da-CNBPz** and **Ac-CNBPz** (Figure 1.22), consisting of 11,12-dicyanodibenzo[a,c]phenazine (CNBPz) as a strong acceptor unit.¹³⁷ These were compared with analogue D- π -A TADF materials **Da-CNBQx** and **Ac-CNBQx**, containing 2,3-dicyanodibenzo[f,h]quinoxaline (CNBQx) as a less strong acceptor unit, which contain a less π -conjugated acceptor structure (Figure 1.22). Comparing **Da-CNBQx** and **Da-CNBPz**, the emission red-shifted from 633 to 688 nm and there is a modest decrease in Φ_{PL} from 85 to 72%. The same behavior was observed for **Ac-CNBQx** and **Ac-CNBPz**, with λ_{PL} red-shifted from 561 to 615 nm and Φ_{PL} decreasing from 75 to 67%, respectively. Calculated non-radiative rate constants (k_{nr}) for the emitters showed an increase in non-radiative decay upon extending the π -conjugation of the acceptor, with values of $1.6 \times 10^7 \text{ s}^{-1}$ for **Da-CNBQx** and $2.4 \times 10^7 \text{ s}^{-1}$ for **Da-CNBPz**; the same trends were observed for **Ac-CNBQx** and **Ac-CNBPz**, where an increase of non-radiative decay from 0.16 to $0.25 \times 10^7 \text{ s}^{-1}$ was seen, in line with the energy gap law. Devices with **Da-CNBQx** and **Da-CNBPz** showed EQE_{max} of 15.0% at λ_{EL} of 670 nm and 20.0% at λ_{EL} of 617 nm, respectively, representing some of the highest efficiency red TADF OLEDs to date. However, both of these devices suffered severe efficiency roll-off with EQE_{100} dropping to 3.8 and 7.5%, respectively. Although the devices with **Ac-CNBQx** and **Ac-CNBPz** show lower EQE_{max} (and blue-shifted emission) of 16.2 (λ_{EL} of 630 nm) and 14.0% (λ_{EL} of 685 nm), their EQE_{100} were superior at 14.5 and 13.9%, respectively. This change is due to smaller ΔE_{ST} values when using Ac as the donor of 0.03 and 0.10 eV for **Ac-CNBPz** and **Ac-CNBQx** compared to 0.11 and 0.18 eV for **Da-CNBPz** and **Da-CNBQx**, respectively, all in 6 wt% doped films in CBP.

In a similar approach to the previous example, cyano groups were added to the 3- and 6-positions of a phenazine core to increase the electron-accepting strength, while two TPA groups were employed as the donors.¹³⁸ **TPA-PZCN** (Figure 1.22) emits at 610 nm and has a very

high Φ_{PL} of 97%, a ΔE_{ST} of 0.13 eV and a τ_{d} of 133 μs . The devices with **TPA-PZCN** showed an EQE_{max} of 27.4% at λ_{EL} at 628 nm and CIE coordinates of (0.65, 0.35), which represents the best result with a peak wavelength longer than 600 nm among the reported red TADF devices.

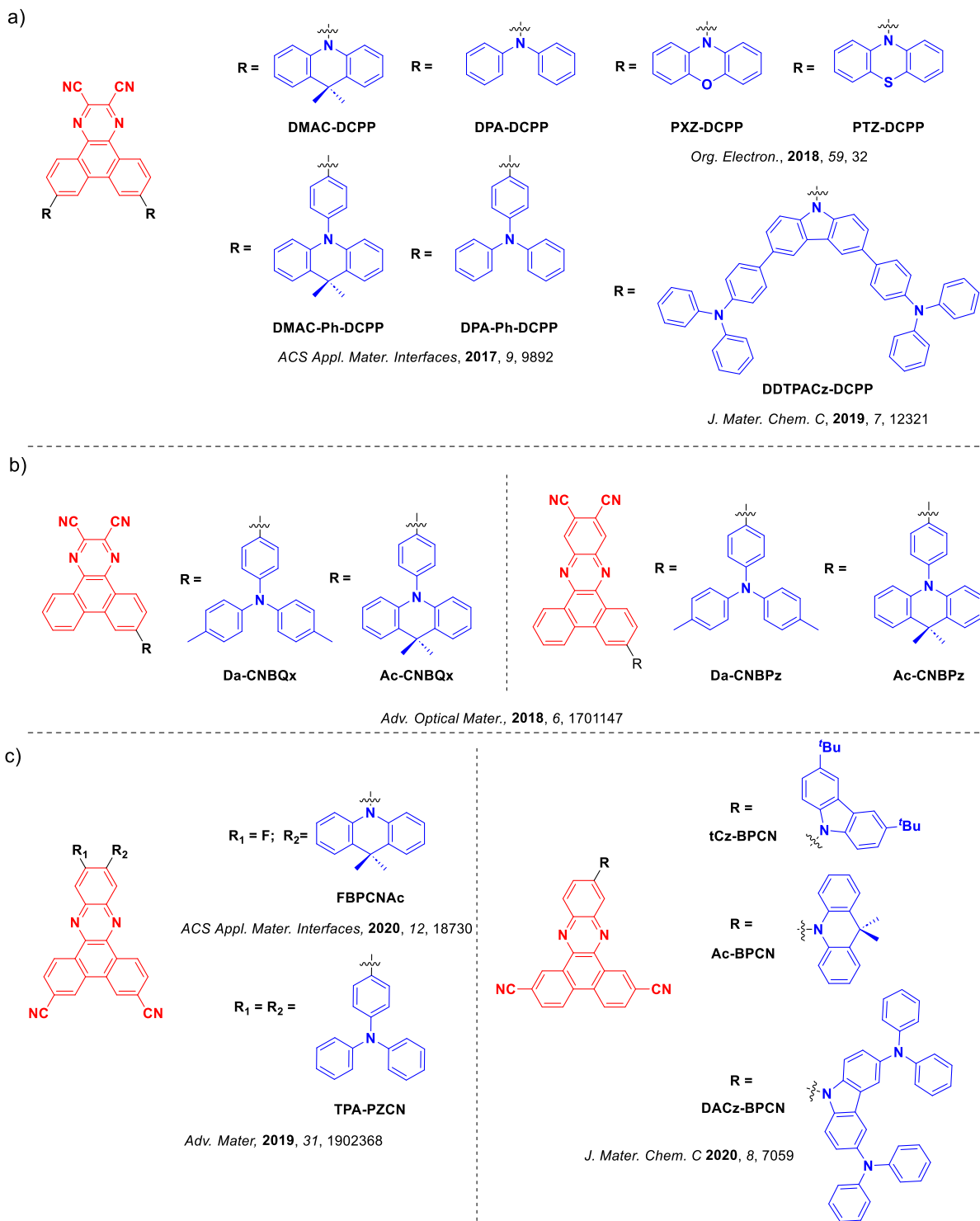


Figure 1.22. Molecular structures of red TADF emitters using a) dibenzo[f,h]quinoxaline-2,3-dicarbonitrile acceptor having two donor groups, b) dibenzo[f,h]quinoxaline-2,3-dicarbonitrile acceptor having one donor group and c) dibenzo[a,c]phenazine-3,6-dicarbonitrile acceptor.

In a subsequent report, Kothavale *et al.* functionalized the same acceptor with a fluorine atom and used DMAC as the donor in **FBPCNAc** (Figure 1.22).¹³⁹ The fluorine substituent was attached *ortho* to the DMAC, which strengthened the electron-acceptor. **FBPCNAc** emits at 607 nm, has a Φ_{PL} of 79%, a small ΔE_{ST} of 0.05 eV, and a τ_{d} of 11.1 μs . The OLEDs with **FBPCNAc** realised an EQE_{max} of 23.8% at λ_{EL} of 597 nm and CIE coordinates of (0.55, 0.44). This blue-shift of the emission compared to the previous examples is likely due to there being only one donor unit in this emitter design compared to two for the others. Kothavale *et al.* also reported two related emitters, **Ac-BPCN** and **DACz-BPCN** (Figure 1.22), which differ in the substitution position of the CN group on the BPCN acceptor unit.¹⁴⁰ **Ac-BPCN** and **DACz-BPCN** emit at 618 and 654 nm, have λ_{PL} of 66 and 47%, ΔE_{ST} of 0.13 and 0.07 eV, and τ_{d} of 11.1 and 7.2 μs , respectively. The OLEDs with **Ac-BPCN** and **DACz-BPCN** in the bipolar host PBICT showed EQE_{max} of 20.7% ($\lambda_{\text{EL}} = 597$ nm) and 11% ($\lambda_{\text{EL}} = 631$ nm) at CIE coordinates of (0.54, 0.45) and (0.60, 0.39), respectively.

Moving away from CN-substituted π -conjugated acceptors, Xie *et al.* developed three TADF molecules **xDMAC-BP** ($x = 1, 2, 3$) containing a rigid planar phenazine acceptor core and different numbers of DMAC donors at the 3-/6-/11-positions (Figure 1.23).¹⁴¹ The emission color of the **xDMAC-BP** series could be tuned from green to orange-red by changing the number of the DMAC units. The reddest emitting analogue **3DMAC-BP** emits at λ_{PL} of 590 nm, has a high Φ_{PL} of 89%, a small ΔE_{ST} of 0.05 eV and a short τ_{d} of 2.9 μs in 20 wt% doped films in mCBP. The OLEDs with **3DMAC-BP** showed an EQE_{max} of 22.0% at λ_{EL} of 606 nm. Crucially, the EQE_{100} of the **3DMAC-BP**-based device still remained as high as 17.5% due to the low efficiency roll-off. The same molecular design was also employed but using PXZ as the donor.¹⁴¹ Expectedly, increasing the number of PXZ units red-shifted the emission from 602 to 682 nm in toluene. The ΔE_{ST} and λ_{PL} values for **1PXZ-BP** are 0.25 eV and 73%, for **2PXZ-BP** are 0.10 eV and 63%, and for **3PXZ-BP** are 0.03 eV and $\Phi_{\text{PL}} = 22\%$, respectively. Thus, as the number of PXZ groups increases, the λ_{PL} decreases as does ΔE_{ST} and also τ_{d} from 4.8 μs , 4.3 μs , and 2.0 μs , respectively. The orange-red OLEDs with **1PXZ-BP**, **2PXZ-BP** and **3PXZ-BP** showed EQE_{max} of 26.3 (λ_{EL} of 590 nm), 19.2 (λ_{EL} of 606 nm) and 7.1% (λ_{EL} of 634 nm). However, compared to **xDMAC-BP** the efficiency roll-off of **xPXZ-BP** are all higher, which the authors speculated may be due to the inferior charge balance of the devices.

Xie *et al.* used a similar dibenzo[*f,h*]pyrido[2,3-*b*]quinoxaline (BPQ) acceptor coupled to three DMAC donors at either the 3-,6-,11-positions or 3-,6-,12-positions in **3,6,11-triAC-BPQ** and **3,6,12-triAC-BPQ**, respectively (Figure 1.23).¹⁴² In 15 wt% doped films in mCBP **3,6,11-triAC-BPQ** and **3,6,12-triAC-BPQ** emit at λ_{PL} of 516 and 611 nm in toluene, have λ_{PL} of 75 and 53% and λ_{d} of 2.50 and 2.25 μs , respectively. **3,6,11-triAC-BPQ** was claimed to have hybridized local and charge-transfer (HLCT) character due to intramolecular hydrogen bonding between the isolated donor and the adjacent pyridine nitrogen, whilst the **3,6,12-triAC-BPQ** displayed typical CT character. **3,6,11-triAC-BPQ** and **3,6,12-triAC-BPQ** have λ_{EST} of 0.10 and 0.03 eV, respectively. Devices with **3,6,11-triAC-BPQ** and **3,6,12-triAC-BPQ** showed EQE_{max} of 22.0% [λ_{EL} of 581 nm, CIE coordinates of (0.51,0.48)] and 16.5% [λ_{EL} of 616 nm, CIE coordinates of (0.58,0.39)], respectively. Zhou *et al.* developed two pairs of emitters **DMAC-11-DPPZ** and **DMAC-10-DPPZ**, and **PXZ-11-DPPZ** and **PXZ-10-DPPZ**, differing only in the nature of the donor (DMAC or PXZ) connected through 10- or 11-positions on the acceptor BP moiety (Figure 1.23).¹⁴³ The compounds substituted at the 11-position ($\Phi_{\text{PL}} = 57.4\%$ and 40.9%) achieved much higher Φ_{PL} than those substituted at the 10-position ($\Phi_{\text{PL}} = 28.6\%$ and 5.3%), owing to suppressed non-radiative vibrational modes. The PL spectra of **DMAC-11-DPPZ** in toluene shows two emission peaks at 567 nm and 490 nm, attributed to the coexistence of quasi-equatorial (QE) and quasi-axial (QA) conformations. **DMAC-10-DPPZ** exhibits a red-shifted emission peak at 620 nm due to stronger CT properties. **PXZ-11-DPPZ** shows a red emission peak at 630 nm, while **PXZ-10-DPPZ** unexpectedly exhibits a blue-shifted emission peak at 573 nm in toluene. The τ_{d} for **DMAC-11-DPPZ**, **DMAC-10-DPPZ**, **PXZ-11-DPPZ**, and **PXZ-10-DPPZ** are 1.53, 0.83, 0.72, and 0.51 μs , respectively. These values are in good agreement with the decrease in the corresponding ΔE_{ST} of 0.112, 0.075, 0.062, and 0.057 eV, respectively. The **DMAC-11-DPPZ** based device showed orange emission at λ_{EL} of 588 nm [CIE coordinates of (0.53, 0.46)] with an EQE_{max} of 23.8%, while the device with **DMAC-10-DPPZ** showed a much lower EQE_{max} of 8.3%, albeit with a red-shifted λ_{EL} of 624 nm [CIE coordinates of (0.61, 0.38)]. Similarly, the **PXZ-10-DPPZ** device showed a red-shifted emission at λ_{EL} of 655 nm [CIE coordinates of (0.63, 0.37)] yet with a higher EQE_{max} of 8.7% compared to the device with **PXZ-11-DPPZ** at λ_{EL} of 627 nm [CIE coordinates of (0.65, 0.35)], which showed an EQE_{max} of only 0.8%.

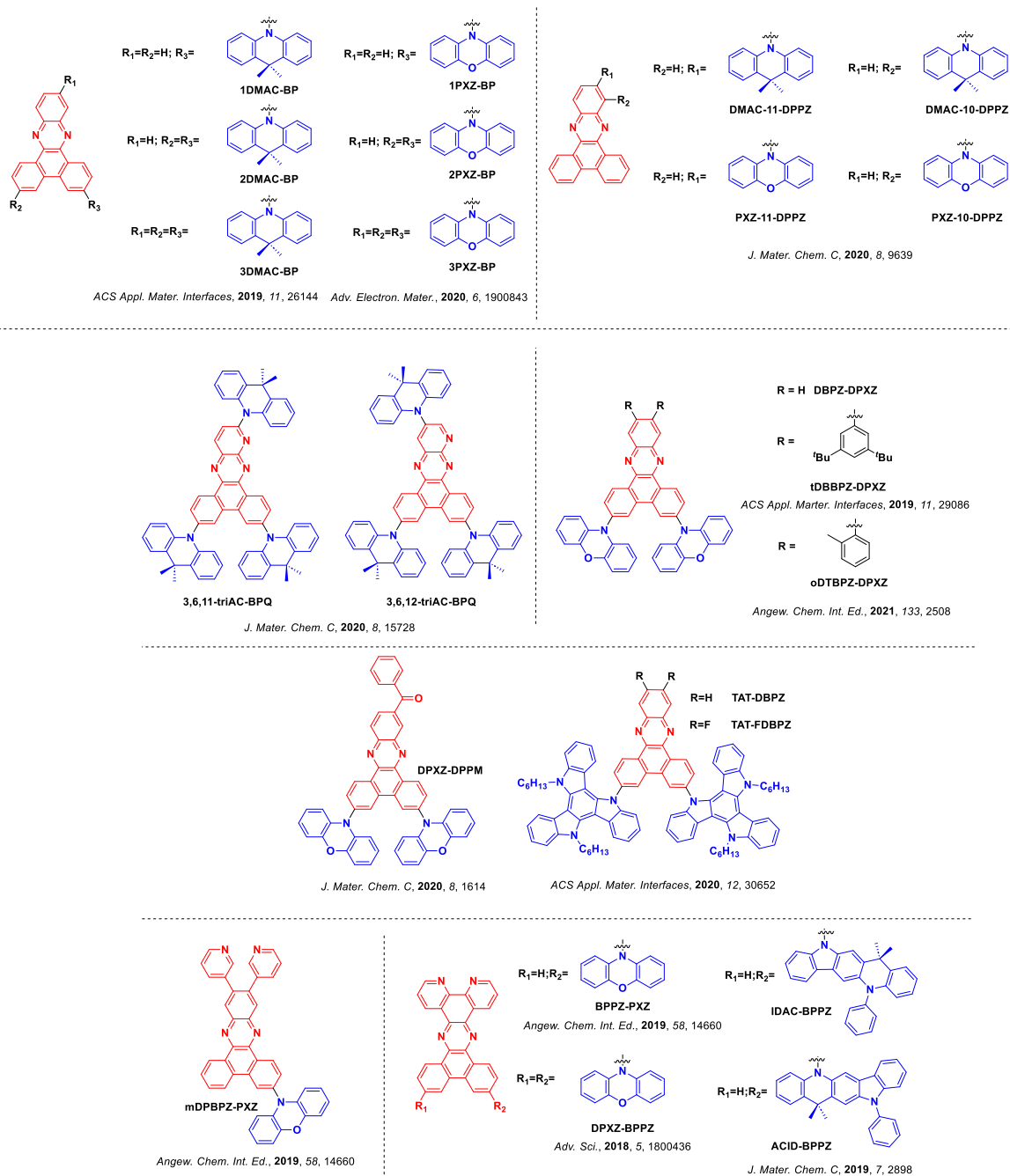


Figure 1.23. Molecular structure of red TADF emitters featuring pyrazino-phenanthrene acceptors.

Introduction of two 3,5-di-*tert*-butylphenyl groups in **tDBBPZ-DPXZ** improved the solubility compared to **2PXZ-BP** (Figure 1.23).¹⁴⁴ **tDBBPZ-DPXZ** emits at λ_{PL} of 617 nm, has a λ_{PL} of 83%, and a small ΔE_{ST} of 0.03 eV in 10 wt% doped films in CBP. A solution-processed **tDBBPZ-DPXZ** OLED emitted at λ_{EL} of 620 nm and CIE coordinates of (0.62,

0.37), and showed an EQE_{max} of 10.1%. **tDBBPZ-DPXZ** has nearly the same photophysical properties as **2PXZ-BP** (**DBBPZ-DPXZ** in that work). Vacuum-deposited devices with **tDBBPZ-DPXZ** and **DBBPZ-DPXZ** both emitted at λ_{EL} 608 nm, corresponding to CIE coordinates of (0.58,0.42) and (0.57,0.43), respectively, and showed EQE_{max} of 17.0 and 17.8% respectively. In a subsequent report from the same group, a similar compound **oDTBPZ-DPXZ** (Figure 1.23) containing *o*-tolyl groups in lieu of *tert*-butylphenyl groups shows comparable photophysics.¹⁴⁵ **oDTBPZ-DPXZ** emits at 622 nm, has a high Φ_{PL} of 87% and a small ΔE_{ST} of 0.04 eV. Solution-processed OLEDs with **oDTBPZ-DPXZ** achieved an EQE_{max} of 18.5% at λ_{EL} of 612 nm and CIE coordinates of (0.60, 0.40).

Liang *et al.* used a weakly electron-withdrawing benzoyl group attached to **2PXZ-BP** to construct the emitter **DPXZ-DPPM** (Figure 1.23).¹²⁵ **DPXZ-DPPM** doped in 5,5'-bis(carbazol-9-yl)-3,3'-bipyridine (DCzDPy) films emits at λ_{PL} of 630 nm, has a Φ_{PL} of 61%, a ΔE_{ST} of 0.05 eV and a τ_{d} of 3.53 μs . Compared to **2PXZ-BP** (λ_{EL} of 606 nm), **DPXZ-DPPM**-based devices display a much redder emission at λ_{EL} of 630 nm corresponding to CIE coordinates of (0.61, 0.38), and showed an EQE_{max} of 11.5%.

Fan *et al.* reported two TADF emitters, **mDPBPZ-PXZ** and **BPPZ-PXZ** (Figure 1.23), which have, respectively substituted or annelated pyridyl groups onto the acceptor.¹⁴⁶ In 14 wt% doped films in CBP, **mDPBPZ-PXZ** emits at λ_{PL} of 638 nm, has a small ΔE_{ST} of 0.04 eV and a high Φ_{PL} of 95%, whereas the neat film has only a moderate Φ_{PL} of 33% with a λ_{PL} of 607 nm. This suggests the introduction of pyridine moieties somewhat relieves concentration-induced quenching. The OLEDs with **mDPBPZ-PXZ** showed an EQE of 21.7% at λ_{EL} of 624 nm and CIE coordinates of (0.62, 0.38). Non-doped devices showed a much lower EQE of 5.2% at λ_{EL} of 680 nm with CIE coordinates of (0.68, 0.32). The fused analogue **BPPZ-PXZ** emits at 607 nm and has a high Φ_{PL} of 100%, ΔE_{ST} of 0.03 eV and a τ_{d} of 3.6 μs . The doped OLED with **BPPZ-PXZ** showed an EQE_{max} of 25.2% at λ_{EL} at 604 nm, whereas the non-doped device showed a much lower EQE_{max} of only 2.5% at λ_{EL} at 656 nm. This contrast was attributed to more serious concentration quenching due to close molecular packing of this more planar emitter compared to **mDPBPZ-PXZ**. A pyridyldisubstituted analogue **DPXZ-BPPZ** was also reported by Chen *et al.* and has similar optoelectronic properties.¹⁴⁷ The **DPXZ-BPPZ** OLED emitted at λ_{EL} of 612 nm and showed an EQE_{max} of 20.1%, and $\text{EQE}_{100}/\text{EQE}_{1000}$ that remained

at ~19.7/16.7%, an efficiency roll off that was superior to the device with **BPPZ-PXZ**. The superior performance of the devices was in part due to the excellent Φ_{PL} of 97%, the reasonably fast k_{RISC} of $2.24 \times 10^5 \text{ s}^{-1}$ and suppressed k_{nr} of $0.5 \times 10^4 \text{ s}^{-1}$, the latter of which was attributed to the rigid nature of the molecule.

Chen *et al.* used the same acceptor in combination with fused donors in **IDAC-BPPZ** and **ACID-BPPZ** (Figure 1.23).¹⁴⁵ Similar emission properties were observed for both compounds with λ_{PL} of 583 and 596 nm and Φ_{PL} of 84 and 75%, respectively. **IDAC-BPPZ** and **ACID-BPPZ** have ΔE_{ST} of 0.06 and 0.01 eV, respectively, and similar τ_{d} of 14 and 12 μs . The OLEDs with **IDAC-BPPZ** showed EQE_{max} of 18.3% at $\lambda_{\text{EL}} = 580 \text{ nm}$ as compared to only 14.7% for the device with **ACID-BPPZ** at $\lambda_{\text{EL}} = 588 \text{ nm}$. A greater efficiency roll-off was observed for the device with **IDAC-BPPZ** compared to that with **ACID-BPPZ**, decreasing from maximum values by ~39 and ~68% for the OLEDs with **ACID-BPPZ** and **IDAC-BPPZ** at 1000 cd m^{-2} , respectively, which was ascribed to the faster τ_{d} alleviating triplet quenching processes in **ACID-BPPZ**.

Liu *et al.* developed two red TADF emitters by incorporating a triazatruxene (TAT) as the electron donor (Figure 1.23).¹⁴⁶ Fluorine-substituted **TAT-FDBPZ** displayed a red-shifted emission ($\lambda_{\text{PL}} = 601 \text{ nm}$) compared to that of **TAT-DBPZ** ($\lambda_{\text{PL}} = 572 \text{ nm}$) as a result of the electron-withdrawing nature of the two fluorine atoms. The large steric hindrance between TAT and DBPZ was suggested to be responsible in a reduced ΔE_{ST} of 0.16 eV and suppressed ACQ, enabling AIE and high Φ_{PL} in the 20 wt% doped films in CBP (Φ_{PL} of 76% for **TAT-DBPZ** and 62% for **TAT-FDBPZ**). **TAT-DBPZ** and **TAT-FDBPZ** have small ΔE_{ST} of 0.16 and 0.10 eV and short τ_{d} of 2.30 and 1.51 μs , respectively. Solution-processed OLEDs with **TAT-DBPZ** showed an EQE_{max} of 15.4% at λ_{EL} of 604 nm, while the **TAT-FDBPZ** based OLEDs showed a red-shifted at λ_{EL} of 611 nm and a smaller EQE_{max} of 9.2%. These values were accompanied by very low efficiency roll-off of only 1.0 % at 100 cd m^{-2} and 19% at 1000 cd m^{-2} .

Rather than installing fused pyridine groups onto phenanthrene, Xu *et al.* developed phenanthroline-based D-A red TADF emitters **oTPA-DPPZ** and **pTPA-DPPZ** (Figure 1.24).¹⁴⁸ In a 30 wt% DBFDPO (4,6-bis(diphenylphosphoryl)-dibenzofuran) doped film, **oTPA-DPPZ** emits at λ_{PL} of 605 nm, has a Φ_{PL} of 75%, a ΔE_{ST} of 0.07 eV and a τ_{d} of 12 μs . OLEDs with **oTPA-DPPZ** showed an EQE_{max} of 18.5% at λ_{EL} of 600 nm. Through adjusting the position of

the donor groups, the T-shaped **pTPA-DPPZ** emits to the red at λ_{PL} of 644 nm in neat film (Figure 1.24). The spatial arrangement of D and A groups in **pTPA-DPPZ** dramatically accelerated the rate of singlet emission without an increase in non-radiative decay, resulting in an increased Φ_{PL} of 87% in the neat film. This change in optical properties was accompanied by a remarkably improved carrier transport in the neat film. As a result, a high-efficiency bilayer non-doped OLED was demonstrated, displaying deep-red emission at $\lambda_{\text{EL}} = 652$ nm and CIE coordinates of (0.67, 0.33) and showing an EQE_{max} of 12.3% and EQE_{1000} of 10.4%.

Zhang *et al.* reported the red TADF emitter (**DBPz-2spAc**, Figure 1.24) based on an 8b,14a dihydrodibenzo[a,c]phenazine-10,13-dicarbonitrile acceptor and containing two spiro-acridines as donors.¹⁴⁹ **DBPz-2spAc** has an Φ_{PL} of 27% ($\lambda_{\text{PL}} = 632$ nm) in toluene and 65% ($\lambda_{\text{PL}} = 632$ nm) in 1 wt% doped films in CBP. OLEDs at 1 wt % doping ratio showed high EQE_{max} of 13.3%, with the emission λ_{EL} ranging from 630 nm. However, the devices suffer from severe efficiency roll-off where the EQE is about 1% at 100 cd/m², attributed to triplet-triplet annihilation (TTA). Tan *et al.* reported two isomeric orange-red TADF emitters, **oPDM** and **pPDM** (Figure 1.24), with the same basic donor-acceptor backbone but with pyrimidine (Pm) attached at different positions.¹⁵⁰ **oPDM** and **pPDM** emit at λ_{PL} of 582 and 573 nm, have moderate ΔE_{ST} of 0.11 and 0.15 eV and high Φ_{PL} of ca. 100 and 88% in 8 wt% doped films in CBP. OLEDs with **oPDM** or **pPDM** exhibited orange-red EL emission at λ_{EL} of 596 and 582 nm and CIE coordinates of (0.56, 0.44) and (0.52, 0.47), respectively. Despite similar PL properties, a significant difference in efficiency was seen in the two devices, with the OLEDs with **oPDM** or **pPDM** showing an EQE_{max} of 28.2 and 11.8%, respectively. The difference was attributed to the differing molecular packing of the emitters in the aggregated state, resulting in very different charge transport performance.

Kothavale *et al.* reported two red TADF emitters, **oDMAC-DPPZ** and **pDMAC-DPPZ** (Figure 1.24), whose structures differ in the regiochemistry of the DMAC donor.¹⁵¹ The Φ_{PL} in toluene of the more red-shifted compound, **pDMAC-DPPZ** ($\lambda_{\text{PL}} = 669$ nm, $\lambda_{\text{PL}} = 15\%$) is lower than that of **oDMAC-DPPZ** ($\lambda_{\text{PL}} = 652$ nm, $\lambda_{\text{PL}} = 63\%$). In the bipolar host 2-phenyl-4,6-bis(12-phenylindolo[2,3-a]carbazole-11-yl)-1,3,5-triazine (PBICT, 1 wt%) the emission of **oDMAC-DPPZ** is blue-shifted to $\lambda_{\text{PL}} = 614$ nm with CIE coordinates (0.59, 0.40), while **pDMAC-DPPZ** emits at λ_{PL} of 638 nm with CIE coordinates (0.64, 0.35). Aligning with their

Φ_{PL} , the device with **oDMAC-DPPZ** showed a higher EQE_{max} of 13.4% at λ_{EL} of 614 nm, while the device with **pDMAC-DPPZ** displayed a lower EQE_{max} of 4.0%.

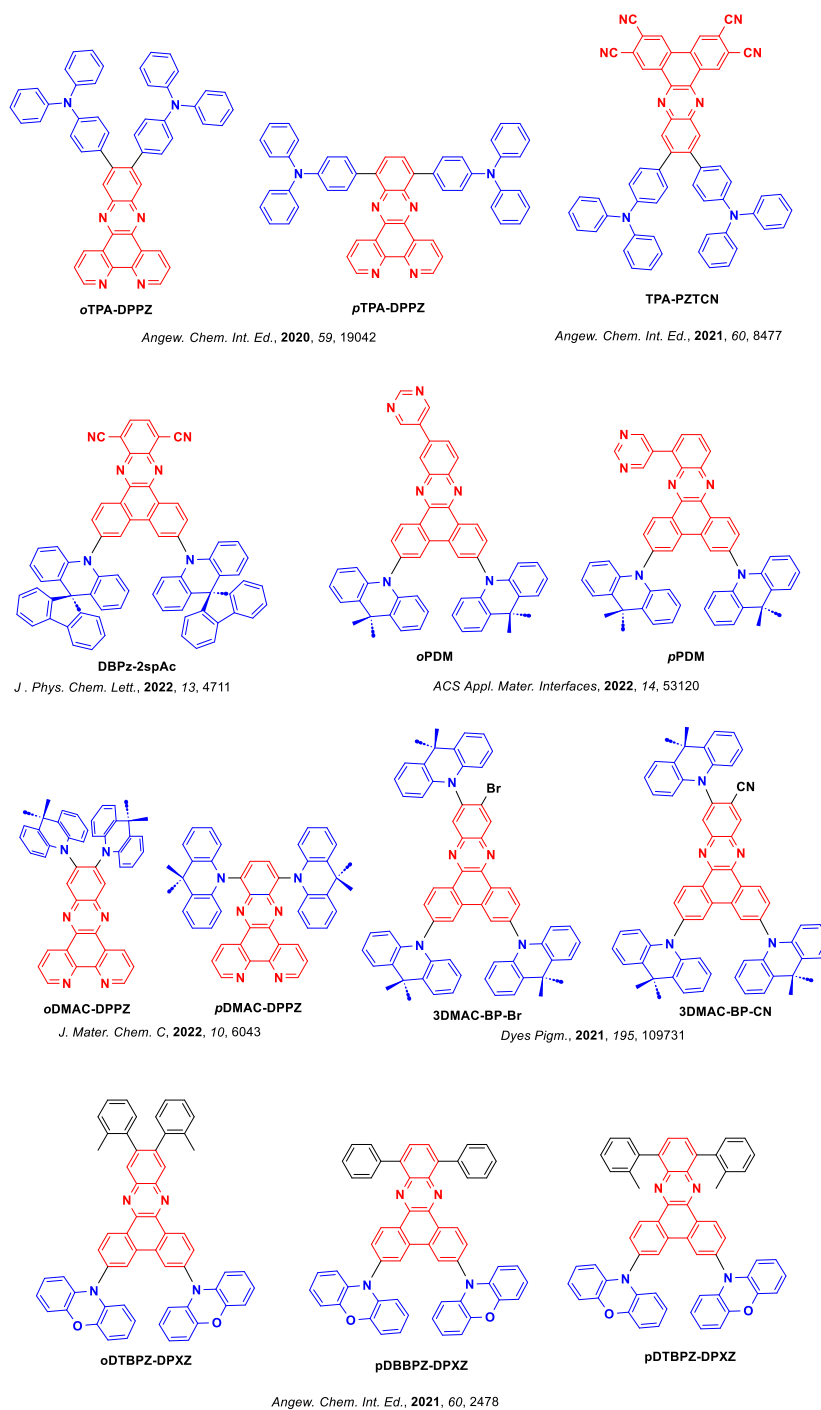


Figure 1.24. Molecular structures of red TADF emitters using phenanthrene acceptors.

Huang *et al.* synthesized two orange-red TADF emitters with D₃-A structures, and modified by either an inductively electron-withdrawing bromine atom (**DMAC-BP-Br**) or a cyano- group (**DMAC-BP-CN**, Figure 1.24).¹⁵² **DMAC-BP-Br** and **DMAC-BP-CN** emit at

λ_{PL} of 612 and 617 nm in toluene, have Φ_{PL} of 83 and 92%, ΔE_{ST} of only 0.04 and 0.02 eV and τ_{d} of 3.8 and 4.6 μs , respectively, in 15 wt% doped films in CBP. The OLEDs with **DMAC-BP-Br** and **DMAC-BP-CN** showed EQE_{max} of 18.9% and 22.4% at λ_{EL} of 596 and 586 nm, respectively.

Balijapalli *et al.* reported a D-A deep-red/NIR emitting compound, **TPA-PZTCN**, featuring multiple cyano groups about the acceptor (Figure 1.24).¹⁵³ **TPA-PZTCN** emits at λ_{PL} of 674 nm and has a Φ_{PL} of 77% in toluene. Doped at 1 wt% in mCBP, the emission of **TPA-PZTCN** at 672 nm maintains the high Φ_{PL} of 78%, while at 10 wt% loading the Φ_{PL} decreases to 40%, accompanied by a much red-shifted λ_{PL} at 729 nm. OLEDs with 1, 3, or 6 wt% **TPA-PZTCN** showed $\text{EQE}_{\text{max}} = 19.3\%$ ($\lambda_{\text{EL}} = 651$ nm), $\text{EQE}_{\text{max}} = 17.7\%$ ($\lambda_{\text{EL}} = 671$ nm), and $\text{EQE}_{\text{max}} = 15.8\%$ ($\lambda_{\text{EL}} = 712$ nm), respectively.

Chen *et al.* reported three red TADF emitters **pDBBPZ-DPXZ**, **pDTBPZ-DPXZ**, and **oDTBPZ-DPXZ** (Figure 1.24) using phenoxazine as donors and differently functionalised acceptors.¹⁴⁵ **pDBBPZ-DPXZ**, **pDTBPZ-DPXZ**, and **oDTBPZ-DPXZ** have distinctive Φ_{PL} of 49, 66, and 87%, respectively, in 8 wt% doped films in CBP. Despite the differing λ_{PL} , the photophysical properties of the three compounds are quite similar, [**pDBBPZ-DPXZ** ($\lambda_{\text{PL}} = 622$ nm, $\Delta E_{\text{ST}} = 0.23$ eV and $\tau_{\text{d}} = 53.3$ μs , **pDTBPZ-DPXZ** ($\lambda_{\text{PL}} = 621$ nm, $\Delta E_{\text{ST}} = 0.10$ eV and $\tau_{\text{d}} = 5.6$ μs and **oDTBPZ-DPXZ** ($\lambda_{\text{PL}} = 621$, $\Delta E_{\text{ST}} = 0.04$ and $\tau_{\text{d}} = 3.3$ μs], except for the differences in the energies of the T_1 states. From **pDBBPZ-DPXZ** to **pDTBPZ-DPXZ** and **oDTBPZ-DPXZ**, the ${}^3\text{LE}_A$ energy levels gradually approach the CT states from one where they are far stabilized to one where they are isoenergetic with the ${}^3\text{CT}$ state and this results in a faster k_{RISC} . The OLEDs with **pDBBPZ-DPXZ**, **pDTBPZ-DPXZ**, and **oDTBPZ-DPXZ** showed very similar red emission spectra, with $\lambda_{\text{EL}} \sim 604$ nm and CIE coordinates of (0.59, 0.40), (0.58, 0.41), and (0.59, 0.41), respectively. Following the ordering of Φ_{PL} , the device with **oDTBPZ-DPXZ** showed the highest EQE_{max} of 20.1%, compared to the devices with **pDTBPZ-DPXZ** and **pDBBPZ-DPXZ**, showing EQE_{max} of 16.0 and 8.0%, respectively.

1.5.5 Phenanthro[4,5-abc]phenazine-11,12-dicarbonitrile Acceptor

The phenanthro[4,5-abc]phenazine-11,12-dicarbonitrile (PPDCN) acceptor was

combined with a TPA donor to form the D–A-type NIR TADF emitter, **TPA-PPDCN**. (Figure 1.25).¹⁵⁴ By replacing the phenanthrene in the acceptor core with pyrene, the π -conjugation of the acceptor is increased. This substitution results in a significantly deeper LUMO energy and a red-shifted emission. The ΔE_{ST} of **TPA-PPDCN** is 0.23 eV in toluene and the neat film emits at 725 nm, has a Φ_{PL} of 21%, and a τ_d of 1.96 μ s. The PL spectra of the doped films gradually red-shift from 650 to 687 nm with increasing doping concentration (5 to 20 wt% in CBP), indicating a shift from monomolecular emission to emission from aggregates. The highest Φ_{PL} is 87% in the 10 wt% doped film in CBP with λ_{PL} of 663 nm, although the Φ_{PL} is maintained at 77% when the doping concentration is 20 wt%. The OLEDs with **TPA-PPDCN** (10 and 20% doped in CBP) showed deep red and NIR emission with respective λ_{EL} of 664 nm and CIE coordinates of (0.68, 0.32) and at 692 nm CIE = (0.70, 0.30), at EQE_{max} of 20.2 and 16.4%, respectively. However, all devices exhibited large efficiency roll-off, with EQE_{100} decreasing to 4.7 and 3.7%, respectively.

The same group reported two pairs of isomers employing either the same PPDCN as the acceptor or shortened analogue PDCN acceptor in combination with acridine donors attached at two different locations (**T/C-DA-1/2**, Figure 1.25).¹⁵⁵ In a 10 wt% doped films in mCBP, **T-DA-1**, **T-DA-2**, **C-DA-1**, and **C-DA-2** emit at λ_{PL} of 601, 640, 640 and 689 nm, respectively. The Φ_{PL} of the *trans*-isomers (**T-DA-1** and **T-DA-2**, 78 and 89% respectively) are significantly higher than those of their corresponding *cis*-isomers (**C-DA-1** and **C-DA-2**, 12 and 14%). The ΔE_{ST} values are 0.16, 0.05, 0.02, and 0.02 eV for **T-DA-1**, **T-DA-2**, **C-DA-1**, and **C-DA-2**, respectively, in toluene at 77 K. The OLEDs with **T-DA-1**, **T-DA-2**, **C-DA-1**, and **C-DA-2** doped at 10 wt% in mCBP showed orange-red to deep-red emission at λ_{EL} of 596, 640, 648, and 684 nm and CIE coordinates of (0.54, 0.46), (0.62, 0.37), (0.66, 0.34), and (0.67, 0.31), all respectively. Due to their low Φ_{PL} , the devices with **C-DA-1** (EQE_{max} of 3.5%) and **C-DA-2** (EQE_{max} of 3.1%) showed much poorer efficiencies compared to the devices with **T-DA-1** and **T-DA-2**, which instead showed EQE_{max} of 22.6 and 26.3%, respectively. Crucially the EQE_{100} of the **T-DA-2** based device still remained as high as 24%, corresponding to efficiency roll-off of just 8.8%.

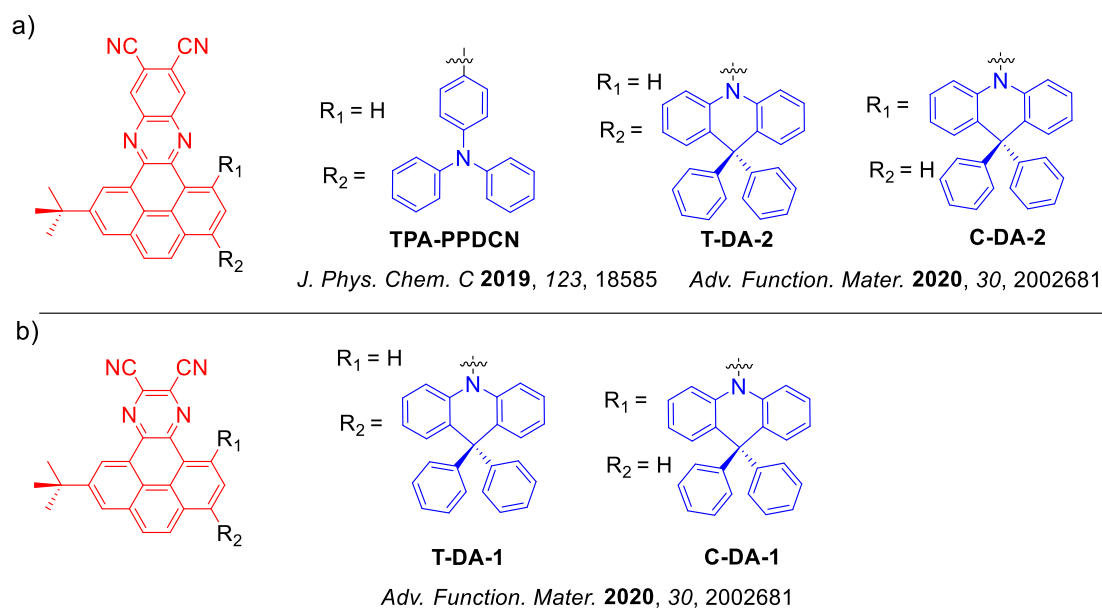


Figure 1.25. Molecular structures of red TADF emitters using phenanthro[4,5-abc]phenazine-11,12-dicarbonitrile.

1.5.6 Conclusion

As discussed in Section 1.5, red TADF emitters based on N-doped PAH acceptors have drawn much attention for efficient red OLEDs due to their ability to reduce nonradiative decay pathways. However, acceptors with smaller π -conjugation such as pyridine, quinoxaline, and acenaphtho[1,2-b]pyrazine, require the introduction of strong electron-withdrawing units like nitrile or fluorine to stabilize the singlet energy to obtain red emission. ANQDC-DMAC and ANQDC-MeFAC, which incorporate acenaphtho[1,2-b]-pyrazine as the acceptor, demonstrated impressive EQE_{max} values of 27.5 and 26.3%, respectively, at λ_{EL} at 615 nm and 614 nm. Larger π -conjugated acceptors like phenanthro[4,5-fgh]quinoxaline often led to higher ΔE_{ST} due to the larger LE content of the excited states. Among the N-PAH acceptors, dibenzo[a,c]phenazine stands out as a favorable choice due to its rigid, planar structure and strong electron-withdrawing ability, reflected in its deep LUMO. As for the donors, TPA, PXZ and DMAC are often used as these are relatively strongly electron donating and they adopt highly twisted conformations with respect to the acceptor, leading to small ΔE_{ST} values.

However, these examples illustrate the challenge in obtaining the desired deep-red emission and the devices showed significant efficiency roll-off. Thus, there is still a need for

emitters that address these deficiencies in device performance. Due to long excited-state lifetimes, the probability of biexponential non-radiative decay pathways like TTA and triplet-polaron quenching (TPQ) will increase, especially at high luminance where the triplet exciton density is high. Intermolecular interactions can adversely affect the efficiency and stability of the device, yet aggregates are one major way to access NIR emission in organic semiconductors. So, it is worth finding the balance of efficiency and red emission by controlling the intermolecular interaction.

1.6 The Development of TADF Emitters for Bioimaging

TADF emitters have also increasingly been used in bioimaging. This section will review the reported TADF compounds from design strategies, photophysical properties and their application in bioimaging. On the scale of individual cells, most living tissue is both optically transparent and has minimal intrinsic contrast (in refractive index or otherwise) between different cellular components. Bioimaging dyes and stains are therefore a frequently necessary tool for observing cell structures, offering the potential to visualize internal organelles and biological processes optically, and often without damaging the cell.^{156,157} While conventional fluorescent emitters are established as contrast agents in bioimaging, issues can arise as a result of the autofluorescence of cells. Autofluorescence is the emission from photoactive materials endogenous to the cell itself, which can mask the desired signal from the contrast bioimaging agent.¹⁵⁸ One strategy to overcome this issue is to employ phosphorescent emitters, as by virtue of their long-lived emission they can allow autofluorescence and phosphorescence to be distinguished in the time-domain. However, while phosphorescent metal complexes have the additional complication of potential toxicity,^{159–162} all-organic TADF materials can potentially also address autofluorescence with their suitably long-lived emission. The large Stokes shifts for D-A TADF materials can also potentially allow autofluorescence to be addressed and eliminated in the spectral domain. However, for both phosphorescent and TADF materials, quenching of triplet states and any delayed emission by physiological dissolved oxygen must also be carefully considered.

To date, there is a small but rapidly growing body of work in which organic TADF compounds have been developed for bioimaging applications, including for time-resolved luminescence imaging (TRLI) for living cells. Many TADF compounds can also emit in the red to NIR region, which is especially transparent to living tissue, even in bulk. These wavelengths are therefore advantageous for *in vivo* bio-imaging because of reduced photo-damage to the biological samples, greater deep tissue penetration allowing optical signal to emerge, and minimal interference from background (typically blue) autofluorescence from biomolecules in the living systems. In this section we will discuss recent examples of TADF emitters that have been used as bioimaging agents.

1.6.1 TADF Emitters Capped with Bovine/Human Serum Albumin

One strategy to circumvent the quenching of TADF emission by oxygen is to use either human serum albumin (HSA) or bovine serum albumin (BSA). Both contain tryptophan, which is a chromophoric amino acid that can react with singlet oxygen, preventing the quenching of the triplet excited states and thus the delayed fluorescence of emitters.¹⁶³ BSA has been used in living-cell imaging experiments to enhance the signal originating from the bioimaging agent and also to help cellular uptake by masking the hydrophobic TADF molecule and rendering the TADF-BSA assembly more hydrophilic,^{164,165} increasing their solubility and stability in aqueous media. In addition, BSA can also protect the emitters from degradation by cellular enzymes and improve their biological compatibility, making them less toxic to cells. In 2014,^{163,166} Xiong *et al.* were the first to propose a TADF emitter, **DCF-MPYM**, that was used in conjunction with BSA. This adduct was employed as the contrast agent in TRLI of MCF-7 cells, and showed long-lived luminescence ($\tau_{\text{PL}} = 22.11 \mu\text{s}$ in deaerated ethanol) at λ_{PL} of 649 nm with a small ΔE_{ST} (0.03 eV) in 5:4 MeOH:EtOH (v/v). The BSA protein provides a hydrophobic cavity and a reductive environment that shields the emitter from oxygen, thus permitting the long-lived delayed emission of **DCF-MPYM** to persist in the cells. TRLI of MCF-7 cancer cells using this contrast agent much stronger red luminescence signals and significantly suppressed background signal in time-resolved imaging mode, compared to equivalent images obtained in steady-state mode.

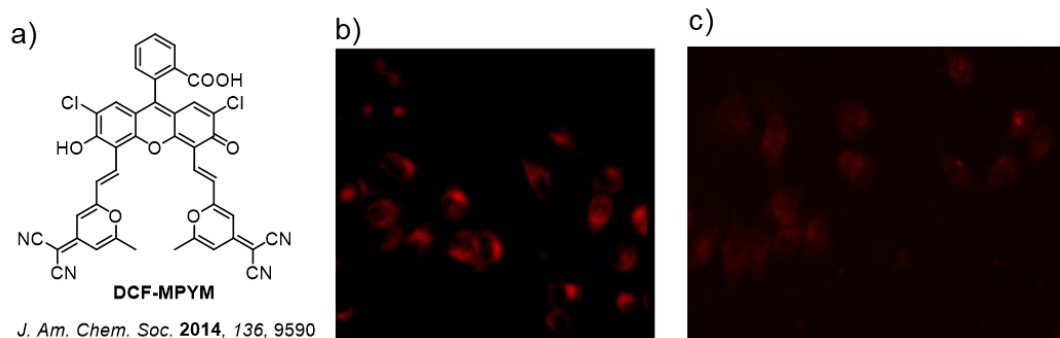


Figure 1.26. (a) Chemical structure of **DCF-MPYM**; b) time-resolved luminescence and (c) steady-state luminescence ($\lambda_{\text{exc}} = 510\text{--}560 \text{ nm}$) images of MCF-7 stained with **DCF-MPYM** (20 μM) and BSA (40 μL , 10 mM) at 37 $^{\circ}\text{C}$. Copyright 2014, American Chemical Society.¹⁶³

The same group later developed two derivatives of **DCF-MPYM** through the introduction of aromatic carbonyl groups, with the goal of enhancing the ISC process to increase the population of triplet excitons and the DF contribution to total emission by augmenting SOC (Figure 1.27).¹⁶⁷ Indeed, derivatives **DCF-MPYM-Ph** and **DCF-MPYM-Th** possess much longer τ_d of 31.29 μ s and 52.05 μ s, respectively, than that of **DCF-MPYM** ($\tau_d = 22.11 \mu$ s). With the assistance of HSA, these two emitters were also used in the TRLI of MCF-7 cells.¹⁶⁷

Another family of TADF emitters used as contrast agents through encapsulation with BSA include **BP-PXZ**, **BP-2PXZ**, **BP-PTZ**, and **BP-2PTZ** (Figure 1.27). These compounds reflect typical D-A TADF emitter designs developed for OLED applications, containing benzophenone (**BP**) as the acceptor (A) and **PXZ** or **PTZ** as donor. This motif also confers AIE properties to the molecule, especially active in aqueous environments.¹⁶⁸ **BP-2PXZ**, **BP-PXZ**, **BP-2PTZ**, and **BP-PTZ** in the neat films possess τ_d of 0.73, 0.96, 0.66 and 1.36 μ s at λ_{PL} of 558, 546, 551 and 544 nm, respectively. After their encapsulation within BSA, the obtained water-soluble nanoparticles demonstrated strong green or yellow luminescence, low cytotoxicity, and good performance in fluorescence lifetime imaging which provided a clear map of intracellular viscosity.¹⁶⁹

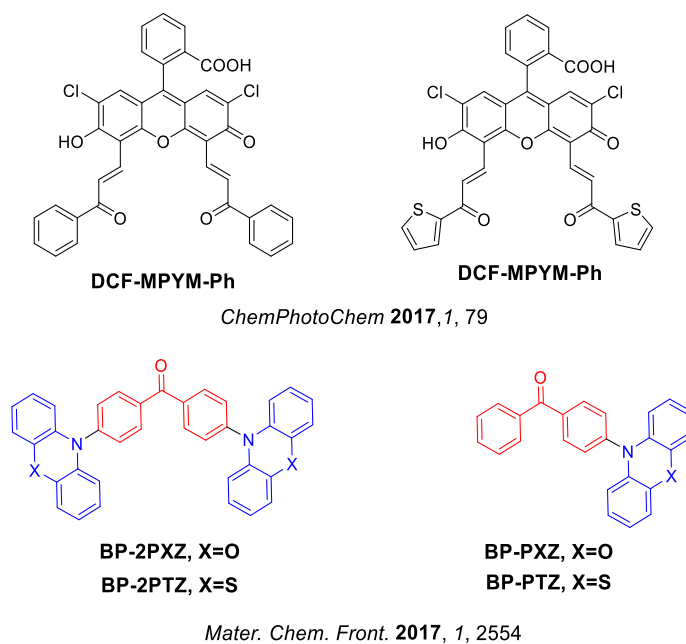


Figure 1.27. Chemical structures of organic TADF molecules used as imaging agents with the assistance of BSA/HSA.

1.6.2 Organic Dots

Organic dots (Odots) have emerged as a class of fluorescent nanoprobes for biological imaging as they are very bright, possess good photostability, do not blink, and are nontoxic.^{170–172} Currently, Odots have mainly been used in cell imaging, biosensing, drug and gene delivery, photothermal and photodynamic therapy, and two-photon-excited fluorescence imaging.^{173–175} However, these applications largely rely on the fluorescence intensity signals instead of their fluorescence lifetime.^{176,177} Odots based on TADF emitters would combine the merits of fluorescent Odots but also feature much longer-lived fluorescence suitable for time-domain microscopy.^{178–182}

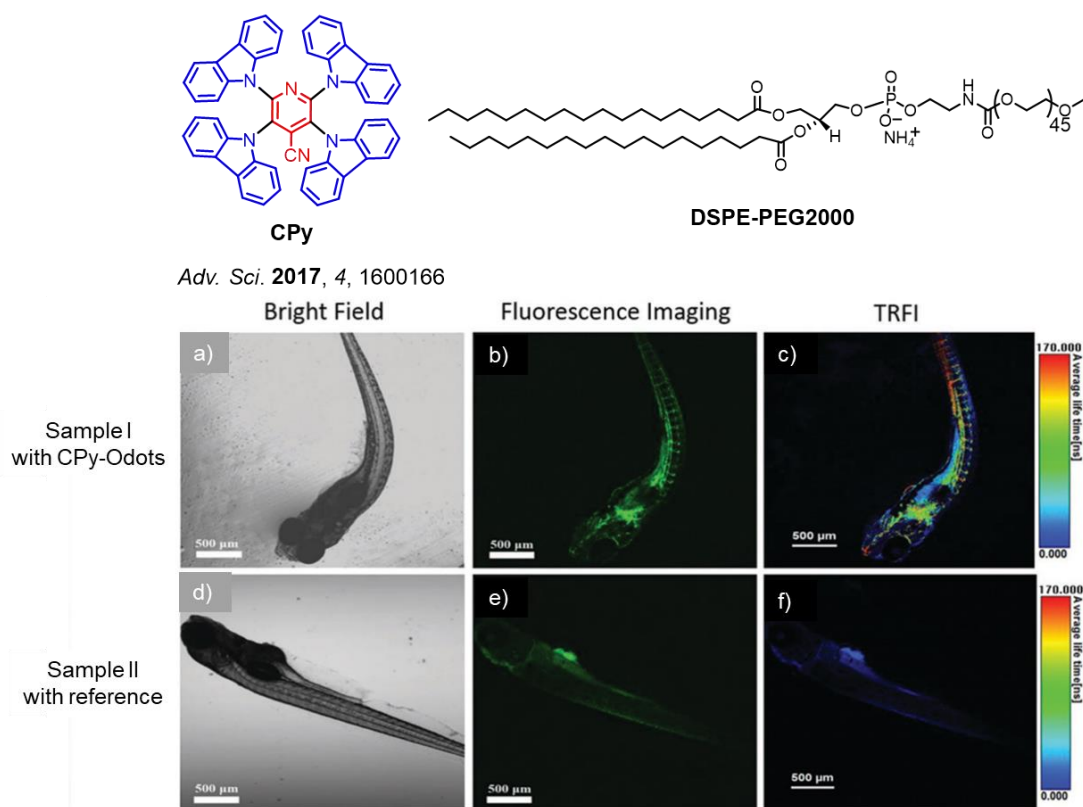


Figure 1.28. Top, chemical structure of CPy and DSPE-PEG2000; Bottom, confocal fluorescence images of zebrafish: (a–c) zebrafish injected with CPy-Odots; (d–f) zebrafish reference non-TADF Odots; Copyright 2017, Wiley-VCH²³

Li *et al.* fabricated CPy-based Odots (CPy-Odots) by encapsulating the high-performance TADF emitter CPy¹⁸³ into DSPE-PEG2000, an amphiphilic and biocompatible polymer that was chosen as the encapsulation matrix due to its ability to encapsulate small,

neutral, organic compounds (Figure 1.28).¹⁸⁴ The **CPy-Odots** are water-soluble and bright (Φ_{PL} of 38% in Milli-Q water), with a $\tau_{\text{d}} = 9.3 \mu\text{s}$ under ambient atmosphere. **CPy-Odots** were consequently employed in time-resolved and confocal fluorescence imaging of living HeLa cells and in living zebrafish. As shown in Figure 1.28, by comparing the images captured with fluorescence lifetime imaging microscopy (FLIM), the vivid green-to-red signals of the **CPy-Odots** were easily distinguished from the autofluorescence (bioluminescence) as the latter possesses a t_{PL} shorter than 3 ns ($\lambda_{\text{ex}} = 405 \text{ nm}$). This study demonstrated that **CPy-Odots** can be used as bright microangiography agents for FLIM in living zebrafish.²³

In addition to **CPy**, another well-known TADF emitter **4CzIPN** was reported to show two-photon absorption as an Odot in HeLa cells.¹⁸⁵ Odots of **4CzIPN** were formed upon encapsulation into PEG-*b*-PPG-*b*-PEG (Figure 1.29). This Odot material possessed a $\tau_{\text{d}} \approx 1.47 \mu\text{s}$ and has good biocompatibility and biodegradability, low toxicity, and shows specificity for uptake into malignant cells that were imaged by confocal fluorescence imaging in living cells. Ran and co-workers similarly prepared nanoprobe micelles by coating **Al-Cz** (Figure 1.29) in glucose-PEG2000-DSPE, which were then used for malignant cell imaging diagnosis. The Glucose-PEG2000-DSPE TADF micelles emitted at $\lambda_{\text{PL}} \sim 500 \text{ nm}$ and were nontoxic, biocompatible, and even biodegradable. They could be efficiently transported into the cancer cells by an over-expressed glucose transporter on the tumor cell membrane, and then once taken into the HepG2 tumor cells localized in the lysosome.

Xiao *et al.* prepared two TADF molecules, **PT** and **AT**, containing different electron-donating moieties to demonstrate a rational design of photosensitizers and fluorescence imaging agents, respectively. The proposed TADF emitters exhibit a tailored balance between two-photon singlet oxygen generation and fluorescence emission (Figure 1.29).^{186,187} **PT** possesses both a smaller calculated ΔE_{ST} of 0.06 eV and f of 0.03 compared to a larger calculated ΔE_{ST} of 0.1 eV and an f of 0.07 for **AT**. In a mixture of 1:99 THF:water, the Φ_{PL} of **PT** and **AT** were 2.2% and 9.1%, respectively, while in the corresponding neat thin films, the Φ_{PL} of **PT** and **AT** increased to 7.9% and 17%, respectively. In this study, DSPE-PEG2000 was employed to encapsulate **AT** and **PT** to produce nanoparticles (**PT NPs** and **AT NPs**) which improved both the stability and biocompatibility of **PT** and **AT** in aqueous environment. The cell studies further indicated that, in line with their contrasting DE_{ST} and F_{PL} values, the **PT**

NPs show much stronger singlet oxygen generation capability and photodynamic therapy (PDT) performance compared to the AT NPs, while the AT NPs produced a much brighter fluorescence image.³¹

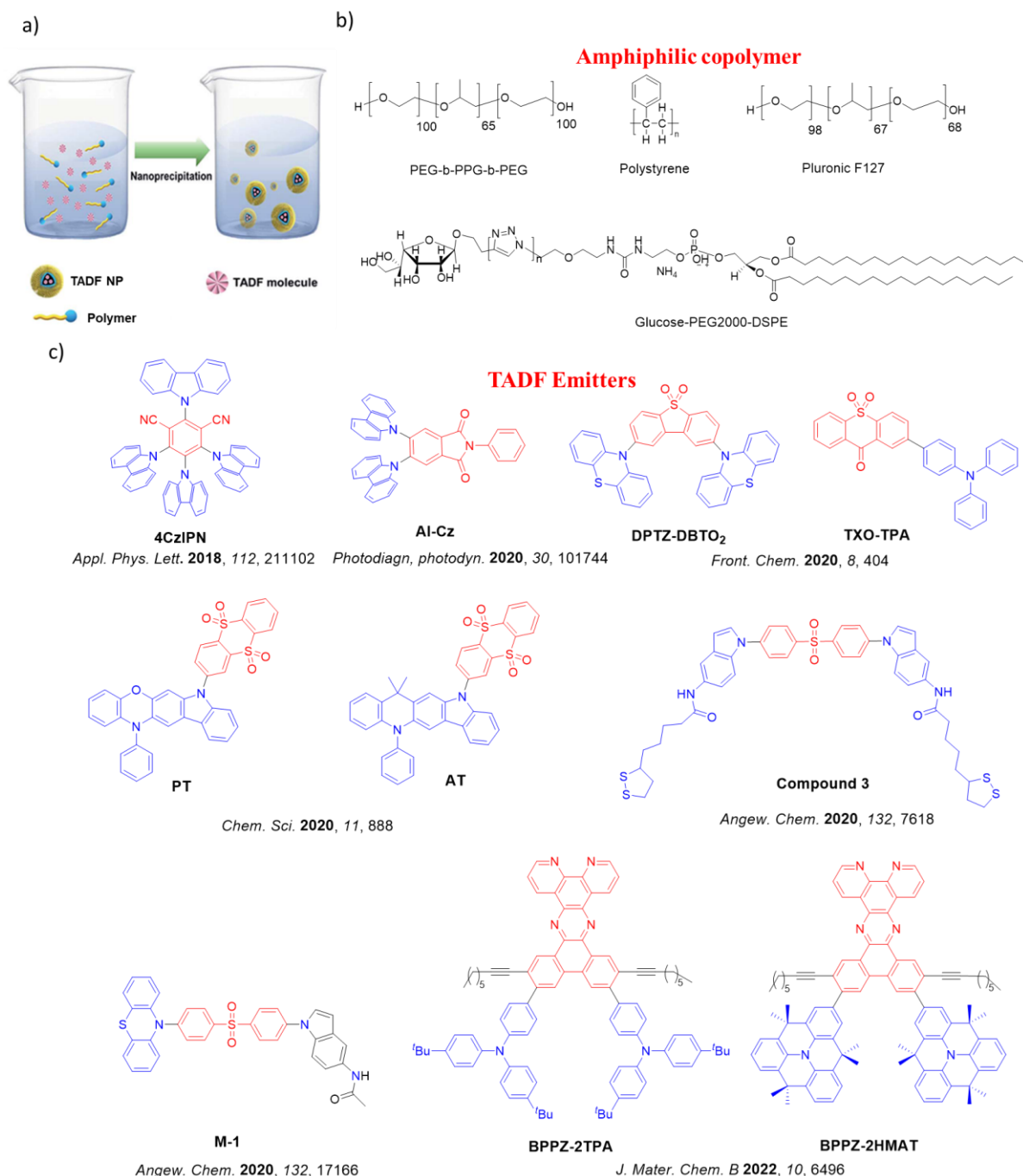


Figure 1.29 (a) Schematic illustration of the nanoprecipitation for nanoparticle preparation Copyright 2020, The Royal Society of Chemistry¹⁸⁶; (b) Chemical structures of amphiphilic copolymer and (c) organic TADF molecules used for fluorescence imaging applications.

Besides DSPE-PEG2000, polystyrene has also been used to encapsulate TADF emitters.

In one study **DPTZ-DBTO₂** and **TXO-TPA** (Figure 1.29) were encapsulated in order to conserve their photophysical properties as nanoparticles in biological media.¹⁸⁷ While for **DPTZ-DBTO₂** the effect of encapsulation on its photophysical properties was not significant (e.g. $\lambda_{\text{PL}} = 563$ nm and $\lambda_{\text{PL-NP}} = 556$ nm), for **TXO-TPA** the emission was markedly blue-shifted when the dye was incorporated in the nanomaterial (e.g. $\lambda_{\text{PL}} = 629$ nm and $\lambda_{\text{PL-NP}} = 555$ nm). Both NPs possessed microsecond-long $\tau_{\text{d}} = 2.89$ μs for **DPTZ-DBTO₂ NP** and $\tau_{\text{d}} = 9.56$ μs for **TXO-TPA**, respectively. The authors found that upon using amino-modified NPs the reagents could be more efficiently internalized with more uniform dispersion inside the cells.

Zhu and co-workers designed an asymmetric donor-acceptor-donor compound that showed dual TADF emission resulting from CT states from each of the phenothiazine and N-(1*H*-indole-5-yl) acetamide donors with the diphenylsulfone acceptor (Figure 1.29).¹⁸⁸ The two emission bands of **M-1** were at $\lambda_{\text{PL}} = 420$ nm and $\lambda_{\text{PL}} = 580$ nm, each showing distinct τ_{d} of 5.2 μs and 12.9 μs , respectively with a total Φ_{PL} of 20.1% in THF. Compound **M-1** was encapsulated within the amphiphilic block copolymer Pluronic F-127, and dispersion of **M-1** in the cell culture medium led to an enhanced average τ_{PL} of 33 μs and 36 μs , respectively, in the dual-channel luminescence imaging studies [the DAPI (4',6-diamidino-2-phenylindole) and FITC (*fluorescein isothiocyanate*) channels, dual-channel luminescence imaging here referring to capturing separate images from different spectral bands, usually blue (DAPI) and green (FITC)]. By calibrating the two time-resolved signals, serialized and integrated intracellular local imaging information could also be observed. The same group also designed a new TADF emitter based on an indole-derived D-A-D skeleton linked with long α -lipoic alkyl chains (Figure 1.29). Compound **3** exhibited blue emission at $\lambda_{\text{PL}} = 487$ nm with DF in both pure DMF ($\tau_{\text{PL}} = 1.4$ μs , Φ_{PL} of 35.3%) and DMF:H₂O 1:99 mixtures ($\tau_{\text{PL}} = 3.6$ μs , Φ_{PL} of 30.8%). Both the aggregates of Compound **3** and NPs formed by encapsulation into Pluronic F-127 were investigated as imaging reagents by TRLI, which demonstrated that the dual emission was conserved in the cells.¹⁸⁹

Moving away from emitters in non-doped aggregated states, Tsuchiya *et al.* recently reported an alternative strategy where the Odot is composed of an emitter (**4CZIPN**), a host (mCP) and a surfactant (DSPE-PEG2k).²⁵ This design mitigates possible aggregation-caused quenching (ACQ) by effectively diluting the emitter within the micelle in an analogous manner

to the emissive layers in OLEDs. These Odots showed near unity Φ_{PL} of 94% and an associated τ_{d} of 3.1 μs under air-free conditions in water. The conditions and ratios involved in the preparation of the Odots affected the properties, where oxygen-free processing gave Odots with higher Φ_{PL} and greater photostability. Further, upon using a host to surfactant ratio of 10:1, the best photostability was achieved, with photo-degradation causing emission to drop to 50% of the initial intensity after 360 mins, which was superior to a reference blue quantum dot sample. Once the Odot is formed, the photophysics was observed to be insensitive to external oxygen. HEK293 cell imaging was demonstrated and the Odots remained stable for at least 7 days after uptake into the cells (Figure 1.30).²⁵

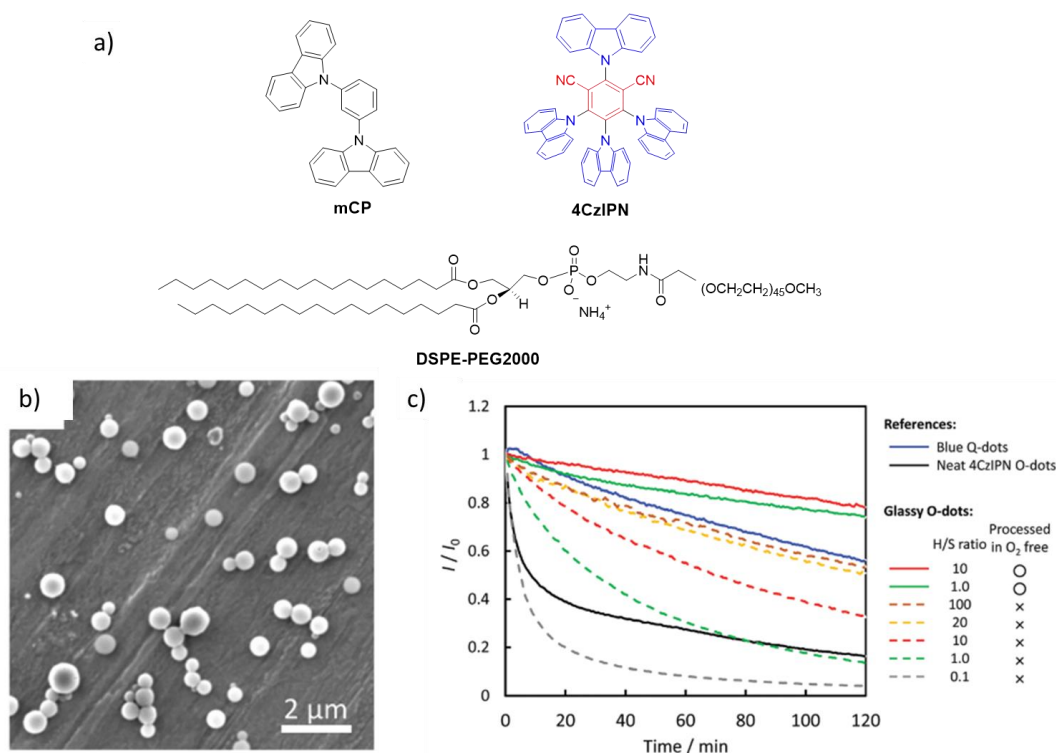


Figure 1.30. (a) Chemical structures of materials for Odot preparation, (b) SEM images of 6 wt% 4CzIPN/mCP glassy Odots; (c) Photo-degradation properties of 6 wt% 4CzIPN/mCP glassy Odots under various preparation conditions, neat 4CzIPN Odots and blue Qdots in water (air saturated); the monitored emission wavelengths were $\lambda_{\text{PL}} = 515, 548$ and 450 nm, respectively; $\lambda_{\text{ex}} = 300\text{--}400$ nm; excitation light intensity 5mWcm^{-2} . Copyright 2019, The Royal Society of Chemistry.²⁵

Using a similar methodology as Tsuchiya and co-workers, Hudson and co-workers

developed two TADF emitters, **BPPZ-2TPA** and **BPPZ-2HMAT** (Figure 1.31).¹⁹¹ Based on a rigid and strongly electron-withdrawing dibenzo[a,c]dipyrido[3,2-h:20-30-j]phenazine-12-yl (BPPZ) motif, they demonstrated two approaches for the encapsulation of these emitters to yield water-dispersible nanoparticles suitable for TRLI.¹⁹¹ Although Odots prepared with the undoped emitters did not show long-lived emission, their prompt fluorescence lifetimes were long, ranging from 8.5 to 11.9 ns in aqueous solution. Glassy organic nanoparticles (g-Odots) were also prepared with 5 wt% doped emitters in mCP surrounded by the amphiphilic polymer DSPE-PEG2000. The g-Odots by contrast showed long-lived emission in aerated aqueous solutions, with t_{PL} of 123 ms for **TPA g-Odots**, and 85 ms for **HMAT g-Odots**. Both approaches yielded nanoparticles suitable for imaging of human cervical (HeLa) and liver (HepG2) cancer cell lines.

Hudson and co-workers also explored other g-Odots based on heptazine-type TADF emitters (Figure 1.31). In this study three s-heptazine TADF materials, **HAP-3Cz**, **HAP-3MeOTPA**, and **HAP-3MeOCz**, showed green to deep-red emission ($\lambda_{PL} = 525\text{--}664$ nm) and variable Φ_{PL} ($\Phi_{PL} = 73\%$ for 2 wt% **HAP-3Cz**, 33% for 2 wt% **HAP-3MeOTPA**, and 7% for 2 wt% **HAP-3MeOCz** in *poly*-mCP).¹⁹⁰ For **HAP-3MeOCz** and **HAP-3Cz**, the g-Odots synthesized in air showed both shorter emission lifetimes and substantially lower Φ_{PL} values (30–41%) relative to those synthesized under nitrogen ($\Phi_{PL} = 99\text{--}100\%$). By contrast, unity F_{PL} was observed for the **HAP-3MeOTPA** g-Odots for samples synthesized both under air and under nitrogen. Similar delayed fluorescence lifetimes were observed for the **HAP-3MeOTPA** (50 μ s under air, 52 μ s under nitrogen) and **HAP-3Cz** g-Odots (1.1 μ s under air, 1.2 μ s under nitrogen), but no delayed fluorescence was observed for **HAP-3MeOCz** g-Odots. These g-Odots were then used as biological imaging probes of immortalized human kidney cancer (HEK293) cells, and both for single- and multi-photon excited microscopy coupled with time-gated luminescence measurements (Figure 1.31). This work therefore not only described new routes to efficient heptazine-based TADF materials, but also demonstrated their potential as nanoparticle-based bioimaging probes.

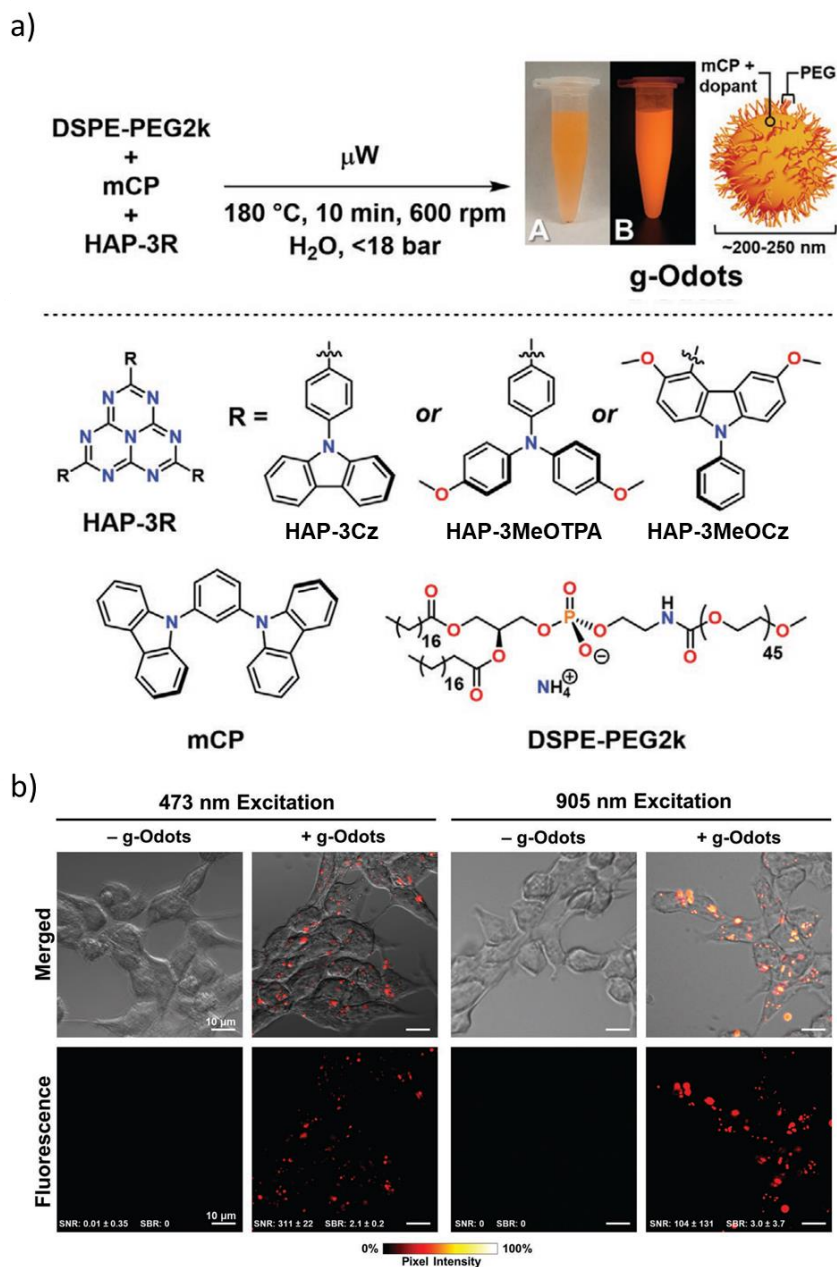


Figure 1.31. (a) Synthesis of g-Odots with examples of isolated nanoparticle suspensions shown for dopant **HAP-3MeOTPA**, where A is photographed under ambient room lighting, and B under 365 nm irradiation. μW = microwave irradiation;))) = ultrasonication. (b) Single-photon excitation ($\lambda_{exc} = 473$ nm, $\lambda_{em} = 485$ – 545 nm) and multi-photon excitation ($\lambda_{exc} = 905$ nm, $\lambda_{em} = 575$ – 630 nm) of HEK293 cells incubated with **HAP-3MeOTPA** g-Odots (+g-Odots) for 24 h. Corresponding control samples (-g-Odots) are shown as well. SNR and SBR calculated with $N = 8$ cells for 473 nm excitation samples, and $N = 22$ cells for 905 nm excitation samples. Copyright 2022, Wiley-VCH GmbH.¹⁹⁰

Hudson and co-workers also reported two boron difluoride curcuminoid (BFC)-based polymers, **CzBN-co-DtaB** and **CzBN-co-HmatB** (Figure 1.32), exhibiting TADF in the deep red/NIR region with λ_{PL} of 694 nm and 717 nm in toluene, respectively.¹⁹² **CzBN-co-DtaB** and **CzBN-co-HmatB** showed τ_{d} of 4.7 and 5.2 μs and Φ_{PL} of 18% and 12%, respectively, in the solid state. Both polymers were incorporated into water-soluble Odots using the amphiphilic polymer poly(styrene-co-maleic anhydride) [PSMA; PS11-co-MA6] that had an average diameter of 65 nm and 58 nm for the Odots with **CzBN-co-DtaB** and **CzBN-co-HmatB**, respectively. There was only a small red-shift in the emission noted for the Odots compared to the neat films (λ_{PL} =730 and 752 nm and 731 and 764 nm in the neat film and in the Odots for **CzBN-co-DtaB** and **CzBN-co-HmatB**, respectively), while the delayed lifetimes were considerably shortened compared to those in the solid state, with τ_{d} of 0.86 μs and 0.95 μs , respectively. These Odots were used in specific extracellular immunolabeling experiments with human SK-BR3 cells and showed nonspecific binding. Using a similar experimental design strategy, Hsu *et al.* prepared several types of NIR-II emissive Odots using polymer TADF emitters, with a **DMAC-TRZ** derivative as a TADF monomer and 3-alkoxy-substituted thiophene as conjugated linker, encapsulated within amphiphilic lipids (Figure 1.32).¹⁹³ These Odots exhibited λ_{PL} of 1064–1100 nm and Φ_{PL} of 0.40–1.58% in aqueous solution, a significant departure from the typical properties of the **DMAC-TRZ** monomer. Although no delayed fluorescence was detected for these Odots, they were nonetheless used successfully in *in vivo* whole-body vascular imaging and 3D bond mapping.

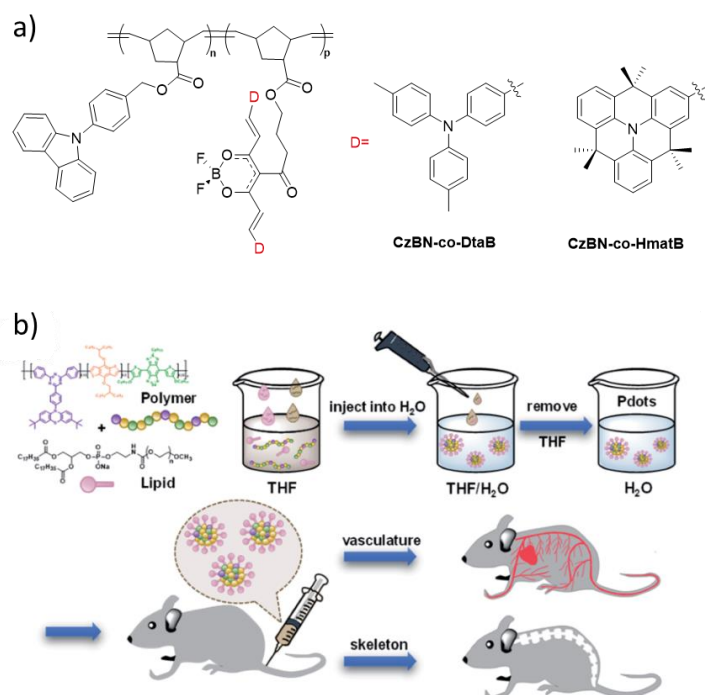


Figure 1.32. (a) Chemical structures of **CzBN-co-DtaB** and **CzBN-co-HmatB**; (b) Schematic diagram representing the preparation of lipid- encapsulated Odots for *in vivo* vascular and bone imaging. Copyright 2022, Royal Society of Chemistry.¹⁹³

Besides using amphiphilic molecules or polymers to encapsulate luminophores, amphiphilic peptides have also been used as a delivery vector in the construction of NPs containing TADF emitters. Zhu *et al.* reported the use of the amphiphilic cell-penetrating peptide (CPP), [F₆G₆(rR)₃R₂] (Figure 1.33), to transport hydrophobic fluorophores across cellular barriers.¹⁸¹ Three known TADF molecules, **4CzIPN**, **NAI-DPAC**, and **BTZ-DMAC**, were incorporated in well-dispersed nanoparticles (NPs) employing CPP in aqueous solution. The CPP-functionalized NPs of **4CzIPN**, **NAI-DPAC**, and **BTZ-DMAC** showed much lower Φ_{PL} of 12%, 2.5% and 0.8% in aqueous solution at λ_{PL} of 555, 607, and 657 nm, respectively, compared to that observed for the emitters in dilute toluene or doped thin films [(**4CzIPN**: $\lambda_{\text{PL}} = 507$ nm, $\Phi_{\text{PL}} = 94\%$),⁴⁸ (**NAI-DPAC**: $\lambda_{\text{PL}} = 570$ nm, $\Phi_{\text{PL}} = 94\%$ in 6 wt% doped into mCPCN film),¹⁹⁴ [(**BTZ-DMAC**: $\lambda_{\text{PL}} = 638$ nm, $\Phi_{\text{PL}} = 56\%$ in 3 wt% doped CBP film)¹⁹⁵]. These three NPs still maintained long-lived luminescence with τ_{d} of 1.8, 6.1 and 31.0 μs for the NPs based on **4CzIPN**, **NAI-DPAC**, and **BTZ-DMAC**, respectively. The low cytotoxicity and high cytomembrane permeability of the NPs enabled them to be exploited for TRLI of living

cells. These findings expanded the applications of cell-penetrating peptides for delivery of molecules and NPs using only noncovalent interactions.

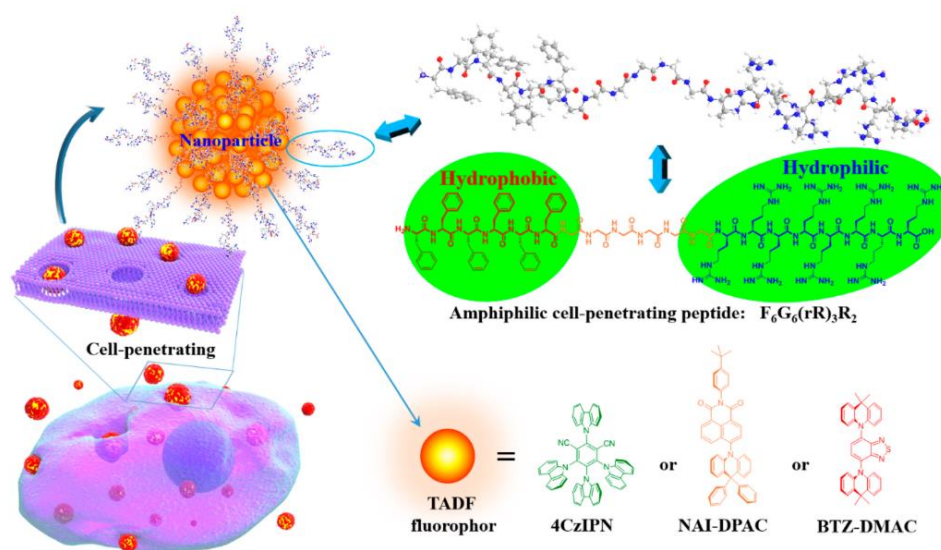


Figure 1.33. Schematic illustration showing the cell-penetrating NPs assembled from the amphiphilic peptide [F6G6(rR)3R2] and TADF molecules. Copyright 2018, American Chemical Society.¹⁸¹

1.6.3 Silica Nanoparticles

Silica-based nanoparticles (SiNPs) have been extensively used as delivery vectors of conventional fluorescent dyes in optical imaging and sensing applications. Avó *et al.* described a method for producing TADF emitter-doped SiNPs that conserve their delayed luminescence in aqueous media. SiNPs (Figure 1.34a) were prepared using a modified Stöber process from tetraethoxysilane and Compound **3** in water.¹⁹⁶ The SiNPs emitted at ca. 585 nm and with a τ_d of 1.20 ms and a Φ_{PL} of 6% in H₂O. To address the low Φ_{PL} of the SiNPs, a modified silica source bearing small PEG chains was prepared. The Φ_{PL} of PEG-SiNPs was higher at 20% and these SiNPs possess a longer τ_d of 1.25 ms, but with an accompanied red-shift in the λ_{PL} to 610 nm. The TADF PEG-SiNPs were effectively internalized by human cells, even at low incubation concentration, localizing primarily in the cytosol and enabling fluorescence microscopy imaging at low dye concentrations.¹⁹⁷ Mo *et al.* encapsulated fluorine and nitrogen co-doped carbon dots (FCDs, NCDs) within amorphous silica using a sol-gel method to obtain TADF materials in aqueous solution (F, NCDs@SiO₂).¹⁹⁸ The presence of a hydrogen

bond network between the CDs and the amorphous silica contributed to reducing non-radiative transitions and producing a long-lived afterglow. The **F, NCDs@SiO₂** had a ΔE_{ST} of 0.32 eV, a high Φ_{PL} of 58.8%, and a $\tau_d = 0.48$ s. This versatile material was used separately in optical information encryption, temperature monitoring, and TRLI studies.

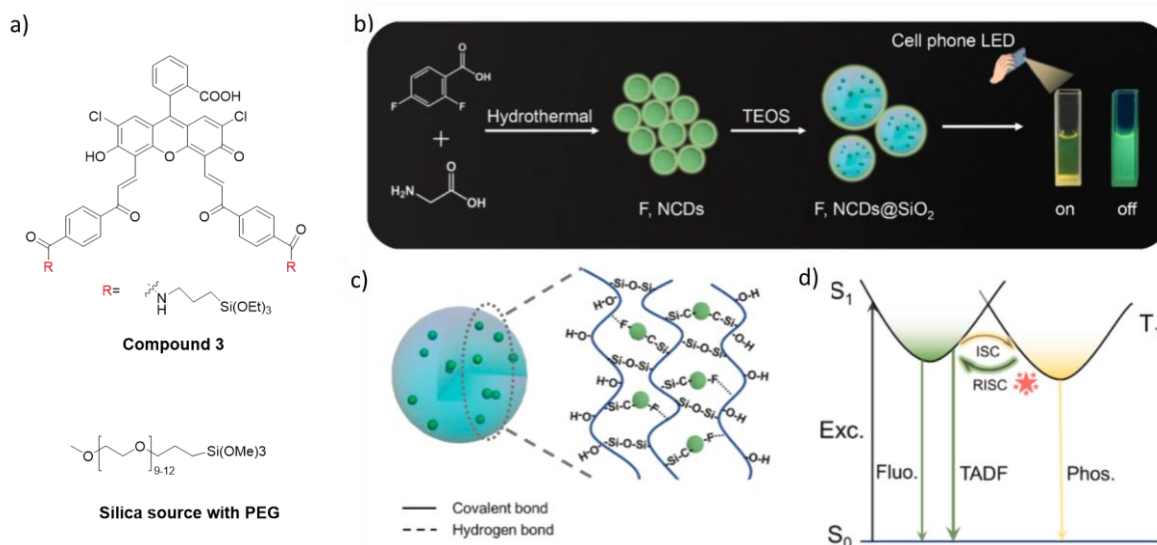


Figure 1.34. a) Chemical structures of materials for Odot preparation; b) Schematic illustration of the preparation procedure for **F, NCDs@SiO₂** and the photographs of **F, NCDs@SiO₂** in aqueous solution after LED excitation; c) Schematic illustration of the possible structural formation; d) delayed fluorescence mechanism of **F, NCDs@SiO₂**. Copyright 2021 Elsevier B.V.¹⁹⁸

1.6.4 Self-Assembled Nanoparticles

Small-molecule fluorescent organic nanoprobe (FONs) have emerged as promising competitors to inorganic semiconductor quantum dots and fluorescent polymer dots in terms of their wide structural variability, low toxicity, and good biodegradability.^{175,199–201} Self-assembled water-dispersible TADF nanostructures based on three known TADF emitters (**2CzPN**, **4CzIPN**, and **4CzIPN-Ph**) were reported by Lee *et al.* that relied on the limited water solubility of these compounds to form the nanostructures (Figure 1.35).²⁰² The FONs were made by self-assembly of each of these three TADF emitters into water dispersible NPs/nanorods (NRs), with sizes ranging from 80 to 200 nm. Under nitrogen environment the reference λ_{PL} (and Φ_{PL} and τ_d) of **2CzPN**, **4CzIPN**, and **4CzIPN-Ph** in toluene solutions are

$\lambda_{\text{PL}} = 473 \text{ nm}$ ($\Phi_{\text{PL}} = 21.5\%$; $\tau_{\text{d}} = 166 \text{ ms}$), 507 nm ($\Phi_{\text{PL}} = 33.5\%$; $\tau_{\text{d}} = 5.1 \text{ ms}$), and 577 nm ($\Phi_{\text{PL}} = 6.6\%$; $\tau_{\text{d}} = 1.1 \text{ ms}$), respectively.

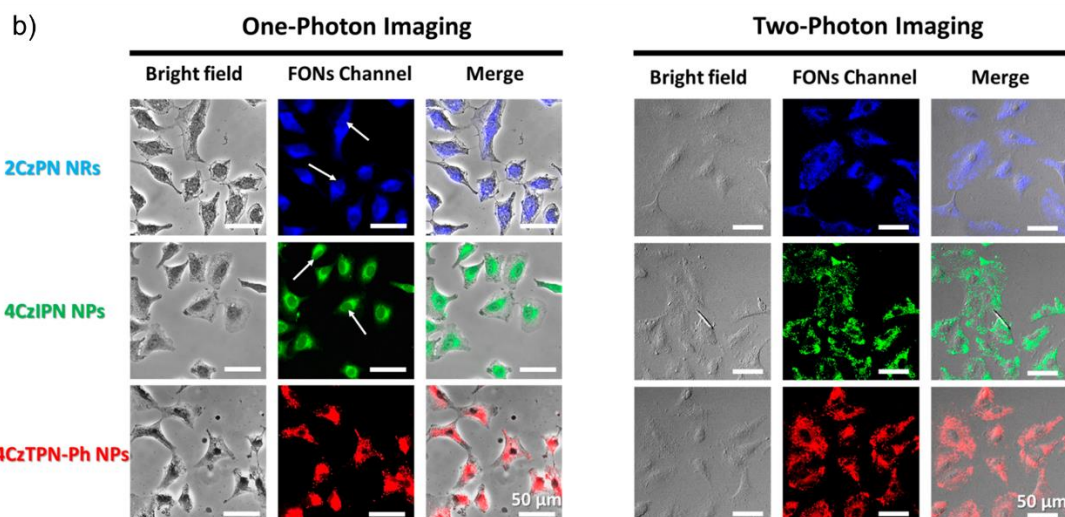
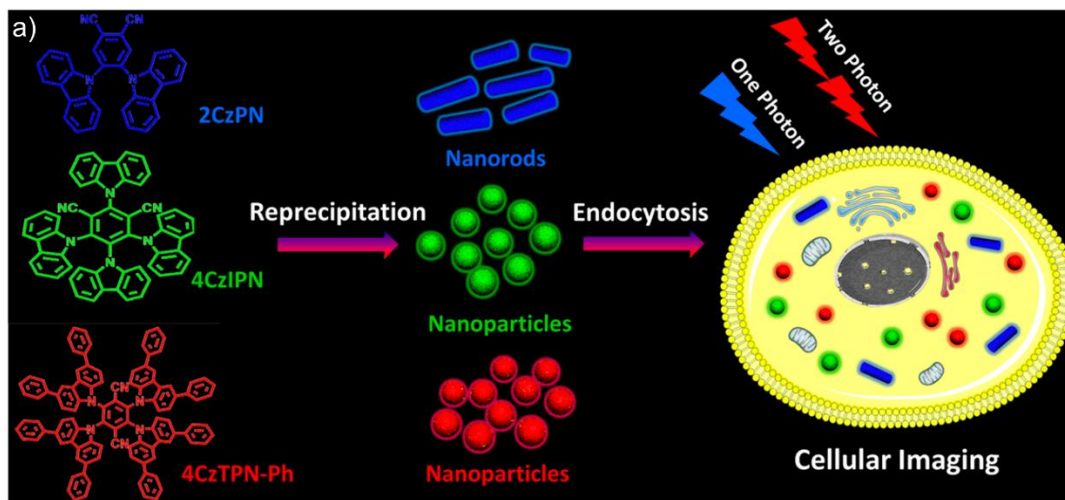


Figure 1.35. (a) Schematic illustration of the preparation of blue/green/red FONs by a reprecipitation method for one- and two-photon cellular imaging; (b) Cellular imaging and localization of the three FONs, monitored with a fluorescence microscope (one-photon λ_{exc} : 380–420 nm) and a laser scanning confocal fluorescence microscope (two-photon λ_{exc} : 800 nm) in an A549 cell (final concentration: 8 $\mu\text{g}/\text{mL}$): left column bright-field channel; middle column FON channel; right column overlay of the bright and FON images. The scale bar is 50 μm . Copyright 2016, American Chemical Society.²⁰²

All three FONs showed a slight red-shift in their λ_{PL} compared to those in toluene ($\lambda_{\text{PL}} = 503 \text{ nm}$ for 2CzPN NRs, $\lambda_{\text{PL}} = 518 \text{ nm}$ for 4CzIPN NPs and $\lambda_{\text{PL}} = 588 \text{ nm}$ for 4CzTPN-Ph NPs) coupled with a slight decrease of their respective Φ_{PL} ($\Phi_{\text{PL}} = 19.4\%$ for 2CzPN NRs,

$\Phi_{\text{PL}} = 11.9\%$ for **4CzIPN NPs** and $\Phi_{\text{PL}} = 3.6\%$ for **4CzTPN-Ph NPs**). In order to evaluate the imaging capabilities of the three FONs, one- and two-photon fluorescence images were obtained in an A549 cell using fluorescence microscopy and laser scanning confocal fluorescence, respectively. Figure 1.35b shows the strong cytoplasmic blue, green, and red fluorescence signals from the **2CzPN**, **4CzIPN**, and **4CzTPN-Ph** nanoprobe, respectively. Two-photon fluorescence imaging for FONs showed greater cytoplasmic details and no fluorescence signal from the nucleus, indicating that the FONs do not penetrate into the cell nucleus. These results suggest that self-assembled nanostructures of carbazole-containing TADF emitters are also promising high-performance fluorescence probes for bioimaging.²⁰²

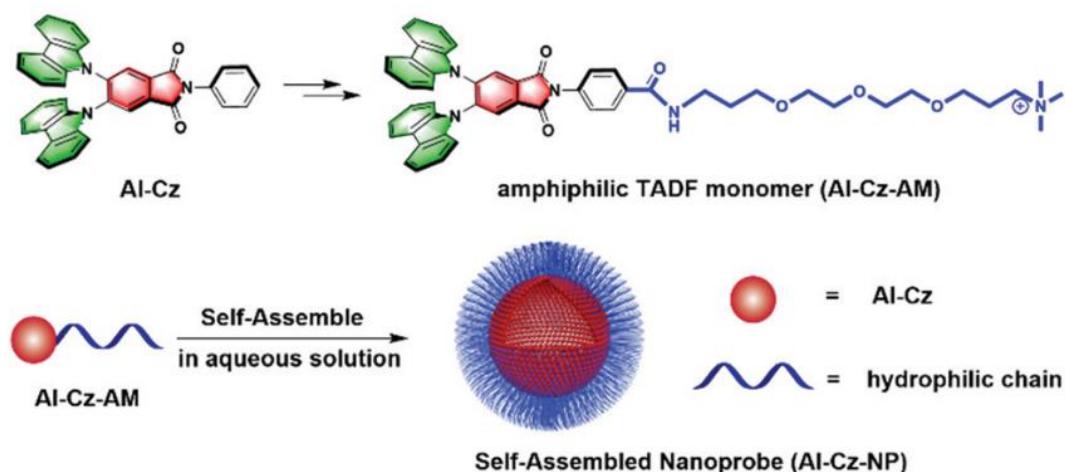


Figure 1.36. Chemical structure of the amphiphilic TADF monomer (**AI-Cz-AM**) based on **AI-Cz** and the design of the single component self-assembled TADF nanoprobe **AI-Cz-NP**. Copyright 2020 Royal Society of Chemistry.²⁰³

Another reported self-assembled TADF amphiphilic monomer (**AI-Cz-AM**) is based on the coupling of the lipophilic aromatic imide-based TADF emitter (**AI-Cz**) with a hydrophilic chain containing a positively charged ammonium terminus.²⁰³ Its amphiphilic nature allowed this TADF monomer to spontaneously form a water-soluble and biocompatible nanoprobe, **AI-Cz-NP** (Figure 1.36). The λ_{PL} of **AI-Cz-AM** and **AI-Cz-NP** were nearly identical at 517 and 514 nm, and the two materials had moderately small and similar ΔE_{ST} values of 0.10 and 0.12 eV although with very low Φ_{PL} of 1.36% and 0.94%, respectively. Interestingly, the τ_{d} increased from 6.08 μs for **AI-Cz-AM** in degassed THF to 10.68 μs for **AI-Cz-NP** in oxygenic aqueous solution, indicating significant resistance to ambient oxygen

quenching. The latter material was subsequently used in FLIM studies of HepG2 cells where long-lived fluorescence signals lasting about 15 μ s were detected. This study illustrated how a self-assembly strategy could be used to effectively eliminate emission quenching by oxygen in living cells, without the need for either a polymerization step or biooligomer encapsulation.

1.6.5 Aggregation-induced Delayed Fluorescence

One strategy to bypass the oxygen sensitivity of delayed fluorescence in TADF emitters is to use aggregated states. The quenching of emission by oxygen can be suppressed due to its limited ability to make physical contact with the emitter in the aggregated state, as demonstrated in some of the previous examples (Figure 1.29).²⁰⁴ ACQ often takes place in TADF emitters in their aggregated states though, which would be detrimental for bioimaging applications. Therefore, emitters that enjoy AIE instead of suffering from ACQ (Figure 1.37a) are viewed as particularly advantageous. For example, the known AIDF emitter **TXO** was encapsulated in the amphiphilic polymer PEG-*b*-PPG-*b*-PEG.²⁰¹ As shown in Figure 1.37b, **TXO NPs** can readily enter the cytoplasm and exhibit strong red emission by two-photon confocal fluorescence imaging. The two-photon FLIM of **TXO NPs** revealed localization in the cytoplasm, where the lifetime of the **TXO NPs** was distributed over a range from ~2.8 to 3.8 ns. Furthermore, **TXO NPs** were used for *in vivo* two-photon FLIM of living zebrafish.²⁰¹

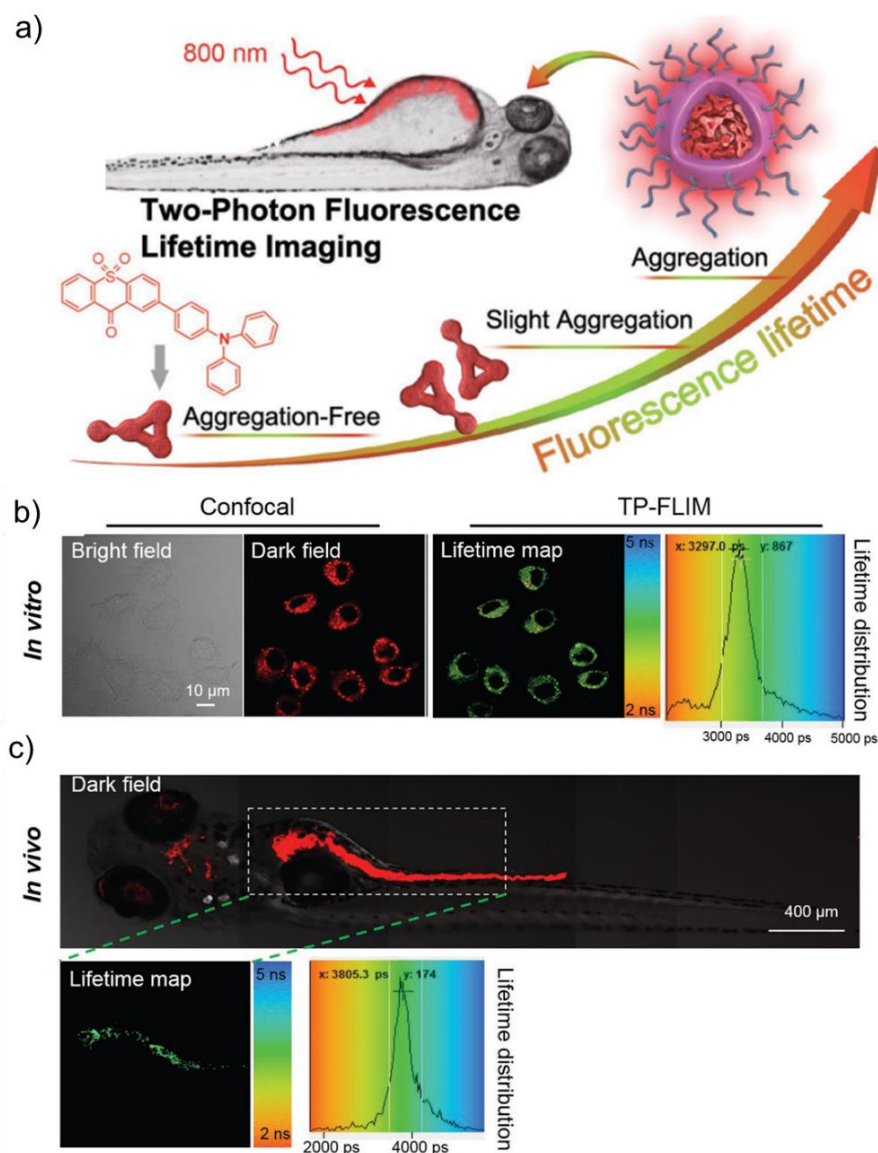


Figure 1.37. (a) Schematic illustration for maximizing aggregation of organic fluorophores to prolong fluorescence lifetime for two-photon FLIM; (b) *In vitro* two-photon confocal fluorescence imaging and two-photon FLIM of HepG2 cells stained with **TXO NPs** ($10 \mu\text{g mL}^{-1}$) after 2 h incubation. Using $\lambda_{\text{exc}} = 760 \text{ nm}$ the fluorescence was recorded between 600–650 nm. (c) *In vivo* two-photon confocal fluorescence imaging and two-photon FLIM of zebrafish stained with **TXO NPs** ($10 \mu\text{g mL}^{-1}$) after 4 h incubation. The $\lambda_{\text{exc}} = 760 \text{ nm}$, and fluorescence emissions were recorded 600–650 nm. Copyright 2018, WILEY-VCH.²⁰¹

Qi *et al.* reported the use of three AIDF emitters, **PXZ-NI**, **PTZ-NI** and lysosome-targeting **Lyso-PXZ-NI** (Figure 1.38), each based on a 1,8-naphthalimide (NI) acceptor.²⁰⁵ The τ_{d} of the 10 wt% PMMA films of **PXZ-NI**, **PTZ-NI**, and **Lyso-PXZ-NI** were 1.0, 1.7, and 1.3

μs , respectively. In aqueous solutions that produced the aggregated form, all three TADF materials demonstrated markedly enhanced delayed fluorescence when concentrations were increased. Subsequently, confocal fluorescence and lifetime imaging studies were performed using laser scanning microscopy and time-resolved fluorescence microscopy. The confocal fluorescence and lifetime images of HeLa cells after incubation with **PXZ-NI**, **PTZ-NI**, and **Lyso-PXZ-NI** for 2 h were captured and exhibited not only strong red fluorescence signals but also long fluorescence lifetime signals in the HeLa cells. In another report, Xu and co-workers presented two phosphine oxide-decorated TADF molecules, **CzPOTCF** and **tBCzPOTCF** (Figure 1.38).²⁰⁶ **CzPOTCF** and **tBCzPOTCF** in neat films exhibited red emission with $\lambda_{\text{PL}} = 634$ and 647 nm, small ΔE_{ST} values of 0.05 and 0.07 eV, moderate Φ_{PL} of 24.5% and 32.7%, and τ_{d} of 8.95 and 8.69 μs , respectively. Steady-state and time-resolved luminescence imaging of HeLa cells was demonstrated using these emitters in their aggregated form. The delayed lifetimes were slightly shortened compared to the neat films at $\tau_{\text{d}} = 6.69$ and 7.41 μs for **CzPOTCF** and **tBCzPOTCF**, respectively, yet nonetheless leading to high signal-to-noise ratios in the microscopy applications.

Sarkar *et al.* reported the first example of a TADF material that is not a D-A structure but rather an oligothiophene derivative, Compound **1** (Figure 1.38).²⁰⁷ In DMSO solution the compound acts as a conventional fluorophore, however in a DMSO/H₂O mixture the emitter aggregates exhibiting AIDF at $\lambda_{\text{PL}} = 600$ nm ($\tau_{\text{PL}} = 4.2$ μs and 8.0 μs , $\Phi_{\text{PL}} = 11\%$). Time-dependent luminescence imaging and cytotoxicity studies of Compound **1** were carried out in HeLa cells, showing low cytotoxicity to the cells and excellent signal-to-noise ratios.

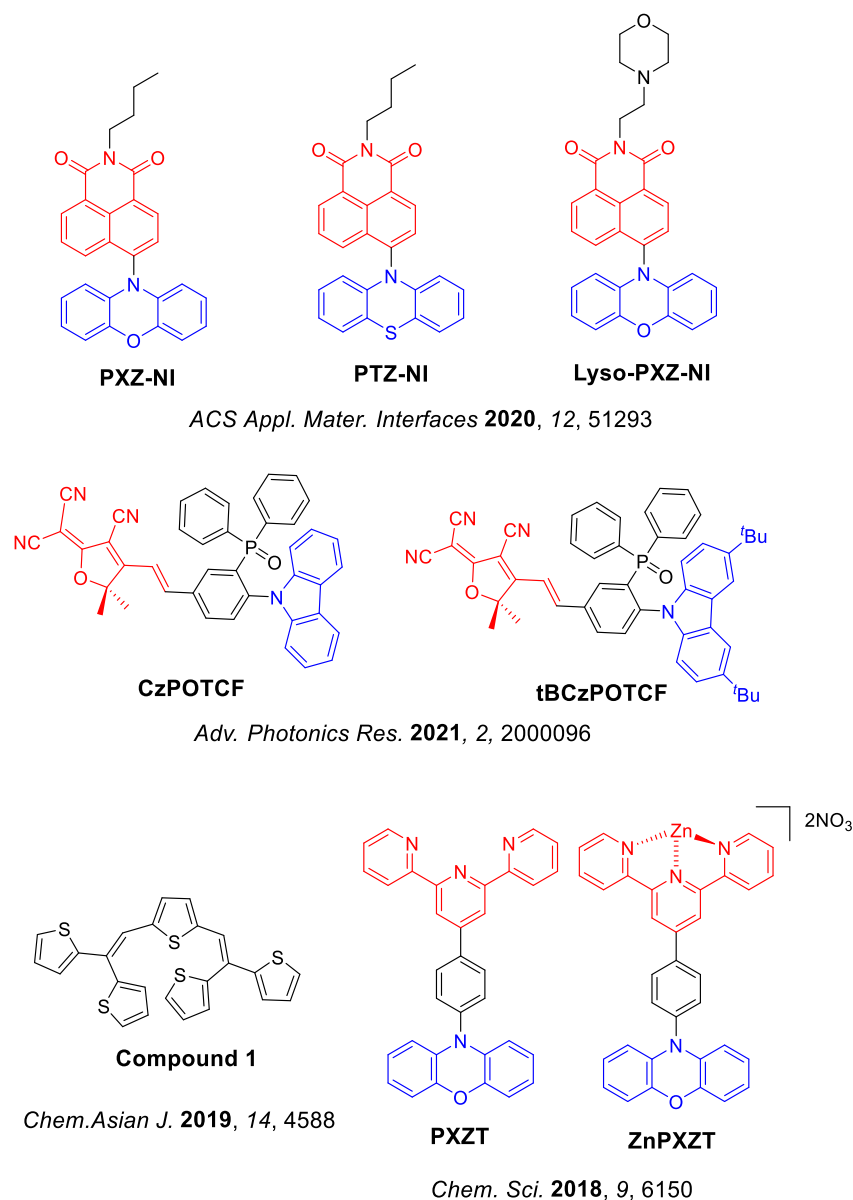


Figure 1.38. Chemical structures of organic TADF molecules with aggregation-induced delayed fluorescence used for microscopy applications.

Instead of preparing aggregates before entry into cells as described in the previous examples, Ni *et al.* proposed a strategy where aggregates would only form within the cells. With an increase of the water content in THF/water mixtures, the lifetimes and the fraction of delayed emission contribution both increased for **PXZT** (Figure 1.38), demonstrating AIDF.²⁰⁸ In 20 wt% PMMA films, **PXZT** likewise showed a long-lived emission with a τ_d of 1.4 μs . However, as with most organic TADF emitters this compound was insoluble in water, which limits its applications to biological microscopy. Incorporation of $[\text{Zn}(\text{NO}_3)_2]^{4+}$ resulted in the formation of a water-soluble complex, although the emission was also quenched. It was

proposed that once in the cell the complex becomes kinetically labile and the zinc ions dissociate when the complex is close to a channel or protein that acts upon zinc. Dissociation of the metal complex thus leads to precipitation of the ligand, and the formation of TADF aggregates which can then be visualized. When the compound was added to HeLa cells and allowed to incubate for 5 hours TADF could indeed be observed, suggesting zinc complex dissociation. The same method was then used for detection of chelating ligand EDTA, as EDTA complexes strongly with zinc leading to dissociation of the zinc from the TADF complex and turning on that ligand's own TADF.

1.6.6 Others TADF Bioimaging Reagents

Another strategy to render small molecule TADF emitters biocompatible for imaging studies is to develop hydrophilic TADF luminophores, which can be achieved through the introduction of a hydrophilic group.^{209,210} Ni *et al.*, for instance, designed a hydrophilic TADF luminophore (**NID-TPP**) by introducing a triphenylphosphonium (TPP⁺) group onto 6-(9,9-dimethylacridin-10(9*H*)-yl)-2-phenyl-1*H*-benzo[*de*]isoquinoline-1,3(2*H*)-dione (**NID**), Figure 1.39. The pristine **NID** exhibits TADF with an emission at λ_{PL} of 610 nm, a small ΔE_{ST} of 0.03 eV, and a τ_{d} of 5.58 μs in toluene. **NID-TPP** possesses the same ΔE_{ST} value of 0.03 eV, but with a shorter τ_{d} of 902 ns in the solid state. The Φ_{PL} of the **NID-TPP** is 0.015% in aqueous solution; however, a 40-fold enhancement was observed ($\Phi_{\text{PL}} = 0.6\%$) upon addition of sodium tetraphenylborate. Due to the strong electrostatic interactions between the TPP⁺ group and BPh₄⁻, **NID-TPP** aggregates and there is a resulting AIE associated with an emission peak at 618 nm and τ_{d} of 1.2 μs . In both the plasma and mitochondria the membrane potential is negatively charged, allowing positively charged species such as **NID-TPP** to gradually accumulate in the cytoplasm as well as into the mitochondrial matrix through passive transport. Thus, **NID-TPP** was utilized for TRLI and two-photon luminescence imaging of HeLa cells and their substructures (Figure 1.39b). As shown in Figure 1.39, at short incubation times no fluorescence signal could be detected in the extracellular medium, while with longer incubation time enhanced fluorescence signals could be observed in HeLa cells.²¹⁰

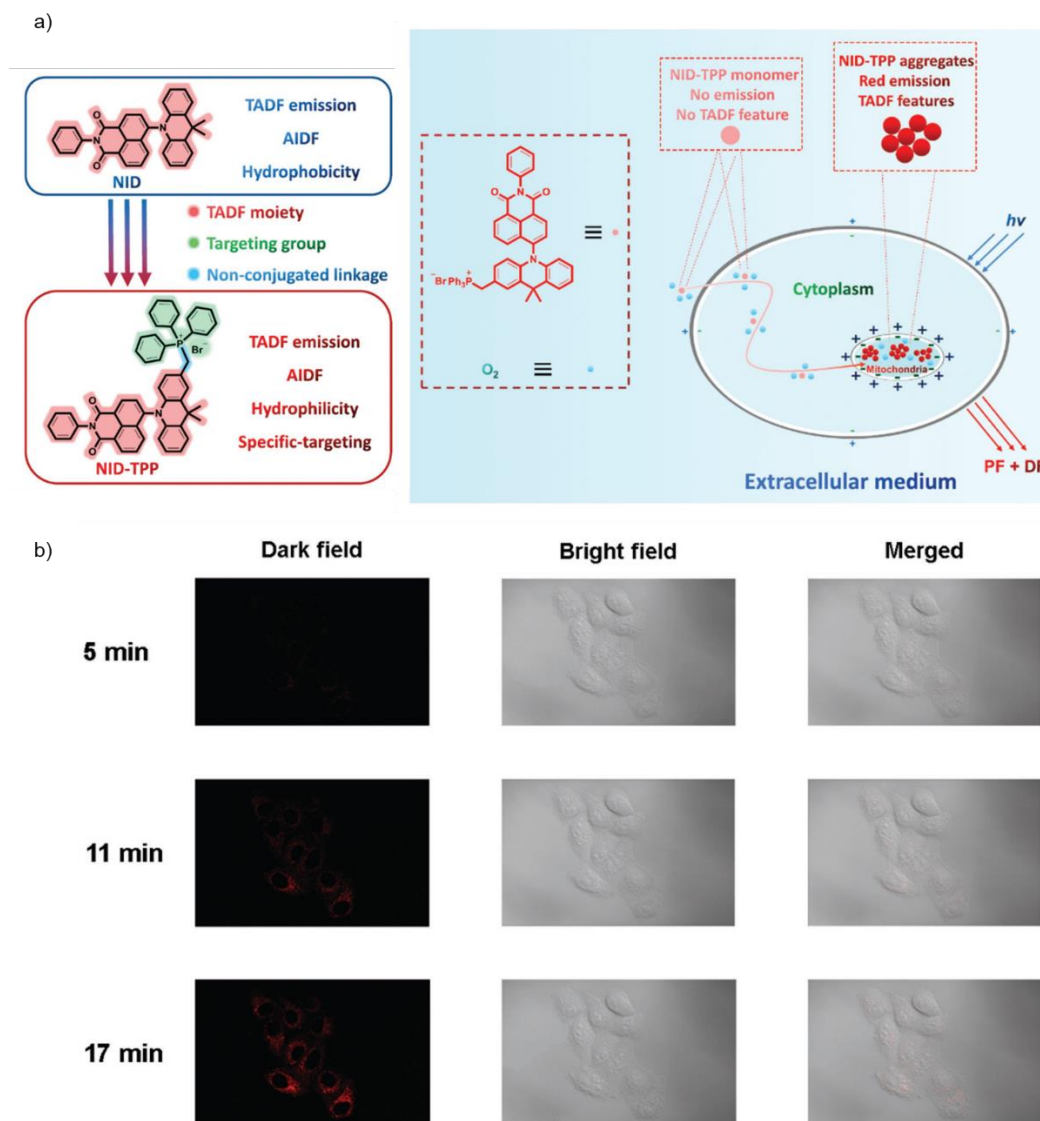


Figure 1.39. (a) Design and proposed uptake mechanism of **NID-TPP** for TRLI of mitochondria in HeLa cells; (b) Two-photon luminescent images of HeLa cells incubated with 10×10^{-6} M **NID-TPP** for 5 min, 11 min and 17 min. $\lambda_{\text{exc}} = 810$ nm, $\lambda_{\text{em}} = 540\text{--}660$ nm. Copyright 2019, WILEY-VCH.²¹⁰

Hudson and co-workers developed multifunctional compartmentalized nanoparticles based on block copolymers, with a hydrophilic cell-penetrating corona surrounding the TADF-active co-monomer block (Figure 1.40).²⁰⁶ This was the first system to employ a single polymer as both the emitter and the cell-penetrating moiety. The polymer nanoparticles (**Pdot**), **BGN_{10-b-P20Pdot}**, exhibited a Φ_{PL} of up to 19% in water and significant delayed fluorescence ($\tau_{\text{d}} > 26$ μs) under both air and inert atmospheres. These all-organic polymer

nanoparticles were shown to efficiently enter HeLa, CHO, and HepG2 cells within 30 min, with cell viabilities remaining high for Pdot concentrations of up to 25 mg mL⁻¹. When used for fixed cellular imaging, Pdot-incubated cells showed high signal-to-background ratios compared to control samples with no Pdot exposure. Using time-resolved spectroscopy, the delayed emission of the Pdots was effectively separated from that of both a biological serum as well as from a secondary fluorescent dye.

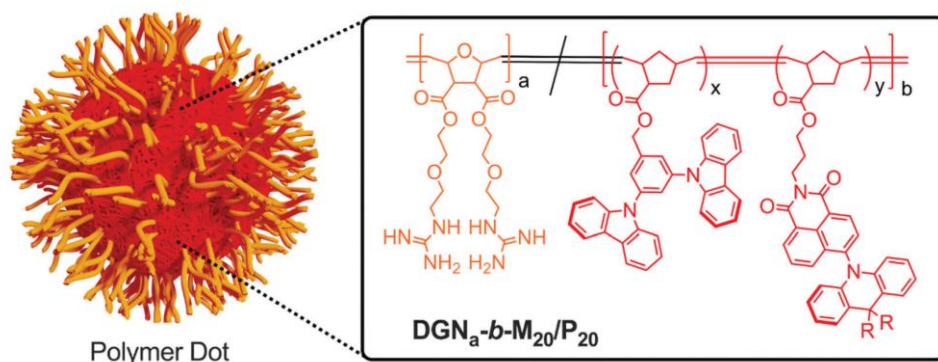


Figure 1.40. Polymer dots formed by self-assembly of an amphiphilic block copolymer containing a water-soluble cell-penetrating guanidinium unit, and a hydrophobic host material and TADF emitter used to deliver TADF emitters to biological targets. Copyright 2021 American Chemical Society.²⁰⁶

By covalently incorporating a TADF monomer (**PDC-DA**) and a photochromic spiropyran derivative (**SPMA**), Yang and co-workers reported a two-component photoswitchable TADF polymeric nanoparticle (**PDFPNs**) (Figure 1.41).²¹¹ The polymerizable luminophore, **PDC-DA**, was used as the energy donor while the photoresponsive SPMA was employed as the energy acceptor. The green emission of **PDC-DA** can be converted into red fluorescence when the SP unit is converted into its red-emissive ring-open merocyanine (**MC**) state using 365 nm UV light, enabling FRET from **PDC-DA** to **MC**. Subsequently, 525 nm visible light can be used to efficiently recycle the SPMA into a FRET-inactive form, recovering the green emission of **PDC-DA**. The **PDFPNs** possesses a τ_d of 3.3 μ s under degassed conditions and a shorter lifetime of 2.73 μ s in aerated aqueous solution. After being irradiated by 365 nm light, the τ_d was remarkably reduced to 1.61 μ s, which the authors ascribed to an efficient FRET process that was switched on between the donor and acceptor. These

nanoparticles showed negligible oxygen-sensitivity, high FRET efficiency, rapid and reversible photo responsiveness, and long-term fluorescence stability. They were thus used to realize reversible dual-color confocal and time-resolved luminescence imaging.

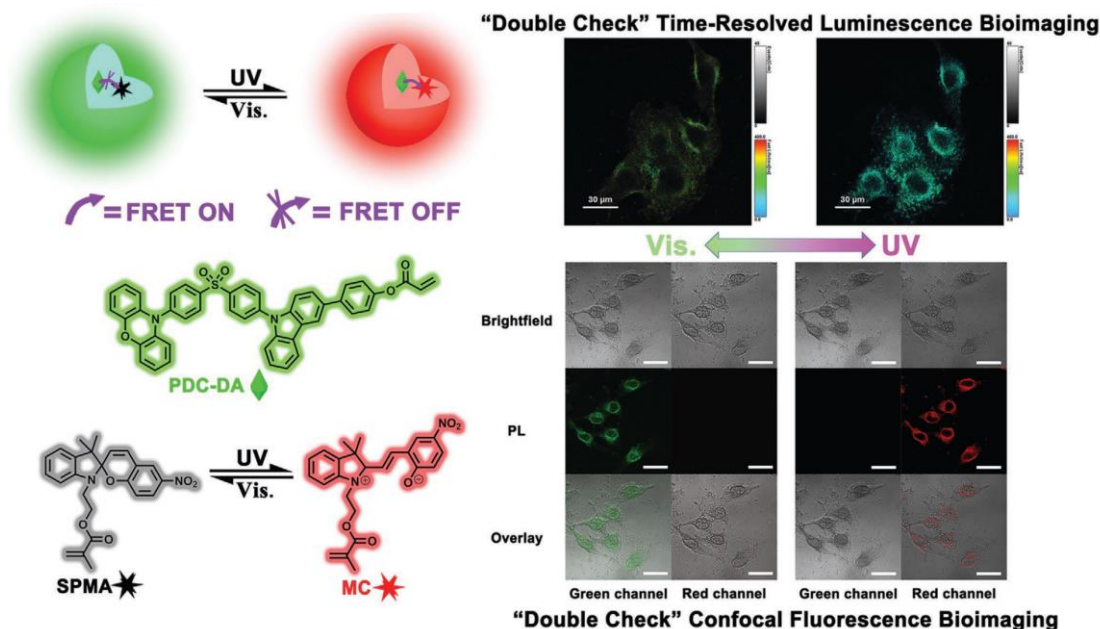


Figure 1.41. Schematic of photochromism and long-lived luminescent “double-check” bioimaging using PDFPNs. Copyright 2022, WILEY-VCH.²¹¹

1.6.7 Conclusions

The aforementioned examples illustrate the promise of TADF materials to act as bioimaging agents, primarily due to their efficient and long-lived emission. The principal design criteria for TADF luminophores for conventional fluorescence imaging and time-resolved imaging applications include a sufficiently long lifetime, good biocompatibility, and tolerance of both atmospheric and intracellular oxygen. To achieve these properties, the design strategies reviewed in this section include: 1) TADF emitters capped with BSA/HSA; 2) TADF-based Odots formed by encapsulating TADF emitters in an amphiphilic polymer; 3) Silica-based nanoparticles as hosts for the encapsulation of the TADF emitter; 4) Self-assembled nanoparticles; 5) Aggregation-induced delayed fluorescence; and 6) Other TADF bioimaging agents such as like water-soluble TADF polymers.

Despite the recent wave of efforts dedicated to exploring TADF materials in bioimaging, its development is still very much in its infancy. Consequently, TADF materials offer

significant opportunities, but also present various challenges that need to be addressed before they can be extensively applied or translated for preclinical/clinical use. Of these we highlight in particular the following: 1) focusing on developing more effective designs to improve the inherent water solubility and poor bioavailability of these organic emitters; 2) designing high brightness deep red /NIR TADF emitters for deep-tissue theragnostic, thereby mitigating possible tissue damage and improving the signal-to-noise ratio; 3) Design of TADF bioimaging agents that show targeted uptake for imaging of specific organelles.

1.7 Aims for the Thesis

Developing high-performance red TADF emitters is challenging, as their photoluminescence quantum yield is limited by the energy-gap law. This thesis aims to develop novel red TADF emitters and makes efforts to understand the origins of efficient red TADF emitters. These materials are then not only exploited in OLEDs, but also in sensors and bioimaging. Specifically, I will focus on the exploration of novel acceptors and investigate the effect of their electron withdrawing abilities, conjugation degree, planarity, and the number and positions of donor substitutions on the photophysical properties of these new red TADF emitters. The goal is to establish the link between molecular structure and their photophysics.

To find out the effect of N doping on the PAH acceptor, **DMACBP**, **DMACPyBP**, **DMACBPN** and **DMACPyBPN** (Figure 1.42a, Chapter 2) are investigated through a combination of theoretical calculations, photophysical and electrochemical characterization, and electroluminescence studies.

To increase Φ_{PL} and gain a deeper insight into the effect of N at 10-position of BP, we refined the molecular design strategy by increasing the π -conjugation and synthesized three TADF compounds, **TPAPyAP**, **TPAPyBP** and **TPAPyBPN** (Figure 1.42b, Chapter 3). These three emitters exhibit color-tuning over a wide gamut from green to deep-red with higher Φ_{PL} than the DMAC-based emitters in Chapter 2. By modulating the solid-state solvatochromism and adjusting the π - π stacking interaction, a deep red emission was obtained from the **TPAPyBPN**-doped films. Based on this result, we developed an efficient deep-red OLED. Furthermore, we demonstrated unusually strong and specific spectral response to ZnCl_2 for all three compounds, especially for **TPAPyBP**, which is the first TADF optical sensor of ZnCl_2 .

To investigate the effect of substitution position and strength of the donors on the optoelectronic properties, Here, four orange-red solution-processable TADF dendrimers with the same acceptor as **DMACBP** in Chapter 2, **2GCzBP**, **2DPACzBP**, **2FBP2GCz** and **2FBP2DPACz** (Figure 1.42c, Chapter 4) were synthesized. The solution-processed OLED based on **2DPACzBP** exhibits a pure red λ_{EL} at 640 nm with low efficiency roll-off where the

EQE remained near that of its maximum at 7.5% at a luminance of 1000 cd m^{-2} , which is among the best results for solution-processed red TADF OLEDs at such a high luminance.

To investigate the impact of the acceptor π -conjugation degree on the properties, two TADF dendrimers with different π -conjugated N-doped PAH acceptors were designed and synthesized. Compound **2GCzBPPZ** (Figure 1.42d, Chapter 5), with a much more π -conjugated acceptor, shows unusual dual emission that is both concentration-dependent and temperature-dependent in solution. The distinct photophysical properties of **2GCzBPPZ** motivated us to use it as a temperature sensor. This compound exhibits excellent temperature sensitivity across a very wide temperature range ($-70 \text{ }^\circ\text{C}$ to $70 \text{ }^\circ\text{C}$) in *n*-hexane, accompanied by a significant spectral response, ranging from yellow to blue emission, which is the widest detected temperature range and color response reported for an organic luminescent material in solution. In addition, solution-processed OLEDs based on these dendrimers as emitters are also discussed.

To explore the influence of the acceptor planarity's on the properties, we explored a large π -conjugation and curved PAH, corannulene, as the acceptor and designed a family of multi-D-A motifs, **TCzPhCor**, **TDMACPhCor**, and **TPXZPhCor** (Figure 1.42e, Chapter 6). These three emitters exhibit room-temperature phosphorescence from different excited triplet states. The **TPXZPhCor** doped film was demonstrated to act as an optical temperature sensor in the range from 77 K to 298 K. We also fabricated solution-processed afterglow OLEDs using **TPXZPhCor**.

To investigate the potential of our available compounds for bioimaging applications, we employed two methods to make water-soluble TADF materials (Figure 1.42f, **DMACBP**, **DMACPyBP** in Chapter 2, and **2GCzBPN** in Chapter 5): nanoparticles and water-soluble sodium-salt emitters. We also reported our first trials as bioimaging reagents.

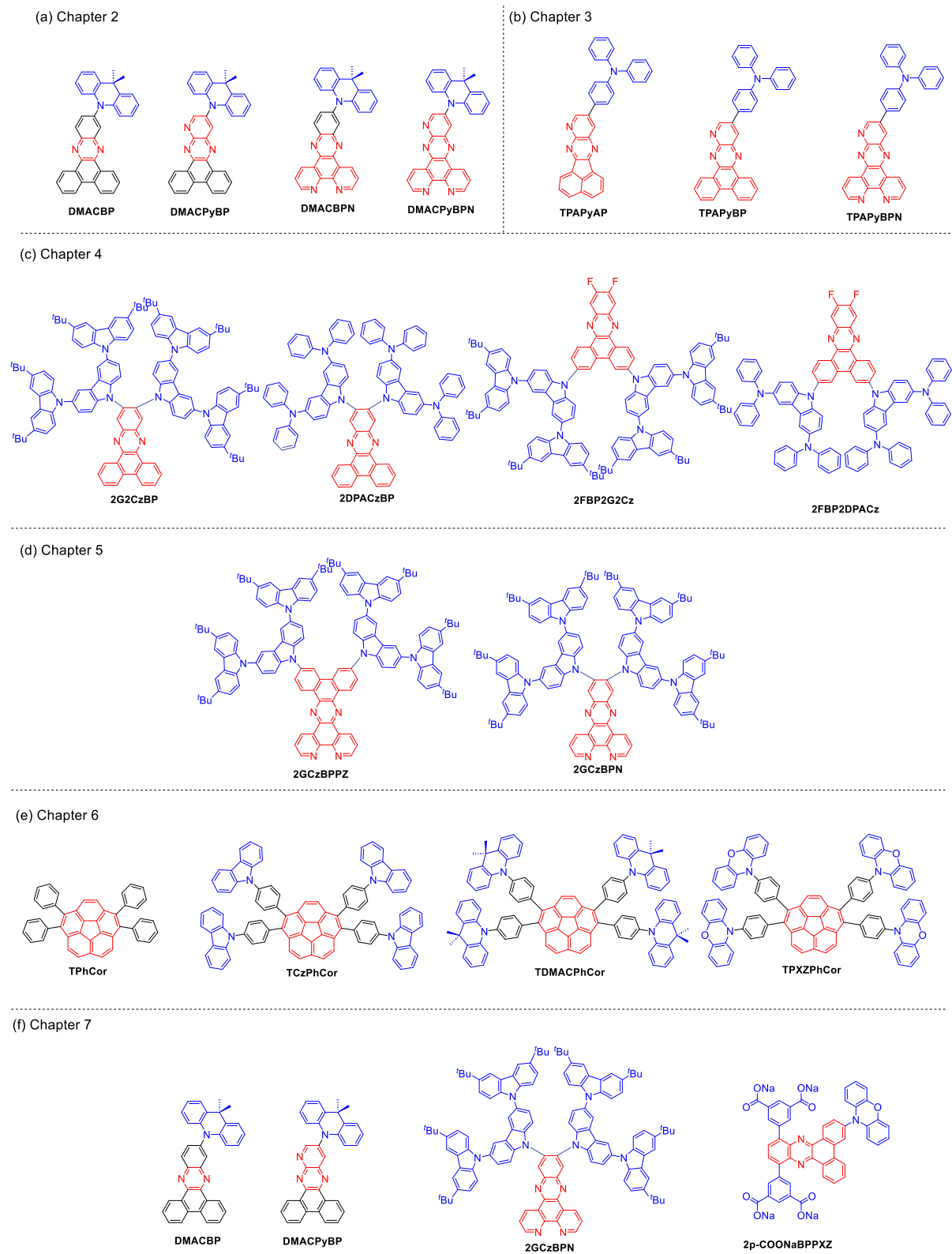
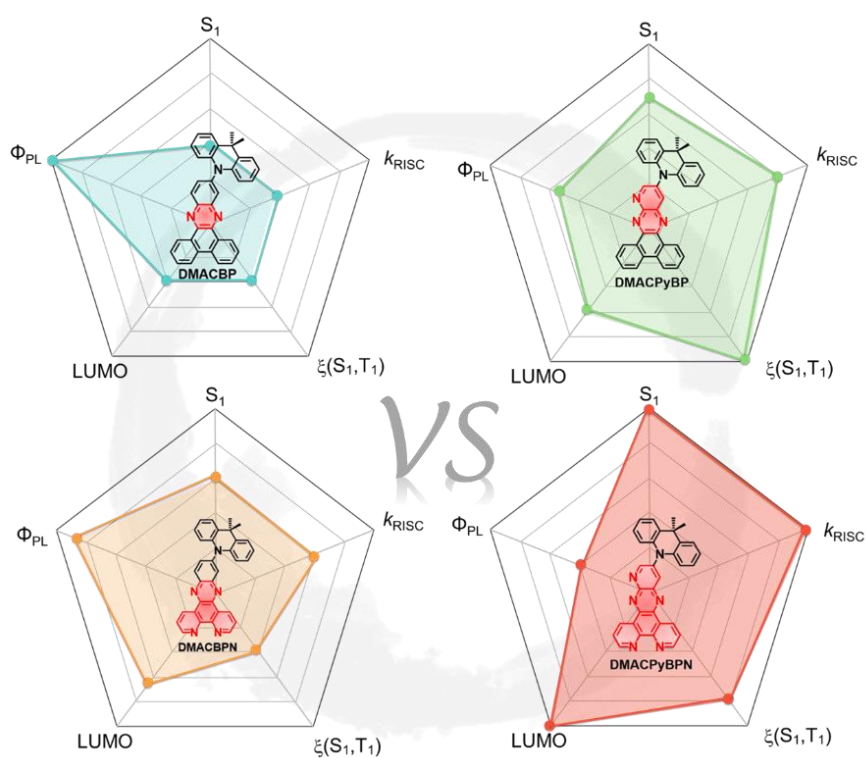
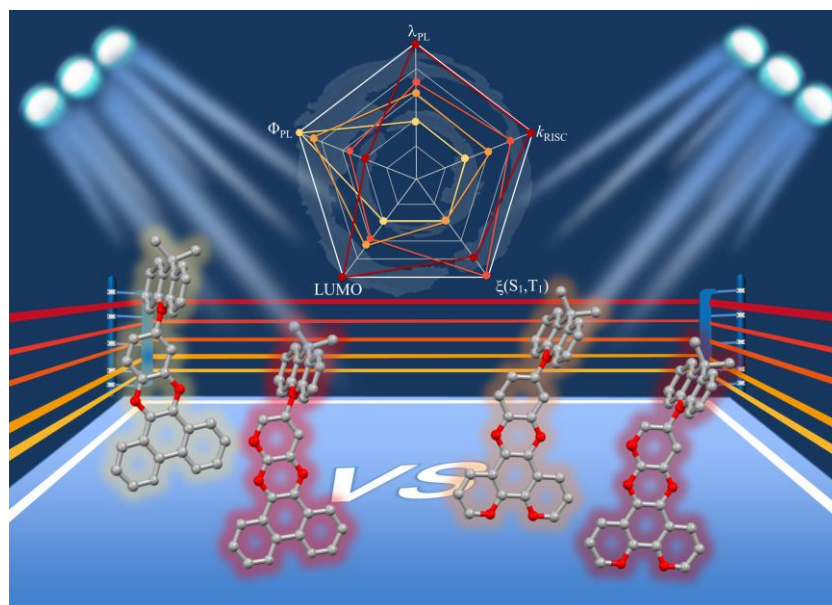


Figure 1.42. Molecular structures of all the materials investigated in this thesis.

Chapter 2: The Influence of Nitrogen Doping of the Acceptor in Orange–Red

Thermally Activated Delayed Fluorescence Emitters and OLEDs



The work presented in this Chapter has been published on Journal of Materials Chemistry C.

Changfeng Si,^{a†} Ya-Nan Hu,^{b†} Dianming Sun,^a Kai Wang^b, Xiao-Hong Zhang^{*b} and Eli Zysman-Colman^{*a} *The influence of nitrogen doping of the acceptor in orange-red thermally activated delayed fluorescence emitters and OLEDs*. (Back cover) *J. Mater. Chem. C*, **2023**, *11*, 12174–12184. <https://doi.org/10.1039/d3tc02352d>.

Collaborators in this Chapter are from:

^b Institute of Functional Nano & Soft Materials (FUNSOM), Joint International Research Laboratory of Carbon-Based Functional Materials and Devices, Soochow University, Suzhou, Jiangsu 215123, P. R. China.

Ya-Nan Hu from Soochow University carried out the OLEDs fabrication. Dr. Dianming Sun helped with the discussion and correction of the manuscript.

I completed all the syntheses and characterization, DFT and TD-DFT calculations, electrochemistry, photophysics measurements and I am the principal author of the text.

2.1 Introduction

As mentioned in Chapter 1.6, most of the reported TADF emitters employ a strongly twisted D-A structure, which leads to localization of the HOMO and the LUMO on the D and A, respectively, and thus to a small ΔE_{ST} . A sufficiently small ΔE_{ST} is necessary to enable endothermic up-conversion of triplet excitons to singlets by RISC.^{112,212,213} The apparent paradox in TADF emitter design is that the design requirements for efficient RISC are in contrast to those to attain high Φ_{PL} , which require significant orbital overlap to maximize the oscillator strength of the transition.^{116,214} Balancing these two criteria in the design of high-performance orange-red emitters becomes that much more difficult as radiative decay decreases while non-radiative decay increases due to the energy-gap law.²¹⁵⁻²¹⁷ The general molecular design principles for red/deep red D-A TADF emitters are: 1) Use of strong donor and acceptor motifs is a common strategy, affording a shallow HOMO and a deep LUMO for D and A, respectively; and 2) Construction of a rigid and typically planar fused ring donor and/or acceptor for the suppression of nonradiative transitions. Within this model, most of the acceptors are derivatives of either acenaphtho[1,2-b]pyrazine-8,9-dicarbonitrile (APDC),¹²⁶ heterocyclic quinoxaline-6,7-dicarbonitrile (QCN),¹²¹ 11,12-dicyanodibenzo[a,c]phenazine (CNBPz),¹³⁷ 2,3-dicyanodibenzo[f,h]quinoxaline (CNBQx),^{218,219} or dibenzo[a,c]-phenazine-3,6-dicarbonitrile (PZCN).²²⁰

Nitrogen-doped polycyclic aromatic hydrocarbons (N-PAH), like dibenzo[a,c]phenazine (BP), have proved particularly popular as moieties in orange-red TADF emitters (Figure 2.1). Zhao *et al.* first reported BP-based TADF compounds, containing one-to-three DMAC donor moieties (Figure 2.1). The orange-red OLEDs with **3DMAC-BP**, an emitter with three DMAC donors situated at the 3-, 6-, and 11-positions of the BP, showed a EQE_{max} of 22.0% with an $\lambda_{EL} = 606$ nm.²²¹ Yang *et al.* reported a related compound using the BP acceptor, **DMAC-11-DPPZ** with the DMAC donor attached at the 11-position of the BP acceptor, which emits at λ_{PL} of 576 nm, has a Φ_{PL} of 57% and a τ_d of 1.53 μ s in 10 wt% doped films in CBP. The optimized OLED with **DMAC-11-DPPZ** displays an orange emission at 588 nm with the EQE_{max} of 23.8%.¹⁴³ Tang *et al.* introduced one more nitrogen at the 10-position of the BP core to generate a new acceptor unit, BPQ. Star-shaped isomers **3,6,11-triAC-BPQ** and **3,6,12-triAC-BPQ** contain three DMAC donors at either the 3,6,11-positions or 3,6,12-positions of BPQ. **3,6,12-triAC-BPQ** showed a small red-shifted emission at 611 nm in toluene and a slightly shorter τ_d of 2.25 μ s in 15 wt% doped films in mCBP compared to **3DMAC-BP** ($\lambda_{PL} = 605$ nm in toluene, $\tau_d = 2.9$ μ s in 20 wt% doped films in mCBP), which is a compound that does not have a N-atom at

the 10-position of the acceptor. By contrast, **3,6,11-triAC-BPQ** exhibited a blue-shifted emission at λ_{PL} of 565 nm compared to **3,6,12-triAC-BPQ**. The devices with **3,6,11-triAC-BPQ** and **3,6,12-triAC-BPQ** showed EQE_{max} of 22.0% [$\lambda_{\text{EL}} = 581$ nm, CIE, coordinates of (0.51,0.48)] and 16.5% [$\lambda_{\text{EL}} = 616$ nm, CIE coordinates of (0.58, 0.39)], respectively.¹⁴² The same group reported an orange-yellow TADF material **DPPZ-DMAC**, where the related DPPZ acceptor contains two additional nitrogen atoms compared to BP. This compound emits at ~ 590 nm, has a smaller ΔE_{ST} of 0.01 eV, and a higher Φ_{PL} of 91.6% in 6 wt% doped films in CBP, compared to that of **DMAC-11-DPPZ**, a compound without the two additional nitrogen atoms in the acceptor. The **DPPZ-DMAC**-based device showed an EQE_{max} of 27.8% with λ_{EL} at 598 nm. Zhang *et al.* reported a similar emitter **SAF-2NP** that employs a structurally related 10H-spiro-(acridine-9,9'-fluorene) (SAF) donor instead of DMAC in combination with the same acceptor as **DPPZ-DMAC**. As expected, **SAF-2NP** shows similar photophysics as **DPPZ-DMAC** but has a slightly blue-shifted emission at λ_{PL} of ~ 580 nm and a much higher Φ_{PL} of 99%. The **SAF-2NP**-based OLED demonstrated a very high EQE_{max} of 32.5% with an λ_{EL} at 576 nm, an efficiency linked to the high Φ_{PL} of 99% and horizontally oriented transition dipole ($\Theta//$) of 85% of the emitter in the host matrix. When DPPZ is coupled with a TPA donor, as in **oTPA-DPPZ**, the emission shifts to the red at 605 nm in the 30 wt% doped films ($\Phi_{\text{PL}} = 75\%$; ΔE_{ST} of 0.07 eV).¹⁴⁸ The OLEDs with **oTPA-DPPZ** showed an EQE_{max} of 18.5% at λ_{EL} of 600 nm. Through adjusting the position of the TPA groups, a “T-shape” deep-red TADF emitter, **pTPA-DPPZ**, was obtained.¹⁴⁸ Compared to **oTPA-DPPZ**, the rational spatial arrangement of D and A groups in **pTPA-DPPZ** accelerated radiative decay from the singlet state by 90-fold, giving rise to a Φ_{PL} of 87% in neat film. The corresponding OLED, having a simplified bilayer non-doped structure, showed an EQE_{max} of 12.3% at λ_{EL} of 652 nm.

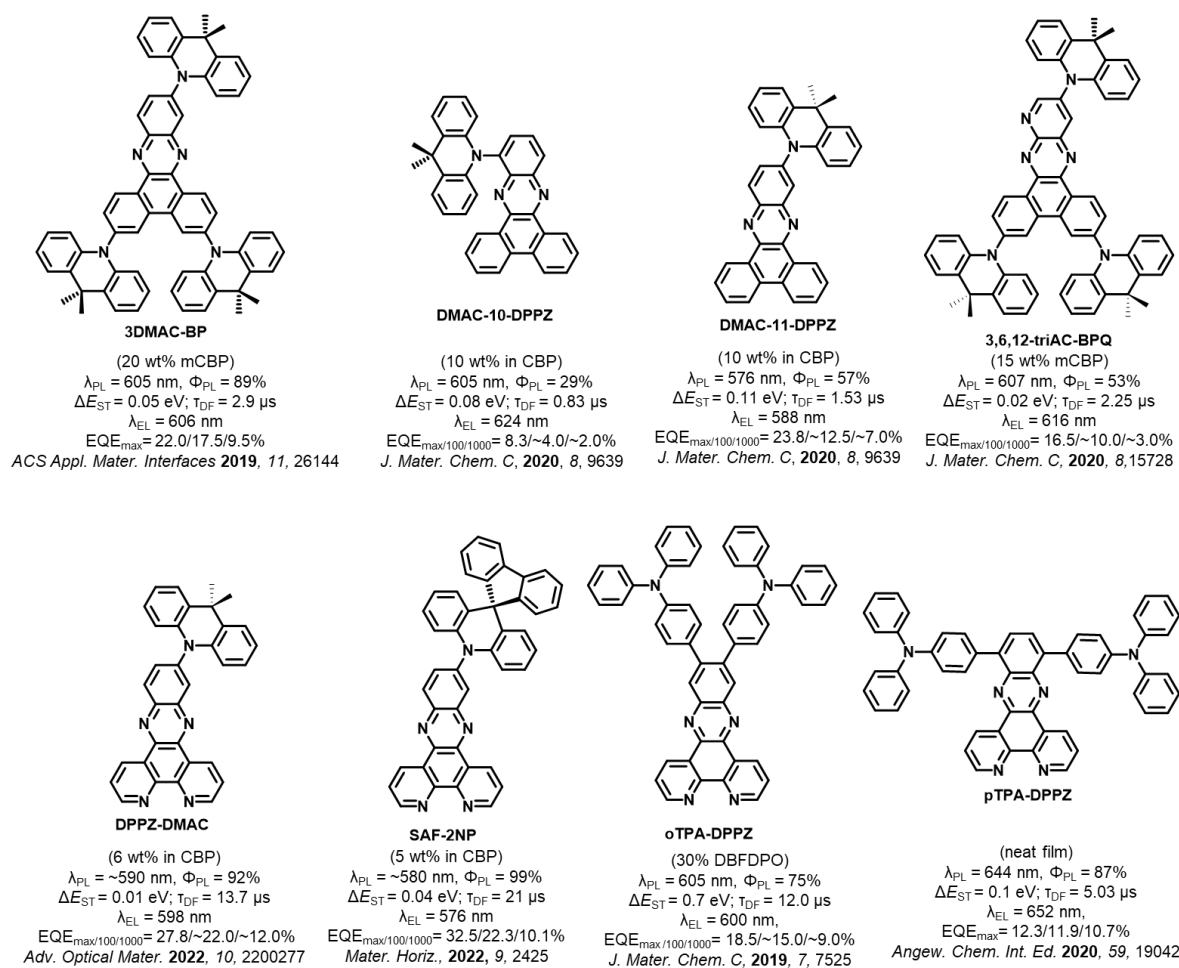


Figure 2.1. Molecular structures of the orange-red TADF emitters based on BP and BP derivatives acceptors.

Examples of D-A TADF emitters have illustrated that the use of N-PAHs like BP or DPPZ accesses orange-to-red emission. Although numerous molecules have been reported, to the best of our knowledge there is no one study that has been conducted to correlate the number of nitrogen atoms in the N-PAH acceptor (Figure 2.2a) to the photophysical properties of the emitter. To address this question we designed and synthesized four DMAC-containing TADF emitters containing different numbers of nitrogen atoms in the N-PAH acceptor: 11-(9,9-dimethylacridin-10(9H)-yl)dibenzo[*a,c*]phenazine (**DMACBP**) (2 nitrogen atoms), 12-(9,9-dimethylacridin-10(9H)-yl)dibenzo[*f,h*]pyrido[2,3-*b*]quinoxaline (**DMACPyBP**) (3 nitrogen atoms), 11-(9,9-dimethylacridin-10(9H)-yl)dipyrido[3,2-*a*:2',3'-*c*]phenazine (**DMACBPN**) (4 nitrogen atoms) and 12-(9,9-dimethylacridin-10(9H)-yl)pyrido[2',3':5,6]pyrazino[2,3-*f*][1,10]phenanthroline (**DMACPyBPN**) (5 nitrogen atoms). Summarized in Figure 2.2b are the variations in key photophysical properties of these four emitters. It becomes clear that the rate of reverse intersystem crossing, k_{RISC} , can be enhanced when the BP acceptor is modified to contain an additional nitrogen atom at the 10-position. The OLED with **DMACBPN**

demonstrated an EQE_{max} of 19.4% at λ_{EL} of 588 nm. The EL spectra shifts to the red when there is increasing nitrogen content in the acceptor, with the reddest device using **DMACPyBPN** emitting at 640 nm.

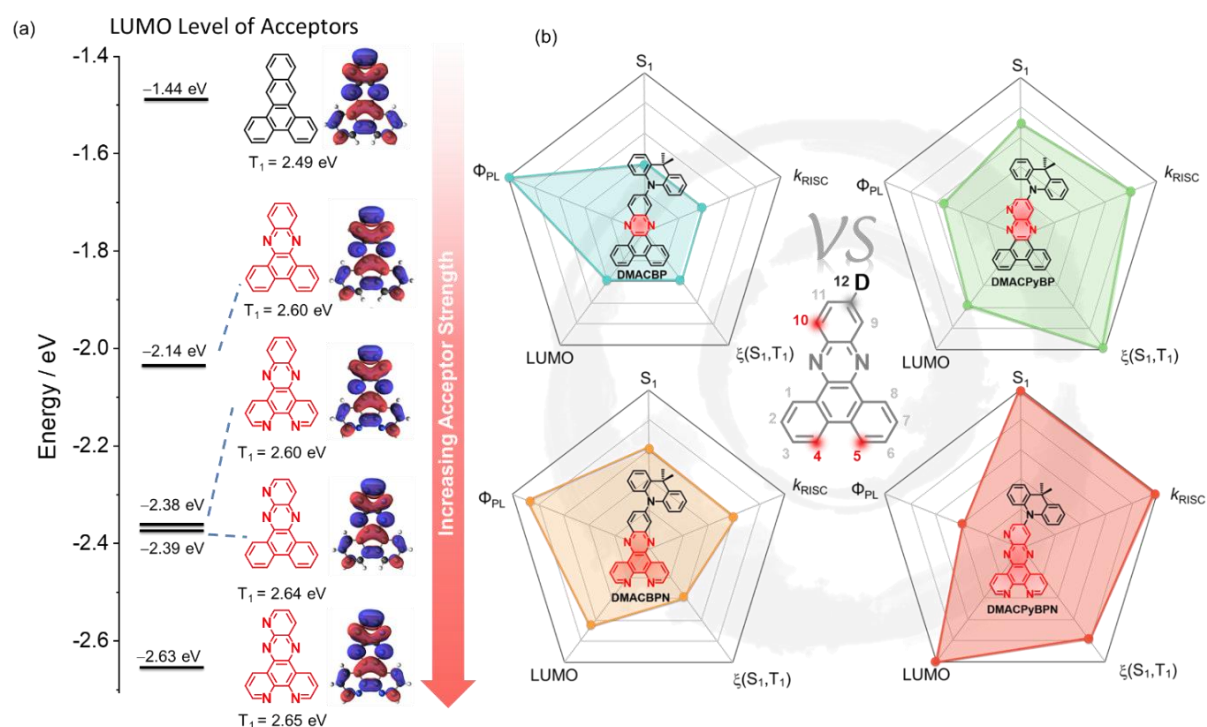
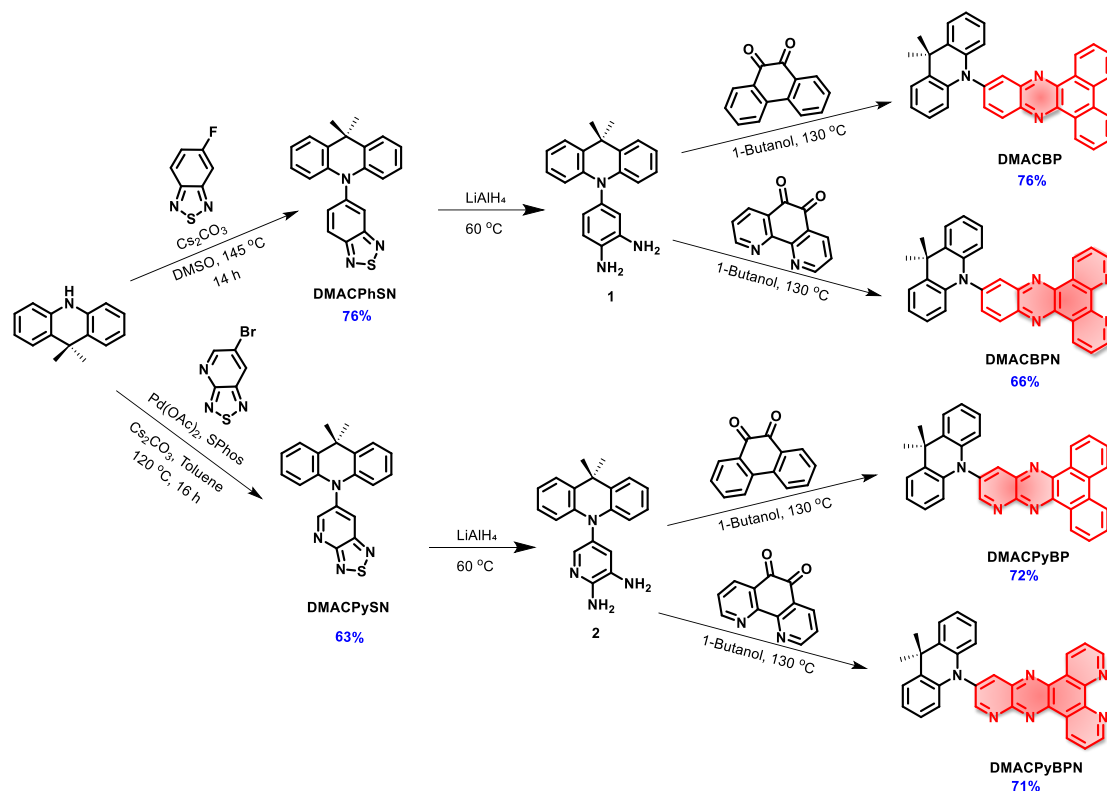


Figure 2.2. (a) Electron-accepting capability (the LUMO level) of nitrogen-doped PAH acceptors units, estimated at the PBE0/6-31G(d,p) level. (b) The main parameters (Φ_{PL} , S_1 , LUMO, k_{RISC} , and $\xi(S_1, T_1)$ values vs four emitters with different N/C ratio acceptor in this Chapter.

2.2 Synthesis

The synthesis of the **DMACBP**, **DMACPyBP**, **DMACBPN** and **DMACPyBPN** is outlined in Scheme 2.1. The intermediate **DMACPhSN** and **DMACPySN** were obtained by nucleophilic substitution reaction between 5-fluorobenzo[*c*][1,2,5]thiadiazole and DMAC, Buchwald-Hartwig coupling between 6-bromo-[1,2,5]thiadiazolo[3,4-*b*]pyridine and DMAC, respectively, followed by the ring-opening of benzothiadiazole (BTD) with lithium aluminum hydride (LiAlH₄). Intermediate **1** was further reacted with phenanthrene-9,10-dione and 1,10-phenanthroline-5,6-dione in 1-butanol reaction condition to obtain **DMACBP** and **DMACBPN**, respectively, in good yield. **DMACPyBP** and **DMACPyBPN** were obtained by the reaction of intermediate **2** with phenanthrene-9,10-dione and 1,10-phenanthroline-5,6-dione in 1-butanol, respectively. The structural identity and purity of the three emitters were verified by ¹H and ¹³C nuclear magnetic resonance (NMR) spectroscopy, melting point determination, high-resolution

mass spectrometry, elemental analyses, and high-performance liquid chromatography (HPLC) (2.9 Experimental section, Figures 2.13-2.35).



Scheme 2.1. Synthetic routes for **DMACBP**, **DMACPyBP**, **DMACBPN** and **DMACPyBPN** emitters.

2.3 Theoretical Calculations

To predict the optoelectronic properties of the four emitters, the modelling was first performed in the gas phase using density functional theory (DFT) at the PBE0/6-31G(d,p) level of theory. The optimized S_0 geometries and calculated energy levels of the HOMO and LUMO are presented in Figure 2.3. As expected, the HOMO is localized on the donor DMAC while the LUMO is localized on N-Rich electron acceptors. The gradually decreased LUMO in **DMACBP**, **DMACPyBP**, **DMACBPN** and **DMACPyBPN** originates from the enhanced electron-withdrawing strength of acceptor with increasing nitrogen content. However, due to the enhanced electronic coupling between the donor and the acceptor, the HOMO levels of **DMACPyBP** and **DMACPyBPN** are more stabilized as these are delocalized over both DMAC and the pyridine (Py) rings, as compared to the DMAC-localized orbitals in **DMACBP** and **DMACBPN** (Figure 2.3). The HOMO-LUMO gap, $\Delta E_{\text{HOMO-LUMO}}$, decreases from 2.84 eV for **DMACBP**, to 2.75 eV for **DMACPyBP**, 2.72 eV for **DMACBPN** and 2.63 eV for **DMACPyBPN**, following a similar trend to that observed for the LUMO and governed by the

strength of the electron-acceptor moiety. As shown in the electrostatic potential maps (Figure 2.3), the nitrogen-rich components have more negative electrostatic potential while the other parts have neutral and positive potential, which correlates with the trend in increasing electron-withdrawing ability of the acceptor with the inclusion of an increasing number of nitrogen atoms within the acceptor moiety.

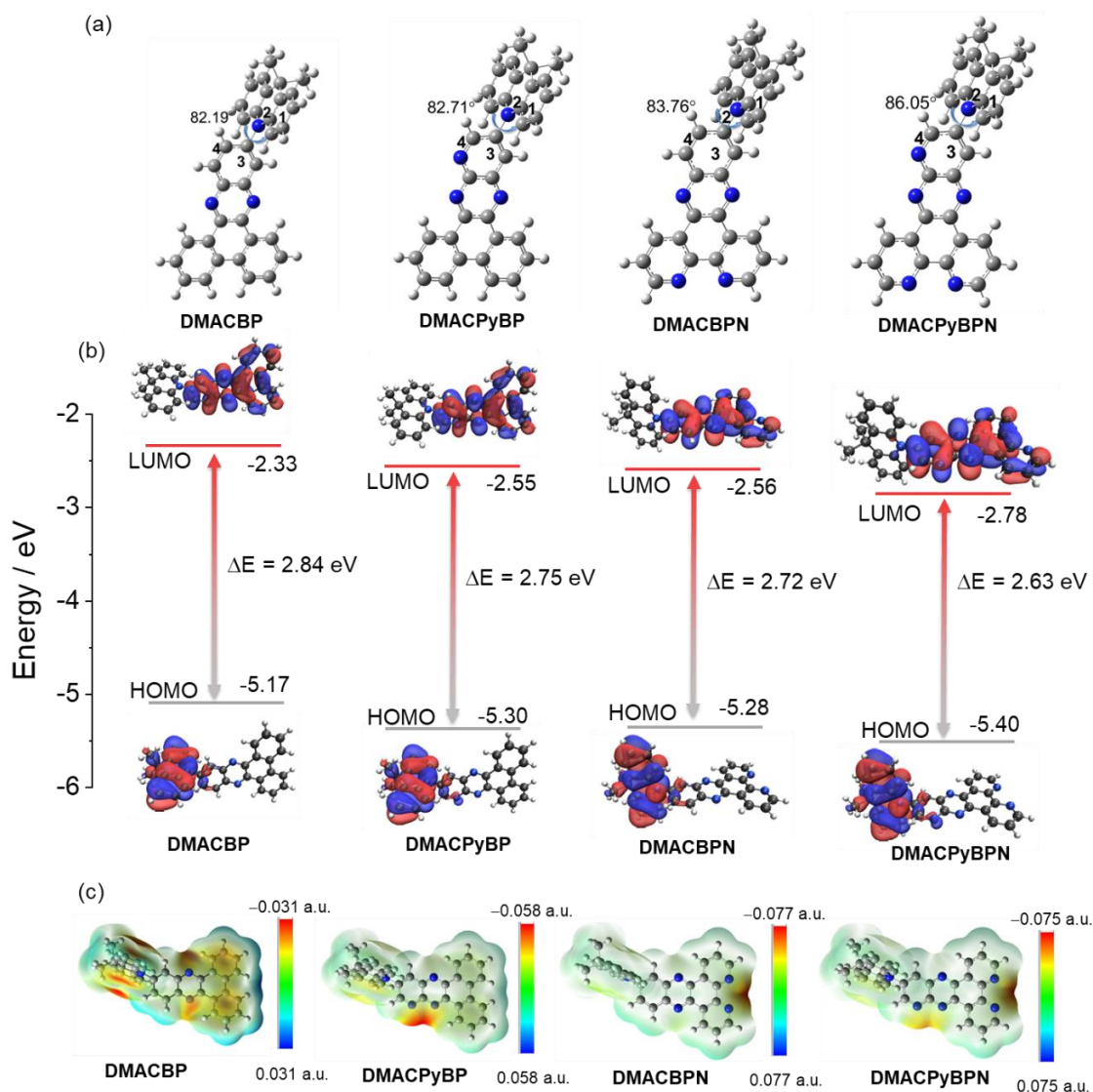


Figure 2.3. (a) Frontier molecular orbitals (isovalued: 0.02) and (b) vertical excitation energy levels of **DMACBP**, **DMACPyBP**, **DMACBPN** and **DMACPyBPN** calculated at the optimized S_0 geometry in the gas phase at the PBE0/6-31G(d,p) level. (c) Electrostatic potential maps of **DMACBP**, **DMACPyBP**, **DMACBPN** and **DMACPyBPN** in ground states with an isodensity surface of 0.004

The excited-state properties were then calculated using time-dependent DFT (TD-DFT) within the Tamm-Dancoff approximation (TDA) based on the optimized ground-state geometry.²²² The S_1 energies are 2.17 eV for **DMACBP**, to 2.04 eV for **DMACPyBP**, 2.05 eV

for **DMACBPN** and 1.91 eV for **DMACPyBPN**, while the T_1 energies likewise decrease from 2.15 eV, to 2.00 eV, 2.03 eV and 1.89 eV, respectively, following a trend of increasingly stabilized excited states with increasing N atom content in the acceptor, although **DMACPyBP** and **DMACBPN** are close in energy (Figure 2.4a). The corresponding ΔE_{ST} values are all relatively small at 0.02, 0.04, 0.02 and 0.03 eV, respectively, due to the large dihedral angles between the DMAC and the acceptor that effectively minimize the electronic coupling [**DMACBP** (82.2°), **DMACPyBP** (82.7°), **DMACBPN** (83.8°) and **DMACPyBPN** (86.1°) based on the optimized S_0 geometries] (Figure 2.3a). To gain insight into the photophysical properties of the S_1 excited states, we performed natural transition orbital (NTO) analyses at the S_0 geometry (Figure 2.4b). The S_1 state of each of the compounds possesses an evident ICT character. Hole and electron distributions mirror HOMO/LUMO localization, respectively. Root-mean-square displacements (RMSDs) between S_0 and S_1 were calculated (Figure 2.4c) using VMD program to evaluate the structural changes that occur upon excitation and intersystem crossing.²²³ The RMSD values of **DMACBP**, **DMACPyBP**, **DMACBPN** and **DMACPyBPN** between S_0 and S_1 were simulated to be 0.17, 0.14, 0.13 and 0.07 Å, respectively. The smaller RMSD of **DMACPyBPN** indicates that the introduction of N at 10-position or 4/5-position reduces the magnitude of structural relaxation. At the relaxed S_1 geometry, there is a larger S_1 - T_1 spin-orbit coupling (SOC) matrix element of 0.05 cm^{-1} in **DMACPyBP** and of 0.04 cm^{-1} in **DMACPyBPN** than that in **DMACBP** (0.01 cm^{-1}) and **DMACBPN** (0.01 cm^{-1}) (Figure 2.4a), indicating that the rate constants of intersystem crossing (k_{ISC}) in **DMACPyBP** and **DMACPyBPN** will be faster than in the latter two compounds.

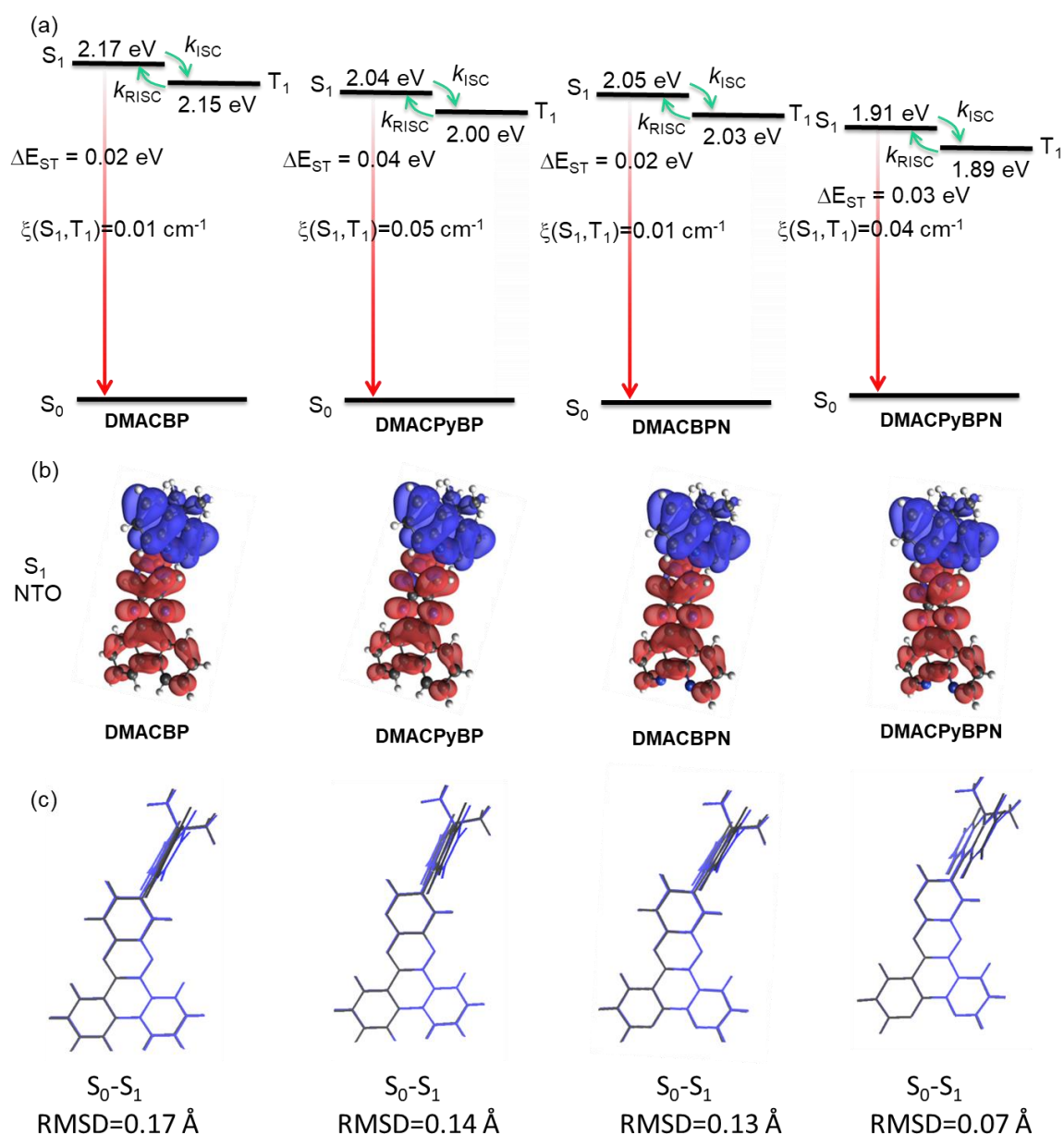


Figure 2.4. (a) vertical excitation energy levels of **DMACBP**, **DMACPyBP**, **DMACBPN** and **DMACPyBPN** calculated at the optimized S₀ geometry in the gas phase at the PBE0/6-31G(d,p) level. (b) Natural transition orbitals (unoccupied (hole, blue) & occupied (electron, red), (isovalue: 0.02) of S₁ for **DMACBP**, **DMACPyBP**, **DMACBPN** and **DMACPyBPN** calculated at the optimized S₀ geometry in the gas phase at the PBE0/6-31G(d,p) level. (c) comparison of optimized structures of **DMACBP**, **DMACPyBP**, **DMACBPN** and **DMACPyBPN** at S₀ (grey) and S₁ (blue) state.

2.4 Electrochemistry

The energies of the frontier molecular orbitals (FMOs) were inferred from the electrochemical behavior of **DMACBP**, **DMACPyBP**, **DMACBPN** and **DMACPyBPN** by

cyclic voltammetry (CV) and differential pulse voltammetry (DPV) in degassed DCM with tetra-*n*-butylammonium hexafluorophosphate ($[n\text{Bu}_4\text{N}]\text{PF}_6$) as the supporting electrolyte (**Figure 2.5**). Electrochemical potentials are reported versus a saturated calomel electrode. The reduction potentials (E_{red}), determined from the DPV peak values, are -1.39 V (**DMACBP**), -1.22 V (**DMACPyBP**), -1.33 V (**DMACBPN**) and -1.11 V (**DMACPyBPN**), respectively, reflecting the expected anodic shift associated with increasing acceptor strength that is mirrored in the trend of the calculated LUMO levels from BP < BPN < PyBP < PyBPN (Figure 2.2a).

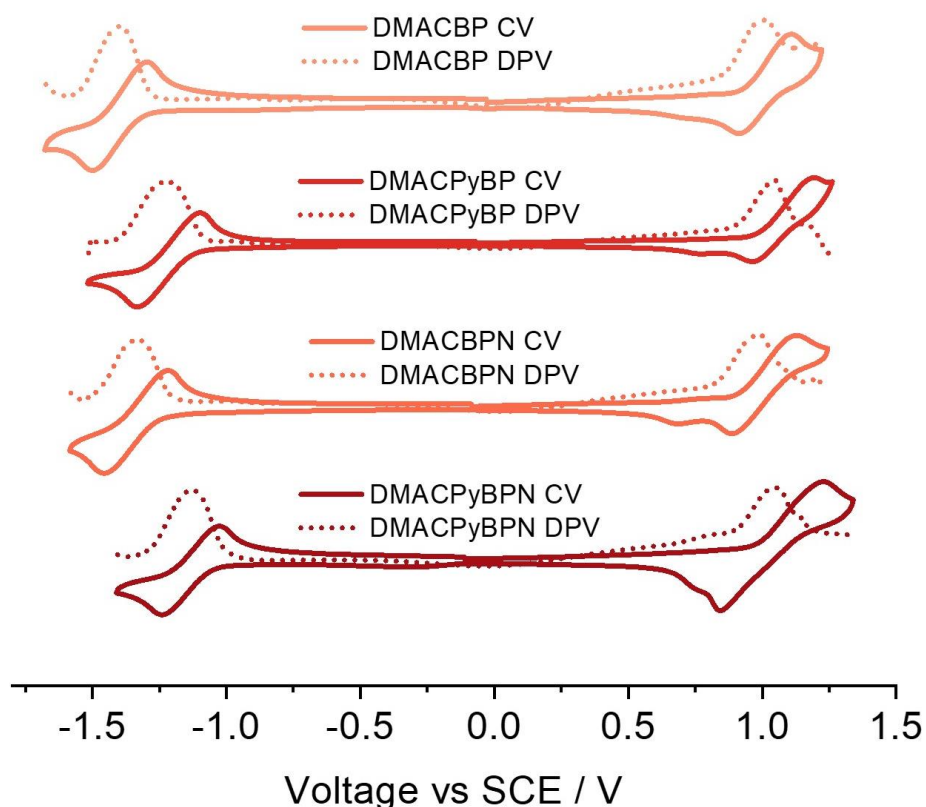


Figure 2.5. Cyclic and differential pulse voltammograms measured in degassed DCM with 0.1 M $[n\text{Bu}_4\text{N}]\text{PF}_6$ as the supporting electrolyte and Fc/Fc^+ as the internal reference (0.46 V vs SCE).²²⁴ Scan rate = 100 mV s^{-1} .

The calculated LUMO energies are -2.94 eV, -3.12 eV, -3.00 eV and -3.20 eV for **DMACBP**, **DMACPyBP**, **DMACBPN** and **DMACPyBPN**, respectively. **DMACPyBP** (1.04 V) and **DMACPyBPN** (1.04 V) have more positive oxidation potentials than those of **DMACBP** (1.00 V) and **DMACBPN** (0.98 V), in line with the DFT calculations. The HOMO levels of **DMACBP**, **DMACPyBP**, **DMACBPN** and **DMACPyBPN** are -5.34 , -5.39 , -5.33 and -5.39 eV, respectively. The HOMO–LUMO gaps for **DMACBP**, **DMACBPN** and **DMACPyBPN** are 2.40, 2.33 and 2.19 eV, respectively, which mirror the trend in the DFT

calculated values of 2.84, 2.72, 2.63 eV; however, **DMACPyBP** exhibits a much smaller HOMO–LUMO gap (2.27 V) inferred from its electrochemistry than **DMACBPN** (2.33 V), which is opposite to the DFT calculated results in the gas phase. However, the inferred LUMO energies obtained from CV exactly mirror the trend from the DFT calculated LUMO of the acceptors as shown in Figure 2.2a. The inconsistency of the data for **DMACPyBP** to its corresponding acceptor likely indicates a deviation of the D-A dihedral angle between the DFT calculated structure in the gas phase and that that exists in solution during the CV acquisition.

2.5 Photophysics in Solution

The UV-Vis absorption spectra of the four emitters in dilute toluene are shown in Figure 2.6a. The spectra show two prominent spectra features, with two intense bands centered at ~390 nm and a hypochromic broad band at ~470 nm, which are assigned to locally excited (LE) $\pi-\pi^*$ transitions of the donors and acceptor moiety,^{225,226} and intramolecular charge transfer (ICT) transitions from the DMAC donor to the acceptor moiety, respectively.^{143,225} The ICT band expectedly shifts to lower energies with the introduction of an increasing number of N atoms at positions 4/5 of the acceptor; for instance, the ICT band at 465 nm of **DMACBPN** ($\epsilon = 2.5 \times 10^3 \text{ M}^{-1} \text{ cm}^{-1}$) is red-shifted compared to that of **DMACBP** ($\lambda_{\text{abs}} = 458 \text{ nm}$, $\epsilon = 1.8 \times 10^3 \text{ M}^{-1} \text{ cm}^{-1}$) while those of **DMACPyBP** and **DMACPyBPN** absorb at essentially the same energy at 474 and 475 nm ($\epsilon = 3.2 \times 10^3 \text{ M}^{-1} \text{ cm}^{-1}$ for both), which match well with the TD-DFT calculated S_1 energies (Figure 2.4a). Positive PL solvatochromism is observed for all compounds (Figure 2.6b), which is consistent with the ICT nature of the emissive excited state.

The steady-state photoluminescence (SSPL) spectra in toluene gradually red-shift from **DMACBP** ($\lambda_{\text{PL}} = 595 \text{ nm}$) to **DMACBPN** ($\lambda_{\text{PL}} = 630 \text{ nm}$) and **DMACPyBPN** ($\lambda_{\text{PL}} = 672 \text{ nm}$), which coincides with an increasing number of nitrogen atoms in the acceptors (Figure 2.2a). However, **DMACPyBP** ($\lambda_{\text{PL}} = 645 \text{ nm}$) containing three nitrogen atoms within the acceptor exhibits a slightly red-shifted emission than **DMACBPN** ($\lambda_{\text{PL}} = 630 \text{ nm}$), which contains four nitrogen atoms within the acceptor. This behavior correlates with the calculated S_1 energies and demonstrated that acceptor **PyBP** with 10-position N showed more stronger electron-withdrawing abilities than **BPN** acceptor with two N in [1,10] phenanthroline, following the trend of acceptor strength as shown in Figure 2.2a. The corresponding optical bandgaps, determined from the intersection point of the normalized absorption and emission spectra, for **DMACBP**, **DMACPyBP**, **DMACBPN** and **DMACPyBPN** are 2.37 eV, 2.20 eV, 2.31 eV and 2.12 eV, respectively (Figure 2.6b), which is consistent with the trend in emission energies (Figure 2.6e, Table 2.1). The Φ_{PL} for **DMACBP**, **DMACPyBP**, **DMACBPN** and

DMACPyBPN in degassed toluene solution are 35%, 20%, 38% and 6%, respectively. When exposed to oxygen, these values significantly decrease to 9%, 7%, 8%, and 3% respectively. The energies of the onsets of the prompt fluorescence and phosphorescence spectra in 2-MeTHF glass at 77 K were used to determine the S_1 and T_1 energies (Figure 2.6c). The S_1 energies are 2.37, 2.26, 2.34 and 2.20 eV, while the T_1 energies are 2.35, 2.26, 2.32 and 2.20 eV, for **DMACBP**, **DMACPyBP**, **DMACBPN** and **DMACPyBPN**, respectively. As both the prompt fluorescence and phosphorescence spectra are structureless, it is reasonable to assign both the S_1 and T_1 states as possessing significant CT character. The corresponding ΔE_{ST} values for **DMACBP**, **DMACPyBP**, **DMACBPN** and **DMACPyBPN** are then 0.02 eV, 0.00 eV, 0.02 eV and 0.00 eV, respectively, which align with the TDA-DFT calculated results (Figure 2.2a).

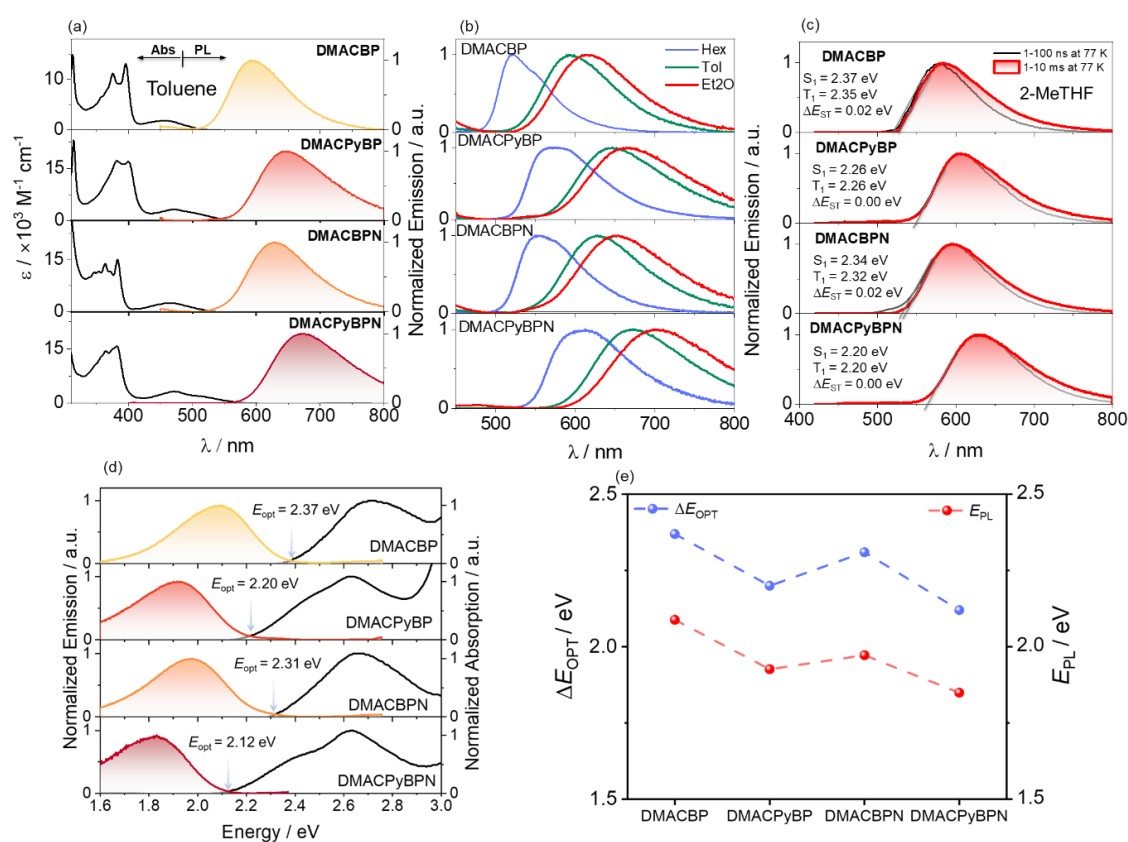


Figure 2.6. (a) UV-vis absorption (in toluene) and steady-state photoluminescence (PL) spectra recorded in toluene at room temperature; (b) PL solvatochromism study ($\lambda_{\text{exc}} = 340 \text{ nm}$); (c) Prompt fluorescence (1-100 ns) and phosphorescence spectra (9-10 ms) in 2-MeTHF at 77 K ($\lambda_{\text{exc}} = 375 \text{ nm}$); (d) The optical bandgaps were determined from the intersection point of the normalized absorption and emission spectra; (e) The relationship between the optical bandgaps and emission energies in toluene for **DMACBP**, **DMACPyBP**, **DMACBPN** and **DMACPyBPN**.

From the difference in the transient PL decay behavior under aerated and degassed conditions in toluene it is clear that the delayed emission is significantly quenched by the presence of oxygen (Figure 2.7); interestingly, the quenching of the PL in **DMACBP** and **DMACBPN** is more significant than in **DMACPyBP** and **DMACPyBPN** that each contain an additional pyridine ring fused to the pyrazine in the acceptor, which may be due to the longer delayed lifetime observed for **DMACBP** and **DMACBPN**. The emission intensity is likewise strongly affected by the presence of oxygen, especially for **DMACBP** and **DMACBPN**, while for **DMACPyBP** and **DMACPyBPN**, the enhancement in intensity upon oxygen removal was much smaller (Figure 2.7). The PL decays with biexponential kinetics, with prompt fluorescence lifetimes, τ_p , of 18 ns, 21 ns, 27 ns and 10 ns, and delayed fluorescence lifetimes, τ_d , of 146.4 μ s, 3.5 μ s, 19.7 μ s and 2.3 μ s, respectively, for **DMACBP**, **DMACPyBP**, **DMACBPN** and **DMACPyBPN**. The corresponding rate constants of intersystem crossing (k_{ISC}) for **DMACBP**, **DMACPyBP**, **DMACBPN** and **DMACPyBPN** are 4.1×10^7 s⁻¹, 3.3×10^7 s⁻¹, 2.9×10^7 s⁻¹ and 5.0×10^7 s⁻¹, respectively, while the rate constants for reverse intersystem crossing (k_{RISC}) for **DMACPyBP** (81.6×10^4 s⁻¹) and **DMACPyBPN** (87.0×10^4 s⁻¹) are much faster than those of **DMACBP** (2.7×10^4 s⁻¹) and **DMACBPN** (24.1×10^4 s⁻¹), due in part to the smaller ΔE_{ST} in the former two that is correlated to the introduction of a nitrogen atom at the 10-position in **DMACPyBP** and **DMACPyBPN**.

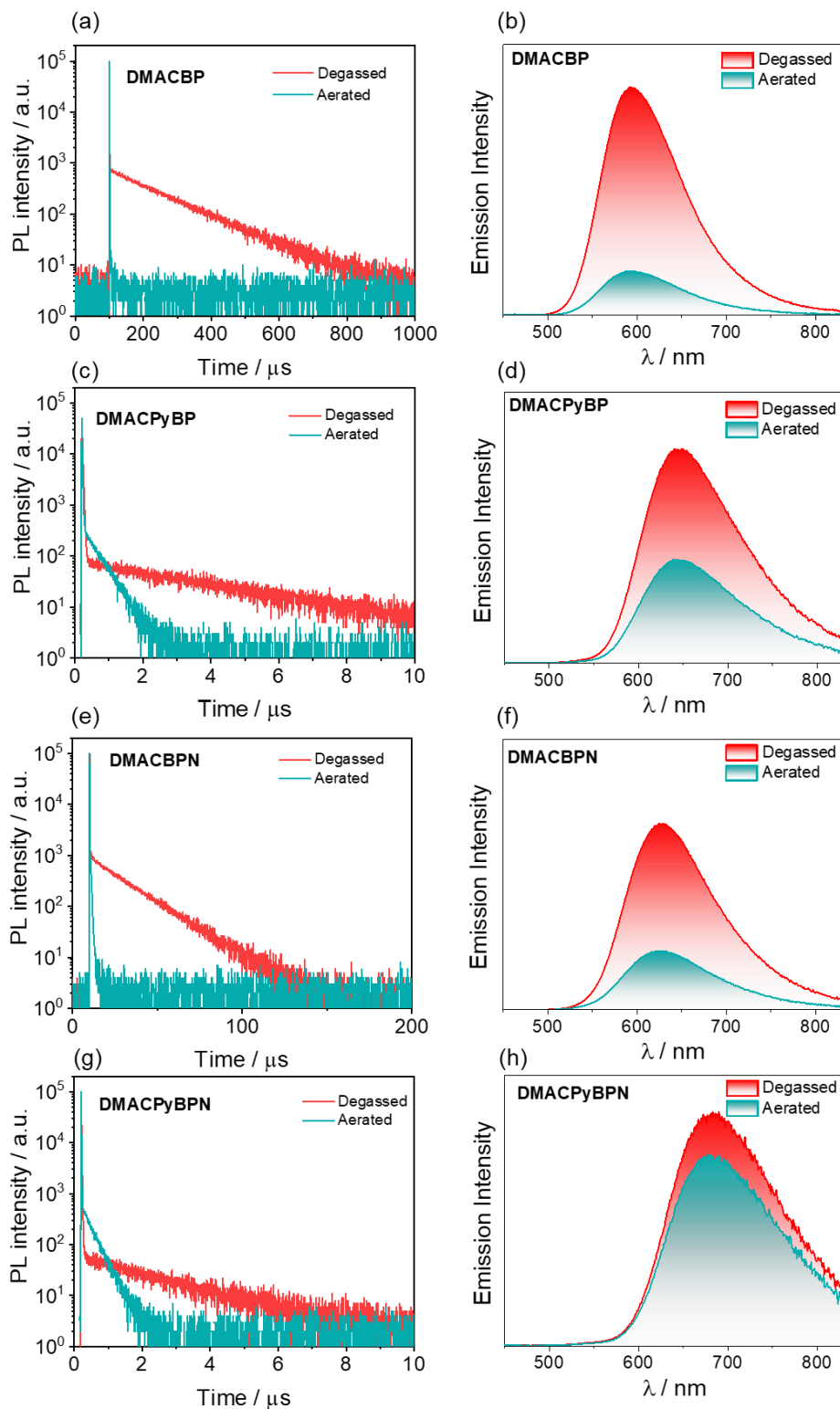


Figure 2.7. Time-resolved PL decay of (a) **DMACBP**, (c) **DMACPyBP**, (e) **DMACBPN** and (g) **DMACPyBPN** and corresponding the PL spectra (b) **DMACBP**, (d) **DMACPyBP**, (f) **DMACBPN** and (h) **DMACPyBPN** in degassed and aerated toluene (time window: 1 ns to 200 μs or 1 ns to 1 ms measured by MCS, 1 ns to 10 μs measured by TCSPC, $\lambda_{\text{exc}} = 375 \text{ nm}$).

2.6 TADF Properties in the Solid State

We next investigated the photophysical properties of the four emitters in an OLED-relevant host, CBP, as this host matrix has a sufficiently high triplet energy ($T_1 = 2.56$ eV) to confine the excitons onto the emitter.^{227,228} The PL of the doped films of varying dopant concentration from 2–10 wt% of emitters were firstly investigated (Figure 2.8) and the corresponding Φ_{PL} values are collated in Table 2.2. As the doping concentration is increased, the emission of all of the compounds is red-shifted from yellow to red (Figure 2.8), and the highest Φ_{PL} values are at a doping concentration of 2 wt%. The SSPL spectra of **DMACBP**, **DMACPyBP**, **DMACBPN** and **DMACPyBPN** at 2 wt% doping concentration exhibit broad and unstructured emission with λ_{PL} at 568, 601, 586, and 606 nm, respectively (Figure 2.9a). The trend in λ_{PL} mirror those in toluene (Figure 2.6a). The Φ_{PL} values of these films of **DMACBP**, **DMACPyBP**, **DMACBPN** and **DMACPyBPN** are 75, 47, 71 and 37%, respectively, under a N_2 atmosphere (Figure 2.9b, Table 2.2).

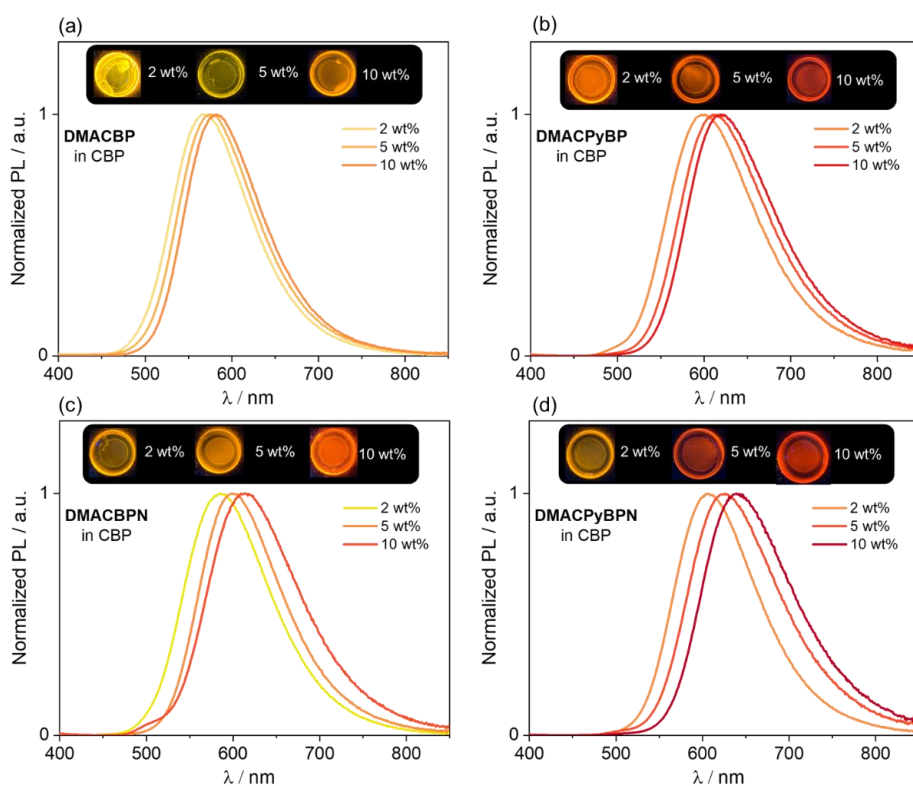


Figure 2.8. PL spectra of the **DMACBP**, **DMACPyBP**, **DMACBPN** and **DMACPyBPN** at different doping concentrations at room temperature ($\lambda_{\text{exc}} = 340$ nm).

Table 2.2. Summary of Φ_{PL} of **DMACBP**, **DMACPyBP**, **DMACBPN** and **DMACPyBPN** at varying dopant concentration from 2–10 wt% in CBP.

Compound	Host	doped ratio ^a	$\Phi_{\text{PL}} / \%$ (in N ₂)	$\Phi_{\text{PL}} / \%$ (in Air)	λ_{PL}
DMACBP	CBP	2%	75	56	568
		5%	70	52	574
		10%	66	43	583
DMACPyBP	CBP	2%	47	41	601
		5%	43	40	610
		10%	41	36	620
DMACBPN	CBP	2%	71	52	586
		5%	67	48	598
		10%	64	46	615
DMACPyBPN	CBP	2%	37	30	606
		5%	36	31	625
		10%	29	25	639

^a Spin-coated 2 -10 wt% emitters doped in CBP films and Φ_{PL} values were determined using an integrating sphere ($\lambda_{\text{exc}} = 340$ nm).

The decrease of Φ_{PL} for **DMACPyBP/DMACPyBPN** can be ascribed to their smaller energy gaps, thus leading to increased non-radiative decay.²²⁹ However, the difference of the distribution of the N atoms in the BP and BPN (two additional nitrogen atoms at the 4- and 5-positions) acceptors has only a relatively minor impact on the overall π -conjugation with a small red-shift in the emission from 568 nm for **DMACBP** to 586 nm for **DMACBPN**; as well, there is only a negligible decrease in the Φ_{PL} between **DMACBP** and **DMACBPN**.²³⁰ The Φ_{PL} values of **DMACBP** and **DMACBPN** exhibited a larger decrease in the presence of air at 56 and 52%, respectively, compared to 41% for **DMACPyBP** and 30% for **DMACPyBPN**, indicating a greater proportion of triplet excitons in **DMACBP** and **DMACBPN**. As shown in Figure 2.9, all four compounds showed multiexponential decay kinetics, with average prompt fluorescence lifetimes, average τ_{p} , of 15.3, 21.1, 22.4, and 23.2 ns and average delayed emission lifetimes, average τ_{d} , of 130.3, 5.9, 47.2, and 2.9 μs at room temperature for **DMACBP**, **DMACPyBP**, **DMACBPN** and **DMACPyBPN**, respectively. The corresponding k_{ISC} for **DMACBP**, **DMACPyBP**, **DMACBPN** and **DMACPyBPN** in the 2 wt% doped films

in CBP are $1.7 \times 10^7 \text{ s}^{-1}$, $0.6 \times 10^7 \text{ s}^{-1}$, $1.2 \times 10^7 \text{ s}^{-1}$ and $0.8 \times 10^7 \text{ s}^{-1}$, respectively, while the k_{RISC} for **DMACPyBP** and **DMACPyBPN** reached $1.94 \times 10^5 \text{ s}^{-1}$ and $4.26 \times 10^5 \text{ s}^{-1}$, more than ten times higher than those of **DMACBP** at $0.10 \times 10^5 \text{ s}^{-1}$ and **DMACBPN** at $0.29 \times 10^5 \text{ s}^{-1}$ (Figure 2.9b), following a similar trend to that observed in toluene. The introduction of a nitrogen atom at the 10-position in **DMACPyBP** and **DMACPyBPN** leads to much stronger CT and faster k_{RISC} .

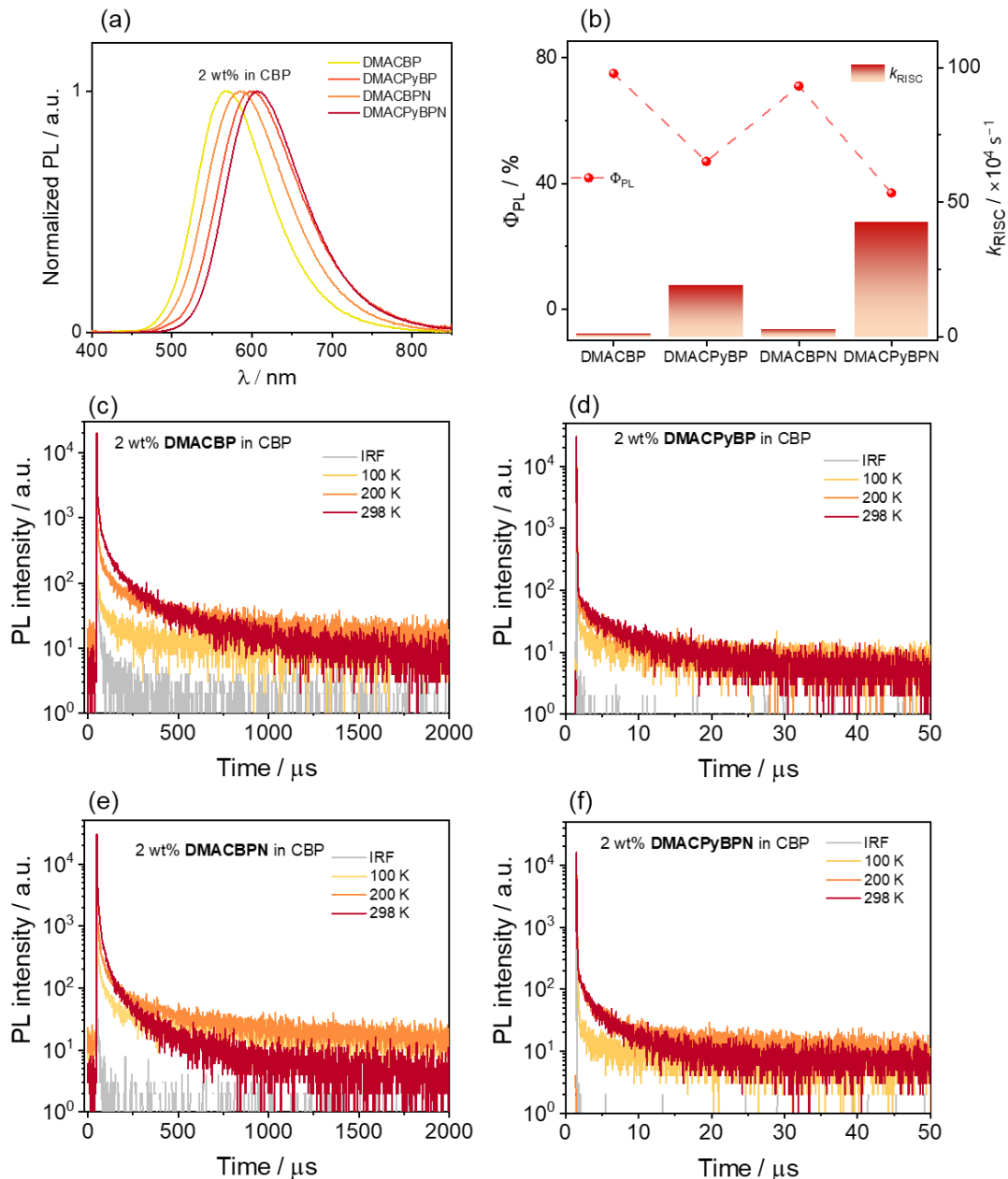


Figure 2.9. (a) PL spectra of 2 wt% **DMACBP**, 2 wt% **DMACPyBP**, 2 wt% **DMACBPN** and 2 wt% **DMACPyBPN** doped CBP film ($\lambda_{\text{exc}} = 360 \text{ nm}$); (b) Φ_{PL} values and k_{RISC} VS four emitter with different N/C ratio acceptor; Temperature-dependent time-resolved PL decay of

(c) 2 wt% **DMACBP**, (d) 2 wt% **DMACPyBP**, (e) 2 wt% **DMACBPN** and (f) 2 wt% **DMACPyBPN** doped CBP film ($\lambda_{\text{exc}} = 375$ nm).

Temperature-dependent time-resolved PL (TRPL) analysis shows that the intensity of the delayed emission increases with increasing temperatures for all 4 compounds, confirming that these compounds emit via TADF (Figure 2.9c-d). The energy levels of the S_1 and T_1 states were estimated from the onsets of the corresponding prompt fluorescence and phosphorescence spectra of the 2 wt% doped films in CBP at 77 K (Figure 2.10). The non-zero tails of the phosphorescence spectra for **DMACBP** and **DMACBPN** might be attributed to the weak emission intensity. As expected, **DMACBP**, **DMACPyBP**, **DMACBPN** and **DMACPyBPN** have, respectively, small ΔE_{ST} values of 0.02, 0.01, 0.01 and 0.01 eV, values that align with those in 2-MeTHF glass.

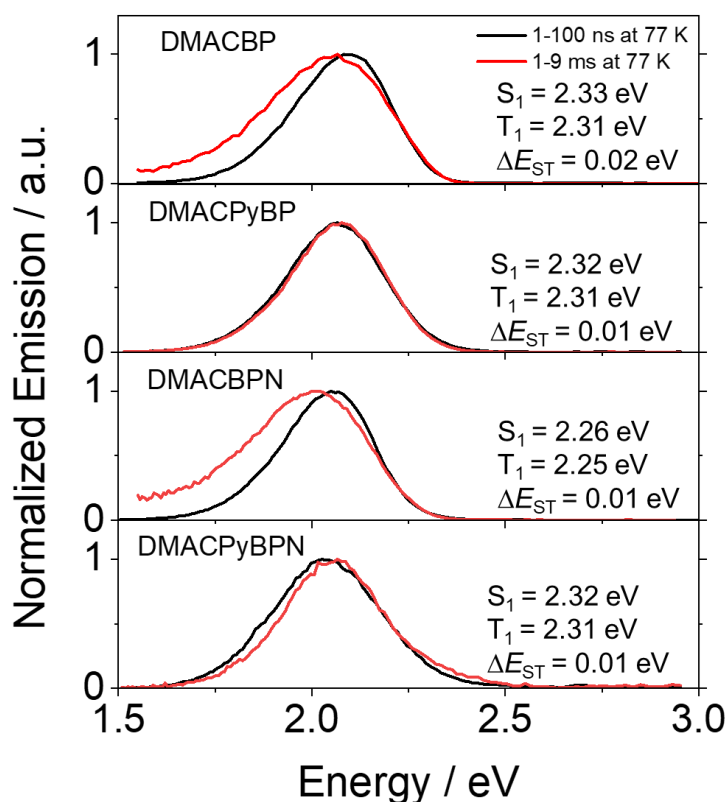


Figure 2.10. Prompt fluorescence (1-100 ns) and phosphorescence spectra (9-10 ms) of the **DMACBP**, **DMACPyBP**, **DMACBPN** and **DMACPyBPN** in 2 wt% doped in CBP film at 77 K ($\lambda_{\text{exc}} = 340$ nm).

Table 2.1. Summary of photophysical properties of Nitrogen-Doped PAH acceptor-based compounds

Molecule	λ_{abs} ($\epsilon / \times 10^3 \text{ M}^{-1} \text{ cm}^{-1}$) / nm ^a	λ_{PL} ^a / nm	τ_{p} / ns ^a	τ_{d} / μs ^a	λ_{PL} ^b / nm	Φ_{PL} ^b / %	S_1/T_1 ^c / eV	ΔE_{ST} / eV	τ_{p} / ns ^d	τ_{d} / μs ^d	$k_{\text{ISC}}^{\text{e}}$ / $\times 10^7 \text{ s}^{-1}$	$k_{\text{RISC}}^{\text{e}}$ / $\times 10^4 \text{ s}^{-1}$	E_{HOMO} ^f / eV	E_{LUMO} ^f / eV	E_{g} ^g / eV
DMACBP	395 (13), 458(1.8)	595	18	146	568	75(56)	2.33/2.31	0.02	15.3	130.3	1.7	1.0	-5.34	-2.94	2.40
DMACPyBP	400 (17), 474(3.2)	645	20	3.5	601	47(41)	2.32/2.31	0.01	21.1	5.9	0.6	19.4	-5.39	-3.12	2.27
DMACBPN	383 (15), 465(2.5)	630	27	19.7	586	71(52)	2.26/2.25	0.01	22.4	47.2	1.2	2.9	-5.33	-3.00	2.33
DMACPyBPN	382 (16), 475(3.2)	672	10	2.3	606	37(30)	2.32/2.31	0.01	23.2	2.9	0.8	42.6	-5.39	-3.20	2.19

^a In PhMe at 298 K ($\lambda_{\text{exc}}=340$ nm). ^b Spin-coated 2 wt% emitters doped in CBP films and Φ_{PL} values were determined using an integrating sphere ($\lambda_{\text{exc}}=340$ nm). Values quoted are under N₂. Values in parentheses are in air. ^c S_1 was obtained from the onset of the prompt emission (time-gated window: 1–100 ns) ms measured in doped film at 77 K and T_1 was obtained from the onset of the phosphorescence spectrum (time-gated window: 1–10 ms) measured in doped film at 77 K. ^d PL lifetime. ^e k_{ISC} = intersystem crossing rate constant from S_1 to T_1 states; k_{RISC} = reverse intersystem crossing rate constant. ^f In DCM with 0.1 M [ⁿBu₄N]PF₆ as supporting electrolyte and Fc/Fc⁺ as the internal reference (0.46 V vs. SCE).²²⁴ The HOMO and LUMO energies were determined using $E_{\text{HOMO/LUMO}} = (E_{\text{ox}}/E_{\text{red}} + 4.8)$ eV where E_{ox} and E_{red} are anodic and cathodic peak potentials, respectively, obtained from the DPV versus Fc/Fc⁺.²²⁴ ^g $E_{\text{g}} = |E_{\text{HOMO}} - E_{\text{LUMO}}|$.

2.7 OLED Device Characterization

To evaluate the EL performance of these emitters, OLEDs employing different concentration emitters doped in CBP films as the emissive layer (EML) were fabricated. The OLEDs has the following configuration: ITO (indium tin oxide)/TAPC (4,4'-(cyclohexane-1,1-diyl)bis(*N,N*-di-*p*-tolylaniline)) (40 nm)/TCTA (tris(4-(9H-carbazol-9-yl)phenyl)amine) (10 nm)/CBP (10 nm)/CBP: *x* wt% dopants (20 nm)/TmPyPB (3,3'-(5'-(3-(pyridin-3-yl)phenyl)-[1,1':3',1''-terphenyl]-3,3''-diyl)dipyridine) (45 nm)/LiF (1 nm)/Al (Figure 2.11a). ITO and Al serve as the anode and cathode, respectively, while TAPC, TCTA and TmPyPB are, respectively, used as the hole-transporting layer, electron-blocking layer, and electron-transporting layer.

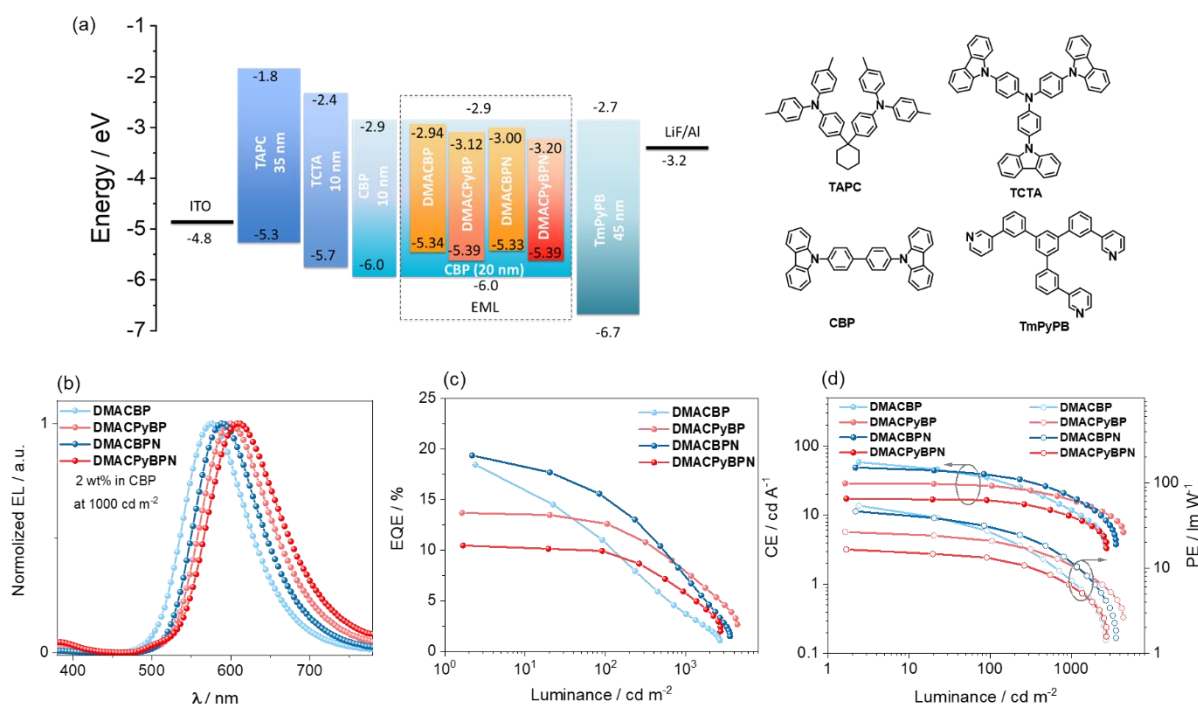


Figure 2.11. (a) Energy level diagram and molecular structure of materials of materials employed in the devices; (b) EL spectra of the devices; (c) external quantum efficiency versus luminance curves for the devices; (d) current efficiency and power efficiency versus luminance curves for the devices.

As shown in Figure 2.11b, the OLEDs with **DMACBP**, **DMACPyBP**, **DMACBPN** and **DMACPyBPN**, at a 2 wt% doping concentration in CBP host exhibit yellow-to-red EL with

the peak emission, λ_{EL} , at 576, 600, 588 and 608 nm, respectively, which match the PL in CBP very well (Figure 2.9a). The corresponding CIE coordinates are (0.48, 0.50), (0.56, 0.44), (0.53, 0.46) and (0.57, 0.42). The devices with **DMACBP**, **DMACPyBP**, **DMACBPN**, and **DMACPyBPN** showed EQE_{max} of 18.5, 13.7, 19.4 and 10.5%, respectively, reflecting the variations in their intrinsic Φ_{PL} (Figure 2.11c and Table 2.3). The maximum current efficiency (CE_{max}) and power efficiency (PE_{max}) values are 58.7 cd A^{-1} and 54.2 lm W^{-1} for the devices with **DMACBP**, 28.9 cd A^{-1} and 26.7 lm W^{-1} for the devices with **DMACPyBP**, 48.9 cd A^{-1} and 46.5 lm W^{-1} for the devices with **DMACBPN**, and 17.4 cd A^{-1} and 16.6 lm W^{-1} for the devices with **DMACPyBPN** (Figure 2.11d). The efficiency roll-off behavior is noticeably different between the four devices. At a luminance of 100 cd m^{-2} , a large efficiency roll-off of 40.5% and 24.7% was observed in the devices with **DMACBP** and **DMACBPN**, respectively, which decreased considerably to 8.0% and 4.7% in the devices with **DMACPyBP** and **DMACPyBPN**, respectively. The EQE decreased to 3.7% at a luminance of 1000 cd m^{-2} for the device with **DMACBP**; however, for the device with **DMACPyBP**, the EQE_{1000} was 7.5%. A plausible explanation for this difference in efficiency roll-off behavior is due to the faster k_{RISC} and shorter τ_{d} in **DMACPyBP** and **DMACPyBPN**, thus leading to smaller triplet exciton populations at high current densities in the devices with these two emitters. The **DMACPyBP**-based OLED showed remarkably low efficiency roll-off, especially compared to other DMAC-containing orange-red TADF OLEDs (Figure 2.1).^{143,221,225} Increasing the doping concentration to 11 wt% does not lead to further improvement in performance and the EL spectra red-shifted progressively (Figure 2.12). At 11 wt% doping, the OLEDs emit in the range of 600–640 nm and showed EQE_{max} of 5.5–15.9% (Table 2.3).

Table 2.3. Electroluminescence data for the devices

Emitter	Concentration/ wt%	V_{on}^a /V	CE_{max}^b /cd A ⁻¹	PE_{max}^c /lm W ⁻¹	$EQE_{max/100/1000}^d$ /%	L_{max}^e /cd m ⁻²	λ_{EL}^f /nm	CIE^g (x, y)
DMACBP	2.0%	3.4	58.7	54.2	18.5/11.0/3.7	2665	576	0.48, 0.50
	5.0%	3.4	40.3	35.1	15.2/12.1/5.4	4146	580	0.52, 0.47
	8.0%	3.5	42.4	38.1	15.7/11.8/5.3	3978	584	0.52, 0.48
	11.0%	3.5	38.1	34.2	14.6/12.0/5.6	4332	584	0.52, 0.47
DMACPyBP	2.0%	3.4	28.9	26.7	13.7/12.6/7.5	4346	600	0.56, 0.44
	5.0%	3.4	18.6	17.2	10.9/10.2/5.8	4045	608	0.58, 0.41
	8.0%	3.4	14.7	13.6	10.2/9.5/5.8	3583	616	0.60, 0.40
	11.0%	3.4	11.6	10.7	9.0/8.3/4.7	3369	620	0.61, 0.39
DMACBPN	2.0%	3.3	48.9	46.5	19.4/14.6/6.7	3551	588	0.53, 0.46
	5.0%	3.2	43.9	43.1	18.4/14.5/7.1	3647	592	0.54, 0.45
	8.0%	3.1	36.1	36.6	16.3/13.9/7.4	4160	596	0.55, 0.44
	11.0%	3.1	31.9	32.3	15.9/13.4/7.5	4315	600	0.57, 0.43
DMACBPN	2%	3.3	17.4	16.6	10.5/10.0/5.0	2723	608	0.57, 0.42
	5%	3.2	8.8	8.6	7.3/7.1/3.5	1918	624	0.61, 0.39
	8%	3.2	5.1	5.0	5.3/5.0/2.1	1421	636	0.62, 0.37
	11%	3.2	4.1	4.0	5.4/5.1/2.0	1428	640	0.63, 0.37

^a Voltage at 1 cd m⁻². ^b Maximum current efficiency. ^c Maximum power efficiency. ^d Maximum external quantum efficiency/ at 100 cd m⁻²/ at 1000 cd m⁻². ^e Maximum luminance. ^f EL emission peak at 1000 cd m⁻². ^g Commission Internationale de L'Éclairage coordinates.

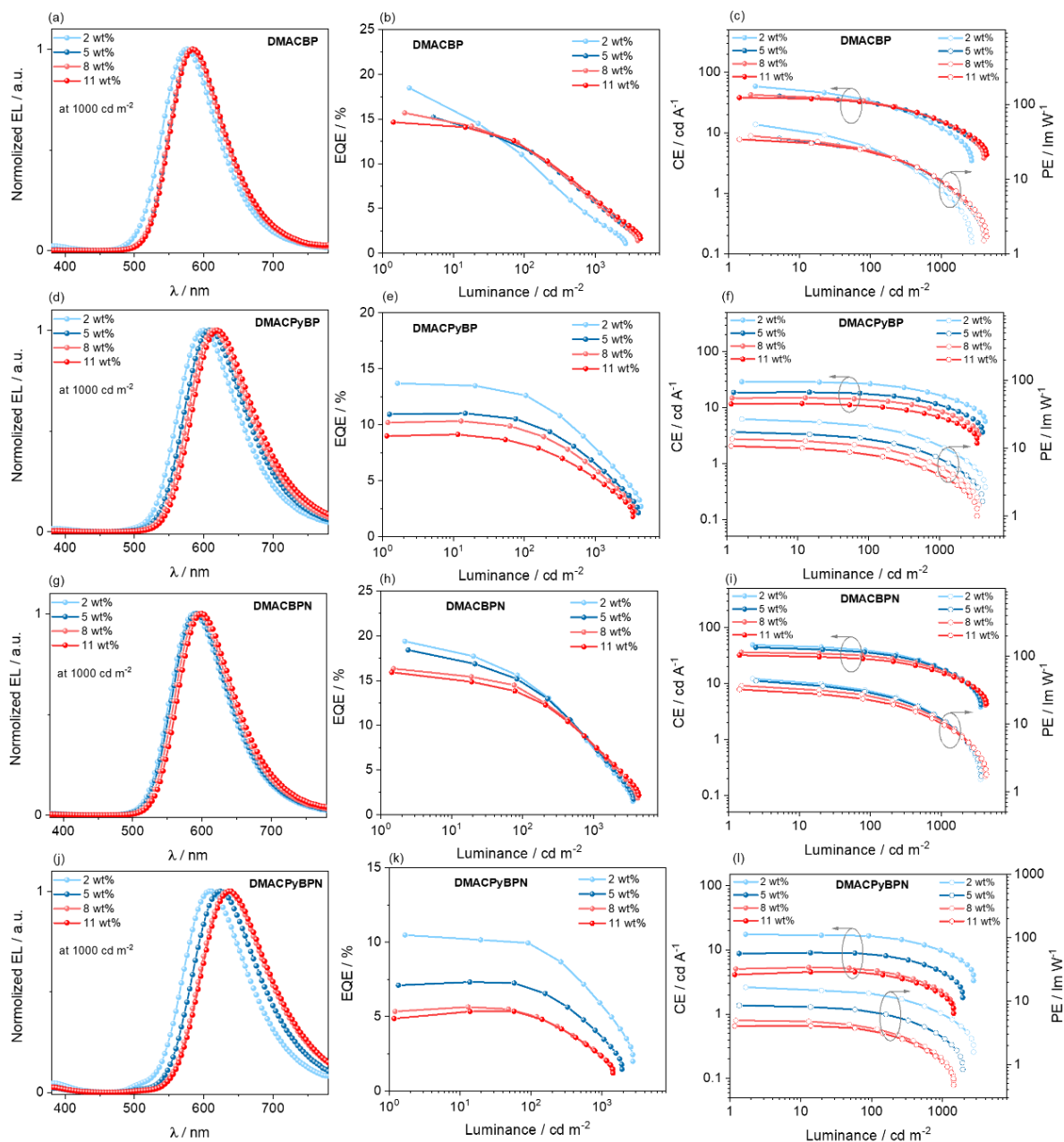


Figure 2.12. OLED performance based on **DMACBP**, **DMACPyBP**, **DMACBPN** and **DMACPyBPN** in 2 wt%, 5 wt%, 8 wt% and 11 wt% doped in CBP as EML.

2.8 Conclusions

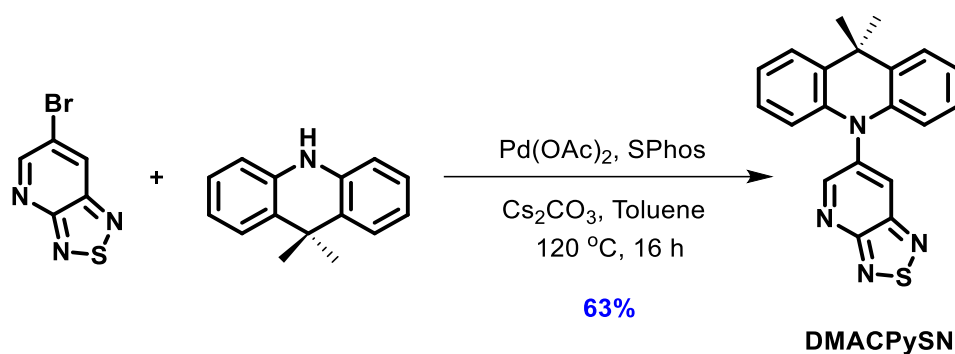
We developed a family of four orange-to-red TADF compounds whose structures differ by the number of nitrogen atoms contained within the conjugated acceptor core. The structure-property relationship among the four compounds has been systematically investigated using DFT calculations, and a combination of photophysical and electrochemical studies; OLEDs

were also fabricated using these materials as emitters. It was found that increasing the nitrogen atom content in the acceptor (BP) of the D-A typed compounds results in a more stabilized LUMO, smaller ΔE_{ST} and faster k_{RISC} . In particular, having a nitrogen at the 10-position of BP notably enhances k_{RISC} , as demonstrated in **DMACPyBP** and **DMACPyBPN** compared to **DMACBP** and **DMACBPN**, despite the small decrease in Φ_{PL} . OLEDs with **DMACBPN** showed a maximum EQE of 19.4% and an electroluminescence maximum of 588 nm. As the N/C ratio increased, the EL spectra of the corresponding devices progressively red-shifted, with the reddest-emitting device ($\lambda_{EL} = 640$ nm) employing **DMACPyBPN**. Furthermore, the **DMACPyBP/ DMACPyBPN**-based OLEDs showed remarkably low efficiency roll-off of only 8 and 5%, compared to 40 and 25% at 100 cd m^{-2} for the devices with **DMACBP/ DMACBPN**, respectively.

2.9 Experimental Section

All commercially available chemicals and reagent grade solvents were used as received. 5-(9,9-dimethylacridin-10(9H)-yl)benzo[*c*][1,2,5]thiadiazole (**DMACPhSN**) was synthesised according to the literature.²³¹

Synthesis of 6-(9,9-dimethylacridin-10(9H)-yl)-[1,2,5]thiadiazolo[3,4-*b*]pyridine (DMACPySN**):**



6-Bromo-[1,2,5]thiadiazolo[3,4-*b*]pyridine (2.00 g, 9.26 mmol, 1.0 equiv.), DMAC (2.13 g, 10.18 mmol, 1.1 equiv.), cesium carbonate (9.05 g, 27.77 mmol, 3.0 equiv.), 2-dicyclohexylphosphino-2',6'-dimethoxybiphenyl (0.23 g, 0.56 mmol, 0.06 equiv.), and palladium(II) acetate (62 mg, 0.28 mmol, 0.03 equiv.) were dissolved in 40 mL of dry toluene and the flask placed under N₂. The mixture was stirred at 120 °C for 16 h. The resulting mixture was cooled to room temperature and then poured into water (30 mL). The organic phase was extracted with DCM (3 × 100 mL). The combined organic layers were dried over anhydrous magnesium sulfate and concentrated under reduced pressure. The crude product was purified by column chromatography on silica gel (17% DCM/Hexane) to afford **DMACPySN** as a red solid (yield = 2.00 g).

6-(9,9-dimethylacridin-10(9H)-yl)-[1,2,5]thiadiazolo[3,4-*b*]pyridine (DMACPySN**):** R_f = 0.3 (17% DCM/Hexane). **Yield:** 63%. **Mp** = 175-176 °C. **¹H NMR (400 MHz, Chloroform-*d*)** δ 9.02 (d, *J* = 2.5 Hz, 1H), 8.47 (d, *J* = 2.5 Hz, 1H), 7.61 – 7.49 (m, 2H), 7.09 – 7.02 (m, 4H), 6.42 – 6.31 (m, 2H), 1.75 (s, 6H). **¹³C NMR (101 MHz, CDCl₃)** δ 160.76, 159.30, 148.25, 140.08, 138.10, 131.44, 131.05, 126.74, 125.74, 122.17, 114.39, 77.36, 77.05, 76.73, 36.22,

30.91. GC-MS Calculated: (C₂₀H₁₆N₃S) 344.11; Found: 344.16, Retention time: 12.42 minutes
in DCM.

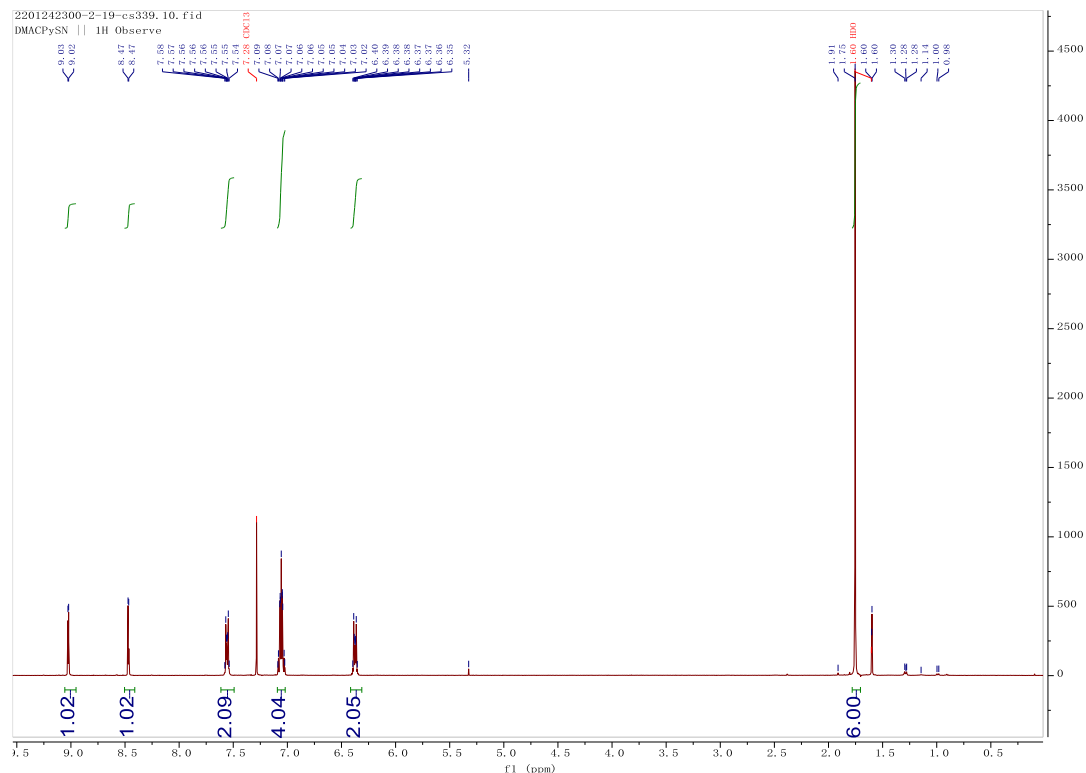


Figure 2.13. ¹H NMR spectra of **DMACPySN** in CDCl₃.

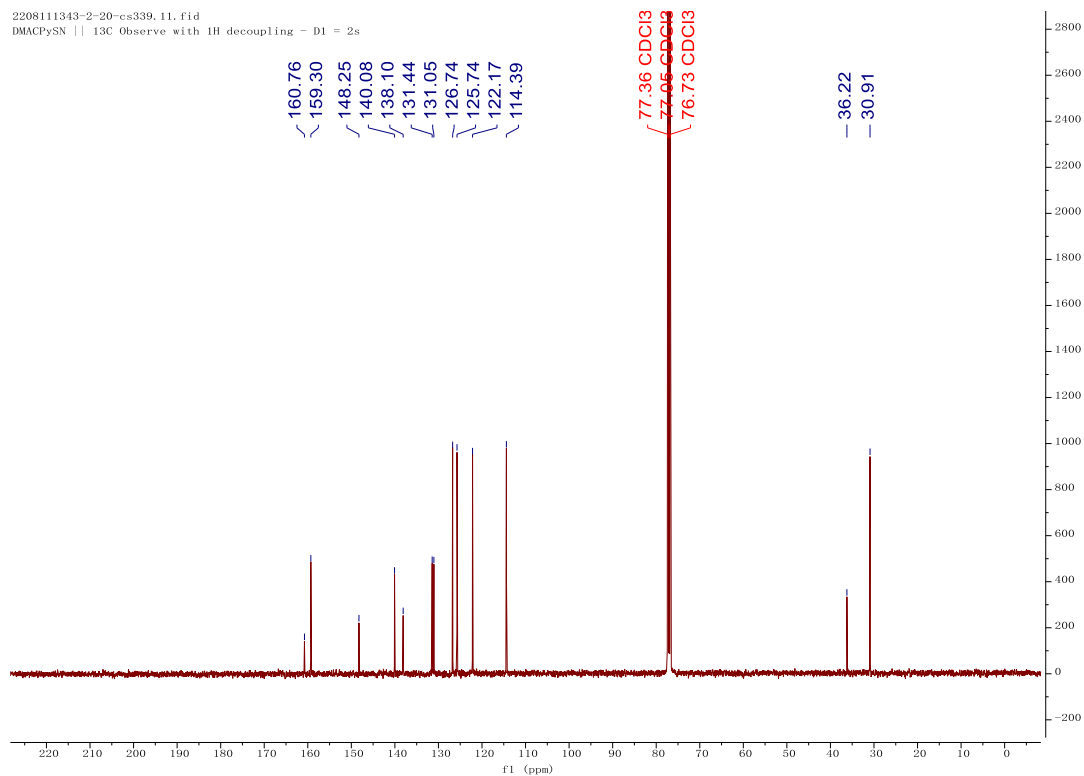


Figure 2.14. ¹³C NMR spectra of **DMACPySN** in CDCl₃.

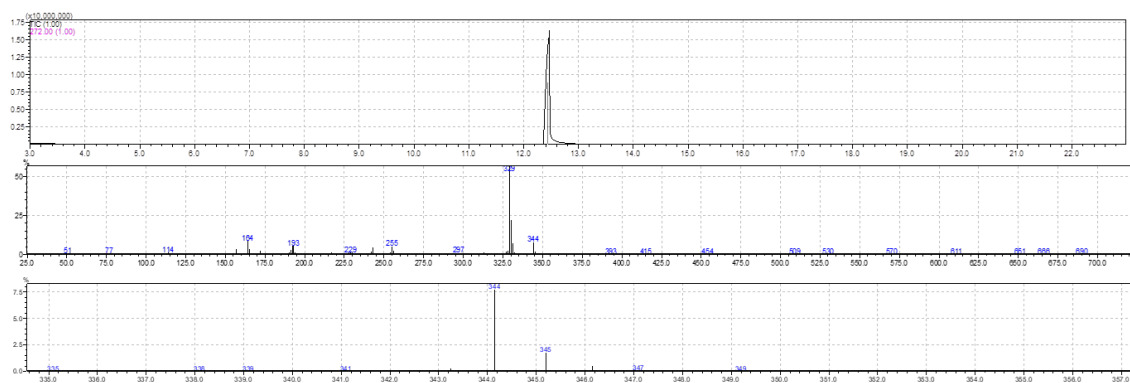
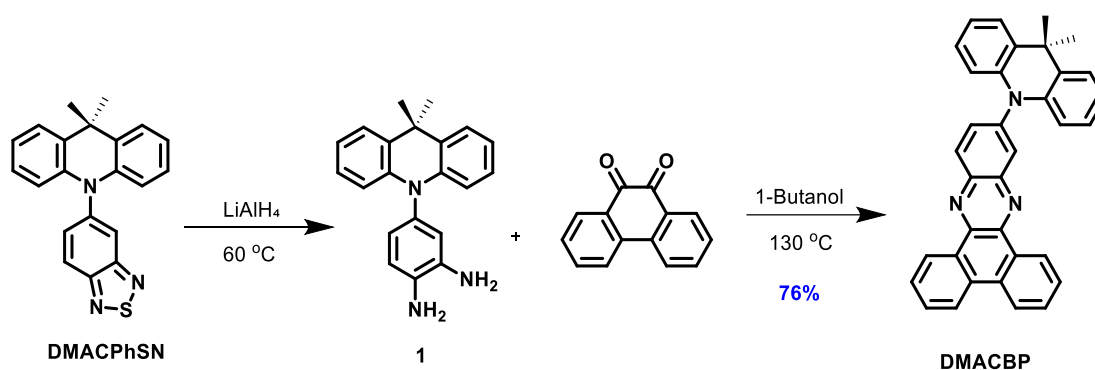


Figure 2.15. GCMS of DMACPySN.

Synthesis of 11-(9,9-dimethylacridin-10(9*H*)-yl)dibenzo[*a,c*]phenazine (DMACBP):



To a solution of **DMACPhSN** (0.5 g, 1.46 mmol, 1.0 equiv.) in dry THF (20 mL) was added lithium aluminum hydride (0.44 g, 11.65 mmol 8.0 equiv.) under a continuous N₂ flow. The resulting mixture was stirred at 60 °C under a N₂ atmosphere for 2 h. After cooling to 0 °C, the reaction mixture was quenched with water (2 mL) and then 2 M NaOH(aq) (2 mL). The above solution was filtered through a pad of Celite, which was subsequently rinsed with ethyl acetate, and the filtrate was then extracted with ethyl acetate (3×30 mL). The organic layer was collected and dried over MgSO₄. After filtration and removal of the solvent, compound **1** was used directly for the next step without further purification. Compound **1** and phenanthrene-9,10-dione (0.30 g, 1.46 mmol, 1.0 equiv.) were added into 20 mL of 1-butanol and then heated to reflux for 12 hours under a N₂ atmosphere. After cooling to room temperature, the solution was poured into water and extracted with DCM (3 × 100 mL). The organic layer was dried over Na₂SO₄ and concentrated under reduced pressure. The residue was purified by column chromatography with (25% DCM/Hexane) to afford the compound **DMACBP** as yellow solid (0.54 g).

11-(9,9-dimethylacridin-10(9H)-yl)dibenzo[*a,c*]phenazine (DMACBP): $R_f = 0.3$ (25% DCM/Hexane). **Yield:** 76%. **Mp** = 257-258 °C. $^1\text{H NMR}$ (500 MHz, CDCl_3) δ 9.49 (dd, $J = 8.0, 1.5$ Hz, 1H), 9.41 (dd, $J = 8.1, 1.4$ Hz, 1H), 8.73 – 8.57 (m, 3H), 8.45 (d, $J = 2.2$ Hz, 1H), 7.91 – 7.75 (m, 5H), 7.58 – 7.51 (m, 2H), 7.04 – 6.96 (m, 4H), 6.52 – 6.39 (m, 2H), 1.79 (s, 6H). $^{13}\text{C NMR}$ (126 MHz, CDCl_3) δ 143.25, 142.76, 142.40, 141.66, 140.69, 132.98, 132.30, 131.41, 130.72, 130.68, 130.64, 128.12, 126.49, 126.44, 125.31, 123.04, 121.15, 114.60, 77.28, 77.02, 76.77, 36.17, 31.06. **HR-MS** $[\text{M}+\text{H}]^+$ **Calculated:** ($\text{C}_{35}\text{H}_{25}\text{N}_3$) 487.2048; **Found:** 487.2043. **Anal. Calcd. for $\text{C}_{35}\text{H}_{25}\text{N}_3$:** C, 86.21%; H, 5.17%; N, 8.62%. **Found:** C, 85.78%; H, 5.11%; N, 8.47%. **HPLC analysis:** 99.04% pure on HPLC analysis, retention time 10.0 minutes in 90% Acetonitrile 10% water.

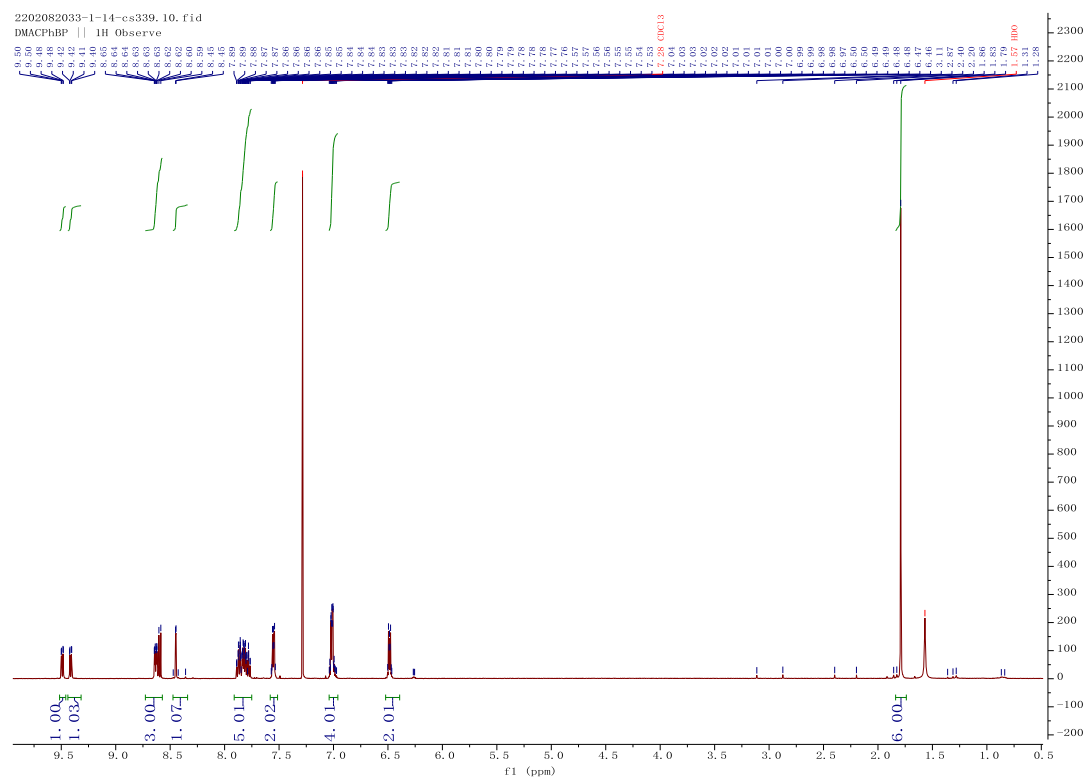


Figure 2.16. $^1\text{H NMR}$ spectra of DMACBP in CDCl_3 .

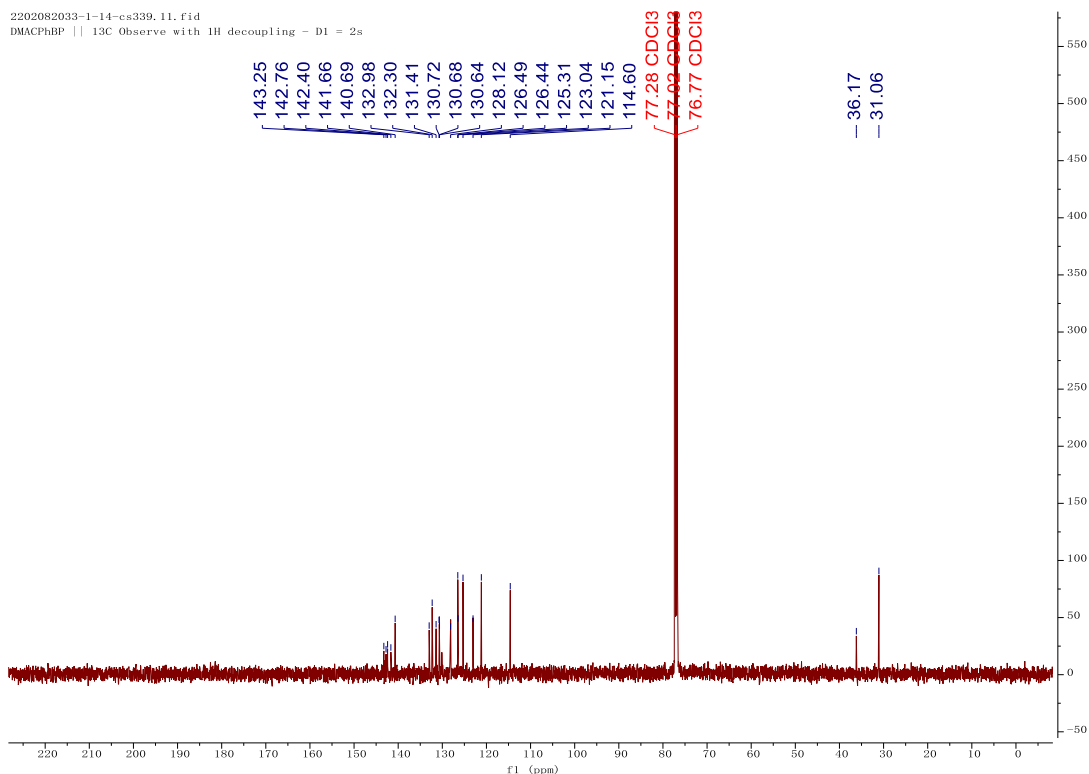


Figure 2.17. ^{13}C NMR spectra of DMACBP in CDCl_3 .

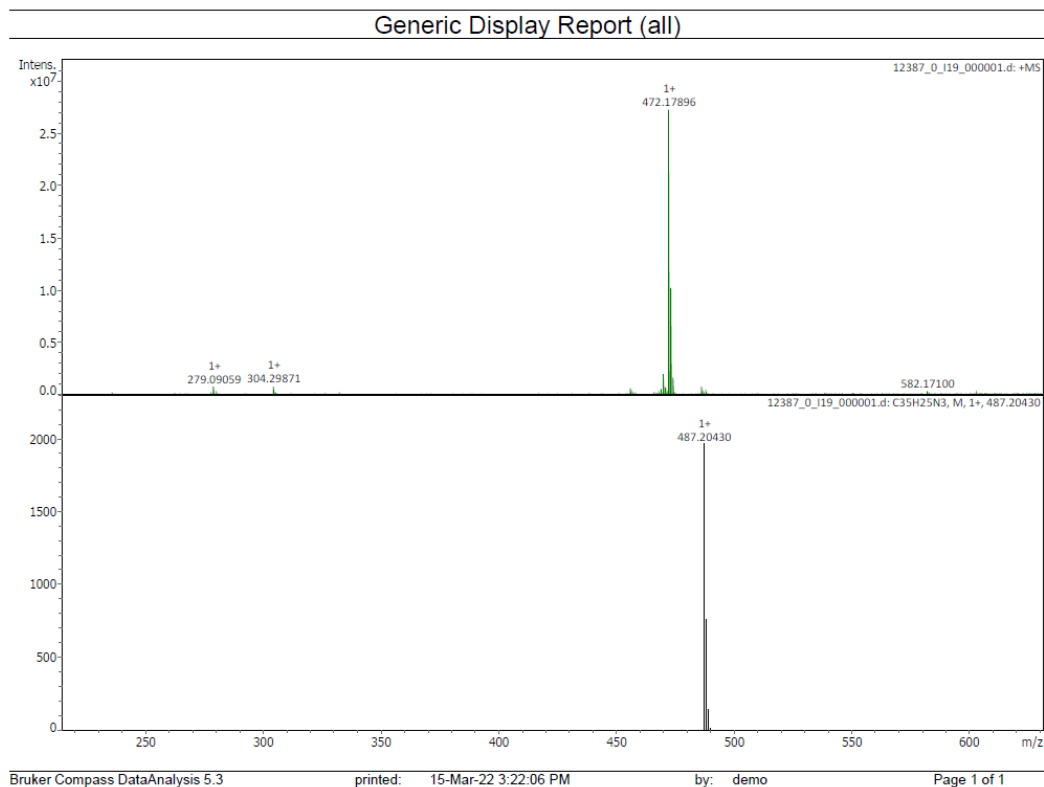


Figure 2.18. HRMS of DMACBP.

Elemental Analysis Service Request Form

Researcher name Changfeng Si

Researcher email cs339@st-andrews.ac.uk

NOTE: Please submit ca. 10 mg of sample

Sample reference number	CFS-230-DMACBP
Name of Compound	DMACBP
Molecular formula	C35H25N3
Stability	
Hazards	
Other Remarks	

Analysis type:

Single Duplicate Triplicate

Analysis Result:

Element	Expected %	Found (1)	Found (2)	Found (3)
Carbon	86.21	84.78	85.78	
Hydrogen	5.17	5.11	5.23	
Nitrogen	8.62	8.38	8.47	
Oxygen				

Authorising Signature:

Date completed	30.03.22
Signature	S-PL
comments	-

Figure 2.19. EA of DMACBP.

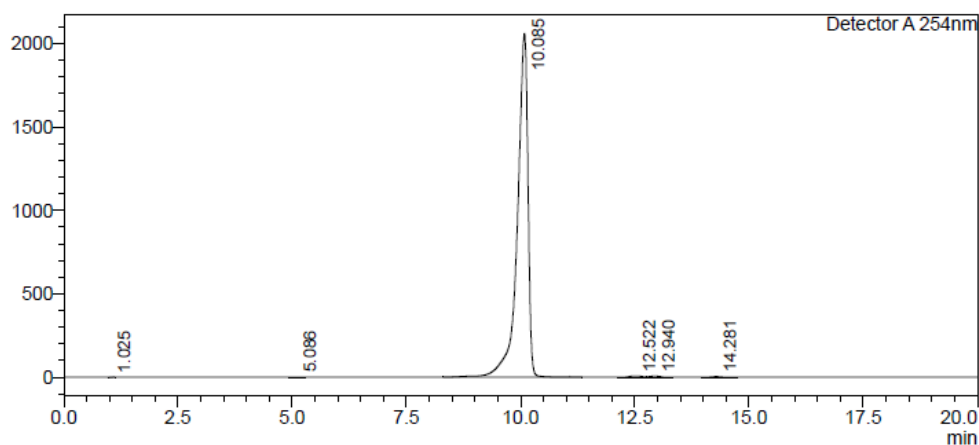
HPLC Trace Report 24 Feb 2022

<Sample Information>

Sample Name : DMACBP
 Sample ID :
 Method Filename : 90% Acetonitrile 10 Water 20 mins.lcm
 Batch Filename : DMACBP.lcb
 Vial # : 1-11
 Injection Volume : 5 uL
 Date Acquired : 24/02/2022 13:55:24
 Date Processed : 24/02/2022 14:15:26
 Sample Type : Unknown
 Acquired by : System Administrator
 Processed by : System Administrator

<Chromatogram>

mV



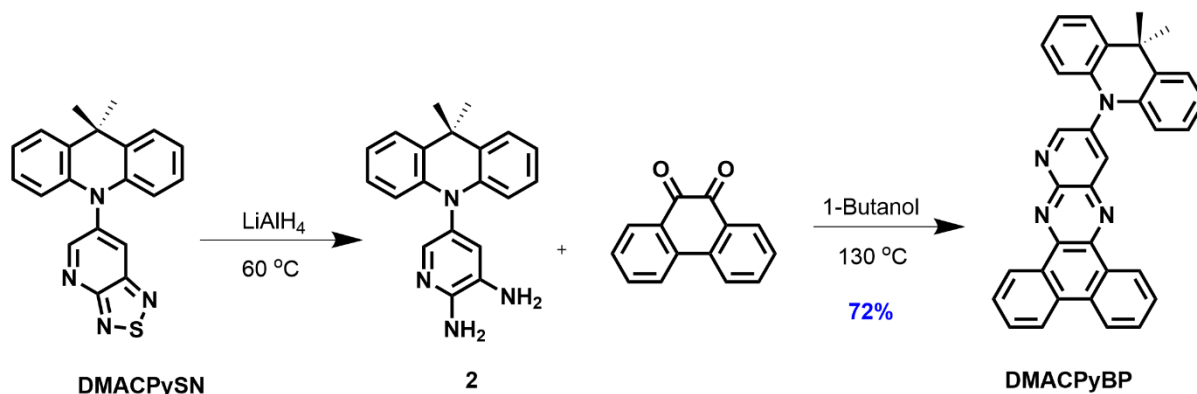
<Peak Table>

Detector A 254nm

Peak#	Ret. Time	Area	Height	Area%	Area/Height	Width at 5% Height
1	1.025	4405	1168	0.013	3.770	--
2	5.086	16955	2157	0.050	7.861	0.259
3	10.085	33284932	2060182	99.044	16.156	0.654
4	12.522	127079	6758	0.378	18.804	--
5	12.940	101215	5912	0.301	17.119	--
6	14.281	71741	3835	0.213	18.705	0.604
Total		33606326	2080013	100.000		

Figure 2.20. HPLC trace of DMACBP.

Synthesis of 12-(9,9-dimethylacridin-10(9H)-yl)dibenzo[*f,h*]pyrido[2,3-*b*]quinoxaline (DMACPyBP):



Compound **DMACPyBP** was synthesized according to the same procedure as described above for the synthesis of **DMACBP**, except that **DMACPySN** (2.2 g, 5.3 mmol) was used as the reactant instead of **DMACPhSN**, yielding a red solid (yield = 0.515 g).

12-(9,9-dimethylacridin-10(9H)-yl)dibenzo[*f,h*]pyrido[2,3-*b*]quinoxaline (DMACPyBP):

R_f = 0.3 (33% DCM/Hexane). **Yield:** 72%. **Mp** = 241-243 $^\circ\text{C}$. **^1H NMR (500 MHz, $\text{DMSO-}d_6$)** δ 9.36 (dd, J = 8.0, 1.5 Hz, 1H), 9.29 – 9.24 (m, 2H), 8.99 (d, J = 2.6 Hz, 1H), 8.92 – 8.84 (m, 2H), 8.02 – 7.83 (m, 4H), 7.63 – 7.58 (m, 2H), 7.07 – 7.00 (m, 4H), 6.49 – 6.44 (m, 2H), 1.72 (s, 6H) ppm. **^{13}C NMR (126 MHz, $\text{DMSO-}d_6$)** δ 158.25, 144.54, 143.28, 140.43, 139.90, 138.43, 138.39, 132.66, 132.42, 132.18, 132.01, 131.20, 129.68, 129.32, 129.16, 129.06, 127.25, 126.71, 126.44, 126.25, 124.38, 122.09, 115.02, 36.29, 31.68 ppm. **HR-MS (Xevo G2-S) $[\text{M}+\text{H}]^+$ Calculated:** ($\text{C}_{34}\text{H}_{24}\text{N}_4$) 488.2001; **Found:** 488.2054. **Anal. Calcd. for $\text{C}_{34}\text{H}_{24}\text{N}_4$:** C, 83.58%; H, 4.95%; N, 11.47%. **Found:** C, 83.57%; H, 4.99%; N, 11.19%. **HPLC analysis:** 98.8% pure on HPLC analysis, retention time 9.11 minutes in 80% MeOH 20% water.

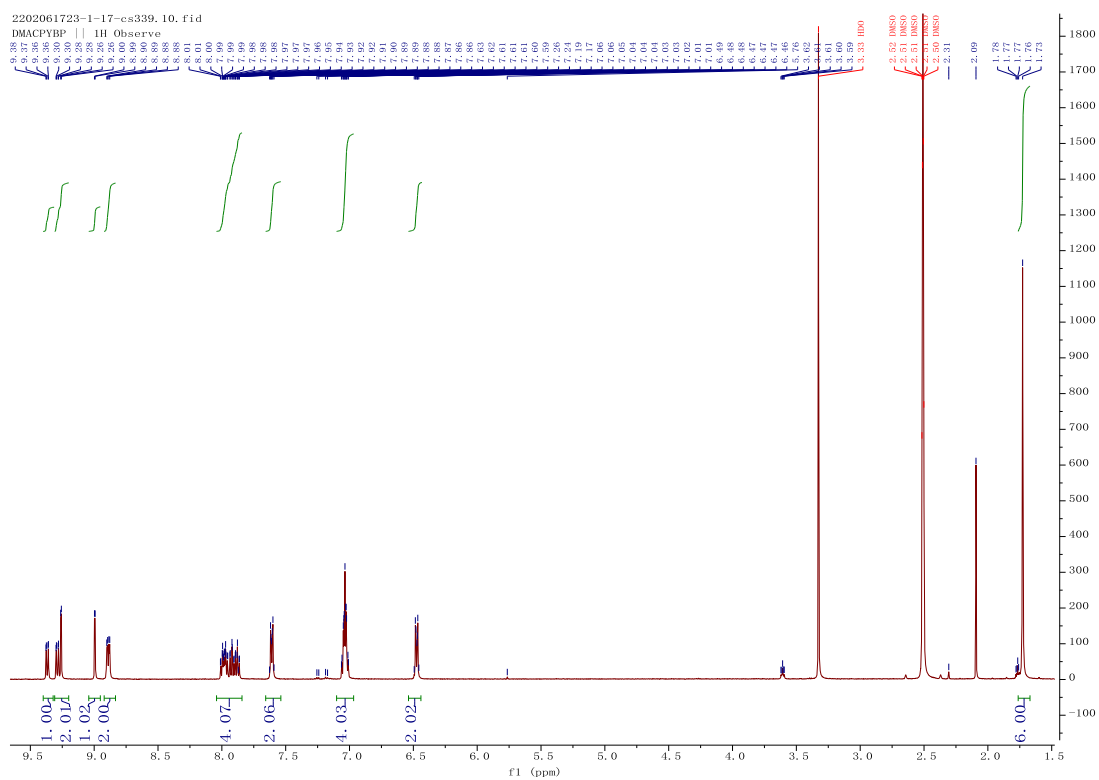


Figure 2.21. ¹H NMR spectra of **DMACPyBP** in DMSO-*d*₆.

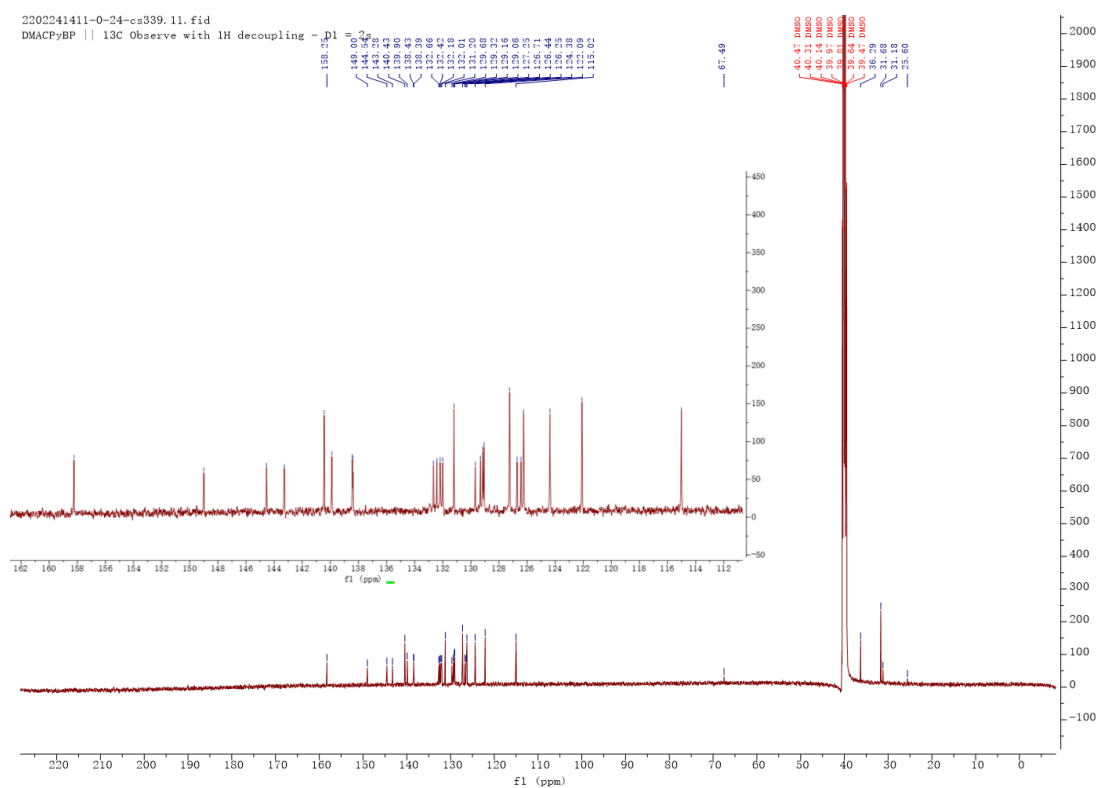


Figure 2.22. ¹³C NMR spectra of **DMACPyBP** in DMSO-*d*₆.

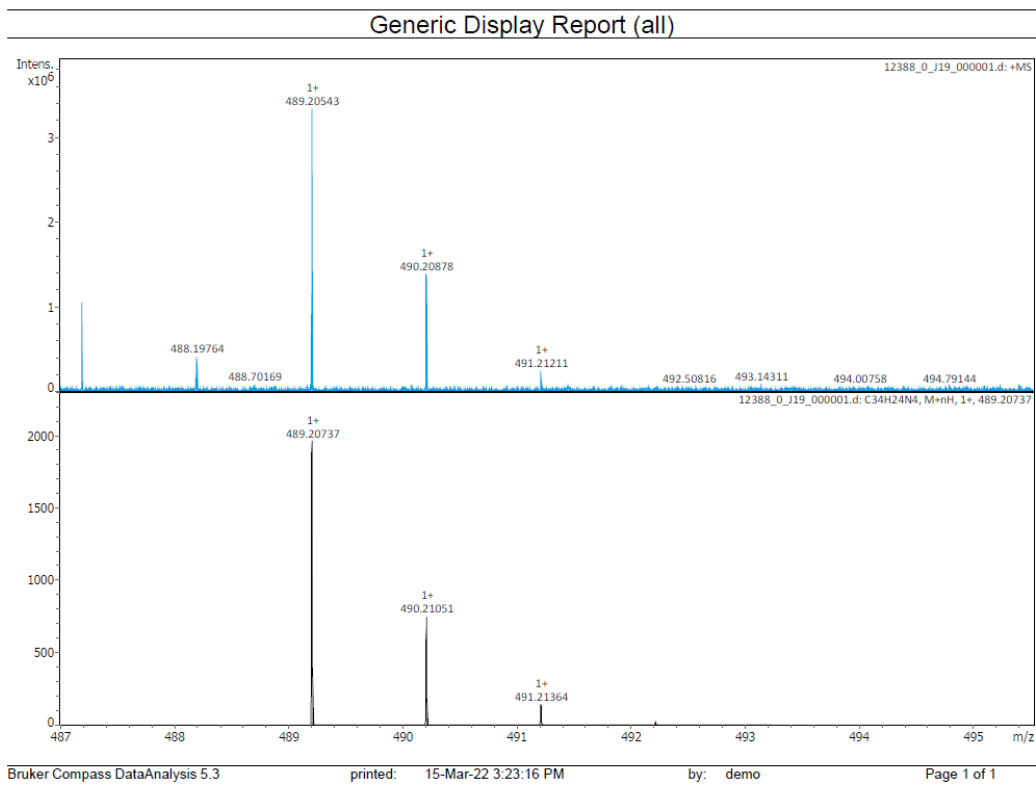


Figure 2.23. HRMS of DMACPyBP.

Elemental Analysis Service Request Form

Researcher name Changfeng Si

Researcher email cs339@st-andrews.ac.uk

NOTE: Please submit ca. 10 mg of sample

Sample reference number	CFS-231-DMACPyBP
Name of Compound	DMACPyBP
Molecular formula	C34H24N4
Stability	
Hazards	
Other Remarks	

Analysis type:

Single Duplicate Triplicate

Analysis Result:

Element	Expected %	Found (1)	Found (2)	Found (3)
Carbon	83.58	83.57	83.61	
Hydrogen	4.95	5.42	4.99	
Nitrogen	11.47	11.18	11.19	
Oxygen				

Authorising Signature:

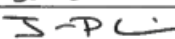
Date completed	30.03.22
Signature	
comments	-

Figure 2.24. EA of DMACPyBP.

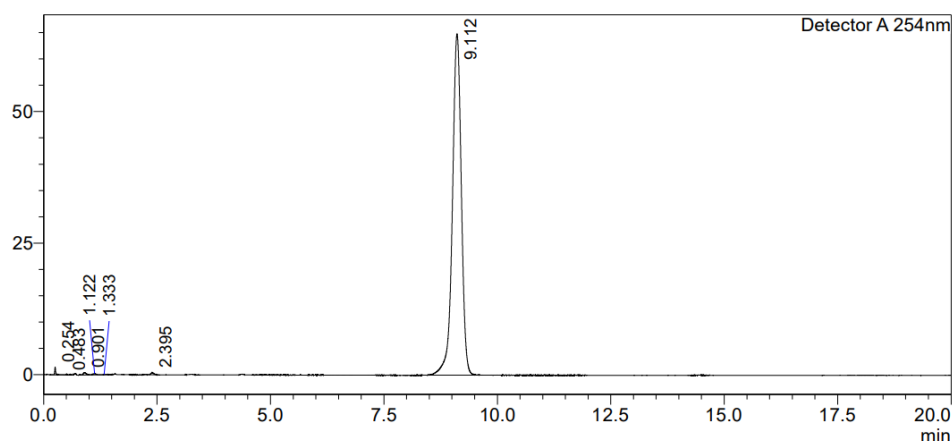
HPLC Trace Report14Oct2021

<Sample Information>

Sample Name : DMACPyBP
 Sample ID :
 Method Filename : 80% Methanol 20 Water 20 mins.lcm
 Batch Filename : DMACPyBP.lcb
 Vial # : 1-2
 Injection Volume : 5 uL
 Date Acquired : 14/10/2021 15:02:41
 Date Processed : 14/10/2021 15:22:44
 Sample Type : Unknown
 Acquired by : System Administrator
 Processed by : System Administrator

<Chromatogram>

mV



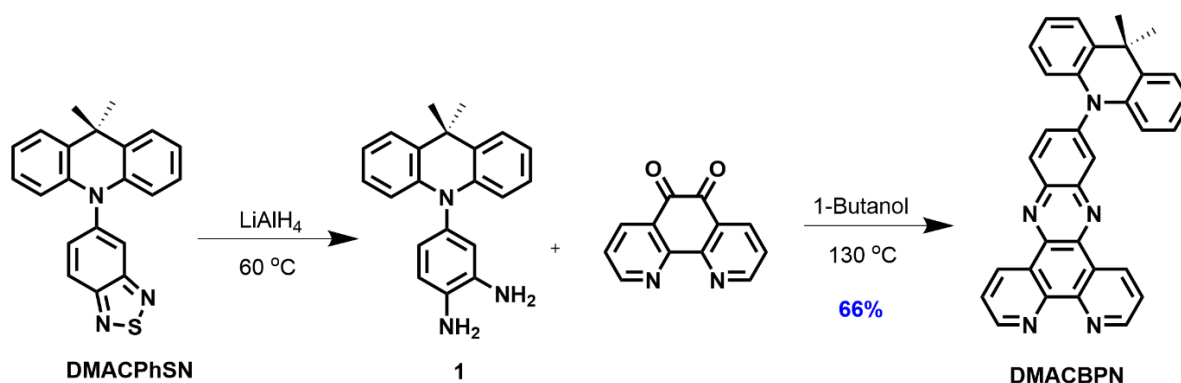
<Peak Table>

Detector A 254nm

Peak#	Ret. Time	Area	Height	Area%	Area/Height	Width at 5% Height
1	0.254	2393	1389	0.266	1.722	0.066
2	0.483	1304	75	0.145	17.451	--
3	0.901	2685	477	0.298	5.628	--
4	1.122	1392	244	0.155	5.704	--
5	1.333	1076	76	0.120	14.100	--
6	2.395	1801	387	0.200	4.655	0.160
7	9.112	889385	64815	98.817	13.722	0.485
Total		900035	67463	100.000		

Figure 2.25. HPLC trace of DMACPyBP.

Synthesis of 11-(9,9-dimethylacridin-10(9H)-yl)dipyrido[3,2-*a*:2',3'-*c*]phenazine (DMACBPN):



Compound **DMACBPN** was synthesized according to the same procedure as described above for the synthesis of **DMACBP**, except that 1,10-phenanthroline-5,6-dione (0.306 g, 1.46 mmol) was used as the reactant instead of phenanthrene-9,10-dione, yielding a red solid (yield = 0.470 g).

11-(9,9-dimethylacridin-10(9H)-yl)dipyrido[3,2-*a*:2',3'-*c*]phenazine (DMACBPN): $R_f = 0.3$ (20% DCM/Hexane). **Yield:** 86%. **Mp** = 312-313 °C. $^1\text{H NMR}$ (400 MHz, CDCl_3) δ 9.74 (dd, $J = 8.1, 1.8$ Hz, 1H), 9.66 (dd, $J = 8.1, 1.8$ Hz, 1H), 9.34 (ddd, $J = 6.5, 4.5, 1.8$ Hz, 2H), 8.62 (dd, $J = 8.9, 0.5$ Hz, 1H), 8.48 (dd, $J = 2.3, 0.5$ Hz, 1H), 7.98 – 7.76 (m, 3H), 7.56 (dd, $J = 6.0, 3.3$ Hz, 2H), 7.09 – 6.98 (m, 4H), 6.55 – 6.47 (m, 2H), 1.78 (s, 6H). $^{13}\text{C NMR}$ (101 MHz, CDCl_3) δ 152.82, 152.75, 143.69, 143.54, 141.90, 140.55, 134.03, 133.68, 132.38, 131.32, 130.68, 127.58, 127.49, 126.52, 125.42, 124.39, 121.54, 114.91, 77.35, 77.04, 76.72, 36.27, 30.93. **HR-MS** (Xevo G2-S) $[\text{M}+\text{H}]^+$ **Calculated:** ($\text{C}_{33}\text{H}_{23}\text{N}_5$) 489.1953; **Found:** 489.2026. **Anal. Calcd. for $\text{C}_{33}\text{H}_{23}\text{N}_5$:** C, 80.96%; H, 4.74%; N, 14.31%. **Found:** C, 81.09%; H, 4.73%; N, 13.81%. **HPLC analysis:** 99.57% pure on HPLC analysis, retention time 3.8 minutes in 98% Methanol 2% water.

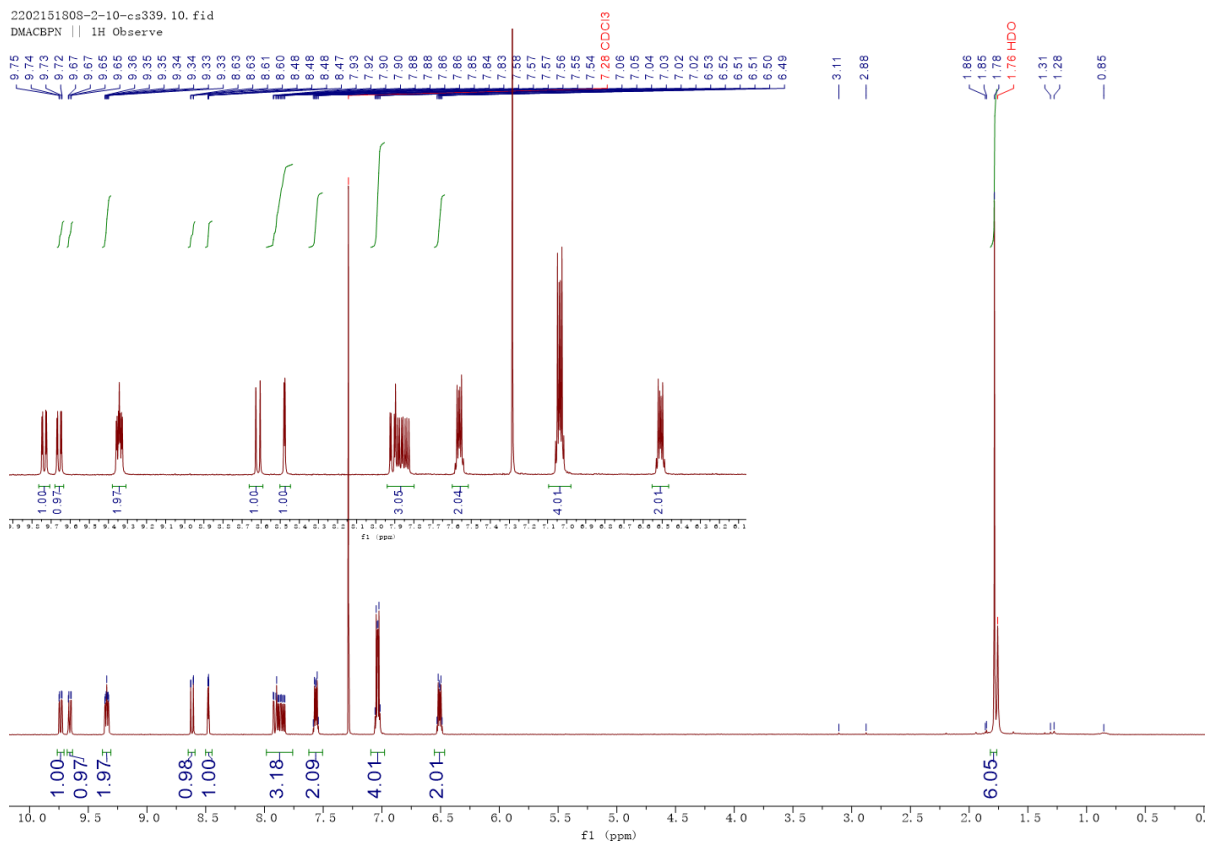


Figure 2.26. ^1H NMR spectra of DMACBPN in CDCl_3 .

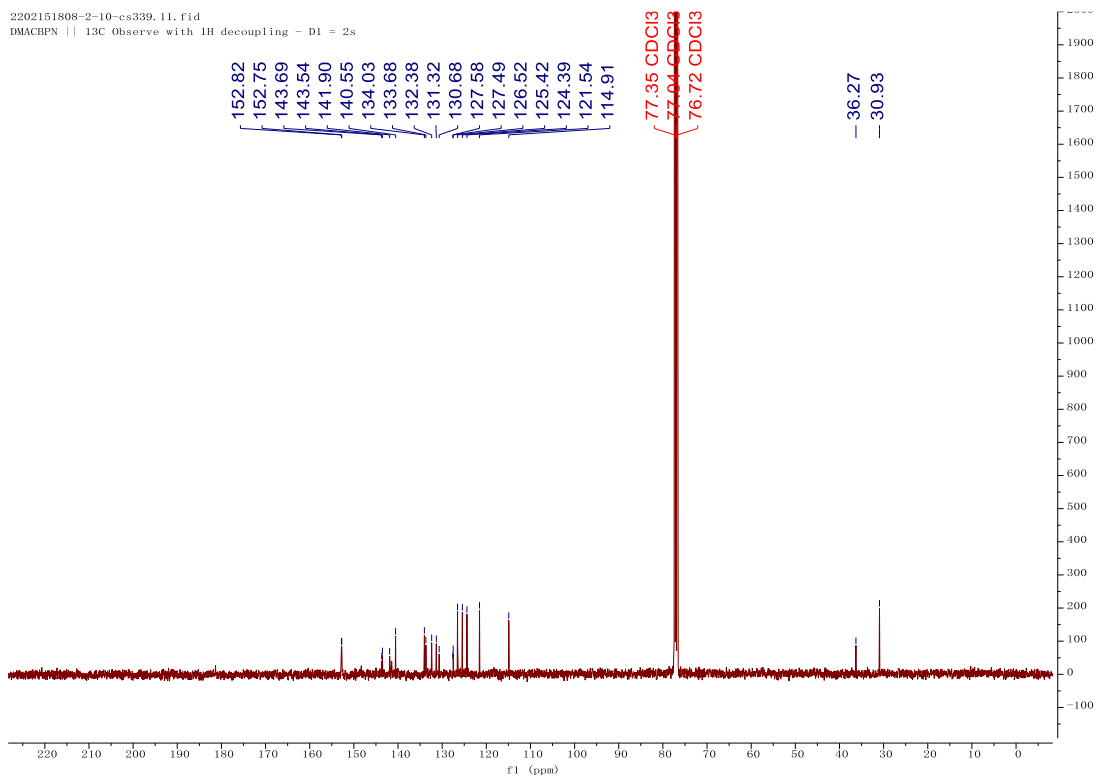


Figure 2.27. ^{13}C NMR spectra of DMACBPN in CDCl_3 .

Generic Display Report (all)

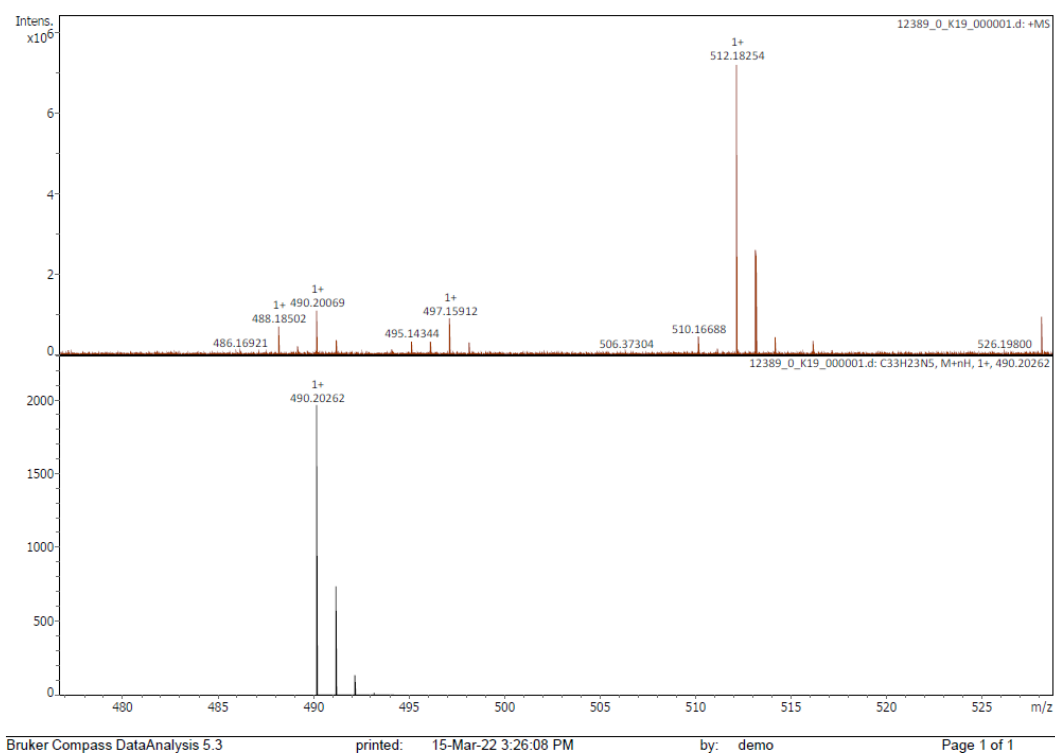


Figure 2.28. HRMS of DMACBPN.

Elemental Analysis Service Request Form

Researcher name Changfeng Si

Researcher email cs339@st-andrews.ac.uk

NOTE: Please submit ca. 10 mg of sample

Sample reference number	CFS-234-DMACBPN
Name of Compound	DMACBPN
Molecular formula	C33H23N5
Stability	
Hazards	
Other Remarks	

Analysis type:

Single Duplicate Triplicate

Analysis Result:

Element	Expected %	Found (1)	Found (2)	Found (3)
Carbon	80.96	79.87	81.09	
Hydrogen	4.74	4.73	4.77	
Nitrogen	14.31	13.63	13.81	
Oxygen				

Authorising Signature:

Date completed	30-03-22
Signature	S-P-L
comments	-

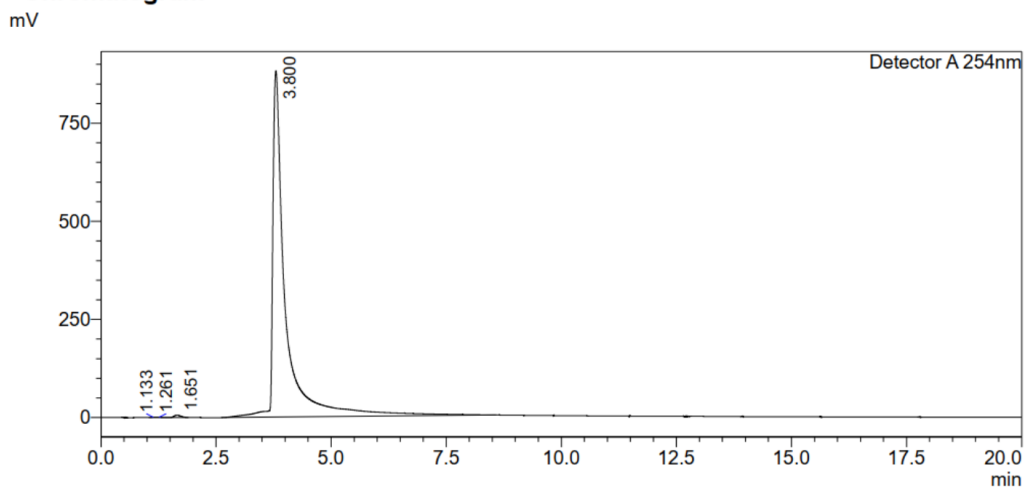
Figure 2.29. EA trace of DMACBPN.

HPLC Trace Report 15 Jan 2023

<Sample Information>

Sample Name : DMACBPN
Sample ID :
Method Filename : 98% Methanol 2 Water 20 mins-NEW.lcm
Batch Filename : DMACBPN3-MeOH.lcb
Vial # : 1-9 Sample Type : Unknown
Injection Volume : 60 uL
Date Acquired : 15/01/2023 17:52:14 Acquired by : System Administrator
Date Processed : 15/01/2023 18:12:16 Processed by : System Administrator

<Chromatogram>



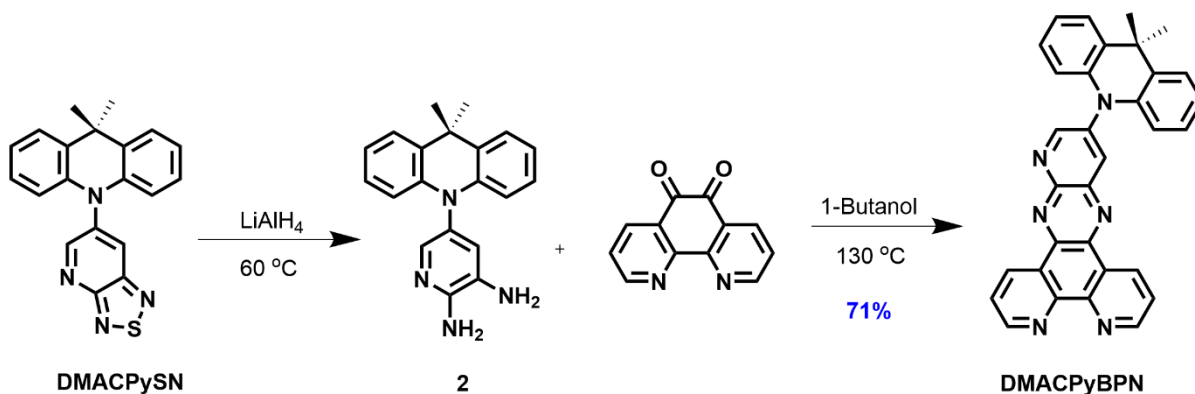
<Peak Table>

Detector A 254nm

Peak#	Ret. Time	Area	Height	Area%	Area/Height	Width at 5% Height
1	1.133	6662	1094	0.039	6.092	--
2	1.261	5379	773	0.032	6.960	--
3	1.651	60325	6076	0.355	9.928	0.312
4	3.800	16912219	880670	99.574	19.204	0.852
Total		16984584	888613	100.000		

Figure 2.30. HPLC trace of DMACBPN.

Synthesis of 12-(9,9-dimethylacridin-10(9*H*)-yl)pyrido[2',3':5,6]pyrazino[2,3-*f*][1,10]phenanthroline (DMACPyBPN):



Compound **DMACPyBPN** was synthesized according to the same procedure as described above for the synthesis of **DMACPyBP**, except that 1,10-phenanthroline-5,6-dione (0.306 g, 1.46 mmol) was used as the reactant instead of phenanthrene-9,10-dione, yielding a red solid (Yield = 0.510 g).

12-(9,9-dimethylacridin-10(9*H*)-yl)pyrido[2',3':5,6]pyrazino[2,3-*f*][1,10]phenanthroline (DMACPyBPN): $R_f = 0.2$ (33% DCM/Hexane). **Yield:** 71%. **Mp** = 325-326 °C. **^1H NMR (500 MHz, DMSO-*d*₆)** δ 9.63 (dd, $J = 8.1, 1.8$ Hz, 1H), 9.54 (dd, $J = 8.1, 1.8$ Hz, 1H), 9.35 – 9.26 (m, 3H), 9.04 (d, $J = 2.7$ Hz, 1H), 8.02 (ddd, $J = 18.0, 8.1, 4.4$ Hz, 2H), 7.65 – 7.57 (m, 2H), 7.09 – 7.00 (m, 4H), 6.56 – 6.47 (m, 2H), 1.72 (s, 6H). **^{13}C NMR (126 MHz, DMSO)** δ 158.67, 153.49, 153.38, 148.92, 148.73, 148.59, 143.56, 142.42, 140.34, 139.18, 139.05, 138.86, 134.15, 133.90, 131.68, 127.32, 127.26, 126.93, 126.26, 125.36, 125.27, 122.36, 115.36, 40.40, 40.23, 40.06, 39.90, 39.73, 39.56, 39.40, 36.35, 31.50. **HR-MS [M+H]⁺ Calculated:** (C₃₂H₂₂N₆) 490.1906; **Found:** 490.1978. **Anal. Calcd. for C₃₂H₂₂N₆:** C, 78.35%; H, 4.52%; N, 17.13%. **Found:** C, 78.38%; H, 4.55%; N, 16.42%. **HPLC analysis:** 97.96% pure on HPLC analysis, retention time 4.84 minutes in 95% Acetonitrile 5% water.

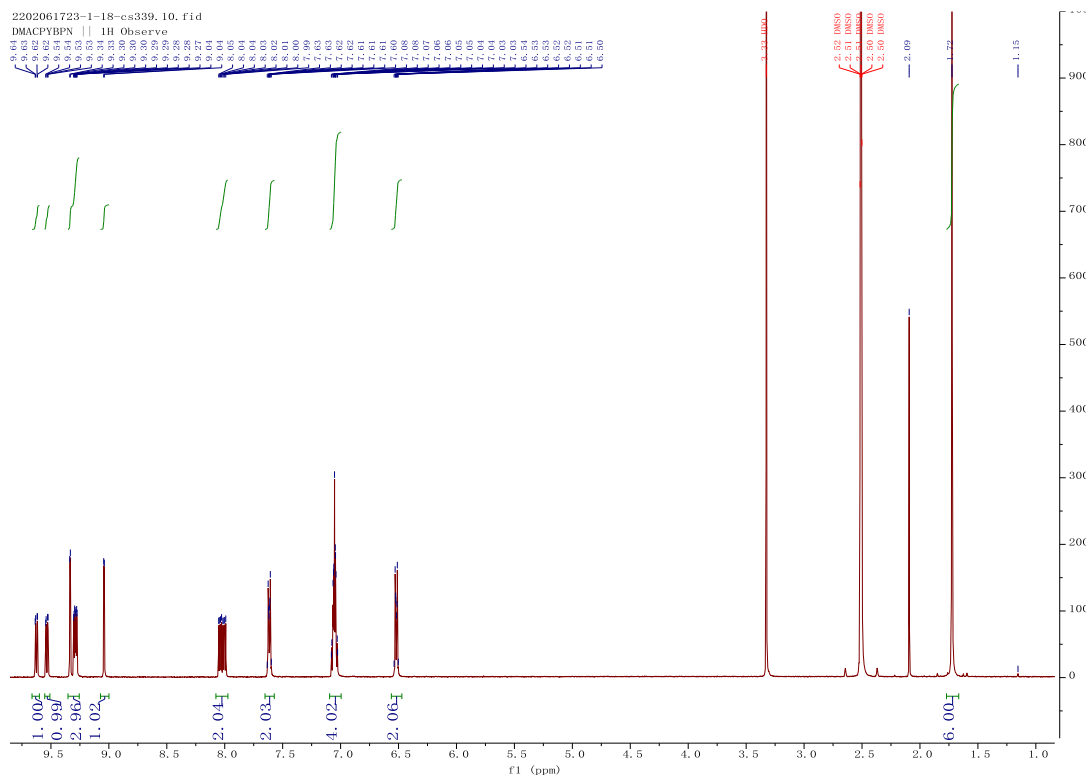


Figure 2.31. ^1H NMR spectra of DMACPyBPN in DMSO- d_6 .

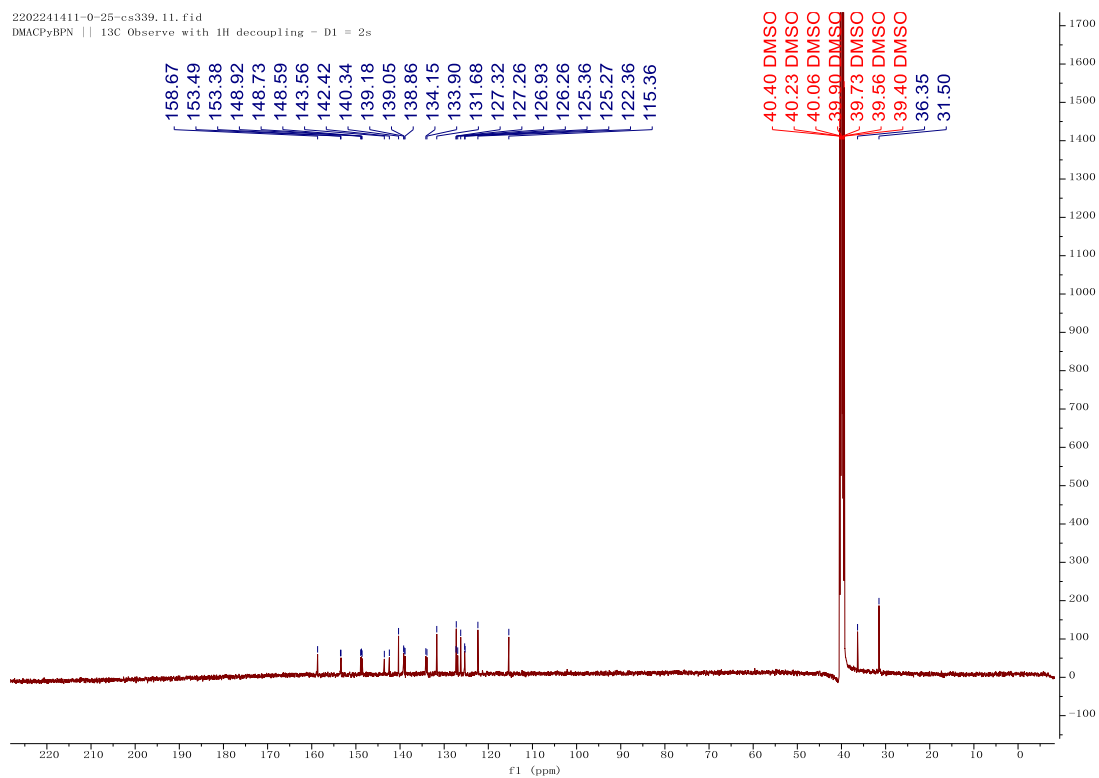


Figure 2.32. ^{13}C NMR spectra of DMACPyBPN in DMSO- d_6 .

Generic Display Report (all)

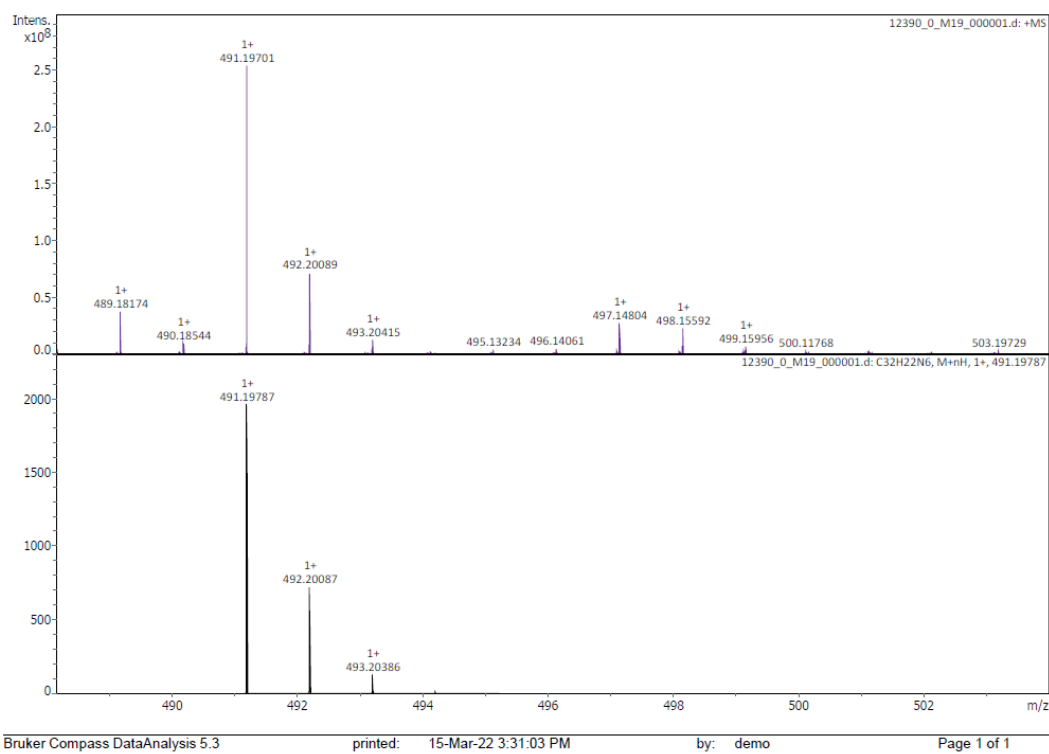


Figure 2.33. HRMS of DMACPyBPN.

Elemental Analysis Service Request Form

Researcher name Changfeng Si

Researcher email cs339@st-andrews.ac.uk

NOTE: Please submit ca. 10 mg of sample

Sample reference number	CFS-236-DMACPyBPN
Name of Compound	DMACPyBPN
Molecular formula	C32H22N6
Stability	
Hazards	
Other Remarks	

Analysis type:

Single Duplicate Triplicate

Analysis Result:

Element	Expected %	Found (1)	Found (2)	Found (3)
Carbon	78.35	78.58	78.17	
Hydrogen	4.52	4.62	4.55	
Nitrogen	17.13	16.42	16.36	
Oxygen				

Authorising Signature:

Date completed	30.03.22
Signature	S-PL
comments	-

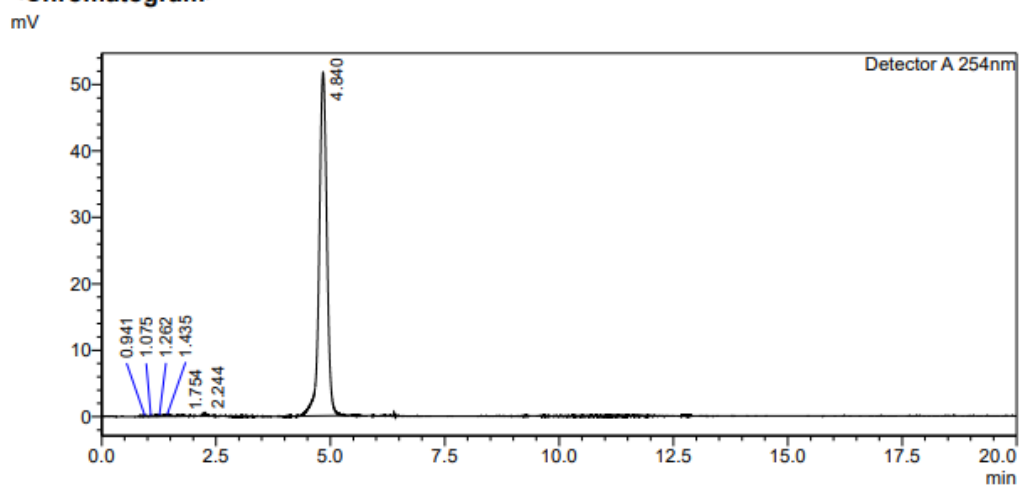
Figure 2.34. HRMS of DMACPyBPN.

HPLC Trace Report25May2023

<Sample Information>

Sample Name : DMACPyBPN
Sample ID : DMACPyBPN
Method Filename : 95% Acetonitrile 5 Water 20 mins.lcm
Batch Filename : DMACPyBPN
Vial # : 1-53
Injection Volume : 10 uL
Sample Type : Unknown

<Chromatogram>



<Peak Table>

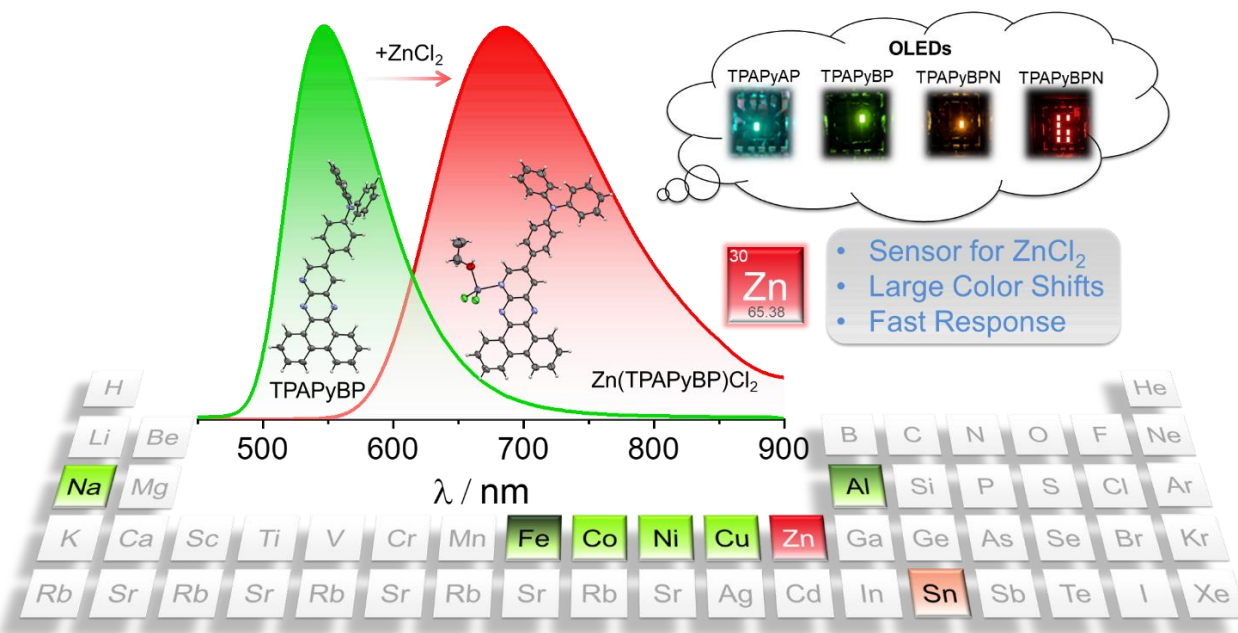
Detector A 254nm

Peak#	Ret. Time	Area	Height	Area%	Area/Height	Width at 5% Height
1	0.941	1151	200	0.187	5.767	--
2	1.075	1107	162	0.180	6.838	--
3	1.262	2654	226	0.431	11.759	--
4	1.435	2672	317	0.434	8.417	--
5	1.754	2250	176	0.366	12.801	--
6	2.244	2713	431	0.441	6.295	--
7	4.840	602826	51622	97.961	11.678	0.421
Total		615371	53133	100.000		

Figure 2.35. HPLC trace of DMACPyBPN.

Chapter 3: Multi-Responsive Thermally Activated Delayed Fluorescence:

ZnCl₂ Sensor and Efficient Green to Deep-red OLEDs



Manuscript of this project is under preparation as

Changfeng Si,^a Abhishek Kumar Gupta,^{a,b} Biju Basumatary,^a David B. Cordes,^a Alexandra M. Z. Slawin,^a Ifor D. W. Samuel,^{b*} and Eli Zysman-Colman^{a*}

Dr. Abhishek Kumar Gupta carried out the OLED devices fabrication and helped with discussion of the sensors part.

Dr. Biju Basumatary helped with discussion and corrections of sensors part.

Dr. David B. Cordes did X-ray crystallography.

I completed all the syntheses and characterization, DFT and TD-DFT calculations, electrochemistry, photophysics measurements, ZnCl₂ sensor measurement and I am the principal author of the text.

3.1 Introduction

In Chapter 2, we fully investigated four different DMAC-based orange-to-red TADF emitters whose structures differed by the number of nitrogen atoms contained within the conjugated acceptor core. We found that increasing the nitrogen atom content in the BP acceptor of the D-A typed compounds results in a more stabilized LUMO, smaller ΔE_{ST} , smaller S_1 and faster k_{RISC} . In particular, having a nitrogen at the 10-position of BP notably enhances k_{RISC} and leads to a large red-shift of the emission but results in a big decrease in the Φ_{PL} . So in this Chapter, emitters **TPAPyAP**, **TPAPyBP** and **TPAPyBPN** were designed by using same acceptor as **DMACPyBP** and **DMACPyBPN** (Chapter 2), respectively, except for **TPAPyAP** (using acenaphtho[1,2-b]pyrido[2,3-e]pyrazine (AP) as acceptor). The DMAC donor was replaced by TPA in order to increase the π -conjugation and overlap between HOMO and LUMO to increase f and thus Φ_{PL} . These three compounds show distinctly different molecular dipole moments based on the conjugation extension and enhancement of the electron-withdrawing ability of the acceptor through the introduction of extra nitrogen atoms within the heterocyclic ring. Depending on the acceptor strength, these three compounds emit at λ_{PL} , of 516 nm, 550 nm, and 575 nm in toluene. In the solid state, the emission of all three compounds progressively red-shifts with increasing polarity of the host. Both **TPAPyBP** and **TPAPyBPN** emit in the pure red ($\lambda_{PL} = 624$ nm) and deep red ($\lambda_{PL} = 675$ nm) in the high-polarity host PPT, respectively, while **TPAPyAP** exhibits a smaller red-shift from green emission ($\lambda_{PL} = 537$ nm) in CBP to yellow emission ($\lambda_{PL} = 584$ nm) in PPT compared to the emission colour change observed for the other two compounds. We also demonstrate that these three emitters can be used in vacuum-deposited OLEDs. The OLEDs based on **TPAPyBPN** in PPT host showed moderated efficiencies of EQE_{max} 12.5% with deep red emission at 657 nm. We also discovered that **TPAPyBP** can act as a selective and sensitive optical sensor for ZnCl₂, which is the first documented TADF optical sensor for ZnCl₂.

Optical sensors are widely used in many applications, including in telecommunications, environmental monitoring, industrial automation, and medical devices.^{232–235} Optical sensors have traditionally employed fluorescent compounds as the basis for their detection mechanism thanks to their numerous benefits including high specificity, low detection limits, fast response time, and technical simplicity.²³⁶ Fluorescent sensors typically work by exhibiting a change in their optical properties, such as fluorescence intensity, emission wavelength or lifetime, in response to interactions with specific analytes or environmental changes.^{237,238} Organic fluorescent compounds such as rhodamines,^{239,240} fluoresceins²⁴¹, cyanine,²⁴² BODIPY,^{243,244}

and coumarin dyes²⁴⁵ have long been used in optical sensing. Phosphorescent complexes have also been explored as sensors in oxygen sensing,²⁴⁶ metal ion detection,²⁴⁷ biomolecule detection,²⁴⁸ and temperature sensing.²⁴⁹ Indeed, both oxygen and temperature sensing rely in particular on accessible triplet excited states of the sensor.

TADF emitters are another class of emissive compounds that have small ΔE_{ST} .^{88,114,115} They have garnered much attention due to their capacity to harvest both singlet and triplet excitons to produce light in electroluminescent devices such as OLEDs applications.^{114,115} They have increasingly been used in other applications, most notably as photocatalysts and as bioimaging reagents.^{103,250,251} However, very few reports exist documenting the use of organic TADF materials as sensors.^{252–254} The first recorded examples employed a TADF compound, **acridine yellow** (Figure 3.1a), as a temperature sensor.²⁵⁵ Steinegger *et al.* subsequently reported a series of carbazole-substituted dicyanobenzene and diphenylamine-substituted anthraquinone D-A TADF emitters (Figure 3.1a) for use as oxygen and temperature sensors.²⁵⁶ In doped films, these dyes exhibit a temperature sensitivity in the investigated temperature range (278–323 K) of 1.4–3.7% K⁻¹ change of the delayed lifetime at 298 K.²⁵⁶ Tonge *et al.* disclosed a TADF polymer, **PTZ-ODA** (Figure 3.1a), which acts as a single-component ratiometric oxygen sensor.²⁵⁷ In addition to oxygen and temperature sensors, Li *et al.* developed a sensor for solvent polarity based on compound **3** (Figure 3.1b), which shows dual emissions at 332 nm (strong LE fluorescence) and 435 nm (weak CT TADF) in DCM under air. Using the solvent-invariant LE fluorescence as an internal reference, the ratio of the intensities of the LE and CT bands as well as the ratios of the prompt and delayed emission lifetimes were used to calibrate against solvent polarity.²⁵⁸ Recently, Yin *et al.* reported a TADF turn-on chemosensor, **DCF-MPYM-lev** (Figure 3.1c), for sulfite ion [SO₃]²⁻ detection. The fluorescence intensity of **DCF-MPYM-lev** solution in CH₃CN/PBS buffer (1/1) significantly increased and dual emissions at 535 nm and 640 nm were observed after the addition of SO₃²⁻. **DCF-MPYM-lev** was also used to monitor exogenous [SO₃]²⁻ in the living cells.²⁵⁹ Qiu *et al.* reported the carbazole-triazine-based donor-acceptor TADF emitter **PhTRZ-OCHO** (Figure 3.1c) as a fluorescence turn-off/fluorescence quenching sensor for the detection of Na⁺, Mg²⁺ and Fe³⁺ ions.²⁵³ The emission intensity at 470 nm of **PhTRZ-OCHO** decreased on the additions of many of the metal ions tested (Ba⁺, Ca⁺, Cd²⁺, Co²⁺, Cr²⁺, Cu²⁺, Fe³⁺, Hg²⁺, K⁺, Mg²⁺, Mn²⁺, Na⁺, Ni²⁺, Pb⁺), the strongest emission quenching occurred in the presence of Na⁺, Mg²⁺ and Fe³⁺. The remarkable fluorescence quenching behavior was attributed to the metal-binding aldehyde group present in **PhTRZ-OCHO** where in the presence of these ions, the CT

state is destabilized and non-emissive.

ZnCl₂, a moderate strength Lewis acid, has found extensive use as a dehydrating and condensation agent, and as a catalyst in chemicals production, metallurgical fluxes, and materials preparation.²⁶⁰ ZnCl₂ is also used in the textile industry as a mordant. Monitoring its levels is essential for both industrial process control and environmental regulation. Additionally, while zinc is vital for biological processes, ZnCl₂ can be toxic and corrosive at high concentrations, making it important to monitor its presence for public health and safety reasons. Although there are plenty of studies on the detection of Zn²⁺, motivated by its importance in various biological processes,^{261,262} there have been few reports of an optical sensor specifically designed for the detection of ZnCl₂. Manandhar *et al.* reported a pyrene-based triazole receptor (**Compound 3**), which formed self-assembled induced excimers upon the addition of ZnCl₂. **Compound 3** showed two distinct emission bands emanating from monomers and excimers.²⁶³ This compound, however, provided a spectral response for other Zn²⁺ salts and was not specific for the detection of ZnCl₂. Sabarinathan *et al.* reported selective colorimetric sensing of ZnCl₂•2H₂O by the polyoxometalate–salt [Himi]₄[SiMo₁₂O₄₀] (**1**). The addition of ZnCl₂•2H₂O into a mixture of **1** in DMSO–H₂O resulted in the formation of blue color; notably, anhydrous ZnCl₂ did not produce the color change under the same conditions. To the best of our knowledge, these are the only two optical sensors for ZnCl₂ that have been reported to date.

Here, we designed three new TADF donor-acceptor emitters with a triphenylamine (TPA) donor and nitrogen-containing heterocyclic pyrazine-based acceptor, 4-(acenaphtho[1,2-b]pyrido[2,3-e]pyrazin-10-yl)-*N,N*-diphenylaniline (**TPAPyAP**), 4-(dibenzo[*f,h*]pyrido[2,3-b]quinoxalin-12-yl)-*N,N*-diphenylaniline (**TPAPyBP**) and *N,N*-diphenyl-4-(pyrido[2',3':5,6]pyrazino[2,3-*f*][1,10]phenanthrolin-12-yl)aniline (**TPAPyBPN**) (Figure **3.1**). Theoretical and experimental results demonstrate that the electron-withdrawing strength of the acceptor increases with both the increased conjugation of the PAH and the number of nitrogen atoms contained within, leading to a red-shift of the emission within the series. These nitrogen atoms can also act as ligands for metal binding and the change in photophysics can be exploited in metal ion sensing.²⁶⁴ We found that these compounds exhibited a stark spectral response to the detection of ZnCl₂. This is due to the formation of zinc chlorido complexes. Of these three emitters, **TPAPyBP** showed the most dramatic and fast fluorescence response toward ZnCl₂ by shifting emission from green (550 nm) to deep red (675 nm). We separately explored these compounds as emitters in OLEDs and documented a rather large host polarity-induced shift in the emission from films doped in 4,4'-Bis(*N*-carbazolyl)-1,1'-biphenyl (CBP) to 2,8-

bis(diphenyl-phosphoryl)-dibenzo[b,d]thiophene (PPT). Especially, the OLEDs with **TPAPyBPN** emitted at 657 nm in PPT and showed an EQE_{max} 12.5%. This electroluminescence was 61 nm red-shifted in comparison to device fabricated in CBP host ($\lambda_{\text{EL}} = 596$ nm, $\text{EQE}_{\text{max}} = 13.6\%$), without significant loss in efficiency. The devices with **TPAPyAP** and **TPAPyBP** doped in CBP emitted at $\lambda_{\text{EL}} = 526$ nm with $\text{EQE}_{\text{max}} = 7.6\%$ and $\lambda_{\text{EL}} = 558$ nm with $\text{EQE}_{\text{max}} = 9.1\%$, respectively.

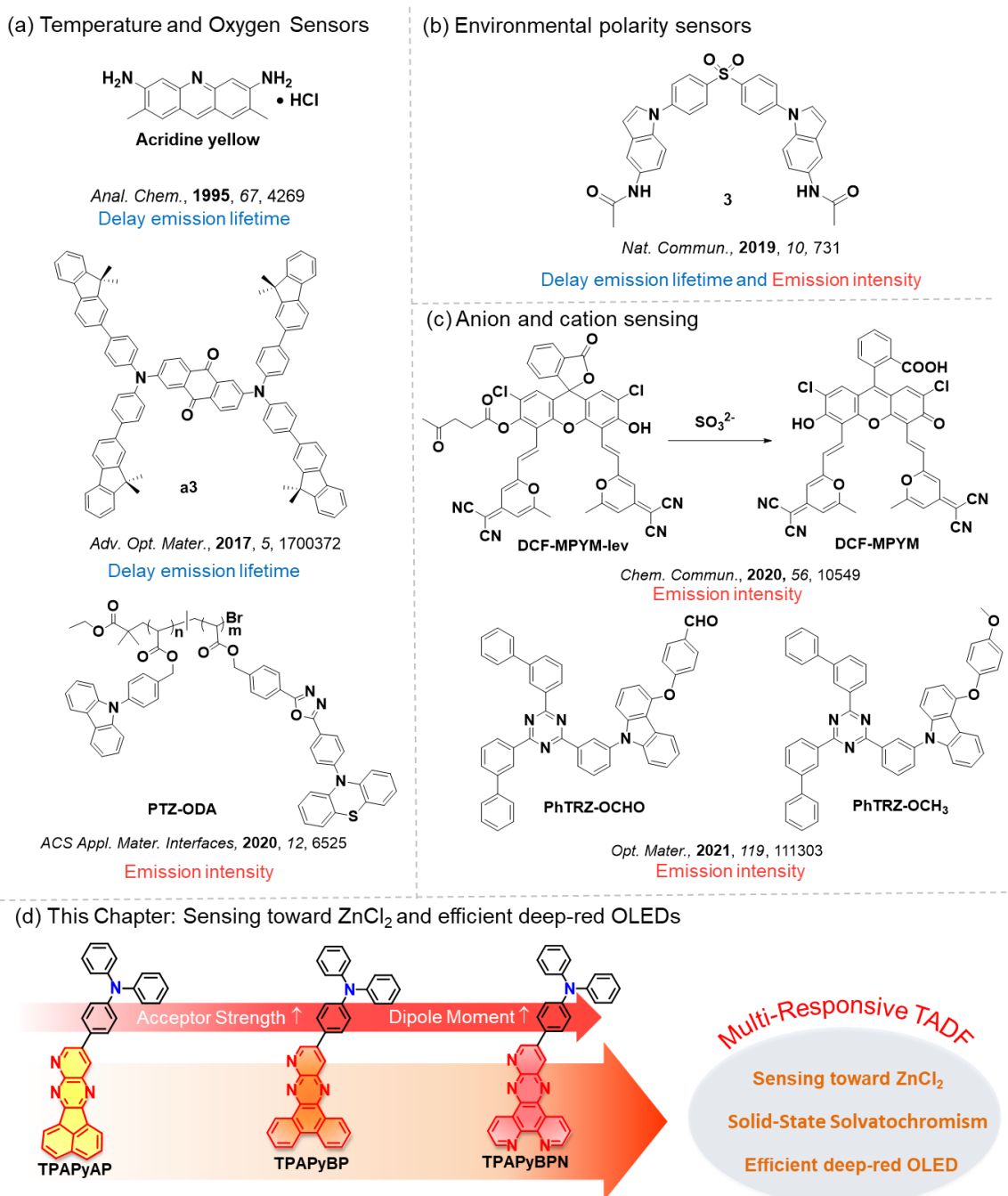
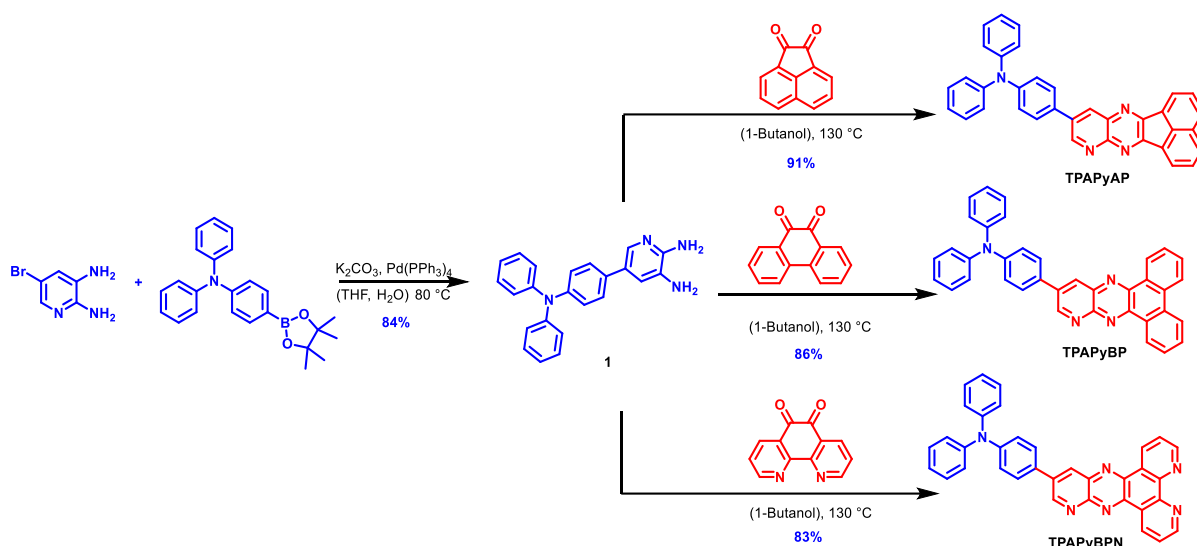


Figure 3.1. Reported TADF emitters' structures for (a) temperature and oxygen sensors; (b) environmental polarity sensors; (c) anion and cation sensing; (d) This Chapter: Multi-responsive TADF based on planar and rich N-type acceptors.

3.2 Synthesis

The synthesis of the family of **TPAPyX** (X = AP, BP, BPN) emitters follows a common route (Scheme 3.1). Intermediate 5-(4-(diphenylamino)phenyl)pyridine-2,3-diamine, **1**, was obtained via a Suzuki-Miyaura cross-coupling of *N,N*-diphenyl-4-(4,4,5,5-tetramethyl-1,3,2-dioxaborolan-2-yl)aniline and 5-bromopyridine-2,3-diamine in 84% yield. The target compounds **TPAPyAP**, **TPAPyBP** and **TPAPyBPN** were each obtained in high yield through a condensation between **1** and the corresponding α -diketones, acenaphthylene-1,2-dione, phenanthrene-9,10-dione (BP) and 1,10-phenanthroline-5,6-dione (BPN), respectively. The identity and purity of the three emitters were verified using a combination of ^1H NMR, ^{13}C NMR spectroscopy, melting point determination, high-resolution mass spectrometry, elemental analysis, single crystal X-ray diffraction studies, and high-performance liquid chromatography. (3.10 Experimental section, Figures 3.18-3.30).



Scheme 3.1. Synthetic routes for **TPAPyAP**, **TPAPyBP** and **TPAPyBPN**.

3.3 X-Ray Diffraction Analysis of **TPAPyBP** and **TPAPyBPN**

Single crystals of **TPAPyBP** and **TPAPyBPN** were obtained by slow evaporation of a saturated toluene solution at room temperature. The structure and packing mode of both molecules in the solid state are shown in Figure 3.2. The dihedral angle between the acceptor and phenylene bridge is around 0° in both compounds. **TPAPyBP** packs as arrays of co-planar compounds along the *c*-axis, reinforced by slipped π - π stacking interactions with adjacent molecules 3.53 Å apart (Figure 3.2a). **TPAPyBPN**, however, adopts an alternating head-to-tail packing pattern, with a shorter π - π distance of 3.40 Å (Figure 3.2b). Along the *a*-axis there are

also C–H···N hydrogen bonds present (2.70 Å and 2.54 Å) that lock neighboring **TPAPyBPN** molecules together, where intermolecular H-bonds exist between the TPA unit and the two nitrogen atoms of the phenanthroline part of the acceptor (Figure 3.2b); there is also a short contact between nitrogen at the 10-position of the BPN acceptor and the TPA at 2.72 Å, while there are no such strong H-bonds observed in the single crystal of **TPAPyBP** (Figure 3.2a).

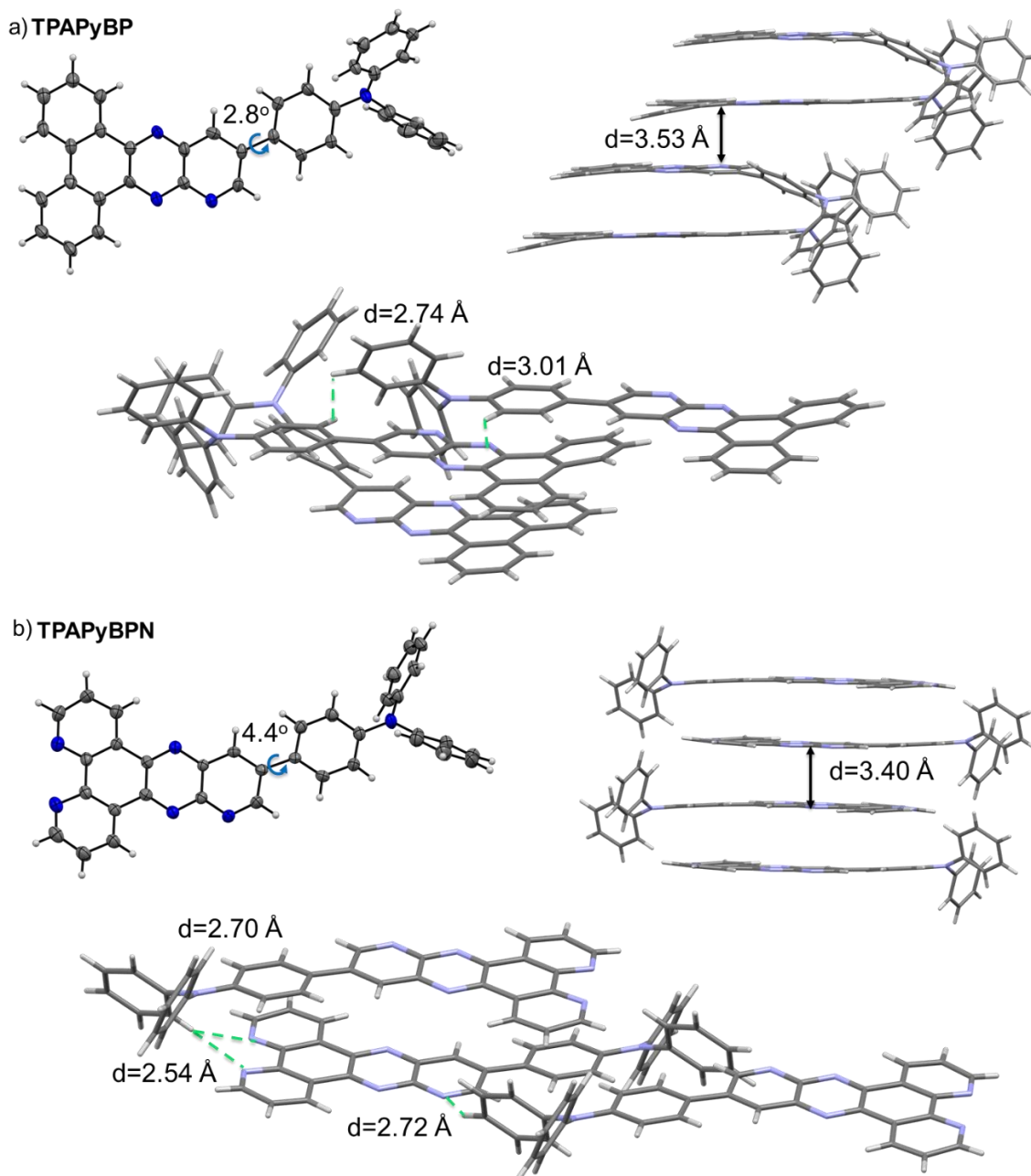


Figure 3.2. Thermal ellipsoid plot of one independent molecule in the single crystal structure (Ellipsoids are drawn at the 50% probability level and solvent molecules have been omitted for clarity), the crystal structure packing and interactions between adjacent molecules of (a) **TPAPyBP** and (b) **TPAPyBPN**, respectively.

3.4 Theoretical Calculations

The S_0 geometries of **TPAPyAP**, **TPAPyBP** and **TPAPyBPN** were optimized using DFT at the PBE0²⁶⁵/6-31G(d,p)²⁶⁶ level of theory in the gas phase. At the optimized S_0 geometries, the dihedral angles between the TPA and acceptor moieties are around 31° for **TPAPyAP**, 39° for **TPAPyBP** and 41° for **TPAPyBPN**, nearly matching those found in the crystal structures of the latter two (Figure 3.2). The calculated energy levels of the HOMOs and LUMOs are shown in Figure 3.3. The HOMOs are localized on the TPA donor, with some minor contribution onto the leading pyridine ring of the acceptor moiety. The LUMOs of all three compounds are localized on the acceptor group, with some contribution also located on the bridging phenylene of the TPA donor. As the acceptor strength increases along the series from **TPAPyAP** to **TPAPyBP** and **TPAPyBPN** both the HOMO and LUMO are stabilized, with the stabilization more significant for the latter. The HOMO-LUMO gap, $\Delta E_{\text{HOMO-LUMO}}$, thus decreases from 3.21 eV for **TPAPyAP** to 3.00 eV for **TPAPyBP** and 2.90 eV for **TPAPyBPN** (Figure 3.3a). The excited-state properties were calculated using TD-DFT within the TDA-DFT based on the optimized ground-state geometries.^{222,267,268} The oscillator strength, f , for the $S_0 \rightarrow S_1$ transition is high at 0.47, 0.39 and 0.36 for **TPAPyAP**, **TPAPyBP** and **TPAPyBPN**, respectively, reflecting a significant overlap of the electron density between the HOMO and LUMO, a result of the relatively small torsions that exist between the TPA and the acceptor moieties. The S_1 energies are 2.82 eV for **TPAPyAP** to 2.59 eV for **TPAPyBP** and 2.48 eV for **TPAPyBPN**, while the T_1 energies likewise decrease from 2.44 eV, 2.25 eV, and 2.17 eV (Figure 3.3b), respectively, following a similar trend to that observed for $\Delta E_{\text{HOMO-LUMO}}$. The degree of spatial separation of the frontier orbitals in **TPAPyBPN** is reflected in a ΔE_{ST} of 0.31 eV, while the larger overlap between HOMO and LUMO for **TPAPyAP** and **TPAPyBP** lead to ΔE_{ST} values that are slightly larger at 0.37 eV and 0.34 eV, respectively.

NTO analyses at the optimized S_1 and T_1 geometry calculated at the TDA-DFT-PBE0/6-31G(d,p) level are shown in Figure 3.3b and c, respectively. For all three compounds, the S_1 states are of CT character from the TPA donor to the acceptor. However, the T_1 states possess mixed CT and LE character on the acceptor. At the relaxed S_1 geometry, there is a decreasing S_1 - T_1 SOC matrix element from 0.27 cm^{-1} in **TPAPyAP** to 0.21 cm^{-1} in **TPAPyBP** and 0.16 cm^{-1} in **TPAPyBPN** (Figure 3.3b). While at the relaxed T_1 geometry, the T_1 - S_1 SOCME are 0.17, 0.22, 0.22 cm^{-1} for **TPAPyAP**, **TPAPyBP** and **TPAPyBPN**, respectively.

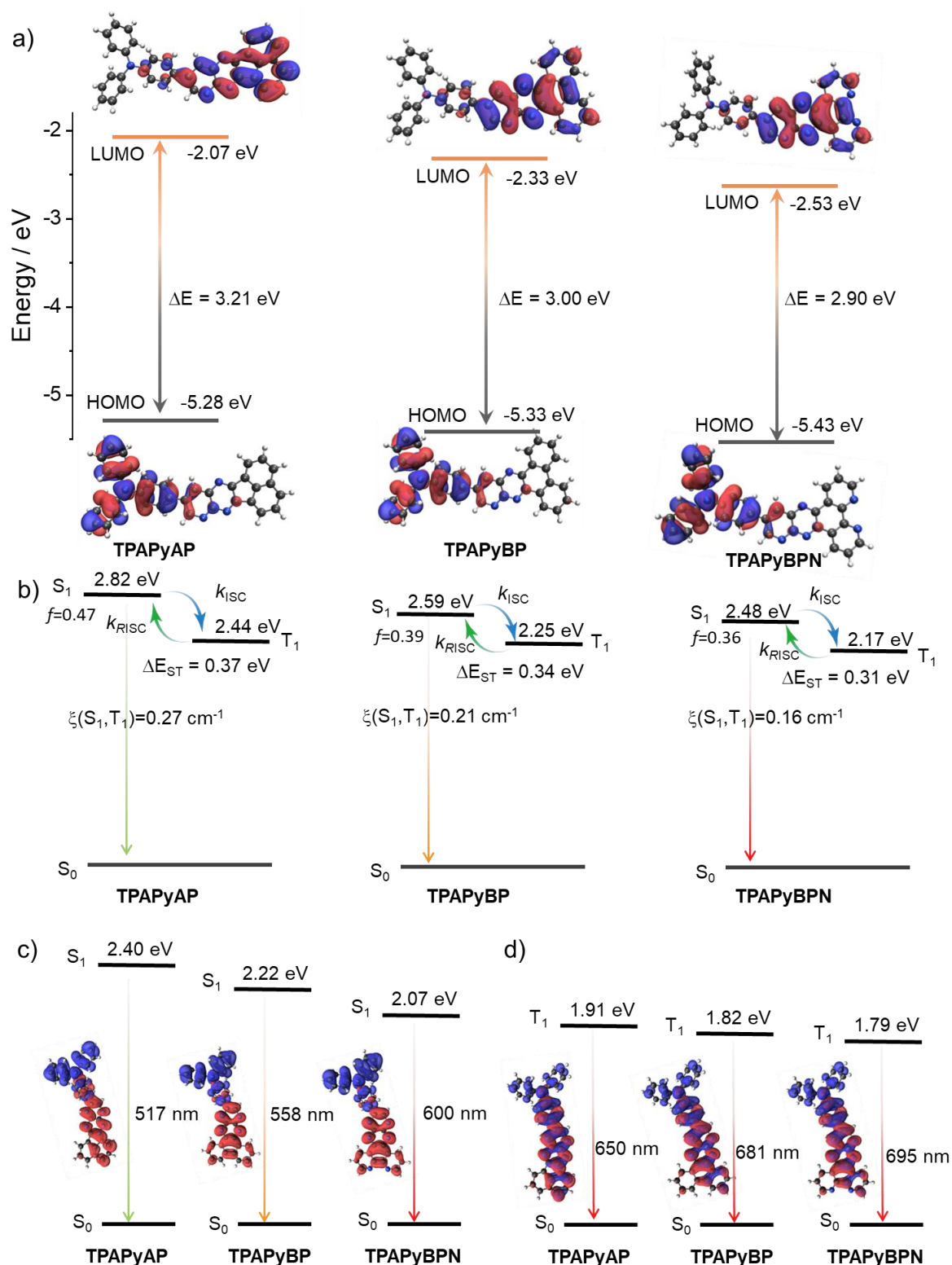


Figure 3.3. (a) Frontier molecular orbitals (isovalue: 0.02) and (b) vertical excitation energy levels of TPAPyAP, TPAPyBP and TPAPyBPN calculated using the optimized S_0 geometry in the gas phase at the PBE0/6-31G(d,p) level. (c) S_1 spin density distributions (isovalue: 0.02) and S_1 vertical emission energies calculated in the gas phase at the S_1 optimized geometry at the TDA-DFT PBE0/6-31G(d,p) level. (d) T_1 spin density distributions (isovalue: 0.02) and T_1

vertical emission energies calculated in the gas phase at the T_1 optimized geometry at the TDA-DFT PBE0/6-31G(d,p) level (hole (blue) & electron (red)).

3.5 Electrochemistry

CV and DPV were employed to investigate the electrochemical characteristics of **TPAPyAP**, **TPAPyBP**, and **TPAPyBPN** in degassed DCM with $n\text{-Bu}_4\text{NPF}_6$ as the supporting electrolyte. Voltammograms are referenced versus Fc/Fc^+ and the data are reported versus a SCE. As shown in Figure 3.4, all three compounds show reversible oxidation and reduction processes. The E_{red} , determined from the DPV peak values, are -1.39 (**TPAPyAP**), -1.21 V (**TPAPyBP**) and -1.09 V (**TPAPyBPN**), respectively, reflecting the expected anodic shift that is mirrored in the trend of calculated stabilized LUMO levels due to the increasing π -accepting ability of the acceptor units from AP < BP < BPN. The corresponding LUMO levels are -2.95 eV, -3.13 eV and -3.25 eV for **TPAPyAP**, **TPAPyBP** and **TPAPyBPN**, respectively. All three emitters possess similar oxidation potentials ($E_{\text{ox}} = 1.01$ V for **TPAPyAP**, 1.00 V for **TPAPyBP** and 1.02 V for **TPAPyBPN**) due to the use of the same TPA donor unit. The HOMO levels of **TPAPyAP**, **TPAPyBP** and **TPAPyBPN** are -5.33, -5.35 and -5.35 eV, respectively. The HOMO–LUMO gaps for **TPAPyAP**, **TPAPyBP** and **TPAPyBPN** are thus 2.38, 2.22 and 2.10 eV, respectively, which mirror the trend in the DFT calculated values of 2.79, 2.62, 2.46 eV.

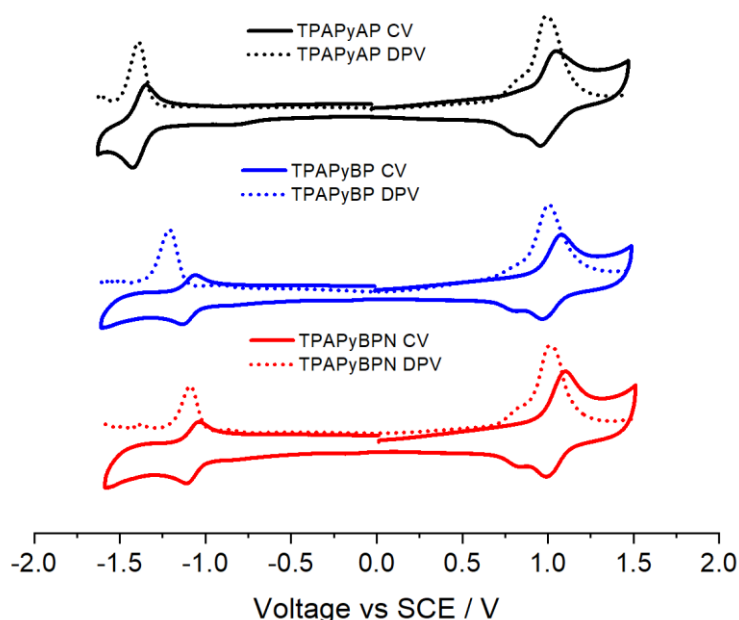


Figure 3.4. CVs and DPVs measured in degassed DCM with 0.1 M $[\text{nBu}_4\text{N}]\text{PF}_6$ as the supporting electrolyte and Fc/Fc^+ as the internal reference (0.46 V vs SCE).²²⁴ Scan rate = 100 mV s^{-1} .

3.6 Photophysical Properties in Solution

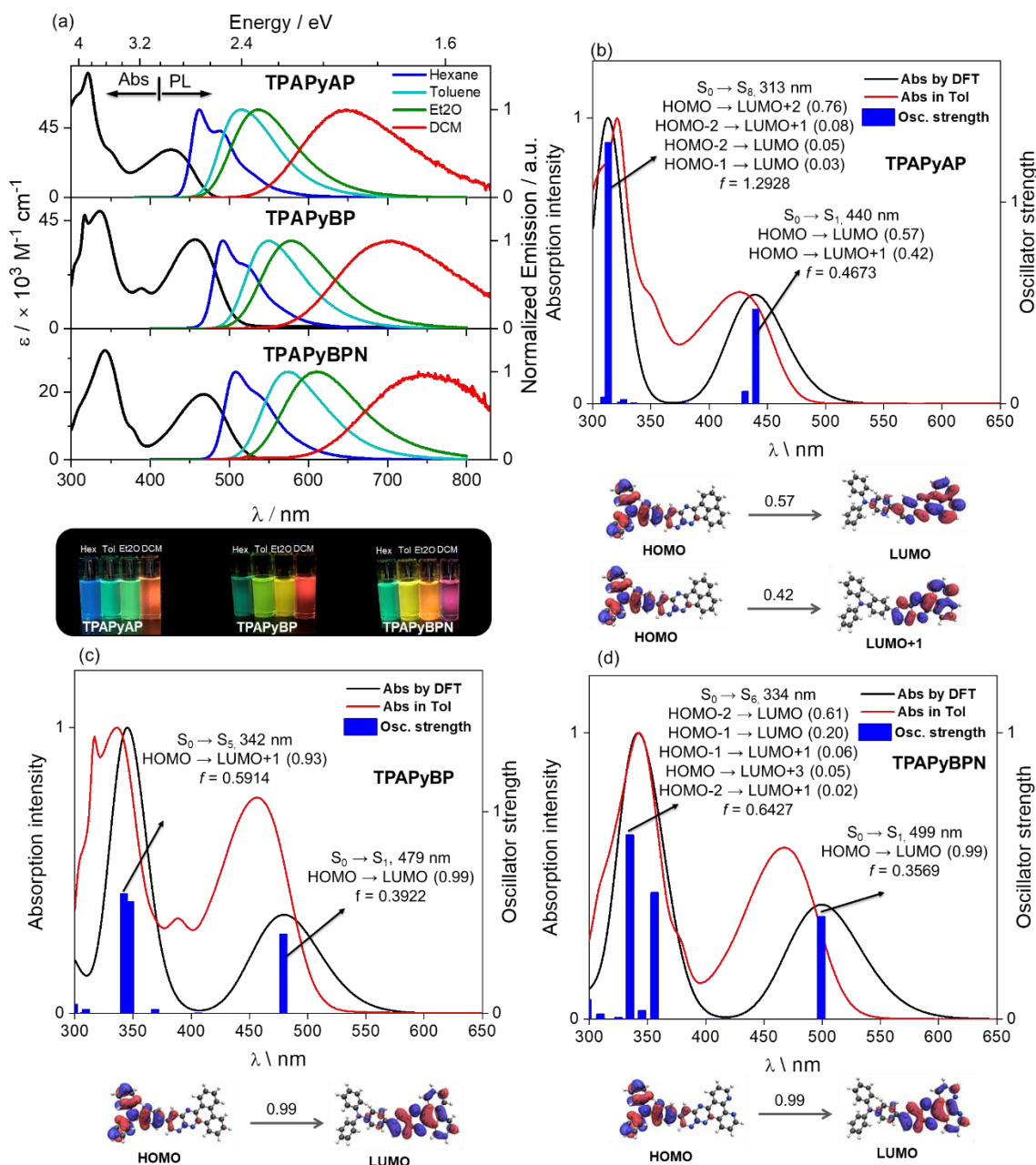


Figure 3.5. (a) UV-vis absorption and PL solvatochromism study ($\lambda_{exc} = 340$ nm, Et₂O= diethyl ether, DCM = dichloromethane); TDA-DFT simulation and experimental UV-Vis absorption spectra in the gas phase of (b) TPAPyAP, (c) TPAPyBP and (d) TPAPyBPN, corresponding the calculated distribution of molecular orbitals (isovalue = 0.02).

The UV-Vis absorption spectra of the three emitters in dilute toluene are shown in Figure 3.5a and the photophysical properties are summarized in Table 3.1. All three compounds exhibit strong absorption bands at around 320 nm, which are assigned to LE π - π^* transitions

of the donors and acceptor moieties, corresponding to the TDDFT shown in Figure 3.5b-d. A strong and broad absorption band is observed at 427 nm ($\epsilon = 31 \times 10^3 \text{ M}^{-1} \text{ cm}^{-1}$) for **TPAPyAP**, 456 nm ($\epsilon = 37 \times 10^3 \text{ M}^{-1} \text{ cm}^{-1}$) for **TPAPyBP** and 469 nm ($\epsilon = 19 \times 10^3 \text{ M}^{-1} \text{ cm}^{-1}$) for **TPAPyBPN**, which is assigned in each case to an ICT transitions from the TPA donor to the acceptor moiety. The molar absorption coefficient of the ICT band at 427 nm of **TPAPyAP** is higher than that of ICT band at 469 nm of **TPAPyBPN**, which aligns with the TD-DFT calculated oscillator strength ($f = 0.47$ for **TPAPyAP** and $f = 0.36$ for **TPAPyBPN**, Figure 3.5), while **TPAPyBP** exhibits the highest ϵ at 456 nm (f of 0.39). The ICT absorption bands of these three compounds also expectedly shift to lower energies as the acceptor strength increases. All compounds show unstructured and broad PL spectra in toluene (Figure 3.5a), indicative of an excited state of ICT character, with peak maxima, λ_{PL} , at 513 nm, 550 nm, and 575 nm for **TPAPyAP**, **TPAPyBP** and **TPAPyBPN**, respectively. Positive solvatochromism is observed for all three compounds (Figure 3.5a), which is consistent with the ICT nature of the emissive excited state. The optical bandgaps, E_{g} , calculated from the intersection point of the normalized absorption and emission spectra, are 2.62 eV, 2.46 eV, and 2.38 eV for **TPAPyAP**, **TPAPyBP** and **TPAPyBPN**, respectively (Figure 3.6a). The photoluminescence quantum yields, Φ_{PL} , in degassed toluene solution of **TPAPyAP**, **TPAPyBP** and **TPAPyBPN** are 93%, 89%, and 86%, respectively, decreasing to 85%, 81%, and 78% upon exposure to oxygen (Table 3.1 Table).

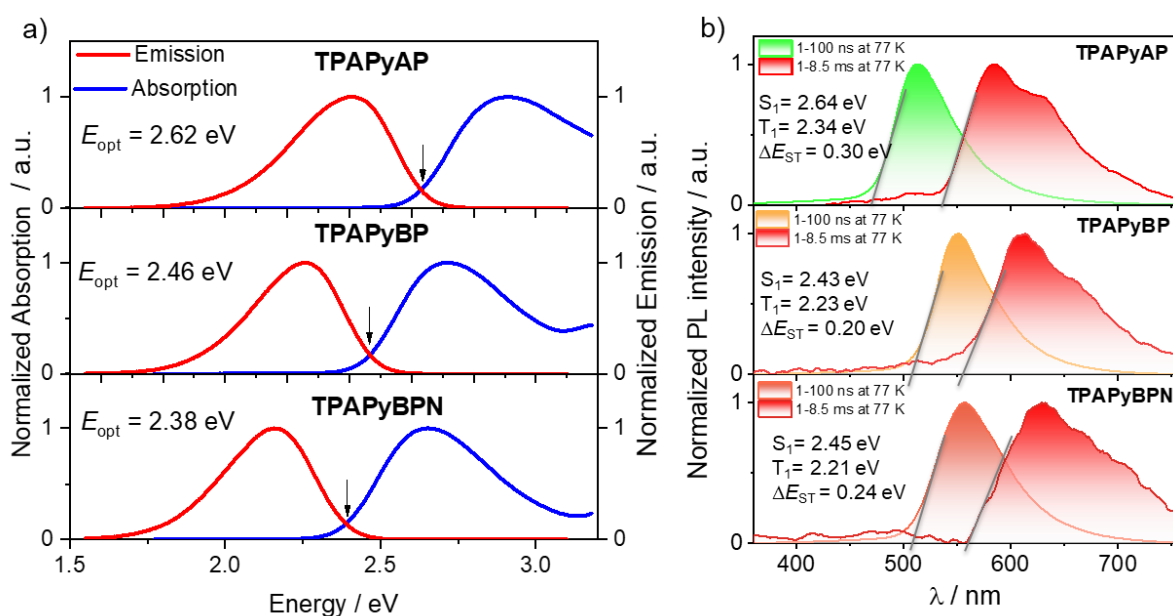


Figure 3.6 (a) The optical bandgaps calculated from the intersection point of the normalized absorption and emission spectra; (b) prompt fluorescence and phosphorescence spectra of **TPAPyAP**, **TPAPyBP** and **TPAPyBPN** toluene at 77 K ($\lambda_{\text{exc}} = 343 \text{ nm}$, prompt and delayed fluorescence spectra were acquired across a 1–100 ns and a 1–8.5 ms time range, respectively).

The PL decays of the three emitters in toluene under degassed and aerated conditions were measured using TCSPC (Figure 3.7). There is only a single decay component (monoexponential) observed for all three compounds, with lifetimes, τ_p , of 4.6 ns for **TPAPyAP**, 5.6 ns for **TPAPyBP** and 7.2 ns for **TPAPyBPN**. While there is no long-lived TADF emission observed, which may be completely quenched by nonradiative decay in solution, as revealed by some previously reported TADF compounds, especially for TPA-based TADF emitters.^{128,138,269,270} The S_1 and T_1 energies of the three emitters were elucidated from the onsets of the respective fluorescence and phosphorescence spectra determined in frozen toluene at 77 K (Figure 3.6b Table 3.1). The S_1 energies of **TPAPyAP**, **TPAPyBP** and **TPAPyBPN**, are 2.64 eV, 2.43 eV, and 2.38 eV, while the T_1 energies are 2.34 eV, 2.23 eV, and 2.21 eV, respectively. The phosphorescence spectra of all three compounds are structured, and each is assigned from the TDA-DFT calculations as a mixed locally excited triplet (3LE) state of the acceptor and 3ICT state (Figure 3.6b). The ΔE_{ST} values of **TPAPyAP**, **TPAPyBP** and **TPAPyBPN** are 0.30 eV, 0.20 and 0.17 eV, respectively, which though smaller than the calculated values nonetheless mirror the trend predicted in the theoretical study. Similar to the other TPA-based TADF emitters,^{269,271} these three compounds also have large ΔE_{ST} in solution, yet TADF is observed in the solid state.

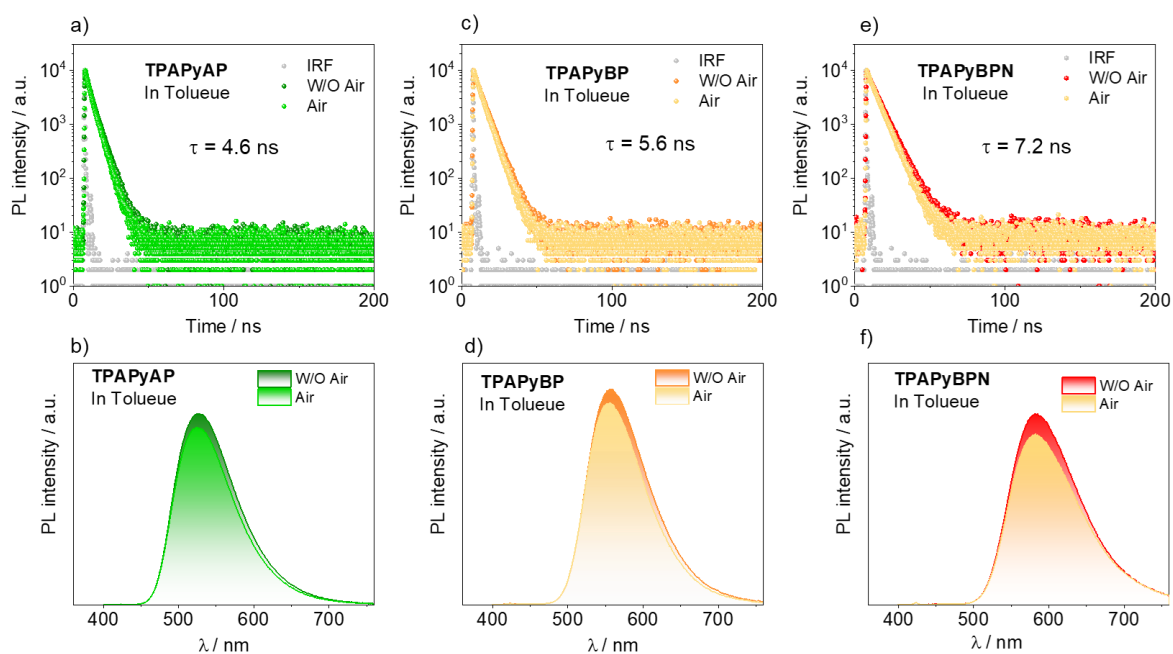


Figure 3.7 Time-resolved PL decay profiles ($\lambda_{exc}=379$ nm) and steady-state PL spectra ($\lambda_{exc}=360$ nm) of (a) (b) **TPAPyAP**, (c) (d) **TPAPyBP** and (e) (f) **TPAPyBPN** in aerated and degassed toluene, respectively.

3.7 Fluorescence Sensing toward Lewis Acids

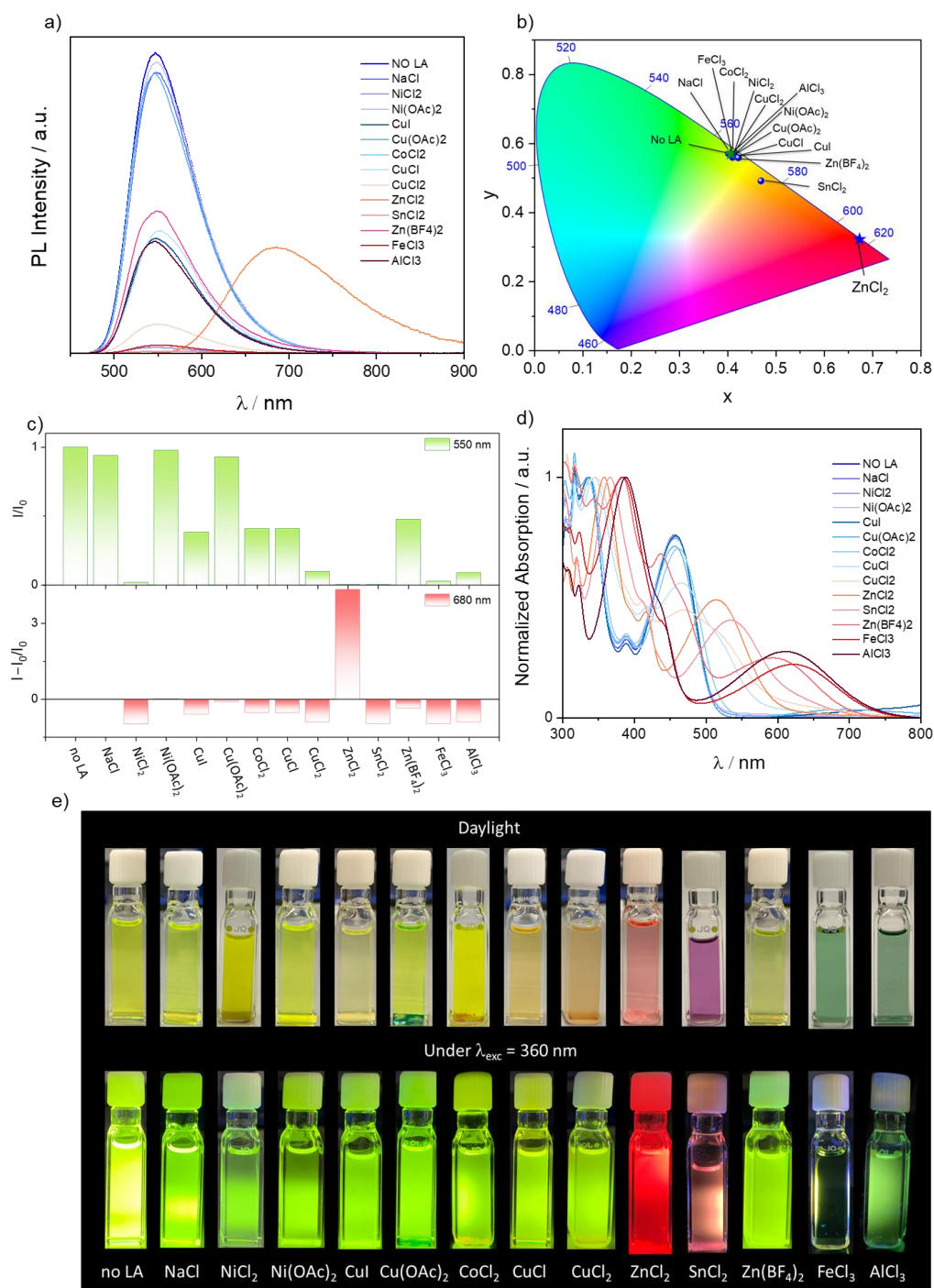


Figure 3.8. (a) PL measurements of TPAPyBP (1.3×10^{-4} M) with different metal salts (10 equiv.); (b) The related CIE diagram; (c) Variation of the PL intensity at 550 nm and 680 nm ($\lambda_{exc} = 410$ nm) of TPAPyBP (0.1 μ M) in the presence of 10 equiv. of metal salt (ethanol/toluene(1/99, v/v)); (d) Absorption measurements of 0.1 μ M TPAPyBP with different metal salts (10 equiv.) (e) Samples in daylight and excited by UV torch ($\lambda_{exc} = 360$ nm) of TPAPyBP upon addition of 10 equiv. of different metal salt (mixture of ethanol and toluene).

Recognizing that the acceptors contain Lewis basic nitrogen atoms of differing number and strength and we decided to assess the potential of these compounds to act as selective optical sensors of Lewis acids. Although TADF luminophores have shown great potential as sensors,^{103,104} such as for oxygen,^{272–274} as temperature probes,^{254,256,275} and for acid–base sensing.²⁷⁶ There is to date no report on the use of TADF luminophores for Lewis acids sensing. We first investigated the optical sensing responses of **TPAPyBP** (1.3×10^{-4} M) towards different metal ions. There is a quenching of the PL intensity of **TPAPyBP** at 550 nm with varying degrees of efficiency upon addition of excess of various metal salts (NaCl, NiCl₂, Ni(OAc)₂, CuI, Cu(OAc)₂, CoCl₂, CuCl, CuCl₂, ZnCl₂, SnCl₂, Zn(BF₄)₂, FeCl₃, AlCl₃) in ethanol/toluene(1/99, v/v) solvent (Figure 3.8a and e). Remarkably, the emission response upon addition of ZnCl₂ is particularly distinct, as there is the emergence of a new, strong emission band at 675 nm (Figure 3.8b and c). As shown in Figure 3.8d, new, strong absorption bands were observed for ZnCl₂, SnCl₂, Zn(BF₄)₂, FeCl₃ and AlCl₃. However, it is noteworthy that only the addition of ZnCl₂ to the **TPAPyBP** toluene solution resulted in a distinct red emission.

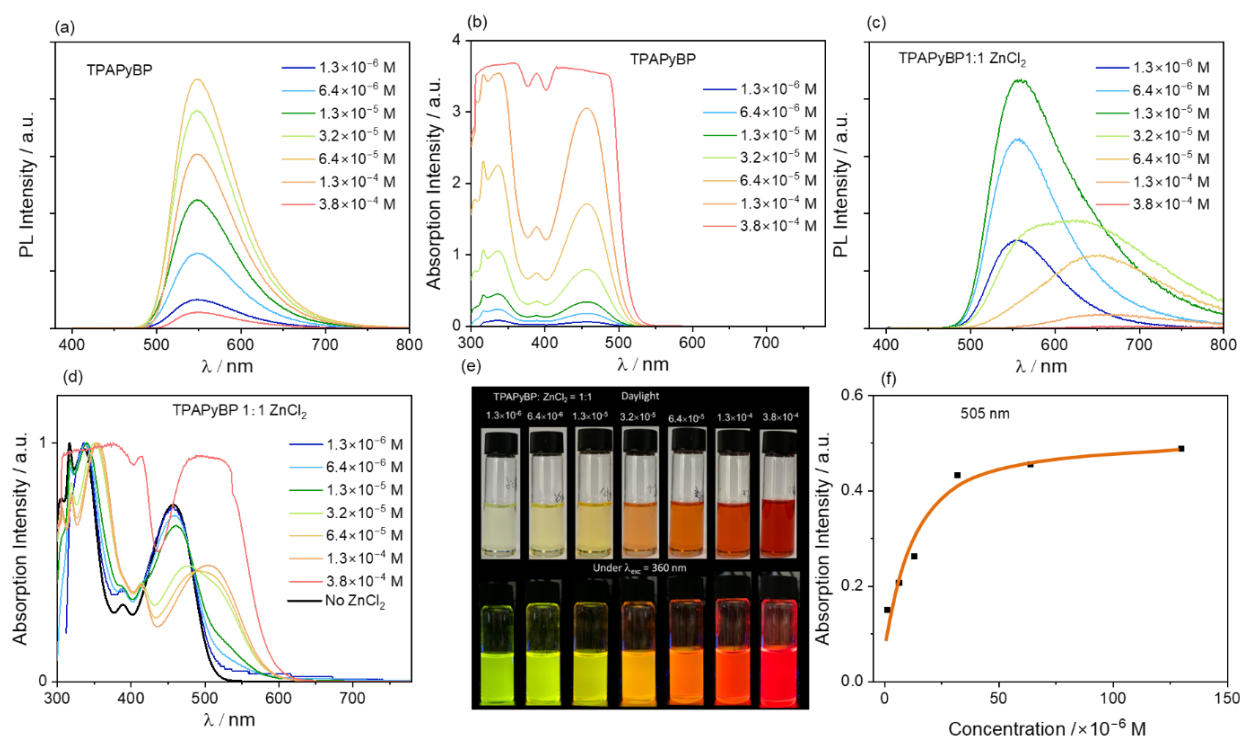


Figure 3.9. (a) The fluorescence spectra and (b) absorption measurements of **TPAPyBP** with different concentrations; (c) The fluorescence spectra and (d) absorption measurements of **TPAPyBP** with different concentrations upon 1 equiv. ZnCl₂; (e) Samples in daylight and excited by UV torch ($\lambda_{\text{exc}} = 360$ nm) of **TPAPyBP** upon 1 equiv. ZnCl₂; (f) the calibration curve corresponding to the absorption spectra.

The intriguing observation of this selective ZnCl_2 sensing prompted us to explore the underlying mechanism. We first investigated the detection limit of ZnCl_2 , which is correlated with the concentration of the emitter. As shown in Figure 3.9, the fluorescence spectra of different concentrations of **TPAPyBP** in a mixture of ethanol and toluene (0.0012/1 v/v) upon addition of 1 equivalent of ZnCl_2 were measured. As the concentration of **TPAPyBP**: ZnCl_2 (1:1 equiv.) increases, the fluorescence intensity at 555 nm increases until the concentration reaches 1.3×10^{-5} M. When the concentration increases further, the intensity of 555 nm emission band decreases while concomitantly a new emission band at 680 nm emerges and gradually becomes the principal emission band, reflecting the observed color change from green to deep red (Figure 3.9c and e). As expected, the corresponding absorption spectrum exhibits a new band at 505 nm, which increases in intensity as the concentration of **TPAPyBP**: ZnCl_2 (1:1 equiv.) increases. As shown in Figure 3.9f, the calibration curve of the absorption spectra demonstrated that the detection limit of ZnCl_2 is around 5.0×10^{-5} M as this is the concentration of its 1:1 adduct with **TPAPyBP**. Furthermore, it's important to highlight the remarkable speed of the reaction time, which occurs within several seconds. This rapid response is highly desirable for sensing applications.

We then systematically investigated the PL response of **TPAPyBP** (1.3×10^{-4} M) in toluene upon gradual addition of ZnCl_2 (0.10 M) in ethanol. As shown in Figure 3.10a-c, the PL intensity of **TPAPyBP** at 550 nm decreases progressively upon addition of ZnCl_2 with concomitant increase of a new emission band at 675 nm. This leads to stark spectral response where the emission changes from greenish yellow to deep-red (Figure 3.10b), with corresponding CIE coordinates from (0.44, 0.55) to (0.61, 0.38), shown in Figure 3.10c. The TRPL of **TPAPyBP** with 10 equiv. of ZnCl_2 still shows monoexponential decay kinetics; however, the lifetime is shorter at 2.9 ns compared to 4.9 ns in the absence of ZnCl_2 . Similarly, there are distinct spectral changes in the UV/vis absorption spectrum whereupon gradual addition of ZnCl_2 , the absorption band at 338 nm was bathochromically shifted to 358 nm while the new CT band 505 nm, which is probably due to the formation of a Zn complex (Figure 3.10d). An isosbestic point at 487 nm and the 1:1 stoichiometry identified in the Job plot indicates that only a single ZnCl_2 is coordinated to **TPAPyBP** (Figure 3.10). Single crystals were grown by slow liquid/liquid diffusion of a saturated toluene solution of **TPAPyBP** and ZnCl_2 dissolved ethanol at room temperature. The structure of $\text{Zn}(\text{TPAPyBP})\text{Cl}_2$ is shown in Figure 3.10f and reveals that the Zinc ion adopts a distorted tetrahedral geometry, coordinated through the pyridyl nitrogen of **TPAPyBP** (10-position N), two chlorido ligands and a molecule

of ethanol solvent (N-Zn-Cl bond angle of 107.54° and N-Zn-O bond angle of 96.42°). This, or a structurally related tetrahedral complex, is the likely putative species in solution. The ^1H NMR spectrum of **TPAPyBP** with increasing concentration of ZnCl_2 in CDCl_3 revealed that the resonances at positions 1 and 3 (Figure 3.11a) of **TPAPyBP** were the most perturbed upon addition of ZnCl_2 , suggesting a possible coordination of Zn^{2+} ion through pyrido[3,4-b]pyrazine core of the acceptor (Figure 3.10f). Furthermore, HRMS of **TPAPyBP** with excess ZnCl_2 confirms the formation of $\text{Zn}(\text{TPAPyBP})\text{Cl}_2$ (Figure 3.11b).

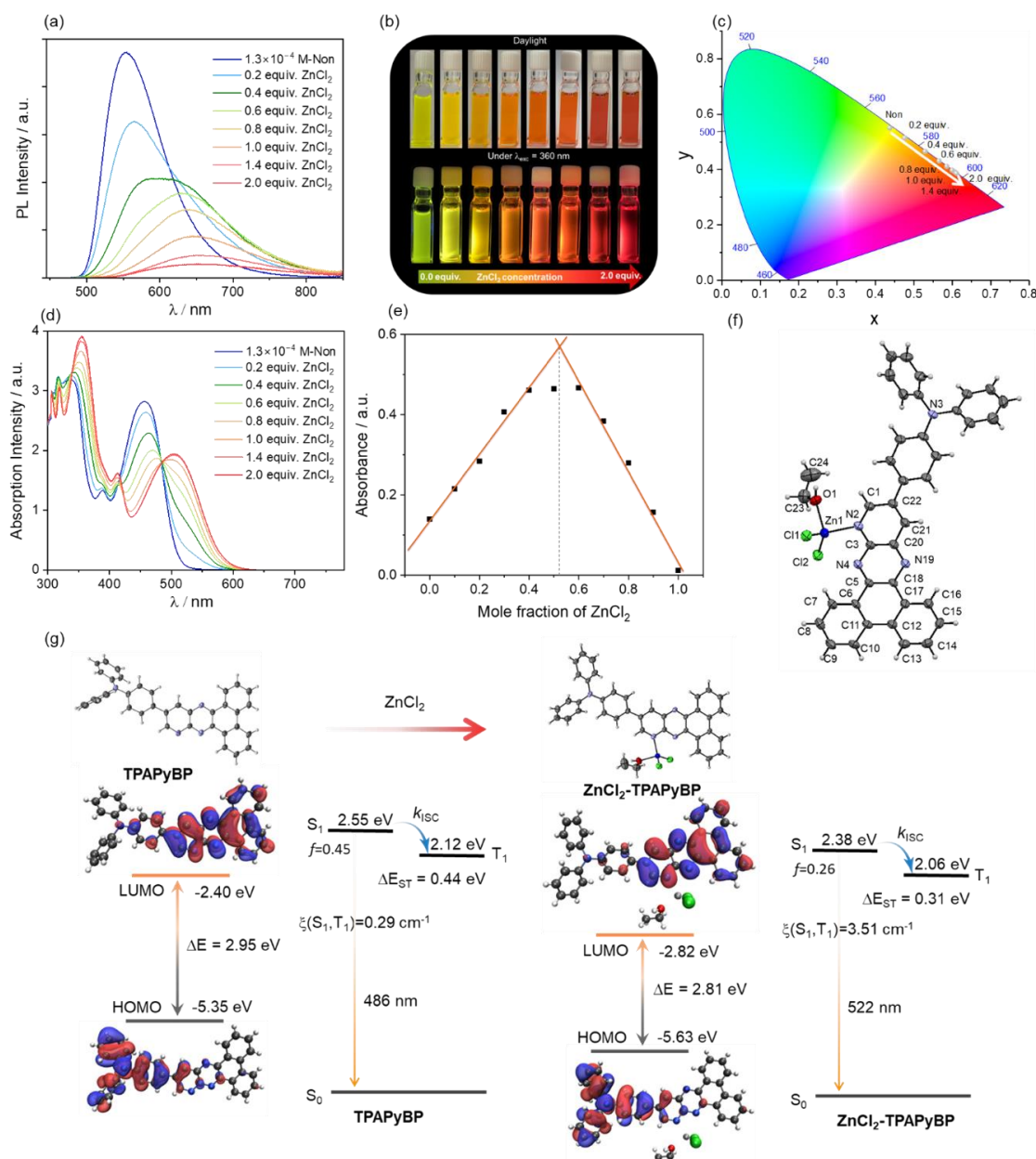


Figure 3.10. (a) PL of **TPAPyBP** (1.3×10^{-4} M) with the addition of ZnCl_2 from 0 to 2.0 equiv. ($\lambda_{\text{exc}} = 487$ nm); (b) Samples in daylight and excited by UV torch ($\lambda_{\text{exc}} = 360$ nm) of **TPAPyBP** ZnCl_2 from 0 to 2.0 equiv.; (c) The corresponding CIE coordinates and (d) UV-Vis absorption spectra obtained from **TPAPyBP** with the addition of ZnCl_2 from 0 to 2.0 equiv.; (e) Job plot

of absorbance for the determination of binding stoichiometry between **TPAPyBP** and ZnCl_2 ($\lambda_{\text{PL}} = 510 \text{ nm}$). (f) Thermal ellipsoid plot (50% probability level) of one independent molecule in the single crystal structure of $\text{Zn}(\text{TPAPyBP})\text{Cl}_2$; (g) Single crystals of **TPAPyBP** and $\text{Zn}(\text{TPAPyBP})\text{Cl}_2$ and corresponding frontier molecular orbitals (isovalue: 0.02) calculated using single crystal geometry in the gas phase at the PBE0/6-31G(d,p) level.

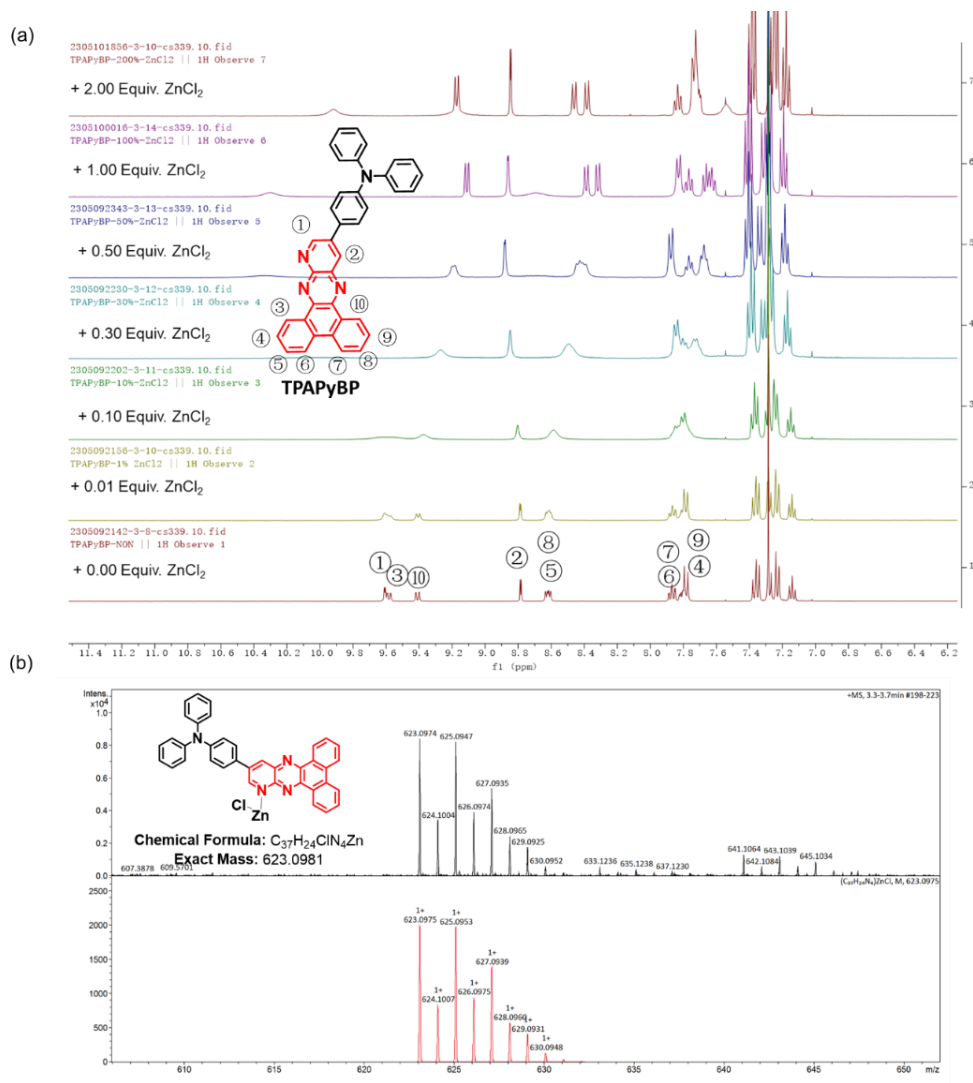


Figure 3.11. (a) ^1H NMR spectrum of **TPAPyBP** with increasing concentration of ZnCl_2 in CDCl_3 ; (b) HRMS of **TPAPyBP** with excessive ZnCl_2 .

For more insights into the origin of new deep red emission in solution, the HOMOs and LUMOs of **TPAPyBP** and $\text{Zn}(\text{TPAPyBP})\text{Cl}_2$ calculated at the PBE0/6-31G(d,p) level (based on the structure obtained from the single crystal X-ray diffraction study) are shown in Figure 3.10f. The energy levels of both the LUMO (-2.82 eV) and the HOMO (-5.63 eV) for $\text{Zn}(\text{TPAPyBP})\text{Cl}_2$ are significantly stabilized compared to -2.40 eV (LUMO) and -5.35 eV (HOMO) for **TPAPyBP**, leading to decrease in the $\Delta E_{\text{HOMO-LUMO}}$ from 2.95 eV to 2.81 eV . As

excepted, the S_1 energy decreases to 2.38 eV for **Zn(TPAPyBP)Cl₂** from 2.55 eV of **TPAPyBP**, corresponding to a large red-shift of both the CT band of the absorption and the emission of **TPAPyBP** upon addition of **ZnCl₂**. Similarly, the emitters **TPAPyAP** and **TPAPyBPN** also showed selectivity towards **ZnCl₂** and there is a new, red-shifted emission band at 650 nm and 655 nm, respectively (Figure 3.12). The Job plots for both compounds indicate the same 1:1 stoichiometry of binding as that observed for **TPAPyBP** (Figure 3.12). Given the more distinct and stronger optical response with **TPAPyBP** compared to **TPAPyAP** and **TPAPyBPN**, here we only focused on **TPAPyBP**.

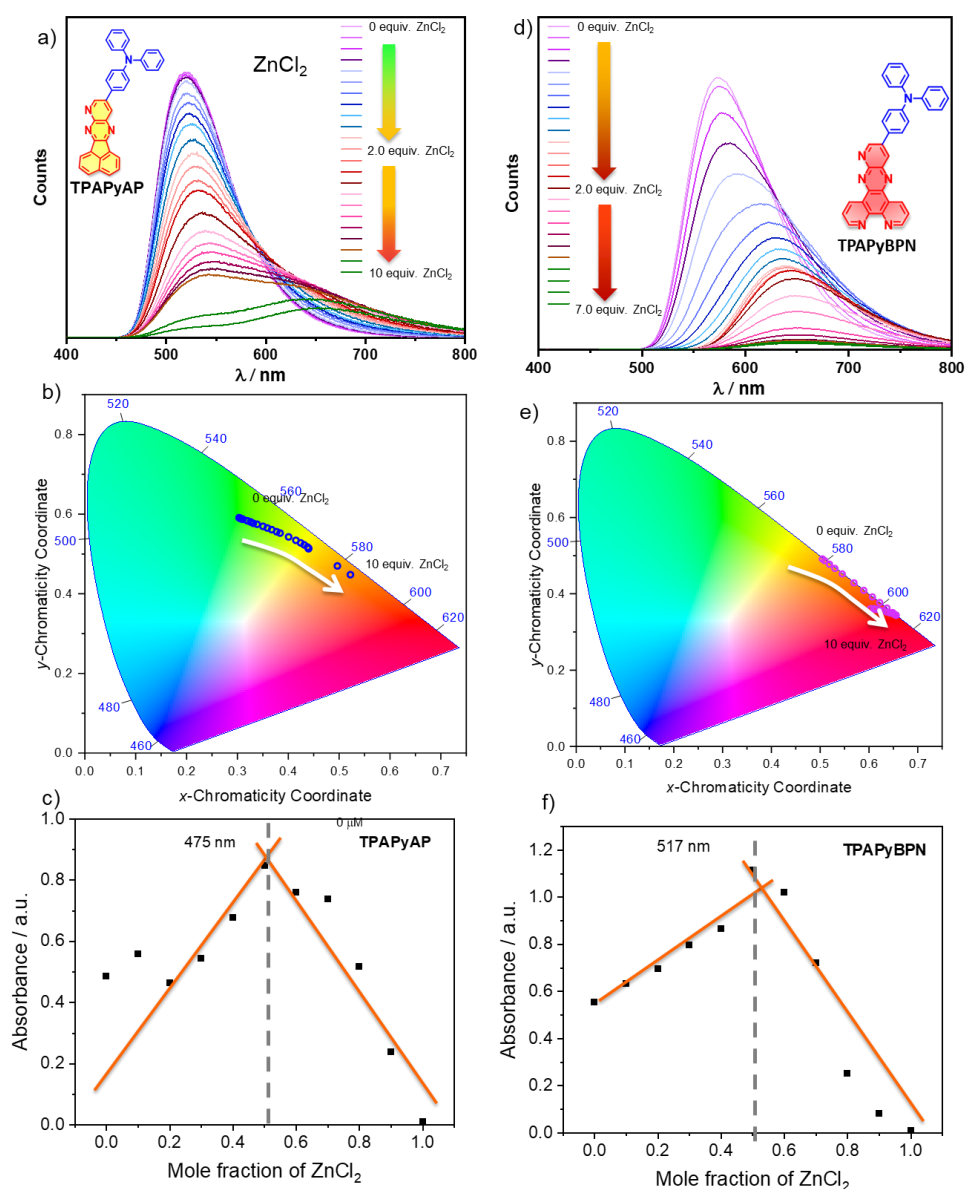


Figure 3.12 Emission measurements for 0.1 μM a) **TPAPyAP**, d) **TPAPyBPN** with the addition of **ZnCl₂** from 0 to 10 equiv., 0 to 7 equiv., respectively. And the related CIE diagrams b) **TPAPyAP** and e) **TPAPyBPN**; Job plot for the determination of binding stoichiometry between c) **TPAPyAP** (λ_{abs} = 475 nm) and f) **TPAPyBPN** (λ_{abs} = 517 nm) and **ZnCl₂**.

3.8 TADF Properties in the Solid State

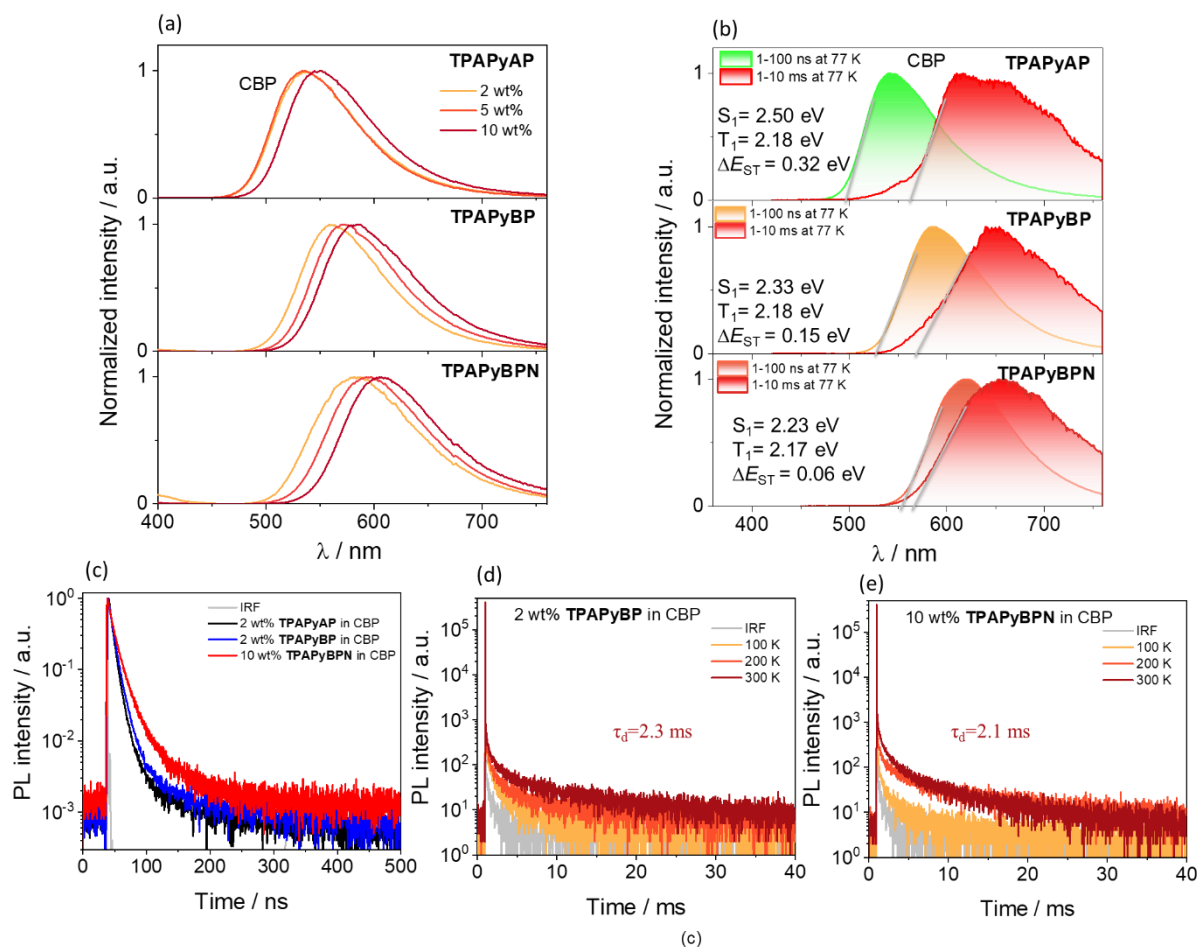


Figure 3.13. (a) PL spectra of **TPAPyAP**, **TPAPyBP** and **TPAPyBPN** doped in **CBP** at various doping concentrations from 2 wt% to 10 wt%; (b) Prompt fluorescence and phosphorescence spectra of 2 wt% **TPAPyAP**, 2 wt% **TPAPyBP** and 10 wt% **TPAPyBPN** doped in **CBP** and (b) PPT ($\lambda_{exc} = 343$ nm, prompt and delayed fluorescence spectra were obtained in the 1–100 ns and 1–10 ms time range, respectively). (c) Transient PL decay of 2 wt% **TPAPyAP**, 2 wt% **TPAPyBP** and 10 wt% **TPAPyBPN** ($\lambda_{exc} = 379$ nm) doped in **CBP** with a time window of 500 ns; Temperature-dependent time-resolved PL decay of (d) 2 wt% **TPAPyBP** and (e) 10 wt% **TPAPyBPN** in **CBP**.

We next measured the photophysical properties of all three compounds in an OLED-relevant nonpolar host **CBP** at different weight concentrations ranging from 2 to 10 wt% (Figure 3.13). The 2 wt% doped **CBP** films of **TPAPyAP**, **TPAPyBP** and **TPAPyBPN** emit at λ_{PL} of 537, 560 and 585 nm, respectively, corresponding closely those in dilute toluene solutions. The Φ_{PL} of the 2 wt% **CBP** doped films of **TPAPyAP**, **TPAPyBP** and **TPAPyBPN**

are 62, 60 and 62%, respectively. All three compounds show unstructured ICT-based emission at room temperature (Figure 3.13a).

Table 3.1. Photophysical properties of **TPAPyAP**, **TPAPyBP**, and **TPAPyBPN** in solution and the solid state.

	λ_{PL}^a /nm	τ_p^a / ns	τ_d / ms	S_1/T_1^b / eV	ΔE_{ST} / eV	Φ_{PL}^c /%
in solution						
TPAPyAP	516	4.6	-	2.64/2.34	0.30	93 (85)
TPAPyBP	550	5.6	-	2.43/2.23	0.20	89 (81)
TPAPyBPN	575	7.2	-	2.45/2.21	0.24	86 (78)
in CBP^d						
TPAPyAP (2 wt%)	537	8.4	-	2.50/2.18	0.32	62 (61)
TPAPyBP (2 wt%)	559	10.0	2.3	2.33/2.18	0.15	60 (58)
TPAPyBPN (10 wt%)	605	15.0	2.1	2.23/2.17	0.06	56 (53)
in PPT^d						
TPAPyAP (2 wt%)	584	6.8	1.42	2.41/2.33	0.11	75 (70)
TPAPyBP (2 wt%)	624	9.7	0.61	2.31/2.28	0.03	63 (58)
TPAPyBPN (10 wt%)	675	14.0	0.11	2.12/2.11	0.01	57 (47)

^a At 298 K, values quoted are in degassed toluene solutions prepared by three freeze-pump-thaw cycles: for λ_{PL} the $\lambda_{\text{exc}} = 340$ nm; for lifetime $\lambda_{\text{exc}} = 379$ nm. ^b Obtained from the onset of the prompt fluorescence (time window: 1 ns – 100 ns) and phosphorescence spectra (time window: 1 ms – 8.5 ms) measured in 2-MeTHF glass at 77 K, $\lambda_{\text{exc}} = 343$ nm. ^c Quinine sulfate in H_2SO_4 (aq) was used as the reference ($\Phi_{\text{PL}} = 54.6\%$, $\lambda_{\text{exc}} = 360$ nm) for the solution-state measurements.²⁷⁷ Values quoted are in degassed solutions, which were prepared by three freeze-pump-thaw cycles. Values in parentheses are for aerated solutions, which were prepared by bubbling air for 10 min. The thin films were determined using an integrating sphere ($\lambda_{\text{exc}} = 340$ nm) under N_2 atmosphere at 298 K. Values quoted inside the parentheses are in the presence of O_2 . ^d Thin films of CBP and PPT were prepared as spin-coated films. Average lifetime ($\tau_{\text{avg}} = \Sigma A_i \tau_i^2 / \Sigma A_i \tau_i$, where A_i is the pre-exponential for lifetime τ_i). Prompt and delayed emissions were measured by TCSPC and MCS, respectively ($\lambda_{\text{exc}} = 379$ nm).

Similar to that observed in toluene at 77 K, the prompt fluorescence of 2 wt% **TPAPyAP**, **TPAPyBP** and **TPAPyBPN** doped in CBP film at 77 K are structureless (Figure 3.13b), with associated S_1 energies of 2.50, 2.33 and 2.23 eV, respectively. As expected, the phosphorescence spectra of all three compounds are structured, with T_1 values of 2.18, 2.18 and 2.17 eV, matching well with the TDA-DFT calculations as a mixed $^3\text{LE}/\text{ICT}$ state. The ΔE_{ST} of these films of **TPAPyAP**, **TPAPyBP** and **TPAPyBPN** are 0.32 eV, 0.15 and 0.06 eV, respectively (Figure 3.13b). As shown in Figure 3.13c-d, **TPAPyBP** and **TPAPyBPN** each showed multiexponential decay kinetics at room temperature, with average prompt fluorescence lifetimes, λ_p , of 10.0 ns and 15.0 ns, respectively, and average delayed emission lifetimes, τ_d , of 2.3 ms and 2.1 ms, respectively. The relative intensity of the delayed PL increases with increasing temperature from 100 K to 300 K for both compounds, thereby corroborating the TADF nature of the emission of these three compounds in the CBP films. However, **TPAPyAP** showed monoexponential decay kinetics with a fluorescence lifetime of 8.4 ns (Figure 3.13a), which can be explained by the large ΔE_{ST} (*vide infra*) and inefficient

TADF in the doped CBP film.

Due to the strong CT effects of **TPAPyAP**, **TPAPyBP** and **TPAPyBPN**, we further investigate how different polarities of host materials (Figure 3.14a) can affect luminescent properties and understand the interactions between guest and host molecules, but also aim to enhance the efficiency of TADF by decreasing ΔE_{ST} in high polarity host.^{278,279} Firstly, we calculated the dipole moment of ground state for CBP (0.0 D), mCP (1.2 D), TPBi (1.92 D), DPEPO (7.29 D) and PPT (2.08 D) by the TDDFT method at PBE0/6-31G(d,p) level. The PL spectra of 2 wt% emitters doped in five different host compounds measured at room temperature are shown in Figure 3.14b-c. Generally, there is an observed red-shifting of the PL with increasing polarity of the host matrix. Due to largest dipole moment of 5.97 D, **TPAPyBPN** exhibited the largest red shifted emission with 53 nm from nonpolar to high polar host, compared that of **TPAPyAP** (42 nm) and **TPAPyBP** (48 nm).

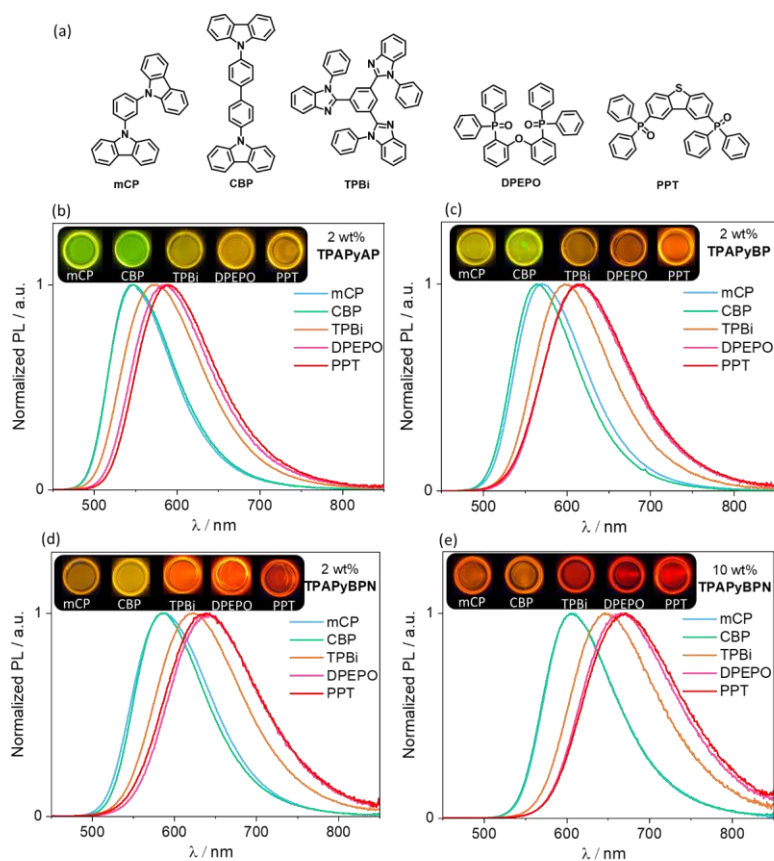


Figure 3.14. (a) The molecular structures of different hosts; (b) PL of **TPAPyAP** in different hosts; (c) PL of **TPAPyBP** in different hosts; (d) PL of **TPAPyBPN** in different hosts.

As shown in Figure 3.15, the doped PPT films of **TPAPyAP**, **TPAPyBP** and **TPAPyBPN** all show multiexponential decay kinetics with average τ_p of 6.8 ns, 9.7 ns, and 14.0 ns and average τ_d of 1.4 ms, 0.68 ms and 0.11 ms at room temperature, respectively. Temperature-

dependent time-resolved PL decays evidence the TADF nature of the emission in the PPT doped films (Figure 3.15a-c). The S_1 levels of **TPAPyAP**, **TPAPyBP** and **TPAPyBPN** are stabilized modestly from 2.48 to 2.41 eV, 2.33 to 2.31 eV, 2.22 to 2.11 eV, respectively, in PPT host compared to that in CBP host. The corresponding ΔE_{ST} values decrease (Table 3.1, Figure 3.15d), implying more efficient RISC in PPT than in CBP.

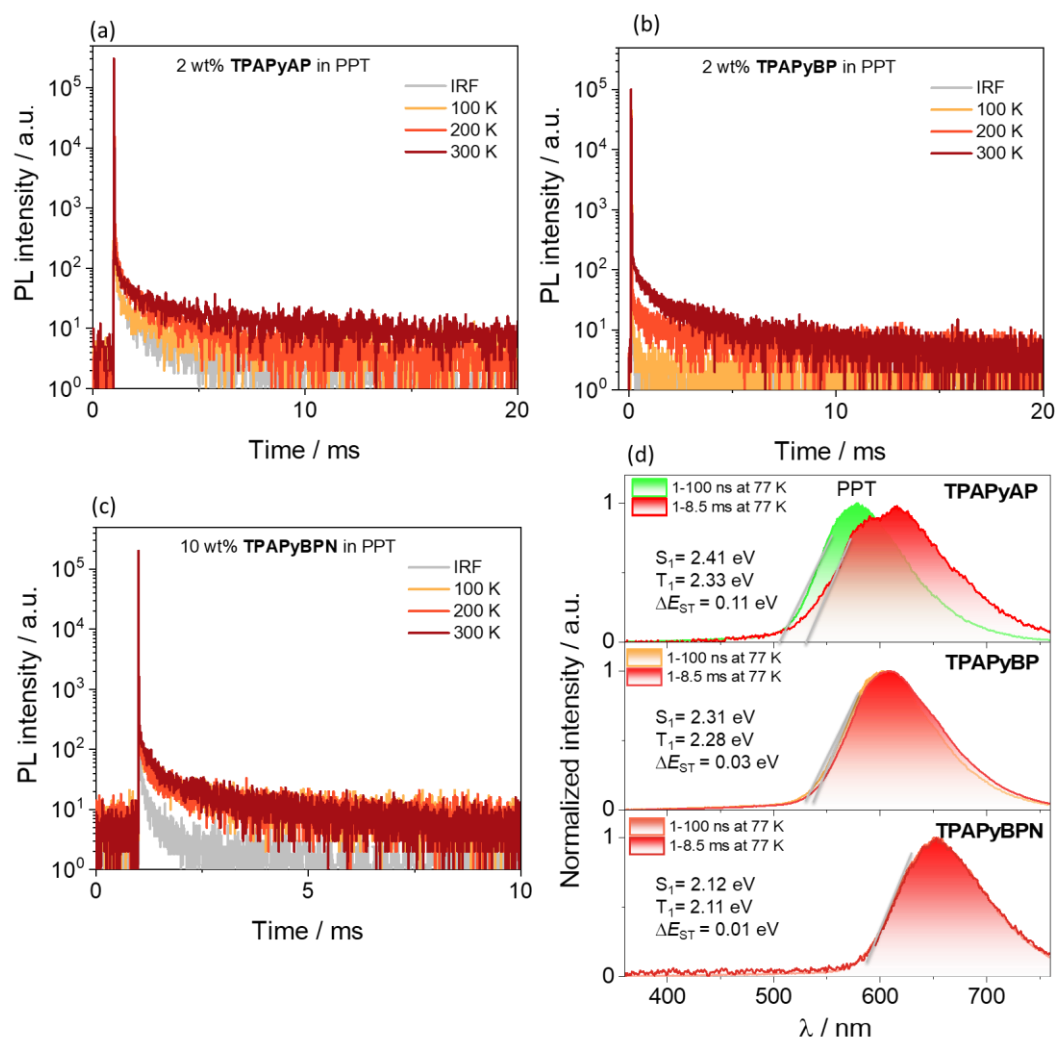


Figure 3.15. Temperature-dependent time-resolved PL decay of (a) 2 wt% **TPAPyAP** (b) 2 wt% **TPAPyBP** and (c) 10 wt% **TPAPyBPN** in PPT. (d) Prompt fluorescence and phosphorescence spectra of 2 wt% **TPAPyAP**, 2 wt% **TPAPyBP** and 10 wt% **TPAPyBPN** doped in PPT ($\lambda_{exc} = 343$ nm, prompt and delayed fluorescence spectra were obtained in the 1–100 ns and 1–8.5 ms time range, respectively).

To further assess the formation of aggregates (π - π packing), we investigated the PL spectra of the doped films of **TPAPyAP**, **TPAPyBP** and **TPAPyBPN** in PMMA at varying concentrations ranging from 0.01 to 100 wt%. As shown in Figure 3.16, the 0.01 wt% doped

films of **TPAPyAP**, **TPAPyBP** and **TPAPyBPN** exhibit green, greenish–yellow and orange emissions with peak wavelengths at 520, 547 and 568 nm, respectively, which are similar to the emission of the monomers in dilute toluene solutions (Figure 3.7). There is a gradual red-shift of the PL into orange region ($\lambda_{\text{max}} = 602$ nm) for **TPAPyAP** and red region ($\lambda_{\text{max}} = 626$ nm) for **TPAPyBP** as the doping concentrations increase from 0.01 to 100 wt% with a wavelength change of 82 nm and 79 nm, respectively. While **TPAPyBPN** exhibits a significant red-shift PL into pure red ($\lambda_{\text{max}} = 647$ nm) at 10 wt% PMMA. This shift continues further into the NIR emission ($\lambda_{\text{max}} = 695$ nm) in neat film with the largest red-shifted wavelength of 127 nm, which indicates that **TPAPyBPN** likely forms much stronger intermolecular interactions than **TPAPyAP** and **TPAPyBP**. As the doping concentrations increase, the Φ_{PL} of the doped films of all three compounds gradually decrease due to in part to the energy gap law,¹¹¹ as shown in Figure 3.16d-f. The red-shifted emission of these three emitters could be explained by the synergistic effect of the transformation of exciton states due to the formation of π - π interactions between adjacent molecules,^{38,280,281} further leading to the J-aggregation. This finding demonstrates that modulating π - π interactions between neighbouring molecules is an effective strategy for achieving red TADF emitters.

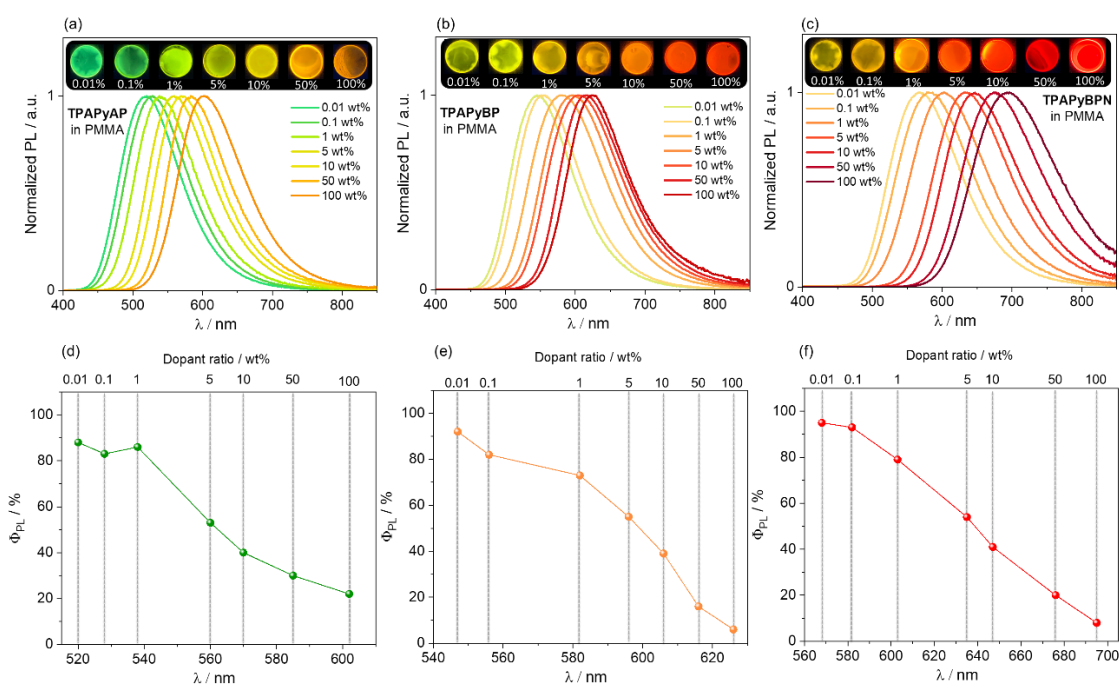


Figure 3.16. PL spectra of (d) **TPAPyAP**, (e) **TPAPyBP** and (f) **TPAPyBPN** in PMMA films at various doping concentrations at room temperature; Φ_{PL} and emission peak wavelengths of (d) **TPAPyAP**, (e) **TPAPyBP** and (f) **TPAPyBPN** in PMMA films at various doping concentrations ($\lambda_{\text{exc}} = 340$ nm).

3.9 OLED Device Characterization

We next proceeded to fabricate vacuum-deposited bottom-emitting OLED devices using **TPAPyAP**, **TPAPyBP** and **TPAPyBPN** as emitters. As shown in Figure 3.17, we fabricated OLEDs with two different device architectures that differ in terms of the host matrix used in the emissive layer (EML): CBP (device **A**); and PPT (device **B**). As shown in Figure 3.17a, the general device architecture consists of ITO/ 1,4,5,8,9,11-hexaazatriphenylenehexacarbonitrile (HATCN) (5 nm)/ 1,1-bis[(di-4-tolylamino)phenyl]cyclohexane (TAPC) (40 nm)/tris(4-carbazoyl-9-ylphenyl)amine (TCTA) (10 nm)/ mCP (10 nm)/EML (20 or 35 nm)/ TmPyPB (50 or 75 nm)/ LiF (0.8 nm)/ Al (100 nm). Here, HATCN was used as a layer for HIL, TAPC and TCTA play the role in HTL, mCP acts as an EBL, TmPyPB acts as both an ETL and a HBL due to its deep HOMO (-6.7 eV),²⁸² and LiF acts as an EIL by modifying the work function of the aluminum cathode. Device **A** consists of a 20 nm EML comprising 2 wt% of **TPAPyAP**, 2 wt% **TPAPyBP** or 10 wt% of **TPAPyBPN** doped into CBP and a 50 nm thick TmPyPB layer, while device **B** consists of a 35 nm thick EML of 10 wt% **TPAPyBPN** doped in PPT and a 70 nm thick TmPyPB layer. The molecular structures of the materials used in both devices are shown in Figure 3.17b.

The performance of the OLEDs is summarized in Table 3.2. The EQE–luminance, current density–voltage–luminance (J – V – L) curves, and EL are given in Figure 3.16c–e. Initially, we fabricated devices using device structure **A** and observed that each EL spectrum is similar to that of the corresponding PL spectrum in the CBP doped thin film, with EL maxima, λ_{EL} , of 526 nm for **TPAPyAP**, 558 nm for **TPAPyBP** and 597 nm for **TPAPyBPN**, with corresponding CIE coordinates of (0.317, 0.578), (0.434, 0.547) and (0.565, 0.433), respectively (Figure 3.16e). The EQE_{max} of the **TPAPyAP**-based device is 7.6% while that of the **TPAPyBP**-based device is 9.1% and that of the **TPAPyBPN**-based device is 13.6% (Table 3.2). Devices of **TPAPyAP** and **TPAPyBP** showed moderate and similar efficiency roll-off, with the EQE at 100 cd/m² (EQE₁₀₀) at 4.9%, and the EQE at 1,000 cd/m² (EQE₁₀₀₀) at 4.3%; however, the **TPAPyBPN**-based device showed much stronger roll-off efficiency with EQE₁₀₀ at 4.6% and EQE₁₀₀₀ at 3.2%. The theoretical EQE_{max} is 13.9% for **TPAPyBPN** in CBP when

considering an outcoupling efficiency of $\chi_{\text{out}} \approx 25\%$ that assumes that the film is isotropic. We next fabricated device **B** with an EML containing **TPAPyBPN** doped into a high polarity host of PPT at the same 10 wt% doping concentration as that in CBP. As expected, the λ_{EL} is red-shifted to 657 nm [CIE coordinates (0.651, 0.348)], close to the λ_{PL} for the 10 wt% doped PPT film. The EQE_{max} of **TPAPyBPN**-based device **B** is 12.5%, close to **TPAPyBPN**-based device **A** in CBP host and is also close to the theoretical $\text{EQE}_{\text{max}} = 14.2\%$. However, the **TPAPyBPN**-based device **B** showed much higher efficiency roll-off, despite the short τ_{d} and small ΔE_{ST} in **TPAPyBPN** doped in PPT host.

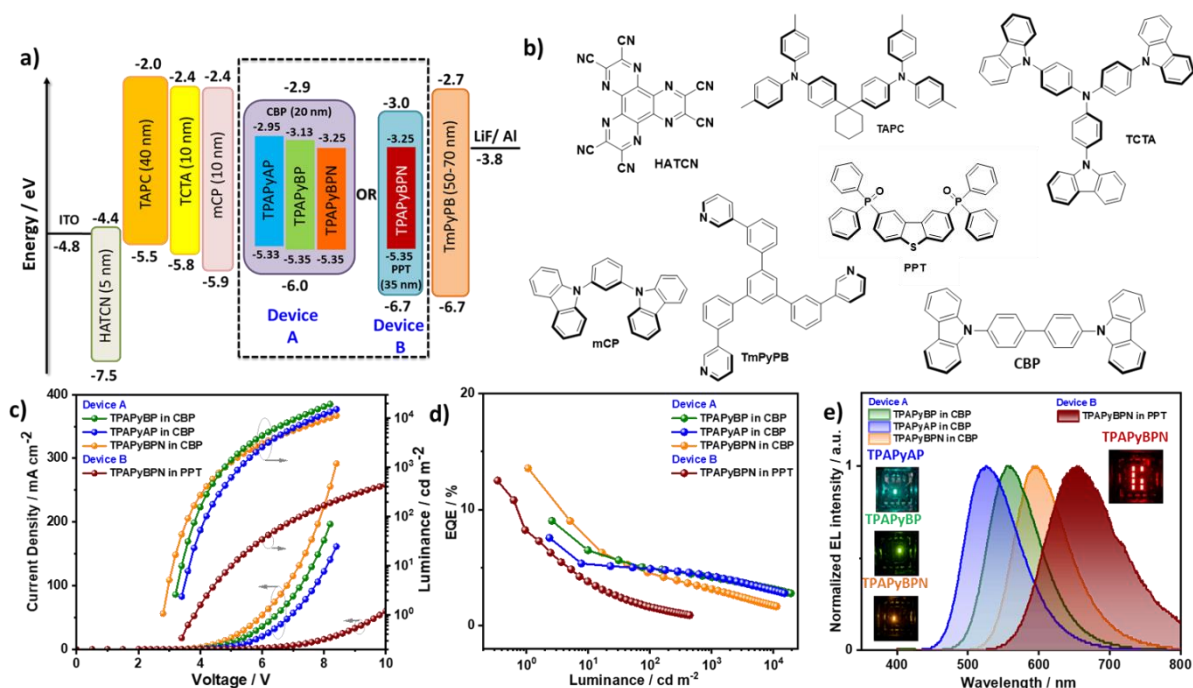


Figure 3.17. (a) Energy level diagram of materials employed in the devices with device **A**: ITO/HATCN (5nm)/ TAPC (40nm)/ TCTA (10 nm)/ mCP (10 nm)/ EML:CBP (20 nm)/ TmPYPB (50 nm)/ LiF (0.8 nm)/ Al (100 nm) and device **B**: ITO/ HATCN (5nm)/ TAPC (40nm)/ TCTA (10 nm)/ mCP (10 nm)/ **TPAPyBPN**:PPT (35 nm)/ TmPyPB (70 nm)/ LiF (0.8 nm)/ Al (100 nm); (b) Molecular structure of materials used in the devices; (c) Current density and luminance versus voltage characteristics for the devices; (d) External quantum efficiency versus luminance curves for the devices, the inset is the electroluminescence of **TPAPyAP**, **TPAPyBP** and **TPAPyBPN** in CBP and **TPAPyBPN** in PPT; (e) Electroluminescence spectra of the device.

Table 3.2. Electroluminescence data for the devices.^a

Emitter	Host	V _{on} ^c / V	λ _{EL} ^d / nm	CE _{max} / cd A ⁻¹	PE _{max} / lm W ⁻¹	EQE ^e / %	CIE ^d / x,y
TPAPyAP^a	CBP (2.0%)	3.4	526	25.24	23.35	7.6/4.9/4.3	0.317, 0.578
TPAPyBP^a	CBP (2.0%)	3.2	558	31.57	29.17	9.1/4.9/4.3	0.434, 0.547
TPAPyBPN^a	CBP (10%)	2.8	596	31.52	35.36	13.6/4.6/3.2	0.565, 0.433
TPAPyBPN^b	PPT (10%)	3.4	657	10.14	9.4	12.5/1.6/-	0.651, 0.348

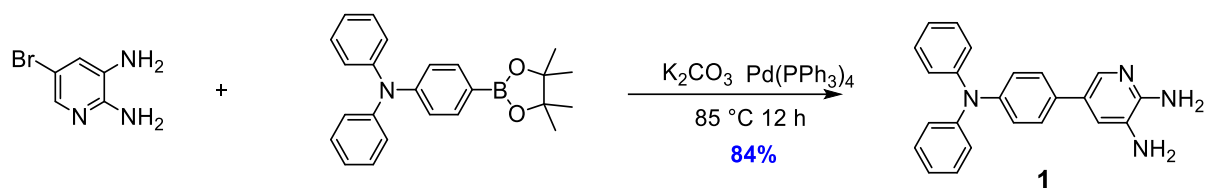
^a Device structure **A**: ITO/ HATCN (5nm)/ TAPC (40nm)/ TCTA (10 nm)/ mCP (10 nm)/ EML:CBP (20 nm)/ TmPYPB (50 nm)/ LiF (0.8 nm)/ Al (100 nm). ^b Device structure **B**: ITO/ HATCN (5nm)/ TAPC (40nm)/ TCTA (10 nm)/ mCP (10 nm)/ TPAPyBPN:PPT (35 nm)/ TmPyPB (70 nm)/ LiF (0.8 nm)/ Al (100 nm). ^c The turn-on voltage at EQE_{max}. ^d The electroluminescence maximum and CIE recorded at 6 V. ^e EQE_{max}/EQE₁₀₀/ EQE₁₀₀₀.

3.10 Conclusions

A family of TPA derivatives, **TPAPyAP**, **TPAPyBP** and **TPAPyBPN**, shows progressively red-shifted emission in toluene as a function of the increasing number of nitrogen atoms in the heterocyclic pyrazine-based acceptors. All three compounds exhibit a spectral response to the detection of ZnCl₂ in toluene, with the most notable being for **TPAPyBP**, where the emission rapidly changed from green (λ_{PL}=550 nm) to deep red (λ_{PL}=675 nm), which is distinct from the typical response of most Zn²⁺ or ZnCl₂ sensors that only rely on changes in emission intensity. We also investigated the potential of these compounds as emitters in OLEDs. Both **TPAPyBP** and **TPAPyBPN** emit in the deep red in PPT, while **TPAPyAP** exhibits a smaller red-shift from green emission in CBP to yellow emission in PPT compared to the other two compounds. The OLEDs showed moderated efficiencies, with the device with **TPAPyBPN** doped in PPT emitting at λ_{EL} = 657 nm and showing an EQE_{max} 12.5%. This electroluminescence was red-shifted by 61 nm compared to device the with CBP as the host (λ_{EL}= 596 nm, EQE_{max} = 13.6%), a reflection of the impact of solid-state solvatochromism.

3.11 Experimental Section

Synthesis of 5-(4-(diphenylamino)phenyl)pyridine-2,3-diamine (1):



A mixture of 5-bromopyridine-2,3-diamine (1.5 g, 8 mmol, 1.0 equiv.), **2** (3.55 g, 9.6 mmol, 1.2 equiv.), $Pd(PPh_3)_4$ (460 mg, 0.4 mmol, 0.05 equiv.), K_2CO_3 (3.31 g, 24 mmol, 0.05 equiv.), 1,4-dioxane (50 mL) and H_2O (25 mL) was heated at $85\text{ }^\circ\text{C}$ for 12 hours under nitrogen. After cooling to room temperature, the solution was poured into water and extracted with DCM ($3 \times 100\text{ mL}$). The organic layer was dried over Na_2SO_4 and concentrated under reduced pressure. The residue was purified by flash column chromatography with 50% EA/Hexane to afford compound **1** as black solid (2.35 g).

5-(4-(diphenylamino)phenyl)pyridine-2,3-diamine (1): $R_f = 0.4$ (50% EA/Hexane). **Yield:** 84%. **Mp** = $219\text{--}222\text{ }^\circ\text{C}$. (Lit. Mp: $218\text{--}219\text{ }^\circ\text{C}$)²⁸³ **1H NMR (400 MHz, $CDCl_3$)** δ 7.89 (d, $J = 2.0\text{ Hz}$, 1H), 7.39 (d, $J = 8.4\text{ Hz}$, 2H), 7.30 (d, $J = 1.7\text{ Hz}$, 2H), 7.26 (s, 2H), 7.14 (dd, $J = 8.4, 2.3\text{ Hz}$, 7H), 7.05 (t, $J = 7.3\text{ Hz}$, 2H), 4.41 (s, 2H), 3.46 (s, 2H) ppm. **^{13}C NMR (101 MHz, $CDCl_3$):** δ 148.05, 147.67, 146.94, 136.03, 132.39, 129.29, 129.15, 128.95, 127.13, 124.34, 124.14, 122.90, 120.95. Analytical data match those previously reported.²⁸³

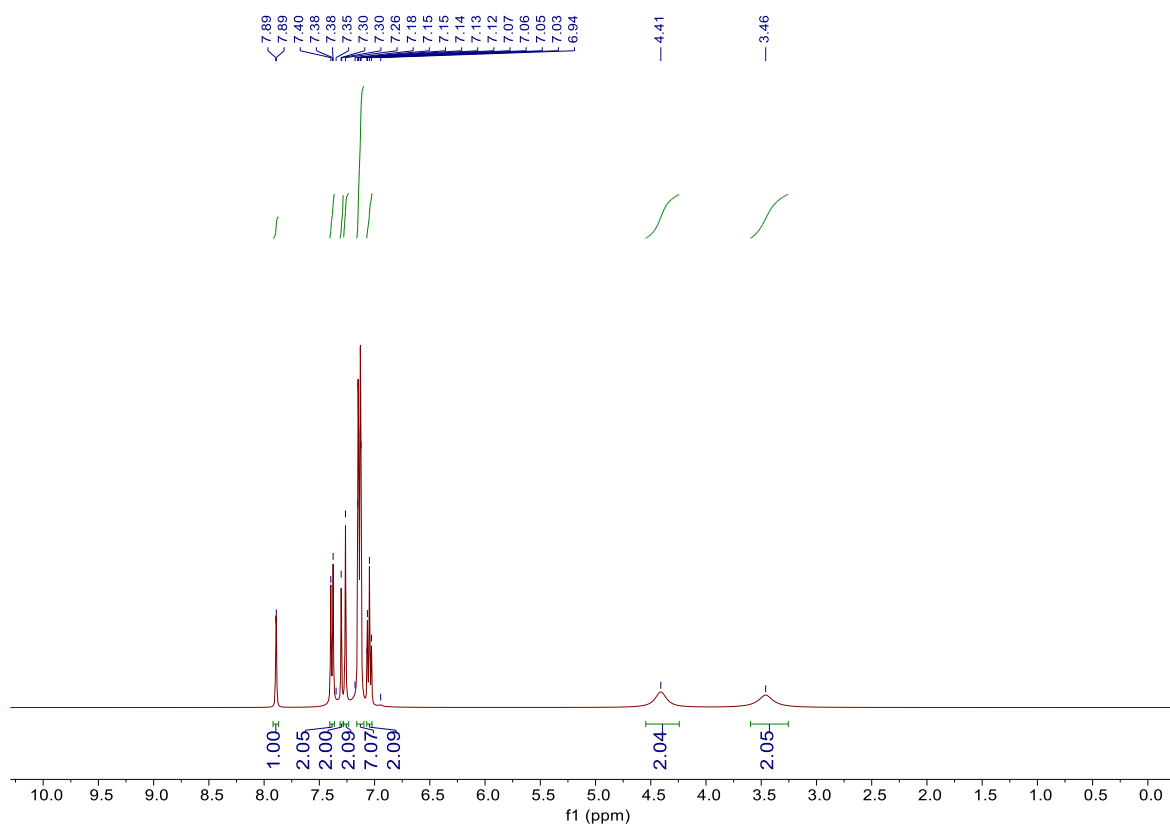


Figure 3.18. ^1H NMR spectra of **1** in CDCl_3 .

2208111343-2-19-cs339.11.fid
 TPAPyNH2 || 13C Observe with 1H decoupling - D1 = 2s

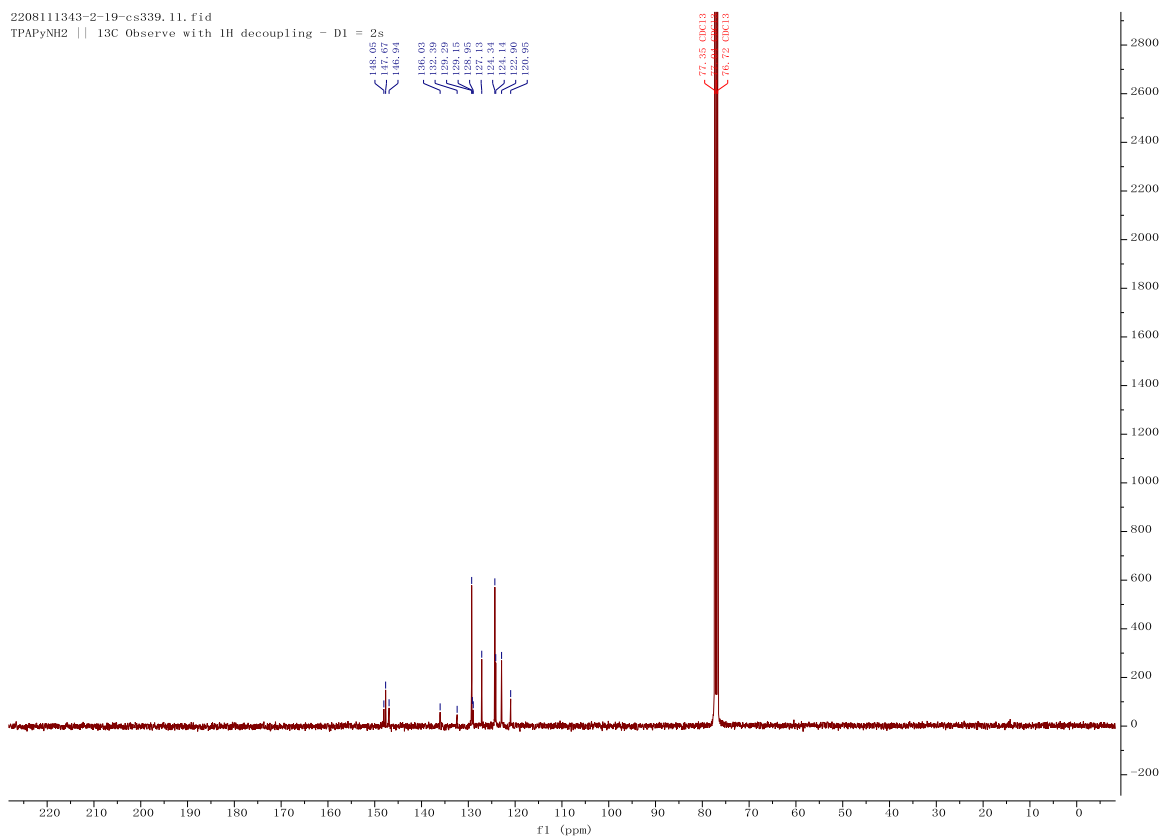
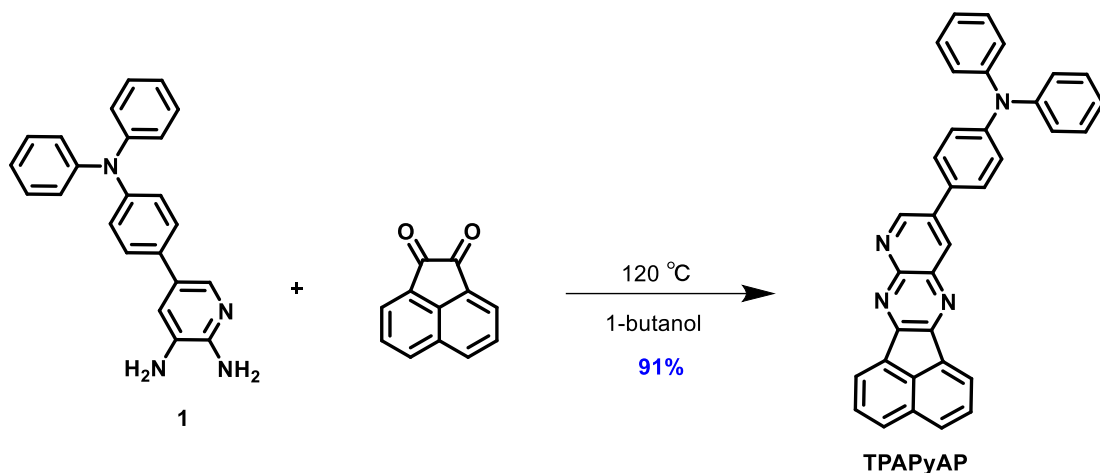


Figure 3.19. ^{13}C NMR spectra of **1** in CDCl_3 .

Synthesis of 4-(acenaphtho[1,2-b]pyrido[2,3-e]pyrazin-10-yl)-N,N-diphenylaniline (TPAPyAP):



1 (0.58 g, 1.65 mmol, 1.0 equiv.) and acenaphthylene-1,2-dione (0.3 g, 1.65 mmol, 1.0 equiv.) were added into 10 mL of 1-butanol and then heated at reflux for 12 hours under a nitrogen atmosphere. After cooling to room temperature, the solution was poured into water and extracted with DCM (3 × 50 mL). The organic layer was dried over Na₂SO₄ and concentrated under reduced pressure. The residue was purified by column chromatography with (dichloromethane/hexane = 1: 3, v/v) to afford the compound **TPAPyAP** as yellow solid (0.75 g).

4-(acenaphtho[1,2-b]pyrido[2,3-e]pyrazin-10-yl)-N,N-diphenylaniline (TPAPyAP): $R_f = 0.3$ (10% DCM/Hexane). **Yield:** 91%. **Mp** = 216-218 °C. **¹H NMR (400 MHz, DMSO-*d*₆)** δ 9.49 (d, $J = 2.5$ Hz, 1H), 8.85 (d, $J = 2.5$ Hz, 1H), 8.53 (dd, $J = 7.0, 0.7$ Hz, 1H), 8.46 (dd, $J = 7.0, 0.7$ Hz, 1H), 8.37 (dt, $J = 8.3, 0.8$ Hz, 2H), 8.04 – 7.96 (m, 4H), 7.44 – 7.36 (m, 4H), 7.18 – 7.07 (m, 8H). **¹³C NMR (101 MHz, DMSO)** δ 155.98, 154.92, 151.53, 149.31, 148.56, 147.14, 136.62, 136.52, 136.14, 133.59, 131.21, 130.92, 130.85, 130.25, 130.13, 129.70, 129.61, 129.08, 128.87, 125.38, 124.40, 123.32, 122.95, 122.66. **HR-MS [M+H]⁺ Calculated:** (C₃₅H₂₂N₄) 498.1844; **Found:** 498.1912. **Anal. Calcd. for C₃₅H₂₂N₄:** C, 84.31%; H, 4.45%; N, 11.24%. **Found:** C, 84.74%; H, 4.58%; N, 11.22%. **HPLC analysis:** 99.33% pure on HPLC analysis, retention time 6.0 minutes in 80% acetonitrile:20% water mix.

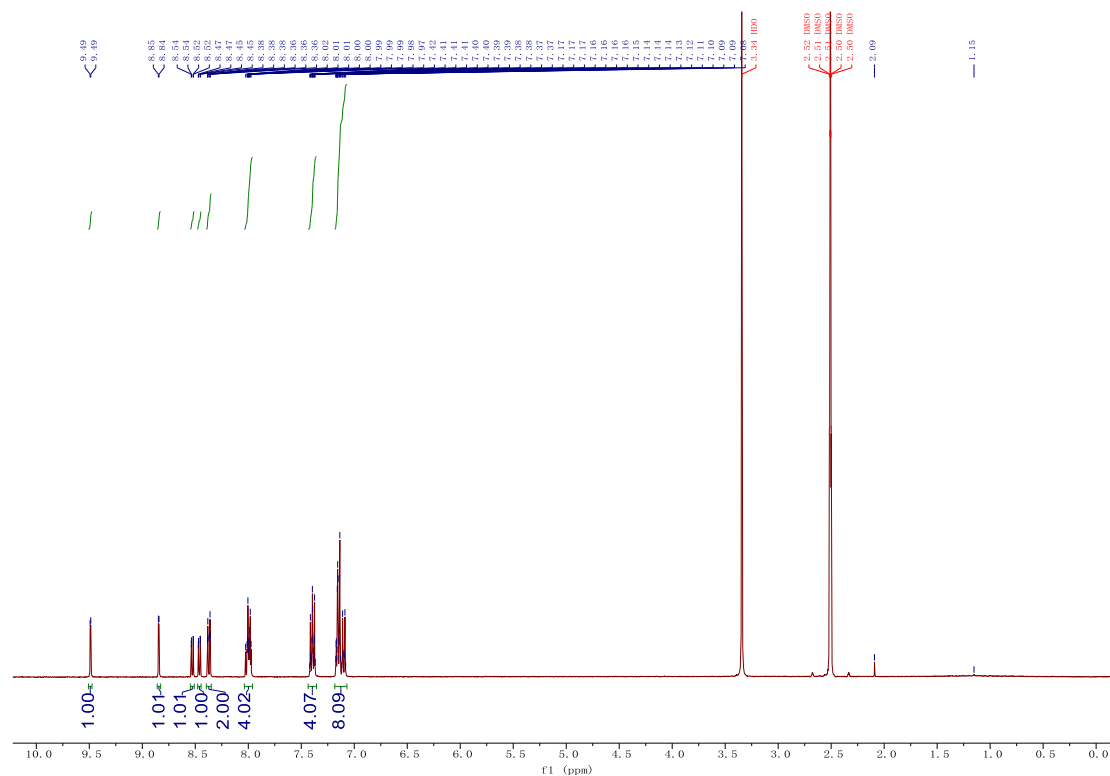


Figure 3.20. ¹H NMR spectra of TPAPyAP in DMSO-*d*₆

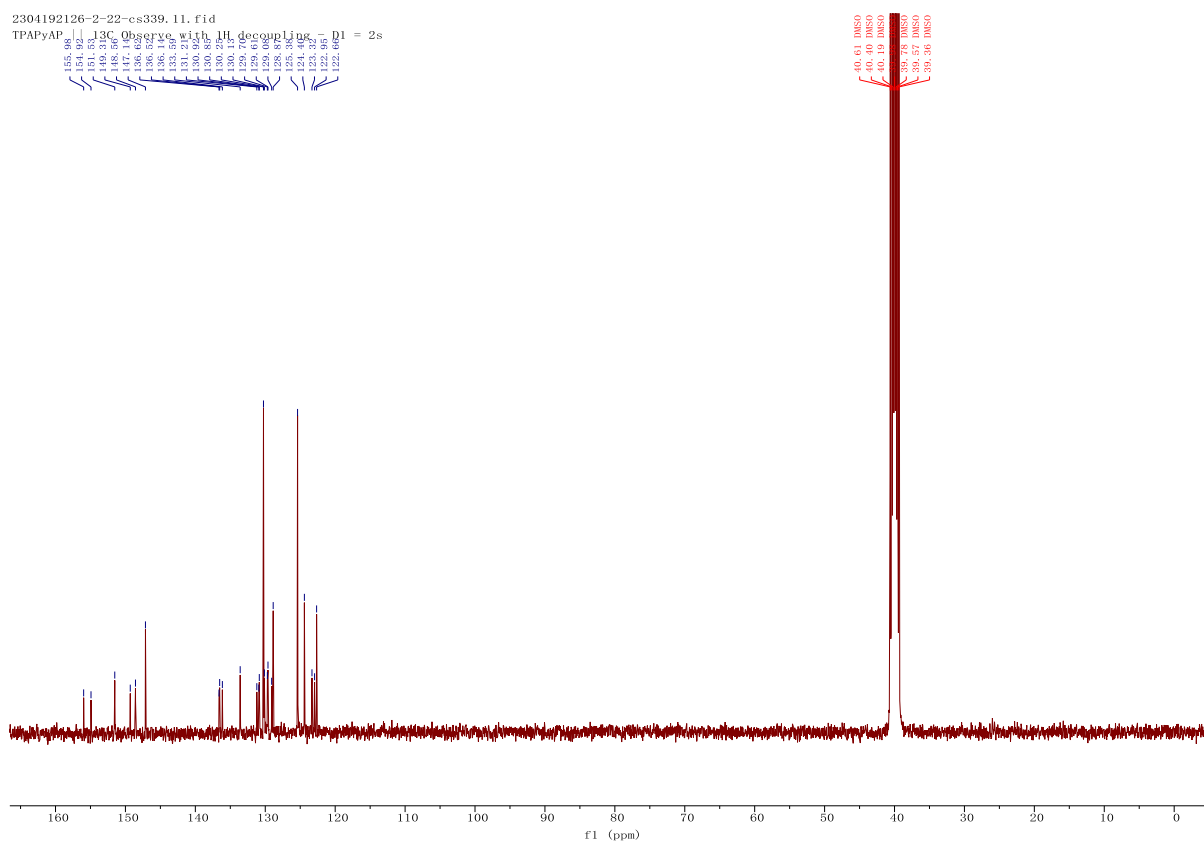


Figure 3.21. ¹³C NMR spectra of TPAPyAP in DMSO-*d*₆.

Display Report

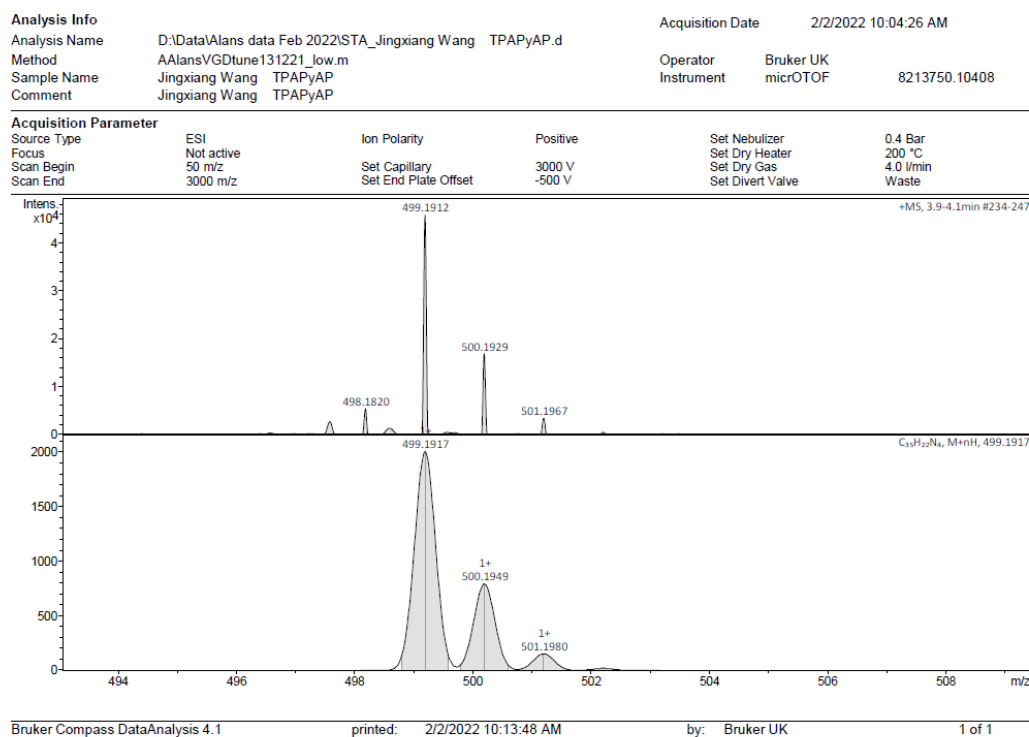


Figure 3.22. HRMS of TPAPyAP.

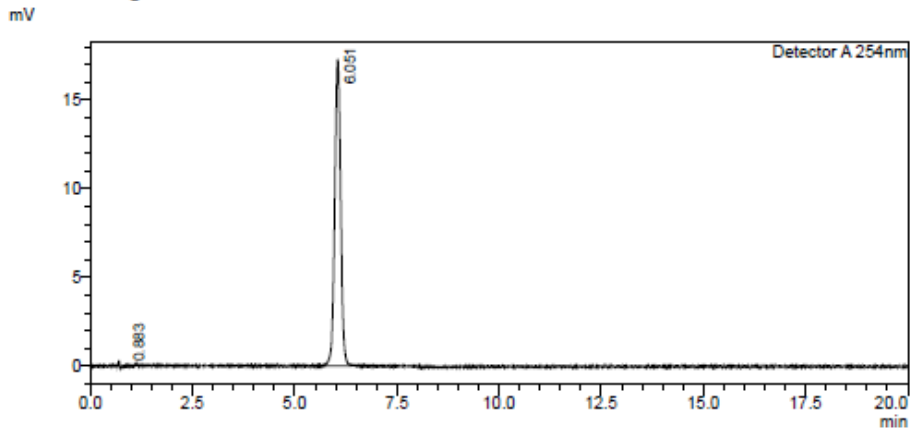
HPLC Trace Report 14 Sep 2021

<Sample Information>

Sample Name : TPAPyAP
 Sample ID :
 Method Filename : 80% Acetonitrile 20 Water 20 mins.lcm
 Batch Filename : TPAPyAP.lcb
 Vial # : 2-52
 Injection Volume : 5 uL
 Date Acquired : 13/09/2021 20:41:57
 Date Processed : 13/09/2021 21:02:00

Sample Type : Unknown
 Acquired by : System Administrator
 Processed by : System Administrator

<Chromatogram>

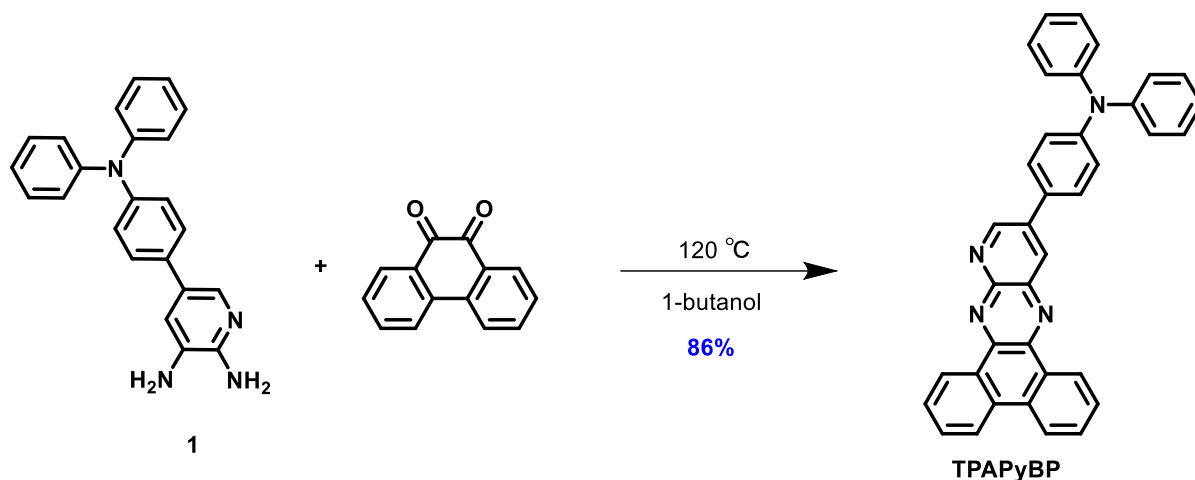


<Peak Table>

Detector A 254nm						
Peak#	Ret. Time	Area	Height	Area%	Area/Height	Width at 5% Height
1	0.883	1169	89	0.663	13.095	-
2	6.051	175182	17236	99.337	10.164	0.347
Total		176351	17326	100.000		

Figure 3.23. HPLC trace of TPAPyAP.

Synthesis of 4-(dibenzo[*f,h*]pyrido[2,3-*b*]quinoxalin-12-yl)-*N,N*-diphenylaniline (TPAPyBP):



Compound **TPAPyBP** was synthesized according to the same procedure as described above for the synthesis of **TPAPyAP**, except that phenanthrene-9,10-dione (0.34 g, 1.63 mmol, 1.0 equiv.) was used as the reactant instead of acenaphthylene-1,2-dione, yielding a red solid (Yield = 0.74 g).

4-(dibenzo[*f,h*]pyrido[2,3-*b*]quinoxalin-12-yl)-*N,N*-diphenylaniline (TPAPyBP): $R_f = 0.3$ (20% DCM/Hexane). **Yield:** 86%. **Mp** = 266-268 °C. **$^1\text{H NMR}$ (400 MHz, DMSO- d_6)** δ 9.72 (d, $J = 2.6$ Hz, 1H), 9.30 (td, $J = 7.7, 1.5$ Hz, 2H), 8.92 (d, $J = 2.5$ Hz, 1H), 8.85 (d, $J = 8.1$ Hz, 2H), 8.10 – 8.03 (m, 2H), 7.98 – 7.91 (m, 2H), 7.90 – 7.84 (m, 2H), 7.44 – 7.36 (m, 4H), 7.21 – 7.08 (m, 8H). **$^{13}\text{C NMR}$ (126 MHz, DMSO- d_6)** δ 154.67, 148.80, 148.69, 147.10, 143.63, 143.33, 137.60, 136.82, 132.39, 132.32, 132.20, 131.71, 131.64, 130.26, 129.77, 129.39, 129.06, 128.89, 128.82, 126.52, 126.29, 125.48, 124.50, 124.16, 122.53, 40.55, 40.38, 40.21, 40.05, 39.88, 39.71, 39.54. **HR-MS** $[\text{M}+\text{H}]^+$ **Calculated:** (C₃₇H₂₄N₄) 524.2001; **Found:** 524.2074. **Anal. Calcd. for C₃₇H₂₄N₄:** C, 84.71%; H, 4.61%; N, 10.68%. **Found:** C, 85.14%; H, 4.72%; N, 10.54%. **HPLC analysis:** 99.57% pure on HPLC analysis, retention time 15.0 minutes in 80% acetonitrile:20% water mix.

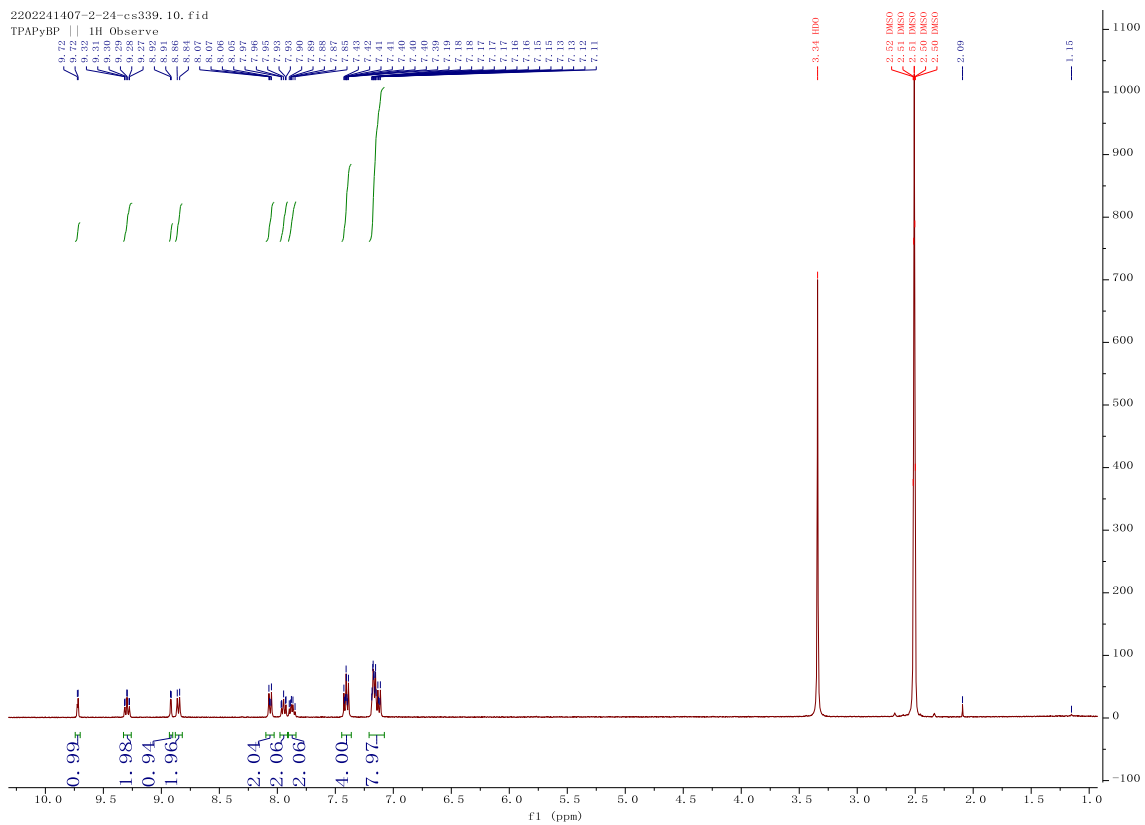


Figure 3.24. ^1H NMR spectra of TPAPyBP in $\text{DMSO-}d_6$

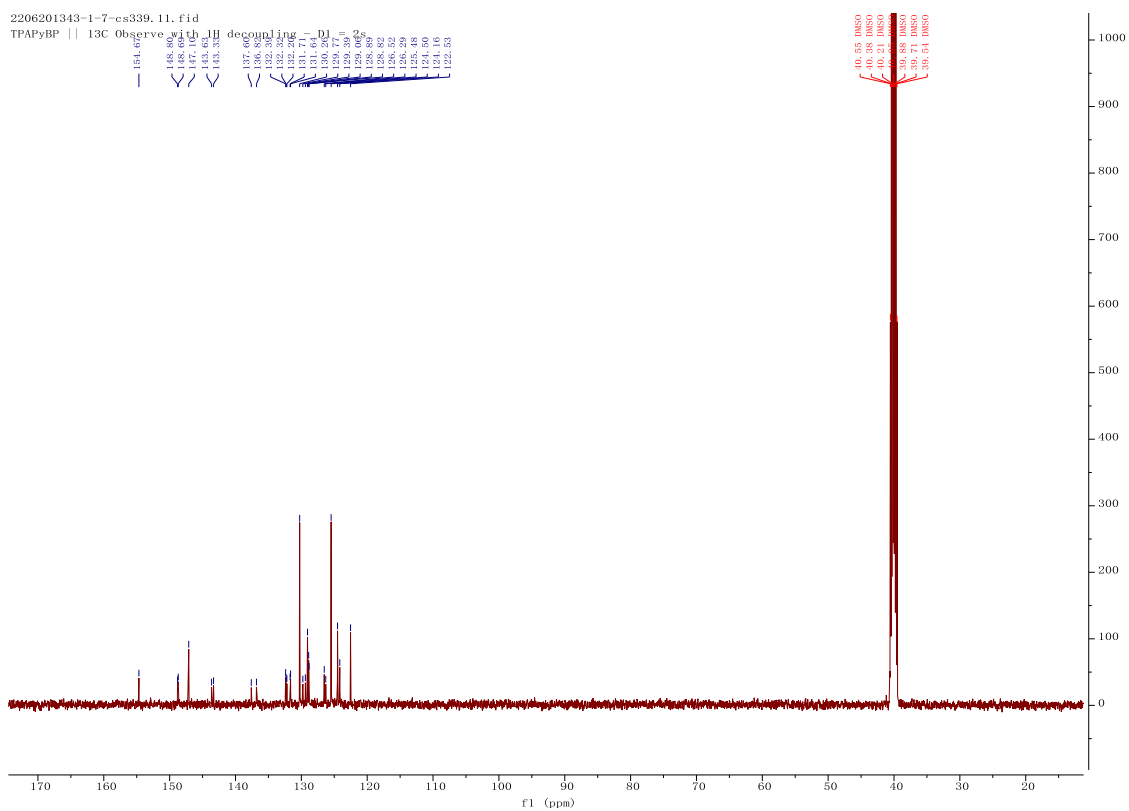


Figure 3.25. ^{13}C NMR spectra of TPAPyBP in $\text{DMSO-}d_6$

Display Report

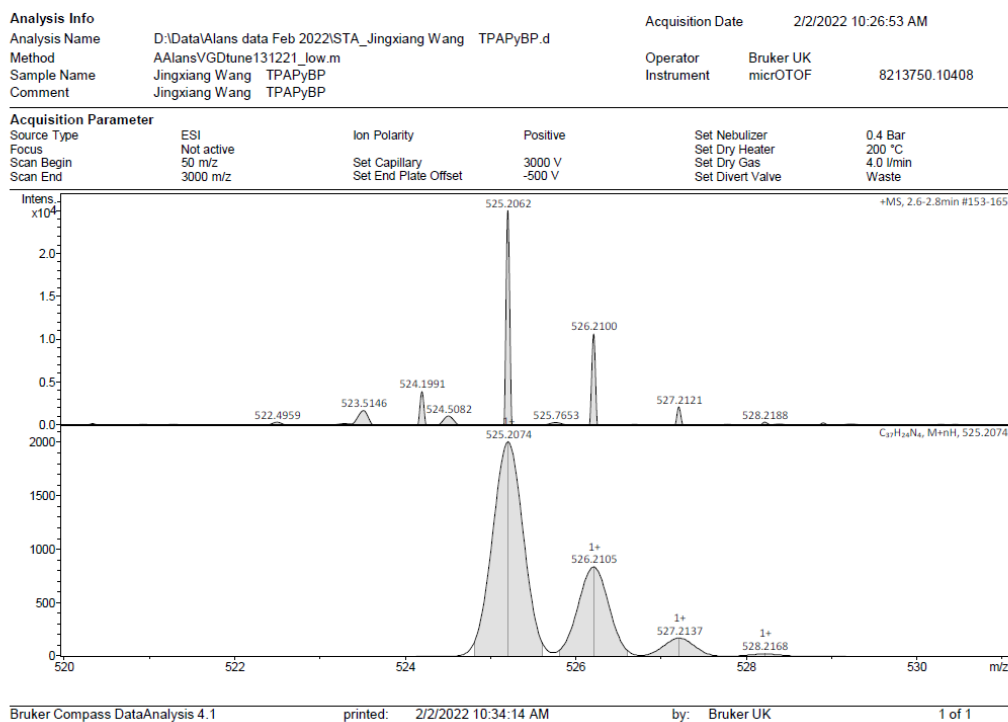


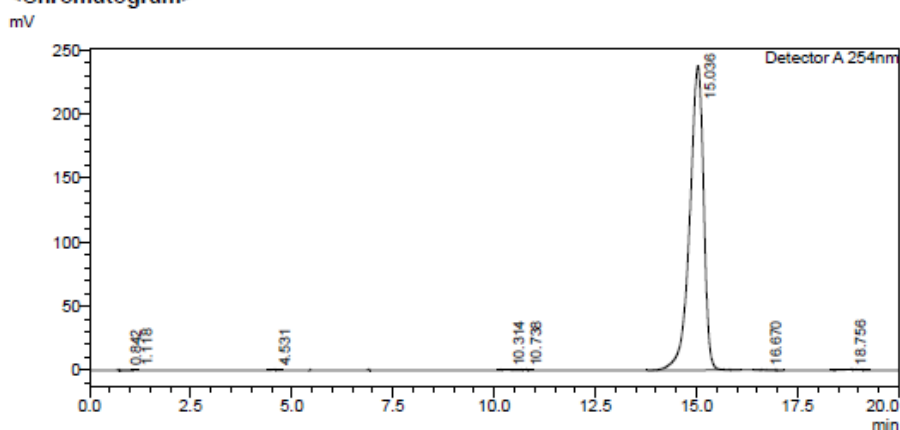
Figure 3.26. HRMS of TPAPyBP.

HPLC Trace Report14Sep2021

<Sample Information>

Sample Name : OSL-I91-090821
 Sample ID :
 Method Filename : 80% Acetonitrile 20 Water 20 mins.lcm
 Batch Filename : TPAPyBP.lcb
 Vial # : 2-52
 Injection Volume : 5 uL
 Date Acquired : 13/09/2021 21:37:24
 Date Processed : 13/09/2021 21:57:27
 Sample Type : Unknown
 Acquired by : System Administrator
 Processed by : System Administrator

<Chromatogram>



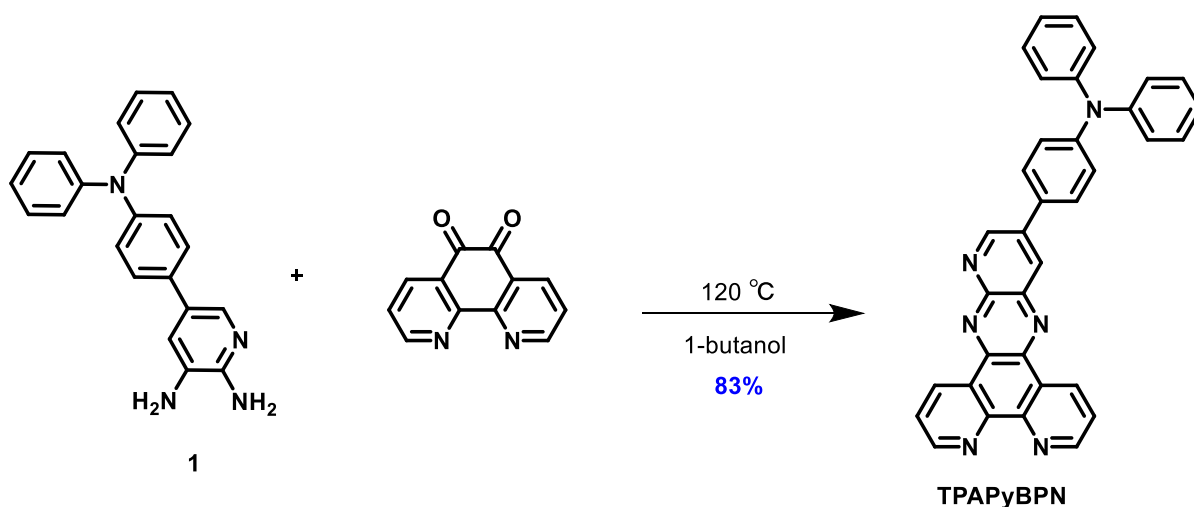
<Peak Table>

Detector A 254nm

Peak#	Ret. Time	Area	Height	Area%	Area/Height	Width at 5% Height
1	0.842	1276	85	0.022	15.079	-
2	1.118	1111	232	0.019	4.779	-
3	4.531	1269	151	0.022	8.382	0.272
4	10.314	2974	189	0.052	15.728	-
5	10.738	1697	114	0.030	14.908	-
6	15.036	5686875	237369	99.569	23.958	0.841
7	16.670	3645	180	0.064	20.305	0.557
8	18.756	12659	473	0.222	26.749	0.810
Total		5711506	238793	100.000		

Figure 3.27. HPLC trace of TPAPyBP.

Synthesis of *N,N*-diphenyl-4-(pyrido[2',3':5,6]pyrazino[2,3-*f*][1,10]phenanthrolin-12-yl)aniline (TPAPyBPN):



Compound **TPAPyBPN** was synthesized according to the same procedure as described above for the synthesis of **TPAPyAP**, except that 1,10-phenanthroline-5,6-dione (0.35 g, 1.65 mmol, 1.0 equiv.) was used as the reactant instead of acenaphthylene-1,2-dione, yielding a dark red solid (Yield = 0.72 g).

***N,N*-diphenyl-4-(pyrido[2',3':5,6]pyrazino[2,3-*f*][1,10]phenanthrolin-12-yl)aniline**

(TPAPyBPN): $R_f = 0.3$ (33% DCM/Hexane). **Yield:** 83%. **Mp** = 330-332 °C. **^1H NMR (500 MHz, DMSO- d_6)** δ 9.78 (s, 1H), 9.59 (s, 2H), 9.26 (s, 2H), 8.94 (s, 1H), 8.06 (d, $J = 8.5$ Hz, 4H), 7.41 (dd, $J = 8.5, 7.2$ Hz, 4H), 7.23 – 7.07 (m, 8H). **^{13}C NMR** measurement was not possible due to low solubility. **HR-MS (Xevo G2-S) [M+H] $^+$ Calculated:** (C₃₅H₂₂N₆) 526.1906; **Found:** 526.1960. **Anal. Calcd. for C₃₅H₂₂N₆:** C, 79.83%; H, 4.21%; N, 15.96%. **Found:** C, 78.40%; H, 4.55%; N, 15.69%. **HPLC analysis:** 99.39% pure, retention time: 6.73 minutes in 80% methanol:20% water.

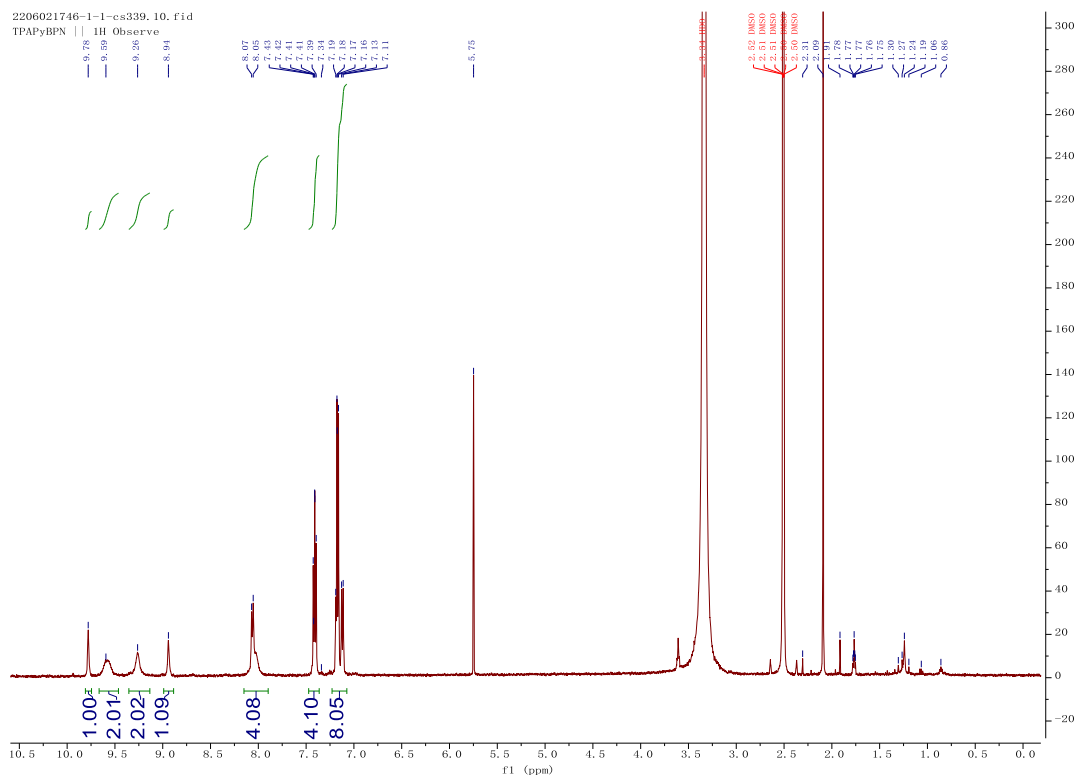


Figure 3.28. ^1H NMR spectra of TPAPyBPN in $\text{DMSO-}d_6$

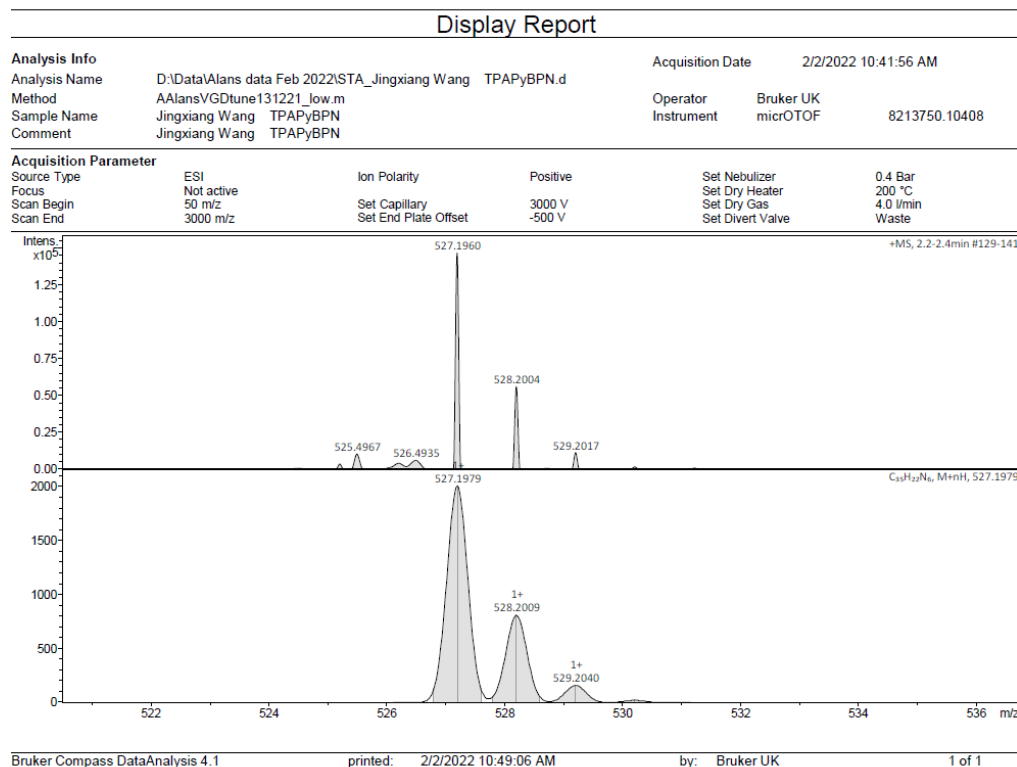


Figure 3.29. HRMS of TPAPyBPN.

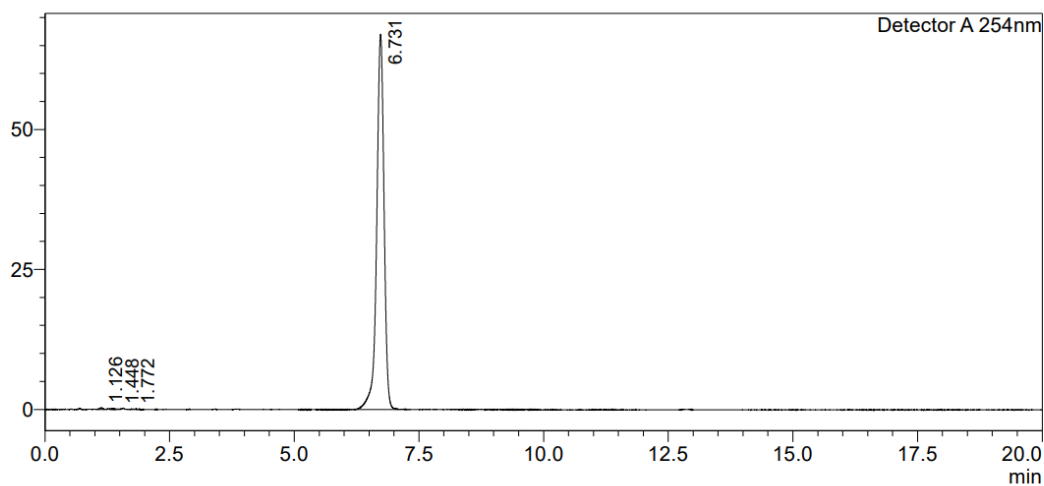
HPLC Trace Report 31 Mar 2023

<Sample Information>

Acquired by : System Administrator
Sample Name : TPAPyBPN
Sample ID :
Tray# : 1
Vial# : 2
Injection Volume : 5 uL
Data Filename : TPAPyBPN.lcd
Method Filename : 80% Methanol 20 Water 20 mins.lcm
Batch Filename : TPAPyBPN
Report Filename : DEFAULT.Isr
Date Acquired : 14/10/2021 19:01:37
Date Processed : 14/10/2021 19:21:38

<Chromatogram>

mV



<Peak Table>

Detector A 254nm

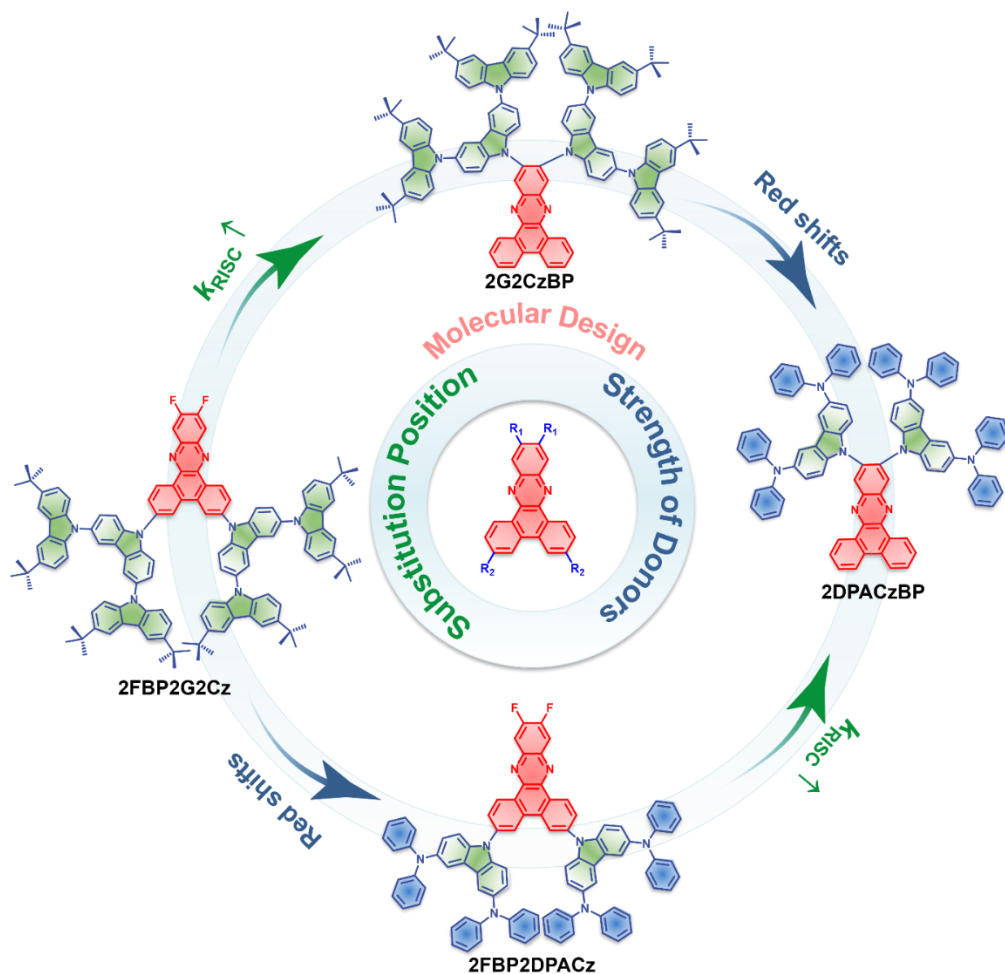
Peak#	Ret. Time	Area	Height	Area%	Area/Height	Width at 5% Height
1	1.126	1847	360	0.266	5.135	--
2	1.448	1285	118	0.185	10.915	--
3	1.772	1115	106	0.161	10.534	--
4	6.731	689580	66942	99.388	10.301	0.375
Total		693827	67525	100.000		

Figure 3.30. HPLC of TPAPyBPN.

Chapter 4: Rational Molecular Design of Efficient Yellow-Red Dendrimer

TADF for Solution Processed OLED: A Combined Effect of Substitution

Position and Strength of Donors



Manuscript of this project is under preparation as

Changfeng Si, Dianming Sun, David B. Cordes, Alexandra M. Z. Slawin, Eli Zysman-Colman*

Dr. Dianming Sun carried out the OLED device fabrication.

Dr. David B. Cordes and Prof. Alexandra M. Z. Slawin did X-ray crystallography.

I completed all the syntheses and characterization, DFT and TD-DFT calculations, electrochemistry, photophysics measurements and I am the principal author of the text.

4.1 Introduction

In **Chapters 2** and **3** we explored two families of orange to deep red small molecules by modifying the BP acceptor through the introduction of additional nitrogen atoms at different positions and also substituting these acceptors with a single donor, like DMAC or TPA at the 12-position of the acceptor. We then systematically investigated the effect of nitrogen number and nitrogen substitutions on the photophysical properties of the emitters. We finally demonstrated efficient vacuum-deposited red TADF OLEDs. In this Chapter, we will explore four new yellow to red TADF dendrimer emitters containing the same BP acceptor. These compounds were designed to be solution-processable. Here, we systematically investigated the effect of substitution position and the strength of the donors, namely 3,3''',6,6'''-tetrakis(*tert*-butyl-9''H-9,3'':6'',9'''-tercarbazole) (**G2Cz**) and N³,N³,N⁶,N⁶-tetraphenyl-9*H*-carbazole-3,6-diamine (**DPACz**), on the optoelectronic properties of these four dendrimers. Finally, we employed these emitters in solution-processed OLEDs (SP-OLEDs).

Although OLEDs have demonstrated their practical applications in displays and solid-state lighting,^{48,114,115,284–286} most OLEDs are fabricated using vacuum deposition technology that has high operating costs and a complicated multilayered device architecture. An alternative strategy would be to make the OLEDs using lower-cost solution-processing techniques such as spin coating or ink-jet printing, which shows great potential in enabling large-area applications.^{287,288} To achieve comparable performance metrics as vacuum-deposited devices, the key requirement for the SP-OLEDs is high-performance solution-processable emitter materials. Although small molecule TADF emitters have satisfied critical industry requirements for vacuum-deposition OLEDs, they tend to crystallize and lead to non-uniform solution-processed film, which can negatively impact the efficiency and longevity of the OLED. Different from small molecules, macromolecules such as dendrimers or polymers are perfect candidates for SP-OLEDs because of their superior film-forming ability, excellent thermal and morphological stability, and high affinity for substrates.^{101,102,289–291} Significant progress has been made in the development of green and blue solution-processable TADF materials, and their corresponding SP-OLEDs exhibit outstanding EQE_{max} of over 20%.^{101,102,292–296}

Despite this achievement, it remains a formidable challenge to develop efficient solution-processable red TADF emitters because of their high k_{nr} governed by the energy gap law.^{215–217} So far, there are only a few reports of relatively efficient red TADF emitters for SP-OLEDs (Figure 4.1). Zhang *et al.* reported an orange-red emitter **4t-BuCzTTR** by using thianthrene 5,5,10,10-tetraoxide as acceptor, *t*Cz as the donor and its SP-OLEDs exhibit an orange-red emission ($\lambda_{EL} = 592$ nm) with an EQE_{max} of 6.2%, which drop to around ~4.0% at 1000 cd m⁻²

(EQE₁₀₀₀).²⁹⁷ A deep red wedge-shaped organic fluorophore, **2TPA-PPDC**, was reported by Zhang *et al.*, whose SP-OLEDs show deep red emission ($\lambda_{\text{EL}} = 670$ nm) with an EQE_{max} of 3.2%.²⁹⁸ Zeng *et al.* reported a SP-OLED containing orange-red emitter **NAI_R3** that contains an extended donor moiety and using *tert*-butylbenzene groups to improve solubility, which emits at 622 nm and has an EQE_{max} of 22.5%, but the device shows quite large efficiency roll-off with an EQE₁₀₀₀ of 3.4%.²⁹⁹ Liu *et al.* developed a D–A–D type red TADF emitter **TAT-FDBPZ** by combining a triazatruxene (TAT) donor and a fluorine-substituted BP as the acceptor. The SP-OLED with **TAT-DBPZ** reached an EQE_{max} of 9.2% at $\lambda_{\text{EL}} = 611$ nm and showed low efficiency roll-off (EQE₁₀₀₀ = 7.4%). Using the same BP acceptor, Chen *et al.* developed a D-A type red emitter, **oDTBPZ-DPXZ** using two PXZs as donor moieties. SP-OLED based on **oDTBPZ-DPXZ** realized red emission at $\lambda_{\text{EL}} = 612$ nm, with EQE_{max} of 18.5%; however, efficiency roll-off was severe (EQE₁₀₀₀ = ~3.0%).¹⁴⁵ This survey of the state-of-the-art in red TADF SP-OLEDs reveals that BP can be used effectively in red emitter design due to its rigid, large π -conjugated system. However, the efficiency of SP-OLEDs using BP-based red emitters still lags behind vacuum-deposited red TADF OLEDs with emitters containing the BP moiety, especially at high luminance. In this Chapter, we address this issue by employing this rigid BP core as acceptor and strategically introducing two different donor dendrons, G2Cz and DPACz at different positions. Four novel orange-red TADF dendrimers, 11,12-bis(3,3",6,6"-tetra-*tert*-butyl-9'*H*-[9,3':6',9"-tercarbazol]-9'-yl)dibenzo[*a,c*]phenazine (**2GCzBP**), 9,9'-(dibenzo[*a,c*]phenazine-11,12-diyl)bis(N³,N³,N⁶,N⁶-tetraphenyl-9'*H*-carbazole-3,6-diamine) (**2DPACzBP**), 11,12-difluoro-3,6-bis(3,3",6,6"-tetra-*tert*-butyl-9'*H*-[9,3':6',9"-tercarbazol]-9'-yl)dibenzo[*a,c*]phenazine (**2FBP2G2Cz**) and 9,9'-(11,12-difluorodibenzo[*a,c*]phenazine-3,6-diyl) bis(N³,N³,N⁶,N⁶-tetraphenyl-9'*H*-carbazole-3,6-diamine) (**2FBP2DPACz**) were developed. We systematically investigated the effect of substitution position and strength of the donors on the optoelectronic properties of the emitters. The k_{RISC} values for **2GCzBP** and **2DPACzBP** are more than 10 times faster than those of **2FBP2G2Cz** and **2FBP2DPACz**. **2DPACzBP**, containing stronger donors, exhibits red shifted emission and smaller singlet–triplet energy splitting of 0.01 eV compared to **2GCzBP** with weak donors. The SP-OLED based on **2DPACzBP** exhibits a pure red emission peak, λ_{EL} at 640 nm, with an EQE_{max} of 7.8%. Surprisingly, the devices show an outstanding efficiency roll-off where the EQE remains high at 7.5% at a luminance of 1000 cd m⁻², which is among the best results in solution-processed red TADF OLEDs at such a high luminance. Furthermore, the efficiency for the devices with all four dendrimers was improved significantly by using 4CzIPN as an assistant dopant in hyperfluorescence (HF) devices, where the **2DPACzBP** HF device shows an EQE_{max}

of 20.0% at λ_{EL} of 605 nm and remains at 11.8% at a luminance of 1000 cd m⁻².

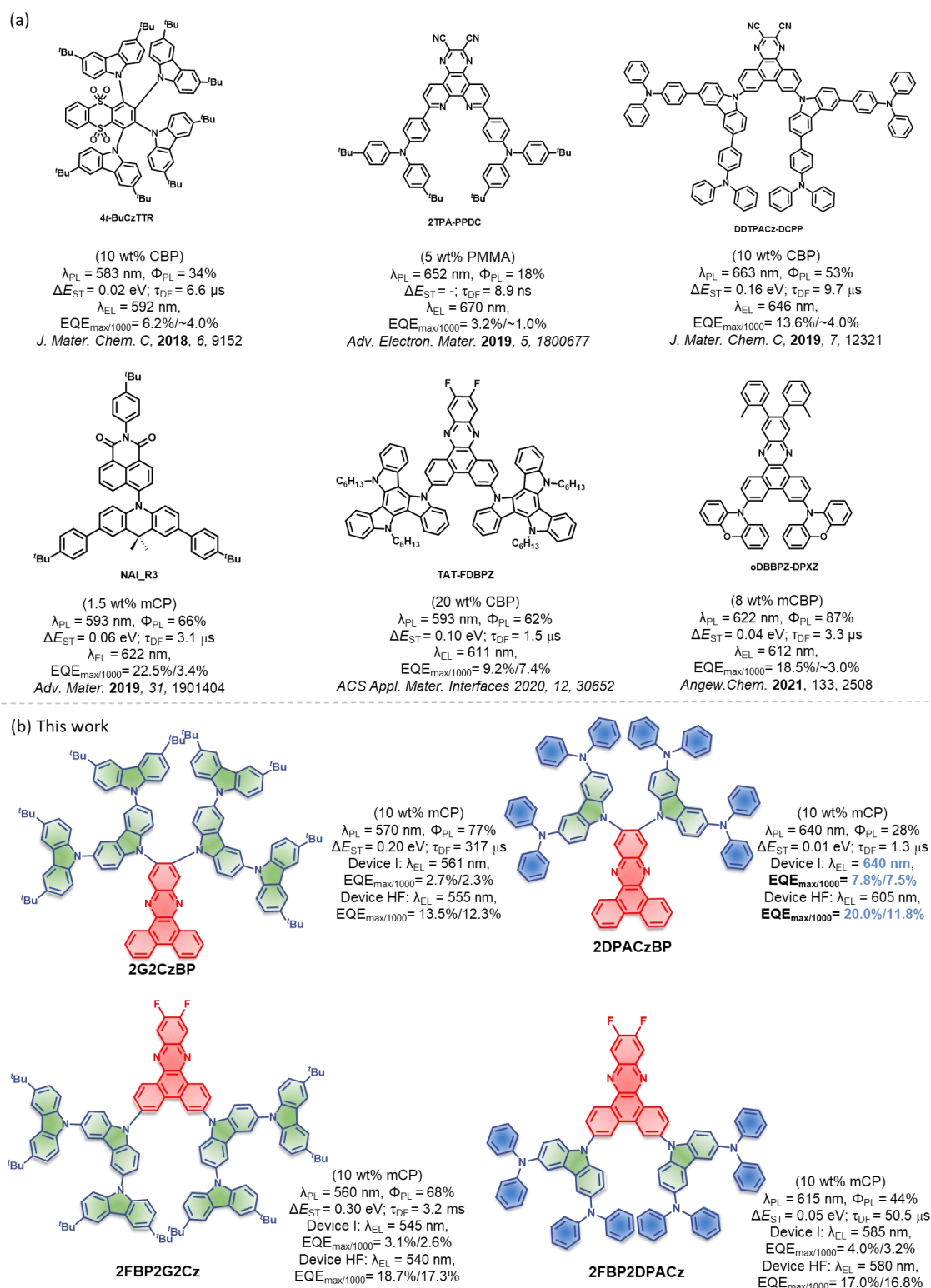
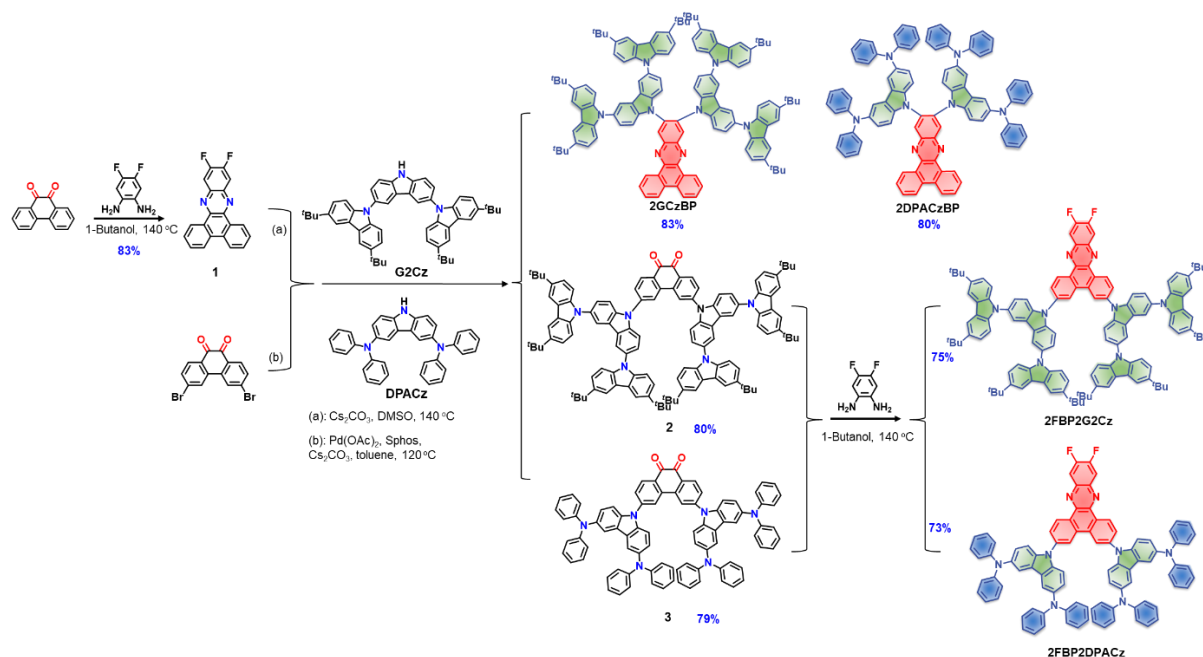


Figure 4.1. (a) Reported solution-processable red TADF emitter materials. (b) Structures of the dendrimers **2GCzBP**, **2DPACzBP**, **2FBP2GCz** and **2FBP2DPACz** reported in this study based on second-generation GCz, DPACz donor dendrons and dibenzo[*a,c*]phenazine (BP) acceptor.

4.2 Synthesis

The synthetic routes for **2GCzBP**, **2DPACzBP**, **2FBP2GCz** and **2FBP2DPACz** are shown in Scheme 4.1. Intermediate **1** was synthesized in 83% yield through the cyclization reaction of 4,5-difluorobenzene-1,2-diamine and phenanthrene-9,10-dione in 1-butanol. **2GCzBP** and **2DPACzBP** were synthesized with good yields (over 80%) through a nucleophilic aromatic substitution reaction between intermediate **1** and dendron G2Cz, DPACz, respectively. Intermediates **2** and **3** were obtained by coupling N-hexane-substituted G2Cz, DPACz and 3,6-dibromophenanthrene-9,10-dione in good yields of 80 and 79%, respectively. Then, the other two final products **2FBP2GCz** and **2FBP2DPACz** were obtained via the cyclization reaction of 4,5-difluorobenzene-1,2-diamine and intermediates **2** and **3**, respectively. The identity and purity of the three emitters were verified by ^1H NMR and ^{13}C NMR spectroscopy, melting point determination, HRMS, EA, single crystal XRD and HPLC.



Scheme 4.1. Synthetic Routes for **2GCzBP**, **2DPACzBP**, **2FBP2GCz** and **2FBP2DPACz**.

4.3 X-Ray Diffraction Analysis of 2DPACzBP

Single crystals of **2DPACzBP** were obtained by slow evaporation of a saturated toluene solution at room temperature. Single crystal analysis of **2DPACzBP** revealed a twisted D-A geometry, where the dihedral angles between the BP acceptor and two DPACz donor dendrons are 57.8° and 57.2° , respectively (Figure 4.2a). As shown in Figure 4.2b-c, there are no significant π - π interactions in the packing mode. Abundant $\text{CH}\cdots\pi$ interactions exist in the dimers (Figure 4.2b) with associated $\text{H}\cdots\pi$ of BP distances of 2.81 and 2.61 Å, which may

contribute to the suppression of non-radiative excitonic transitions. Neighboring molecules show weak $\pi \cdots \pi$ (BP \cdots adjacent BP distance of 3.38 Å) interactions.

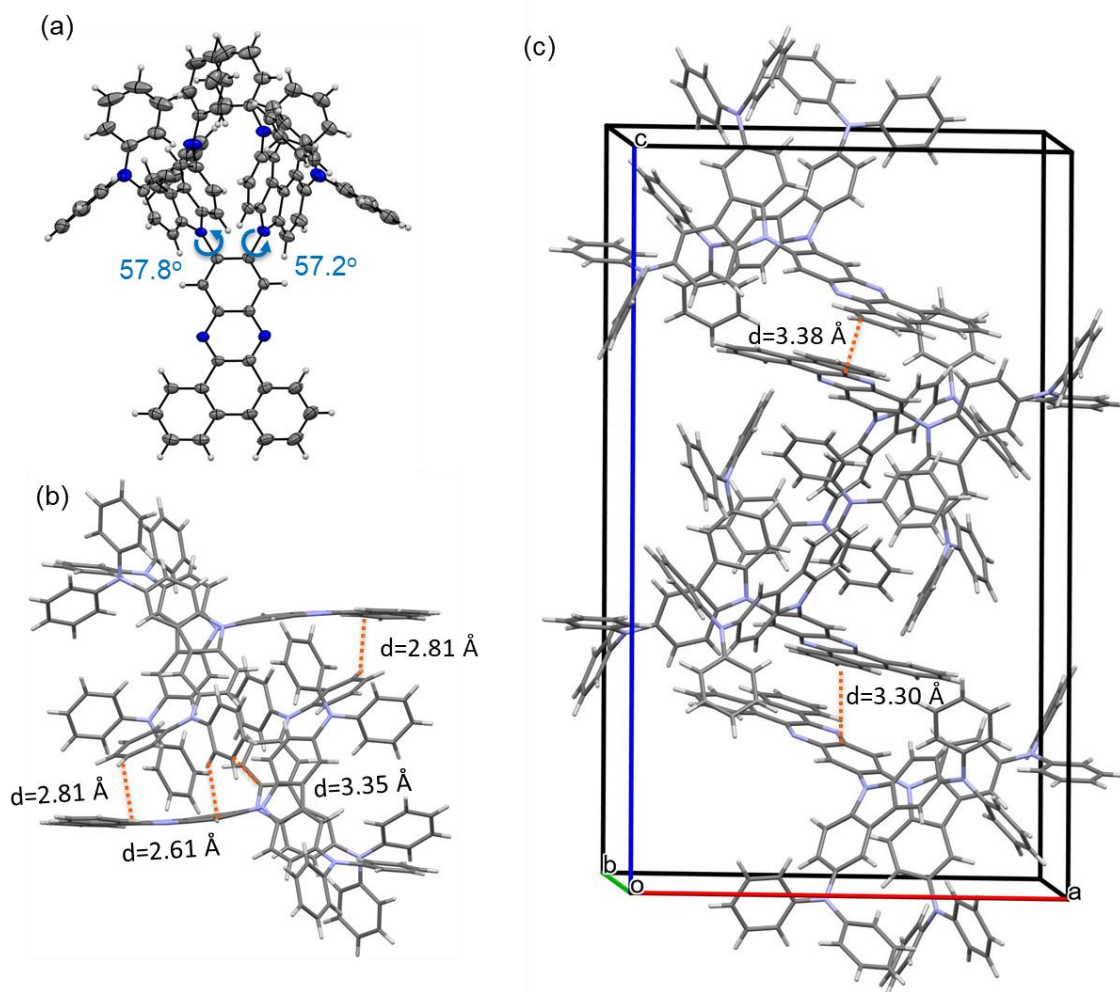


Figure 4.2. (a) Thermal ellipsoid plot of one independent molecule in the single crystal structure of **2DPACzBP**. Ellipsoids are drawn at the 50% probability level and solvent molecules have been omitted for clarity; (b) Views of the crystal dimer structure of **2DPACzBP** and (c) packing mode with interactions between adjacent molecules.

4.4 Theoretical Calculations

The S_0 geometries of **2GCzBP**, **2DPACzBP**, **2FBP2GCz** and **2FBP2DPACz** were optimized using DFT at the PBE0²⁶⁵/6-31G(d,p) level²⁶⁶ of theory in the gas phase starting from a geometry generated in Chem3D.³⁰⁰ At the optimized S_0 geometries, the dihedral angles between the donors at the 11 and 12 positions and the acceptor moiety in **2GCzBP** ($\sim 67^\circ$) and **2DPACzBP** ($\sim 58^\circ$) are much larger than those where the donors are at the 3 and 6 positions in **2FBP2GCz** ($\sim 43^\circ$) and **2FBP2DPACz** ($\sim 44^\circ$). This behavior results from larger steric hindrance between the donors in **2GCzBP** and **2DPACzBP** (Figure 4.3a). Furthermore,

2GCzBP exhibits a highly twisted geometry with a torsion angle between D and A of $\sim 67^\circ$, slightly higher than that ($\sim 58^\circ$) for **2DPACzBP**.

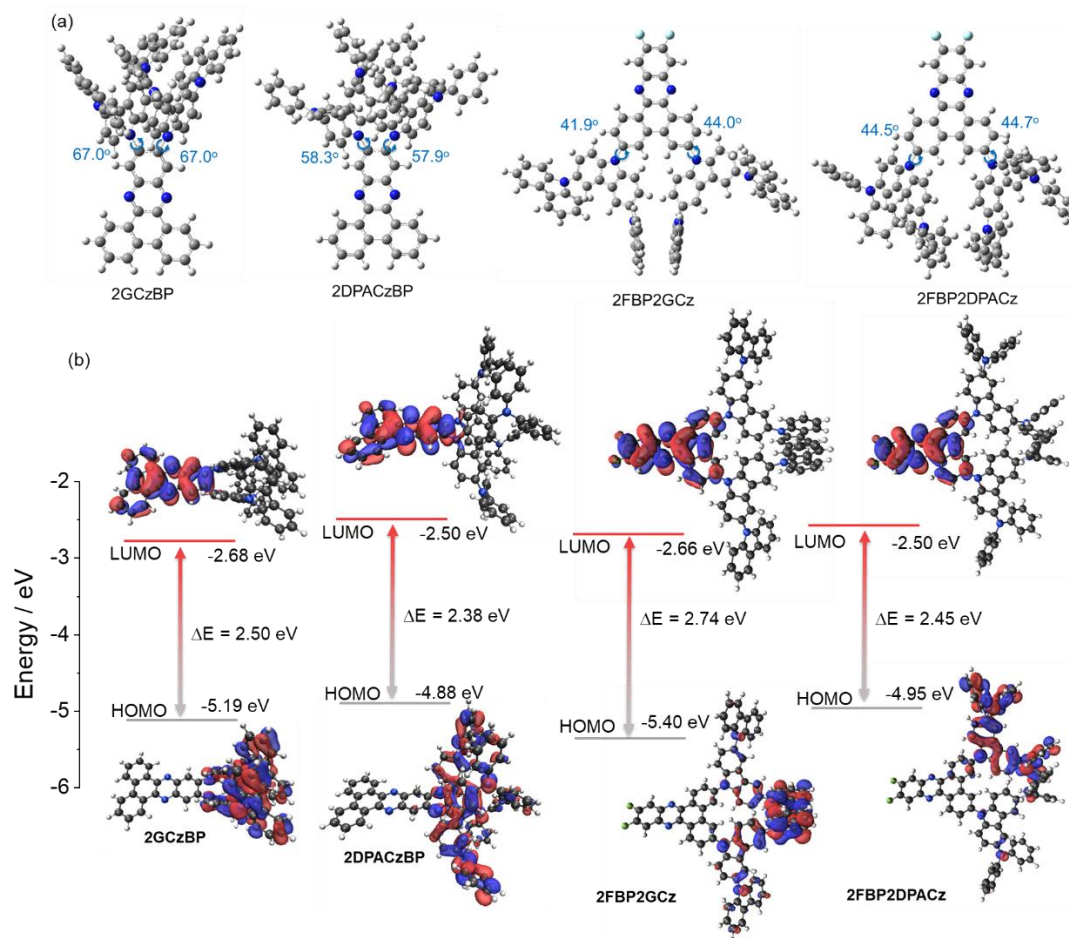


Figure 4.3. (a) DFT-optimized molecular geometries of ground state of **2GCzBP**, **2DPACzBP**, **2FBP2GCz** and **2FBP2DPACz**; (b) Frontier molecular orbitals (isovalue: 0.02) of **GCzBP**, **2DPACzBP**, **2FBP2GCz** and **2FBP2DPACz**.

The calculated energy levels of the HOMOs and LUMOs are shown in Figure 4.3b. The HOMOs are localized on the donors, while the LUMOs of all four compounds are localized on the BP acceptor group. As the donor strength increases from **2GCzBP** to **2DPACzBP** and from **2FBP2GCz** to **2FBP2DPACz**, the HOMOs are destabilized. As expected, the LUMOs are also destabilized with increasing donor strength from **2GCzBP** to **2DPACzBP**. When using the same donor, the HOMO of **2GCzBP** (-5.19 eV) is more destabilized compared to that of **2FBP2GCz** (-5.40 eV). This destabilization is attributed to the presence of two donors at adjacent positions exhibiting a cooperative effect, where their combined electronic influence is greater than the sum of their individual effects in **2FBP2GCz**. So, the overall electron-donating ability of **2DPACzBP** is amplified leading to a more destabilized HOMO. The HOMO-LUMO gap, $\Delta E_{\text{HOMO-LUMO}}$, thus decreases from 2.50 eV for **2GCzBP** to 2.38 eV for **2DPACzBP**, while

the $\Delta E_{\text{HOMO-LUMO}}$ decreases from 2.72 eV in **2FBP2GCz** to 2.50 eV in **2GCzBP**.

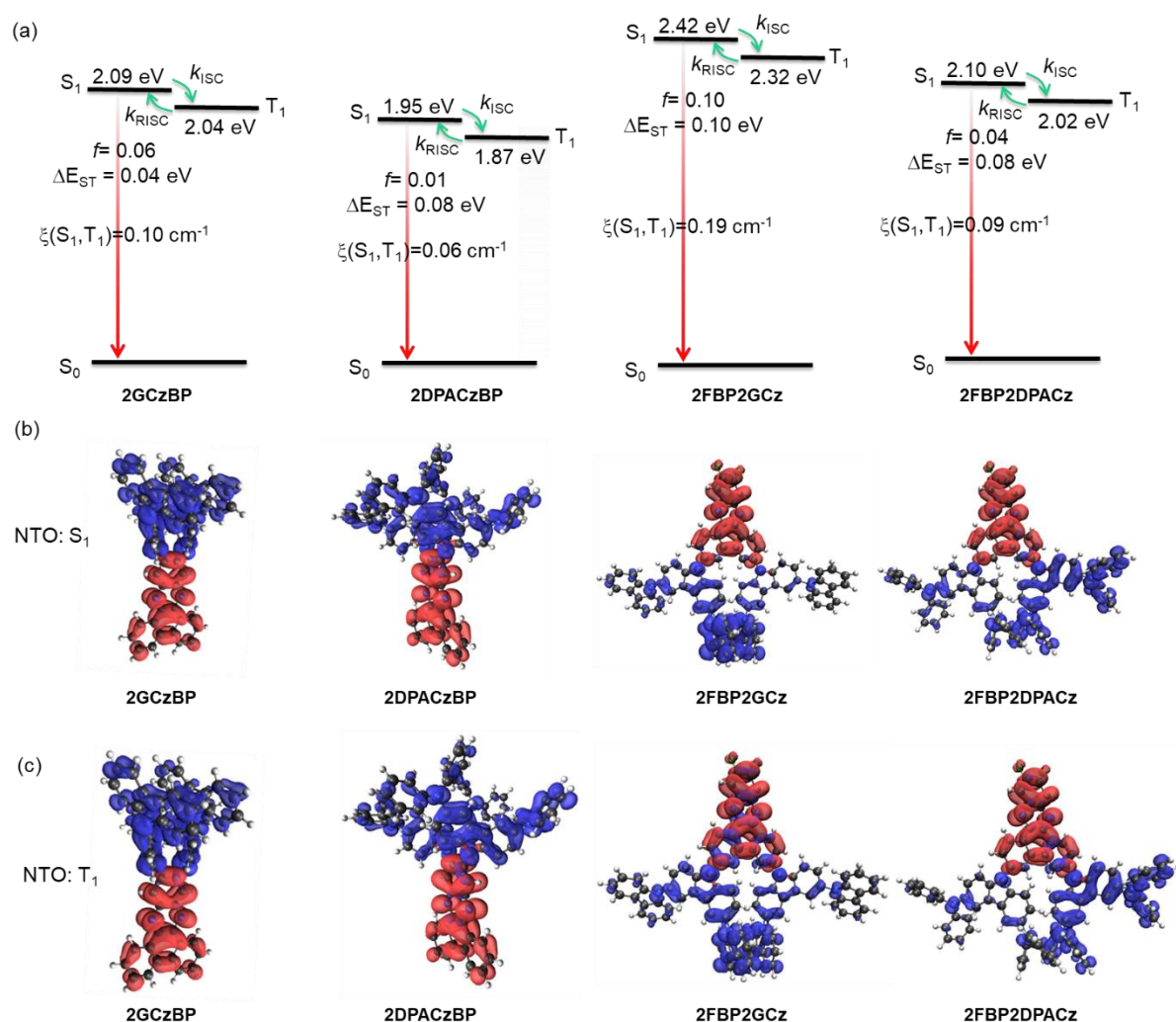


Figure 4.4. (a) vertical excitation energy levels of **2GCzBP**, **2DPACzBP**, **2FBP2GCz** and **2FBP2DPACz**; Natural transition orbitals (unoccupied (hole, blue) & occupied (electron, red), (isovalue: 0.02) of (b) S_1 and (c) T_1 for **2GCzBP**, **2DPACzBP**, **2FBP2GCz** and **2FBP2DPACz** calculated at the optimized S_0 geometry in the gas phase at the PBE0/6-31G(d,p) level.

The excited-state properties were calculated using TD-DFT within the TDA-DFT based on the optimized ground-state geometries (Figure 4.4a).^{222,267,268} The oscillator strength, f , for the S_0 to S_1 transition is 0.06, 0.01, 0.10 and 0.08 for **2GCzBP**, **2DPACzBP**, **2FBP2GCz** and **2FBP2DPACz**, respectively, reflecting a result of the relatively smaller torsions that exist between the position 3, 6 donors and the acceptor moieties. The S_1 energies are 2.09 eV for **2GCzBP**, 1.95 eV for **2DPACzBP**, 2.42 eV for **2FBP2GCz** and 2.10 eV for **2FBP2DPACz**, while the T_1 energies decrease from 2.04 eV, 1.87 eV, 2.32 eV and 2.02 eV, respectively, following a similar trend to that observed for $\Delta E_{\text{HOMO-LUMO}}$. All four compounds exhibit small ΔE_{ST} of less than 0.10 eV, suggesting that these compounds should emit via TADF. At the

relaxed S_1 geometry, there is a larger S_1 - T_1 SOC matrix element (0.19 cm^{-1}) in **2FBP2GCz** and (0.10 cm^{-1}) in **2GCzBP** than that in **2FBP2DPACz** (0.09 cm^{-1}) and **2DPACzBP** (0.06 cm^{-1}) (Figure 4.4a), indicating that the ISC will be faster in **2FBP2GCz** and **2GCzBP** than that in the latter two compounds. NTO analyses at the S_0 geometry (Figure 4.4b) demonstrated that the low-lying excited states in all compounds show an obvious ICT character. Holes and electrons are well separated in the donor segments and acceptor cores, respectively. There is somewhat less separation in the T_1 for **2FBP2GCz** and **2FBP2DPACz**, so the state can better be described as a mixture LE and CT character (Figure 4.4c).

4.5 Electrochemistry

The energies of the FMOs of **2GCzBP**, **2DPACzBP**, **2FBP2GCz** and **2FBP2DPACz** were inferred from the electrochemical behavior by CV and DPV in degassed DCM with tetra-*n*-butylammonium hexafluorophosphate ($^n[\text{Bu}_4\text{N}]\text{PF}_6$) as the supporting electrolyte, as shown in Figure 4.5. The reduction potential (E_{red}), determined from the DPV peak values, are -1.24 V (**2GCzBP**), -1.38 V (**2DPACzBP**), -1.28 V (**2FBP2GCz**) and -1.35 V (**2FBP2DPACz**) reflecting the expected cathodic shift with the increase in donor strength. The LUMO energies are -3.11 eV , -3.07 eV , -3.08 eV and -3.02 eV for **2GCzBP**, **2DPACzBP**, **2FBP2GCz** and **2FBP2DPACz**, respectively, and align with the trend found for the DFT calculations. **2GCzBP** and **2FBP2GCz** both have two resolvable quasi-reversible oxidation waves, with similar first oxidation potentials at E_{ox} of 1.03 V , and second oxidation potentials at 1.13 V , which correspond to the oxidation of the inner carbazole and the peripheral *tert*-butylcarbazole, respectively.^{102,301} A similar trend is observed for **2DPACzBP** ($E_{\text{ox}} = 0.66 \text{ V}$) and **2FBP2DPACz** ($E_{\text{ox}} = 0.65 \text{ V}$). The HOMO levels of **2GCzBP**, **2DPACzBP**, **2FBP2GCz** and **2FBP2DPACz** are -5.38 , -5.01 , -5.37 and -5.02 eV , respectively. The electrochemical data indicate that compounds with the same donors have effectively the same E_{ox} . However, this behavior is not reproduced in the DFT calculations where the calculated HOMO of **2FBP2GCz** (-5.40 eV) is more stabilized than that of **2GCzBP** (-5.19 eV), implying that there is a cooperative effect amongst the two donors in the later, an interaction that is not reproduced in the electrochemical measurements. The corresponding HOMO–LUMO gaps are 2.27 , 2.04 , 2.30 and 2.00 eV for **2GCzBP**, **2DPACzBP**, **2FBP2GCz** and **2FBP2DPACz**, respectively, which mirror the trend in the DFT calculated values of 2.50 , 2.38 , 2.74 , 2.45 eV . (Figure 4.3b).

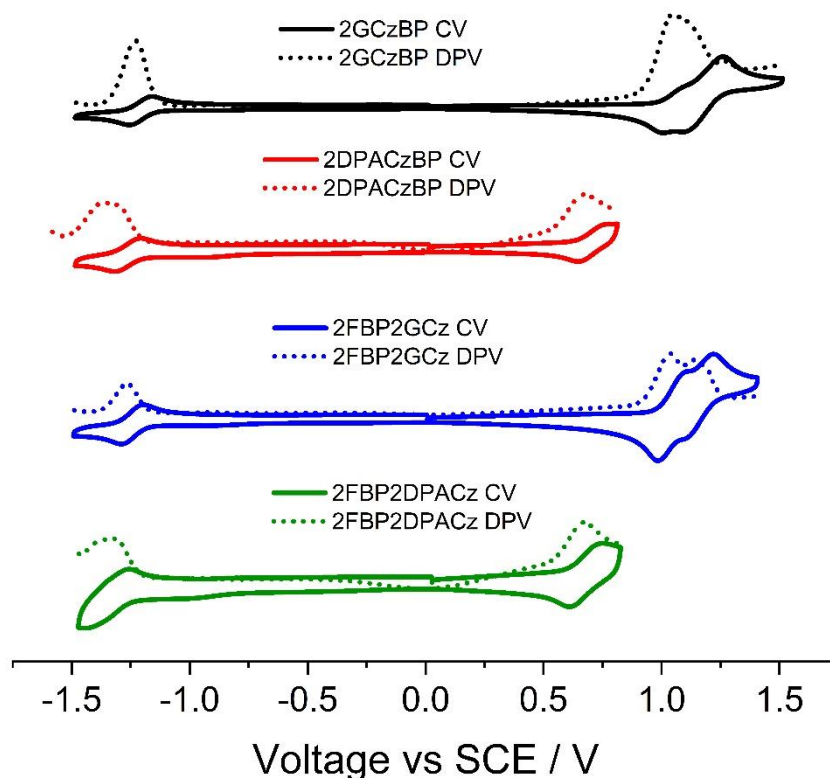


Figure 4.5. Cyclic and differential pulse voltammograms (CV and DPV) measured in degassed DCM with 0.1 M $[\text{nBu}_4\text{N}]\text{PF}_6$ as the supporting electrolyte and Fc/Fc^+ as the internal reference (0.46 V vs SCE).²²⁴ Scan rate = 100 mV s^{-1} .

4.6 Photophysics in Solution

The UV-Vis absorption spectra of the four emitters in dilute toluene are shown in Figure 4.6a, and the photophysical properties are summarized in Table 4.1. All four compounds exhibit strong absorption bands at below 400 nm [**2GCzBP** (346 nm, $\epsilon=5.7\times 10^4 \text{ M}^{-1} \text{ cm}^{-1}$), **2DPACzBP** (353 nm, $\epsilon=3.3\times 10^4 \text{ M}^{-1} \text{ cm}^{-1}$), **2FBP2GCz** (348 nm, $\epsilon=4.7\times 10^4 \text{ M}^{-1} \text{ cm}^{-1}$) and **2FBP2DPACz** (354 nm, $\epsilon=4.1\times 10^4 \text{ M}^{-1} \text{ cm}^{-1}$], which are attributed to LE $\pi-\pi^*$ transitions of both the donors and acceptor moieties based on a comparison with literature data of BP and GCz.^{101,102,145} Weak and broad absorption bands are observed at 460 nm ($\epsilon=1.6\times 10^4 \text{ M}^{-1} \text{ cm}^{-1}$) for **2GCzBP**, 506 nm ($\epsilon=0.7\times 10^4 \text{ M}^{-1} \text{ cm}^{-1}$) for **2DPACzBP**, 436 nm ($\epsilon=1.4\times 10^4 \text{ M}^{-1} \text{ cm}^{-1}$) for **2FBP2GCz** and 464 nm ($\epsilon=1.1\times 10^4 \text{ M}^{-1} \text{ cm}^{-1}$) for **2FBP2DPACz**, which are assigned to ICT transitions from the donor units to the acceptor core, assignments that are corroborated by the relative oscillator strengths ($f = 0.04, 0.01, 0.10$ and 0.04 for **2GCzBP**, **2DPACzBP**, **2FBP2GCz** and **2FBP2DPACz**, respectively) calculated by the TD-DFT (Figure 4.6b). There is the expected

shift to lower energies of the ICT band aligned with increasing donor strength (from **2GCzBP** to **2DPACzBP**) and donor substitution position from position 3, 6 to position 11, 12 (**2FBP2GCz** to **2GCzBP**). All compounds exhibit unstructured and broad PL spectra in toluene (Figure 4.6c), indicative of an excited state with strong ICT character, with peak maxima, λ_{PL} , at 585 nm, 690 nm, 565 nm and 675 nm for **2GCzBP**, **2DPACzBP**, **2FBP2GCz** and **2FBP2DPACz**, respectively. Positive solvatochromism is observed for all compounds (Figure 2.c), which is consistent with the ICT nature of the emissive excited state. The optical bandgaps, E_g , calculated from the normalized absorption and emission spectra intersection point, are 2.38 eV, 2.09 eV, 2.54 eV, and 2.21 eV for **2GCzBP**, **2DPACzBP**, **2FBP2GCz** and **2FBP2DPACz**, respectively (Figure 4.6d). The corresponding Φ_{PL} values in degassed toluene solution are 59%, 6%, 47% and 9%, respectively, for **2GCzBP**, **2DPACzBP**, **2FBP2GCz** and **2FBP2DPACz**. When exposed to oxygen, these values significantly decrease to 38% and 27% for **2GCzBP** and **2FBP2GCz**, respectively, and slightly decrease to 5%, and 5% for **2DPACzBP** and **2FBP2DPACz**. The prompt fluorescence and phosphorescence spectra of all compounds in 2-MeTHF at 77 K were measured to determine the S_1 and T_1 energies from their respective onsets (Figure 4.6e). The S_1 energies of **2GCzBP**, **2DPACzBP**, **2FBP2GCz** and **2FBP2DPACz** are 2.45 eV, 2.12 eV, 2.56 eV, and 2.34 eV, and the T_1 energies are 2.25 eV, 2.12 eV, 2.33 eV and 2.33 eV, respectively. The phosphorescence spectra of **2GCzBP** and **2FBP2GCz** are structured, and each is assigned from TDDFT calculations as a mixed locally excited triplet (^3LE) state of the acceptor (**BP-F**) and charge-transfer (^3CT) state (Figure 4.4c). The ΔE_{ST} of **2GCzBP**, **2DPACzBP**, **2FBP2GCz** and **2FBP2DPACz** are 0.20 eV, 0.00 eV, 0.23 eV and 0.01 eV, respectively, which are similar to the trend of the calculated values, where **2FBP2GCz** has the largest calculated ΔE_{ST} of 0.10 eV compared to **2GCzBP** (0.04 eV), **2DPACzBP** (0.08 eV) and **2FBP2DPACz** (0.04 eV) as shown in Figure 4.4a.

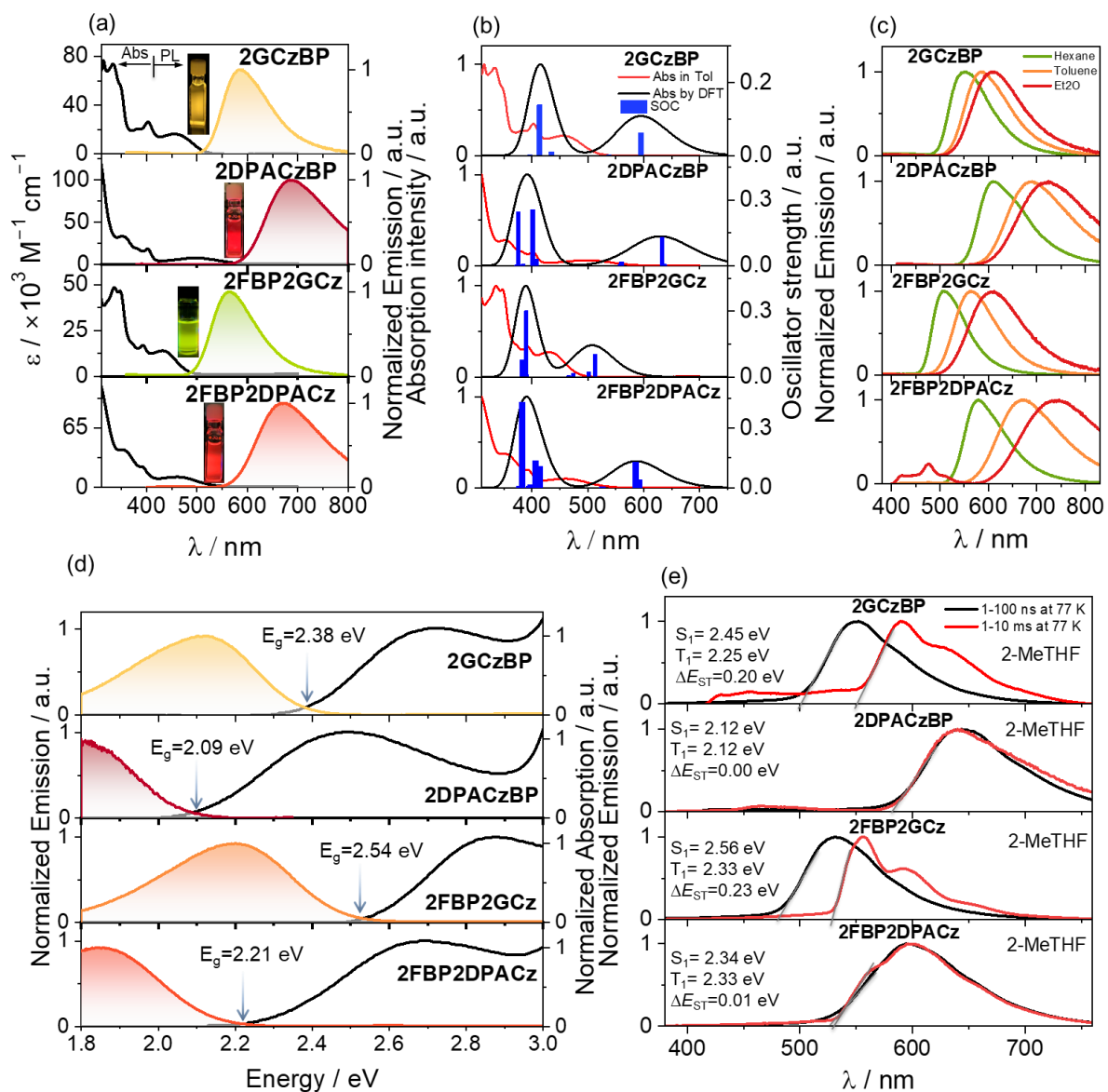


Figure 4.6. (a) UV-vis absorption (in toluene) and steady-state photoluminescence (PL) spectra; (b) TDA-DFT simulation and experimental UV-Vis absorption spectra; (c) PL solvatochromism study of **2GCzBP**, **2DPACzBP**, **2FBP2GCz** and **2FBP2DPACz** recorded at room temperature ($\lambda_{\text{exc}} = 340 \text{ nm}$); (d) The optical bandgaps were determined from the intersection point of the normalized absorption and emission spectra for all compounds; (e) Prompt fluorescence (1-100 ns) and phosphorescence spectra (1-10 ms) in 2-MeTHF at 77 K of **2GCzBP**, **2DPACzBP**, **2FBP2GCz** and **2FBP2DPACz** ($\lambda_{\text{exc}} = 343 \text{ nm}$).

The PL decays of all molecules in toluene under degassed conditions were measured using a combination of TCSPC/MCS techniques (Figure 4.7). The ICT bands of **2GCzBP**, **2DPACzBP**, **2FBP2GCz** and **2FBP2DPACz** all decay with biexponential kinetics, with prompt fluorescence lifetimes, τ_p , of 22.2 ns, 4.2 ns, 14.2 ns and 3.2 ns, and delayed fluorescence lifetimes, τ_d , of 79.1 μs , 0.24 μs , 102.6 μs and 0.25 μs , respectively. The delayed

components of **2GCzBP** and **2FBP2GCz** are much longer-lived and were totally quenched by oxygen, due to the larger ΔE_{ST} in these two compounds. The corresponding PL intensity of toluene solutions was enhanced upon the oxygen removal for all four compounds (Figure 4.7e-f), demonstrating that oxygen could quench triplet states.

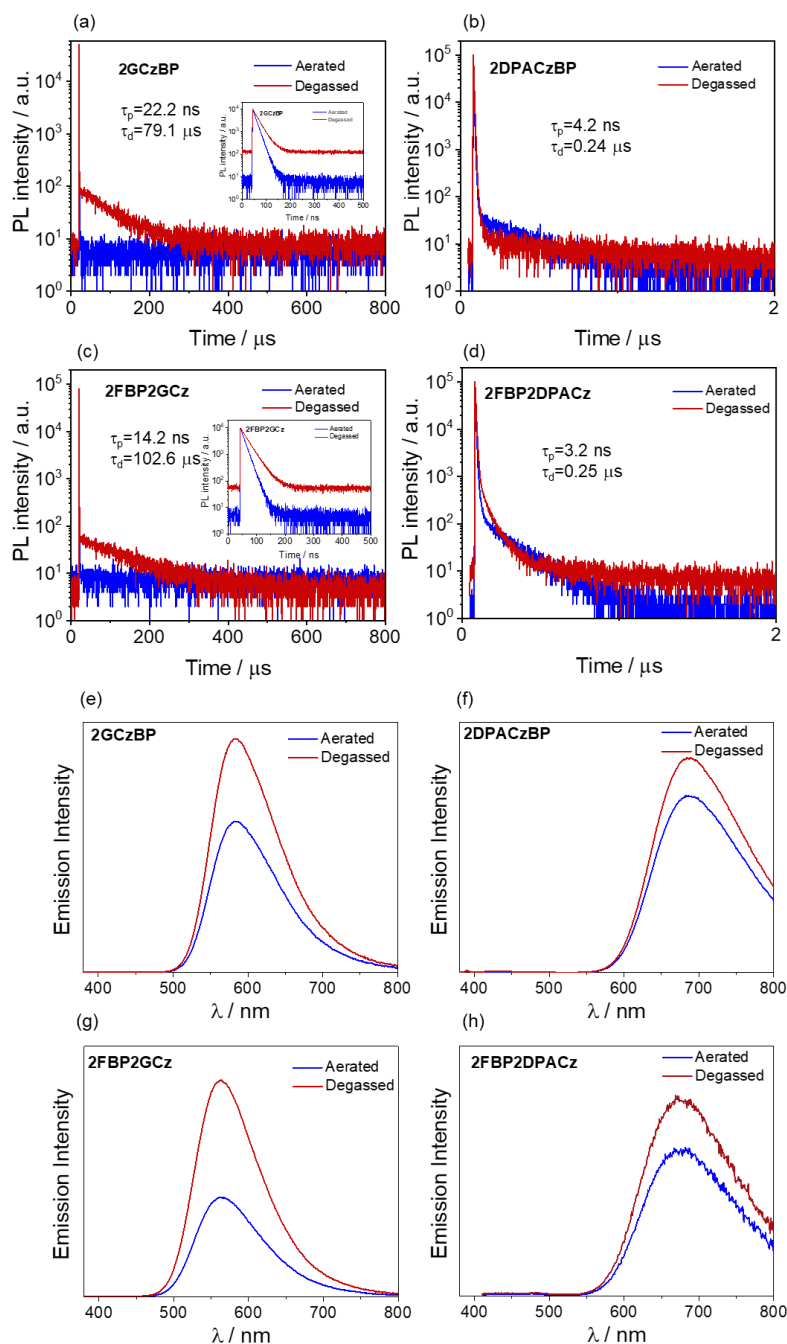


Figure 4.7. Time-resolved PL decay of (a) **2GCzBP**, (b) **2DPACzBP**, (c) **2FBP2GCz** and (d) **2FBP2DPACz** in degassed and aerated toluene ($\lambda_{exc} = 379$ nm) and Steady-state PL spectra of (e) **2GCzBP**, (f) **2DPACzBP**, (g) **2FBP2GCz** and (h) **2FBP2DPACz** in degassed and aerated toluene ($\lambda_{exc} = 340$ nm).

4.7 Photophysics in the Solid State

To assess the emission properties of these emitters in the solid-state, their photophysical properties were investigated in an OLED-relevant host mCP as this host matrix has a sufficiently high triplet energy ($T_1 = 2.91$ eV) to confine the excitons onto the emitter. Figure 4.8 shows the PL spectra of the 1 wt% and 10 wt% doped films in mCP and the neat film, the latter showing an obviously red shifted due to strong intermolecular interaction.³⁸ The optimized doping concentration for **2GCzBP**, **2DPACzBP**, **2FBP2GCz** and **2FBP2DPACz** is 10 wt%, and the corresponding Φ_{PL} values under a N_2 atmosphere are 77%, 28%, 68% and 44%, respectively, which decrease to 68%, 27%, 53% and 41%, respectively, under air. At 10 wt% doping in mCP, the PL spectra are all unstructured with λ_{PL} at 570, 640, 560 and 615 nm for **2GCzBP**, **2DPACzBP**, **2FBP2GCz** and **2FBP2DPACz**, respectively (Figure 4.8, Table 4.1). The S_1/T_1 energy levels of **2GCzBP** (2.45/2.25 eV), **2DPACzBP** (2.12/2.12 eV), **2FBP2GCz** (2.56/2.33 eV) and **2FBP2DPACz** (2.34/2.33 eV) in 10 wt% doped films in mCP film were estimated from the onsets of the fluorescence and phosphorescence spectra at 77 K (Figure 4.8b). The corresponding ΔE_{ST} values of **2GCzBP**, **2DPACzBP** and **2FBP2GCz** are 0.22 eV, 0.01 eV and 0.30 eV, respectively, align with similar results acquired in 2-MeTHF at 77 K. However, **2FBP2DPACz** has a larger ΔE_{ST} of 0.19 eV in solid state than that in 2-MeTHF (0.04 eV) at 77 K, due to the solvent polarity affects.³⁰²

As shown in Figure 4.8c-f, all four compounds showed multiexponential decay kinetics with average prompt fluorescence lifetimes, average τ_{p} , of 22.9 ns, 15.6 ns, 21.1 ns, and 23.0 ns, and average delayed emission lifetimes, average τ_{d} , of 0.3 ms, 1.3 μs , 3.2 ms and 50.5 μs at room temperature for **2GCzBP**, **2DPACzBP**, **2FBP2GCz** and **2FBP2DPACz**, respectively. The corresponding k_{ISC} for the four compounds in mCP films are $0.52 \times 10^7 \text{ s}^{-1}$, $0.23 \times 10^7 \text{ s}^{-1}$, $1.12 \times 10^7 \text{ s}^{-1}$ and $0.29 \times 10^7 \text{ s}^{-1}$ for **2GCzBP**, **2DPACzBP**, **2FBP2GCz** and **2FBP2DPACz**, respectively. The k_{RISC} in mCP films for **2DPACzBP** reached $7.98 \times 10^5 \text{ s}^{-1}$, a value much faster than **2GCzBP** of $0.36 \times 10^4 \text{ s}^{-1}$, **2FBP2GCz** of $0.04 \times 10^4 \text{ s}^{-1}$ and **2FBP2DPACz** of $2.13 \times 10^4 \text{ s}^{-1}$, respectively. Liu *et al.* reported a similar TADF emitter **TAT-FDBPZ** (Figure 4.1) by using two triazatruxene donors and the same acceptor as **2FBP2GCz/2FBP2DPACz**.³⁰³ **TAT-FDBPZ** emits at λ_{PL} of 593 nm, has a much shorter τ_{d} of 1.51 μs and faster k_{RISC} of $1.71 \times 10^6 \text{ s}^{-1}$ than those of **2FBP2GCz/2FBP2DPACz**, which could result from the greater rigidity and larger planar conjugated structure of TAT than those of GCz and DPACz in our work.

For the same donor, the k_{RISC} for the compounds substituted in position 11 and 12 is more than 10 times faster than that of compounds substituted in position 3 and 6, due to the short CT

from donor to electron withdrawing units. For the same substitution position, the k_{RISC} for the compounds substituted by strong donors is more than 50 times faster than that of compounds with weak donors, due to its smaller ΔE_{ST} . Xie *et al.* reported a TADF molecule, **2DMAC-BP**, which contains two DMAC donors attached to the BP acceptor.²²¹ **2DMAC-BP** emits at λ_{PL} of 553 nm, has a τ_{d} of 7.5 μs and k_{RISC} of $4.74 \times 10^5 \text{ s}^{-1}$ in 20 wt% doped films in mCBP. Zeng *et al.* developed another TADF emitter **DPPZ-2DMAC**, which consists of a similar acceptor to BP (same as the acceptor **BPN** shown in Chapter 5) and two DMAC donors substituted at the 10 and 11 positions.²²⁵ Similar to what we observed, **DPPZ-2DMAC** exhibits a red-shifted emission of $\lambda_{\text{PL}} = 620 \text{ nm}$ and has shorter τ_{d} of 4.5 μs and fast k_{RISC} of $5.52 \times 10^5 \text{ s}^{-1}$ compared with **2DMAC-BP**. As shown in Figure 4.8c-f, the relative intensities of the delayed PL increased with increasing temperature from 100 K to 300 K, thereby corroborating the TADF nature of the emission of these four compounds in the mCP films.

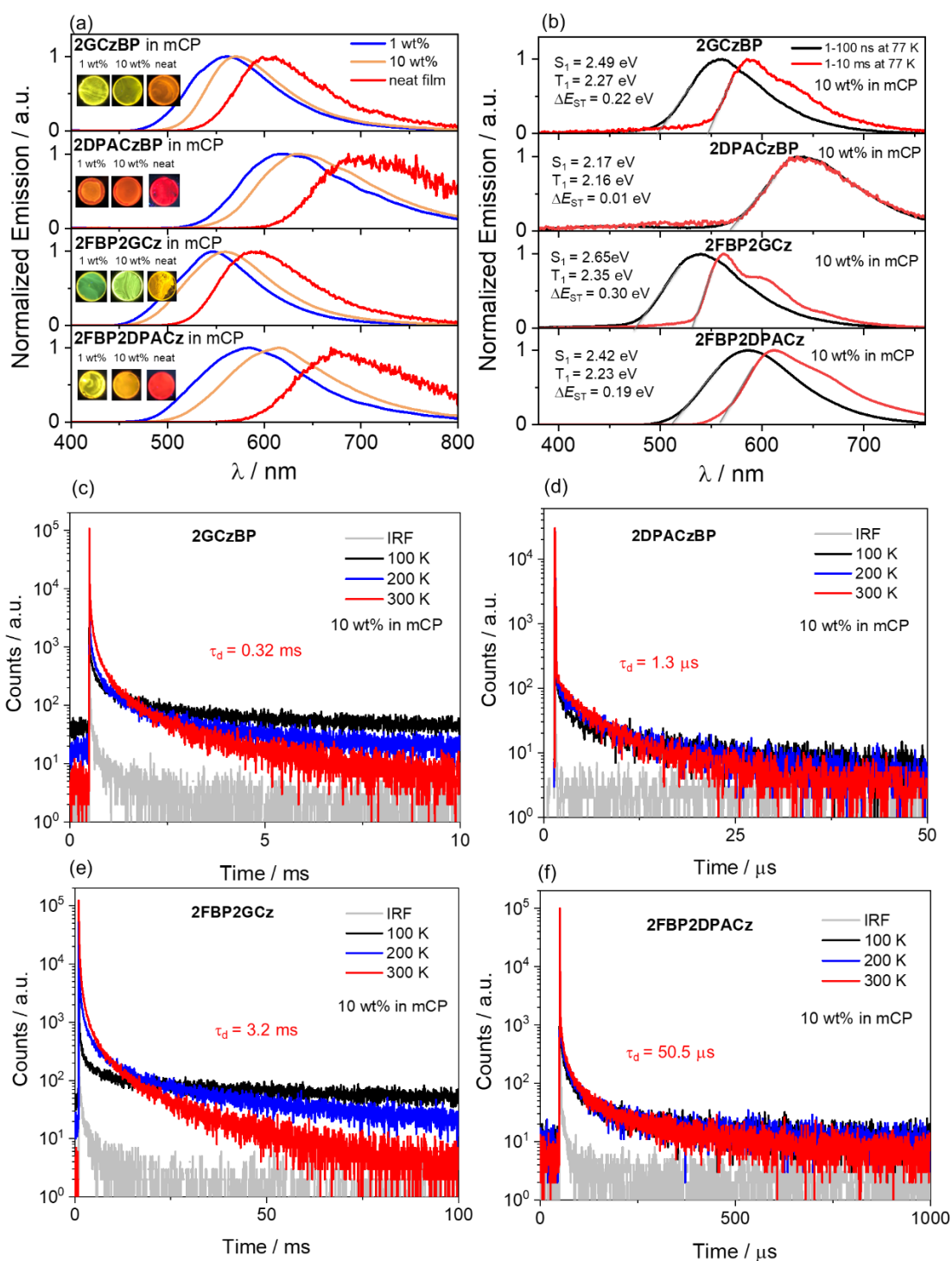


Figure 4.8. (a) SSPL spectra of **2GCzBP**, **2DPACzBP**, **2FBP2GCz** and **2FBP2DPACz** recorded in doped mCP film at room temperature ($\lambda_{exc} = 340$ nm). (b) Prompt fluorescence (1-100 ns) and phosphorescence spectra (1-10 ms) in 10 wt% doped in mCP at 77 K of **2GCzBP**, **2DPACzBP**, **2FBP2GCz** and **2FBP2DPACz** ($\lambda_{exc} = 343$ nm). Temperature-dependent time-resolved PL decay of 10 wt% (c) **2GCzBP**, (d) **2DPACzBP**, (e) **2FBP2GCz** and (f) **2FBP2DPACz** doped mCP film ($\lambda_{exc} = 379$ nm).

Table 4.1. Photophysical properties of **2GCzBP**, **2DPACzBP**, **2FBP2GCz** and **2FBP2DPACz**.

	$\lambda_{\text{abs}} / (\epsilon / \times 10^3 \text{ M}^{-1} \text{ cm}^{-1}) / \text{nm}$	$\lambda_{\text{PL}}^{\text{a}}$ / nm	$\tau_{\text{p}} / \text{ns}^{\text{a}}$	$\tau_{\text{d}} / \mu\text{s}^{\text{a}}$	S_1/T_1^{b} / eV	$\Delta E_{\text{ST}}^{\text{b}}$ / eV	$\lambda_{\text{PL}}^{\text{c}}$ / nm	$\Phi_{\text{PL}}^{\text{c}}$ / %	$\tau_{\text{p}}^{\text{d}}$ / ns	$\tau_{\text{d}}^{\text{d}}$ / μs	S_1/T_1^{e} / eV	$\Delta E_{\text{ST}}^{\text{f}}$ / eV	$k_{\text{ISC}}^{\text{f}}$ / $\times 10^7 \text{ s}^{-1}$	$k_{\text{RISC}}^{\text{f}}$ / $\times 10^4 \text{ s}^{-1}$	$k_{\text{s,r}}^{\text{f}}$ / $\times 10^7 \text{ s}^{-1}$	$k_{\text{s,nr}}^{\text{f}}$ / $\times 10^7 \text{ s}^{-1}$	HOMO ^g / eV	HOMO ^g / eV	E _g ^g / eV
2GCzBP	346 (57), 460(16)	585	22.2	79.1	2.45/ 2.25	0.20	570 (68)	77	22.9	317	2.49/ 2.27	0.22	0.52	0.36	2.96	0.88	-5.38	-3.11	2.27
2DPACzBP	353 (33), 403(18), 506(7)	690	4.2	0.24	2.12/ 2.12	0.00	640 (27)	28	15.6	1.3	2.17/ 2.16	0.01	0.23	79.8	1.73	4.45	-5.01	-2.97	2.04
2FBP2GCz	348 (47), 394(17), 436(14)	565	14.2	102.6	2.56/ 2.33	0.23	560 (53)	68	21.1	3200	2.65/ 2.35	0.30	1.12	0.04	2.51	1.18	-5.37	-3.07	2.30
2FBP2DPACz	354(41), 394(22), 464(11)	675	3.2	0.25	2.35/ 2.30	0.05	615 (41)	44	23.0	50.5	2.42/ 2.23	0.19	0.29	2.13	1.78	2.27	-5.02	-3.02	2.00

^a In PhMe at 298 K ($\lambda_{\text{exc}}=340 \text{ nm}$). ^bObtained from the onset of the prompt fluorescence (time window: 1 ns – 100 ns) and phosphorescence spectra (time window: 1 ms – 10 ms) measured in 2-MeTHF glass at 77 K, $\lambda_{\text{exc}} = 343 \text{ nm}$. ^cThin films of 10 wt% emitters doped in mCP were prepared by spin-coating and Φ_{PL} values were determined using an integrating sphere ($\lambda_{\text{exc}}=340 \text{ nm}$). Values quoted are under N_2 . Values in parentheses are in air. ^dAverage lifetime ($\tau_{\text{avg}} = \Sigma A_i \tau_i^2 / \Sigma A_i \tau_i$, where A_i is the pre-exponential for lifetime τ_i). ^e S_1 was obtained from the onset of the prompt emission (time-gated window: 1–100 ns) ms measured in doped film at 77 K and T_1 was obtained from the onset of the phosphorescence spectrum (time-gated window: 1–10 ms) measured in doped film at 77 K. ^f $k_{\text{ISC}} =$ intersystem crossing rate from S_1 to T_1 states; $k_{\text{RISC}} =$ reverse intersystem crossing rate. ^g In DCM with 0.1 M [$n\text{Bu}_4\text{N}$]PF₆ as supporting electrolyte and Fc/Fc⁺ as the internal reference (0.46 V vs. SCE).²²⁴ The HOMO and LUMO energies were determined using $E_{\text{HOMO/LUMO}} = -(E_{\text{ox}}/E_{\text{red}} + 4.8) \text{ eV}$ where E_{ox} and E_{red} are anodic and cathodic peak potentials, respectively, obtained from the DPV.²²⁴ $E_{\text{g}} = |E_{\text{HOMO}} - E_{\text{LUMO}}|$.

4.8 Device Characterization

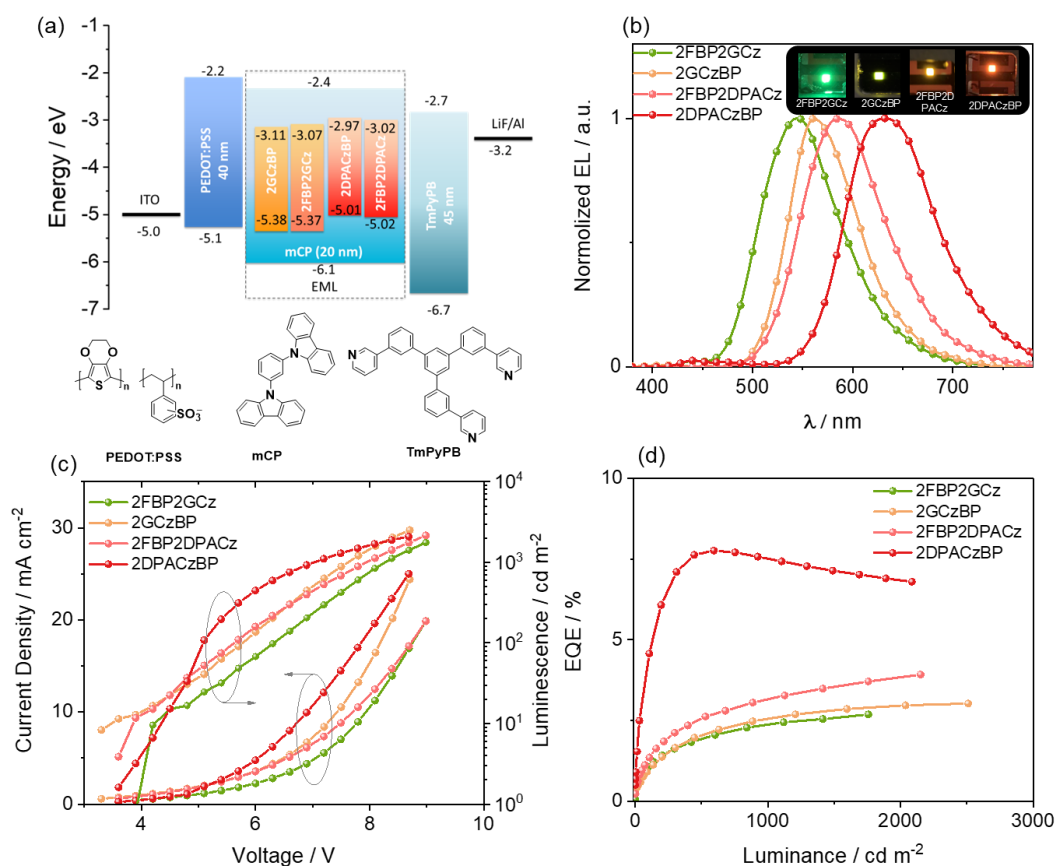


Figure 4.9. (a) Energy level diagram and molecular structure of materials employed in the devices; (b) EL spectra of OLED devices with the structure of ITO/PEDOT:PSS (40 nm)/ mCP:10 wt% dopants (20 nm)/TmPyPB (45 nm)/LiF (1 nm)/Al; (c) Current density and luminance versus voltage characteristics; (d) external quantum efficiency versus luminance curves.

To evaluate the EL performance of these emitters, solution-processed OLEDs employing the optimised doping concentration of 10 wt% emitters doped in mCP films as the EML were fabricated with a typical configuration of indium ITO (indium tin oxide)/ poly(3,4-ethylenedioxythiophene):poly(styrenesulfonate) (PEDOT:PSS) (40 nm)/ mCP : 10wt% dopants (20 nm)/TmPyPB (45 nm)/LiF (1 nm)/Al (Figure 4.9a), where ITO and Al serve as the anode and cathode, respectively. PEDOT:PSS and TmPyPB are sequentially used as the hole-transporting layer electron-transporting layer, respectively.

As shown in Figure 4.9b, the OLEDs of **2FBP2GCz**, **2GCzBP**, **2FBP2DPACz** and **2DPACzBP** at a doping concentration of 10 wt% in mCP host exhibit green, yellow and red emission with λ_{EL} at 545, 561, 585 and 640 nm and CIE coordinates of (0.37, 0.57), (0.46, 0.53), (0.51, 0.48) and (0.61, 0.36) in the device, which match the PL emission of the 10 wt% doped films in mCP very well. As depicted in Figure 4.9c-d, the devices with **2DPACzBP** showed the highest EQE_{max} of 7.8% at 600 cd m^{-2} with negligible efficiency roll-off at 1000 cd m^{-2} ($EQE_{1000} = 7.6\%$), which is the highest EQE_{1000} in reported solution-processed red OLEDs (Figure 4.11), and even still maintain 87% of its EQE_{max} at 2000 cd m^{-2} ($EQE_{2000} = 6.8\%$).

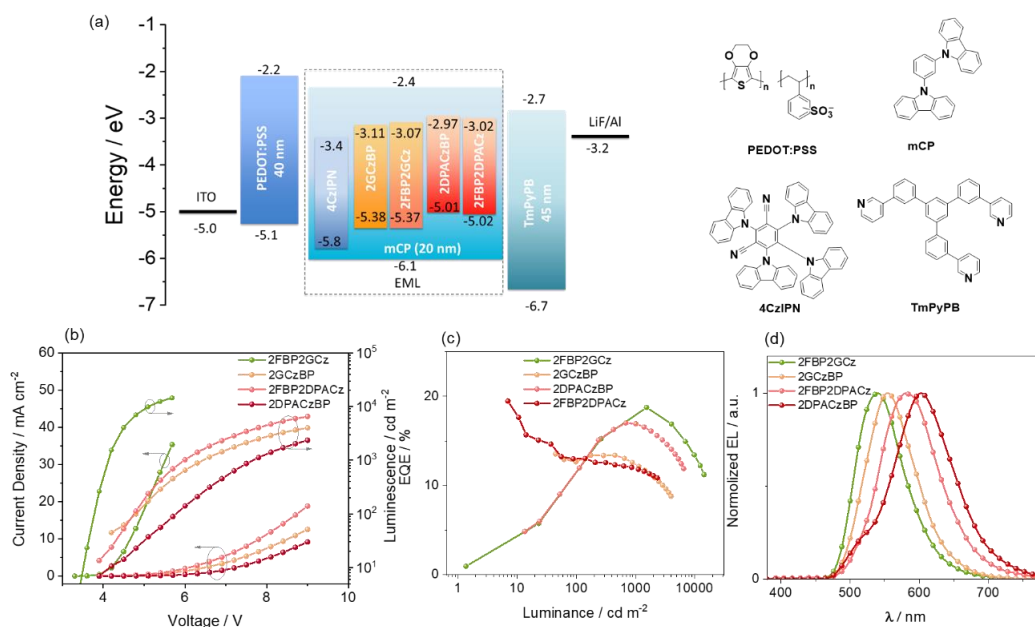


Figure 4.10. (a) Energy level diagram and molecular structure of materials of materials employed in the devices; (b) Current density and luminance versus voltage characteristics for the HF devices; (c) external quantum efficiency versus luminance curves for the HF devices; (d) Electroluminescence spectra of the HF devices.

To further improve the OLED performance, TADF-sensitized-fluorescence HF devices were fabricated.³⁰⁴ Here, **4CzIPN** was selected as the TADF assistant dopant because of its high Φ_{PL} and short τ_d in mCP.^{305–307} The optimized ratio of mCP/4CzIPN/emitters was established in the literature to be 65 : 32 : 3.^{304,308,309} The

device performance is shown in Figure 4.10a, and the data are summarized in Table 4.2. As shown in Figure 4.10, the EQE of the HF devices with all four compounds have been greatly improved compared to the mCP host only device. Furthermore, all the emission spectra of the HF devices are slightly blue-shifted compared to the corresponding mCP host-only devices, due to weak intermolecular interaction at low doping concentration (3 wt% emitters) than that of the 10 wt% doped EML in mCP devices (Figure 4.9).³⁸ The HF devices based on **2DPACzBP** showed an EQE_{max} of 20.0% at λ_{EL} = 605 nm, much higher than 7.8% in the mCP only devices. Furthermore, the HF devices with **2FBP2GCz**, **2GCzBP** and **2FBP2DPACz** showed high EQE_{max} of 18.7, 13.5 and 17.0% with the emission peak λ_{EL} , at 540, 555 and 585, respectively. The EQEs at 1000 cd m⁻² in the HF devices with **2FBP2GCz**, **2GCzBP**, **2FBP2DPACz** and **2DPACzBP** remained at 17.3%, 12.3%, 16.8% and 11.8%, respectively (Table 4.2), which, to the best of our knowledge, is amongst the best performance for orange to red HF SP-OLED. To date, there have been few reports of solution-processed HF OLEDs.^{308,310–312} Chen *et al.* firstly reported a red all-fluorescent SP-OLED using the TADF sensitizing assistant host, 1,2-bis(4-(3,6-di-*tert*-butyl-9H-carbazol-9-yl)phenyl)ethane-1,2-dione (DC-TC), and tetraphenyldibenzoperiflanthene (DBP) as the red fluorescent emitter, which showed EQE_{max} of 8.0% that dropped to 6.7% at 100 cd m⁻².³⁰⁸ Wallwork *et al.* demonstrated HF SP-OLED with an EQE_{max} of 15.3% (EQE₁₀₀₀=8.4%) using cibalackrot as the fluorescent emitter and 4CzIPN-tBu as the TADF assistant host in CBP.³¹¹ Recently, the same group report the first HF SP-OLEDs based on Cibalackrot dendrimers, which showed an EQE_{max} of 12.5% and an EQE₁₀₀₀ of 12.0% at λ_{EL} of ~600 nm.³¹⁰

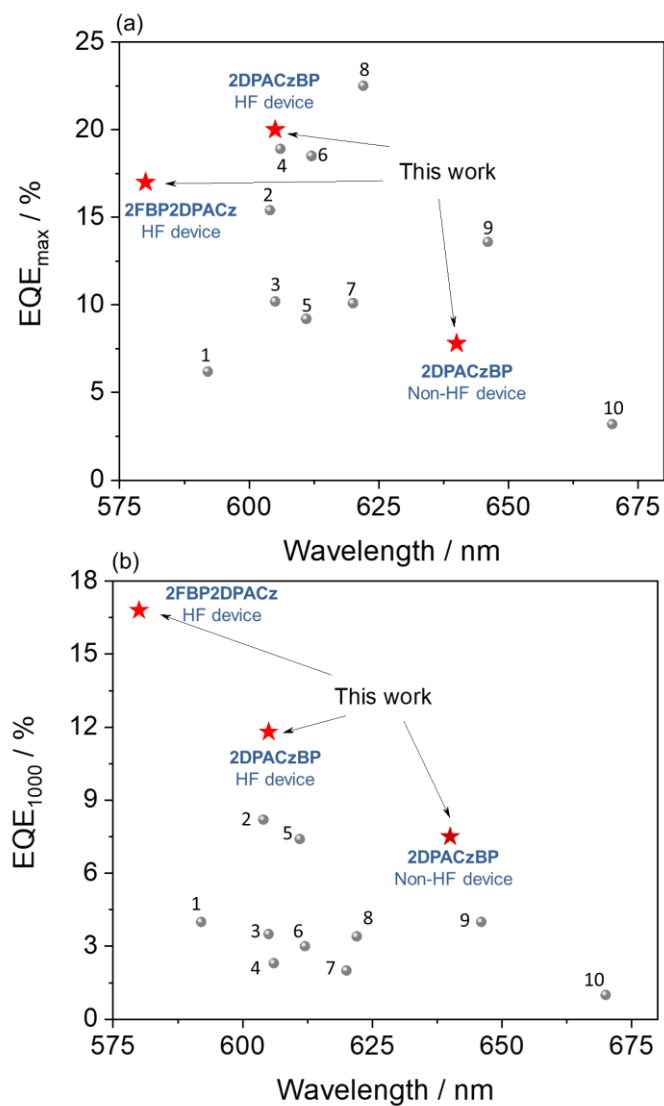


Figure 4.11. The EQE values at 1000 cd m^{-2} of all reported solution-processed orange to red ($\lambda_{\text{EL}} > 575 \text{ nm}$) TADF OLEDs as a function of wavelength.

Table 4.2. Electroluminescence data for the devices

Emitter	V _{on} ^a /V	EL ^b /nm	CE/PE ^c / cd A ⁻¹ /lm W ⁻¹	EQE _m ax /%	EQE ₁ 00 /%	EQE ₁₀ 00 /%	CIE ^d	L _{max} / cd ^e m ⁻²	Ref.
2FBP2GCz	3.9	545	8.8/3.1	2.7	1.1	2.3	(0.37, 0.57)	1757	This work
2GCzBP	3.0	561	10.3/3.8	3.1	1.0	2.6	(0.46, 0.53)	2509	This work
2FBP2DPACz	3.2	585	10.8/3.8	4.0	1.4	3.2	(0.51, 0.48)	2151	This work
2DPACzBP	3.4	640	9.6/4.9	7.8	4.6	7.5	(0.61, 0.36)	2086	This work
3wt% 2FBP2GCz : mCP:4CzIPN(2:1)	3.0	540	68.2/51.0	18.7	11.2	17.3	(0.35, 0.60)	1444 8	This work
3wt% 2GCzBP : mCP:4CzIPN(2:1)	3.9	555	49.0/36.6	13.5	13.1	12.3	(0.41,0.5 7)	3995	This work
3wt% 2FBP2DPACz : mCP:4CzIPN(2:1)	3.2	580	49.5/27.3	17.0	11.3	16.8	(0.49, 0.49)	6516	This work
3wt% 2DPACzBP : mCP:4CzIPN(2:1)	3.4	605	46.1/36.7	20.0	13.1	11.8	(0.53, 0.45)	2348	This work
1 4t-BuCzTTR	4.7	592	13.0/6.4	6.2	~5.0	~4.0	(0.54, 0.45)	~120 0	297
2 TAT-DBPZ	3.2	604	29.7/23.3	15.4	12.3	8.2	(0.56, 0.44)	1348 1	303
3 DBP-4MOTPA	3.9	605	17.4/13.6	10.2	~9.0	~3.5	(0.55,0.4 2)	5200	313
4 2DMAC-DBP- 2tBuCz	2.3	606	34.7/44.7	18.9	8.2	2.3	(0.57,0.4 2)	~500 0	314
5 TAT-FDBPZ	3.2	611	15.6/14.0	9.2	9.1	7.4	(0.58, 0.41)	1646 7	303
6 oDTBPZ-DPXZ	3.3	612	31.0/27.1	18.5	12.1	~3.0	(0.60,0.4 0)	~300 0	145
7 tDBBPZ-DPXZ	4.5	620	12.8/7.3	10.1	8.2	~2.0	(0.62, 0.37)	~100 0	144
8 NAI_R3	7.0	622	28.3/9.4	22.5	-	3.4	(0.60, 0.40)	~200 0	299
9 DDTPACz-DCPP	4.0	646	13.6/9.0	13.6	~10.0	~4.0	(0.61,0.3 8)	1856	136
1 0 2TPA-PPDC	4.6	670	3.26/-	3.2	N/A	~1.0	(0.64, 0.36)	1622	298

^a Turn-on voltage at a brightness ≈ 1 cd m⁻². ^b The electroluminescence maximum recorded at 6 V. ^c PE: power efficiency, CE: current efficiency; ^d The CIE coordinates recorded at 6 V; ^e maximum luminescence.

4.9 Conclusions

Here, we designed and synthesized four novel orange-red solution-processable TADF dendrimers, **2GCzBP**, **2DPACzBP**, **2FBP2GCz** and **2FBP2DPACz**. We systematically investigated the effect of substitution position and strength of the donors on their optoelectronic properties (Figure 4.12). From this study we could draw the following conclusions: 1). The emission color of the compounds not only depends on the donor strength but also shows a large red-shift when same donors are substituted not from position 3 and 6 but to position 11 and 12 of the BP acceptor. 2). The k_{RISC} for

the compounds substituted in position 11 and 12 of BP is more than 10 times faster than that of compounds substituted in position 3 and 6. 3). **2GCzBP** exhibits the highest Φ_{PL} of 77% and the Φ_{PL} slightly decrease to 68% for **2FBP2GCz**, in both compounds where donors are substituted at the 3 and 6 position. However, both **2DPACzBP** and **2FBP2DPACz** show much lower Φ_{PL} , which we attribute to the energy gap law, especially for **2DPACzBP** (the smallest S_1 and lowest Φ_{PL}). 4). Due to the large dihedral angles between the donors at the 11/12 positions and the acceptor, **2GCzBP** and **2DPACzBP** possess much smaller ΔE_{ST} compared to **2FBP2GCz** and **2FBP2DPACz**, respectively. Furthermore, the stronger donor contributes to the smaller ΔE_{ST} in these compounds with same substitution position. The SP-OLED based on **2DPACzBP** exhibits a pure red emission $\lambda_{\text{EL}} = 640$ nm with an excellent EQE_{max} of 7.8%. Further, the devices showed low efficiency roll-off where the EQE remains high at 7.5% at a luminance of 1000 cd m^{-2} , which is among the best results in solution-processed red TADF OLEDs at so high luminance. The much worse device performance using **2GCzBP**, **2FBP2GCz** and **2FBP2DPACz** may be result from the slow k_{RISC} and an unoptimized device structure in these cases. The efficiency of all of the HF devices with **4CzIPN** as the assistant dopant improved significantly, where the **2DPACzBP** HF device showed a particularly attractive performance with an EQE_{max} of 20.0% at $\lambda_{\text{EL}} = 605$ nm that remains high at 11.8% at a luminance of 1000 cd m^{-2} , which is the best performance for the orange-to-red HF SP-OLED.

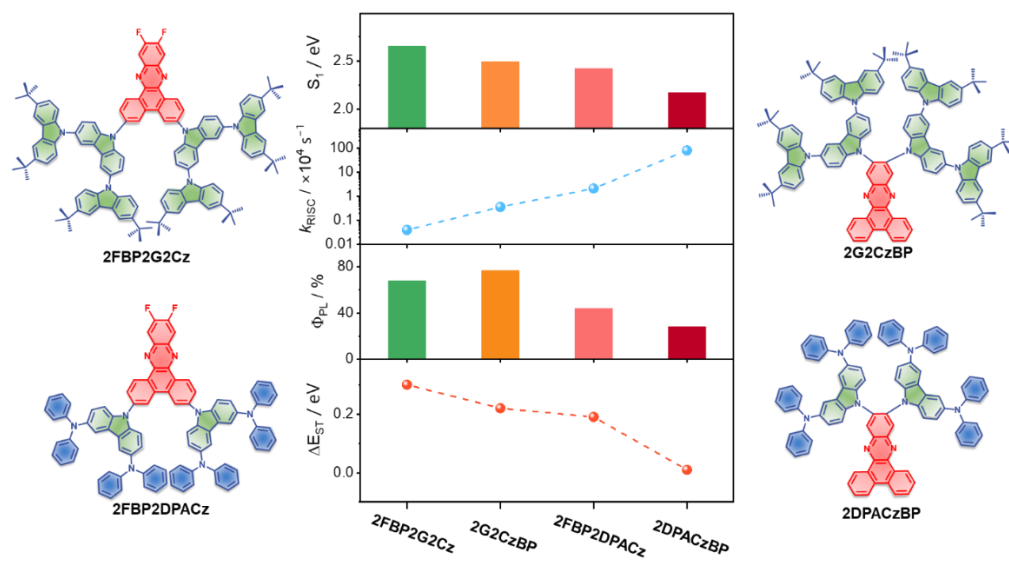
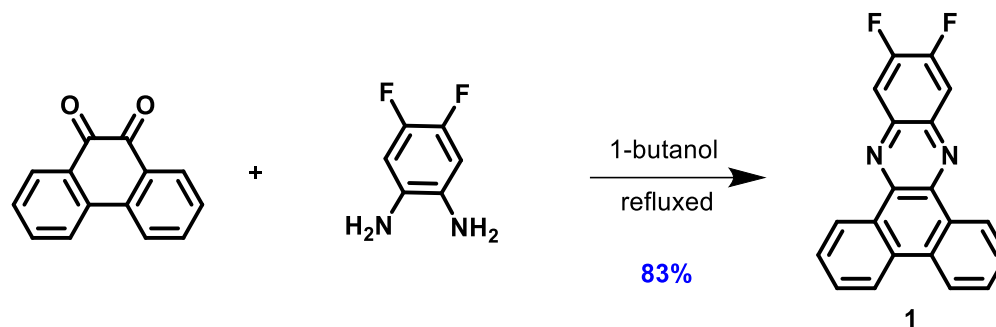


Figure 4.12. The relationship of key parameters among these four TADF dendrimers in this Chapter.

4.10 Experimental Section

The following compounds were synthesised according to the literature: 3,3'',6,6''-tetra-*tert*-butyl-9*H*-9,3':6',9''-tercarbazole (DPACz),³¹⁵ *N*³,*N*³,*N*⁶,*N*⁶-tetraphenyl-9*H*-carbazole-3,6-diamine (GCz),³¹⁶ 3,6-dibromo-9,10-phenanthrenequinone.³¹⁷

Synthesis of 11,12-difluorodibenzo[*a,c*]phenazine (1):



Phenanthrene-9,10-dione (3 g, 14 mmol, 1.0 equiv.) and 4,5-difluorobenzene-1,2-diamine (2.1 g, 14 mmol, 1.0 equiv.) were added into 20 mL of 1-butanol and then refluxed for 12 hours under a nitrogen atmosphere. After cooling to room temperature, the solution was poured into water and extracted with DCM (3×50 mL). The organic layer was dried over Na₂SO₄ and concentrated under reduced pressure. The residue was purified by column chromatography (33% DCM/Hexane) to afford compound **1** as brown solid (4.6 g).

11,12-difluorodibenzo[*a,c*]phenazine (1): Yield: 83%. **R_f** = 0.2 (33% DCM/Hexane). **Mp** = 169-171 °C. (Lit. Mp: 170-173 °C).²²⁵ **¹H NMR (500 MHz, CDCl₃)** δ 9.32 (dd, *J* = 8.0, 1.5 Hz, 2H), 8.57 (dd, *J* = 8.1, 1.2 Hz, 2H), 8.02 (t, *J* = 9.5 Hz, 2H), 7.83 (ddd, *J* = 8.2, 7.1, 1.5 Hz, 2H), 7.76 (ddd, *J* = 8.1, 7.0, 1.2 Hz, 2H). **¹³C NMR (126 MHz, CDCl₃)**: δ = 142.45, 139.43, 132.07, 130.63, 129.76, 128.06, 126.21, 122.97, 114.48. Analytical data match those previously reported.²²⁵

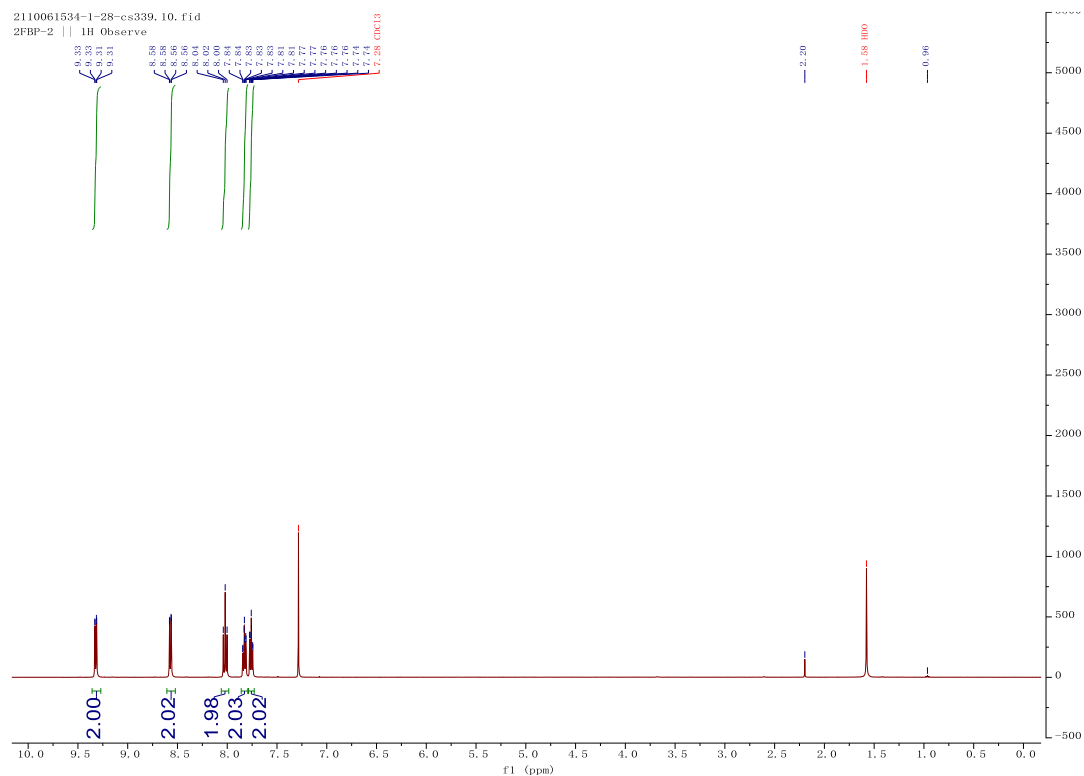


Figure 4.13. ^1H NMR spectra of **1** in CDCl_3 .

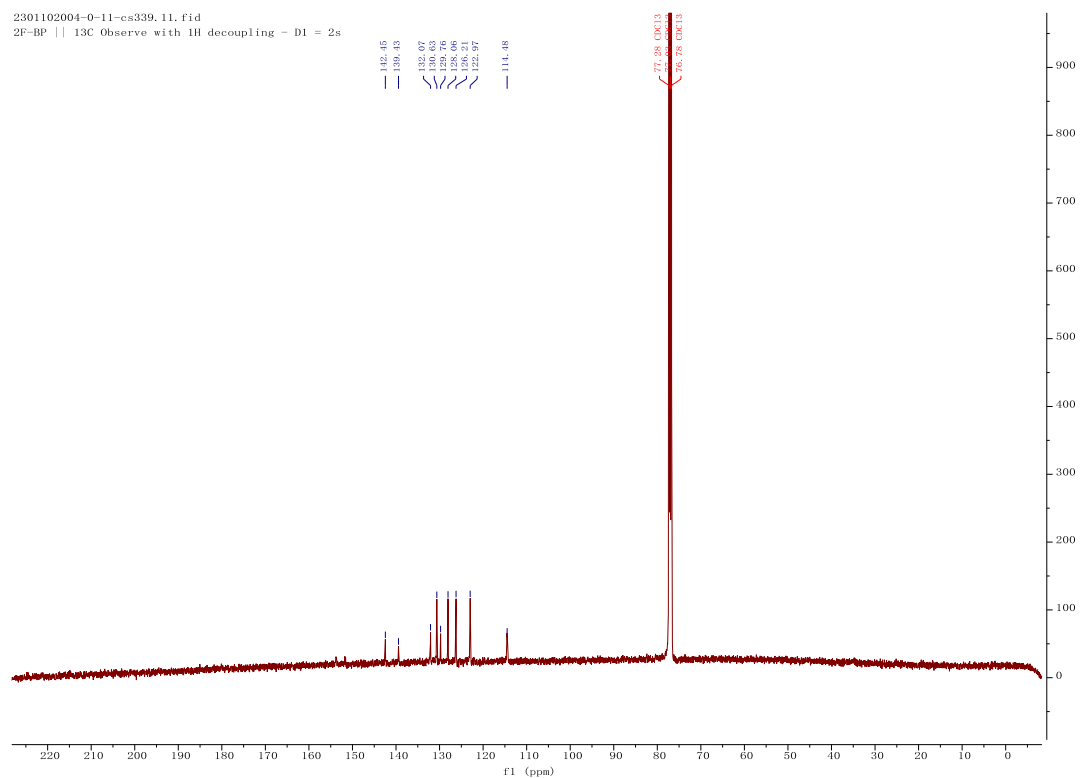
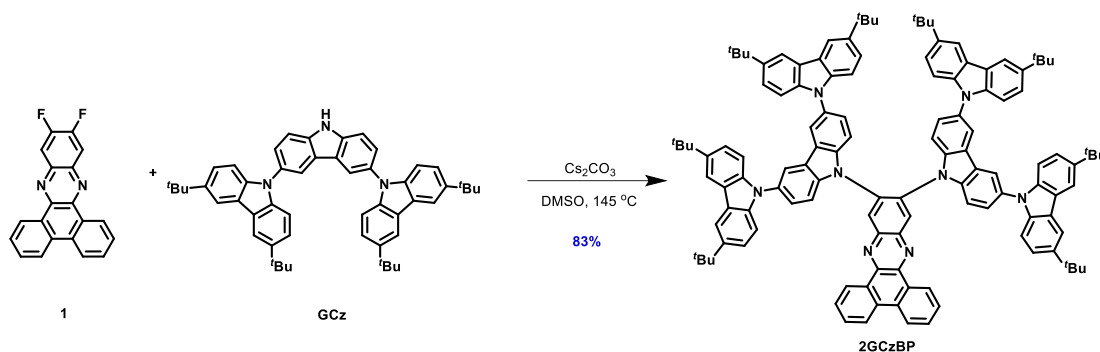


Figure 4.14. ^{13}C NMR spectra of **1** in CDCl_3 .

Synthesis of 11,12-bis(3,3',6,6''-tetra-*tert*-butyl-9'*H*-[9,3':6',9''-tercarbazol]-9'-yl)dibenzo[*a,c*]phenazine (2GCzBP):



1 (0.2 g, 0.6 mmol, 1.0 equiv.), **GCz** (0.67 g, 1.3 mmol, 2.1 equiv.) and Cs₂CO₃ (1.03 g, 3.0 mmol, 5.0 equiv.) were added into 10 mL of DMSO and then heated at 145 °C for 12 hours under a nitrogen atmosphere. After cooling to room temperature, the solution was poured into water and extracted with DCM (3×50 mL). The organic layer was dried over Na₂SO₄ and concentrated under reduced pressure. The residue was purified by column chromatography with (33% DCM/Hexane) to afford the compound **2GCzBP** as yellow solid (0.90 g).

11,12-bis(3,3',6,6''-tetra-*tert*-butyl-9'*H*-[9,3':6',9''-tercarbazol]-9'-yl) dibenzo[*a,c*]phenazine (2GCzBP): Yield: 83%. R_f = 0.3 (33% DCM/Hexane). Mp >400 °C. ¹H NMR (400 MHz, Chloroform-*d*) δ 9.60 (dd, *J* = 7.9, 1.5 Hz, 2H), 9.17 (s, 2H), 8.74 – 8.70 (m, 2H), 8.11 (s, 8H), 8.03 (d, *J* = 2.0 Hz, 4H), 7.93 (dddd, *J* = 26.0, 8.1, 7.1, 1.3 Hz, 5H), 7.49 (d, *J* = 8.6 Hz, 5H), 7.32 (d, *J* = 2.0 Hz, 2H), 7.30 (d, *J* = 2.0 Hz, 2H), 7.10 (s, 14H), 1.37 (s, 72H) ppm. ¹³C NMR (101 MHz, CDCl₃): δ = δ 144.25, 142.49, 141.94, 139.80, 139.46, 135.32, 132.68, 131.57, 131.47, 131.37, 129.87, 128.44, 126.84, 125.21, 124.36, 123.70, 123.27, 123.05, 118.86, 116.11, 111.30, 108.75, 77.37, 77.05, 76.73, 34.64, 32.01. HR-MS [M+H]⁺ Calculated: (C₁₂₄H₁₁₈N₈) 1718.9479; Found: 1718.9474. Anal. Calcd. for C₁₂₄H₁₁₈N₈: C, 86.57%; H, 6.91%; N, 6.51%. Found: C, 86.46%; H, 6.88%; N, 6.52%. HPLC analysis: 99.33% pure on HPLC analysis, retention time 13.25 minutes in 100% THF.

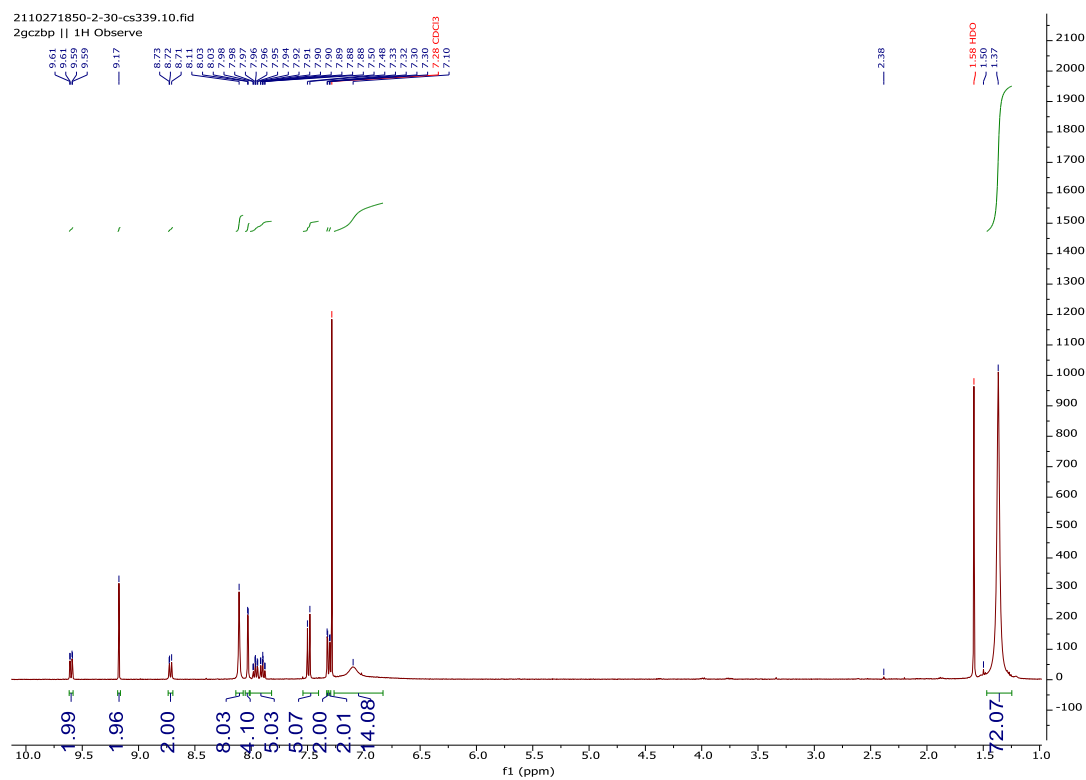


Figure 4.15. ^1H NMR spectra of **2GCzBP** in CDCl_3 .

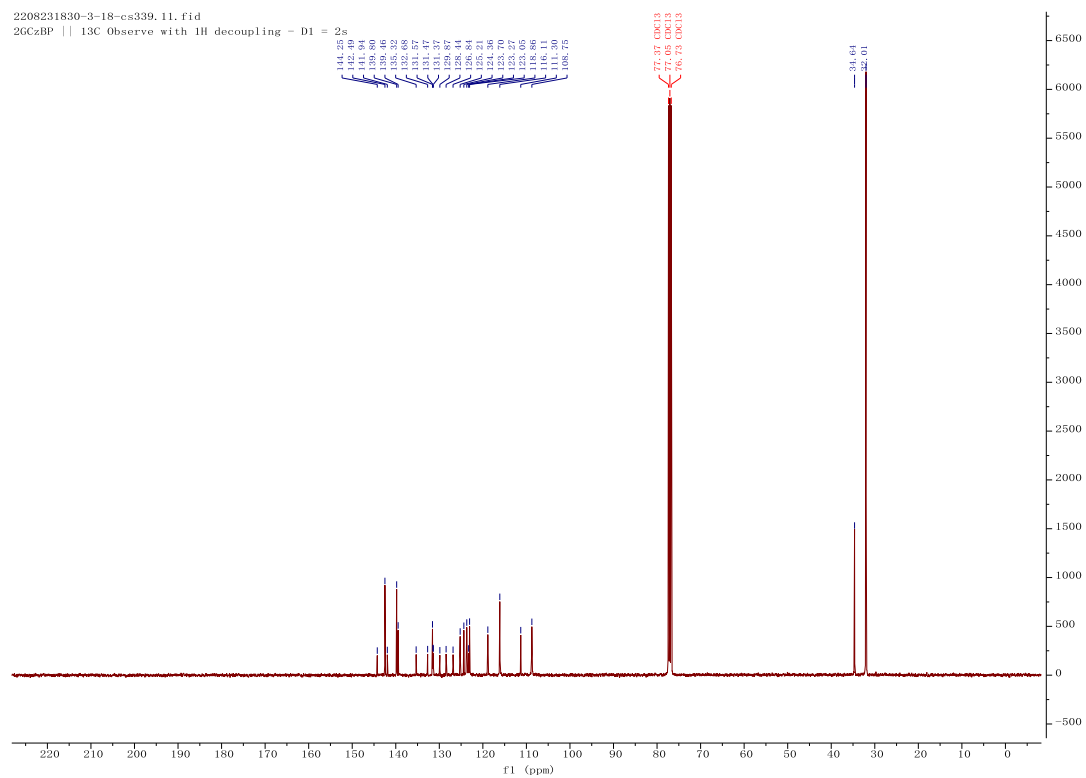


Figure 4.16. ^{13}C NMR spectra of **2GCzBP** in CDCl_3 .

Generic Display Report (all)

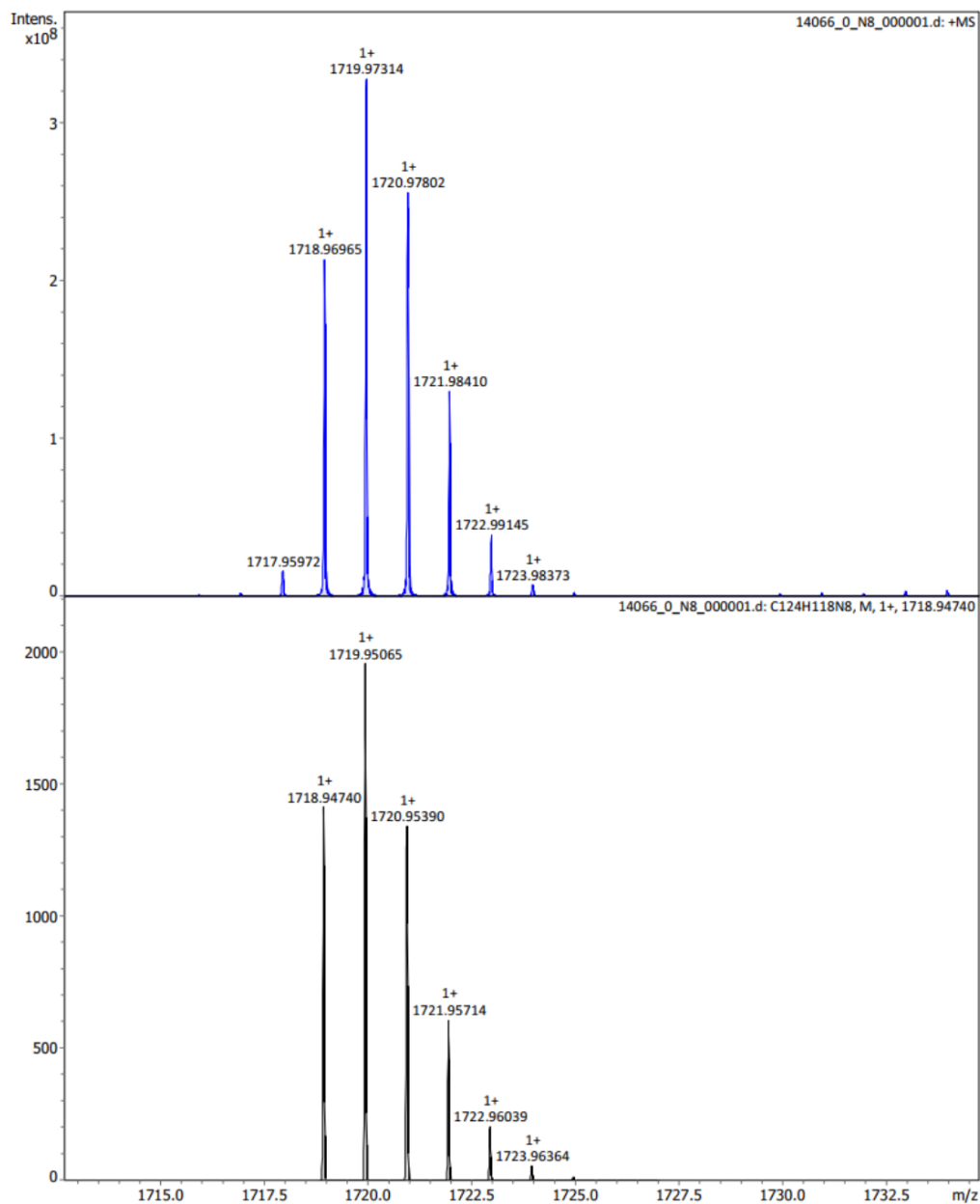


Figure 4.17. HRMS of 2GCzBP.

Elemental Analysis Service Request Form

Researcher name Changfeng Si

Researcher email cs339@st-andrews.ac.uk

NOTE: Please submit ca. 10 mg of sample

Sample reference number	CS160-2GCzBP
Name of Compound	2GCzBP
Molecular formula	C124H118N8
Stability	
Hazards	
Other Remarks	

Analysis type:

Single Duplicate Triplicate

Analysis Result:

Element	Expected %	Found (1)	Found (2)	Found (3)
Nitrogen	6.51	6.55	6.48	
Carbon	86.57	86.26	86.65	
Hydrogen	6.91	6.95	6.88	

Authorising Signature:

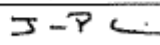
Date completed	28.11.22
Signature	
comments	

Figure 4.18. Elemental analysis of 2GCzBP.

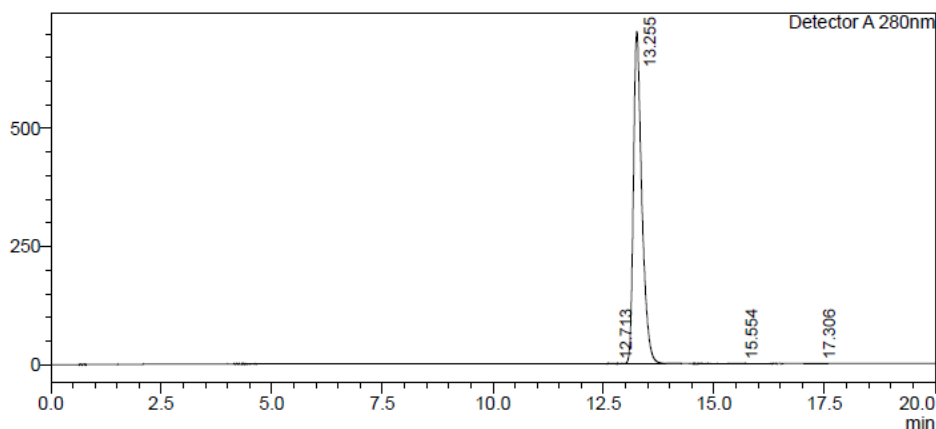
HPLC Trace Report 01 Jul 2022

<Sample Information>

Sample Name : 2GCzBP
Sample ID : 2GCzBP
Method Filename : 100% THF 20 mins 280nm - new-please use.lcm
Batch Filename : 2FBP2GCz.lcb
Vial # : 1-13
Injection Volume : 10 uL
Date Acquired : 01/07/2022 18:27:52
Date Processed : 01/07/2022 18:47:54
Sample Type : Unknown
Acquired by : System Administrator
Processed by : System Administrator

<Chromatogram>

mV



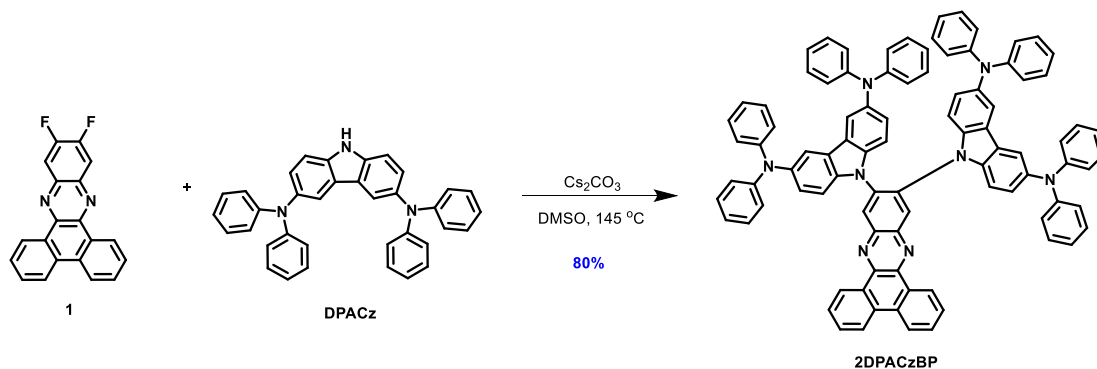
<Peak Table>

Detector A 280nm

Peak#	Ret. Time	Area	Height	Area%	Area/Height	Width at 5% Height
1	12.713	3039	166	0.033	18.276	--
2	13.255	9322916	702865	99.835	13.264	0.474
3	15.554	6702	372	0.072	18.003	0.469
4	17.306	5665	389	0.061	14.562	0.430
Total		9338322	703792	100.000		

Figure 4.19. HPLC trace of 2GCzBP.

Synthesis of 9,9'-(dibenzo[*a,c*]phenazine-11,12-diyl)bis(*N*³,*N*³,*N*⁶,*N*⁶-tetraphenyl-9*H*-carbazole-3,6-diamine) (2DPACzBP):



1 (0.2 g, 0.6 mmol, 1.0 equiv), DPACz (0.67 g, 1.3 mmol) and Cs_2CO_3 were added into

10 mL of DMSO and then heated at 145 °C for 12 hours under nitrogen atmosphere. After cooling to room temperature, the solution was poured into water and extracted with DCM (3×50 mL). The organic layer was dried over Na₂SO₄ and concentrated under reduced pressure. The residue was purified by column chromatography (33% DCM/Hexane, v/v) to afford the compound **2DPACzBP** as dark red solid (0.65 g).

9,9'-(dibenzo[*a,c*]phenazine-11,12-diyl)bis(N³,N³,N⁶,N⁶-tetraphenyl-9*H*-carbazole-3,6-diamine) (2DPACzBP): Yield: 80%. **R_f** = 0.3 (33% DCM/Hexane). **Mp** = 369-370 °C. **¹H NMR (400 MHz, CDCl₃)** δ 9.49 (dd, *J* = 8.0, 1.5 Hz, 2H), 8.87 (s, 2H), 8.66 (d, *J* = 8.1 Hz, 2H), 7.87 (dt, *J* = 29.4, 7.5 Hz, 4H), 7.54 (s, 4H), 7.21 – 7.01 (m, 20H), 7.00 – 6.68 (m, 28H). ppm. **¹³C NMR (126 MHz, CDCl₃)** δ 148.28, 143.76, 141.50, 141.17, 137.17, 135.19, 132.46, 131.04, 130.32, 129.94, 129.09, 128.27, 126.64, 125.43, 124.31, 123.14, 122.63, 121.67, 118.05, 110.77, 77.30, 77.04, 76.79. **HR-MS [M+H]⁺ Calculated:** (C₉₂H₆₂N₈) 1278.5097; **Found:** 1279.5092. **Anal. Calcd. for C₉₂H₆₂N₈:** C, 86.36%; H, 4.88%; N, 8.76%. **Found:** C, 86.42%; H, 4.81%; N, 8.76%. **HPLC analysis:** 98.8% pure on HPLC analysis, retention time 5.568 minutes in the mixture of 50% acetonitrile and 50% water.

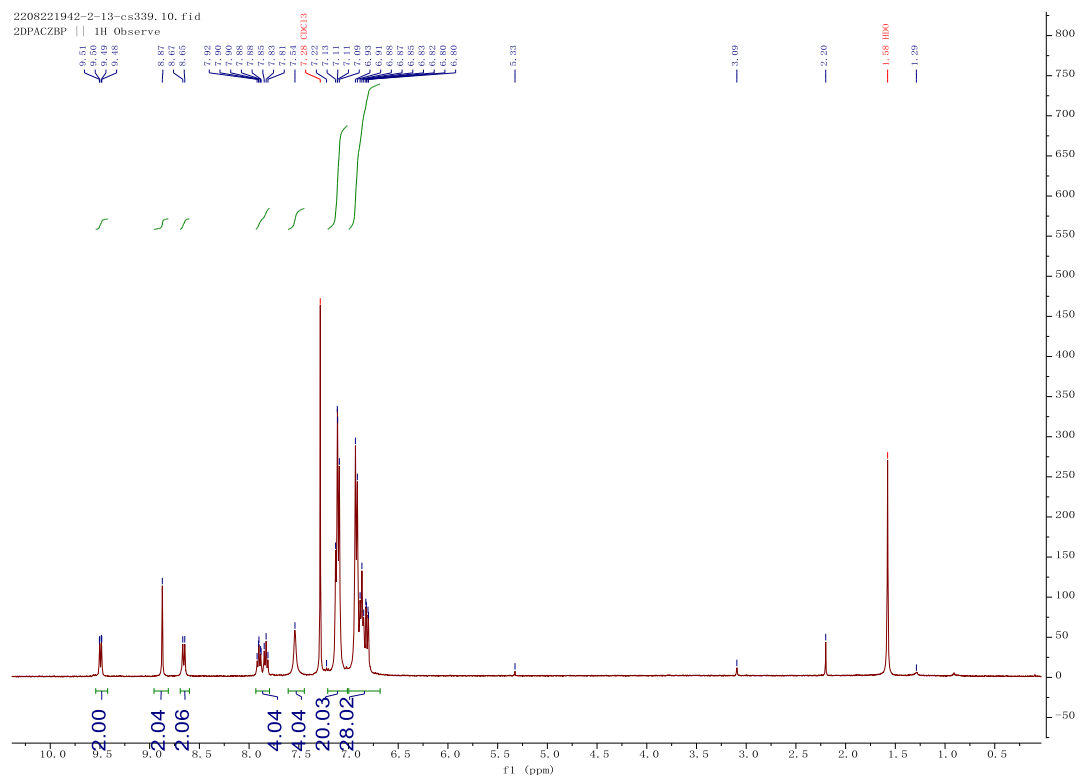


Figure 4.20. ¹H NMR spectra of 2DPACzBP in CDCl₃.

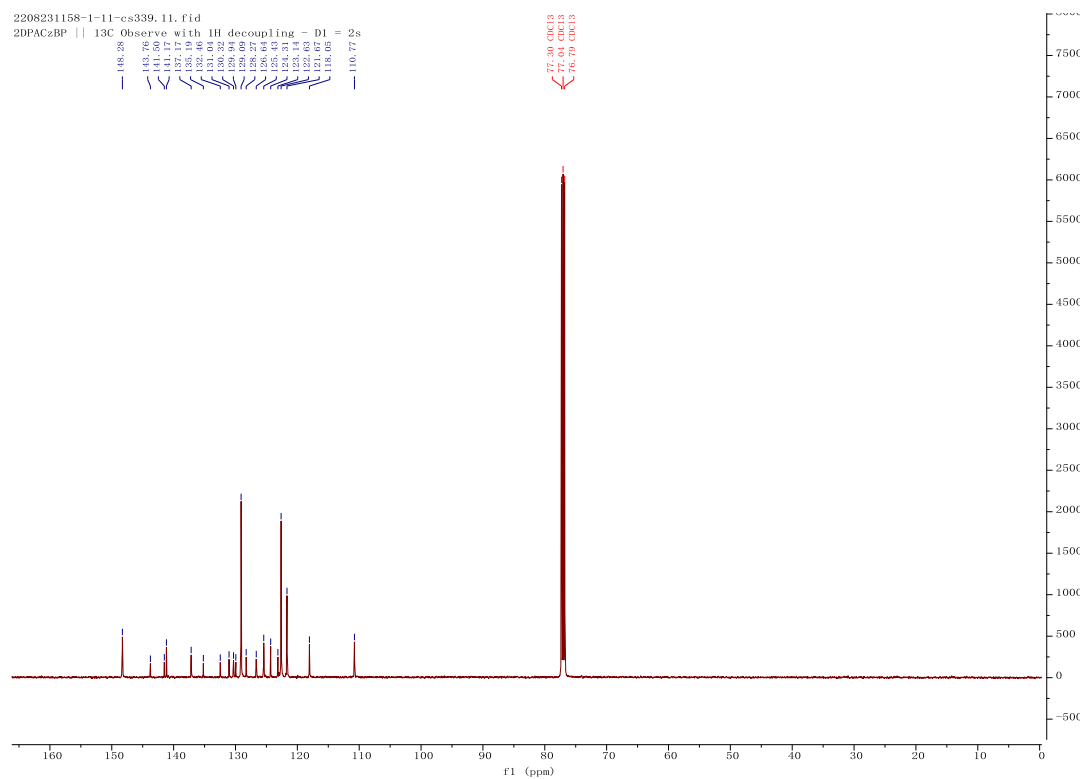
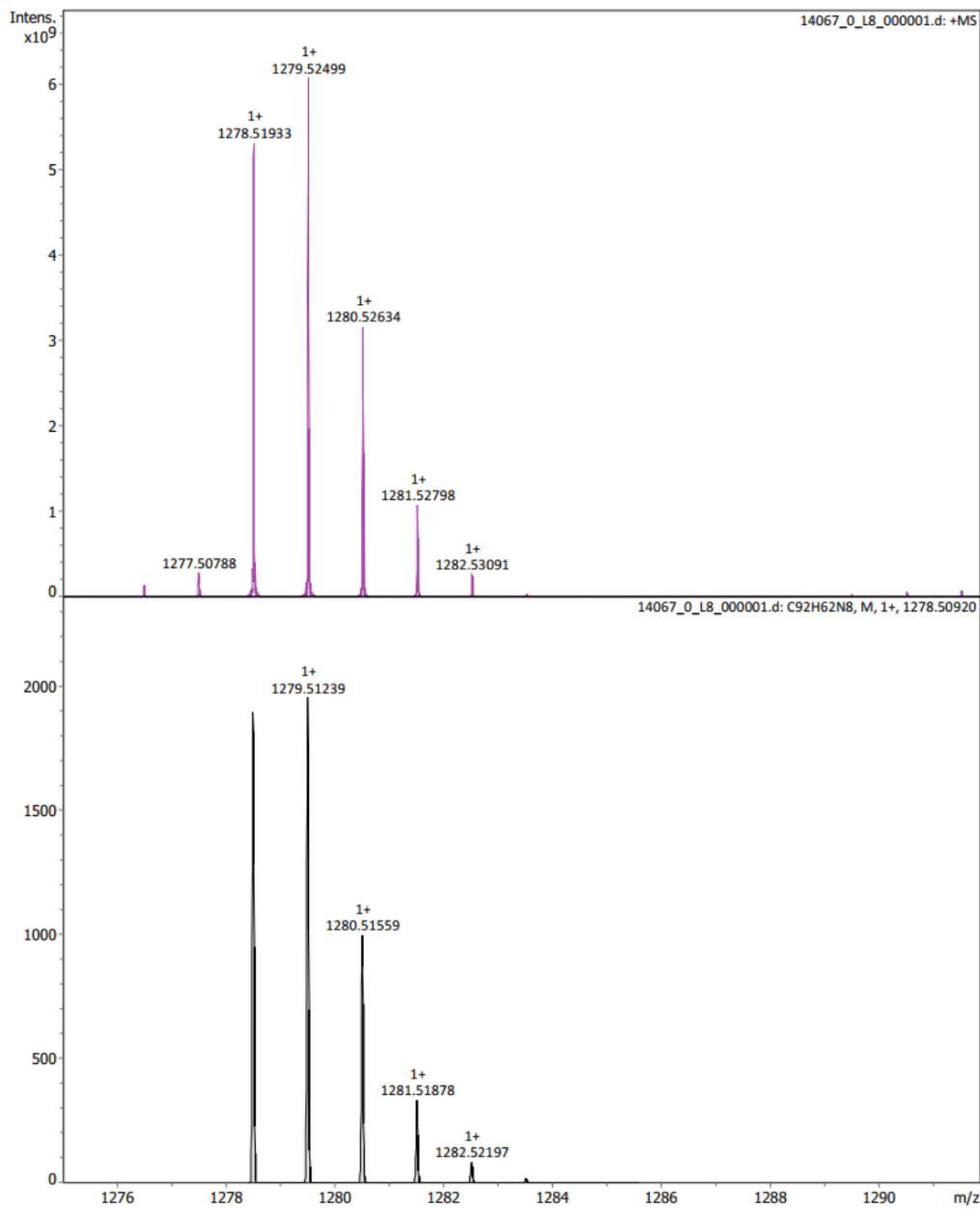


Figure 4.21. ¹³C NMR spectra of 2DPACzBP in CDCl₃.

Generic Display Report (all)



Bruker Compass DataAnalysis 5.3 printed: 24-Oct-22 3:58:21 PM by: demo Page 1 of 1

Figure 4.22. HRMS of 2DPACzBP.

Elemental Analysis Service Request Form

Researcher name Changfeng Si

Researcher email cs339@st-andrews.ac.uk

NOTE: Please submit ca. 10 mg of sample

Sample reference number	CS159-2DPACzBP
Name of Compound	2DPACzBP
Molecular formula	C92H62N8
Stability	
Hazards	
Other Remarks	

Analysis type:

Single Duplicate Triplicate

Analysis Result:

Element	Expected %	Found (1)	Found (2)	Found (3)
Nitrogen	8.76	8.70	8.82	
Carbon	86.36	86.06	86.77	
Hydrogen	4.88	4.79	4.83	

Authorising Signature:

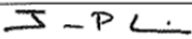
Date completed	09.05.23
Signature	
comments	

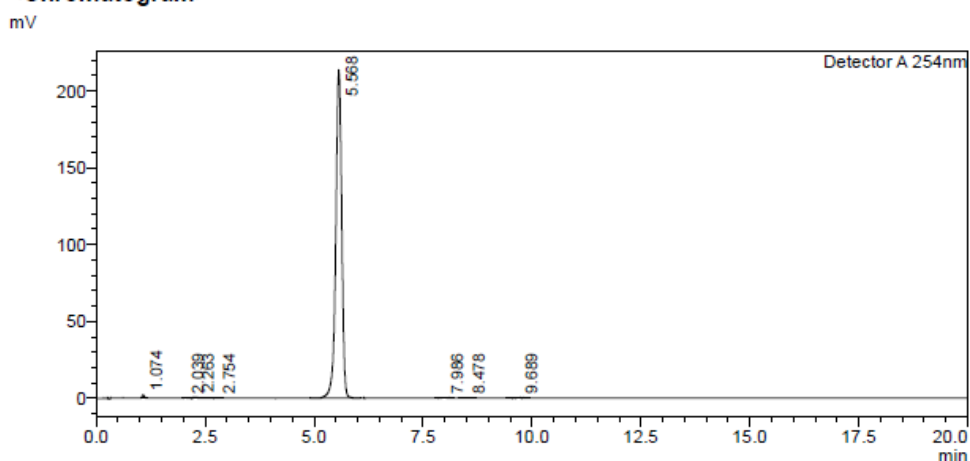
Figure 4.23. Elemental analysis of 2DPACzBP.

HPLC Trace Report 19 Nov 2021

<Sample Information>

Sample Name : 2DPACzBP
Sample ID :
Method Filename : 50% Acetonitrile 50 Water 20 mins.lcb
Batch Filename : 2DPACzBP-2.lcb
Vial # : 1-29
Injection Volume : 10 uL
Date Acquired : 19/11/2021 17:25:45
Date Processed : 19/11/2021 17:45:46
Sample Type : Unknown
Acquired by : System Administrator
Processed by : System Administrator

<Chromatogram>



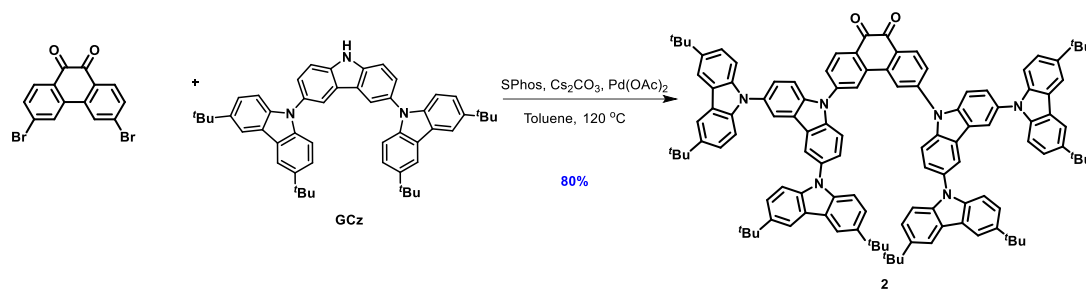
<Peak Table>

Detector A 254nm

Peak#	Ret. Time	Area	Height	Area%	Area/Height	Width at 5% Height
1	1.074	7677	2190	0.375	3.505	0.124
2	2.039	1922	375	0.094	5.122	-
3	2.263	4817	608	0.235	7.928	0.261
4	2.754	1201	138	0.059	8.707	0.256
5	5.568	2024379	213074	98.794	9.501	0.334
6	7.986	3910	344	0.191	11.355	0.351
7	8.478	1187	100	0.058	11.867	0.311
8	9.689	3993	305	0.195	13.086	0.409
Total		2049087	217135	100.000		

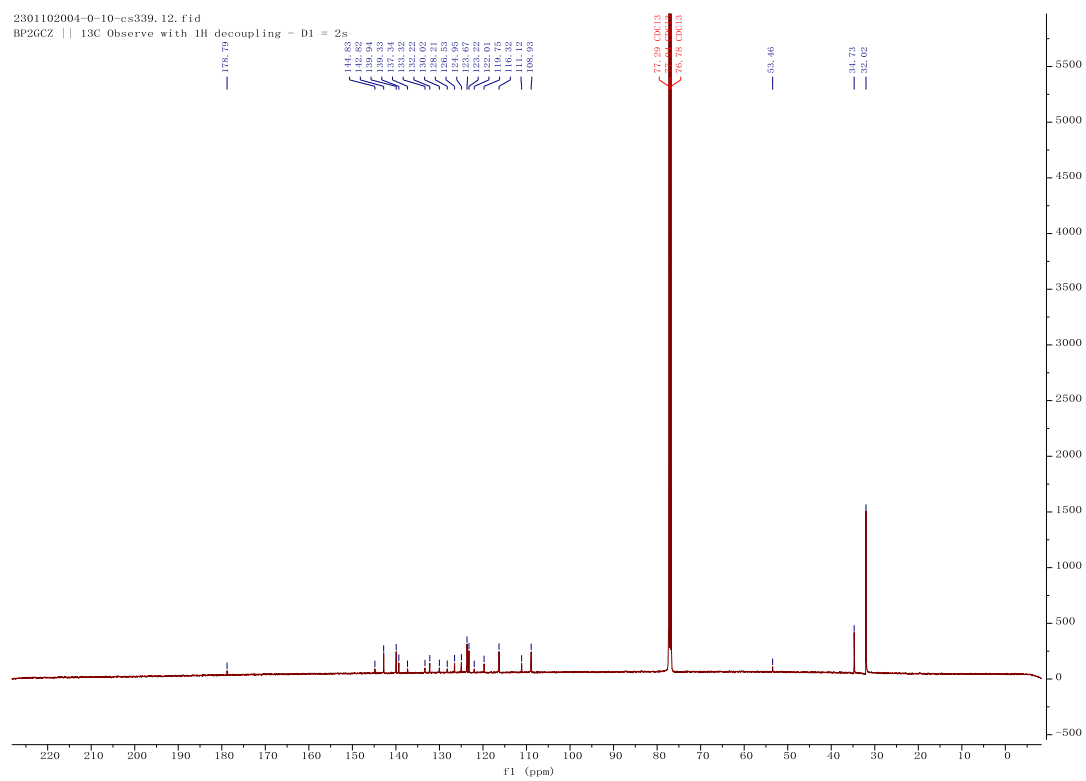
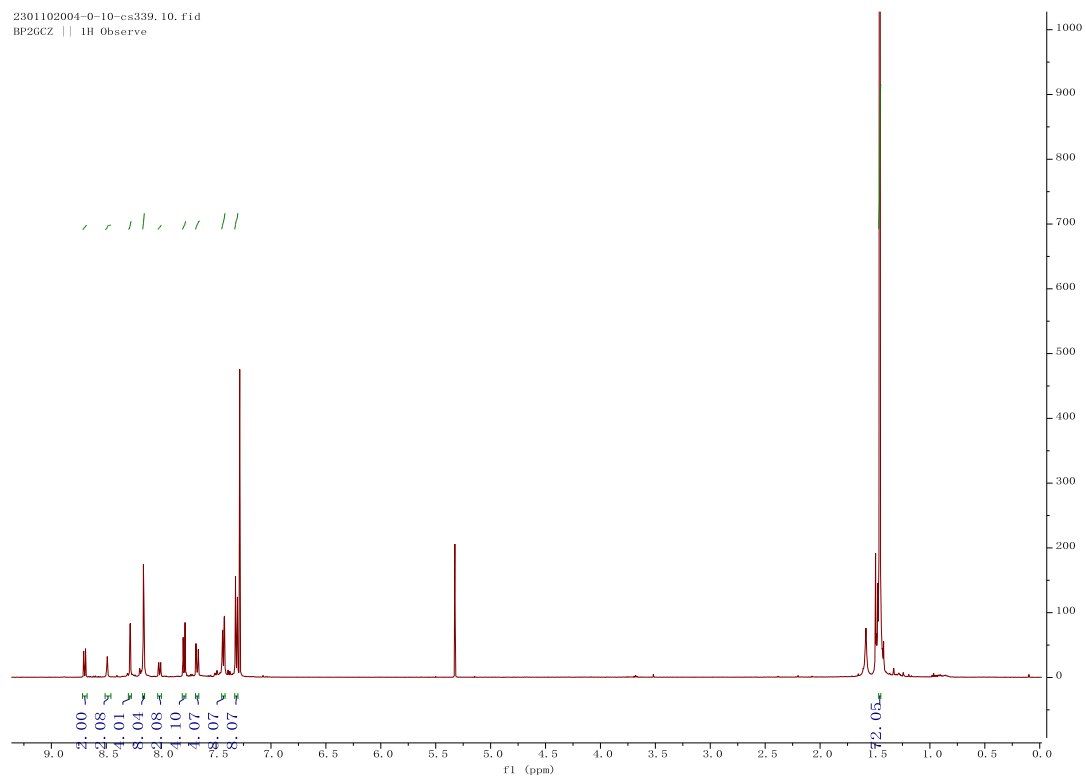
Figure 4.24. HPLC trace of 2DPACzBP.

Synthesis of 3,6-bis(3,3'',6,6''-tetra-*tert*-butyl-9'*H*-[9,3':6',9''-tercarbazol]-9'-yl)phenanthrene-9,10-dione (2):



Under a nitrogen atmosphere, to a 100 mL Schlenk flask were added 3,6-dibromo-9,10-phenanthrenequinone (0.5 g, 1.4 mmol, 1.0 equiv.), **GCz** (2.2 g, 3.0 mmol, 2.2 equiv.), Pd(OAc)₂ (0.015 g, 0.07 mmol, 0.05 equiv.), 2-dicyclohexylphosphino-2',6'-dimethoxybiphenyl (SPhos) (0.084 g, 0.2 mmol, 0.15 equiv.), Cs₂CO₃ (2.7 g, 8.2 mmol, 6.0 equiv.) and toluene (50 mL) was stirred at 110 °C for 24 h. After being cooled to room temperature, this reaction mixture was added aqueous NH₄Cl and was extracted with DCM (3×50 mL). The organic layer was dried over anhydrous Na₂SO₄, filtered, and concentrated to afford the crude product, which was purified by column chromatography. The crude product was purified by column chromatography on silica gel (25% DCM/Hexane) to afford **2** as black solid (yield =1.80 g).

3,6-bis(3,3'',6,6''-tetra-*tert*-butyl-9'*H*-[9,3':6',9''-tercarbazol]-9'-yl)phenanthrene-9,10-dione (2): R_f = 0.2 (25% DCM/Hexane). **Yield:** 80%. **Mp** = 341-343 °C. **¹H NMR (500 MHz, CDCl₃)** δ 8.70 (d, *J* = 8.3 Hz, 2H), 8.49 (d, *J* = 2.0 Hz, 2H), 8.28 (d, *J* = 2.0 Hz, 4H), 8.16 (d, *J* = 1.9 Hz, 8H), 8.01 (dd, *J* = 8.3, 1.8 Hz, 2H), 7.79 (d, *J* = 8.7 Hz, 4H), 7.67 (dd, *J* = 8.7, 2.0 Hz, 4H), 7.43 (dd, *J* = 8.7, 1.9 Hz, 8H), 7.31 (d, *J* = 8.6 Hz, 8H), 1.46 (s, 72H). **¹³C NMR (126 MHz, CDCl₃):** 178.79, 144.83, 142.82, 139.94, 139.33, 137.34, 133.32, 132.22, 130.02, 128.21, 126.53, 124.95, 123.67, 123.22, 122.01, 119.75, 116.32, 111.12, 108.93, 77.29, 77.04, 76.78, 53.46, 34.73, 32.02. **HR-MS [M+H]⁺ Calculated:** (C₁₁₈H₁₁₄N₆O₂) 1646.9003; **Found:** 1646.8998.



Generic Display Report (all)

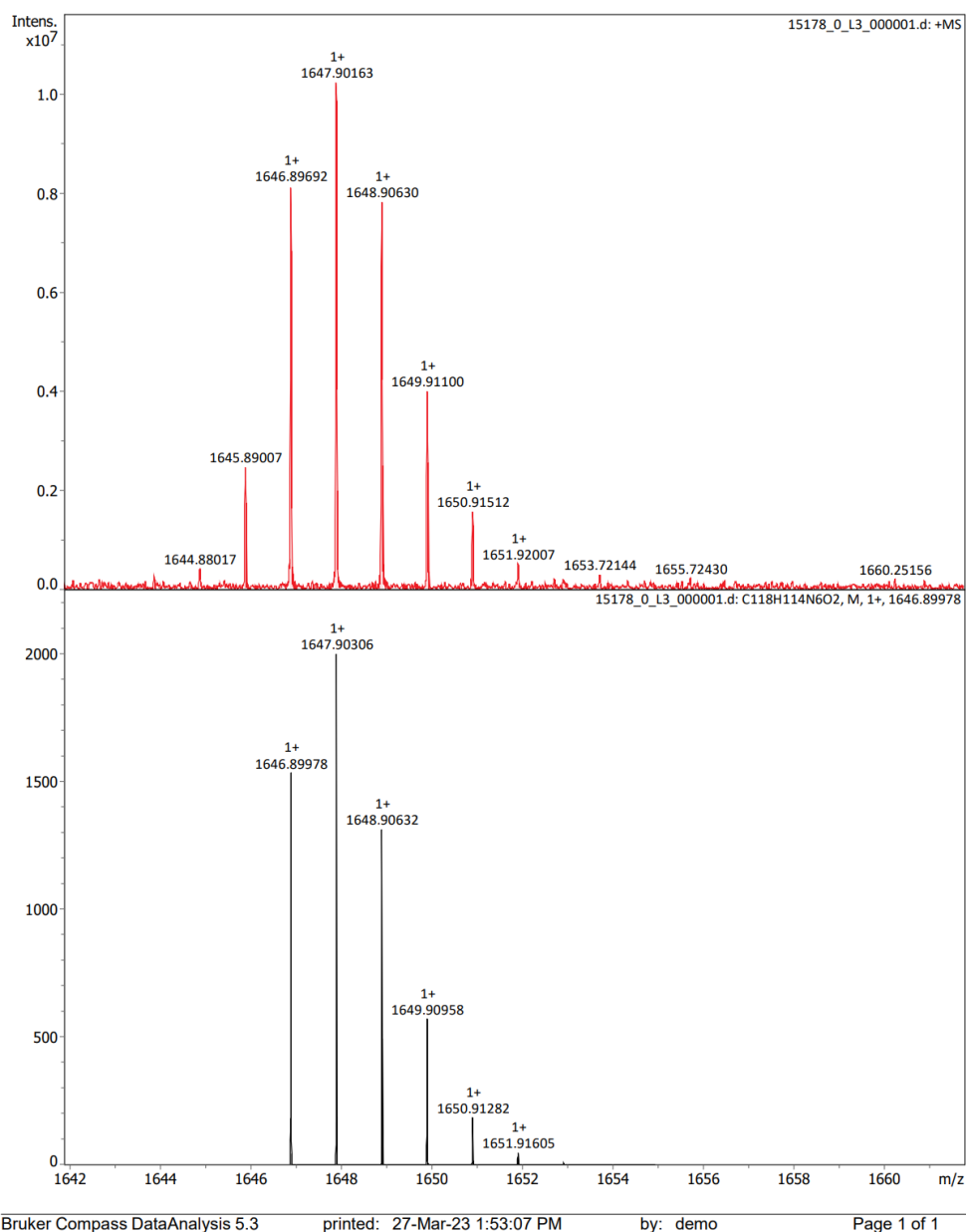
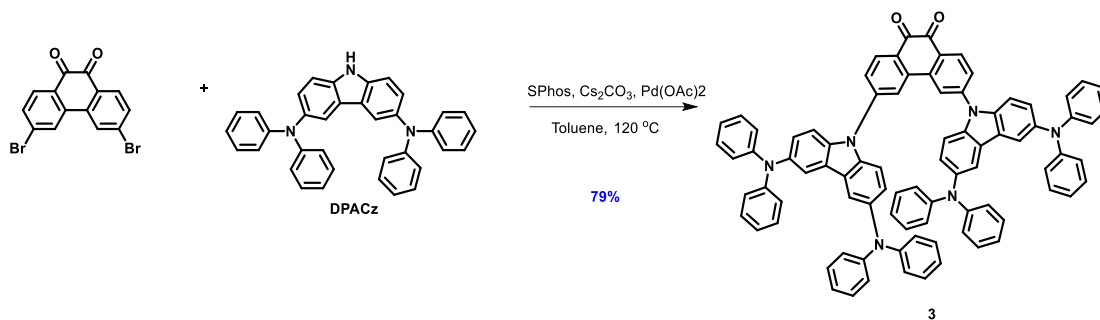


Figure 4.27. HRMS of 2.

Synthesis of 3,6-bis(3,6-bis(diphenylamino)-9H-carbazol-9-yl)phenanthrene-9,10-dione (3):



Under a nitrogen atmosphere, to a 100 mL Schlenk flask were added 3,6-dibromo-9,10-phenanthrenequinone (0.5 g, 1.4 mmol, 1.0 equiv.), **DPACz** (1.5 g, 3.0 mmol, 2.2 equiv.), Pd(OAc)₂ (0.015 g, 0.07 mmol, 0.05 equiv), 2-dicyclohexylphosphino-2',6'-dimethoxybiphenyl (SPhos) (0.084 g, 0.2 mmol, 0.15 equiv), Cs₂CO₃ (2.7 g, 8.2 mmol, 6.0 equiv.) and toluene (50 mL) was stirred at 110 °C for 24 h. After cooling to room temperature, the reaction mixture was added aqueous NH₄Cl and was extracted with DCM (3×50 mL). The organic layer was dried over anhydrous Na₂SO₄, filtered, and concentrated to afford the crude product, which was purified by column chromatography. The crude product was purified by column chromatography on silica gel (25% DCM/Hexane, v/v) to afford **3** as black solid (yield =1.30 g).

3,6-bis(3,6-bis(diphenylamino)-9H-carbazol-9-yl)phenanthrene-9,10-dione (3):

Yield: 79%. **R_f** = 0.2 (25% DCM/Hexane). **Mp** = 320-322 °C. **¹H NMR (400 MHz, CDCl₃)** δ 8.54 (d, J = 8.3 Hz, 2H), 8.24 (d, J = 2.0 Hz, 2H), 7.81 (dd, J = 8.2, 1.8 Hz, 2H), 7.78 (d, J = 2.1 Hz, 4H), 7.47 (d, J = 8.8 Hz, 4H), 7.25 – 7.20 (m, 20H), 7.09 – 7.05 (m, 16H), 6.97 (tt, J = 7.3, 1.2 Hz, 8H) ppm. **¹³C NMR (126 MHz, CDCl₃):** δ = 178.80, 148.29, 145.11, 142.04, 137.14, 136.97, 132.93, 129.20, 129.06, 128.25, 127.18, 126.02, 125.16, 123.05, 122.08, 121.06, 118.50, 110.85, 77.28, 77.03, 76.78. **HR-MS [M+H]⁺ Calculated:** (C₈₆H₅₈N₆O₂) 1206.4621; **Found:** 1206.4616.

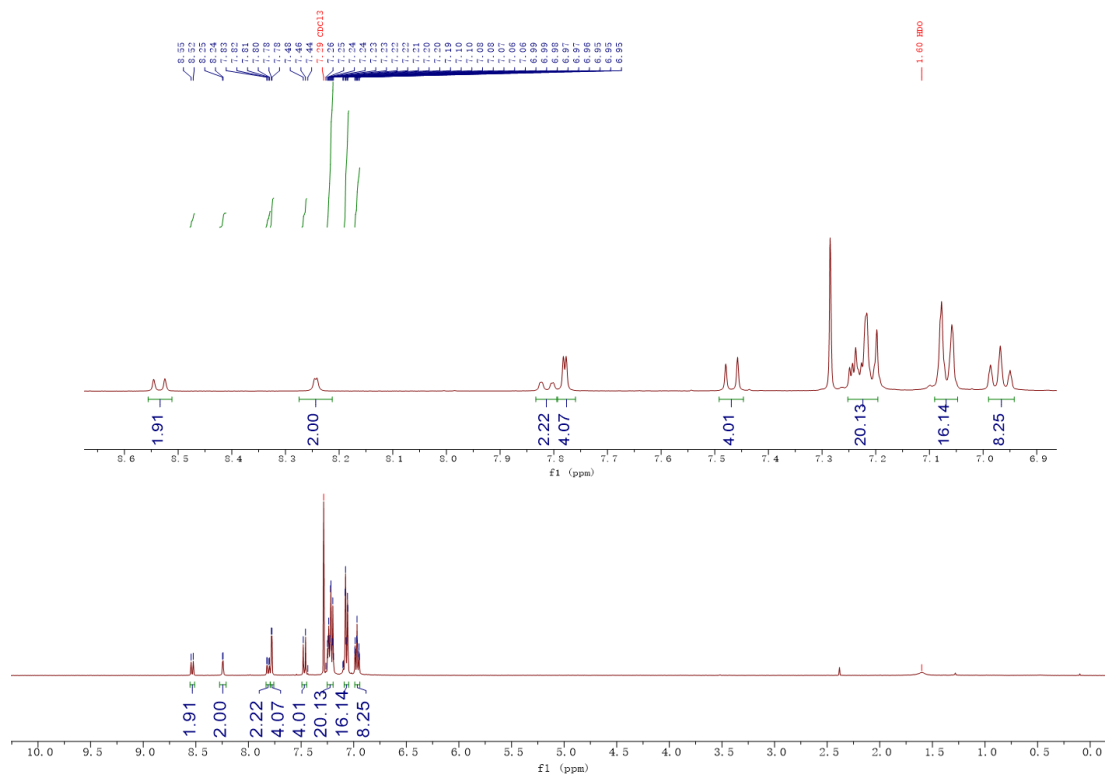


Figure 4.28. ^1H NMR spectra of **3** in CDCl_3 .

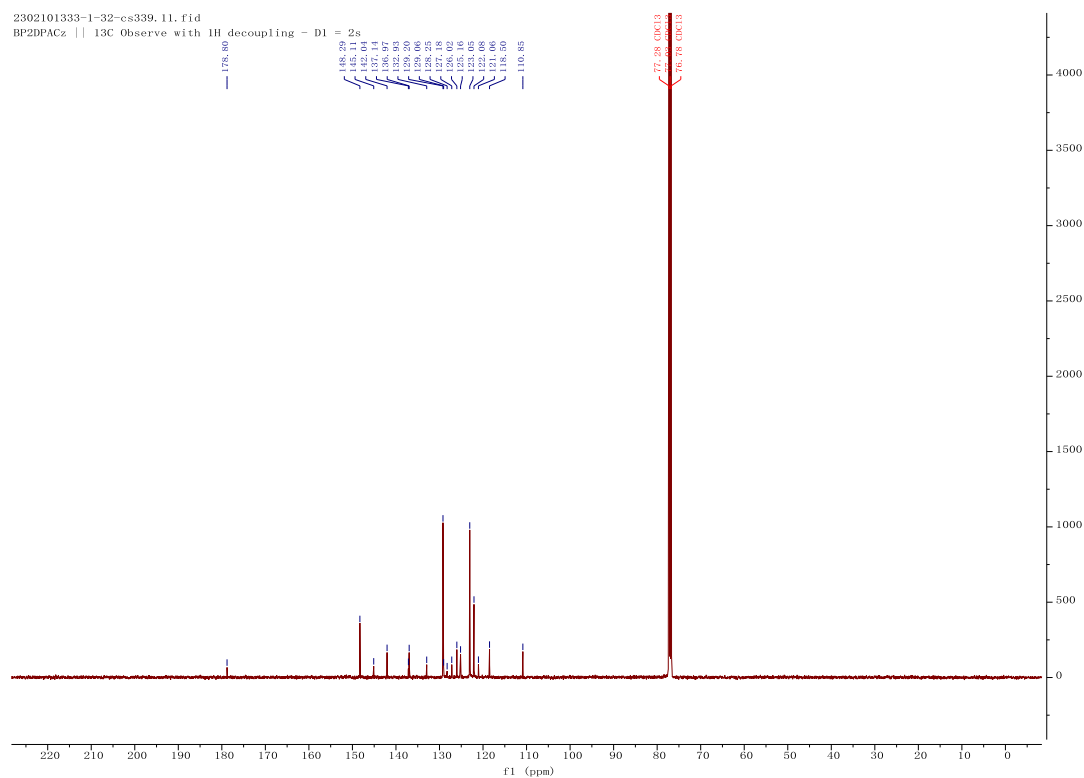
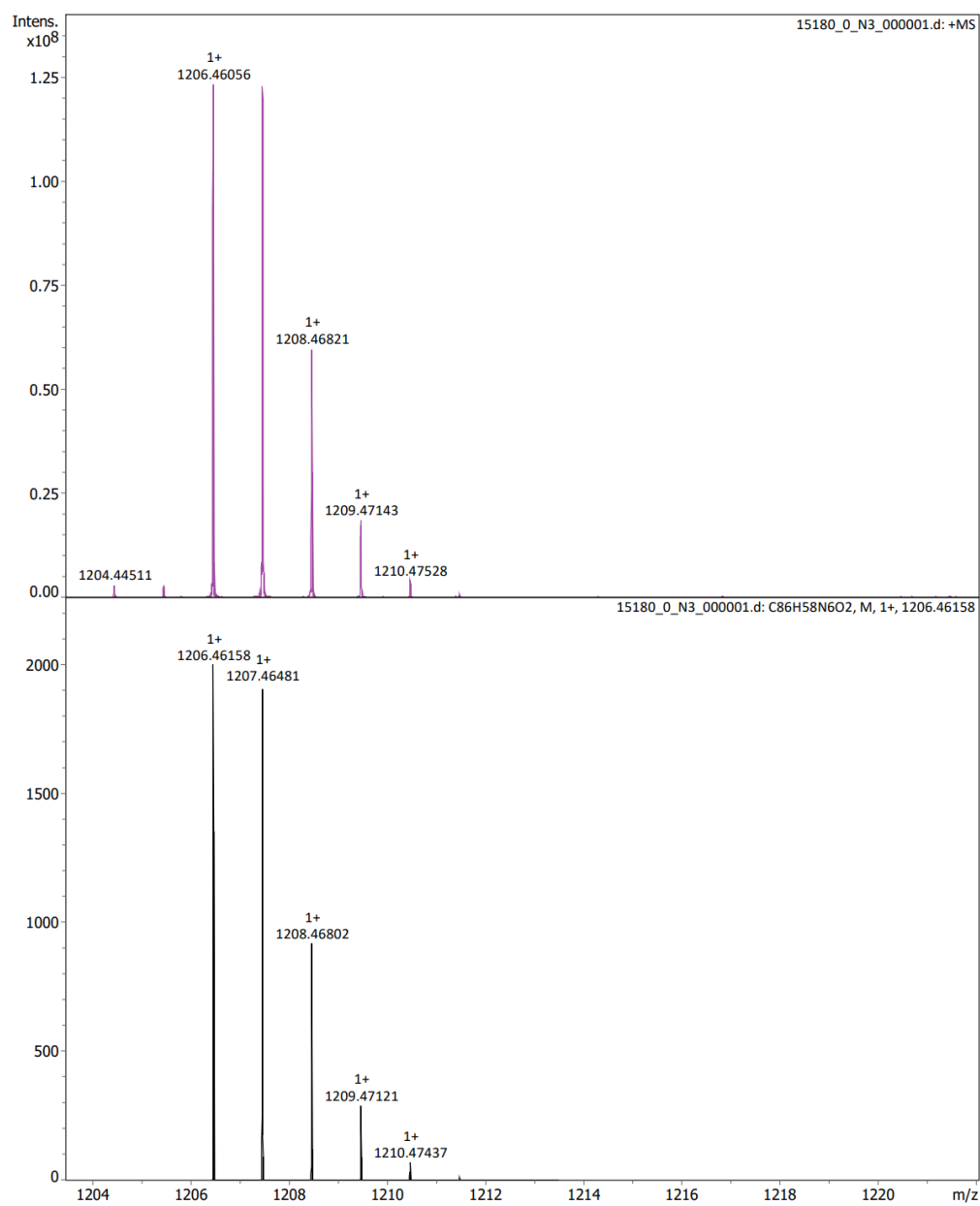


Figure 4.29. ^{13}C NMR spectra of **3** in CDCl_3 .

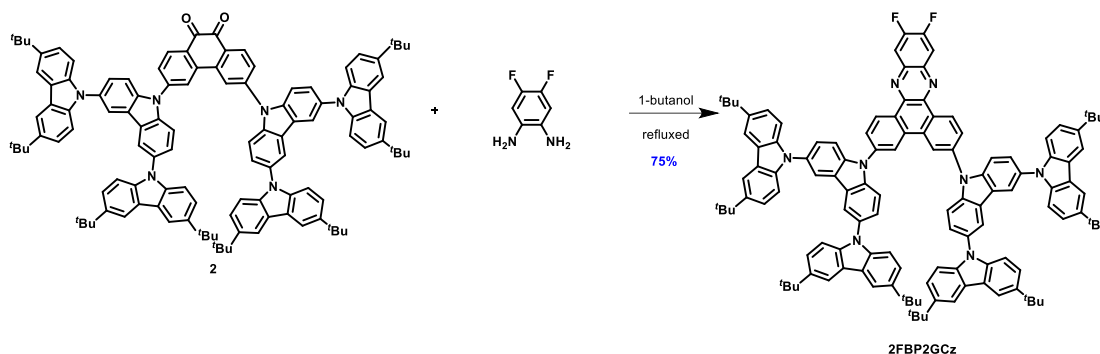
Generic Display Report (all)



Bruker Compass DataAnalysis 5.3 printed: 27-Mar-23 1:57:06 PM by: demo Page 1 of 1

Figure 4.30. HRMS of 3.

Synthesis of 11,12-difluoro-3,6-bis(3,3'',6,6''-tetra-*tert*-butyl-9'*H*-[9,3':6',9''-tercarbazol]-9'-yl)-8b,14a-dihydrodibenzo[*a,c*]phenazine (2FBP2GCz):



2 (0.4 g, 0.24 mmol, 1.0 equiv) and 4,5-difluorobenzene-1,2-diamine (0.035 g, 0.24 mmol, 1.0 equiv.) were added into 10 mL of 1-butanol and then heated at 130 °C for 14 h under a nitrogen atmosphere. After cooling to room temperature, the solution was poured into water and extracted with DCM (3×50 mL). The organic layer was dried over Na₂SO₄ and concentrated under reduced pressure. The residue was purified by column chromatography with (33% DCM/Hexane, v/v) to afford the compound **2FBP2GCz** as red solid (0.32 g).

11,12-difluoro-3,6-bis(3,3'',6,6''-tetra-*tert*-butyl-9'*H*-[9,3':6',9''-tercarbazol]-9'-yl)-8b,14a-dihydrodibenzo[*a,c*]phenazine (2FBP2GCz): Yield: 75%. R_f = 0.3 (33% DCM/Hexane). Mp = 368-370 °C. ¹H NMR (500 MHz, CDCl₃) δ 9.83 (d, *J* = 8.6 Hz, 2H), 9.01 (d, *J* = 2.1 Hz, 2H), 8.34 (d, *J* = 2.0 Hz, 4H), 8.25 (dd, *J* = 8.6, 1.9 Hz, 2H), 8.20 (t, *J* = 2.0 Hz, 10H), 7.83 (d, *J* = 8.7 Hz, 4H), 7.69 (dd, *J* = 8.7, 2.0 Hz, 4H), 7.63 – 7.30 (m, 18H), 1.49 (s, 72H). ¹³C NMR (126 MHz, CDCl₃): δ = 154.40, 154.25, 152.33, 152.18, 142.69, 141.84, 140.30, 140.11, 140.03, 139.83, 133.19, 131.55, 129.81, 129.03, 127.68, 126.39, 124.43, 123.66, 123.18, 121.61, 119.69, 116.28, 114.83, 111.07, 109.07, 77.32, 77.06, 76.81, 34.76, 32.07. HR-MS [M+H]⁺ Calculated: (C₁₂₄H₁₁₈F₂N₈) 1754.9291; Found: 1754.9285. Anal. Calcd. for C₁₀₄H₇₈N₄: C, 84.80%; H, 6.66%; N, 6.38%. Found: C, 84.81%; H, 6.68%; N, 6.39%. HPLC analysis: 99.49% pure on HPLC analysis, retention time 13.01 minutes in 100% THF.

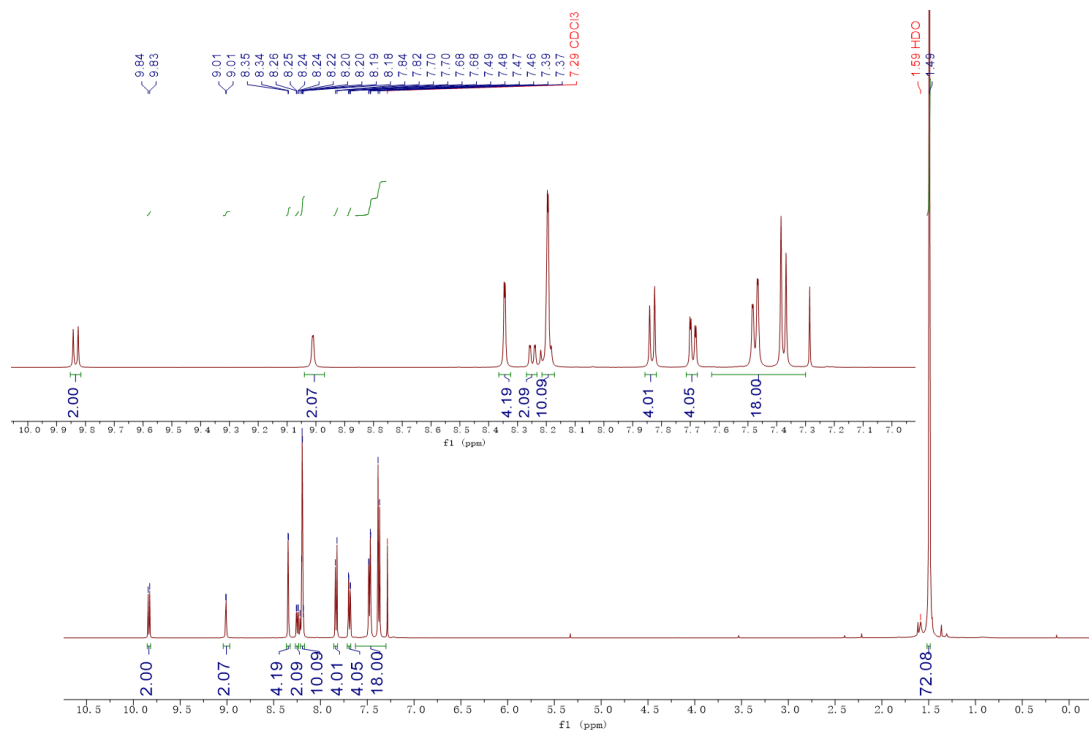


Figure 4.31. ^1H NMR spectra of **2FBP2GCz** in CDCl_3 .



Figure 4.32. ^{13}C NMR spectra of **2FBP2GCz** in CDCl_3 .

Generic Display Report (all)

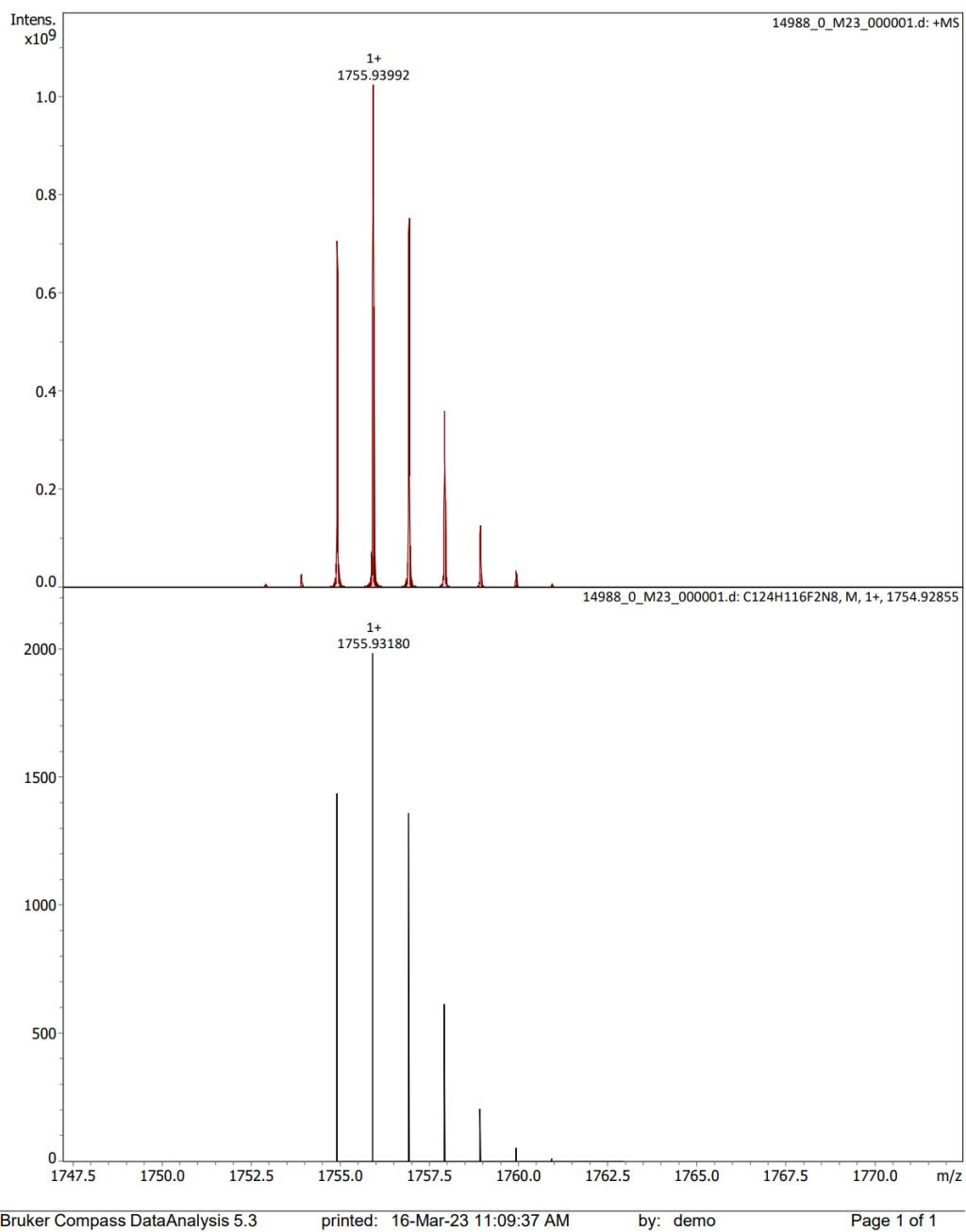


Figure 4.33. HRMS of 2FBP2GCz.

Elemental Analysis Service Request Form

Researcher name Changfeng Si

Researcher email cs339@st-andrews.ac.uk

NOTE: Please submit ca. 10 mg of sample

Sample reference number	CS146-2FBP2GCz
Name of Compound	2FBP2GCz
Molecular formula	C124H116F2N8
Stability	
Hazards	
Other Remarks	

Analysis type:

Single Duplicate Triplicate

Analysis Result:

Element	Expected %	Found (1)	Found (2)	Found (3)
Nitrogen	6.38	6.36	6.42	
Carbon	84.80	84.90	84.72	
Hydrogen	6.66	6.65	6.70	

Authorising Signature:

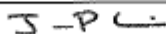
Date completed	09.05.23
Signature	
comments	

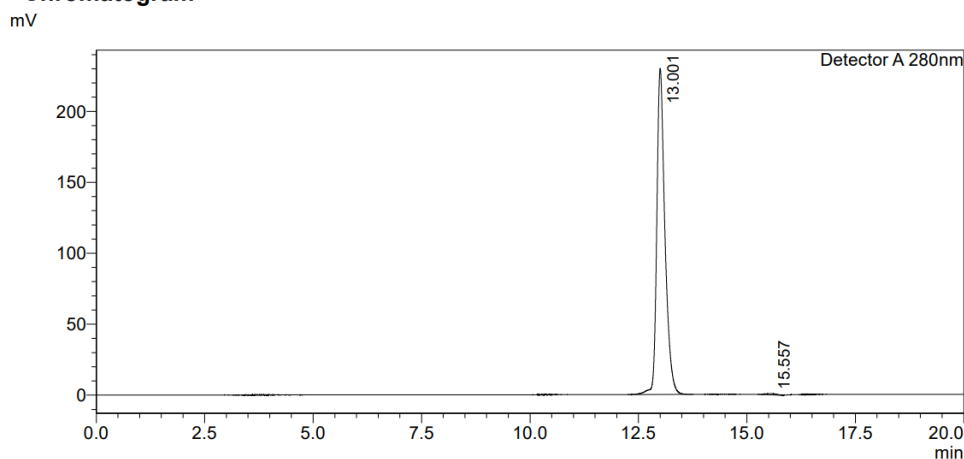
Figure 4.34. EA of 2FBP2GCz.

HPLC Trace Report01Jul2022

<Sample Information>

Sample Name : 2FBP2GCz
Sample ID : 2FBP2GCz
Method Filename : 100% THF 20 mins 280nm - new-please use.lcm
Batch Filename : 2FBP2GCz.lcb
Vial # : 1-11
Injection Volume : 10 uL
Date Acquired : 01/07/2022 15:09:09
Date Processed : 01/07/2022 15:29:11
Sample Type : Unknown
Acquired by : System Administrator
Processed by : System Administrator

<Chromatogram>

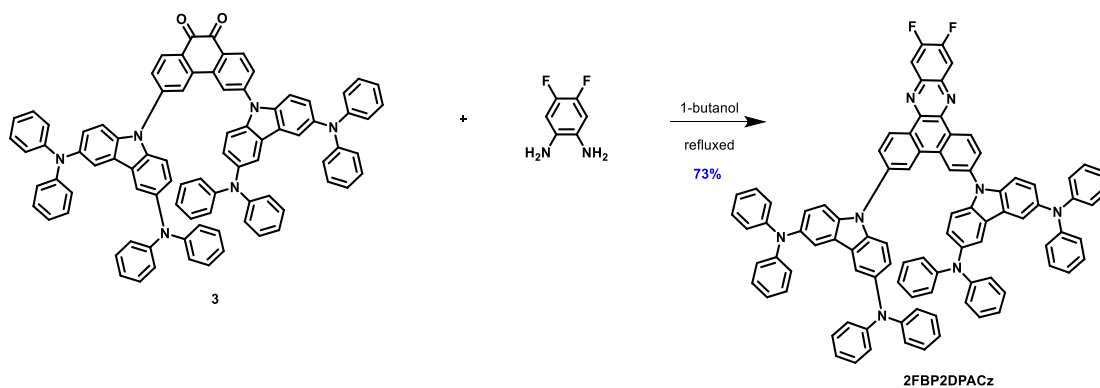


<Peak Table>

Peak#	Ret. Time	Area	Height	Area%	Area/Height	Width at 5% Height
1	13.001	3004828	229459	99.491	13.095	0.465
2	15.557	15368	866	0.509	17.747	0.495
Total		3020196	230325	100.000		

Figure 4.35. HPLC of 2FBP2GCz.

Synthesis of 9,9'-(11,12-difluorodibenzo[*a,c*]phenazine-3,6-diyl)bis(*N*³,*N*³,*N*⁶,*N*⁶-tetraphenyl-9*H*-carbazole-3,6-diamine) (2FBP2DPACz):



3 (0.3 g, 0.25 mmol, 1.0 equiv.) and 4,5-difluorobenzene-1,2-diamine (0.036 g, 0.25 mmol, 1.0 equiv.) were added into 10mL of 1-butanol and then heated at 130 °C for 14

h under a nitrogen atmosphere. After cooling to room temperature, the solution was poured into water and extracted with DCM (3×50 mL). The organic layer was dried over Na₂SO₄ and concentrated under reduced pressure. The residue was purified by column chromatography with (33% DCM/Hexane) to afford the compound **2FBP2DPACz** as red solid (0.24 g).

9,9'-(11,12-difluorodibenzo[*a,c*]phenazine-3,6-diyl)bis(N³,N³,N⁶,N⁶-tetraphenyl-9*H*-carbazole-3,6-diamine) (2FBP2DPACz): Yield: 73%. R_f = 0.3 (33% DCM/Hexane). Yield: 73%. Mp = 265-266 °C. ¹H NMR (400 MHz, CDCl₃) δ 9.64 (d, *J* = 8.5 Hz, 2H), 8.73 (d, *J* = 2.0 Hz, 2H), 8.18 – 8.01 (m, 6H), 7.84 (d, *J* = 2.2 Hz, 4H), 7.50 (d, *J* = 8.7 Hz, 4H), 7.27 – 7.21 (m, 20H), 7.10 (d, *J* = 7.6 Hz, 14H), 6.97 (t, *J* = 7.3 Hz, 8H). ¹³C NMR (126 MHz, CDCl₃): δ 148.45, 141.88, 141.26, 140.15, 139.81, 138.08, 133.04, 129.15, 128.98, 128.57, 127.07, 126.14, 124.55, 122.88, 121.83, 120.86, 118.77, 114.70, 110.72. HR-MS (Xevo G2-S) [M+H]⁺ Calculated: (C₉₂H₆₀F₂N₈) 1314.4909; Found: 1314.4903. Anal. Calcd. for C₉₂H₆₀F₂N₈: C, 84.00%; H, 4.60%; N, 8.52%. Found: C, 85.76%; H, 4.66%; N, 8.43%. HPLC analysis: 99.70% pure on HPLC analysis, retention time 13.57 minutes in 100% THF.

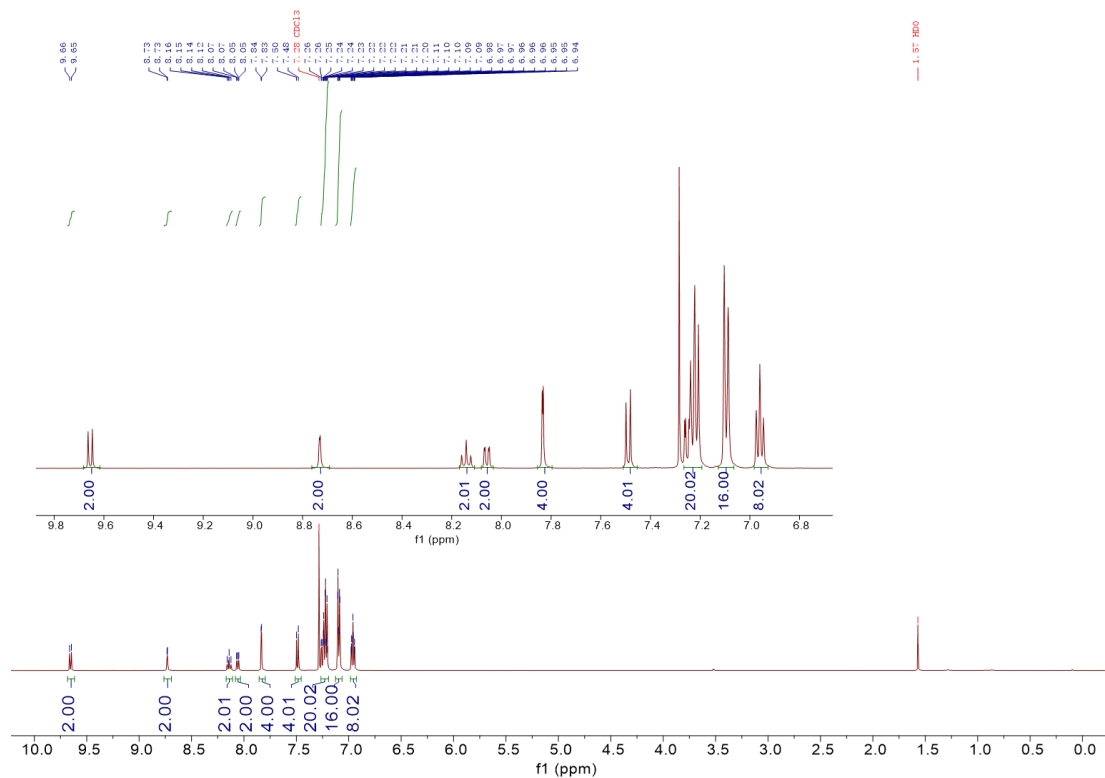


Figure 4.36. ^1H NMR spectra of **2FBP2DPACz** in CDCl_3 .

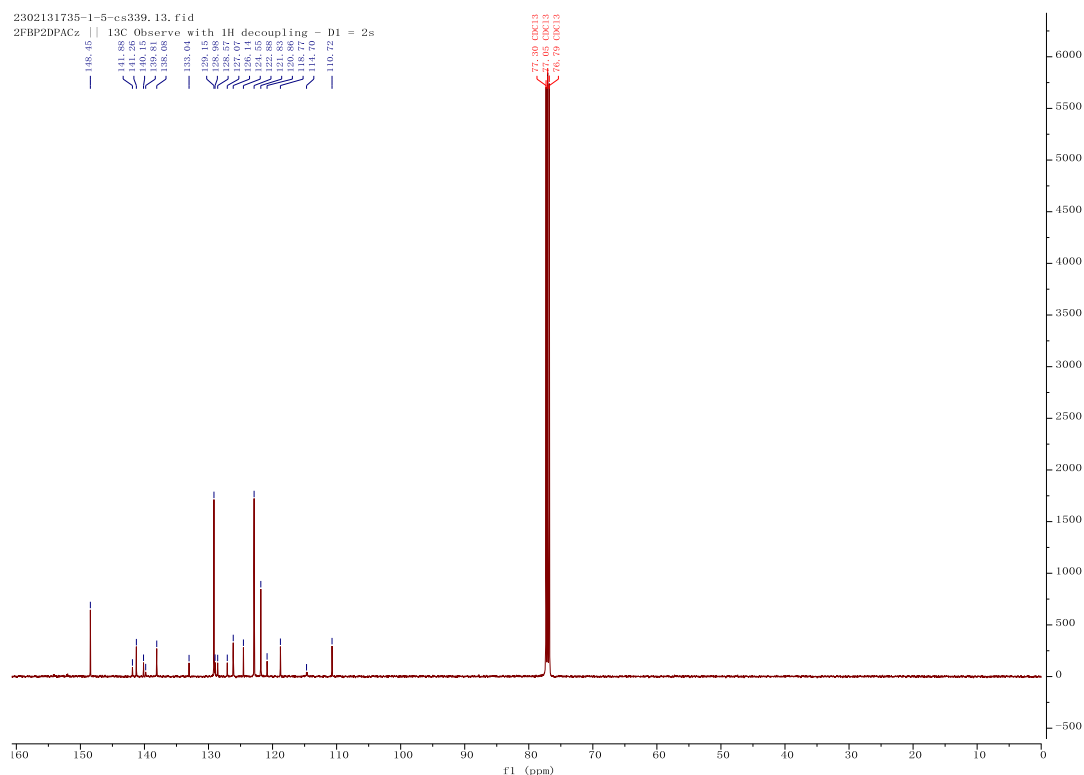


Figure 4.37. ^{13}C NMR spectra of **2FBP2DPACz** in CDCl_3 .

Generic Display Report (all)

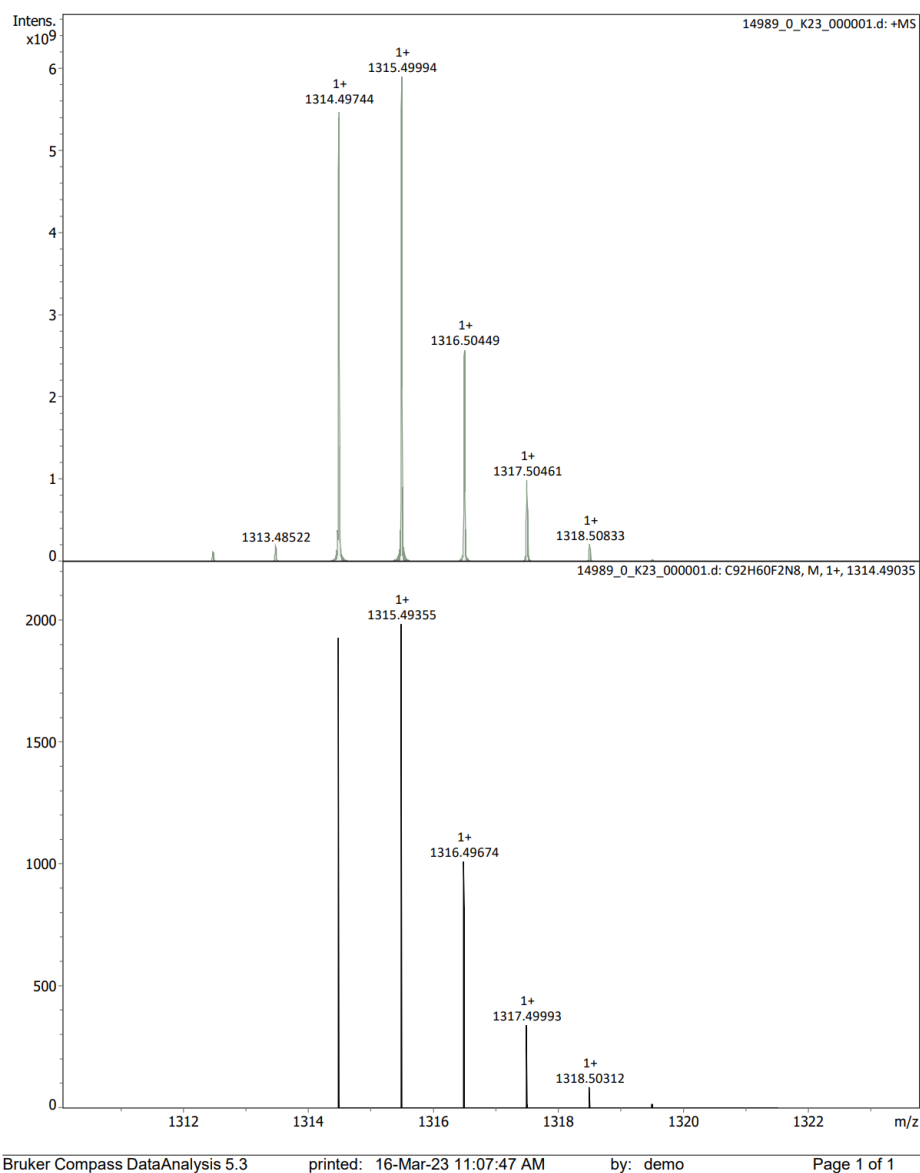


Figure 4.38. HRMS of 2FBP2DPACz.

Elemental Analysis Service Request Form

Researcher name Changfeng Si

Researcher email cs339@st-andrews.ac.uk

NOTE: Please submit ca. 10 mg of sample

Sample reference number	CS204-2FBPDPACz
Name of Compound	2FBPDPACz
Molecular formula	C92H60F2N8
Stability	
Hazards	
Other Remarks	

Analysis type:

Single Duplicate Triplicate

Analysis Result:

Element	Expected %	Found (1)	Found (2)	Found (3)
Nitrogen	8.52	8.43	8.37	
Carbon	84.00	85.76	85.77	
Hydrogen	4.60	4.70	4.66	

Authorising Signature:

Date completed	09.05.23
Signature	J - P L.
comments	

Figure 4.39. EA of 2FBP2DPACz.

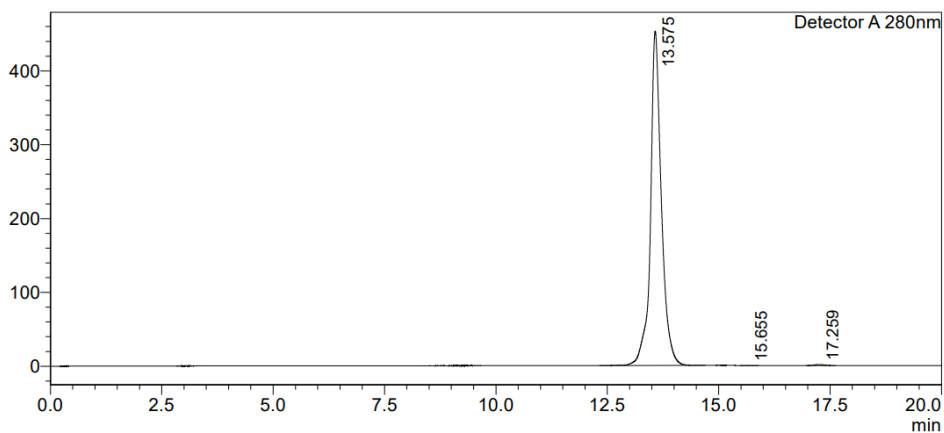
HPLC Trace Report12Sep2022

<Sample Information>

Sample Name : 2FBP2DPACz
Sample ID : 2FBP2DPACz
Method Filename : 100% THF 20 mins 280nm - new-please use.lcm
Batch Filename : 2FBP2GCz.lcb
Vial # : 1-11
Injection Volume : 20 uL
Date Acquired : 12/09/2022 19:31:21
Date Processed : 12/09/2022 19:51:23
Sample Type : Unknown
Acquired by : System Administrator
Processed by : System Administrator

<Chromatogram>

mV



<Peak Table>

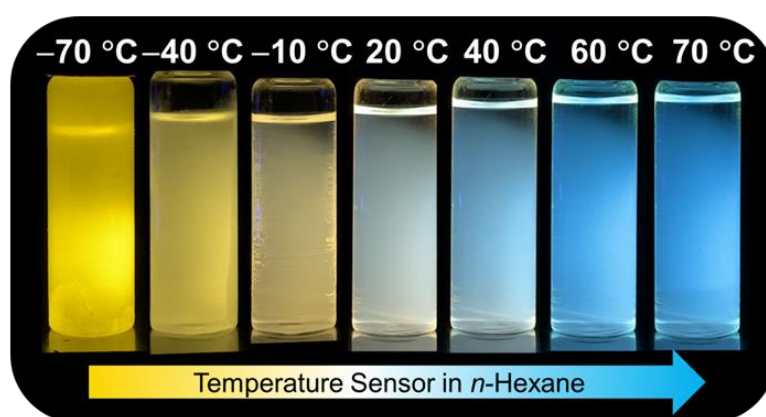
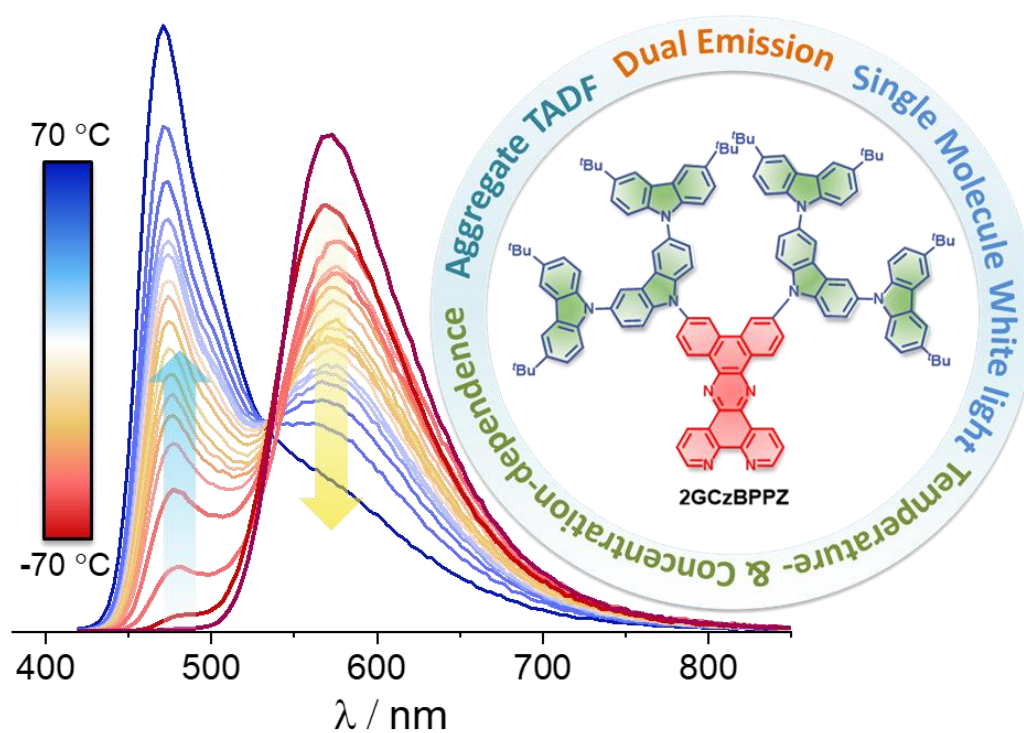
Detector A 280nm

Peak#	Ret. Time	Area	Height	Area%	Area/Height	Width at 5% Height
1	13.575	7728085	452445	99.703	17.081	0.724
2	15.655	2590	220	0.033	11.779	0.319
3	17.259	20430	1363	0.264	14.990	0.472
Total		7751105	454028	100.000		

Figure 4.40. HPLC of 2FBP2DPACz.

Chapter 5: A Sensitive Temperature Sensor with a Large Dynamic Spectral Range Based on a Dual-emissive Thermally Activated Delayed Fluorescence

Dendrimer Material



Manuscript of this project is under preparation as

Changfeng Si, Dianming Sun, Eli Zysman-Colman*

Dr. Dianming Sun carried out the OLED device fabrication.

I completed all the syntheses and characterization, DFT and TD-DFT calculations, electrochemistry, photophysics measurements, temperature sensor measurement and I am the principal author of the text.

5.1 Introduction

In **Chapter 4**, we systematically investigated the effect of substitution position and the strength of the donors on the optoelectronic properties of four dendrimers containing BP as the acceptor. In this Chapter, a related BPN acceptor is combined with two G2Cz donors, forming a more red-shifted emission compound **2GCzBPN**, compared to **2GCzBP** (in **Chapter 4**). In addition, a much larger planarity and π -conjugation acceptor BPPZ has been designed, derived from the BPN acceptor. The target compound **2GCzBPPZ** was synthesized using the same donor as **2GCzBPN**. Interestingly, **2GCzBPN** and **2GCzBPPZ** exhibit totally different photophysical properties, due to their different geometry. Especially, **2GCzBPPZ** shows unusual dual emission that is both concentration-dependent and temperature-dependent in solution, which is the first observation of aggregate emission from TADF dendrimers in solution.

As discussed in **Chapter 1**, TADF relies on there being a relatively small ΔE_{ST} to enable RISC at ambient temperatures. To obtain a small ΔE_{ST} in purely organic molecules, the most widely adopted strategy is to introduce a strongly twisted D-A system, that produces an S_1 state of intramolecular charge transfer character, and which also results in a compound where there is a small overlap of the electron density between the HOMO and the LUMO.^{115,318} Most of TADF, and indeed most emissive, compounds only emit from a single, low-lying excited state, adhering to Kasha's rule.^{319,320}

Several strategies have been advanced to design organic TADF molecules that show dual-emission characteristics from a single component, behavior that could be exploited to produce white-light emission,³²¹ or in sensing²⁵⁴ or bioimaging.³²² Dual emission can be induced where an emissive compound exists in multiple conformations, each with their distinct photophysical properties. First reported by Adachi and co-workers, who designed a D-A TADF emitter, **PTZ-TRZ** (Figure **5.1a**), this compound exists in both a quasi-axial (A) and quasi-equatorial (E) conformation and shows dual ICT fluorescence.³²³ Li *et al.* reported the compound **a-DMAc-TRZ** (Figure **5.1a**), which shows emission from two different conformations.³²⁴ Dual emission can also arise from equilibrated LE and CT excited states.²⁵⁸ Geng *et al.* designed two molecules, **TMCz- σ -TRZ** and **DMAc- σ -TRZ** (Figure **5.1b**), that contain a

hexafluoroisopropylidene σ -bridging unit between the D and A moieties. Both of these D- σ -A compounds showed simultaneous emission from LE and CT states, the latter of which showed TADF character.³²⁵ Another design involves the dual emission from hybrid intramolecular and intermolecular CT excited states. Most TADF systems emit from either an intramolecular CT (intra-CT) excited state or an intermolecular CT (inter-CT) excited state, such as exists in an exciplex; however, there are a limited number of reports of TADF systems where there is a coexistence of intra- and inter-CT states.^{326,327} For instance, Chi and co-workers explored four asymmetrical D-A-D' compounds, **CPzP**, **CPzPO**, **SPzP** and **SPzPO** (Figure 5.1c), each showing dual emission. In solution, as the concentration increased, the emission maximum of the high-energy intra-CT bands remained unchanged whereas the low-energy inter-CT bands increased in intensity significantly, which the authors attributed to the enhanced C-H \cdots O hydrogen bonding between adjacent molecules.³²⁶ Finally, some TADF molecules containing an asymmetric triad structure showed dual emission emanating from two different ICT transitions from different donors to a common acceptor. For examples, Zhu *et al.* developed a TADF emitter (Figure 5.1d) that combined PTZ (D) and N-(1H-indole-5-yl) acetamide (D') as donors each attached to the same diphenylsulfone acceptor that showed dual emission.³²² The formation of an intermolecular H-bonding network and the quasi-equatorial conformation of the PTZ made the dual TADF emission strong both in dilute solution and in the aggregated state.

In addition to the aforementioned strategies, modulating the ratio of excimers/aggregates versus monomer species would be another strategy to obtain dual emission systems.³²⁸⁻³³⁴ Generally, excimer formation is favored when the structure of the emitter is rigid and planar, such as is found in anthracene,³³⁵ pyrene,³³⁶ and fluorene.³³⁷ However, those type of polycyclic aromatic hydrocarbons (units) are not suitable for constructing TADF compounds as their triplet energies are too low in energy, leading invariably to compounds with large ΔE_{ST} , regardless of donor substitution. Excimers are uncommon in highly twisted D-A TADF compounds due to sterics that impede the required intermolecular π -stacking interactions.^{338,339} Aggregates are clusters of molecules that are held together by intermolecular interactions and form in the ground state, unlike excimers that form in the excited state.³⁴⁰ However, most emissive aggregates exhibit a single emission band that is red-shifted (J-aggregation) or blue-

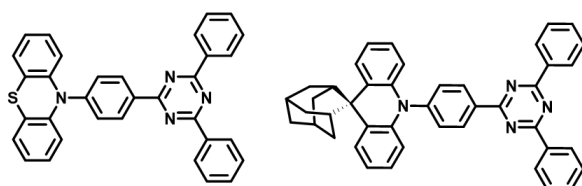
shifted (H-aggregation) compared to the emission of the monomeric species.^{36,341,342} There are relatively few examples of dual emission TADF systems resulting from a combination of monomer and aggregate emission, especially in the solution state.³⁴³

Optical temperature sensing using organic fluorophores has been developed over the past two decades, there are now examples of organic temperature sensors that show high sensitivity, fast response, simple operation, and have been used in diverse applications such as bioimaging,^{344–349} fluorescent thermometers,³⁴⁴ and microfluidic.³⁵⁰ Detection using these sensors typically relies on the temperature dependence of one of the emission intensity,³⁵¹ wavelength,^{352,353} and lifetime.³⁵⁴ Most of the small molecule temperature-sensitive fluorescent probes are derived from rhodamine, BODIPY or molecules emitting from a twisted intramolecular charge transfer (TICT) state, whose emission intensity and/or lifetime are temperature dependent and where the sensors operate typically over a temperature range from around 20 °C to 70 °C.^{345,355–357} Organic TADF materials have also shown promise as temperature sensors.^{8,33–39} However, most TADF-based temperature sensors rely only on changes in the emission lifetimes or emission intensity of the materials, which are governed by the endothermic nature of the RISC processes. For example, Farinha and co-workers reported the encapsulation of C₇₀ in polymer nanoparticles, this system shows a emission intensity increase with increasing temperature, corresponding to a working range from –75 °C to 105 °C.³⁶¹ Borisov and co-workers developed TADF-based temperature probes by encapsulating TADF compounds in a low-oxygen permeability polymer (P(VDC-*co*-AN)), these materials feature good temperature sensitivity in the range of 5 °C to 50 °C with 1.4–3.7% K⁻¹ change of delayed lifetime, τ_d , at 298 K.³⁵⁹ However, these two examples of temperature sensors that rely on emission lifetime or intensity change are generally more complex to integrate into devices than traditional temperature sensors due to the need for specialized instrumentation for their excitation and detection, thereby limiting their wider use. A second class of TADF-based temperature sensors rely on changes in emission color; however, there are very few reports of spectral TADF temperature sensors. Hudson and co-workers designed a temperature-responsive polymer by co-polymerization of the TADF monomer, **NAI-DMAC**, with *N*-isopropylacrylamide and a blue fluorescent dopant (*t*BuODA) as a Förster resonance energy transfer (FRET) acceptor. The polymer was used as a ratiometric temperature sensors that

varied its color from red TADF emission at room temperature to blue fluorescence at 70 °C, showing a high ratiometric fluorescent thermal response of $32 \pm 4\% \text{ K}^{-1}$ over a temperature range from 20 °C to 70 °C.

In this Chapter, two different rigid and planar N-doped PAHs were employed as the acceptors in two TADF dendrimers containing a second-generation tercarbazole donor dendron, GCz. The chemical structures of the dendrimers 12,15-bis(3,3'',6,6''-tetra-*tert*-butyl-9'*H*-[9,3':6',9''-tercarbazol]-9'-yl)dibenzo[*a,c*]dipyrido[3,2-*h*:2',3'-] phenazine (**2GCzBPPZ**) and 11,12-bis(3,3'',6,6''-tetra-*tert*-butyl-9'*H*-[9,3':6',9''-tercarbazol]-9'-yl)dipyrido[3,2-*a*:2',3'-*c*]phenazine (**2GCzBPN**) are shown in Figure 5.1e. Compound **2GCzBPPZ** possesses a complex concentration- and temperature-dependent dual emission where the longer wavelength emission band shows TADF. Through a combination of detailed photophysical studies and theoretical calculations we attribute to the emission from both monomolecular and aggregates species. Due to the more twisted geometry and the presence of bulky substituents, **2GCzBPN** exhibits TADF and aggregates formation is suppressed. The distinct photophysical properties of **2GCzBPPZ** motivated us to use it as a temperature sensor. **2GCzBPPZ** exhibits excellent temperature sensitivity across a very wide temperature range (−70 °C to 70 °C), corresponding to a large color change from yellow at −70 °C through white at room temperature to sky blue at 70 °C, which is to the best of our knowledge one of the best TADF-based temperature sensors based on its large dynamic spectral range and associated wide temperature detection range emanating from a single material. Finally, we also employed these two dendrimers as emitters in solution-processed OLEDs.

(a) Dual-emission from dual conformations



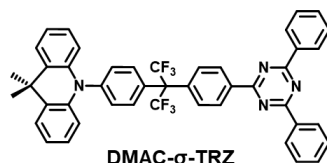
PTZ-TRZ

J. Phys. Chem. C **2014**, *118*, 15985

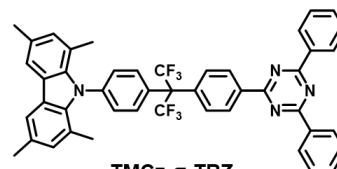
a-DMac-TRZ

Angew. Chem. **2019**, *131*, 592

(b) Dual-emission from equilibrated LE and CT



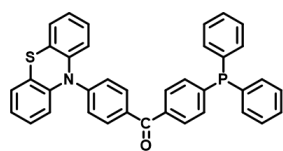
DMAC-σ-TRZ



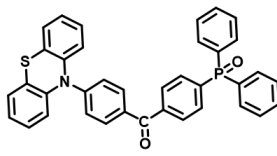
TMCz-σ-TRZ

Angew. Chem. **2017**, *129*, 16763

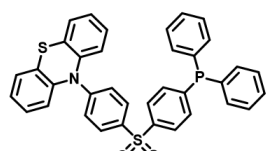
(c) Dual-emission from hybrid intramolecular and intermolecular CT



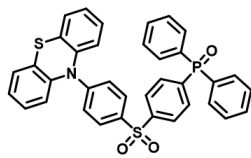
CPzP



CPzPO



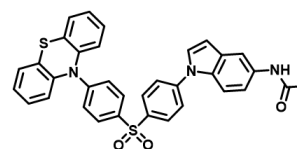
SPzP



SPzPO

Adv. Funct. Mater. **2017**, *27*, 1703918

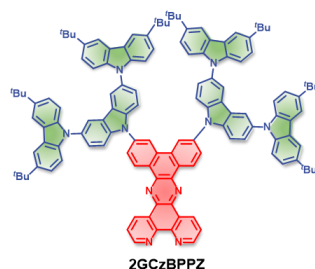
(d) Dual-emission from two ICTs based on asymmetric triad structures



M-1

Angew. Chem. **2020**, *132*, 17166

(e) This work

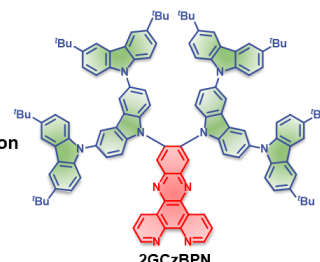


2GCzBPPZ

- Dual emission
- Concentration-dependent
- Temperature-dependent
- Single-molecule white light
- Aggregate TADF

VS

Single emission
TADF



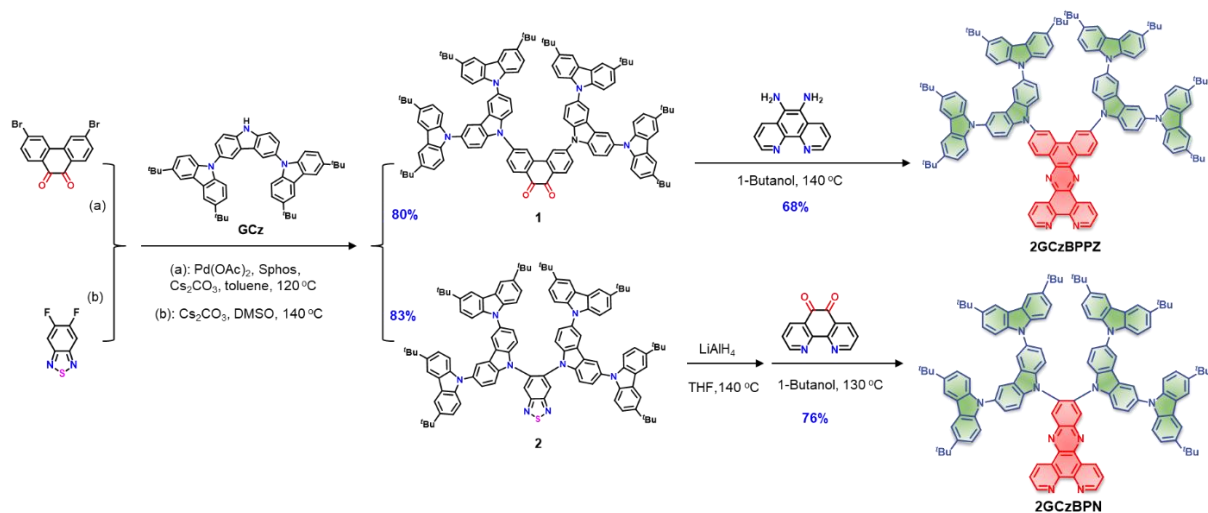
2GCzBPN

Figure 5.1. Dual emission from (a) dual conformations, (b) equilibrated LE and CT states, (c) “hybrid intramolecular and intermolecular CT” states and (d) two ICT states based on asymmetric triad structures; (e) this work: dual emission from TADF monomers and aggregates.

5.2 Synthesis

Scheme 5.1 shows the synthetic routes for 2GCzBPPZ and 2GCzBPN. Intermediates 1 and 2 were synthesized by, respectively, coupling G2Cz to the corresponding halogenated acceptor core via a Buchwald-Hartwig C-N cross-coupling or by nucleophilic aromatic substitution reaction in yields of 80 and 83%. Emitters 2GCzBPPZ and 2GCzBPN were obtained by the condensation reaction of 1 and 2 with 1,10-phenanthroline-5,6-diamine and 1,10-phenanthroline-5,6-dione, respectively. The identity and purity of the two emitters were

verified by ^1H NMR, ^{13}C NMR spectroscopy, melting point determination, high resolution mass spectrometry and elemental analysis and HPLC (Figures 5.12-27 in 5.10 Experimental Section).



Scheme 5.1. Synthetic Routes for **2GCzBPPZ** and **2GCzBPN**.

5.3 Theoretical Calculations

The S_0 geometries of **2GCzBPPZ** and **2GCzBPN** were optimized using DFT at the PBE0²⁶⁵/6-31G(d,p) level²⁶⁶ of theory in the gas phase starting from a geometry generated using Chem3D.³⁰⁰ At the optimized S_0 geometries (Figure 5.2a), due to the larger steric hindrance caused by two of the 2GCz donors substituted on neighboring positions of the BPN acceptor, **2GCzBPN** possesses a much more twisted geometry than that of **2GCzBPPZ**, where the torsion angles between donor and acceptor were on average about 67° and 43° , respectively. Furthermore, **2GCzBPPZ** possesses a much longer molecular length (22 Å) than that of **2GCzBPN** (18 Å). The FMO of **2GCzBPPZ** and **2GCzBPN** are shown in Figure 5.2b. As expected, the HOMOs are localized on the donors, while LUMOs are localized on the acceptor group. Notably, as shown in Figure 5.2b, BPNBP (LUMO = -2.19 eV) is a much weaker electron-acceptor than BPN (LUMO = -2.38 eV). Thus, the HOMO-LUMO gap, $\Delta E_{\text{HOMO-LUMO}}$, decreases from 2.87 eV for **2GCzBPPZ** to 2.36 eV for **2GCzBPN**.

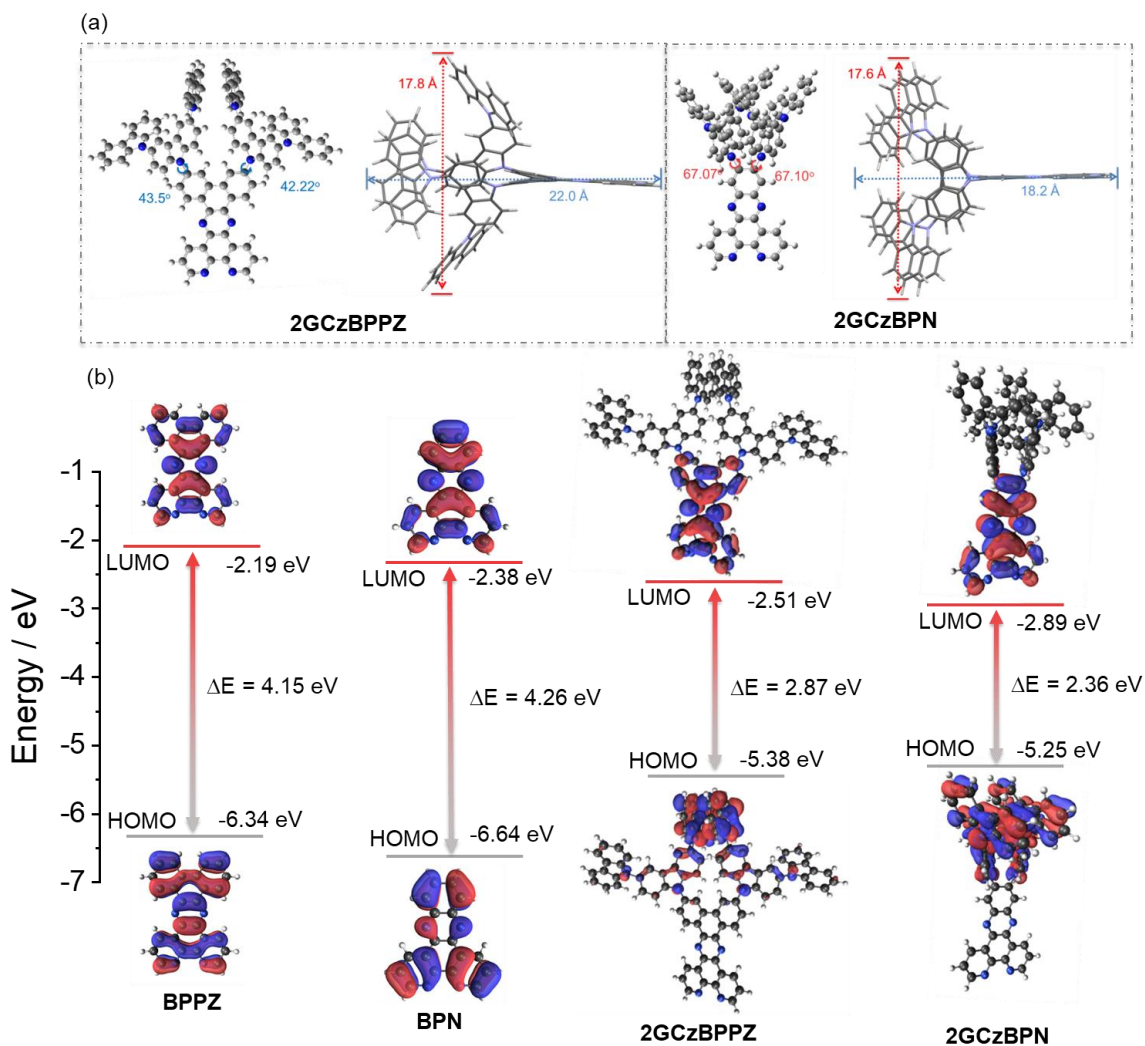


Figure 5.2. (a) DFT-optimized molecular geometries of ground state of **2GCzBPPZ** and **2GCzBPN**; (b) Frontier molecular orbitals (isovalue: 0.02) of **BPPZ**, **BPN**, **2GCzBPPZ** and **2GCzBPN**.

The excited-state properties were calculated using TD-DFT within the TDA-DFT based on the optimized S_0 geometries (Figure 5.3a).^{222,267,268} The S_1 energies are 2.54 eV for **2GCzBPPZ** and 1.95 eV for **2GCzBPN**, while the T_1 energies are 2.43 eV to 1.91 eV, respectively, corresponding to ΔE_{ST} values of 0.11 eV for **2GCzBPPZ** and only 0.04 eV for **2GCzBPN** (Figure 5.3a), due to its more twisted conformation. Figure 5.3b displays the NTOs for S_1 and T_1 . For both compounds, the hole and electron densities are clearly separated for S_1 , indicating CT transitions from the ground state. While the T_1 state of **2GCzBPN** is also CT in nature, that of **2GCzBPPZ** is better described as one having a mixed LE and CT character.

Reflecting the somewhat stronger overlap between the HOMO and LUMO electron densities, the calculated oscillator strength, f , for the S_0 - S_1 transition in **2GCzBPPZ** ($f = 0.13$) is larger than in **2GCzBPN** ($f = 0.06$). To evaluate the geometric rigidity of the compounds, we calculated the RMSD value (Figure 5.3c) using the VMD program²²³ between S_0 and S_1 geometries each optimized at the PBE0/6-31G(d,p) level. **2GCzBPN** shows a relatively smaller geometry relaxation (RMSD = 0.22 Å) compared to **2GCzBPPZ** (RMSD = 0.41 Å), suggesting that **2GCzBPN** possess a more rigid geometry, so nonradiative decay should be relatively attenuated for this compound compared to **2GCzBPPZ**.

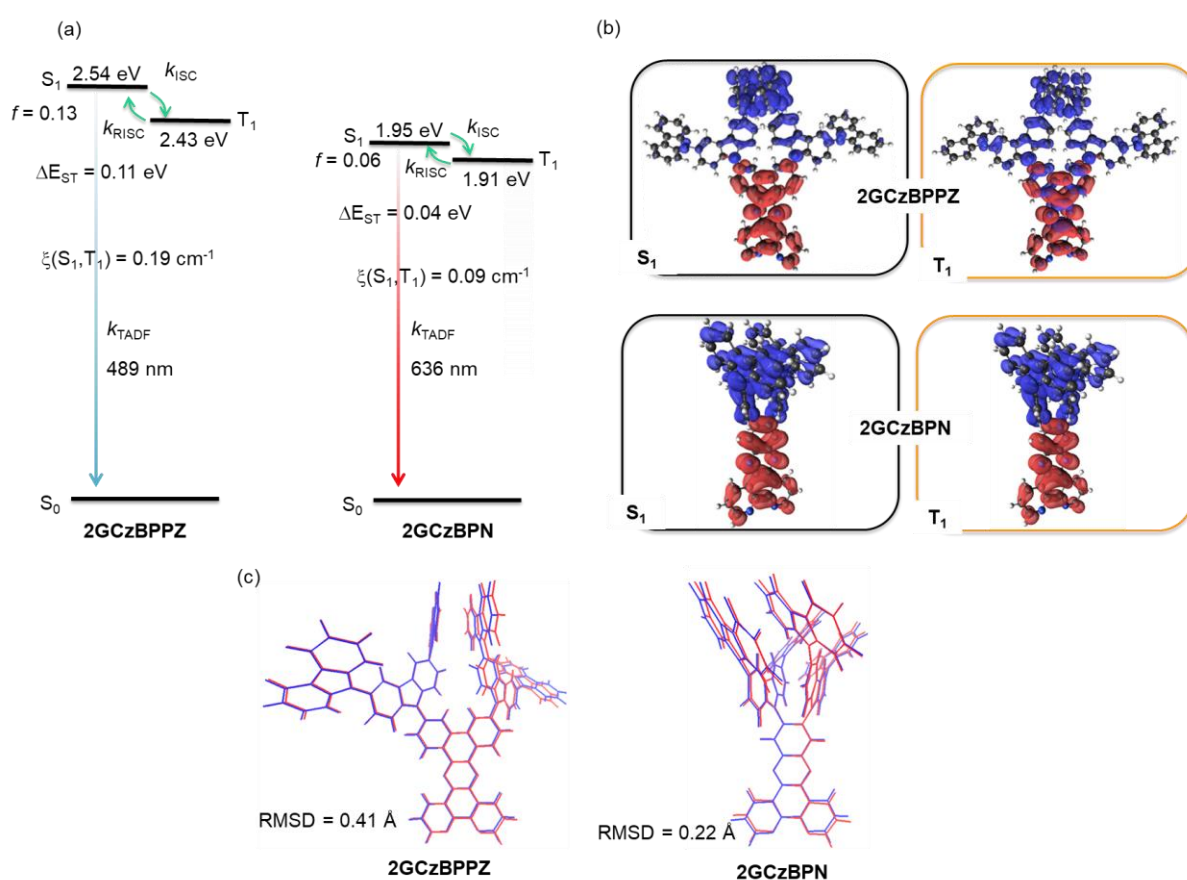


Figure 5.3. (a) vertical excitation energy levels of **2GCzBPPZ** and **2GCzBPN**, (b) Natural transition orbitals (unoccupied (hole, blue) & occupied (electron, red), (isovalue: 0.02) of S_1 and T_1 for **2GCzBPPZ** and **2GCzBPN** calculated at the optimized S_0 geometry in the gas phase at the PBE0/6-31G(d,p) level. (c) comparison of optimized structures of **2GCzBPPZ** and **2GCzBPN** at S_0 (blue) and S_1 (red) state.

5.4 Electrochemistry

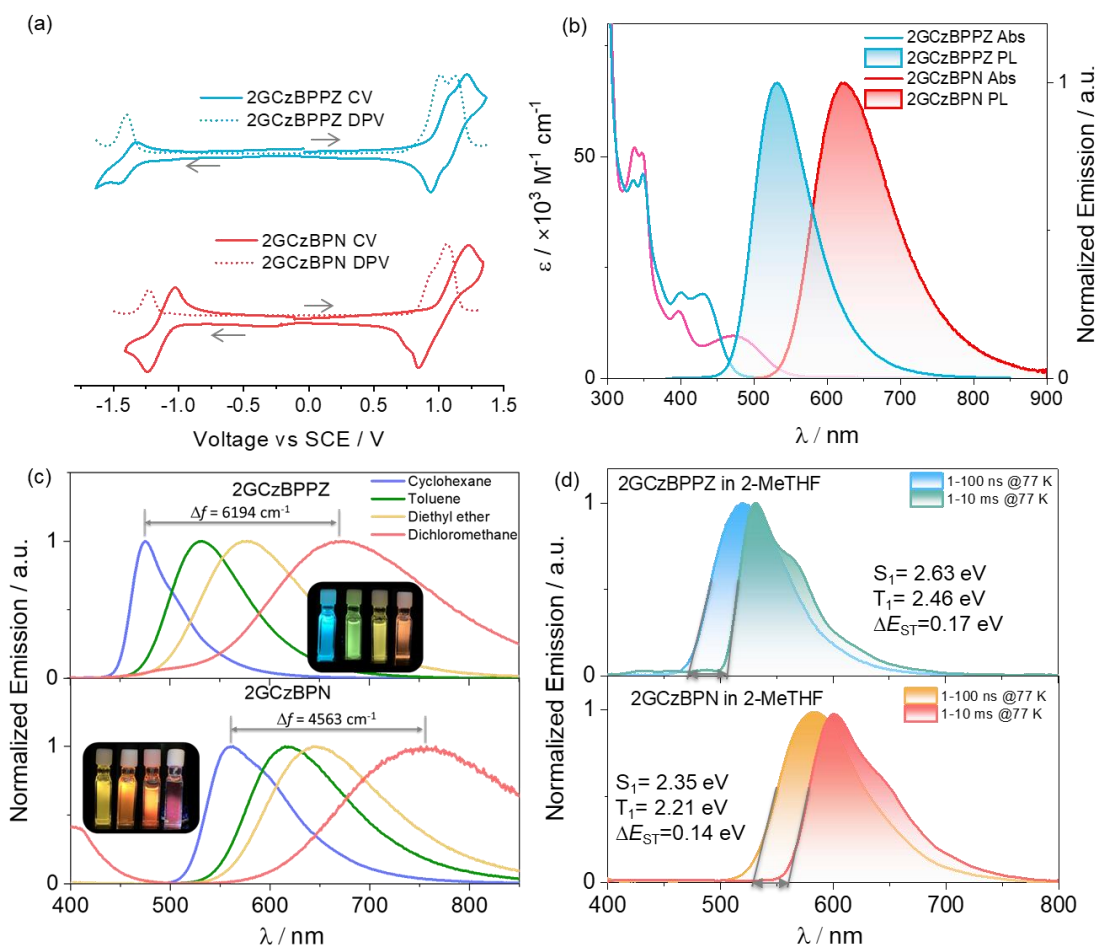


Figure 5.4. (a) Cyclic and differential pulse voltammograms measured in degassed DCM with 0.1 M $[\text{nBu}_4\text{N}]\text{PF}_6$ as the supporting electrolyte and Fc/Fc^+ as the internal reference (0.46 V vs SCE).²²⁴ Scan rate = 100 mV s^{-1} . (b) UV-vis absorption and SSPL spectra of **2GCzBPPZ** and **2GCzBPN** recorded in toluene at room temperature ($\lambda_{\text{exc}} = 340 \text{ nm}$). (c) PL solvatochromism study of **2GCzBPPZ** and **2GCzBPN** ($\lambda_{\text{exc}} = 343 \text{ nm}$). (d) Prompt fluorescence and phosphorescence spectra of **2GCzBPPZ** and **2GCzBPN** 2-MeTHF at 77 K ($\lambda_{\text{exc}} = 360 \text{ nm}$, phosphorescence spectra were acquired across a 1–10 ms time range).

Next, the energies of the FMOs were inferred from the electrochemical behavior of **2GCzBPPZ** and **2GCzBPN** by CV and DPV in degassed DCM with $[\text{nBu}_4\text{N}]\text{PF}_6$ as the supporting electrolyte (Figure 5.4a). The E_{red} , determined from the DPV peak values, are -1.36 V for **2GCzBPPZ** and -1.13 V for **2GCzBPN**, respectively. The inferred LUMO energies of

–2.94 eV and –3.21 eV for **2GCzBPPZ** and **2GCzBPN**, respectively, are consistent with the trend of the energies from the theoretical calculation (Figure 5.3a). **2GCzBPPZ** and **2GCzBPN** exhibited a similar oxidation potential ($E_{\text{ox}} = 1.06$ V for **2GCzBPPZ**, 1.04 V for **2GCzBPN**) due to the use of same GCz donor unit, corresponding to HOMO levels of –5.36 and –5.38 eV, respectively. The HOMO–LUMO gaps are 2.42 and 2.17 eV for **2GCzBPPZ** and **2GCzBPN**, respectively, which mirror the trend in the DFT calculated values of 2.87 and 2.36 eV.

5.5 Photophysics in Solution

The UV-Vis absorption spectra of **2GCzBPPZ** and **2GCzBPN** in dilute toluene are shown in Figure 5.4b, and the photophysical properties are summarized in Table 5.1. Both compounds exhibit similar strong double hump absorption with peaks at 337 and 346 nm, which can be attributed to LE transitions of the 2GCz donors based on a comparison with literature data of 2GCz.^{101,102} The absorption band at around 400 nm for both compounds is assigned to an LE transition of the acceptor moieties as these align with the absorption of BPN (Figure 5.5a).¹³⁷ **2GCzBPPZ** possesses a stronger ICT absorption band peaking at 432 nm ($\epsilon = 19 \times 10^3 \text{ M}^{-1} \text{ cm}^{-1}$) than that of **2GCzBPN** (475 nm, $\epsilon = 10 \times 10^3 \text{ M}^{-1} \text{ cm}^{-1}$), which is consistent with the calculated higher $f = 0.13$ for **2GCzBPPZ** ($S_0 \rightarrow S_1$) than $f = 0.06$ for **2GCzBPN** ($S_0 \rightarrow S_1$) (Figure 5.5b and c). The unstructured and broad PL spectra in toluene for both compounds indicate excited states with strong ICT character, with peak maxima, λ_{PL} , at 534 nm and 624 nm for **2GCzBPPZ** and **2GCzBPN**, respectively (Figure 5.4b).

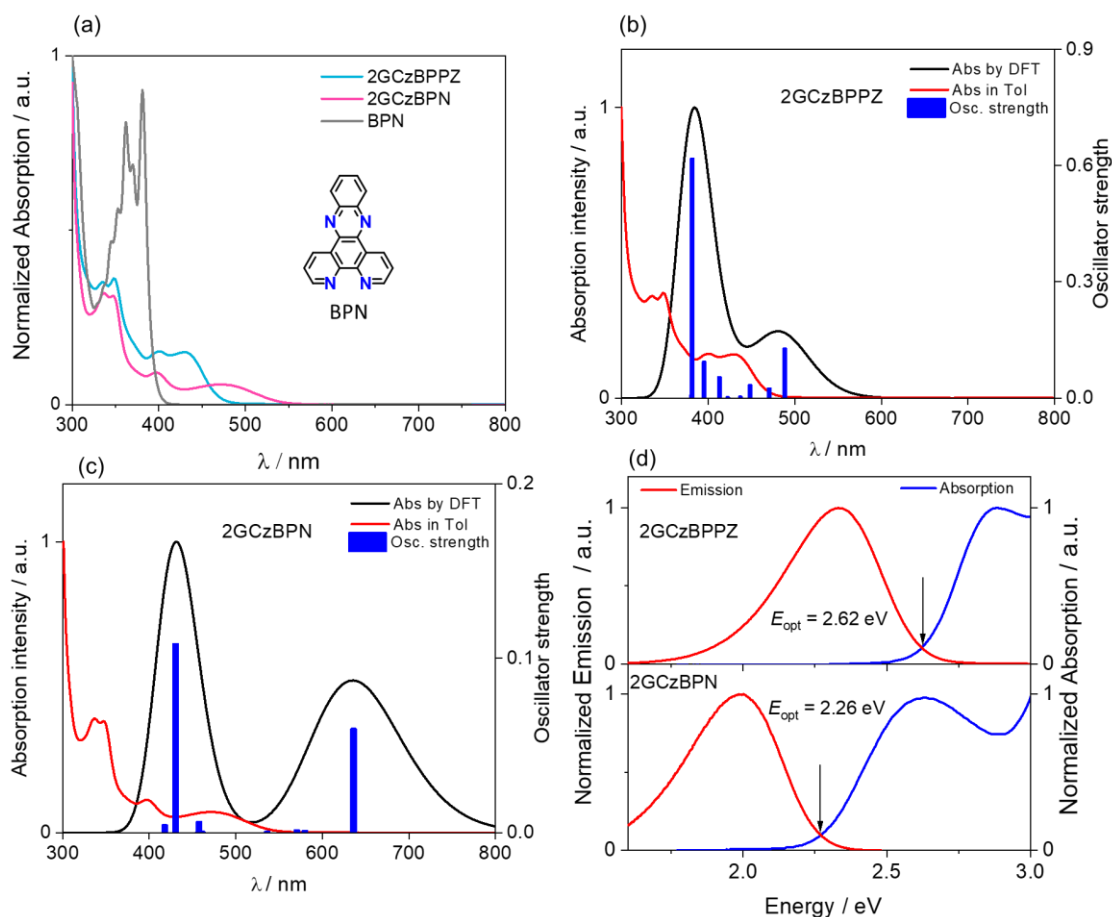


Figure 5.5. (a) Normalized UV-vis absorption for **2GCzBPPZ**, **2GCzBPN** and **BPN**; TDA-DFT simulation and experimental UV-Vis absorption spectra of (b) **2GCzBPPZ** and (c) **2GCzBPN**. (d) The optical bandgaps were determined from the intersection point of the normalized absorption and emission spectra for **2GCzBPPZ** and **2GCzBPN**. ($\lambda_{\text{exc}} = 343$ nm).

A strong positive solvatochromism is observed for both compounds (Figure 5.4c), which is consistent with the CT nature of the emissive excited state. Furthermore, **2GCzBPPZ** exhibits a more significant positive solvatochromism with a $\Delta f = 6194$ cm^{-1} than that ($\Delta f = 4563$ cm^{-1}) of **2GCzBPN**, corresponding to the larger transition dipole moment in the excited state, which is corroborated by DFT calculations, for **2GCzBPPZ** (3.63 D) than **2GCzBPN** (2.83 D). The E_g calculated from the intersection of the normalized absorption and emission spectra (Figure 5.5d), are 2.62 eV and 2.26 eV for **2GCzBPPZ** and **2GCzBPN**, respectively. The prompt fluorescence and phosphorescence spectra in 2-MeTHF glass at 77 K were used to extract the S_1 and T_1 energies from their respective onsets (Figure 5.4d, Table 5.1). The S_1 energies of **2GCzBPPZ** and **2GCzBPN** are 2.63 and 2.35 eV, and the T_1 energies are 2.46 eV

and 2.21 eV, respectively. The corresponding ΔE_{ST} values for **2GCzBPPZ** and **2GCzBPN** are 0.17 eV and 0.14 eV, respectively. The structured character of the phosphorescence spectrum for both emitters implies a T_1 state with LE character, corroborated by the TDA-DFT calculations to mixed $^3CT/^3LE$ state (LE localized on the acceptor, especially for **BPNNB**).

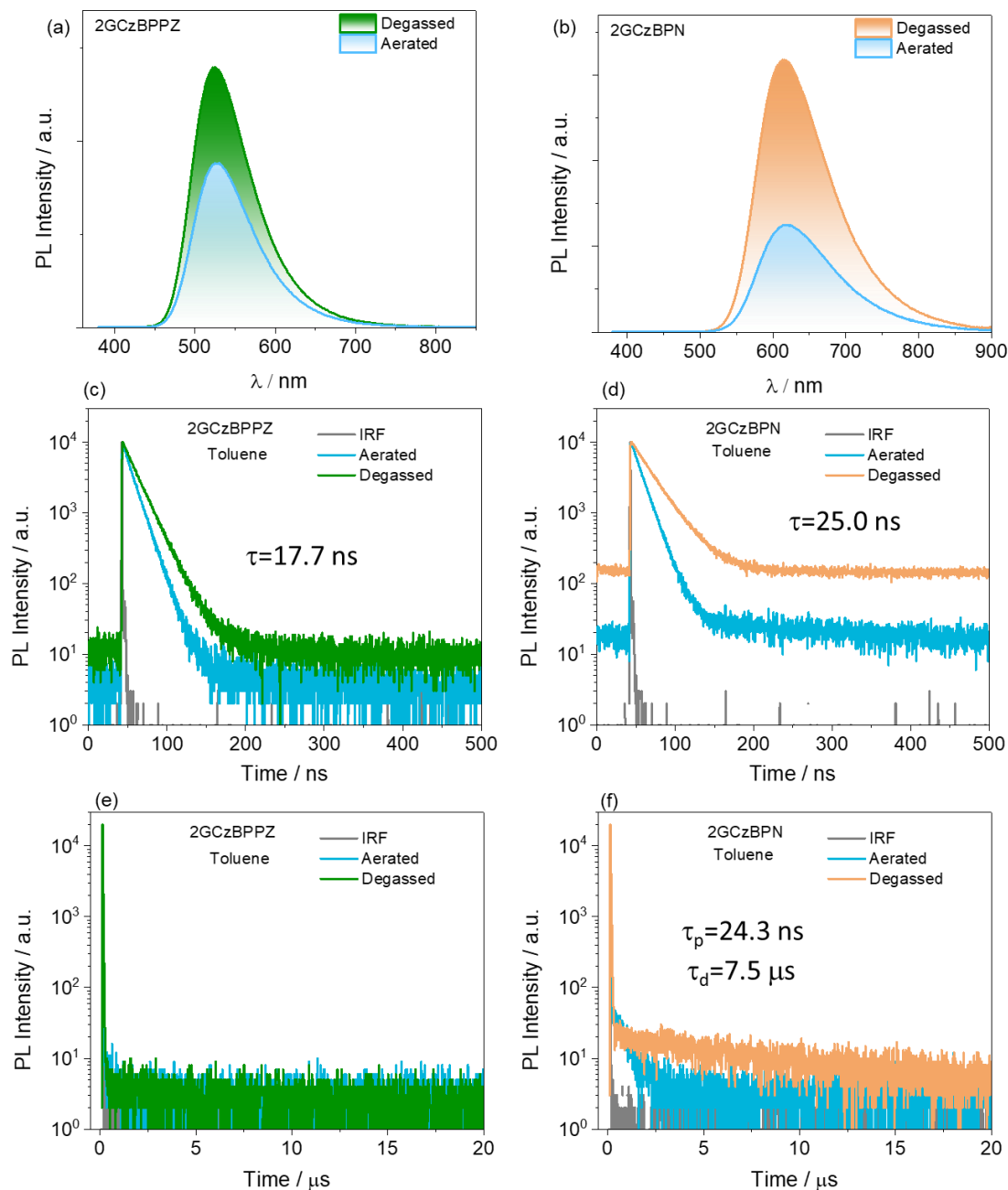


Figure 5.6. Steady-state PL spectra of (a) **2GCzBPPZ**, (b) **2GCzBPN**, in degassed and aerated toluene (λ_{exc} = 343 nm). Time-resolved PL decay profiles of (b) **2GCzBPPZ**, (c) **2GCzBPN** with time window 0-500 ns and (e) **2GCzBPPZ**, (f) **2GCzBPN** with time window 0-20 μs using TCSPC in aerated and degassed toluene (λ_{exc} = 379 nm).

The emission and TRPL decays of **2GCzBPPZ** and **2GCzBPN** in degassed and aerated toluene measured show biexponential kinetics with a prompt fluorescence lifetime, τ_p , of 24.3 ns and a delayed fluorescence lifetime, τ_d , of 7.5 μ s, in **2GCzBPN** (Figure 5.6). However, the emission of **2GCzBPPZ** decays monoexponentially with τ_p of 22.3 ns, and no delayed emission is observed. In both compounds, the emission intensity in the toluene solutions was enhanced upon oxygen removal, demonstrating that oxygen is quenching accessible triplet states in both compounds.

5.6 Aggregate modulation

Due to the large degree of π -conjugation inherent in both acceptors, there is likely to be strong intermolecular π - π interactions leading to excimer/aggregates formation. To explore and modulate the emergence of aggregates emission in **2GCzBPPZ** and **2GCzBPN**, we measured the PL spectra of different concentrations of **2GCzBPPZ** and **2GCzBPN** in *n*-hexane solution (Figure 5.7). As shown in Figure 5.7a, there are two emission peaks observed for **2GCzBPPZ** where the high-energy emission band at 475 nm converts to the low-energy emission band at 575 nm with increasing concentrations, indicating that a new species, either aggregate or excimer is responsible for the low-energy emission; however, there is negligible change in the emission spectra of **2GCzBPN** with increasing concentration (Figure 5.7f). Regardless of changes in concentration or temperature, **2GCzBPN** consistently exhibits a single emission peak, suggesting the absence of aggregation formation in **2GCzBPN**. The corresponding ratios of the intensity of the emission at 475 to 575 nm (I_{475}/I_{575}) and (I_{575}/I_{475}) upon increasing concentration are shown in Figure 5.7b. We found the isosbestic point to be at a concentration of 1.6×10^{-5} M, where the emission intensity of the monomer ($\lambda_{PL} = 475$ nm) is equal to that of the aggregates ($\lambda_{PL} = 575$ nm). Specifically, at low concentrations of **2GCzBPPZ** ($< 1.6 \times 10^{-5}$ M), the system is dominated by emission from the monomer as molecules are on average not sufficiently close to each other to form aggregates to any major extent (Figure 5.7c). As the concentration increases ($> 1.6 \times 10^{-5}$ M), the probability of intermolecular interactions increases, and the population of aggregates begins to grow (Figure 5.7c).

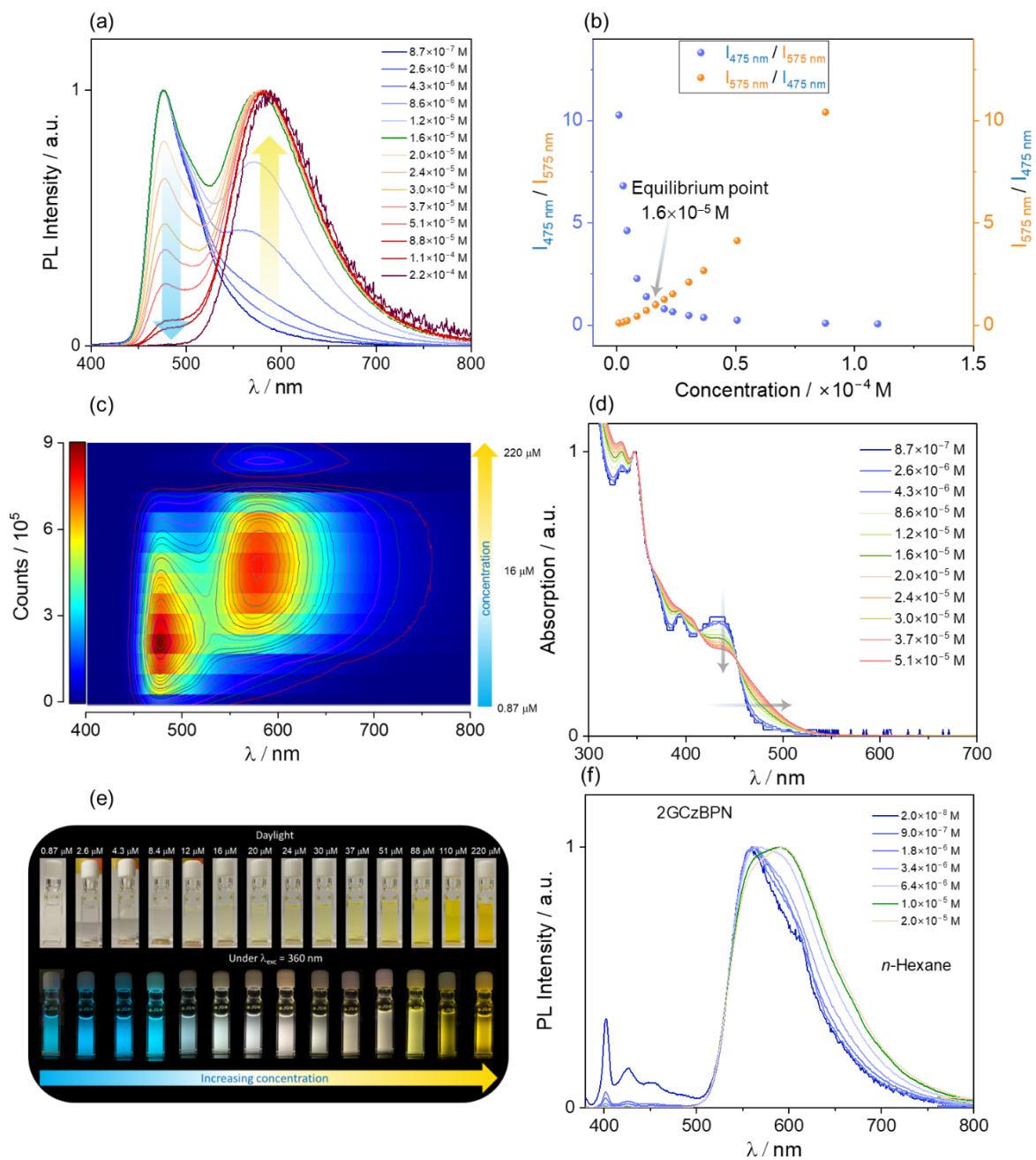


Figure 5.7. (a) Concentration-dependent fluorescence spectra for **2GCzBPPZ** in *n*-hexane solution ($\lambda_{exc} = 340$ nm); (b) Ratiometric plot of I_{475}/I_{575} (blue dots) and I_{575}/I_{475} (orange dots) vs increasing concentration of **2GCzBPPZ**; (c) Concentration-dependent emission mapping; (d) Concentration-dependent absorption spectra for **2GCzBPPZ** in *n*-hexane solution; (e) Corresponding photos under daylight and UV torch ($\lambda_{exc} = 360$ nm); (f) Concentration-dependent emission spectra for **2GCzBPN** in *n*-hexane solution ($\lambda_{exc} = 340$ nm).

Figure 5.7d reveals that with increasing concentration, the absorption maximum associated with the ICT band of **2GCzBPPZ** monomer at ~432 nm gradually decreases along with the emergence of a red-shifted absorption tail from 452 nm to 550 nm, indicating the formation of aggregates through strong intermolecular interactions in the ground state.^{326,363} Furthermore, the absorption of **2GCzBPPZ** in different solvents at the same concentration also demonstrated that the formation of aggregates occurs in *n*-hexane but not in higher polarity solvents like toluene, diethyl ether, or dichloromethane. This is likely due to strong solute-solvent interactions that competitively act to suppress the intermolecular interactions between **2GCzBPPZ** molecules responsible for aggregate formation.^{364,365}

Figure 5.8a shows that white emission can be obtained in 2×10^{-5} M solutions of **2GCzBPPZ** in *n*-hexane as a result of contributions from two distinct emission bands at λ_{PL} of 475 and 575 nm. Both emission bands are quenched upon exposure to oxygen, indicating that triplet states are accessible in both emission processes. TRPL studies in *n*-hexane under degassed and aerated conditions reveal that the emission band at 475 nm decays with a lifetime, τ_{p} , of 7.3 ns (Figure 5.8b), which may reflect the quenching of this emission due to fast Förster resonance energy transfer from the monomers to aggregates. The emission band at 575 nm decays with biexponential kinetics, with τ_{p} of 24.3 ns and τ_{d} of 7.5 μs , (Figure 5.8b bottom), the delayed emission was largely quenched after exposure to air, which could be understood as the quenching of the aggregates-induced TADF in solution.^{328,366} We next investigated the photophysical properties of **2GCzBPPZ** as doped films in polymethyl methacrylate (PMMA) (Figure 5.8c). For the 0.1 wt% doped film in PMMA, **2GCzBPPZ** exhibits a weak green emission with the main peak at 515 nm and shoulder peak at 580 nm. With increasing doping concentration, the intensity of high-energy emission band decreases while the low-energy emission band becomes dominant, reflecting a similar behavior to that observed in *n*-hexane solution. The TRPL decays reveal biexponential decay kinetics with associated τ_{p} and τ_{d} for both emission bands in 0.1 wt % doped film in PMMA. The delayed lifetime of the low-energy emission band decreased from 2.12 ms to 150.5 μs with increasing doping concentration from 0.1 wt% to 50 wt% (Figure 5.8d). While the corresponding prompt lifetime slightly increased from 18.7 ns to 25.9 ns with increasing doping concentration.

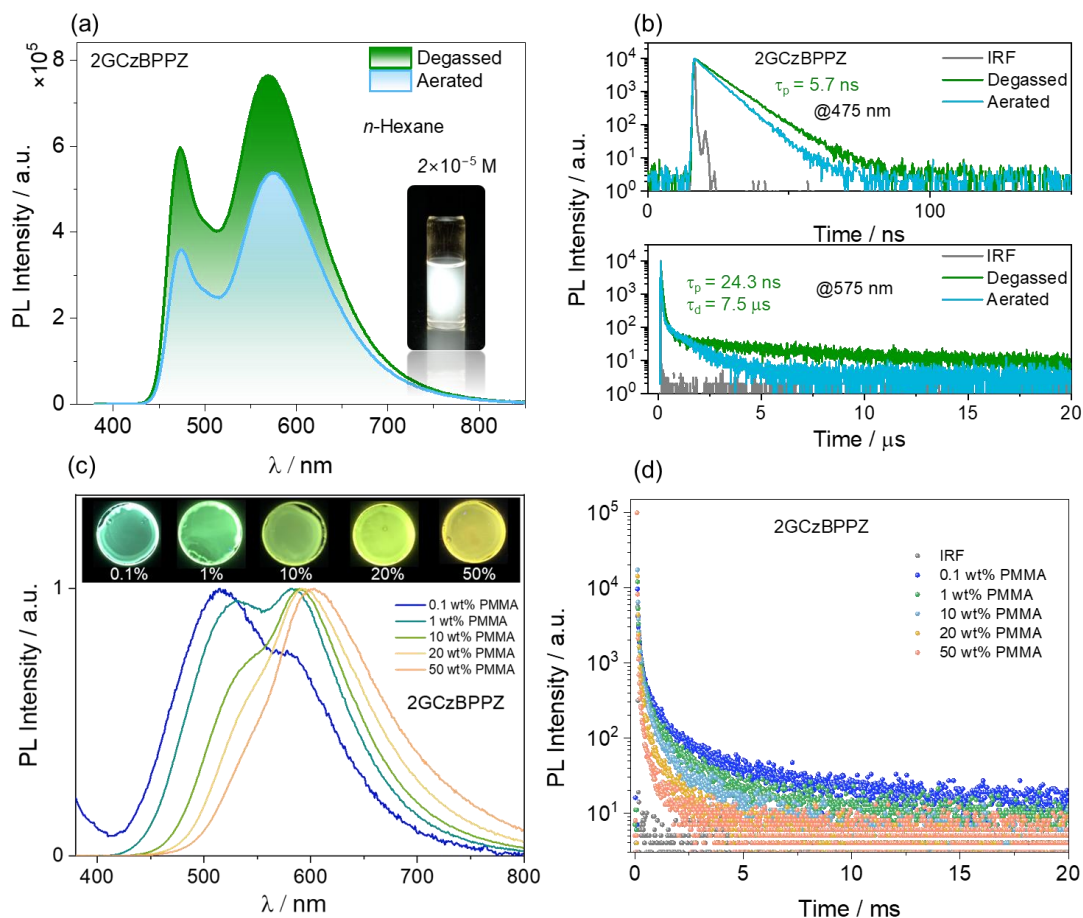


Figure 5.8. (a) PL spectra under degassed and aerated conditions at the concentration of 2.0×10^{-5} M in *n*-hexane; (b) PL decay of the emission $\lambda_{em} = 475$ nm (top) and $\lambda_{em} = 575$ nm (bottom) under degassed and aerated *n*-hexane; (c) Normalized fluorescence spectra of increasing doping concentrations (from 0.1 wt% to 50 wt%) for **2GCzBPPZ** in PMMA; (d) the corresponding PL decay of doing film in PMMA.

5.7 Colorimetric Temperature Sensing

Intrigued by the unusual dual-emissive nature of **2GCzBPPZ**, we sought to explore in greater detail the photophysical properties and studied the temperature-dependence of the emission in *n*-hexane (Figure 5.9). At room temperature, the 1.6×10^{-5} M solution of **2GCzBPPZ** is dual-emissive and the sample appears to emit white light (Figure 5.9a and c), where there is an approximately equal contributions from the emission from the monomer (475 nm) and aggregates (575 nm). Upon decreasing the temperature towards the solvent freezing point, the low-energy emission band increases in intensity dramatically while the high-energy

emission band is completely quenched. The corresponding ratio of the intensity of the emission at 575 to 475 nm (I_{575}/I_{475}) exponentially decreases with increasing temperature from $-70\text{ }^{\circ}\text{C}$ to room temperature ($r^2 = 0.998$) (Figure 5.9d). Such an exponential relationship could result from a combination of various factors at low temperature, like high viscosity and low solubility that will both affect the population of the aggregates.^{367,368} On the other hand, increasing the temperature beyond room temperature reveals a complementary effect where the high-energy emission band becomes more intense and the low-energy emission band all but disappears. In this temperature regime there is a linear relationship between I_{475}/I_{575} versus T ($r^2 = 0.988$ over a temperature region of 25 to $70\text{ }^{\circ}\text{C}$), corresponding to a ratiometric increase of $6.6\% \pm 0.2\% \text{ K}^{-1}$ (Figure 5.9e). Overall, **2GCzBPPZ** features excellent temperature sensitivity across a broad range of $-70\text{ }^{\circ}\text{C}$ to $70\text{ }^{\circ}\text{C}$, manifested in distinct colorimetric readout from yellow at $-70\text{ }^{\circ}\text{C}$ to white at RT and finally to sky blue at $70\text{ }^{\circ}\text{C}$, corresponding to CIE coordinates of (0.50, 0.49) at $-70\text{ }^{\circ}\text{C}$ that shift to CIE coordinates of (0.23, 0.32) associated with blue emission (Figure 5.9b). The broad range of temperature detection coupled with the significant color change exhibited by **2GCzBPPZ** make it a promising temperature sensor, whose properties are much superior to previously reported organic fluorescent temperature sensors.^{345–347} Generally, most organic fluorescent temperature sensors rely only on changes in emission intensity with negligible color change and have a narrow temperature detection range, usually of between RT to $\sim 70\text{ }^{\circ}\text{C}$.^{345–347,355–357} We have interpreted the origin of the wide dynamic spectral range of our optical temperature sensor to result from a temperature-dependent equilibrium between monomeric and aggregate species. Illustrated in Figure 5.9f, upon increasing the temperature, the π -stacking interactions necessary for aggregate formation are disrupted and the monomer population increases, reflected in the emergence of blue emission. As the temperature is decreased, the mobility of the molecules in solution is reduced, which can increase the probability of intermolecular interactions and promote the formation of aggregates as the molecules have less energy to overcome the repulsive forces between them and the attractive forces become more significant. Note that FRET occurs from monomer to the aggregates and so as the population of aggregates increases, so does the FRET rate, leading to an accelerated quenching of the high-energy emission of the monomeric species.

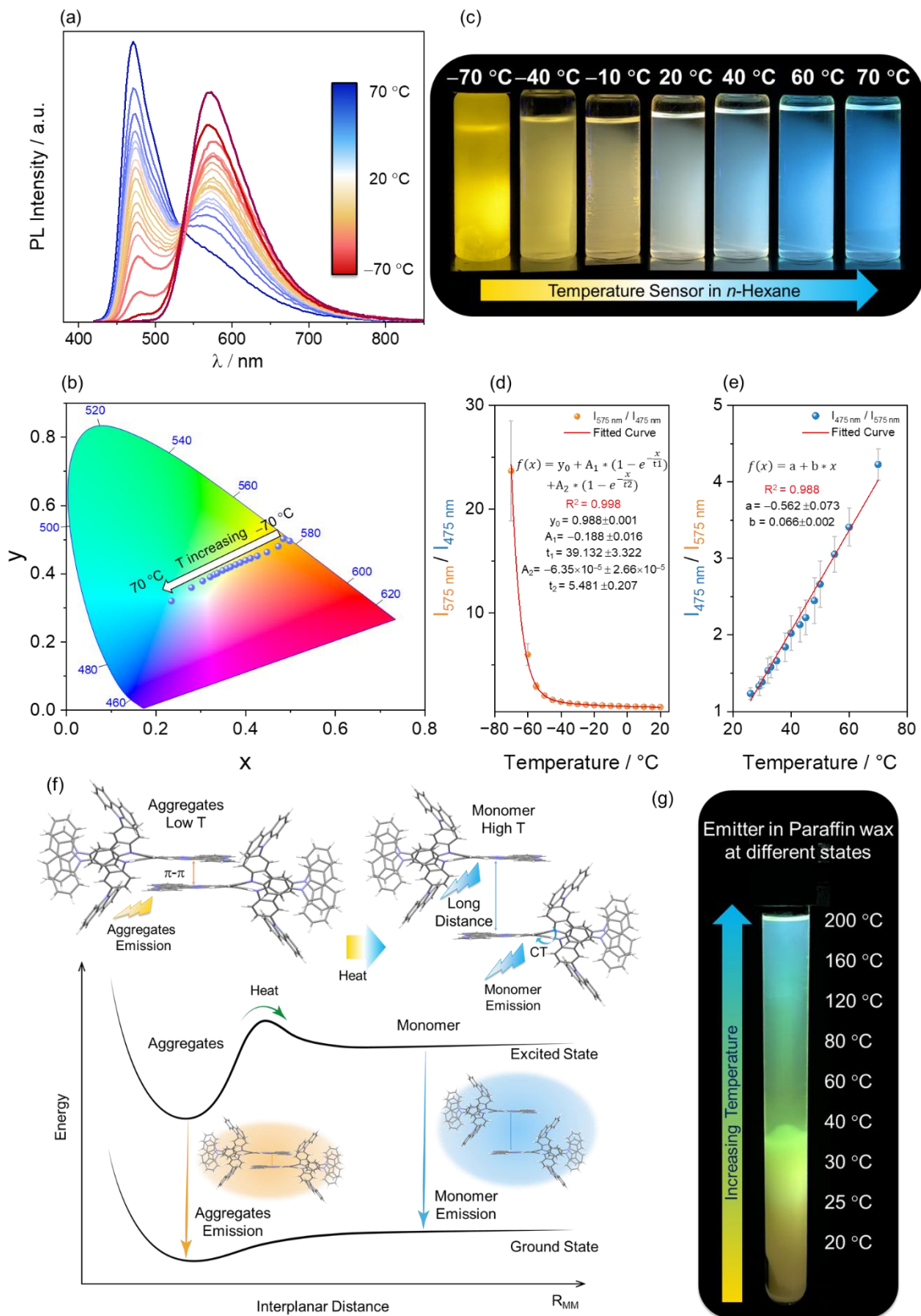


Figure 5.9. (a) Temperature-dependent emission spectra of 2GCzBPPZ in n-hexane at a concentration of 1.6×10^{-5} M ($\lambda_{\text{exc}} = 360$ nm); (b) CIE plot of the emission spectra in (a) of

2GCzBPPZ; (c) Photos of **2GCzBPPZ** at various temperatures (UV torch $\lambda_{\text{exc}} = 360$ nm); (d) Ratiometric plot of I_{575}/I_{475} vs temperature upon decreasing the temperature below RT; (e) Ratiometric plot of I_{475}/I_{575} vs temperature upon increasing the temperature from RT (right); (f) Schematic representation of the thermal response and two-state equilibration model describing the observed abnormal temperature-responsive dual emission phenomenon of **2GCzBPPZ**. (g) Spatio-temperature sensor application in paraffin wax (paraffin embedded with **2GCzBPPZ** in a test tube (length:160 mm, diameter: 16 mm) excited with a UV torch, $\lambda_{\text{exc}} = 360$ nm).

Recognizing the potential of this compound to act as a temperature sensor, we translated its properties into the solid state by embedding the compound into Paraffin. As shown in Figure 5.9g, when photoexcited at 360 nm the solid Paraffin emits in the yellow at room temperature. As the temperature increases from 20 towards 80 °C, paraffin starts to melt at around 50 °C and the emission gradually blue shifts from yellow to green. When the temperature increases beyond 160 °C, the liquid paraffin emits in the blue, emulating the emission observed in *n*-hexane beyond 60 °C. This distinctive performance in paraffin makes it ideal as a spatio-temperature probe. As demonstrated in Figure 5.9g, the **2GCzBPPZ**-embedded paraffin was melted and poured into a test tube (length:160 mm, diameter: 16 mm) and then allowed to solidify upon cooling. At room temperature, the entire test tube with the solid paraffin shows yellow emission. As the top part of the temperature is selectively heated and the local temperature increases, this part of the paraffin sample exhibits a noticeable color change, while the bottom section of the paraffin maintains its yellow emission as this part is still at room temperature. We have correlated the optical response of the **2GCzBPPZ**-embedded paraffin with an external temperature probe to demonstrate that it can act as an accurate temperature sensor (Figure 5.28 in Section 5.10). In an attempt to use a non-polar solid host with a higher melting temperature we also incorporated **2GCzBPPZ** into CBP. However, despite having a similar polarity to paraffin, dual emission was not observed in this host. **2GCzBPPZ** thus shows unrivaled temperature sensitivity and with a broad temperature-dependent spectral response compared to previously reported organic temperature sensors.³⁴⁴⁻³⁴⁹

5.8 TADF Properties in the Solid State

To assess the emission properties of **2GCzBPPZ** and **2GCzBPN** in the solid state, their photophysical properties were investigated in an OLED-relevant host mCP as this host matrix has a sufficiently high triplet energy ($T_1 = 2.91$ eV)³⁶⁹ to confine the excitons onto the emitter. As shown in Figure 5.10, as 10 wt% doped films in mCP, **2GCzBPN** emits at λ_{PL} of 601 nm, which is red-shifted compared to **2GCzBPPZ**, which emits at λ_{PL} of 531 nm (Table 5.1). The corresponding Φ_{PL} of **2GCzBPN** and **2GCzBPPZ** are 71% and 57%, respectively, which decrease to 60% and 45%, respectively, under air. The S_1/T_1 energy levels of **2GCzBPPZ** (2.76/2.50 eV) and **2GCzBPN** (2.38/2.26 eV) were inferred from the onsets of the prompt fluorescence and phosphorescence spectra, respectively, at 77 K (Figure 5.10a and b). For **2GCzBPN**, both the fluorescence and phosphorescence spectra are broad and structureless, indicating that both the S_1 and T_1 states have CT character. However, the phosphorescence spectrum of **2GCzBPPZ** is structured, suggesting that the T_1 state has LE character, while the S_1 state is CT in character. The corresponding ΔE_{ST} values are 0.26 and 0.12 eV for **2GCzBPPZ** and **2GCzBPN**, respectively, which matched the trend observed in 2-MeTHF glass at 77 K (ΔE_{ST} of 0.17 eV for **2GCzBPPZ** and 0.14 eV for **2GCzBPN**).

The room temperature emission from both compounds shows multiexponential decay kinetics, with average prompt fluorescence lifetimes, τ_{p} , of 18.0 ns and 34.1 ns, and average delayed emission lifetimes, τ_{d} , of 73.1 μs and 2.9 μs for **2GCzBPPZ** and **2GCzBPN**, respectively (Figure 5.10d). The corresponding k_{ISC} for both compounds in mCP films are 1.61×10^7 s⁻¹ and 0.45×10^7 s⁻¹ for **2GCzBPPZ**, and **2GCzBPN**, respectively, while the rate k_{RISC} for **2GCzBPN** reached 4.1×10^5 s⁻¹, a value 20 times faster than in **2GCzBPPZ** of 1.93×10^4 s⁻¹. The relative intensities of the delayed PL increased with increasing temperature from 100 K to 298 K, corroborating the TADF nature of the emission of both compounds in the mCP films (Figure 5.10e and f).

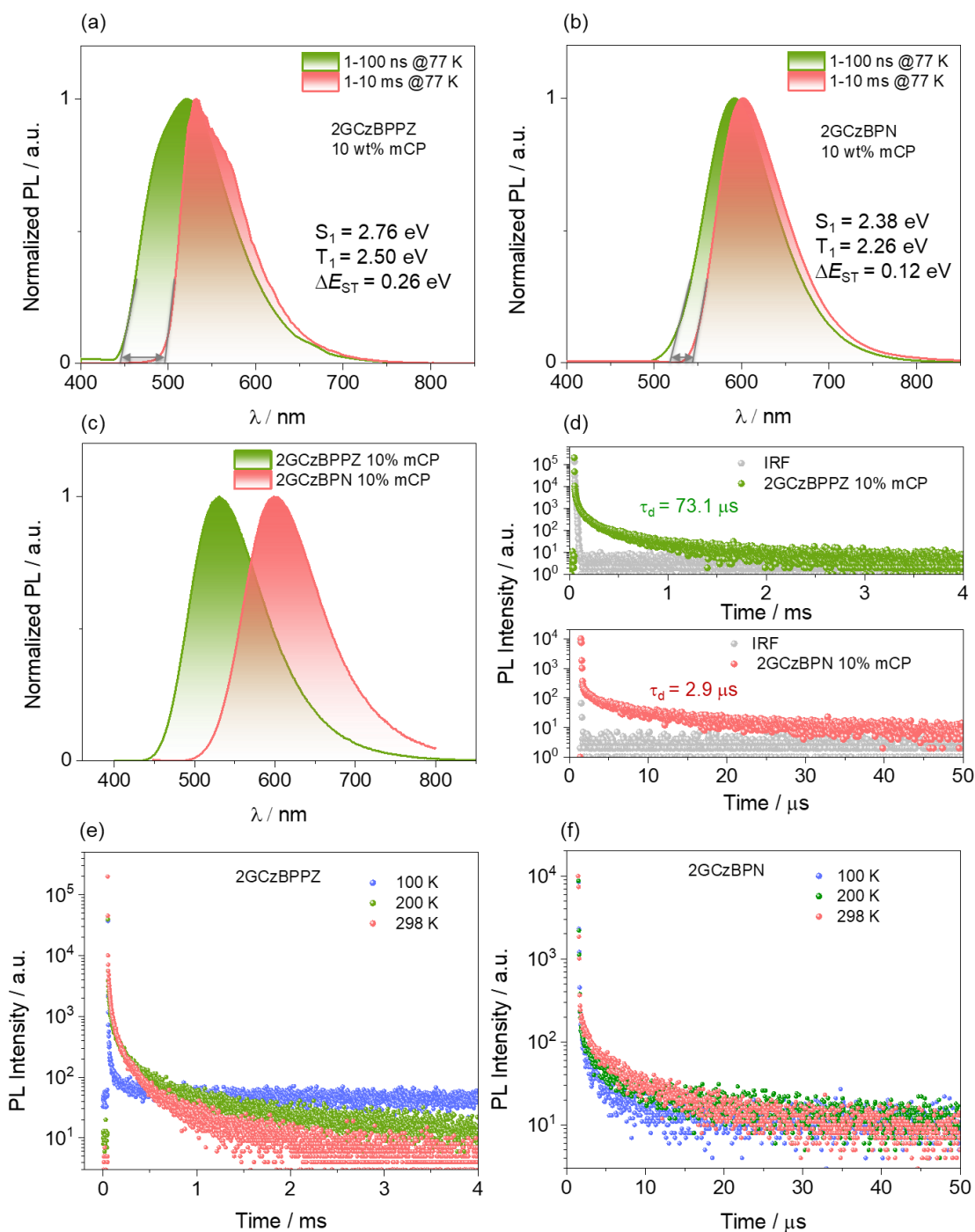


Figure 5.10. Prompt fluorescence (1-100 ns) and phosphorescence spectra (1-10 ms) in 10 wt% doped in mCP at 77 K of (a) **2GCzBPPZ** and (b) **2GCzBPN** ($\lambda_{exc} = 345$ nm). (c) Steady-state PL spectra of 10 wt% doped films of **2GCzBPPZ** and **2GCzBPN** in mCP film at room temperature ($\lambda_{exc} = 345$ nm); (d) PL decay of 10 wt% doped films of **2GCzBPPZ** and **2GCzBPN** in mCP at 298 K ($\lambda_{exc} = 375$ nm); Temperature-dependent PL decay of 10 wt% doped films of (e) **2GCzBPPZ** and (f) **2GCzBPN** in mCP ($\lambda_{exc} = 375$ nm).

Table 5.1. Photophysical properties of **2GCzBPPZ** and **2GCzBPN**.

	$\lambda_{\text{abs}} / (\epsilon / \times 10^3 \text{ M}^{-1} \text{ cm}^{-1})^{\text{a}}$	$\lambda_{\text{PL}}^{\text{a}}$	S_1/T_1^{b}	$\Delta E_{\text{ST}}^{\text{b}}$	$\lambda_{\text{PL}}^{\text{c}}$	$\Phi_{\text{PL}}^{\text{c}}$	$\tau_{\text{p}}^{\text{d}}$	$\tau_{\text{d}}^{\text{d}}$	S_1/T_1^{e}	$\Delta E_{\text{ST}}^{\text{e}}$	HOMO ^f	LUMO ^f	ΔE^{f}
	nm	nm	eV	eV	nm	/ %	/ ns	/ μs	eV	eV	eV	eV	eV
2GCzBPPZ	346 (45), 400(19), 432(19)	534	2.63 /2.46	0.17	531	57 (45)	18.0	73.1	2.71/ 2.50	0.26	-5.36	-2.94	2.42
2GCzBPN	348 (51), 397(15), 475(10)	624	2.35 /2.21	0.14	601	71 (60)	34.1	2.9	2.38/ 2.26	0.12	-5.38	-3.21	2.17

^a In PhMe at 298 K ($\lambda_{\text{exc}} = 340$ nm). ^b Obtained from the onset of the prompt fluorescence (time window: 1 ns – 100 ns) and phosphorescence spectra (time window: 1 ms – 10 ms) measured in 2-MeTHF glass at 77 K, $\lambda_{\text{exc}} = 343$ nm. ^c Thin films of 10 wt% emitters doped in mCP were prepared by spin-coating, and Φ_{PL} values were determined using an integrating sphere ($\lambda_{\text{exc}} = 345$ nm). Values quoted are under N₂. Values in parentheses are in air. ^d Average lifetime ($\tau_{\text{avg}} = \Sigma A_i \tau_i^2 / \Sigma A_i \tau_i$, where A_i is the pre-exponential for lifetime τ_i). Prompt and delayed emissions were measured by TCSPC and MCS, respectively ($\lambda_{\text{exc}} = 379$ nm). ^e S₁ was obtained from the onset of the prompt emission (time window: 1–100 ns) measured in doped film at 77 K and T₁ was obtained from the onset of the phosphorescence spectrum (time window: 1–10 ms) measured in doped film at 77 K. ^f In DCM with 0.1 M [ⁿBu₄N]PF₆ as the supporting electrolyte and Fc/Fc⁺ as the internal reference (0.46 V vs. SCE).²²⁴ The HOMO and LUMO energies were determined using $E_{\text{HOMO/LUMO}} = -(E_{\text{ox}}/E_{\text{red}} + 4.8)$ eV where E_{ox} and E_{red} are anodic and cathodic peak potentials versus Fc/Fc⁺, respectively, obtained from the DPV.^{224g} $\Delta E = |E_{\text{HOMO}} - E_{\text{LUMO}}|$.

5.9 Solution-processed OLED Device Characterization

We next fabricated solution-processed (SP) OLEDs employing 10 wt% emitters doped in mCP films as the EML using the following device stack: ITO / PEDOT:PSS (40 nm)/ mCP (60%): oxadiazolyl]phenylene (OXD-7) (30%): 10 wt% emitters (20 nm)/ TmPyPB (45 nm)/LiF (1 nm)/Al (Figure 5.11a and b), where ITO and Al serve as the anode and cathode, respectively, and PEDOT:PSS and TmPyPB are the hole-transporting layer electron-transporting layer, respectively. As shown in Figure 5.11b, the OLEDs with **2GCzBPPZ** and **2GCzBPN** exhibit green and orange emission with emission maxima, λ_{EL} , of 552 and 608 nm and corresponding CIE coordinates of (0.39, 0.55) and (0.58, 0.40), respectively, which match the PL emission (Figure 5.11c). The devices with **2GCzBPPZ** showed lower turn-on voltages (V_{on}) of 3.5 V and high brightness of up to 8000 cd m⁻² compared to V_{on} of 4.1 V and a maximum luminance of 1068 cd m⁻² for the devices with **2GCzBPN** (Figure 5.11c and Table 5.2). At the same voltages, the current density of the **2GCzBPN**-based device is lower than that of the **2GCzBPPZ**-based device, which we ascribe to the relatively lower electron mobility of **2GCzBPN** in the mCP film. The devices with **2GCzBPPZ** showed a higher EQE_{max} of 15.0% at 581 cd m⁻² with negligible efficiency roll-off at 1000 cd m⁻² ($EQE_{1000} = 14.0\%$), while the devices with **2GCzBPN** showed poorer performance, with EQE_{max} of 5.3% (Figure 5.11d). Considering the measured Φ_{PL} (Table 5.1) and assuming 25% outcoupling efficiency associated with an isotropic orientation of the transition dipole moment of the emitter, the EQE_{max} for devices with **2GCzBPPZ** and **2GCzBPN** are expected to be 14.3% and 17.8%, respectively. This indicates that the device with **2GCzBPPZ** has effectively unity exciton utilization efficiency; however, at this stage it is unclear why the EQE_{max} for **2GCzBPN** is so low.

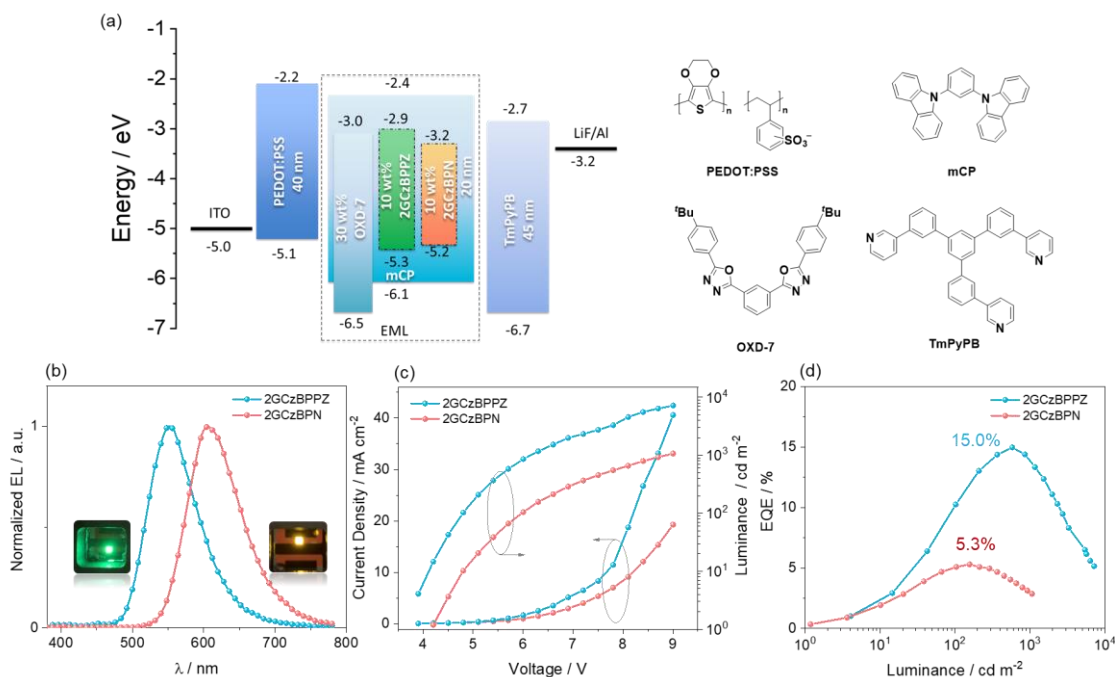


Figure 5.11. (a) Energy level diagram and structure of materials used in the devices; (b) EL spectra, (c) Current density and luminance versus voltage characteristics, (d) External quantum efficiency versus luminance curves for the devices.

Table 5.2. Electroluminescence data for the devices

Emitter	$V_{\text{on}}^a / \text{V}$	$\lambda_{\text{EL}}^b / \text{nm}$	$L_{\text{max}} / \text{cd m}^{-2}$	$\text{CE} / \text{cd A}^{-1}$	$\text{PE}_{\text{max}} / \text{lm W}^{-1}$	$\text{EQE}^c / \%$	$\text{CIE}^d / x,y$
2GCzBPPZ	3.5	552	7207	51.7	28.8	15.0/10.2/14.0	0.39, 0.55
2GCzBPN	4.1	608	1068	10.2	5.1	5.3/5.1/3.0	0.58, 0.40

^a The turn-on voltage at a brightness $\approx 1 \text{ cd m}^{-2}$. ^b The electroluminescence maximum recorded at 6 V. ^c $\text{EQE}_{\text{max}} / \text{EQE}_{100} / \text{EQE}_{1000}$. ^d The CIE coordinates recorded at 6 V.

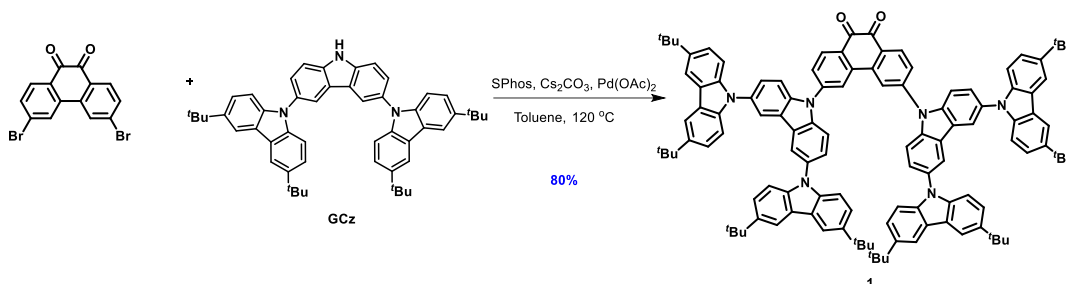
5.10 Conclusions

In this Chapter, we designed two TADF dendrimers **2GCzBPPZ** and **2GCzBPN** by using different rigid and planar nitrogen-doped PAHs as the acceptors combined with two second-generation ter(carbazole) donor dendrons. Due to less twisted geometry adopted and the use of the large π -conjugation acceptor, **2GCzBPPZ** shows an unusual single molecule white

emission in *n*-hexane solution that results from dual emission from a combination of monomer and aggregates emitting, respectively, at 475 nm and 575 nm. The dual emission behavior of **2GCzBPPZ** is quite sensitive to both the concentration and temperature. We exploited this dual emission behavior in a temperature sensor by embedding **2GCzBPPZ** in paraffin. To the best of our knowledge, **2GCzBPPZ** shows the broadest spectra and temperature response of any organic temperature sensor. Due to its more twisted geometry, **2GCzBPN** shows efficient TADF and there is no significant aggregate formation and no dual emission. Finally, we employed these two compounds as emitters in solution-processed OLEDs. The SP-OLEDs with **2GCzBPPZ** showed around a three-times higher EQE_{max} of 15.0% at λ_{EL} of 552 nm than the device with **2GCzBPN** (EQE_{max} = 5.3% at λ_{EL} = 608 nm). We are currently investigating the origin for this divergence in performance.

5.11 Experimental Section

Synthesis of 3,6-bis(3,3',6,6''-tetra-*tert*-butyl-9'*H*-[9,3':6',9''-tercarbazol]-9'-yl)phenanthrene-9,10-dione (1):



Under a nitrogen atmosphere, to a 100 mL Schlenk flask were added 3,6-dibromo-9,10-phenanthrenequinone (0.5 g, 1.4 mmol, 1.0 equiv.), **GCz** (2.2 g, 3.0 mmol, 2.2 equiv.), Pd(OAc)₂ (0.015 g, 0.07 mmol, 0.05 equiv.), 2-dicyclohexylphosphino-2',6'-dimethoxybiphenyl (SPhos) (0.084 g, 0.2 mmol, 0.15 equiv.), Cs₂CO₃ (2.7 g, 8.2 mmol, 6.0 equiv.) and toluene (50 mL) and the reaction was stirred at 110 °C for 24 h. After being cooled to room temperature, the reaction mixture was added to aqueous NH₄Cl (30 mL) and was extracted with DCM (3×50 mL). The organic layer was dried over anhydrous Na₂SO₄, filtered, and concentrated under reduced pressure to afford around 2.0 g of the crude product as a dark solid. The crude product was purified by column chromatography on silica gel (25% DCM/hexane) to afford **1** as a dark red solid (Yield = 1.80 g).

3,6-bis(3,3',6,6''-tetra-*tert*-butyl-9'*H*-[9,3':6',9''-tercarbazol]-9'-yl)phenanthrene-9,10-dione (1): Yield: 80%. R_f = 0.2 (25% DCM/hexane). Mp = 341-343 °C. ¹H NMR (500 MHz, CDCl₃) δ 8.70 (d, *J* = 8.3 Hz, 2H), 8.49 (d, *J* = 2.0 Hz, 2H), 8.28 (d, *J* = 2.0 Hz, 4H), 8.16 (d, *J* = 1.9 Hz, 8H), 8.01 (dd, *J* = 8.3, 1.8 Hz, 2H), 7.79 (d, *J* = 8.7 Hz, 4H), 7.67 (dd, *J* = 8.7, 2.0 Hz, 4H), 7.43 (dd, *J* = 8.7, 1.9 Hz, 8H), 7.31 (d, *J* = 8.6 Hz, 8H), 1.46 (s, 72H). ¹³C NMR (126 MHz, CDCl₃): 178.79, 144.83, 142.82, 139.94, 139.33, 137.34, 133.32, 132.22, 130.02, 128.21, 126.53, 124.95, 123.67, 123.22, 122.01, 119.75, 116.32, 111.12, 108.93, 77.29, 77.04, 76.78, 53.46, 34.73, 32.02. HR-MS [M+H]⁺ Calculated: (C₁₁₈H₁₁₄N₆O₂) 1646.9003; Found: 1646.8998.

2301102004-0-10-cs339.10.fid
BP2GCZ || 1H Observe

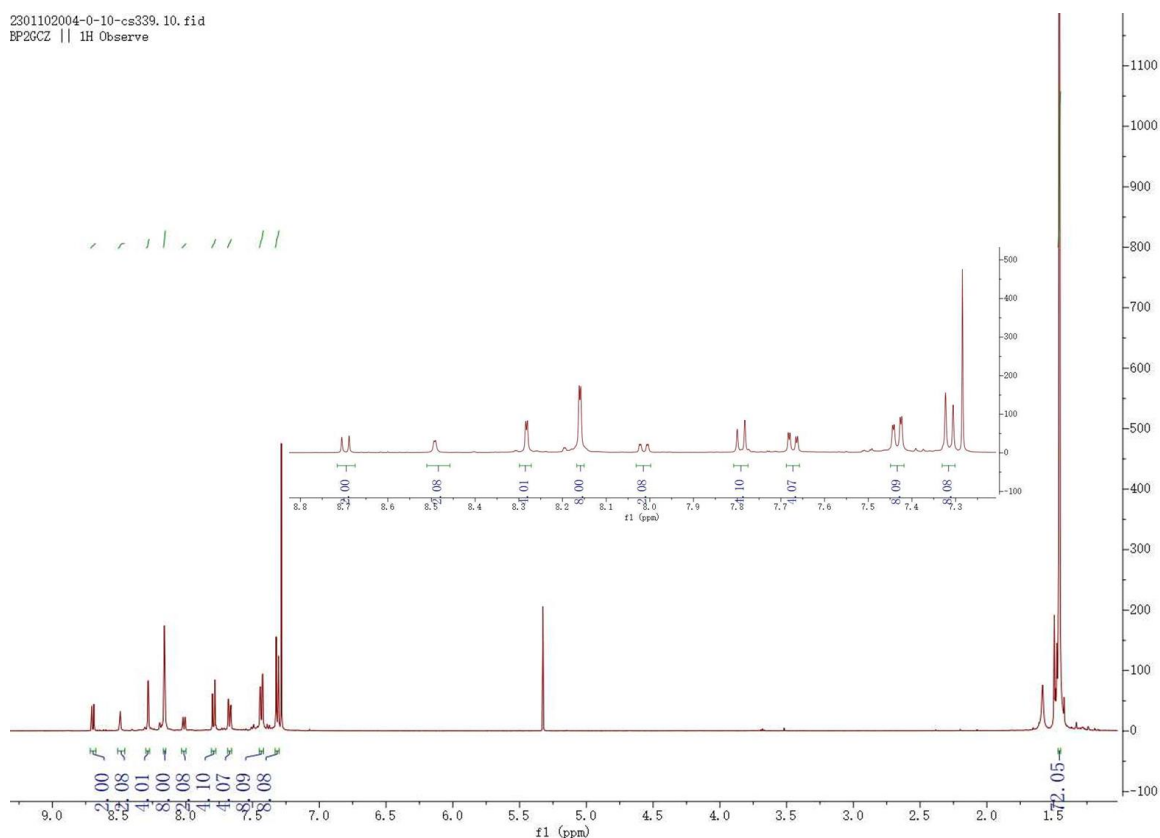


Figure 5.12. ^1H NMR spectra of **1** in CDCl_3 .

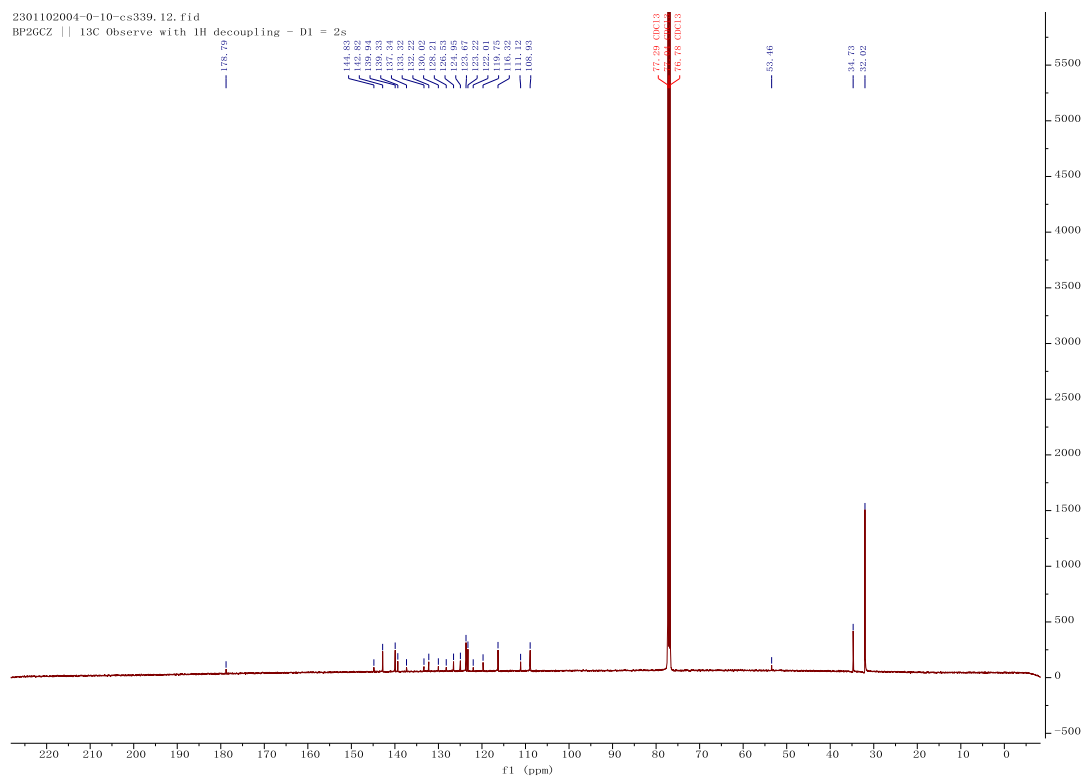


Figure 5.13. ^{13}C NMR spectra of **1** in CDCl_3 .

Generic Display Report (all)

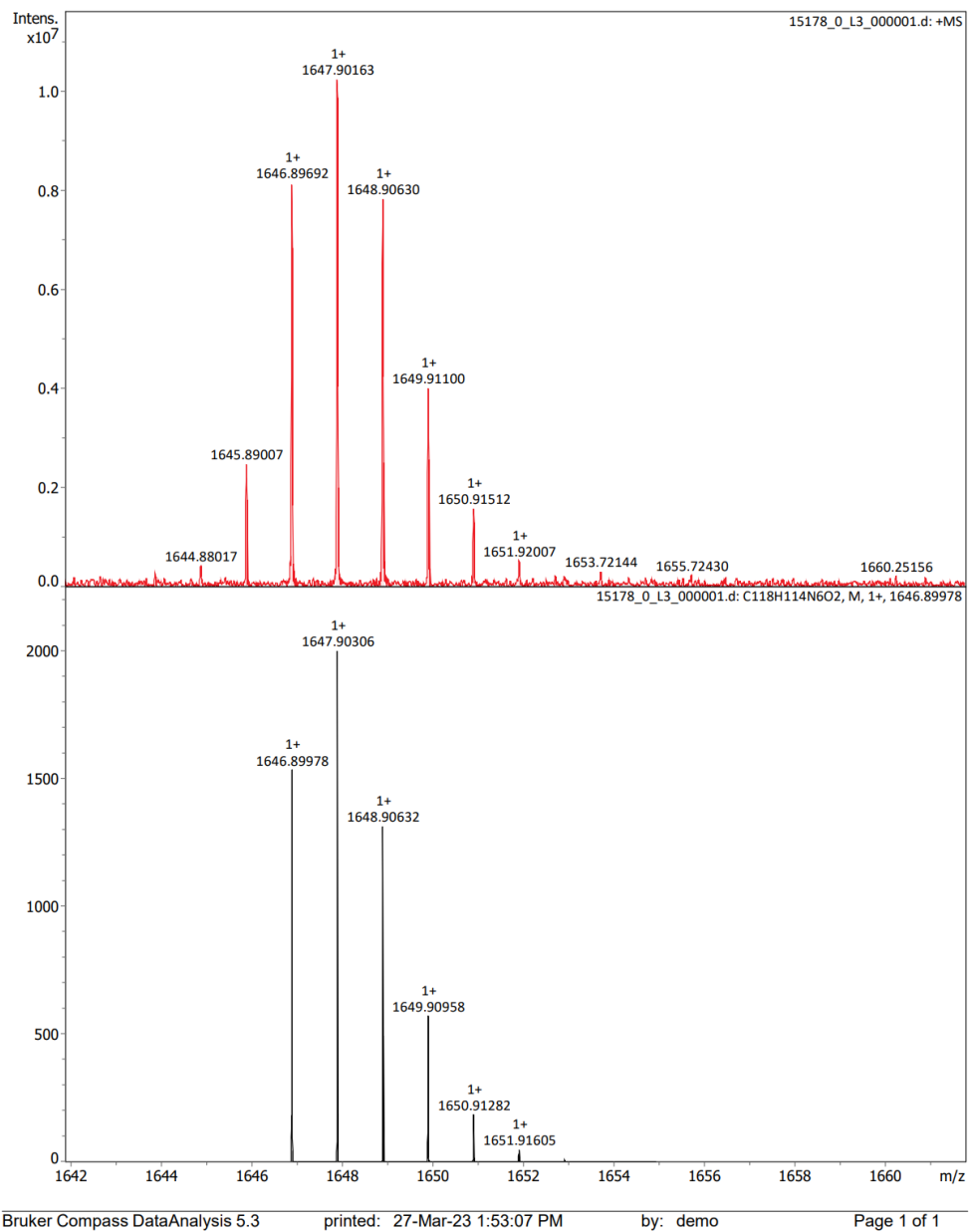
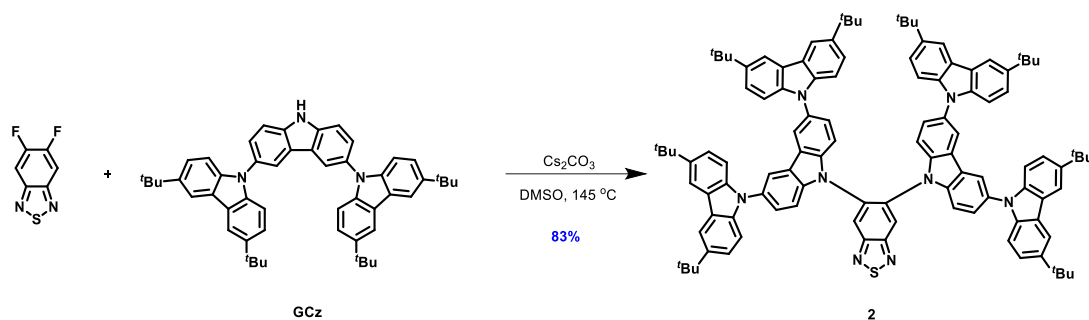


Figure 5.14. HRMS of 1.

Synthesis of 5,6-bis(3,3',6,6''-tetra-*tert*-butyl-9'*H*-[9,3':6',9''-tercarbazol]-9'-yl)benzo[*c*][1,2,5]thiadiazole (2):



To a flask containing 10 mL of DMSO were added 5,6-difluorobenzo[*c*][1,2,5]thiadiazole (0.4 g, 2.32 mmol, 1.0 equiv.), **GCz** (3.52 g, 4.88 mmol, 2.1 equiv.) and Cs₂CO₃ (3.79 g, 11.62 mmol, 5.0 equiv.) and the reaction was heated to 145 °C and stirred under a nitrogen atmosphere for 16 h. After cooling to room temperature, the solution was poured into water (50 mL) and extracted with DCM (3×100 mL). The organic layer was dried over Na₂SO₄, filtered, and concentrated under reduced pressure. The residue (around 3.5 g of a dark yellow solid) was purified by column chromatography with (20% DCM/hexane) to afford the compound **2** as a light-yellow solid (Yield: 3.05 g).

5,6-bis(3,3'',6,6''-tetra-*tert*-butyl-9'*H*-[9,3':6',9''-tercarbazol]-9'-yl)benzo[*c*][1,2,5]

thiadiazole (2): Yield: 83%. **R_f** = 0.4 (20% DCM/Hexane). **Mp** > 400 °C. **¹H NMR (500 MHz, THF-*d*₈)** 9.09 (s, 2H), 8.23 – 8.13 (m, 14H), 7.57 (d, *J* = 8.6 Hz, 4H), 7.33 (dd, *J* = 8.6, 2.0 Hz, 5H), 7.13 (s, 13H), 1.37 (s, 72H). **¹³C NMR (126 MHz, THF-*d*₈):** δ 141.90, 139.81, 139.61, 135.90, 131.37, 124.69, 124.41, 123.37, 118.83, 118.77, 115.82, 111.54, 108.74, 66.96, 66.78, 66.60, 66.43, 66.25, 66.08, 34.28, 31.43, 24.84, 24.67, 24.51, 24.35, 24.19, 24.03. **HR-MS [M+H]⁺ Calculated:** (C₁₁₀H₁₁₀N₈S) 1574.8574; **Found:** 1574.8568.

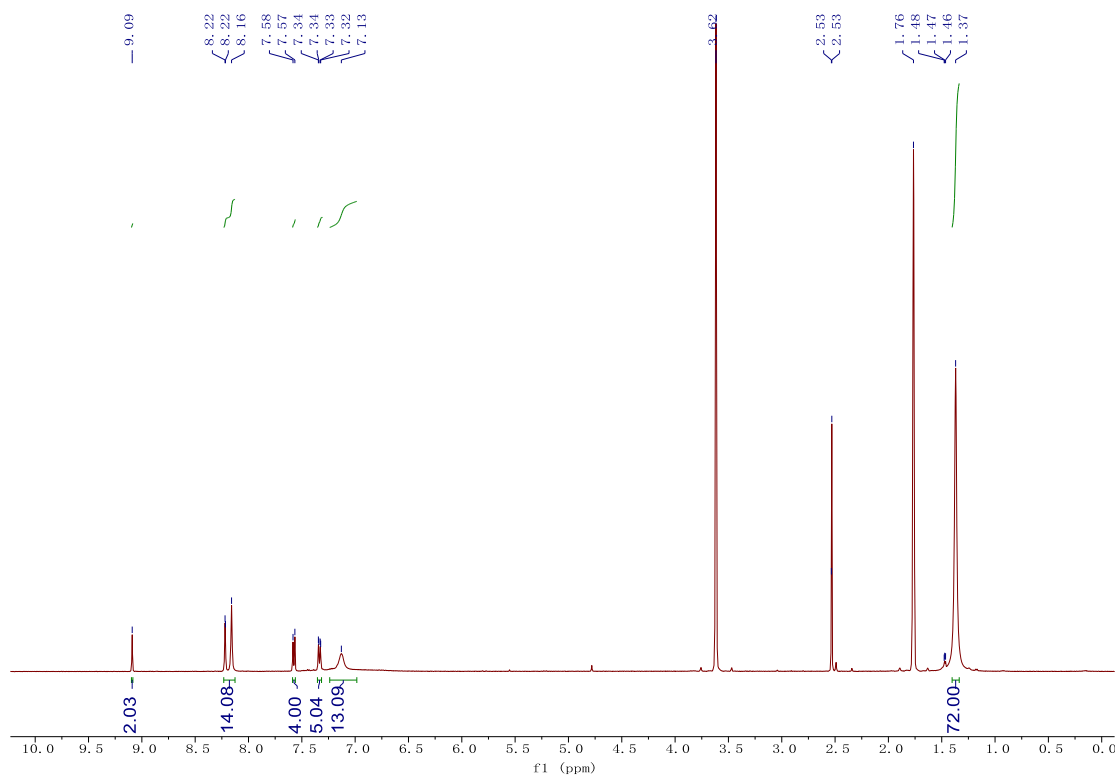


Figure 5.15. ^1H NMR spectra of **2** in $\text{THF-}d_8$.

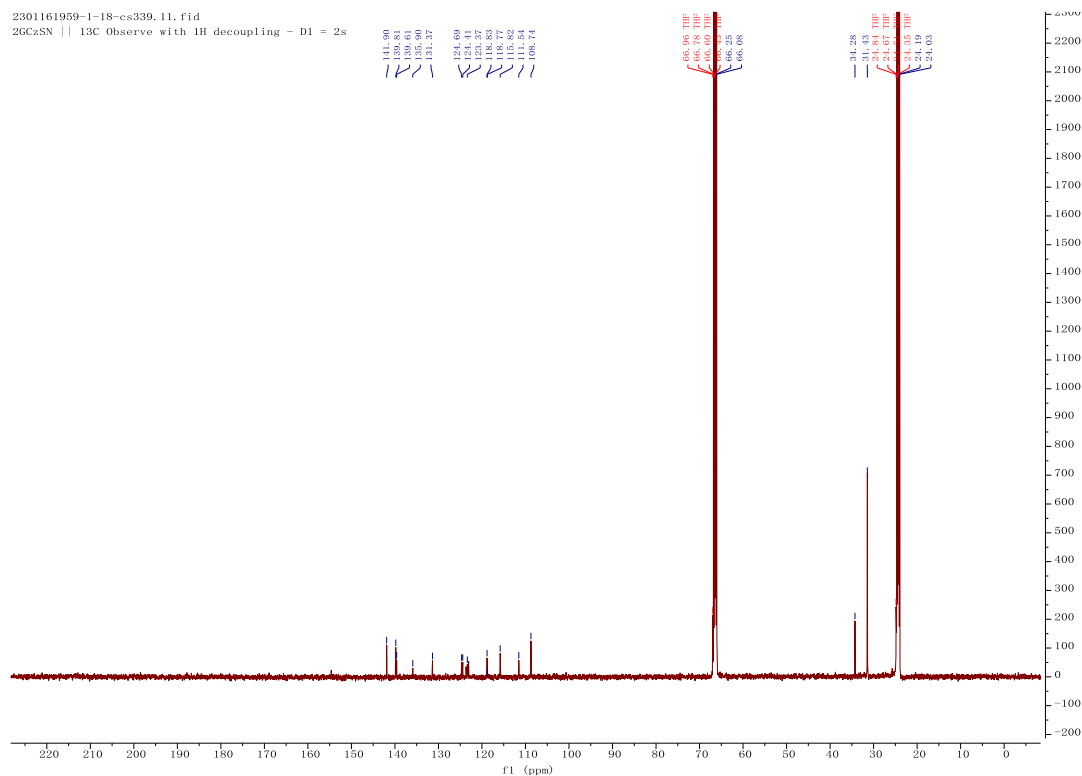


Figure 5.16. ^{13}C NMR spectra of **2** in $\text{THF-}d_8$.

Generic Display Report (all)

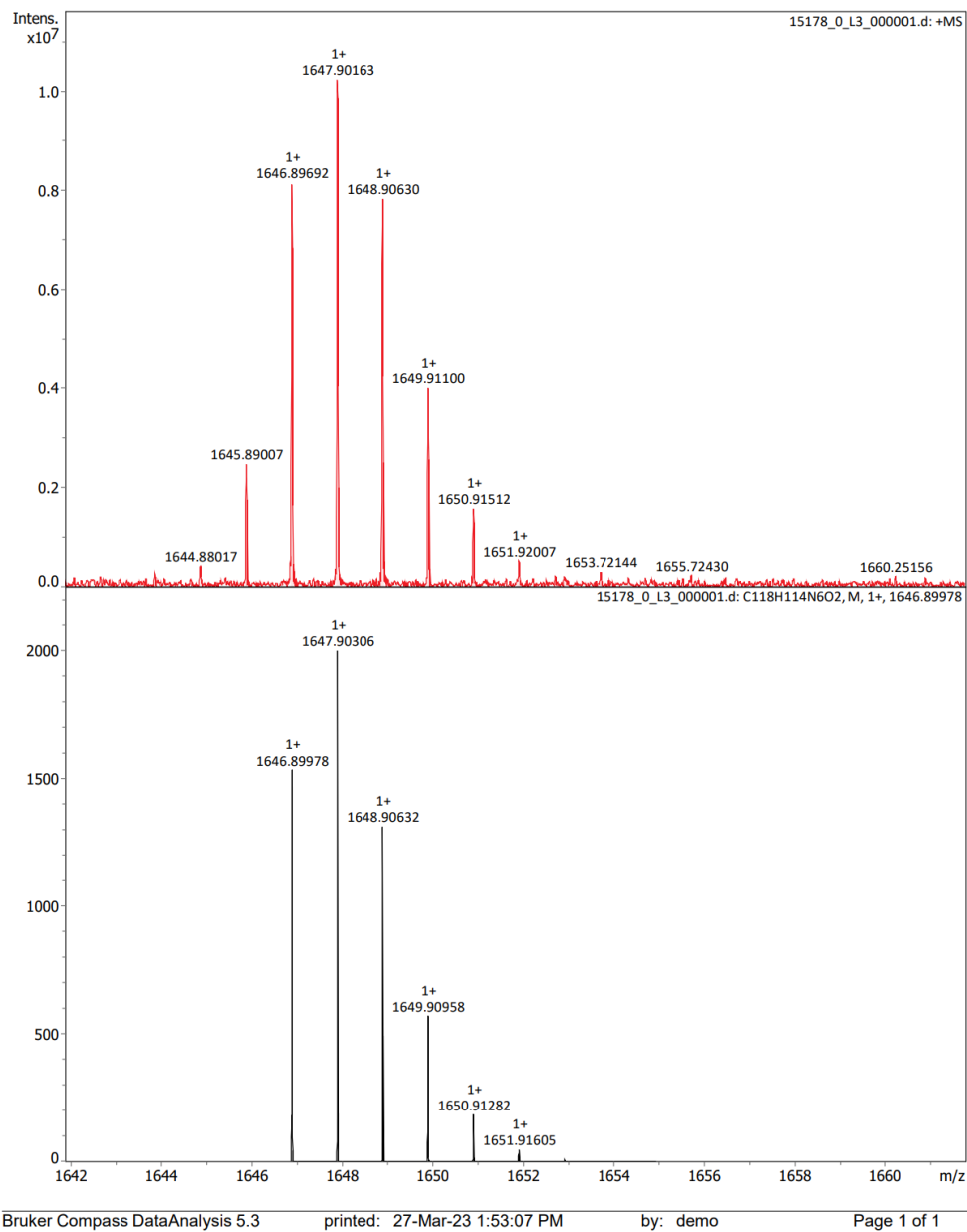
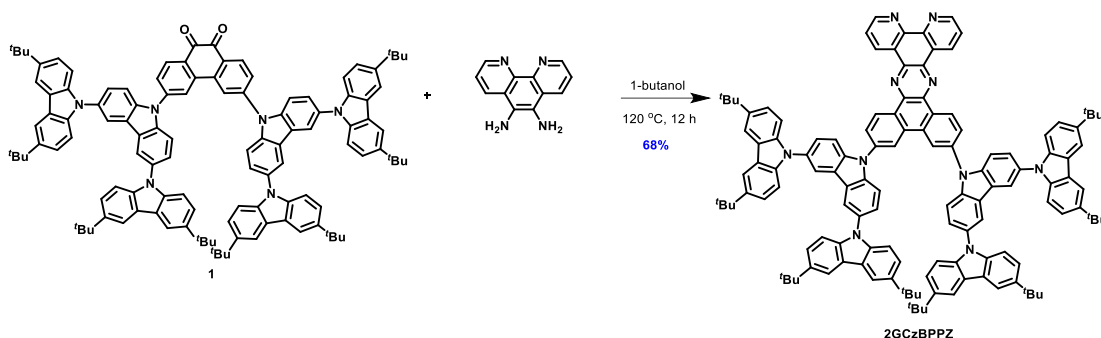


Figure 5.17. HRMS of 2.

Synthesis of 12,15-bis(3,3',6,6''-tetra-*tert*-butyl-9'*H*-[9,3':6',9''-tercarbazol]-9'-yl)dibenzo[*a,c*]dipyrido[3,2-*h*:2',3'-*j*]phenazine (2GCzBPPZ):



To a flask containing 10 mL of 1-butanol were added **1** (0.8 g, 0.48 mmol, 1.0 equiv.) and 1,10-phenanthroline-5,6-diamine (0.1 g, 0.48 mmol, 1.0 equiv.) and the reaction was heated to 120 °C for 12h under a nitrogen atmosphere. After cooling to room temperature, the solution was poured into water (20 mL) and extracted with DCM (3×50 mL). The organic layer was dried over Na₂SO₄, filtered, and concentrated under reduced pressure. The residue (around 0.7 g of a yellow solid) was purified by column chromatography with (20% DCM/hexane) to afford the compound **2GCzBPPZ** as a yellow solid (0.60 g).

12,15-bis(3,3'',6,6''-tetra-*tert*-butyl-9'*H*-[9,3':6',9''-tercarbazol]-9'-yl)dibenzo[*a,c*]

dipyrido[3,2-*h*:2',3'-*j*]phenazine (2GCzBPPZ): Yield: 68%. R_f = 0.3 (20% DCM/hexane).

Mp >400 °C. **¹H NMR (500 MHz, CDCl₃)** δ 10.06 (d, *J* = 8.5 Hz, 2H), 10.00 (dd, *J* = 8.1, 1.8 Hz, 2H), 9.47 (dd, *J* = 4.5, 1.8 Hz, 2H), 9.11 (d, *J* = 2.1 Hz, 2H), 8.34 (p, *J* = 2.3, 1.8 Hz, 6H), 8.18 (d, *J* = 2.0 Hz, 9H), 8.01 (dd, *J* = 8.1, 4.4 Hz, 2H), 7.85 (d, *J* = 8.7 Hz, 4H), 7.69 (dd, *J* = 8.7, 2.0 Hz, 4H), 7.46 (dd, *J* = 8.7, 2.0 Hz, 9H), 7.36 (d, *J* = 8.6 Hz, 8H), 1.47 (d, *J* = 1.8 Hz, 72H). **¹³C NMR (126 MHz, CDCl₃):** δ 152.52, 142.72, 140.96, 140.39, 140.14, 139.68, 133.93, 133.16, 131.66, 129.88, 128.79, 127.70, 127.54, 126.40, 124.48, 123.62, 123.22, 121.73, 119.71, 116.26, 111.02, 109.04, 77.26, 77.01, 76.76, 34.72, 32.03. **HR-MS [M+H]⁺**

Calculated: (C₁₃₀H₁₂₂N₁₀) 1823.9887; **Found:** 1823.9926. **Anal. Calcd. for C₁₃₀H₁₂₂N₁₀:** C, 85.58%; H, 6.74%; N, 7.68%. **Found:** C, 85.77%; H, 6.84%; N, 7.68%. **HPLC analysis:** 98.6% pure on HPLC analysis, retention time 10.190 minutes in mixture of 85% Acetonitrile and 15% Water.

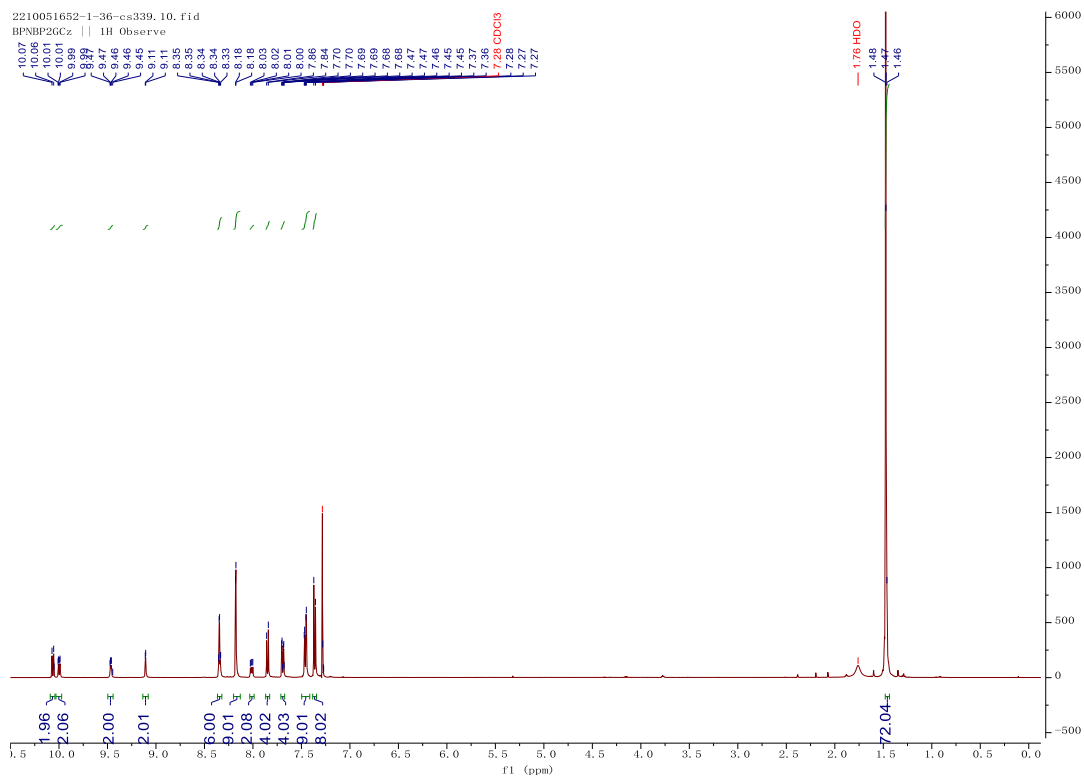


Figure 5.18. ¹H NMR spectra of 2GCzBPPZ in CDCl₃.

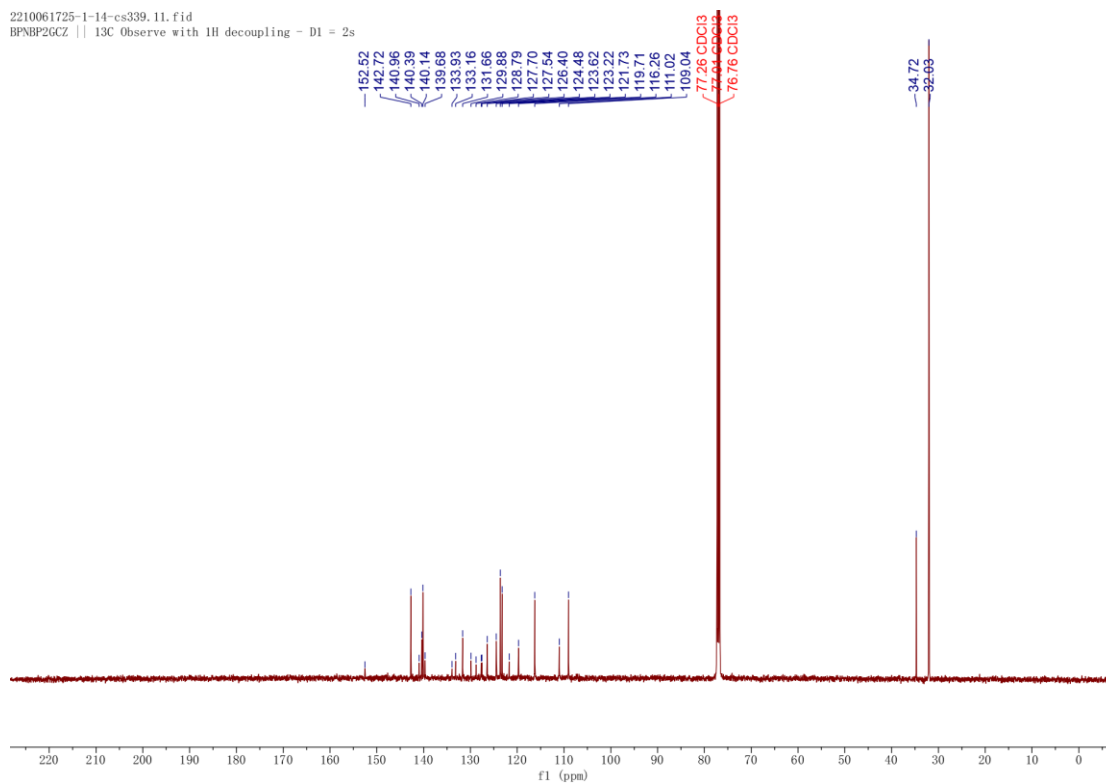


Figure 5.19. ¹³C NMR spectra of 2GCzBPPZ in CDCl₃.

Generic Display Report (all)

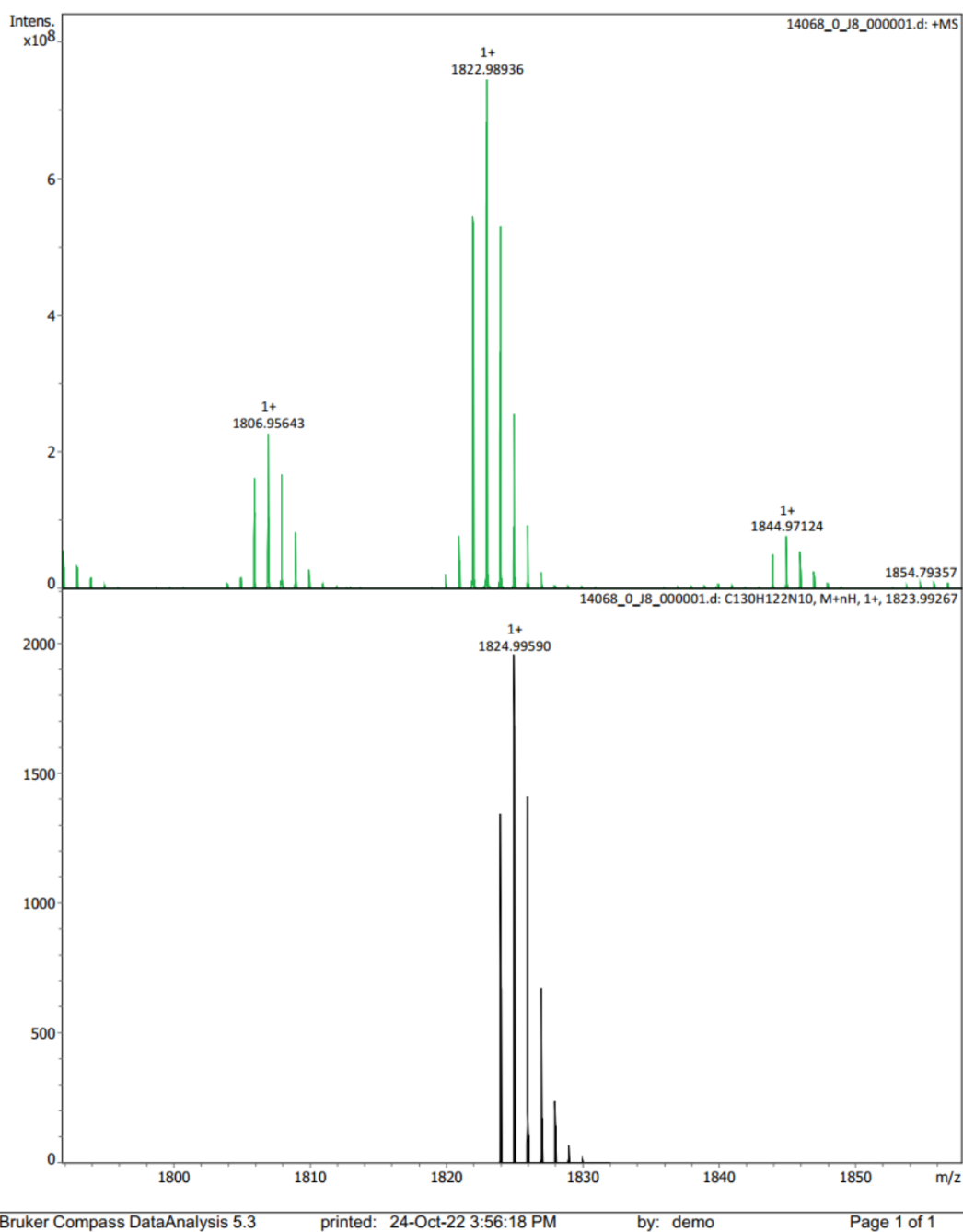


Figure 5.20. HRMS of 2GCzBPPZ.

Elemental Analysis Service Request Form

Researcher name Changfeng Si

Researcher email cs339@st-andrews.ac.uk

NOTE: Please submit ca. 10 mg of sample

Sample reference number	CS289-BPNBP2GCz
Name of Compound	BPNBP2GCz
Molecular formula	C130H122N10
Stability	
Hazards	
Other Remarks	

Analysis type:

Single Duplicate Triplicate

Analysis Result:

Element	Expected %	Found (1)	Found (2)	Found (3)
Nitrogen	7.68	7.70	7.78	
Carbon	85.58	85.77	86.20	
Hydrogen	6.74	6.84	6.88	

Authorising Signature:

Date completed	28.11.22
Signature	J-PC
comments	

Figure 5.21. Elemental analysis of 2GCzBPPZ.

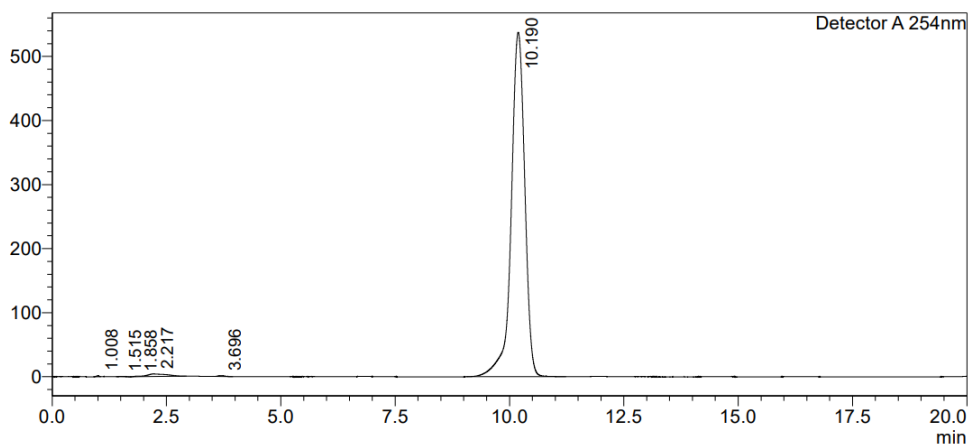
HPLC Trace Report31Mar2023

<Sample Information>

Sample Name : BPNBP2GCZ
 Sample ID :
 Method Filename : 85% Acetonitrile 15 Water 20 mins.lcm
 Batch Filename : BPNBP2GC.lcb
 Vial # : 1-23
 Injection Volume : 20 uL
 Date Acquired : 31/03/2023 21:37:26
 Date Processed : 31/03/2023 21:57:28
 Sample Type : Unknown
 Acquired by : System Administrator
 Processed by : System Administrator

<Chromatogram>

mV



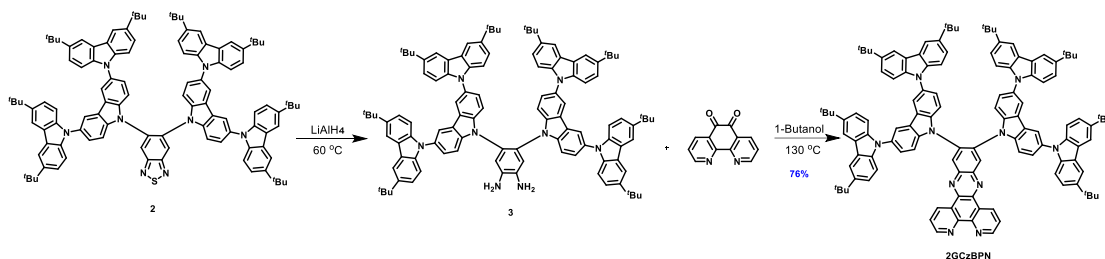
<Peak Table>

Detector A 254nm

Peak#	Ret. Time	Area	Height	Area%	Area/Height	Width at 5% Height
1	1.008	5216	1521	0.046	3.429	0.119
2	1.515	4148	344	0.037	12.050	0.271
3	1.858	7836	870	0.070	9.006	--
4	2.217	124941	4070	1.110	30.699	--
5	3.696	14751	1534	0.131	9.616	0.321
6	10.190	11099732	537490	98.606	20.651	0.767
Total		11256625	545830	100.000		

Figure 5.22. HPLC trace of 2GCzBPPZ.

Synthesis of 11,12-bis(3,3',6,6''-tetra-*tert*-butyl-9'*H*-[9,3':6',9''-tercarbazol]-9'-yl)dipyrido[3,2-*a*:2',3'-*c*]phenazine (2GCzBPN):



To a solution of **2** (1.0 g, 0.63 mmol, 1.0 equiv.) in dry THF (40 mL) were added lithium aluminum hydride (0.19g, 5.08 mmol 8.0 equiv.) under a continuous N₂ flow. The resulting mixture was stirred at 60 °C under N₂ atmosphere for 2 h. After cooling to 0 °C, the reaction mixture was quenched with water (2 mL) and then 2 M NaOH(aq) (2 mL) was added. The solution was filtered through a pad of Celite, which was subsequently rinsed with ethyl acetate (3×50 mL), and the filtrate was then extracted with ethyl acetate (3×50 mL). The organic layer was collected and dried over MgSO₄(s). After filtration and removal of the solvent under reduced pressure, compound **3** was used directly for the next step without further purification. Compound **3** and 1,10-phenanthroline-5,6-dione (0.13 g, 0.63 mmol, 1.0 equiv.) were added into 40 mL of 1-butanol and then heated to reflux for 12h under a nitrogen atmosphere. After cooling to room temperature, the solution was poured into water and extracted with DCM (3 × 100 mL). The organic layer was dried over Na₂SO₄, filtered, and concentrated under reduced pressure. The residue (around 1.0 g of an orange solid) was purified by column chromatography with (25% DCM/hexane) to afford the compound **2GCzBPN** as a yellow solid (0.83 g).

11,12-bis(3,3',6,6''-tetra-*tert*-butyl-9'*H*-[9,3':6',9''-tercarbazol]-9'-yl)dipyrido [3,2-*a*:2',3'-*c*]phenazine (2GCzBPN): Yield: 76%. R_f = 0.3 (25% DCM/Hexane). Mp >400 °C. ¹H NMR (500 MHz, CDCl₃) δ 9.87 (dd, *J* = 8.1, 1.6 Hz, 2H), 9.51 – 9.41 (m, 2H), 9.23 (s, 2H), 8.11 (s, 8H), 8.05 (d, *J* = 2.0 Hz, 4H), 7.98 (dd, *J* = 8.1, 4.4 Hz, 2H), 7.49 (d, *J* = 8.6 Hz, 4H), 7.33 (dd, *J* = 8.7, 2.0 Hz, 4H), 7.09 (s, 16H), 1.37 (s, 72H). ¹³C NMR (126 MHz, CDCl₃): δ 153.43, 148.91, 142.90, 142.62, 142.22, 139.77, 139.29, 136.28, 134.24, 131.85, 131.53, 127.24, 125.34, 124.61, 124.52, 123.74, 123.13, 118.97, 116.19, 111.17, 108.73, 77.36, 77.11, 76.86, 34.68, 32.05. HR-MS [M+H]⁺ Calculated: (C₁₂₂H₁₁₆N₁₀) 1721.9418; Found: 1721.9457. Anal. Calcd. for C₁₂₂H₁₁₆N₁₀: C, 85.08%; H, 6.79%; N, 8.13%. Found: C, 85.23%;

H, 6.96%; N, 8.29%. **HPLC analysis:** 99.2% pure on HPLC analysis, retention time 6.448 minutes in mixture of 90% Acetonitrile and 10% Water.

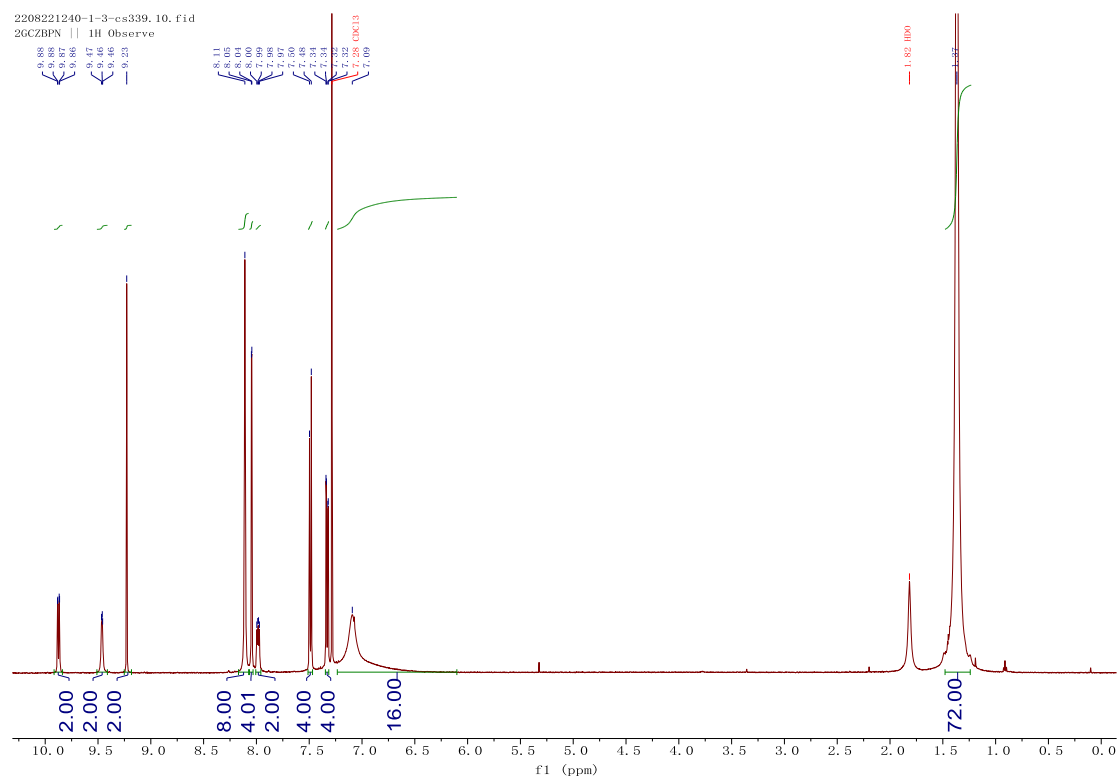


Figure 5.23. ^1H NMR spectra of 2GCzBPN in CDCl_3 .

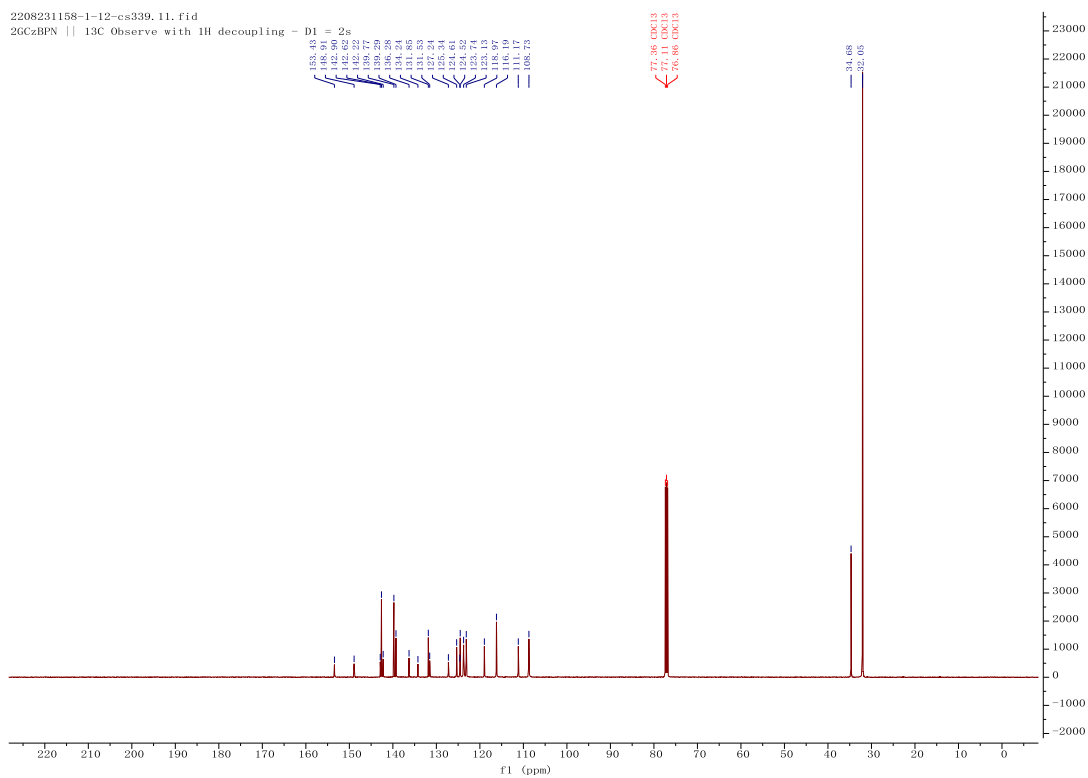
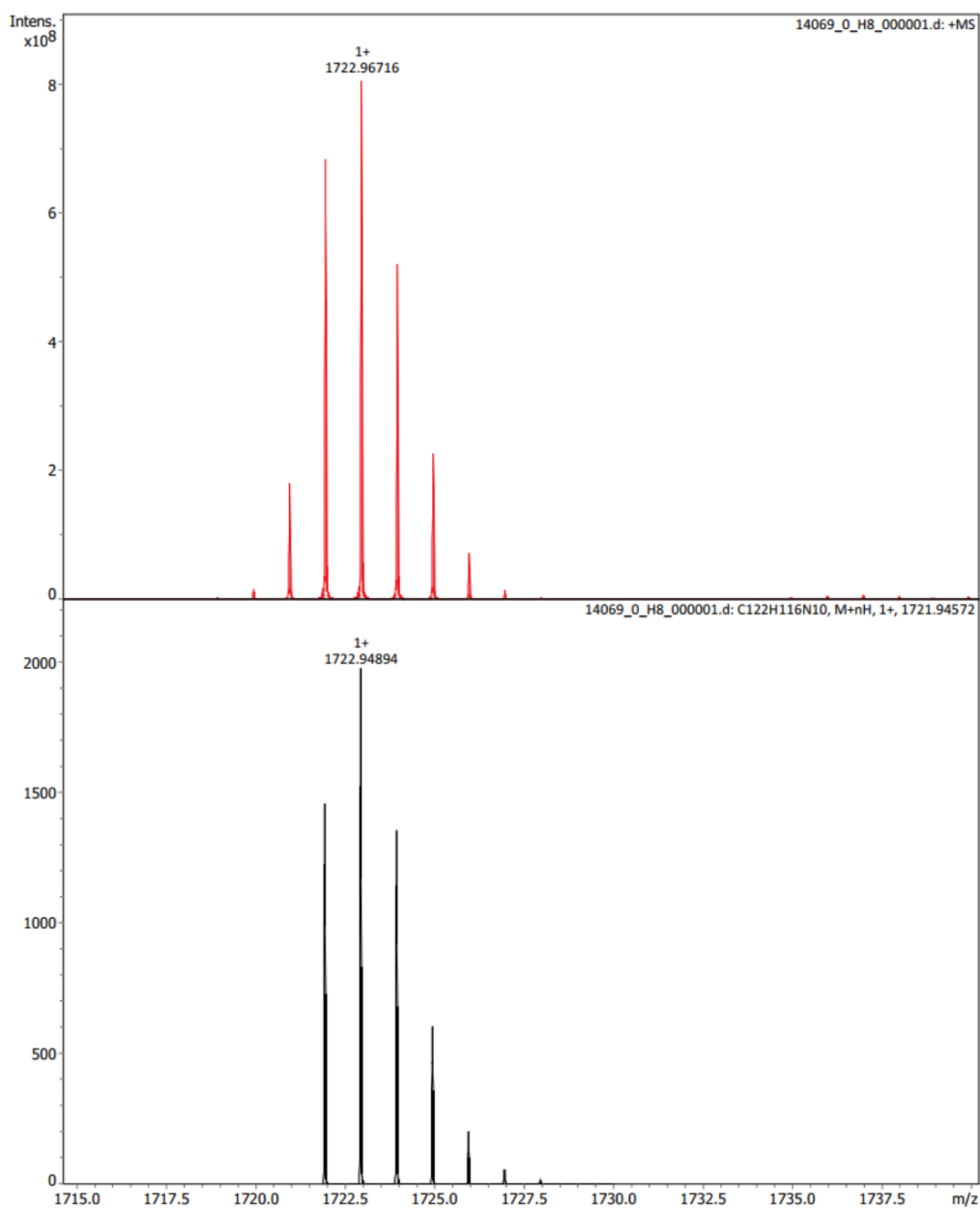


Figure 5.24. ^{13}C NMR spectra of **2GcZBPN** in CDCl_3 .

Generic Display Report (all)



Bruker Compass DataAnalysis 5.3

printed: 24-Oct-22 3:50:19 PM

by: demo

Page 1 of 1

Figure 5.25. HRMS of 2GCzBPN.

Elemental Analysis Service Request Form

Researcher name Changfeng Si

Researcher email cs339@st-andrews.ac.uk

NOTE: Please submit ca. 10 mg of sample

Sample reference number	CS260-2GCzBPN
Name of Compound	2GCzBPN
Molecular formula	C122H116N10
Stability	
Hazards	
Other Remarks	

Analysis type:

Single Duplicate Triplicate

Analysis Result:

Element	Expected %	Found (1)	Found (2)	Found (3)
Nitrogen	8.13	8.32	8.29	
Carbon	85.08	85.76	85.23	
Hydrogen	6.79	7.04	6.96	

Authorising Signature:


Date completed	28.11.22
Signature	
comments	

Figure 5.26. Elemental analysis of 2GCzBPN.

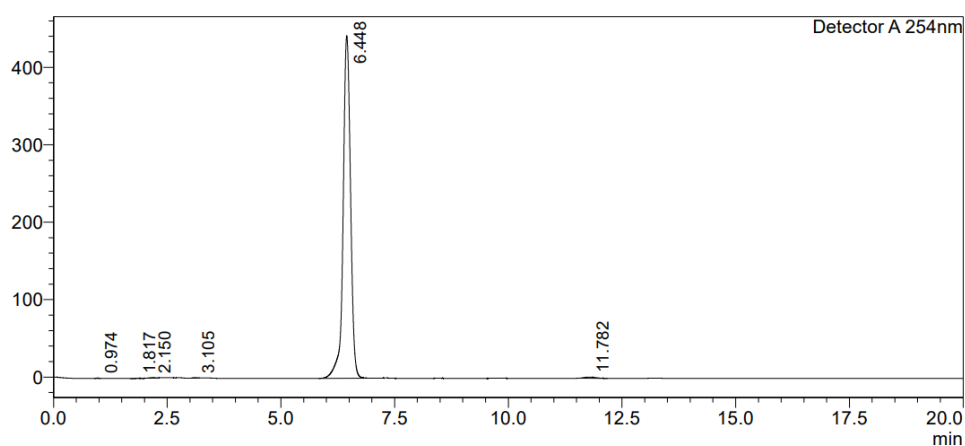
HPLC Trace Report 31 Mar 2023

<Sample Information>

Sample Name : 2GCZBPN
Sample ID :
Method Filename : 90% Acetonitrile 10 Water 20 mins.lcm
Batch Filename : BPNBP2GC.lcb
Vial # : 1-23
Injection Volume : 10 uL
Date Acquired : 31/03/2023 21:57:50
Date Processed : 31/03/2023 22:17:52
Sample Type : Unknown
Acquired by : System Administrator
Processed by : System Administrator

<Chromatogram>

mV



<Peak Table>

Detector A 254nm

Peak#	Ret. Time	Area	Height	Area%	Area/Height	Width at 5% Height
1	0.974	2173	637	0.043	3.412	0.099
2	1.817	2331	284	0.046	8.219	0.234
3	2.150	3258	408	0.064	7.992	0.226
4	3.105	2745	570	0.054	4.814	0.151
5	6.448	5018774	441879	99.242	11.358	0.422
6	11.782	27811	1579	0.550	17.611	0.540
Total		5057092	445357	100.000		

Figure 5.27. HPLC trace of 2GCzBPN.

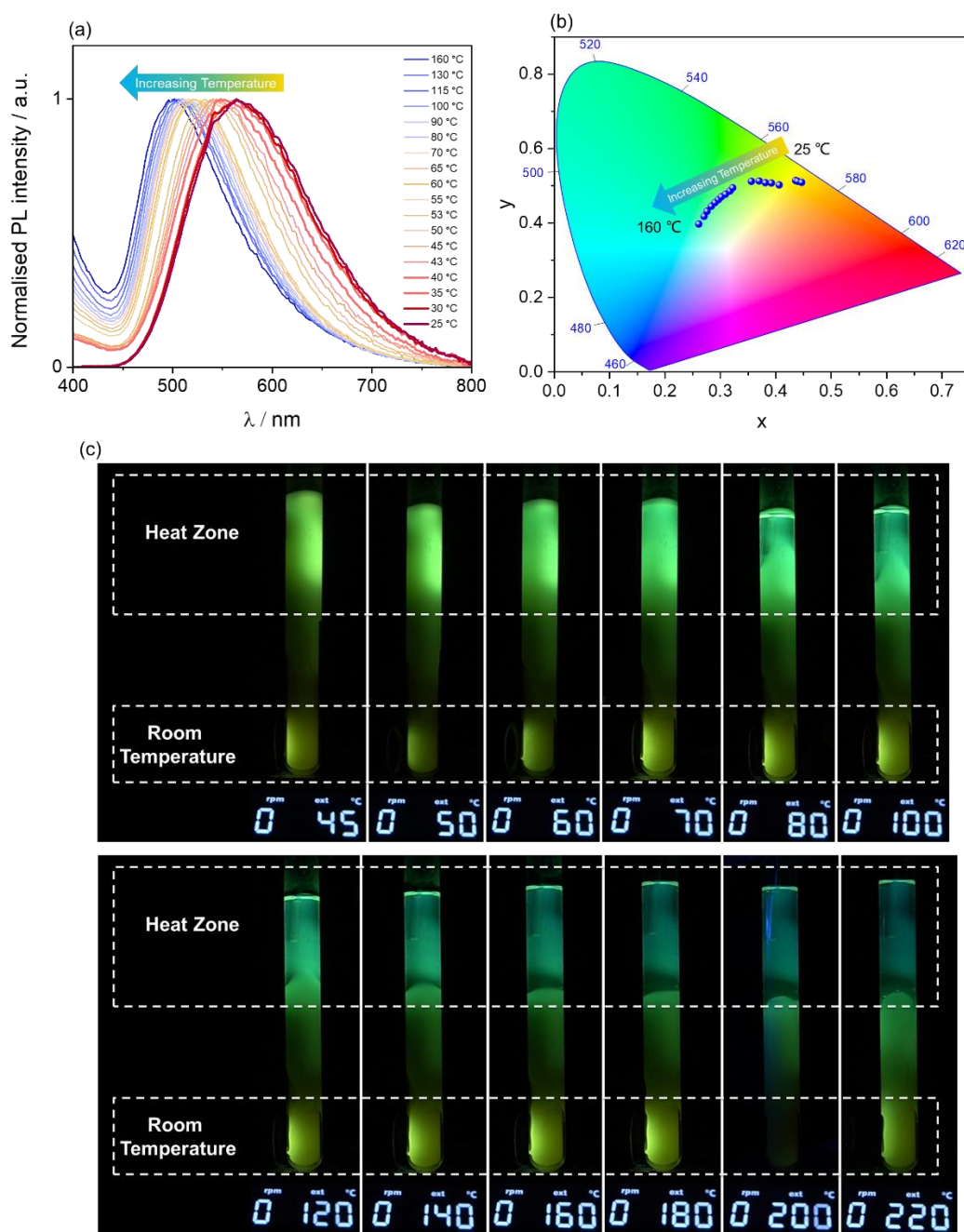
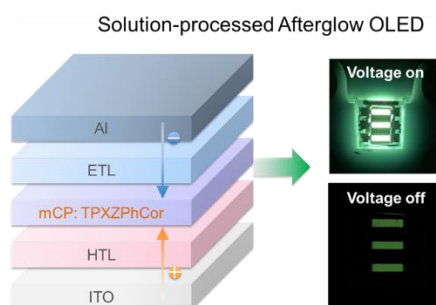
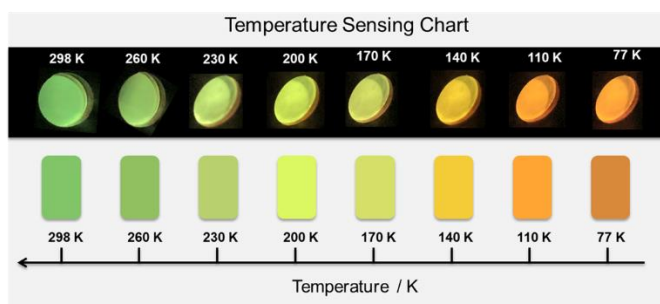
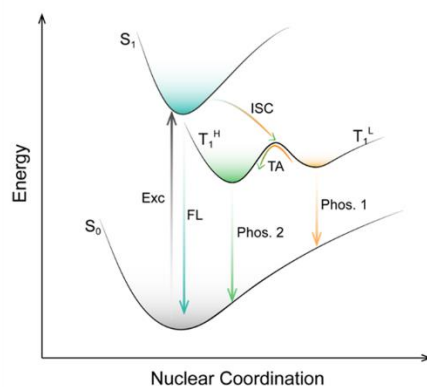
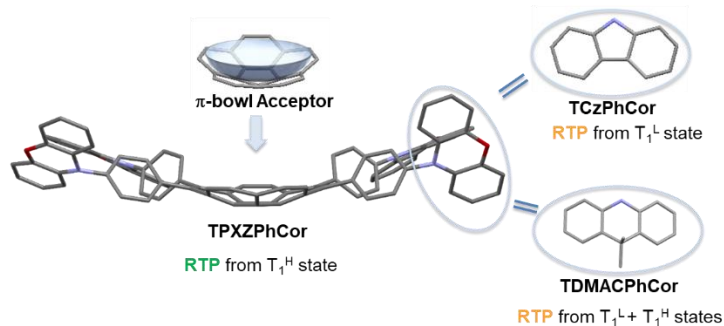


Figure 5.28. (a) Temperature-dependent emission spectra of Paraffin embedded with **2GCzBPPZ** ($\lambda_{\text{exc}} = 340$ nm); (b) Corresponding CIE plot; (c) Paraffin with **2GCzBPPZ** in test tube (length:160 mm, diameter: 16 mm) excited with a UV torch ($\lambda_{\text{exc}} = 360$ nm); The top side (Heat Zone) of the test tube was heated with a heat gun and the temperature was monitored using a Heidolph 509-67910-00 Pt 1000 Temperature Sensor.

Chapter 6: Room-Temperature Multiple Phosphorescence from Functionalized Corannulenes: Temperature Sensing and Afterglow Organic Light-Emitting Diode

Light-Emitting Diode



Manuscript of this project has been published in *Angewandte Chemie*.

Changfeng Si, Tao Wang, Abhishek Kumar Gupta, David B. Cordes, Alexandra M. Z. Slawin, Jay S. Siegel, Eli Zysman-Colman* *Angew. Chem. Int. Ed.* **2023**, e202309718. DOI: 10.1002/anie.202309718.

Dr. Tao Wang performed the mechanism analysis and assisted in updating the writing.

Dr. Abhishek Kumar Gupta carried out the OLED device fabrication.

Dr. David B. Cordes did X-ray crystallography.

Prof. Jay S. Siegel provided the starting material of TBrCor.

I completed all the syntheses and characterization, DFT and TD-DFT calculations, electrochemistry, photophysics measurements, temperature sensor measurements and I am the principal author of the text.

6.1 Introduction

In the previous Chapters, we investigated several families of D-A type orange-red TADF emitters containing BP derivatives as acceptors, which are planar, highly conjugated N-doped PAH. In this Chapter, we will explore a novel family of D-A emitters using a curved PAH without N-doping, corannulene, as the acceptor.

Corannulene, C₂₀H₁₀, also known as a buckybowll, is a curved PAH often visualized as the hydrogen-terminated C₂₀ cap of C₆₀ (Figure 6.1a).^{370,371} The intrinsically curved geometry of corannulene is dynamic, characterized by a rapid bowl-to-bowl inversion at room temperature.³⁷²⁻³⁷⁵ Corannulene has a permanent dipole moment of 2.1 D, good electron-accepting ability (LUMO= -2.65 eV) and redox activity.³⁷⁶⁻³⁷⁸ The rapid development of corannulene derivatives has seen their use as components in energy storage devices,³⁷⁹⁻³⁸¹ solar cells,³⁸²⁻³⁸⁵ organic field-effect transistors³⁸⁶⁻³⁸⁸ and biomedical applications.³⁸⁹⁻³⁹² However, there are only a handful of reports describing the luminescent properties of corannulene-based compounds, despite the fact that more than 1000 publications have focused on corannulene since the discovery of the first synthesis of corannulene in 1966.³⁹³⁻³⁹⁸ For instance, Mack *et al.* reported a corannulene-based blue emitter, 1,4-bis(corannulenylethynyl)benzene ($\lambda_{\text{PL}} = 420$ nm; $\Phi_{\text{PL}} = 60\%$ in CH₂Cl₂), exhibiting a much enhanced fluorescence compared to corannulene ($\lambda_{\text{PL}}=417$ nm; $\Phi_{\text{PL}}=7\%$ in cyclohexane) (Figure 6.1b).^{395,399} In 2018, Hatakeyama *et al.* reported a π -extended B₂N₂-embedded corannulene derivative ($\lambda_{\text{PL}} = 424$ nm; $\Phi_{\text{PL}} = 69\%$ in CH₂Cl₂) and the first reported example of a corannulene-based OLED, which showed a EQE_{max} of 2.61%.³⁹⁶ To date, all of the reported corannulene-based emitters are fluorescent, emitting from the S₁ state. And there are no examples of luminescent corannulene derivatives that harvest triplet excitons in their emission, like TADF and RTP.

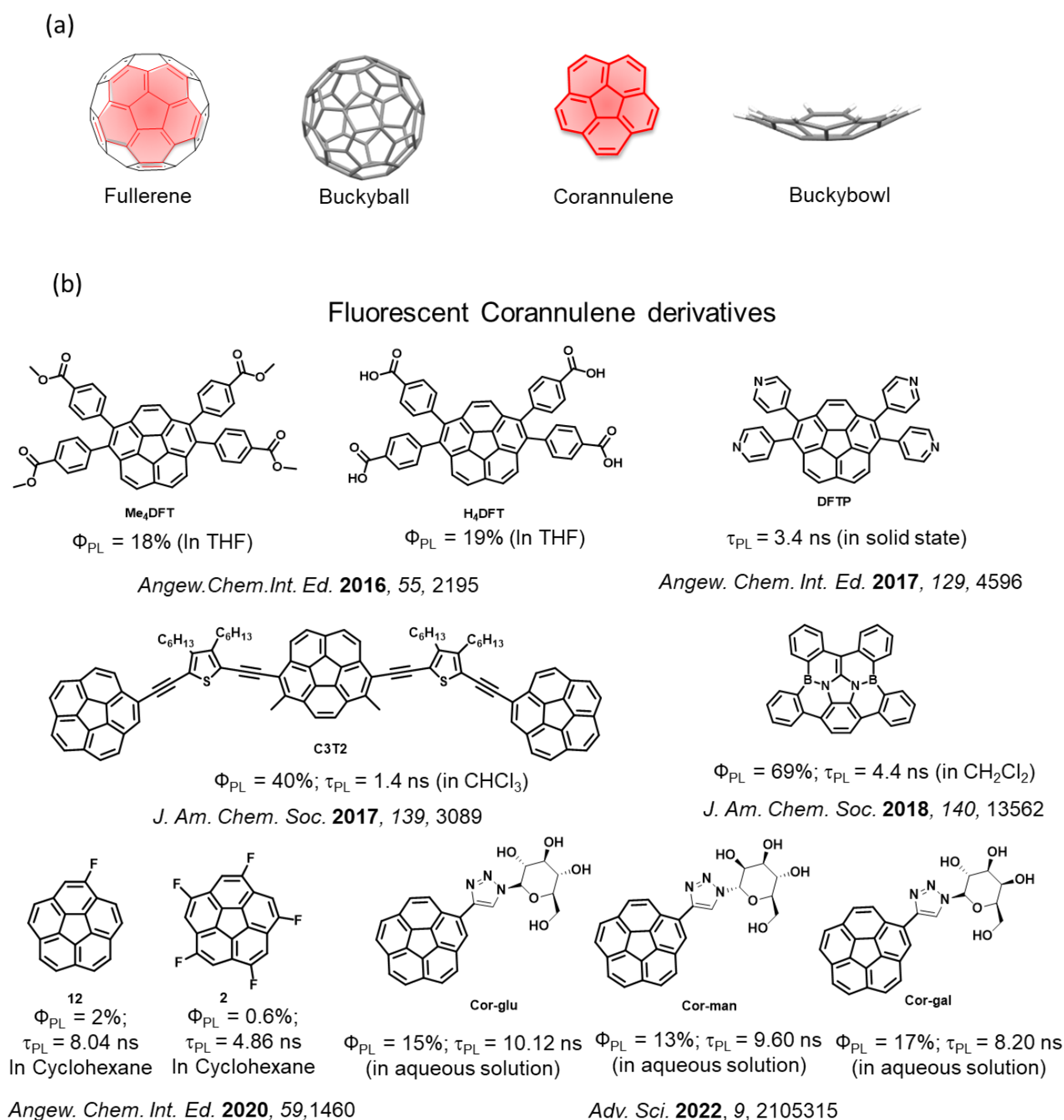


Figure 6.1. (a) Chemical structures of fullerene and corannulene; (b) Reported fluorescence corannulene derivatives.

RTP is the radiative transition from molecular triplet excitons at room temperature, together with a phosphorescence lifetime, τ_{ph} , that is typically on the order of microseconds. OLEDs with RTP emitters are able to harvest 100% of the excitons to produce light. The majority of reported RTP luminophores are organometallic complexes, where the metals, such as platinum (Pt) and iridium (Ir), can effectively enhance spin-orbit coupling and thus boost both ISC and radiative emission rates from the triplet manifold.^{65,400,401} So far, RTP counterparts have been widely investigated, evidenced by their use in myriad applications,

such as bioimaging,^{402–404} X-ray scintillators,^{405,406} nonlinear optics,⁴⁰⁷ sensing,^{408–412} information encryption,^{413–416} and OLEDs.^{417–419} Nevertheless, it remains a significant challenge to develop high-performance purely organic RTP emitters, as in these compounds that have a large ΔE_{ST} there is weak spin-orbit coupling between singlet and triplet states.⁴²⁰ To date, the most popular organic RTP design paradigms mainly follow two strategies: 1) boosting ISC by, for instance, introducing carbonyl groups^{421,422} and/or halogens⁴²³ into a molecule; 2) suppressing triplet nonradiative processes through, for instance, crystallization,^{327,424,425} supramolecular assembly,⁴²⁶ or matrix rigidification.^{427,428}

Most phosphorescent emitters generally obey Kasha's rule, where phosphorescence originates from T_1 .^{319,429} However, the observation of multiple phosphorescence in a single molecule, a violation of Kasha's rule,^{430–435} has rarely been documented. The observation of multiple phosphorescence provides an insight into high-lying triplet excited-state dynamics. For example, several benzothiophene derivatives showing dual phosphorescence that originate from emissions from T_2 and T_1 (Figure **6.2a**, top).⁴³⁰ Huang and co-workers reported a series of triazine derivatives that show dual phosphorescence from the monomer (T_1) and the aggregate (T_1^a) (Figure **6.2b**).⁴³³ Zhang and co-workers developed several AIE-active RTP emitters exhibiting dual phosphorescence from TPA-based donor-acceptor motifs (Figure **6.2c**, top), which was attributed to a high-lying T_1 (T_1^H) state and only be observed at low temperature (<250 K).⁴³⁴ Very recently, our group reported two donor-acceptor naphthalene-based dual phosphorescent luminophores, whose RTP originates from a T_1^H state while low-temperature phosphorescence (LTP) is gradually dominated by a lower-lying T_1 state (T_1^L) (Figure **6.2c**, bottom).⁴³⁵ Despite these examples, there is a dearth of systematic investigations of the origins of dual phosphorescence and insight gleaned for how to regulate the coupling between two triplet excited states, which effectively retards the development and applications of materials that show multiple phosphorescence.

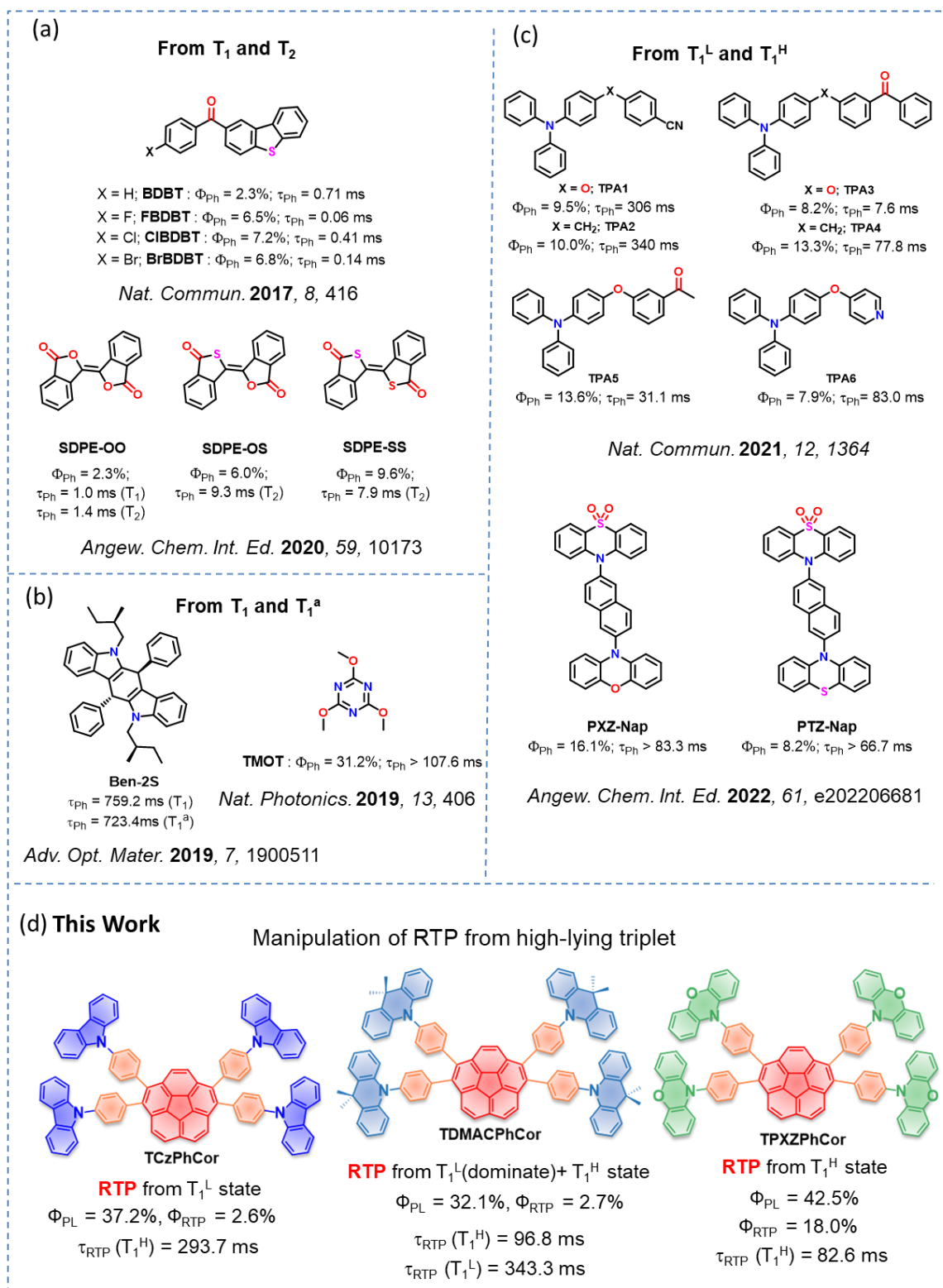
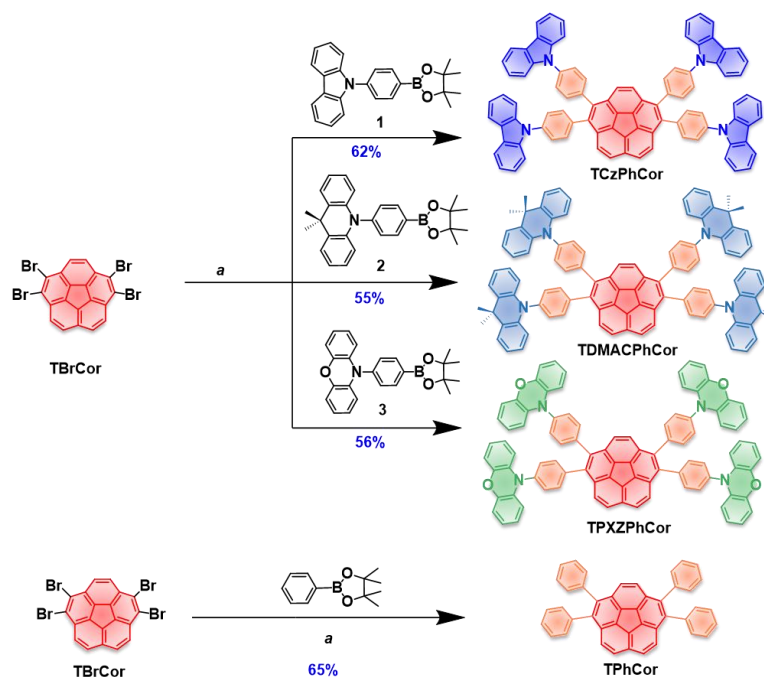


Figure 6.2. Chemical structures of reported RTP emitters: (a) Examples of phosphorescence from T_1 and T_2 in the crystal. (b) Emission from T_1 (monomer) and T_1^a (aggregate) in crystals; (c) Emission from higher-lying and lower-lying triplet excited states (T_1^H and T_1^L); (d) Chemical structures of multi-D-A corannulenes reported in this Chapter.

Here, we devised three tetra(donor)-acceptor compounds **TCzPhCor**, **TDMACPhCor**, and **TPXZPhCor** employing corannulene as the acceptor and **Cz**, **DMAC**, and **PXZ**, respectively, as peripheral donors (Figure 6.2d). In a bid to develop TADF materials, we hypothesized that the introduction of multiple donors would provide multiple avenues for ISC/RISC via spin-vibronic coupling.⁴³⁶ However, instead we discovered unusual RTP behavior in these compounds, showing three different types of RTP from different triplet excited states. We found that using mCP as the host, **TCzPhCor** shows RTP from only one LE state. By contrast, dual RTP from T_1^H and T_1^L , and T_1^H -dominated RTP are observed in **TDMACPhCor**, **TPXZPhCor**, respectively. We have explored colorimetric temperature sensing using **TPXZPhCor** and found that it exhibits excellent sensitivity and exhibits a wide range of color changes, from cyan at 298 K to orange at 77 K. To the best of our knowledge, it represents the most promising performance for temperature sensing using phosphorescent afterglow materials. Further, we have also demonstrated the utility of **TPXZPhCor** as the emitter in an afterglow OLED, which shows the highest device performance reported to date for this class of devices, with an EQE_{max} and L_{max} of 3.3% and 5167 cd m⁻², respectively.

6.2 Synthesis



Scheme 6.1. Synthetic route for **TCzPhCor**, **TDMACPhCor**, **TPXZPhCor** and **TPhCor**.

Reagents and conditions: ^aTHF, (K₂CO₃)_{aq}, Pd(PPh₃)₄ (0.2 equiv.), 80 °C, 12 h.

Compounds **TCzPhCor**, **TDMACPhCor**, **TPXZPhCor** and 1,2,5,6-tetraphenyldibenzo[*ghi,mno*] fluoranthene (**TPhCor**) were synthesized in greater than 55% yield via the Suzuki-Miyaura cross-coupling reaction using 1,2,7,8-tetrabromocorannulene (**TBrCor**) as the core (outlined in Scheme 6.1).³¹⁶ The identity and purity of the three compounds were verified by ¹H & ¹³C NMR spectroscopy, melting point determination, high-resolution mass spectrometry, elemental analyses, and HPLC.

6.3 Single-crystal Analysis

The X-ray single crystals of **TPXZPhCor** and **TPhCor** were obtained from slow evaporation of toluene at room temperature. As shown in Figure 6.3a, **TPXZPhCor** adopts a twisted D-A geometry, indicating no significant π - π interactions is present (Figure 6.3c). The bowl depth, described as the perpendicular distance from the terminal carbon atom of the corannulene skeleton to the parallel planes containing the hub C1-C5 ring, is 0.779 Å (Figure 6.3a bottom). This is shallower than that of **TPhCor** (0.88 Å, Figure 6.3d) and corannulene (0.87 Å).³⁹³ Figure 6.3b illustrates the packing motifs of **TPXZPhCor** dimers in the unit cell. Numerous CH $\cdots\pi$ interactions exist in the dimers with associated H \cdots centroid distances of 2.78 (phenylene to corannulene) and 2.81 Å (phenoxazine to corannulene), which may contribute to the suppression of nonradiative excitonic transitions. Neighboring molecules disposed in a relative concave-convex orientation also show weak CH $\cdots\pi$ (phenylene to phenoxazine, H \cdots centroid distance of 2.52 Å) and π $\cdots\pi$ (corannulene to phenoxazine, centroid \cdots centroid distance of 3.63 Å) interactions. Due to the steric bulk of the PXZ groups, adjacent molecules pack in an offset manner with the shortest distance between the centroids of the central cyclopentadiene ring of the corannulenes being 7.83 Å (Figure 6.3c). To best of our knowledge, corannulene derivatives generally exhibit convex-concave⁴³⁷⁻⁴³⁹ or “clamshell” type packing.³⁹⁸ The picture of the packing motif observed in **TPXZPhCor** is slightly different. The shortest equivalent distance between adjacent **TPXZPhCor** molecules arranged in a concave-convex manner is 11.80 Å, which is longer than those documented in previous reports⁴³⁷⁻⁴³⁹ and in a concave-concave manner is 16.07 Å. (Figure 6.3c).

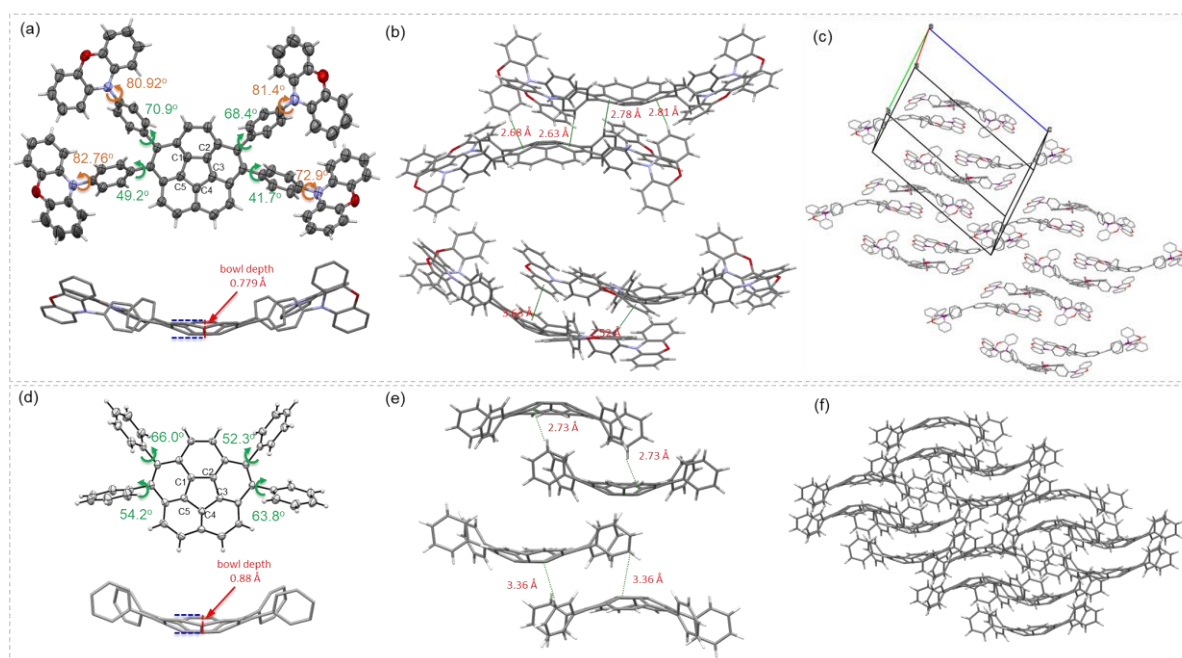


Figure 6.3. Thermal ellipsoid (top) and stick (bottom) plots of one independent molecule in the single crystal structure of (a) **TPXZPhCor** and (d) **TPhCor** (Ellipsoids are drawn at the 50% probability level and solvent molecules have been omitted for clarity); (b) **TPXZPhCor** and (e) **TPhCor** dimers in convex-convex and convex-concave orientations along with relevant intermolecular interactions. Packing of (c) **TPXZPhCor** and (f) **TPhCor** single crystals.

6.4 Theoretical Modelling

We first modelled the photophysical properties of the three compounds in the gas phase using TD-DFT within TDA²²² at the TDA-DFT-M062X/6-31G(d,p) level of theory⁴⁴⁰ based on the optimized ground-state geometries calculated at the same level of theory. At the optimized S_0 geometries, the bowl shape of corannulene is present in all three compounds (Figure 6.4a). The bowl depth slightly decreases as the electron-donating strength of the donors increases from 0.84 Å (**TCzPhCor**) to 0.83 Å (**TDMACPhCor**) and 0.79 Å (**TPXZPhCor**), all shallower than those of corannulene (0.88 Å) and **TPhCor** (0.84 Å). The calculated bowl depths of **TPhCor** and **TPXZPhCor** coincide well with those of the single crystal structures (Figure 6.3a and d). Strongly twisted D–A geometries were computed for **TCzPhCor**, **TDMACPhCor**, and **TPXZPhCor** (Figure 6.4b). Larger dihedral angles between donor and the phenylene bridge exist in **TDMACPhCor** (from 84.9 to 94.8°) and **TPXZPhCor** (from 81.0 to 95.7°) compared to **TCzPhCor** (from 51.0 to 52.5°), while the dihedral angles between

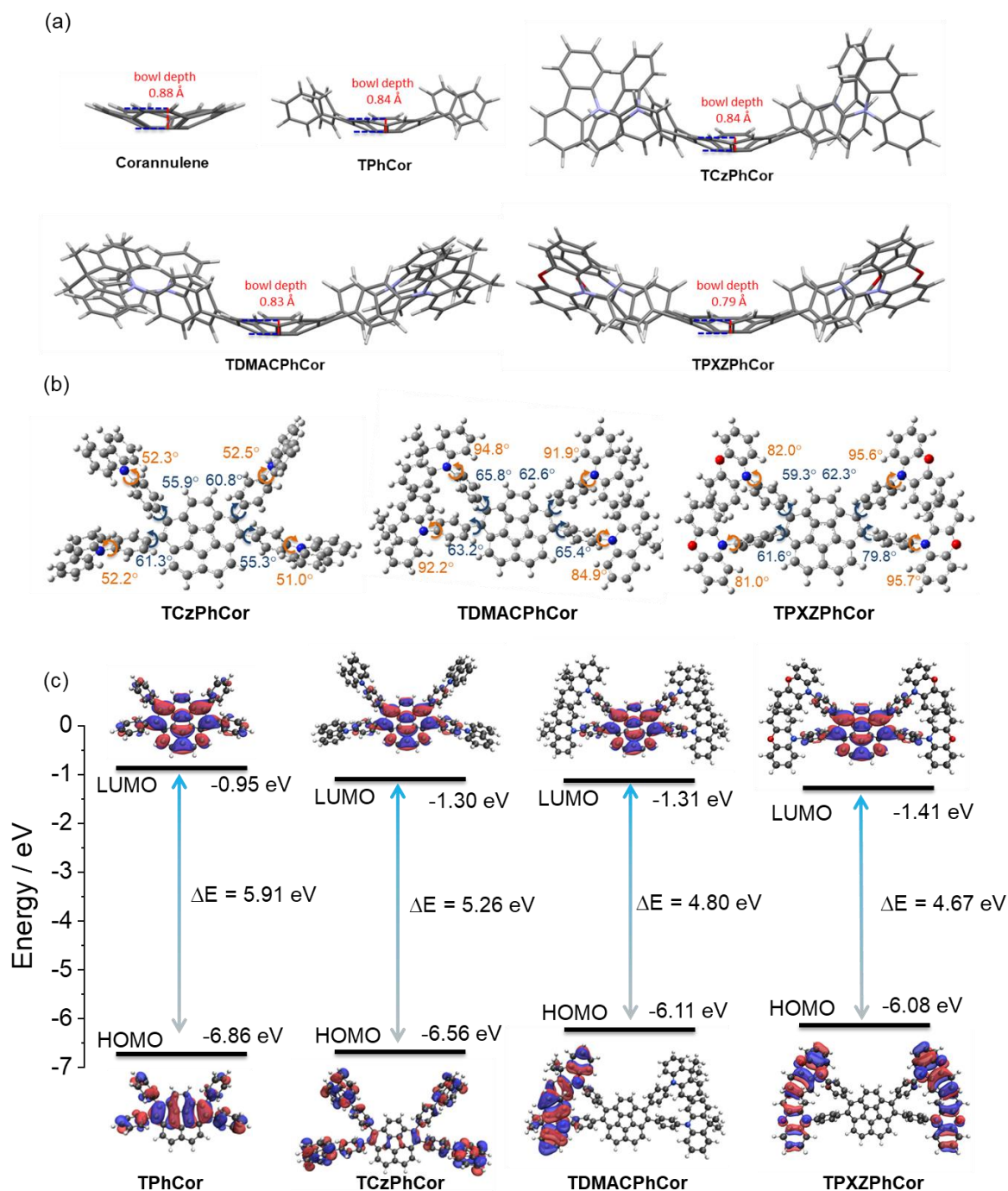


Figure 6.4. (a) Bowl depth of corannulene, **TPhCor**, **TCzPhCor**, **TDMACPhCor** and **TPXZPhCor** at optimized S_0 geometries; (b) Optimized S_0 geometries of **TCzPhCor**, **TDMACPhCor** and **TPXZPhCor** calculated at the DFT-M062X/6-31G(d,p) level (dihedral angles between corannulene and the π bridge in dark blue color; dihedral angles between π bridge and the donor N-heteroaromatics in orange color). (c) Electron density distribution and energy levels of frontier molecular orbitals (isovalue: 0.02).

the phenylene bridge and corannulene slightly increase in **TDMACPhCor** (from 62.6° to 65.8°) and **TPXZPhCor** (from 59.3° to 79.8°) than **TCzPhCor** (from 53.3 to 61.3°). The S_0 geometry of **TPXZPhCor** is similar to that found in the single crystal (Figure 6.3a), where the donor groups are highly twisted with respect to the phenylene bridge and the phenylene bridge is itself strongly twisted with respect to corannulene. The calculated energies of the HOMO and LUMO are displayed in Figure 6.4b. As expected, the HOMO and LUMO are localized on the donors and the corannulene acceptor, respectively. The progressively destabilized HOMO reflects the increasing electron-donating strength of the donors in **TCzPhCor**, **TDMACPhCor**, and **TPXZPhCor**, respectively, while similar LUMO energies reveal negligible electronic coupling between the donors with the corannulene acceptor. The LUMO of **TPhCor** is destabilized (− 0.95 eV) compared to the LUMOs of three corannulene derivatives (Figure 6.4b) as it is a smaller conjugation length.

NTO analyses at the S_0 geometry provide insight into the nature of excited-state transitions (Figure 6.5a). For **TCzPhCor**, the S_1 state possesses a LE character mostly localized on the corannulene core. However, for **TDMACPhCor** and **TPXZPhCor**, the S_1 state is of CT character, reflective of the stabilization of this state compared to the LE states in the presence of the stronger electron-donors; indeed, there is a progressive though very weak stabilization of the S_1 state from 3.77 eV in **TCzPhCor** to 3.76 eV in **TDMACPhCor** and 3.67 eV in **TPXZPhCor** as a result of the near orthogonal conformation of the donor groups relative to the **TPhCor** (Figure 6.5a). The $\Delta E_{S_1T_1}$ values also decrease progressively from 0.63 eV in **TCzPhCor** to 0.56 eV in **TDMACPhCor** and 0.47 eV in **TPXZPhCor**.

The S_1 and T_1 geometries were optimized at the TDA-DFT-M062X/6-31G(d,p) level. **TCzPhCor** exhibits a relatively larger geometry relaxation, where the root-mean-square displacement (RMSD) value calculated using the VMD program²²³ is 0.60 Å between S_0 and S_1 compared to that of **TDMACPhCor** (0.48 Å) and **TPXZPhCor** (0.48 Å). While **TDMACPhCor** shows a quite large RMSD value of 0.92 Å between S_0 and T_1 , **TCzPhCor** and **TPXZPhCor** possess the same value of 0.77 Å (Figure 6.5Figure 2.b). Such large changes in molecular geometries between the S_0 state and excited states probably result in multiple meta-stable excited-state conformers. The bowl depth of corannulene in both the S_1 (bowl depth= ~0.68 Å) and T_1 (bowl depth= ~0.63 Å) geometries decreases by more than 15%

compared to that in the S_0 geometry (bowl depth = ~ 0.82 Å) for all three compounds.

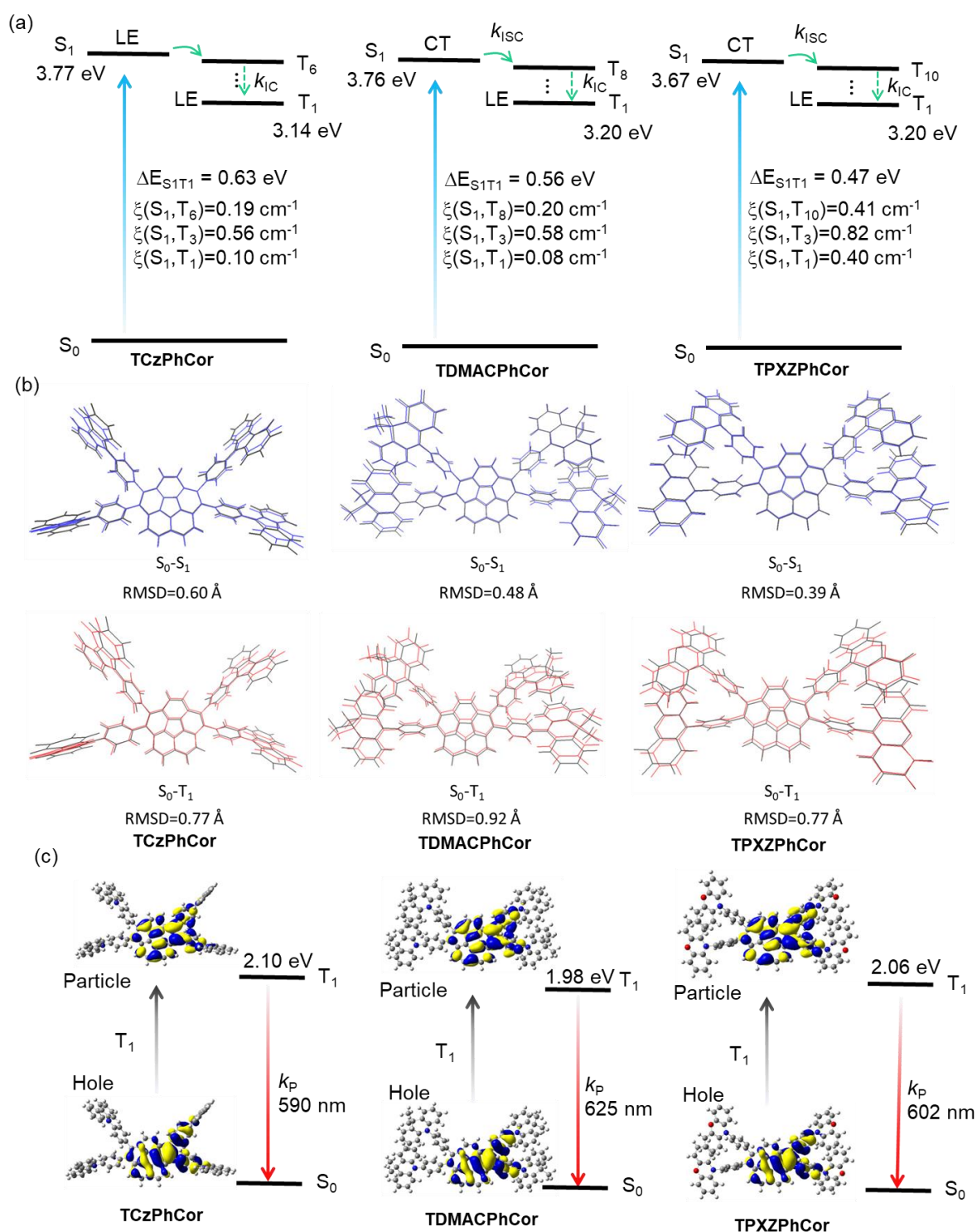


Figure 6.5. (a) Vertical excitation energy levels calculated at the optimized S_0 geometry in the gas phase at the TDA-DFT-M062X/6-31G(d,p) level. (b) Calculated geometric changes between S_0 (black), S_1 (blue) and T_1 (red) states. (c) Natural transition orbitals (isovalue: 0.02) and T_1 vertical emission.

At the relaxed S_1 geometry, there is a much larger S_1 - T_1 SOC matrix element (0.40 cm^{-1}) in **TPXZPhCor** than that in both **TCzPhCor** (0.10 cm^{-1}) and **TDMACPhCor** (0.08 cm^{-1}) (Figure 6.5a), while larger SOC values of greater than 0.56 cm^{-1} are noted from S_1 to T_3 . The density of triplet states and the SOC between these and S_1 should favor ISC, which should be beneficial for producing triplet excitons for RTP. At the optimized T_1 geometry (Figure 6.5c), **TCzPhCor**, **TDMACPhCor** and **TPXZPhCor** possess similar T_1 energies, which indicate the same LE character of the T_1 state on the corannulene core. The relatively stabilized T_1 energy of **TDMACPhCor** probably originates from an LE state that extends onto the phenylene rings, which is possible due to the smaller dihedral angles between the corannulene and the π -linker than exists in **TCzPhCor** and **TPXZPhCor**.

6.5 Electrochemistry

The energies of the FMOs were inferred from the electrochemical behavior of **TCzPhCor**, **TDMACPhCor** and **TPXZPhCor** using CV and DPV in degassed DCM, with tetra-*n*-butylammonium hexafluorophosphate, [$n\text{Bu}_4\text{N}$]PF₆, as the supporting electrolyte (Figure 6.6). The oxidation potentials (E_{ox}), determined from the DPV peak values, are 1.29 V (**TCzPhCor**), 0.81 V (**TDMACPhCor**) and 0.73 V (**TPXZPhCor**) versus SCE. The corresponding HOMO energies are -5.64 eV , -5.13 eV and -5.07 eV for **TCzPhCor**, **TDMACPhCor**, and **TPXZPhCor**, respectively, consistent with the trend in calculated HOMO energies (Figure 6.5) and reflecting the increasing strength of the donor across the series. **TDMACPhCor** exhibited a slightly more negative reduction potential ($E_{\text{red}} = -2.02 \text{ V}$) than **TCzPhCor** ($E_{\text{red}} = -1.94 \text{ V}$), which likely results from the weakly coupled D-A geometry of the former. **TPXZPhCor** exhibits a more anodically shifted E_{red} (-1.78 V) originating from the completely electronically decoupled D-A geometry. The corresponding LUMO energies of **TCzPhCor**, **TDMACPhCor** and **TPXZPhCor** are -2.40 eV , -2.32 eV , and -2.56 eV . The resulting HOMO-LUMO gaps of **TCzPhCor**, **TDMACPhCor** and **TPXZPhCor** are 3.24, 2.81 and 2.51 eV, respectively, mirroring the trend in the calculated values.

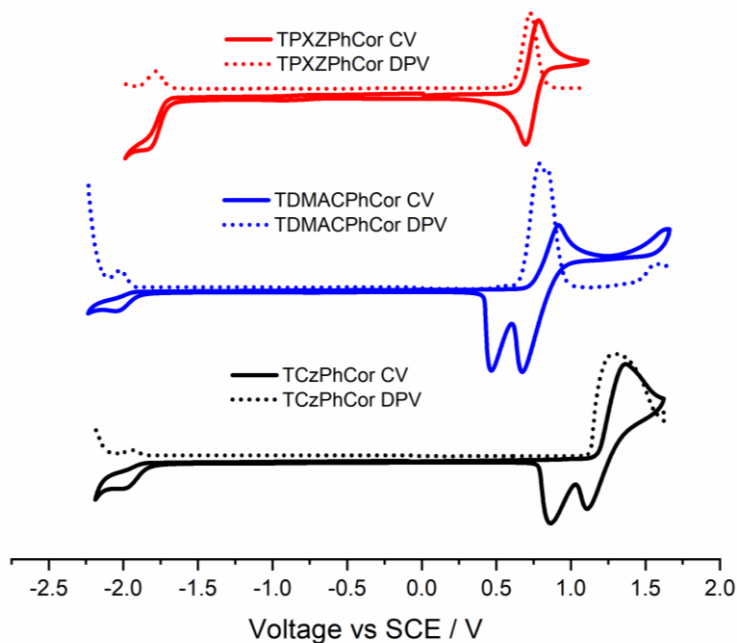


Figure 6.6. Cyclic and differential pulse voltammograms measured in degassed DCM with 0.1 M $[n\text{Bu}_4\text{N}]\text{PF}_6$ as the supporting electrolyte and Fc/Fc^+ as the internal reference (0.46 V vs SCE).²²⁴ Scan rate = 100 mV s^{-1} .

6.6 Photophysics in Solution

The UV-Vis absorption spectra of the three emitters measured in toluene show a strong absorption centered at ~ 300 nm (Figure 6.7a and b, and Table 6.1), originating from the LE π - π^* transitions on the corannulene core.⁴⁴¹ A weak CT transition band at around 400 nm is observed in **TDMACPhCor** and **TPXZPhCor** (Figure 6.7b). The enhanced molar absorptivity coefficients of the band at around 300 nm of the three compounds compared to **TPhCor** and corannulene are the result of contributions from LE transitions on the donors (Figure 6.7b).^{442,443} The optical bandgaps, calculated from the intersection point of the normalized absorption and emission spectra, for **TCzPhCor**, **TDMACPhCor** and **TPXZPhCor** are 3.04 eV, 3.01 eV, 2.90 eV, respectively (Figure 6.7c). SSPL spectra recorded in toluene show a gradual red-shift from **TCzPhCor** to **TDMACPhCor** and **TPXZPhCor**, coinciding with their decreasing optical gaps (Figure 6.7a). A stronger positive solvatochromism is observed in **TPXZPhCor** compared to **TDMACPhCor** (Figure 6.7d-e), which is almost absent in **TCzPhCor**.

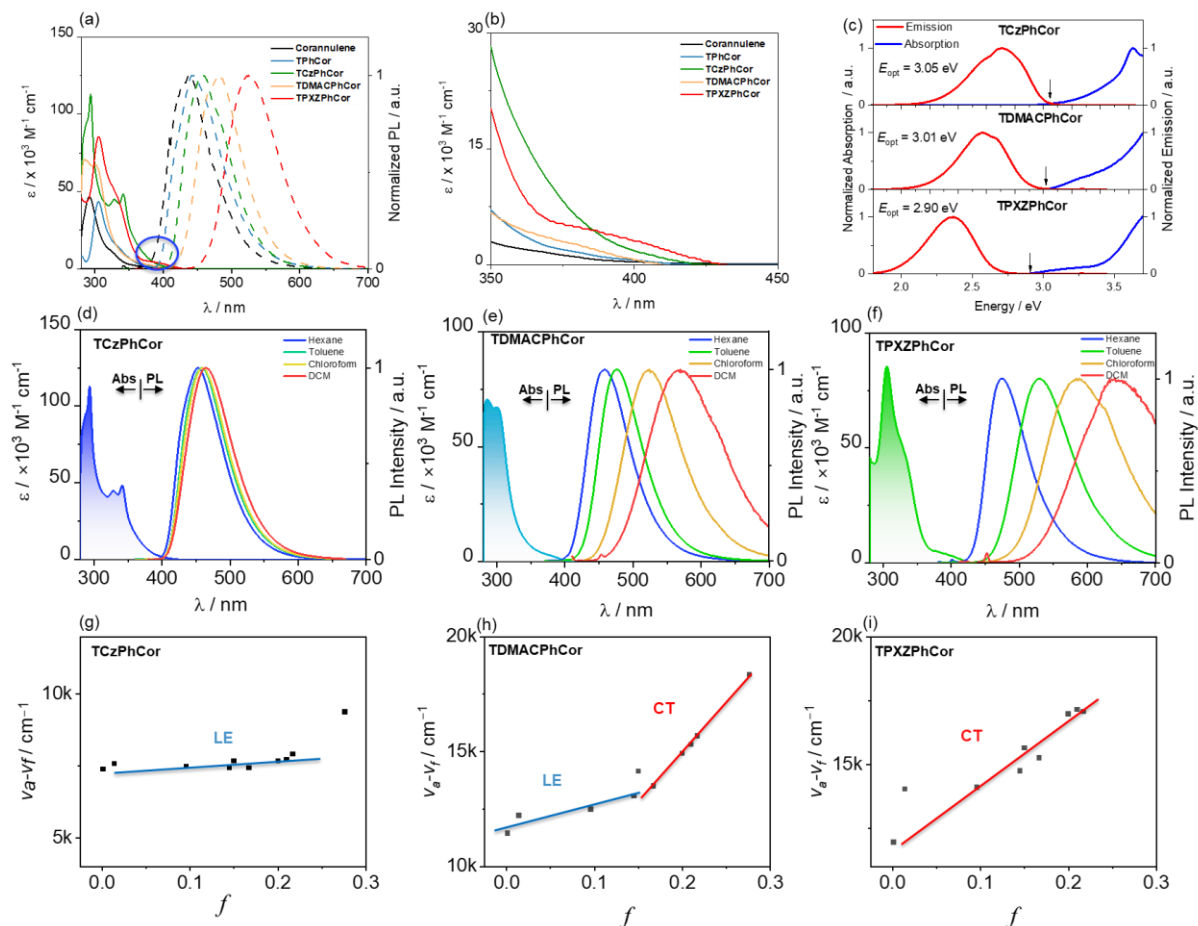


Figure 6.7. (a) UV-vis absorption and steady-state PL spectra for **Corannulene**, **TPhCor**, **TCzPhCor**, **TDMACPhCor** and **TPXZPhCor** in toluene ($\lambda_{\text{exc}} = 340$ nm); (b) Absorption zoom of all the compounds from 350 to 450 nm; (c) The optical bandgaps were determined from the intersection point of the normalized absorption and emission spectra for **TCzPhCor**, **TDMACPhCor** and **TPXZPhCor**. UV-vis absorption (in toluene) and solvatochromism studies of (d) **TCzPhCor**, (e) **TDMACPhCor**, and (f) **TPXZPhCor** recorded in air at room temperature ($\lambda_{\text{exc}} = 340$ nm). Lippert-Mataga plots of (g) **TCzPhCor**, (h) **TDMACPhCor** and (i) **TPXZPhCor**.

As shown in Figure 6.7g-i, the Lippert-Mataga study reveals that the emissive state of **TCzPhCor** is of dominant LE character, while the emissive state of **TDMACPhCor** is better described as having hybrid LE and CT character, that of **TPXZPhCor** is of CT character, matched well with the calculations (Figure 6.5). The related absorption and PL spectra for the solvatochromism study and calculated parameters are presented in Table 6.1. Notably, a linear relationship between the Stokes shift ($u_a - u_f$) and the orientational polarizability f was observed

for **TCzPhCor** and **TPXZPhCor** (Figure 6.7g-i). The relatively small slope for **TCzPhCor** and unstructured emission imply that the S_1 state possesses a small degree of CT character, reflected in a dipole moment, μ_e , of 11.4 D calculated according to the Lippert-Mataga equation. For **TPXZPhCor**, the slope of the Lippert Mataga plot is much steeper, which implies a much stronger CT character to the S_1 , linked with an associated μ_e of 24.7 D. The picture for **TDMACPhCor** is more complex as the Lippert-Mataga plot reveals two distinct regimes with μ_e of 16.9 D and 33.0 D. Such behavior is characteristic of an excited state of mixed LE and CT character (HLCT).^{69,444,445}

The Φ_{PL} values of **TCzPhCor**, **TDMACPhCor** and **TPXZPhCor** in aerated toluene are 34%, 18% and 16%, which slightly increase to 37%, 21% and 19%, respectively (Table 6.2). This minor reduction in value indicates a possible quenching of fluorescence by the oxygen present in the solution.⁴⁴⁶ The time-resolved PL decays are monoexponential, with PL lifetimes, τ_{PL} , in the nanosecond regime (Figure 6.8). The Φ_{PL} and τ_{PL} values rule out emission involving triplet excitons. The ΔE_{ST} for **TCzPhCor**, **TDMACPhCor**, and **TPXZPhCor**, determined from the onsets of prompt and delayed emission in toluene at 77 K, are 0.59 eV, 0.54 eV, and 0.34 eV (Figure 6.8g-i), respectively. Such large ΔE_{ST} values rule out the possibility of TADF. The similar phosphorescence spectra in the three compounds recorded in toluene at 77 K indicate that the nature of the T_1 state is the same and localized on the **TPhCor** core (Figure 6.8j).

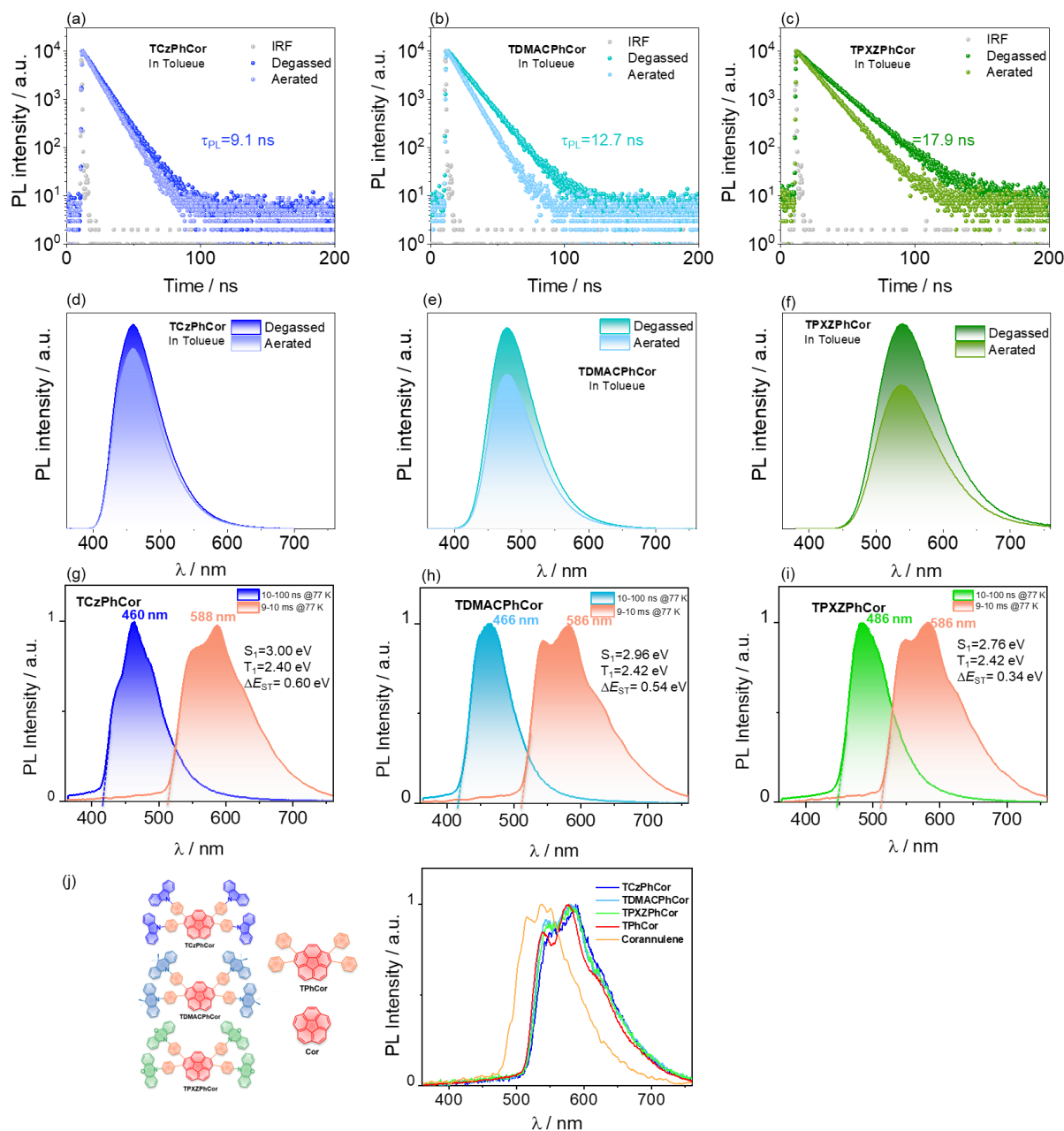


Figure 6.8 Time-resolved PL decay profiles of (a) TCzPhCor, (b) TDMACPhCor and (c) TPXZPhCor in aerated and degassed toluene ($\lambda_{exc} = 379$ nm). Steady-state PL spectra of (d) TCzPhCor, (e) TDMACPhCor and (f) TPXZPhCor in degassed and aerated toluene ($\lambda_{exc} = 340$ nm). Prompt fluorescence (1-100 ns) and phosphorescence spectra (1-10 ms) recorded in toluene at 77 K of (g) TCzPhCor, (h) TDMACPhCor, and (i) TPXZPhCor, (j) phosphorescence of Corannulene, TPhCor ($\lambda_{exc} = 343$ nm).

Table 6.1 Detailed absorption and emission peak positions of the three compounds in different solvents

Solvent	ε	n	$f(\varepsilon, n)$	TCzPhCor			TDMACPhCor			TPXZPhCor		
				λ_a /nm	λ_f /nm	$\nu_a-\nu_f$ /cm ⁻¹	λ_a /nm	λ_f /nm	$\nu_a-\nu_f$ /cm ⁻¹	λ_a /nm	λ_f /nm	$\nu_a-\nu_f$ /cm ⁻¹
Hexane	1.9	1.375	0.0012	340	454	7385	301	459	11436	303	475	11436
Toluene	2.38	1.494	0.014	340	458	7577	301	476	12214	304	530	12214
Butyl ether	3.08	1.399	0.096	340	456	7482	301	482	12475	304	532	12475
Isopropyl ether	3.88	1.368	0.145	340	455	7433	301	496	13061	304	551	13061
Chloroform	4.81	1.443	0.149	340	460	7672	301	524	14138	305	583	14138
Ethyl ether	4.34	1.352	0.167	340	455	7433	301	507	13498	305	570	13498
Ethyl acetate	6.02	1.372	0.200	340	460	7672	301	546	14907	305	632	14907
Tetrahydrofuran	7.58	1.407	0.210	340	461	7720	301	558	15301	305	639	15301
Methylene chloride	8.93	1.424	0.217	340	465	7906	301	570	15678	305	636	15678
Dimethyl formamide	37	1.427	0.276	340	499	9371	301	672	18341	305	-	-

λ_a : The first absorption band; λ_f Peak value of PL spectra obtained at 298 K, concentration 10^{-5} M, $\lambda_{exc} = 340$ nm.

6.7 RTP from Solid States

We next investigated the photophysical properties of the three emitters in PMMA at a 1 wt% doping concentration. As shown in Figure 6.9, the steady-state PL spectra of **TCzPhCor**, **TDMACPhCor**, and **TPXZPhCor** show structureless emission at λ_{PL} of 450 nm, 465 nm, and 500 nm, respectively, with associated τ_{PL} of 9.8 ns, 25.2 ns, and 30.8 ns, respectively. RTP spectra of **TCzPhCor**, **TDMACPhCor** and **TPXZPhCor** were acquired across a time-gated window of 30-200 ms, with maxima, λ_{Ph} , centered at around 580 nm, 530 nm and 550 nm, respectively. The corresponding phosphorescence lifetimes (τ_{Ph}) are 573.0 ms, 286.1 ms, and 34.6 ms, respectively (Figure 6.9d). The low-temperature phosphorescence (LTP) spectra at 77 K are centred at around 575 nm, 576 nm and 580 nm for **TCzPhCor**, **TDMACPhCor** and **TPXZPhCor**, respectively. The LTP emission profiles overlap very well with the phosphorescence spectrum of 1 wt% **TPhCor** in PMMA measured at 77 K. Based on these results, we can conclude that the LTP originates from the LE T_1 state localized on **TPhCor**. It is worth noting that there is a remarkable difference in the phosphorescence spectra at 298 K and 77 K of both **TDMACPhCor** and **TPXZPhCor** (Figure 6.9b and c), reflected also in the different phosphorescence afterglows at 298 K and 77 K (Figure 6.9e and f). Based on similar

observations made in our previous report,⁴³⁵ we assign this dual phosphorescence to T_1^H and T_1^L , associated with phosphorescence from two conformers. Considering the broad RTP of **TDMACPhCor** and **TPXZPhCor**, we contend that the spectra consist of contributions from both T_1^H and T_1^L , which is only possible if there is thermally activated excitonic coupling between T_1^H and T_1^L (*vide infra*).

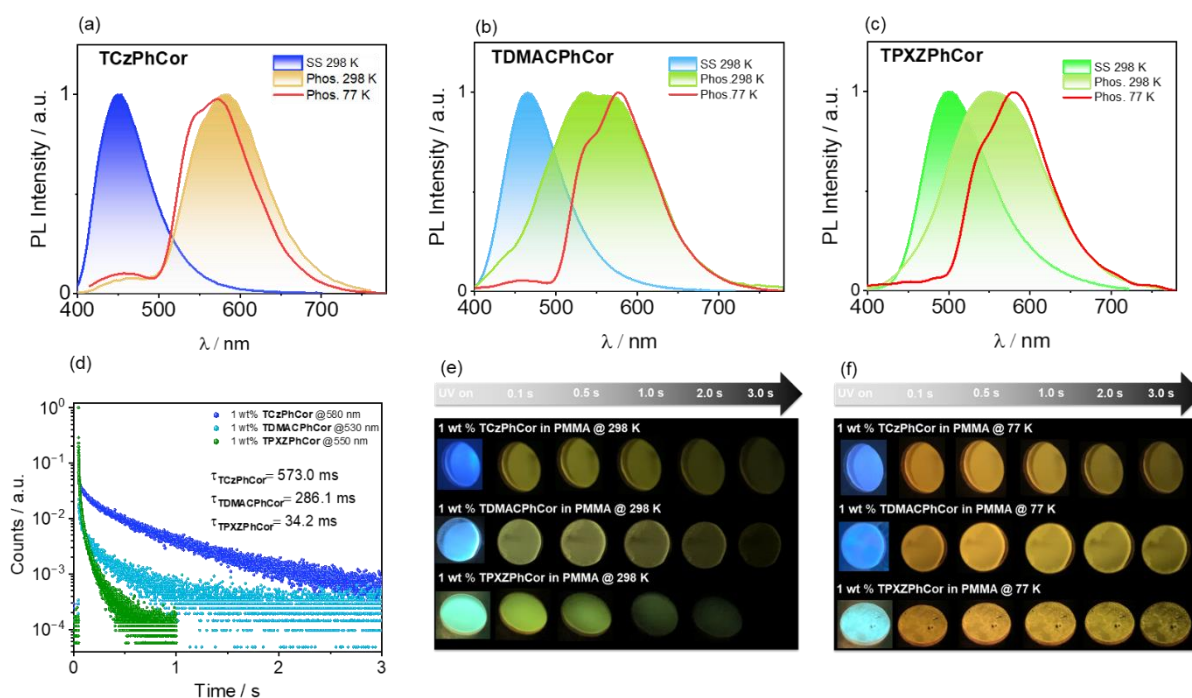


Figure 6.9. Steady-state and time-gated (time-gated window: 30-200 ms) PL spectra of (a) 1 wt% **TCzPhCor**, (b) 1 wt% **TDMACPhCor** and (c) 1 wt% **TPXZPhCor** in PMMA at 298 K and 77 K ($\lambda_{exc}=320$ nm). (d) Time-resolved PL decay profiles of 1 wt% **TCzPhCor**, 1 wt% **TDMACPhCor** and 1 wt% **TPXZPhCor** in PMMA under vacuum. Images of the PMMA films with emitters showing afterglows at (e) 298 K and (f) 77 K under vacuum (excitation source: 365 nm UV torch).

Table 6.2. Summary of photophysical properties of corannulene-based compounds

	$\lambda_{\text{abs}}/(\epsilon / \times 10^3 \text{ M}^{-1} \text{ cm}^{-1})/\text{nm}^a$	λ_{PL}^a / nm	Φ_{PL}^b /%	λ_{PL}^c /nm	Φ_{PL}^c /%	τ_p^c /ns	$\tau_{\text{Ph}}^{\text{Hd}}$ /ms	$\tau_{\text{Ph}}^{\text{Ld}}$ /ms	S_1/T_1^g /eV	ΔE_{ST} /eV
TPhCor	305(43), 336 (13)	442	11(10)	443	13.0 (12.0)	15.1	-	144.2	3.07/ 2.43	0.64
TCzPhCor	238 (211), 229(114), 327(53), 339(64)	458	37 (34)	462	36.2 (35.0)	6.5	-	293.7	3.00/ 2.40	0.60
TDMACPhCor	261(167), 283(163),303(160)	476	21 (18)	485	32.1 (29.4)	19.8	96.8	343.3	2.96/ 2.42	0.54
TPXZPhCor	242(133),260(48) 279(38), 303(48), 333(21)	530	19 (16)	529	42.5 (24.5)	30.7	82.6	-	2.77/ 2.43	0.34

^a In PhMe at 298 K ($\lambda_{\text{exc}}=340$ nm). ^b Quinine sulfate in H₂SO₄ (aq) was used as the reference ($\Phi_{\text{PL}} = 54.6\%$, $\lambda_{\text{exc}}=340$ nm).²⁷⁷ ^c Spin-coated 1 wt% **TPhCor** in PMMA, 1 wt% for **TCzPhCor**, 7 wt% for **TDMACPhCor** and 15 wt% for **TPXZPhCor** doped in mCP films and values were determined using an integrating sphere ($\lambda_{\text{exc}}=340$ nm). Values quoted are under N₂. Values in parentheses are in air. ^d PL decay detected emission wavelength is 585 nm for **TPhCor**, **TCzPhCor** and **TDMACPhCor** for RTP T₁^L, 490 nm for **TDMACPhCor** and 530 nm for **TPXZPhCor** for RTP (T₁^H). ^e In DCM with 0.1 M [*n*Bu₄N]PF₆ as supporting electrolyte and Fc/Fc⁺ as the internal reference (0.46 V vs. SCE).²²⁴ The HOMO and LUMO energies were determined using $E_{\text{HOMO/LUMO}} = -(E_{\text{ox}}/ E_{\text{red}} + 4.8)$ eV where E_{ox} and E_{red} are anodic and cathodic peak potentials, respectively, obtained from the DPV.²²⁴ ^f $E_g = |E_{\text{HOMO}} - E_{\text{LUMO}}|$ ^g S₁ was obtained from the onset of the prompt emission (time-gated window: 1–100 ns) measured in toluene at 77 K and T₁ was obtained from the onset of the phosphorescence spectrum (time-gated window: 1–10 ms) measured in toluene at 77 K ($\lambda_{\text{exc}}=343$ nm).

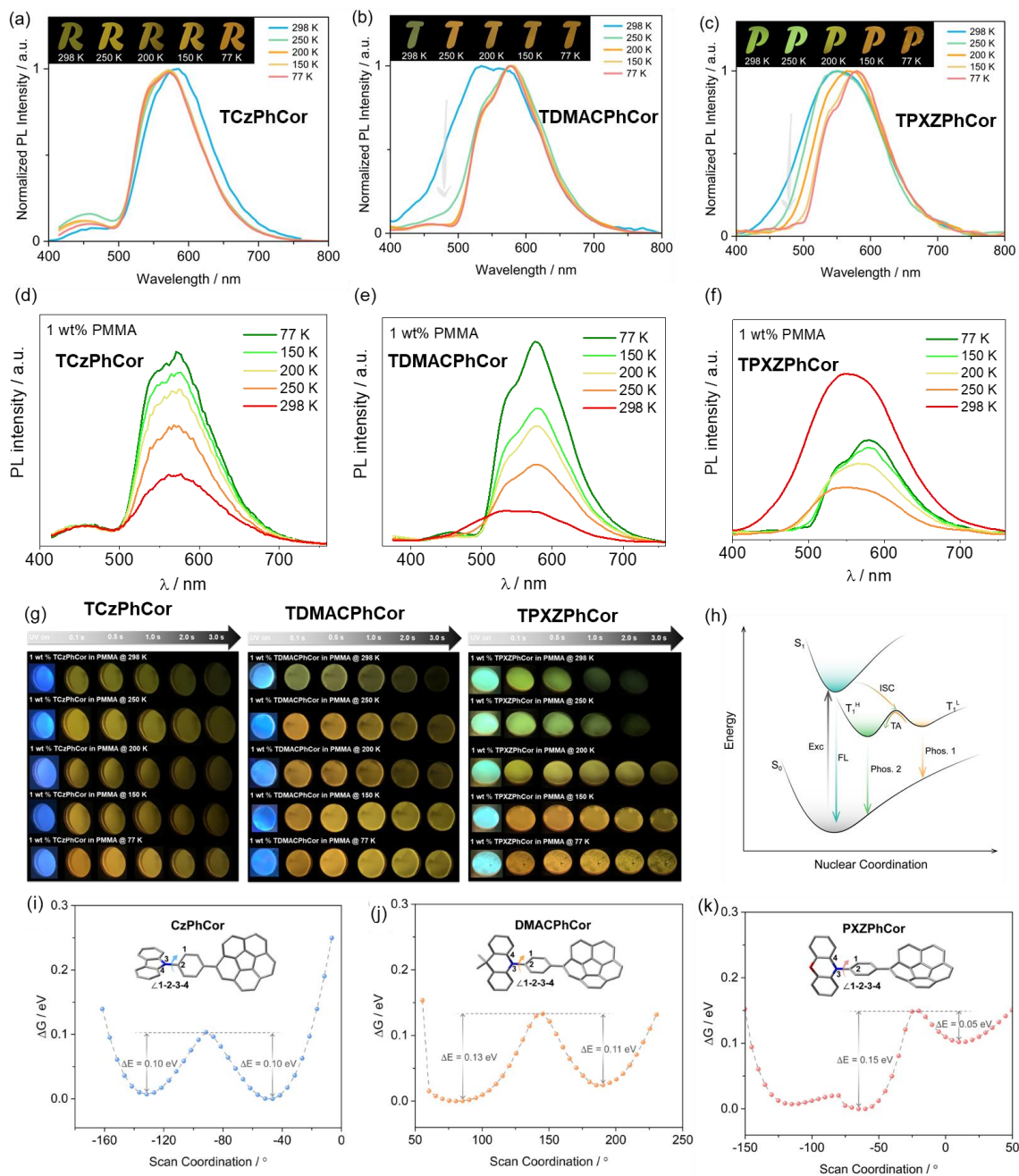


Figure 6.10. Temperature-dependent phosphorescence spectra of (a) (d) 1 wt% **TCzPhCor**, (b) (e) 1 wt% **TDMACPhCor** and (c) (f) 1 wt% **TPXZPhCor** in PMMA (time-gated window: 30–200 ms, $\lambda_{exc} = 320$ nm); (g) images showing phosphorescence in vacuum at different temperatures, excited by a 365 nm UV torch. (h) Mechanistic illustration of dual phosphorescence using a simplified Jablonski diagram; Exc: excitation; FL: fluorescence; TA: thermal activation; Phos.: phosphorescence. Potential energy scan of (i) **CzPhCor**, (j) **DMACPhCor**, and (k) **PXZPhCor** at the optimized T_1 geometry in the gas phase at uM06-2X/6-31G(d,p) level; inset: molecular structures associated with scanned torsion angles ($\angle 1-2-3-4$).

To validate this hypothesis, temperature-dependent phosphorescence spectra were measured from 77 to 298 K. As shown in Figure 6.10a and d, the phosphorescence emission of **TCzPhCor** shows a negligible change across this temperature range; the weak emission band centred at ~460 nm is ascribed to steady-state fluorescence due to the residual background excitation, evidenced by the unchanged PL intensity as a function of temperature. A similar background excitation was observed in the phosphorescence spectrum of the **TCzPhCor**-doped PMMA film. However, for **TDMACPhCor** and **TPXZPhCor**, distinctly red-shifted phosphorescence spectra were obtained with decreasing temperature, also reflected by the change in the phosphorescence afterglows (Figure 6.10b, c, e, f), which is the result of loss of the phosphorescence from T_1^H . Figure 6.10h illustrates a plausible mechanistic explanation, where excitonic coupling between T_1^H and T_1^L is temperature dependent, which explains why at different temperatures, differing phosphorescence afterglows were recorded. To elucidate the mechanism, we also conducted the relaxed potential energy surface calculation based on the optimized T_1 geometry at the uM06-2X/6-31G(d,p) level (Figure 6.10i-k). Notably, it is not feasible to conduct such calculations on these molecules given their size, and so to simplify the calculations, mono-substituted corannulenes were taken as examples. As demonstrated in our previous work,⁴³⁵ the energy barrier is the key to determining which of the two geometries (T_1^H and T_1^L) dominates phosphorescence emission. The PES modelling was carried out by progressively modulating the torsion angle between the donor (Cz, DMAC and PXZ) and benzene bridge. For **CzPhCor**, two triplet conformers were acquired showing the almost identical relative Gibbs energy (ΔG) indicates the same triplet energy (Figure 6.10i), which could explain why dual phosphorescence is not present in **TCzPhCor**. However, two different triplet conformers co-exist in both **DMACPhCor** and **PXZPhCor**. These two conformers are separated by a transition state (TS) geometry. For **DMACPhCor**, the barrier energies between the TS geometry and the two conformers are 0.13 eV and 0.11 eV (Figure 6.10j), which indicate that there is a rapid interconversion between the two conformers at ambient temperatures. As Figures 6.10b indicate, there are two contributions to the phosphorescence emission of **TDMACPhCor**, which we have attributed to T_1^H and T_1^L states. For **PXZPhCor**, the interconversion mainly occurs from T_1^L to T_1^H conformers at room temperature due to a much smaller energy barrier between T_1^L and TS conformers compared to that between T_1^H and TS

conformers (0.05 eV vs 0.15 eV) (Figure 6.10k). This is consistent with the T_1^H -dominated RTP recorded in **TPXZPhCor** (Figures 6.10c). Assuming these model systems accurately reflect the conformational dynamics of the tetrasubstituted compounds in the study then a plausible Jablonski diagram can be formulated (Figure 6.10h), where at room temperature T_1^H RTP can be thermally populated from the T_1^L state. At low temperatures, T_1^L phosphorescence dominates due to the inhibited thermal activation. The energy differences between T_1^H and T_1^L approximated from the onsets of the respective phosphorescence spectra are 0.36 eV, and 0.31 eV for **TDMACPhCor**, and **TPXZPhCor**, respectively.

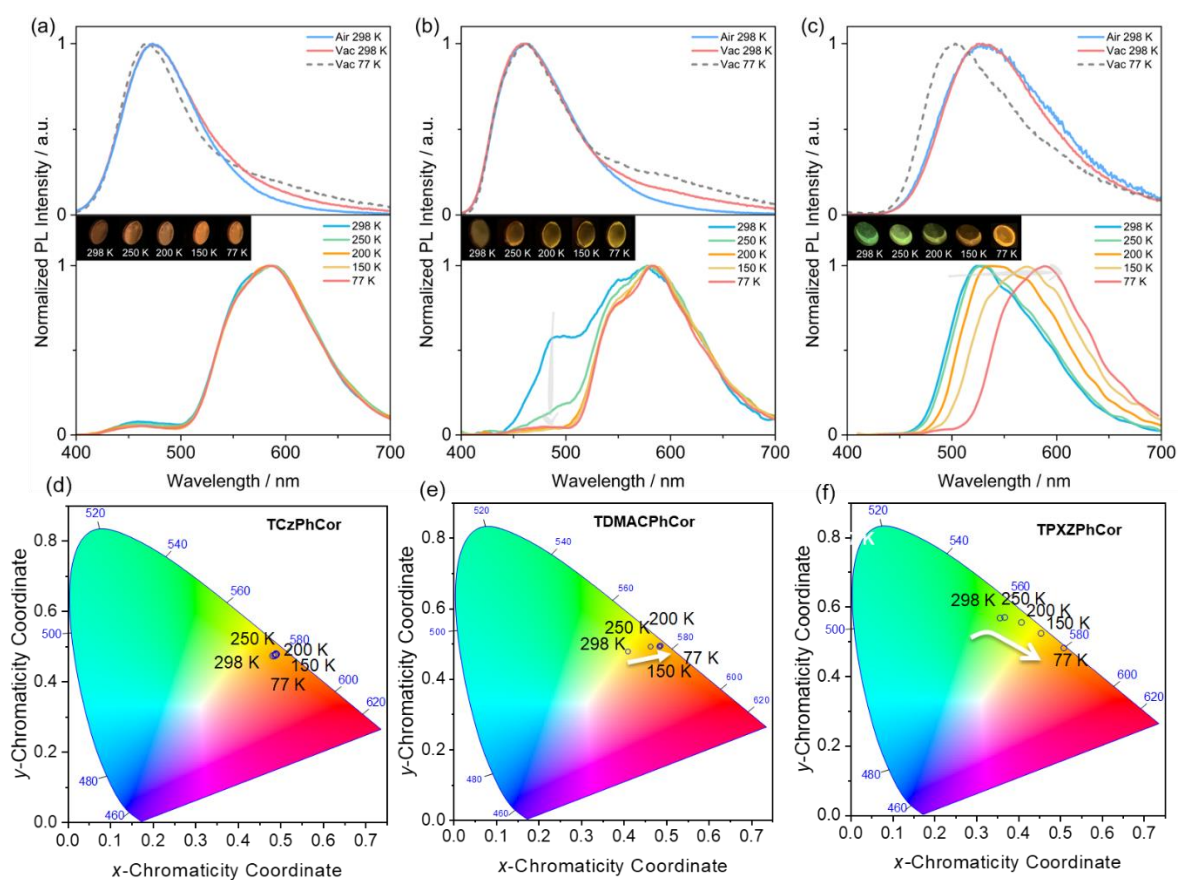


Figure 6.11. Steady-state PL (at 298 K and 77 K) and temperature-dependent phosphorescence spectra of (a) 1 wt% **TCzPhCor**, (b) 7 wt% **TDMACPhCor** and (c) 15 wt% for **TPXZPhCor** in mCP ($\lambda_{exc} = 320$ nm; time-gated window: 30–200 ms; insets: images showing phosphorescence at different temperature excited by a 365 nm UV torch). Time-dependent changes in CIE coordinates of phosphorescence of (d) 1 wt% **TCzPhCor**, (e) 7 wt% **TDMACPhCor** and (f) 15 wt% for **TPXZPhCor** in mCP.

With a potential view to assessing these materials in OLEDs, we explored the photophysics in doped films in mCP as this host has a T_1 energy of ~ 3.0 eV,⁴⁴⁷ thus excitons would be confined onto the RTP emitters. The optimized doping concentrations of **TCzPhCor**, **TDMACPhCor**, and **TPXZPhCor** are 1 wt%, 7 wt%, and 15 wt%, respectively, where the Φ_{PL} values are 37.2%, 32.1%, and 42.5%, respectively (Table 6.3). The varying optimal doping concentrations among these compounds may arise from differences in the efficiency of Förster resonance energy transfer.⁴⁴⁸ The steady-state PL spectra of the three emitters in air and vacuum at 298 K show broad and structureless emission at λ_{PL} of 465 nm, 475 nm, and 530 nm (Figure 6.11a-c, top), with τ_{PL} of 6.5 ns, 19.8 ns and 30.7 ns, for **TCzPhCor**, **TDMACPhCor** and **TPXZPhCor**, respectively. Similar to the result recorded in PMMA, **TCzPhCor** in mCP exhibits RTP at 588 nm with τ_{ph} of 293.7 ms (Figure 6.12aFigure 6.), which originates mostly from T_1^{L} that is localized on the **TPhCor** core. This observation further supports that the RTP form **TCzPhCor** does not originate from any carbazole isomeric impurity.⁴⁴⁹

The unchanged phosphorescence spectra as a function of temperature are consistent with a single origin of the phosphorescence (Figure 6.11a, bottom). For **TDMACPhCor**, dual RTP emission from T_1^{H} and T_1^{L} was observed, centered at 480 nm and 585 nm (Figure 6.11b, bottom) with associated τ_{ph} of 96.8 ms and 343.3 ms (Figure 6.12b), respectively. As the temperature decreases, the high-energy phosphorescence from T_1^{H} decreases in intensity as it can no longer be efficiently populated. For **TPXZPhCor**, the emission at 528 nm is dominated by the RTP from T_1^{H} (Figure 6.12c, bottom), with a τ_{ph} of 82.6 ms. This is reflected by a significant change in the spectral profile as a function of temperature (Figure 6.11d-e). The Φ_{RTP} of **TCzPhCor**, **TDMACPhCor** and **TPXZPhCor** in mCP are 2.6%, 2.7%, and 18.0%, respectively, which are much higher than those measured in 1 wt% doped PMMA films (0.1% for **TCzPhCor**, 0.3% for **TDMACPhCor** and 10.0% for **TPXZPhCor**, respectively) (Figure 6.12d). This divergence in Φ_{RTP} recorded in mCP and PMMA results from different host-guest interactions, which provides a window into an effective strategy to regulate the T_1^{H} and T_1^{L} excitonic coupling.

Table 6.3. Summary of Φ_{PLS} of corannulene-based compounds with different doping concentrations in PMMA and mCP.

Compound	Host	doped ratio	$\Phi_{\text{PL}} / \% (\text{N}_2)$	$\Phi_{\text{PL}} / \% (\text{Air})$	$\Phi_{\text{RTP}} / \%$
TCzPhCor	PMMA	1%	33.9	33.8	0.1
		10%	32.7	30.9	1.8
	mCP	1%	37.2	34.6	2.6
		3%	31.1	28.6	2.5
		5%	35.7	34.6	1.1
		7%	36.3	35	1.3
		10%	32.3	31.6	0.7
		15%	34.3	34.3	0
TDMACPhCor	PMMA	1%	28.5	28.2	0.3
		10%	18.4	17.0	1.4
	mCP	1%	20.9	20.1	0.8
		3%	22.9	22	0.9
		5%	24.4	24.2	0.2
		7%	32.1	28.4	2.7
		10%	25.8	22.7	3.1
		15%	23	20.3	2.7
TPXZPhCor	PMMA	1%	34.5	24.5	10.0
		10%	16.9	32.3	15.4
	mCP	1%	36.8	24.5	14.3
		3%	32.3	22.5	10.2
		5%	36.6	22.1	12.4
		7%	37.5	24.2	13.8
		10%	40.2	23.7	15.7
		15%	42.5	24.5	18.0
20%	42.3	24.5	17.7		

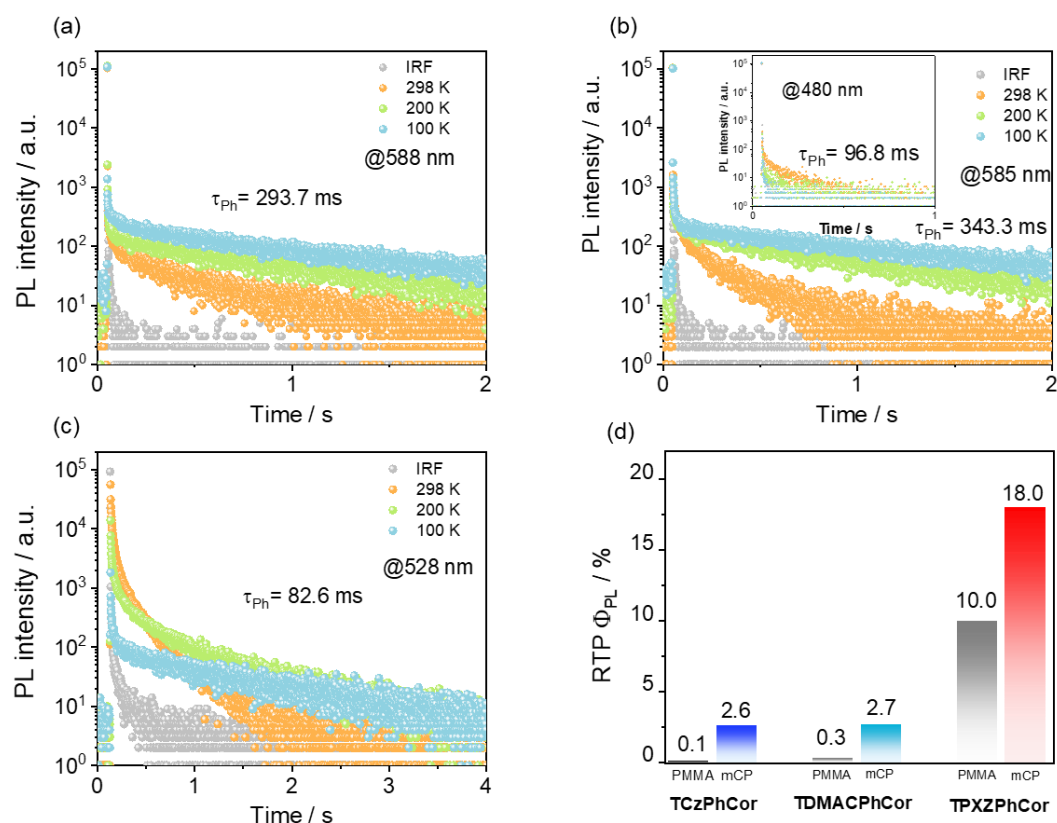


Figure 6.12. Temperature-dependent time-resolved PL decay of (a) 1 wt% **TCzPhCor**, (b) 7 wt% **TDMACPhCor** and (c) 15 wt% **TPXZPhCor** in mCP in vacuum ($\lambda_{exc}=379$ nm); (d) RTP Φ_{PL} values of 1 wt% **TCzPhCor**, 7 wt% **TDMACPhCor** and 15 wt% **TPXZPhCor** in PMMA and mCP.

Given that **TPXZPhCor** shows dual phosphorescence emission in mCP as a function of temperature, we decided to study the photophysics of **TPXZPhCor** in mCP at both lower (1 wt%) and higher (30 wt%) doping concentrations to interrogate the influence of intermolecular interactions on the dual phosphorescence behavior. The Φ_{PL} values measured at these doping concentrations indicate that the 30 wt% **TPXZPhCor** doped mCP film possesses the highest RTP Φ_{PL} (17.8%), higher than that of the 1 wt% doping concentration (RTP $\Phi_{PL} = 10.2\%$) (Figure 6.13a and b). The observed aggregation-enhanced emission originates from twisted geometries, which disfavor unwanted π - π interactions. Both 1 wt% and 30 wt% **TPXZPhCor** doped mCP films exhibit similar temperature-dependent phosphorescence behavior to the 15 wt% doped sample. As temperature decreases, there is a red-shift of the phosphorescence, reflected in the temperature-dependent phosphorescence afterglows (Figure 6.13c and d) and

evolution in the CIE coordinates (Figure 6.13e and f). The photophysical investigation at these two doping concentrations indicates that aggregation has negligible influences on the T_1^H and T_1^L phosphorescence spectra, which implies that the phosphorescence occurs from monomolecular species and not aggregates.

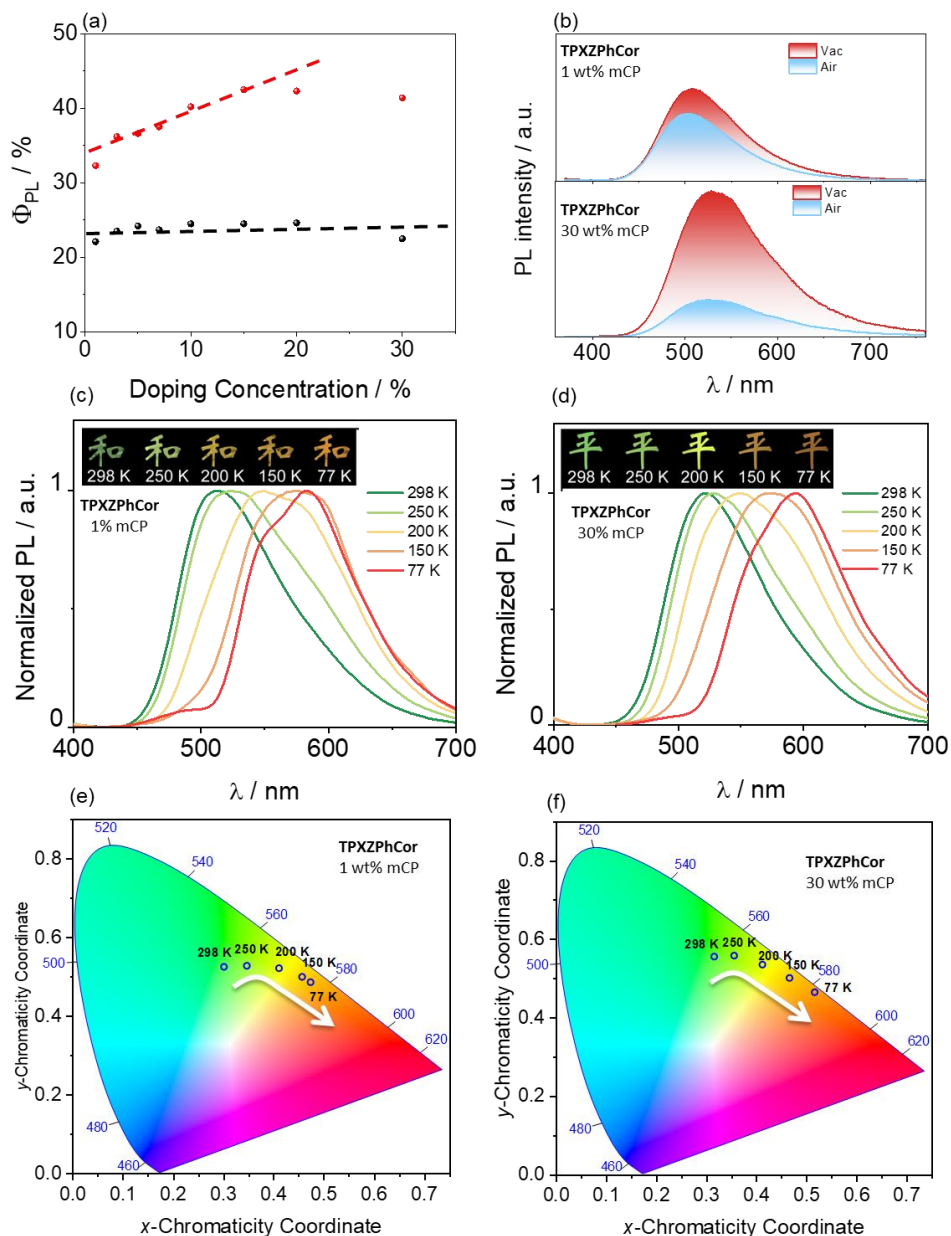


Figure 6.13. (a) Relationship between Φ_{PL} and doping concentration of **TPXZPhCor** in mCP; black dot and red dot represent Φ_{PL} recorded in air and N_2 , respectively; (b) SSPL spectra of 1 wt% and 30 wt% **TPXZPhCor** in mCP at 298 K in vacuum and air. Temperature-dependent phosphorescence spectra of (c) 1 wt% and (d) 30 wt% **TPXZPhCor** in mCP films (time-gated window: 30-200 ms; $\lambda_{exc} = 320$ nm). inset: images showing phosphorescence in vacuum at

different temperatures, where the two Chinese characters together mean “peace”. The characters were generated using a mask on top of the image of the photoexcited film excited by a 365 nm UV torch. Time-dependent changes in CIE coordinates of phosphorescence of (e) 1 wt% **TPXZPhCor** and (f) 30 wt% **TPXZPhCor** in mCP.

6.8 Temperature Sensing and Afterglow OLEDs

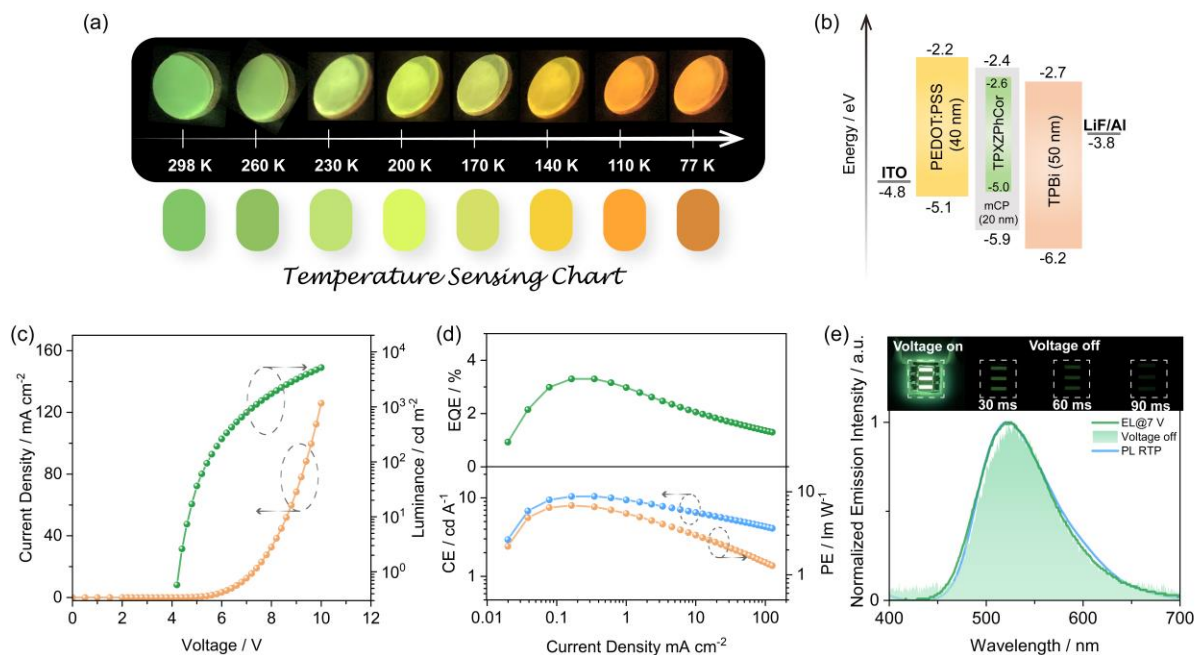


Figure 6.14 (a) Temperature-dependent phosphorescence afterglows of 30 wt% **TPXZPhCor** in mCP and fitted sensing charts. (b) Device configuration and energy level diagram of the materials employed in the devices. (c) current density–voltage–luminance (d) efficiencies-current density, (e) EL spectra during (green) and after electrical excitation (grey line), the inset photos of OLEDs at 7 V and afterglow OLEDs.

In our previous report,⁴³⁵ we developed several temperature sensing charts showing phosphorescence afterglows ranging from blue to green. Considering the remarkable difference in the phosphorescence afterglows of **TPXZPhCor** as a function of temperature, the temperature sensing charts using the 30 wt% **TPXZPhCor** doped mCP films exhibit a much wider color palate than in our previous study,⁴³⁵ ranging from cyan at 298 K to orange at 77 K (Figure 6.14a).

To the best of our knowledge, there are only a limited number of reports of temperature

sensing based on phosphorescence afterglow materials.^{450–452} Lee *et al.*⁴⁵⁰ reported a temperature sensor in a microfluidic device based on an organic RTP compound, **Br6A**, doped in a temperature-sensitive polymer matrix; however, no temperature-dependent emission color change was observed. Liang *et al.*⁴⁵¹ demonstrated that a fluorine-substituted organic phosphor is thermo-responsive in both crystals and doped films, where the phosphorescence lifetime was found to increase linearly with decreasing temperature; however, no afterglow color change was observed, which limits its application as a rapid naked eye temperature sensor. **TPXZPhCor**, by contrast, can be used for rapid temperature sensing in cold environments.

We also explored the potential of **TPXZPhCor** as an emitter in an afterglow OLED (Figure 6.14b-e). To the best of our knowledge, there were only three prior reports of afterglow OLEDs.^{453–455} Adachi and co-workers demonstrated the first afterglow OLED wherein they employed a hydrophobic steroid derivative as the host and a deuterated fluorene-based compound as the dopant in the EML.⁴⁵³ The green OLED only showed an EQE_{max} of ~1%. The same group proposed another strategy and developed an exciplex-based afterglow OLED by reducing the guest concentration to slow the exciton recombination rate and increasing the EML thickness to enhance the charge accumulation process. However, the abnormally low guest concentration and thick EML contribute to the significantly reduced device brightness and necessitate a very high driving voltage (pulse voltage = 70 V), resulting in an EQE_{max} of ~0.8%. Further, the device exhibited a long transient EL decay of more than 10 s.⁴⁵⁴ Xie *et al.* reported an afterglow OLED that used PPT and NPB as host and guest, respectively, within the EML. The devices showed green afterglow emission with an ultralong lifetime of 356 ms; however, the EQE_{max} was 1.47% and the L_{max} reached only 743 cd m⁻².

We fabricated solution-processed OLEDs employing 15 wt% **TPXZPhCor** doped in mCP films as the EML and investigated their performance as well as the afterglow produced from the electroluminescence. The device stack consisted of: ITO/ PEDOT:PSS (30 nm)/ EML (30 nm)/ TPBi (50 nm)/ LiF (1 nm)/ Al (100 nm), where ITO and Al serve as the anode and cathode, respectively, PEDOT:PSS acts as the hole-transporting layer, TPBi acts as the electron-transporting layer, and LiF acts as the electron-injection layer (Figure 6.14b). The afterglow OLED performance is summarized in Table 6.3. The optimized device has a turn-on voltage of 4.3 V and a driving voltage at 100 cd m⁻² of 5.5 V, which is much lower than previously reported

afterglow OLEDs.⁴⁵⁴ The L_{\max} reached 5167 cd m⁻² and the EQE_{max} was 3.3% (Figure 6.14d). Compared to the previous reports of afterglow OLEDs, device A has the highest performance (Table 6.3). The EL spectrum (Figure 6.14e) of the OLED matches the phosphorescence spectrum of the 15 wt% **TPXZPhCor** doped in the mCP film. Furthermore, the steady-state EL and afterglow spectra (Figure 6.14e) are essentially the same, reflecting degenerate S₁ and T₁^H states.

Table 6.3. Summary of afterglow OLED performance

Devices	V _{on} ^a / V	V ₁₀₀ ^b / V	λ _{EL} ^c / nm	λ _{EL} ^d / nm	Luminance ^e /cd m ⁻²	EQE _{max} ^f / %
A	4.3	5.5	525	528	5167	3.30
Ref ⁵³	5.8	8.9	440	544	450	1.47
Ref ⁵⁴	-	-	-	~520	-	~1.00
Ref ⁵⁵	-	-	-	-	-	~0.8

^a Turn-on voltage at 1 cd m⁻². ^b Driving voltage at 100 cd m⁻². ^c EL maximum at 7 V. ^d EL maximum after ceasing electrical excitation. ^e Maximum luminance, ^f Maximum external quantum efficiency.

6.9 Conclusions

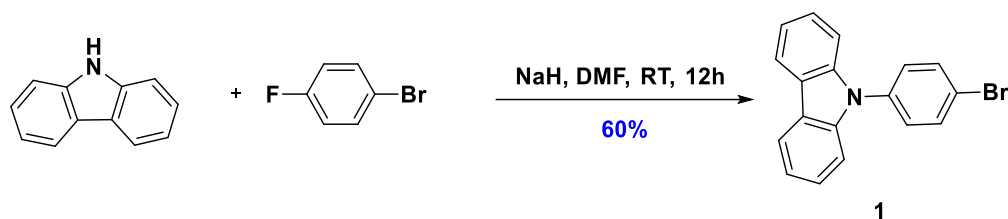
In this Chapter, we have systematically explored how donors regulate multiple phosphorescence in corannulene-based emitters **TCzPhCor**, **DMACPhCor**, and **PXZPhCor**. By endowing corannulene-centered emitter with multiple accessible excited-state geometries, we found that **TCzPhCor** shows ultralong RTP from the lowest T₁, associated with τ_{ph} of 573 ms (in PMMA) and 293.7 ms (in mCP); **TDMACPhCor** possesses dual RTP in both PMMA and mCP due to the balanced distribution of triplet excitons in T₁^H and T₁^L states, whose τ_{ph} values are 96.8 ms and 343.7 ms, respectively, in mCP; however, **TPXZPhCor** exhibits T₁^H-dominated RTP with τ_{ph} of 82.6 ms in mCP in 15 wt% doped mCP, which occurs as a result of thermally activated reverse internal conversion. Exploiting this photophysical behavior, we demonstrated how **TPXZPhCor** can act as an optical temperature sensor in the range from 77 K to 298 K. Benefitting from degenerate S₁ and T₁^H states, we have fabricated record-efficient

solution-processed afterglow OLEDs using **TPXZPhCor**, which showed an EQE_{max} of 3.3% and a L_{max} of 5167 cd m^{-2} .

6.10 Experimental Section

The following compounds were synthesised according to the literature: 9,9-dimethylacridan,³¹⁵ tetrabromocorannulene (TBrCor).³¹⁶ Carbazole was obtained from commercial sources. Before use, carbazole was purified by silica gel column chromatography and further purified by recrystallization in methanol and vacuum sublimation.

Synthesis of 9-(4-bromophenyl)-9H-carbazole (1):



To a solution of carbazole (2.14 g, 12.8 mmol, 1.0 equiv.) in dry DMF (50 mL) at room temperature under a nitrogen atmosphere was added portion-wise sodium hydride (60% in mineral oil, 0.56 g, 14.1 mmol, 1.1 equiv.). The resulting suspension was stirred under nitrogen atmosphere for 30 minutes. Then a solution of 1-bromo-4-fluorobenzene (2.24 g, 12.8 mmol, 1.0 equiv.) in dry DMF (30 mL) was added to the stirred suspension. The resulting reaction mixture was allowed to stir for a further 12 h. The reaction mixture was then slowly added to ice water and then extracted with DCM (3×50 mL). The combined organic layers were dried with anhydrous sodium sulfate and concentrated under reduced pressure. The crude product was purified by silica gel flash column chromatography using DCM: hexane= 1:10 as eluent to afford the desired compound as a white solid (yield = 2.74 g).

9-(4-bromophenyl)-9H-carbazole (1): Yield: 60%. **R_f**=0.4 (Hexane). **Mp** = 143-145 °C. (Lit. Mp:⁴⁵⁶ 144-145 °C) **¹H NMR (500 MHz, CDCl₃):** δ = 8.19 (d, J = 7.8 Hz, 2H), 7.77 (d, J = 8.6 Hz, 2H), 7.51 – 7.46 (m, 3H), 7.45 – 7.41 (m, 3H), 7.35 (ddd, J = 8.0, 6.8, 1.2 Hz, 2H). ppm. **¹³C NMR (126 MHz, CDCl₃):** δ = 140.60, 136.80, 133.14, 128.74, 126.13, 123.50, 120.91, 120.45, 120.25, 109.59 ppm. Analytical data matches that previously reported.⁴⁵⁶

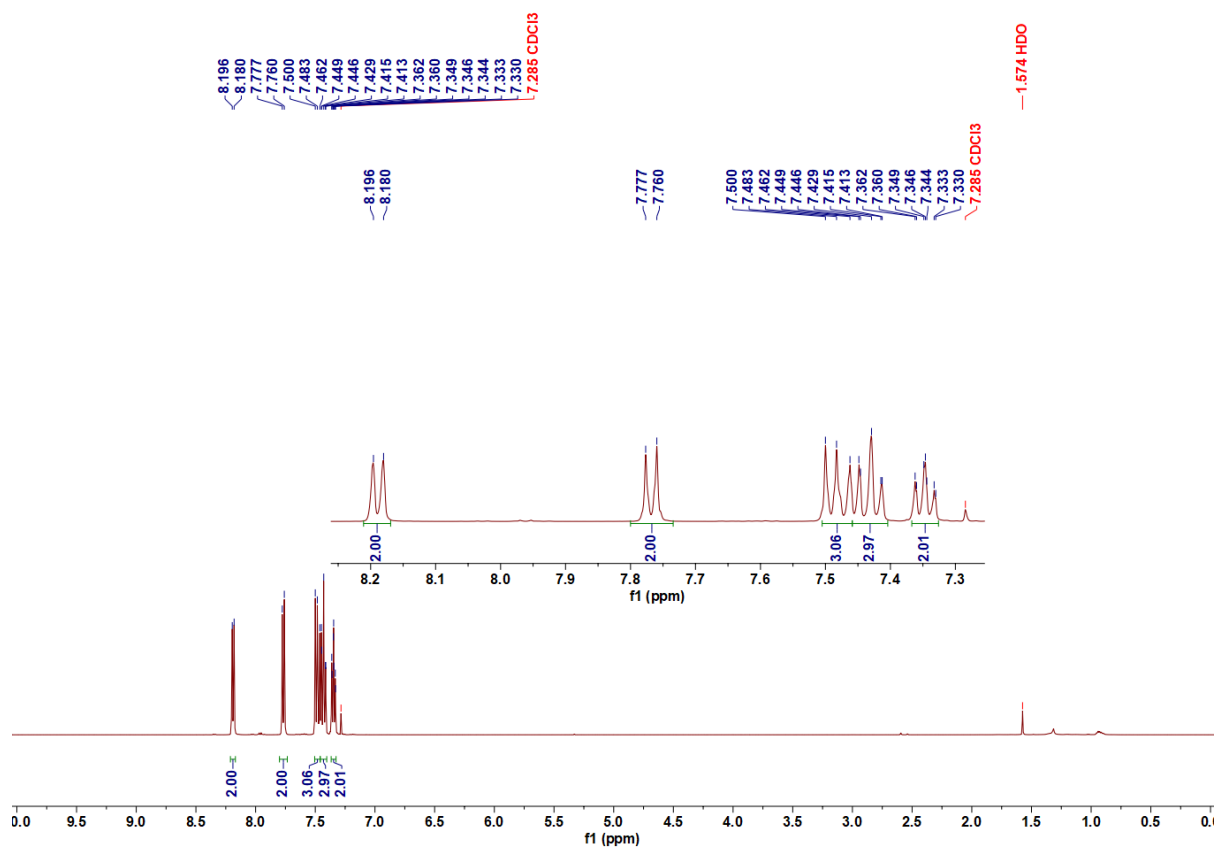


Figure 6.15. ^1H NMR spectra of **1** in CDCl_3 .

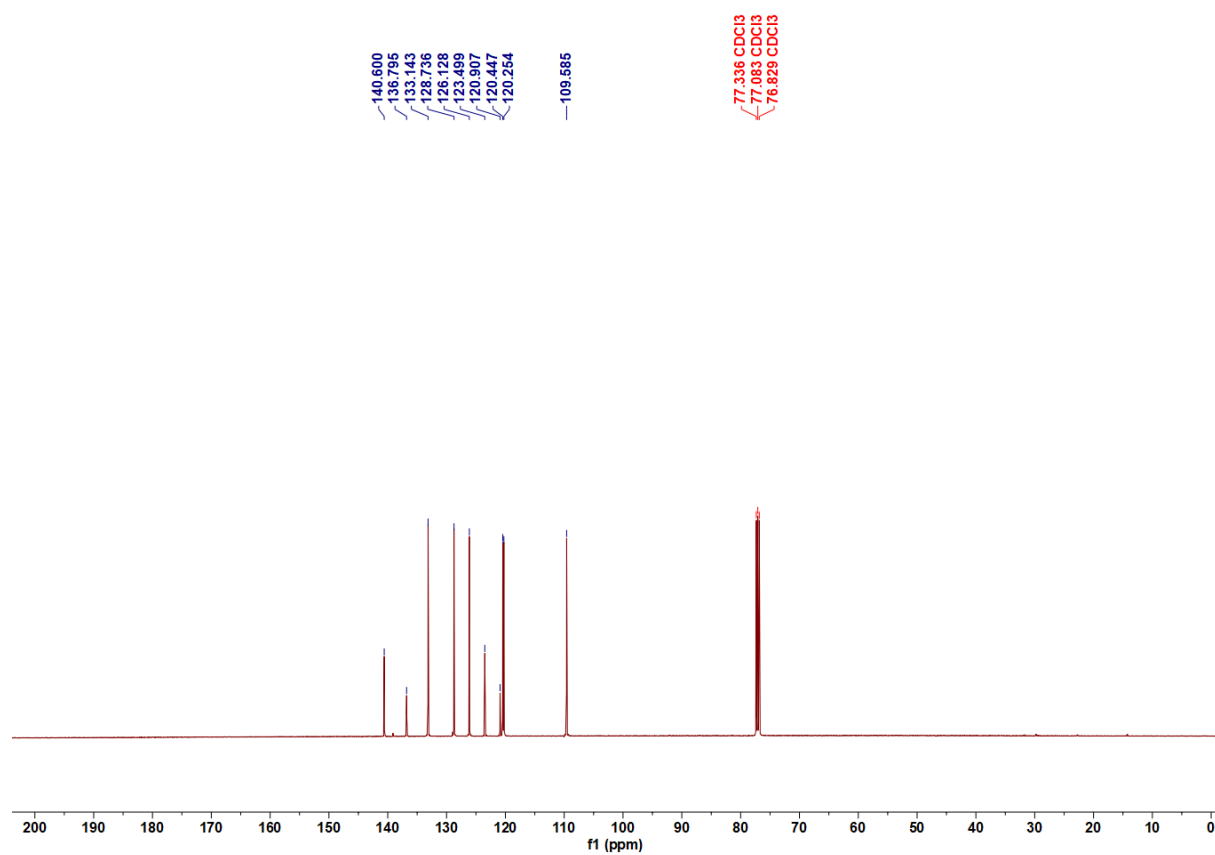
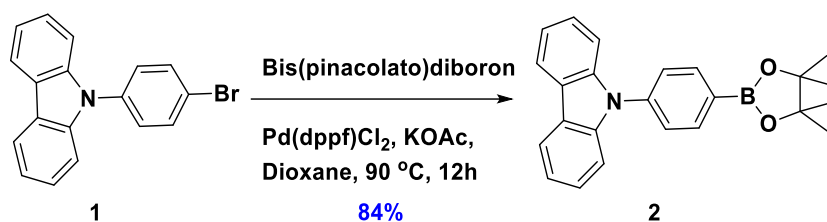


Figure 6.16. ^{13}C NMR spectra of **1** in CDCl_3 .

Synthesis of 9-(4-(4,4,5,5-tetramethyl-1,3,2-dioxaborolan-2-yl) phenyl)-9H-carbazole (2):



A Schlenk flask was charged with **1** (1.29 g, 4.0 mmol, 1.0 equiv.), then bis(pinacolato)diboron (1.52 g, 6.0 mmol, 1.5 equiv.), Pd(dppf)Cl₂ (146 mg, 0.2 mmol, 0.05 equiv.), KOAc (1.18 g, 12.0 mmol, 3.0 equiv.) and dry 1,4-dioxane (40 mL) were added to the flask under nitrogen. The mixture was heated to 90 °C with stirring for about 12 h. Then the mixture was cooled to room temperature and extracted with ethyl acetate (3 × 50 mL). The combined organic layers were dried with anhydrous sodium sulfate and concentrated under reduced pressure. The crude product was purified by silica gel flash column chromatography using EA:hexane = 1:10 as eluent to give compound **2** as a white solid (yield = 1.24 g).

9-(4-(4,4,5,5-tetramethyl-1,3,2-dioxaborolan-2-yl) phenyl)-9H-carbazole (2): R_f = 0.3 (10% EA/Hexane). **Yield:** 84%. **Mp** = 170-171 °C. (Lit. Mp:⁴⁵⁷ 168 °C) **¹H NMR (500 MHz, CDCl₃):** δ = 8.17 (d, J = 7.8 Hz, 2H), 8.08 (d, J = 8.2 Hz, 2H), 7.63 (d, J = 8.2 Hz, 2H), 7.48 (dd, J = 8.2, 1.0 Hz, 2H), 7.46 – 7.41 (m, 2H), 7.32 (ddd, J = 8.0, 7.0, 1.2 Hz, 2H), 1.43 (s, 12H) ppm. **¹³C NMR (126 MHz, CDCl₃):** δ = 140.57, 140.35, 136.39, 126.08, 125.98, 123.51, 120.32, 120.07, 109.85, 84.11, 24.95 ppm. Analytical data matches that previously reported.⁴⁵⁷

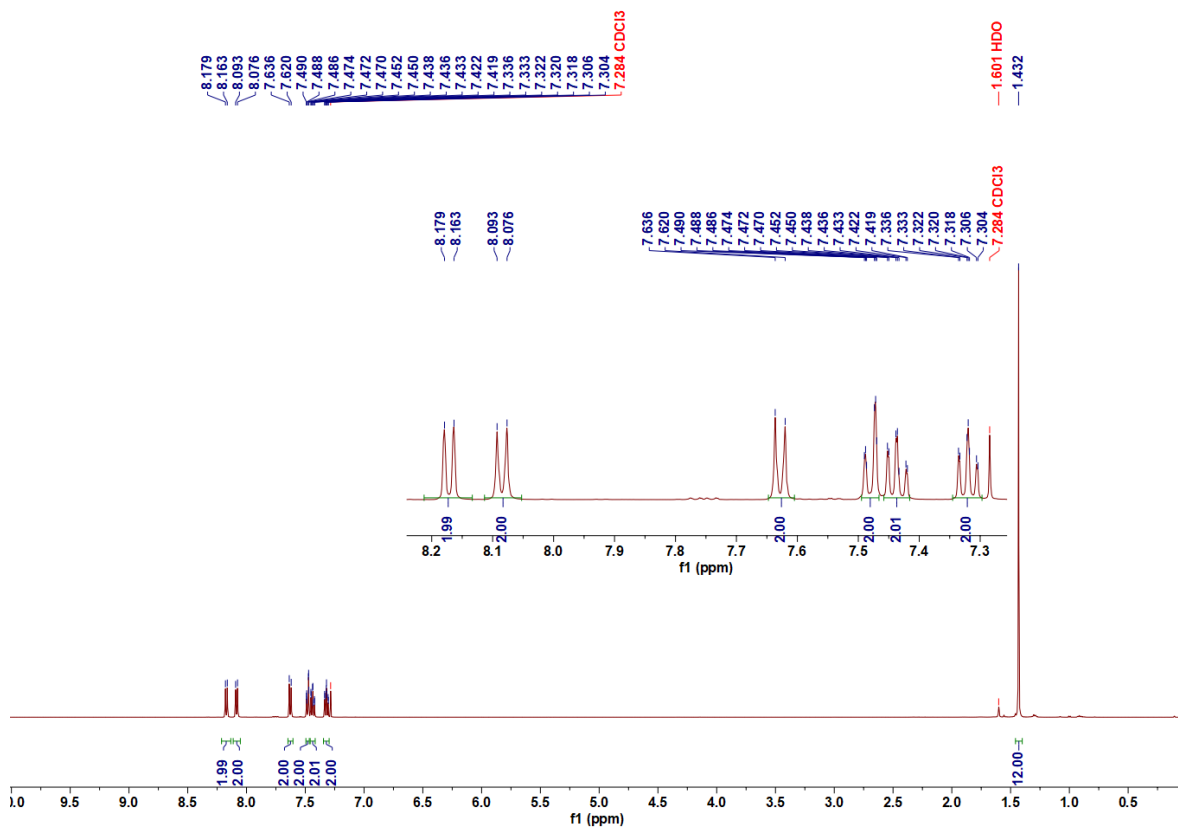


Figure 6.17. ¹H NMR spectra of **2** in CDCl₃.

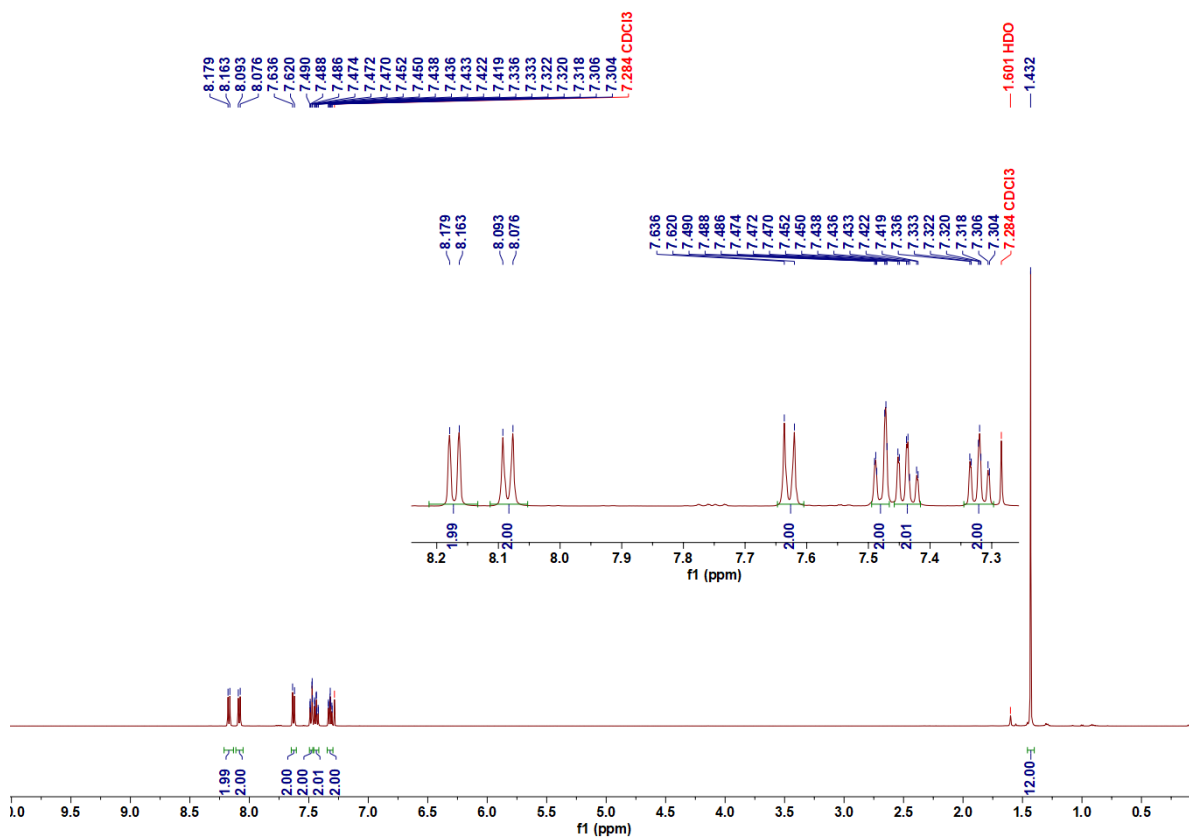
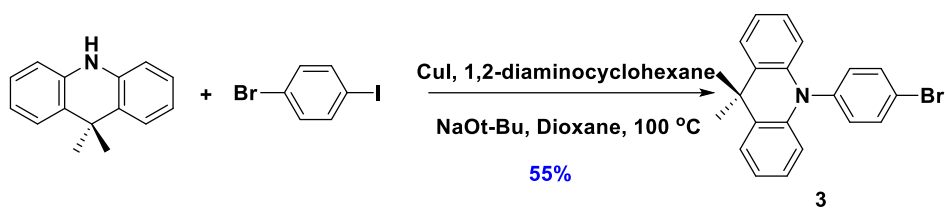


Figure 6.18. ¹³C NMR spectra of **2** in CDCl₃.

Synthesis of 10-(4-bromophenyl)-9,9-dimethyl-9,10-dihydroacridine (3):



A mixture of 9,9-dimethylacridan (5.7 g, 27.25 mmol, 1.0 equiv.), 1-bromo-4-iodobenzene (8.5 g, 30.0 mmol, 1.1 equiv.), copper(I) iodide (0.11 g, 0.55 mmol, 0.02 equiv.), sodium tert-butoxide (5 g, 54 mmol, 2.0 equiv), and 1,2-diaminocyclohexane (0.32 g, 2.8 mmol, 0.1 equiv) in dry 1,4-dioxane (50 mL) was refluxed for 12 h. After cooling to room temperature, the reaction mixture was added into water, and then extracted with DCM. The combined organic layers were dried over anhydrous magnesium sulfate and concentrated under reduced pressure. The crude product was purified by column chromatography on silica gel (DCM: hexane/ = 1:9, v/v) to give **3** as a white solid (yield =5.46 g).

10-(4-bromophenyl)-9,9-dimethyl-9,10-dihydroacridine (3): Yield: 55%. R_f = 0.6 (10% DCM/Hexane). Mp=180-181 °C. $^1\text{H NMR}$ (400 MHz, CDCl_3) δ 7.83 – 7.74 (m, 2H), 7.52 – 7.44 (m, 2H), 7.28 – 7.22 (m, 2H), 7.05 – 6.92 (m, 4H), 6.31 – 6.24 (m, 2H), 1.71 (s, 6H) ppm. $^{13}\text{C NMR}$ (101 MHz, CDCl_3): δ = 140.60, 140.30, 134.24, 133.24, 130.09, 126.43, 125.34, 122.11, 120.82, 113.90, 77.35, 77.04, 76.72, 35.98, 31.25 ppm. Analytical data matches that previously reported.⁴⁵⁸

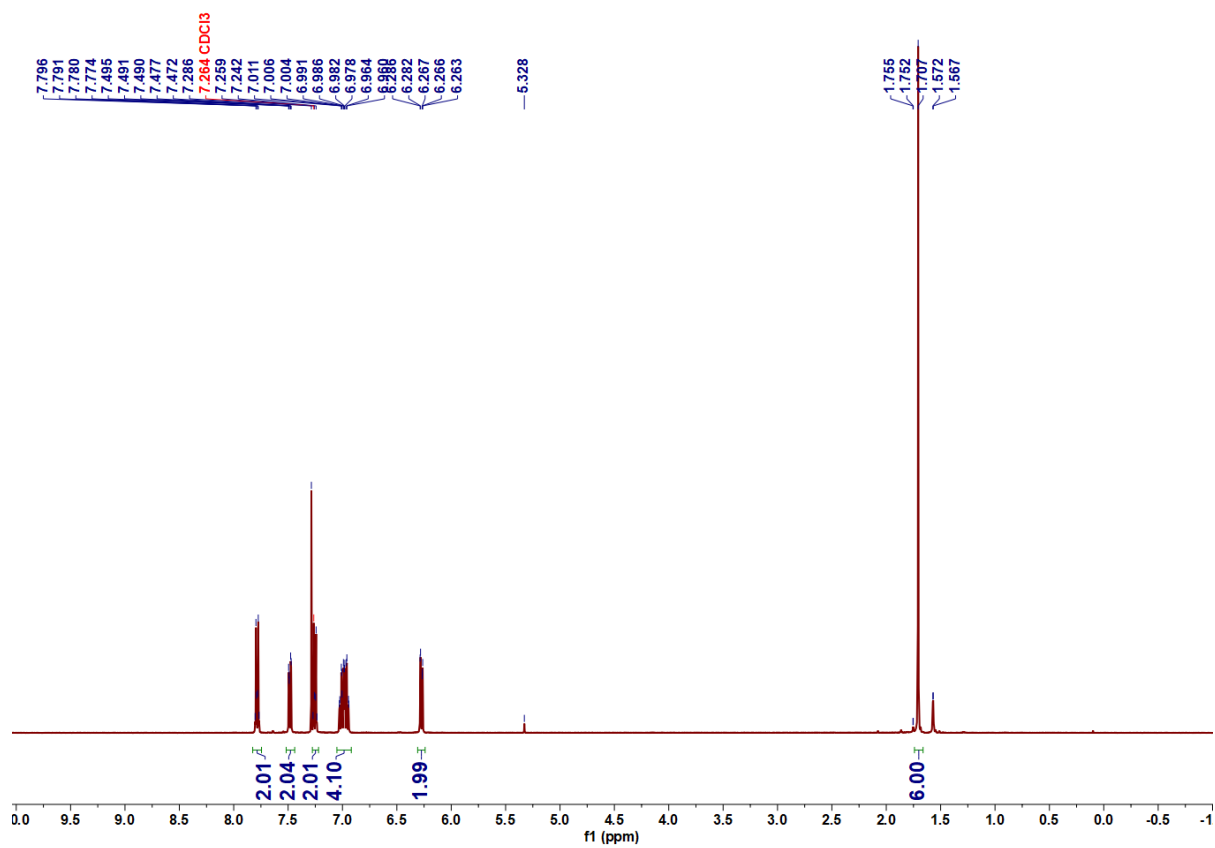


Figure 6.19. ¹H NMR spectra of **3** in CDCl₃.

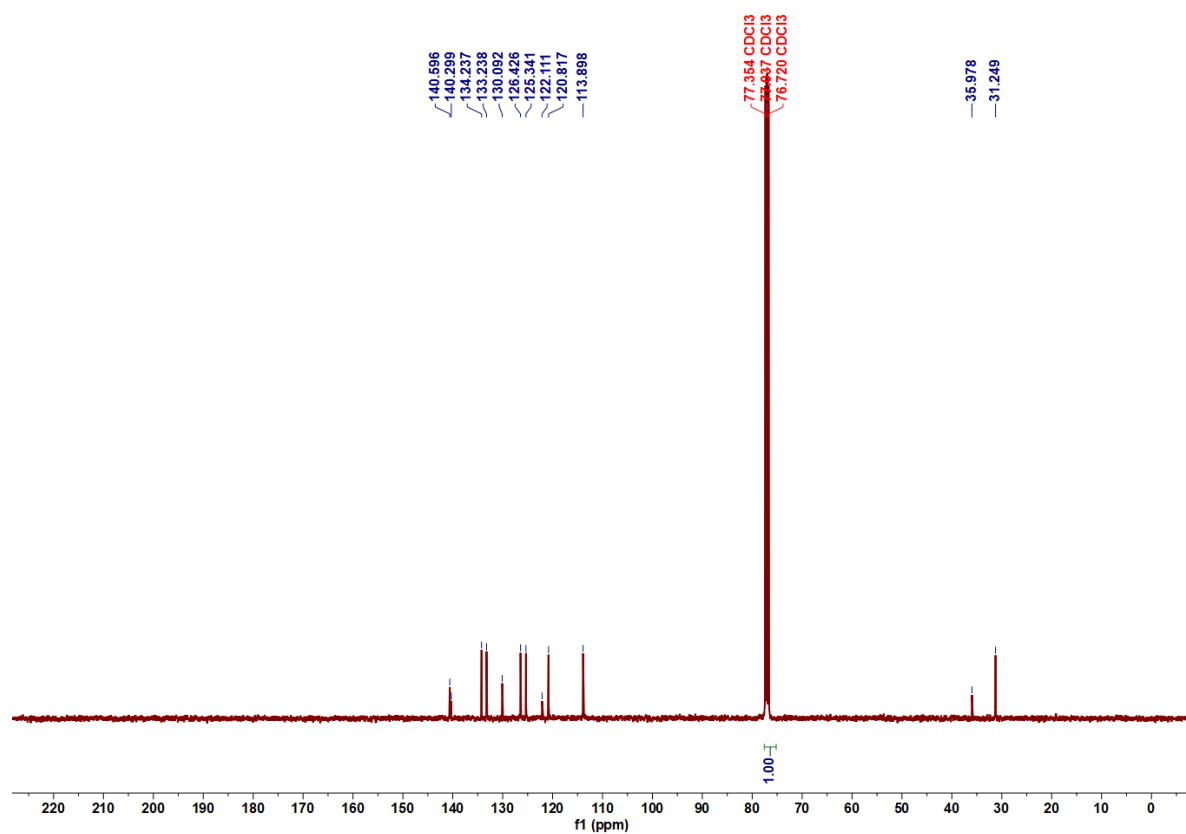
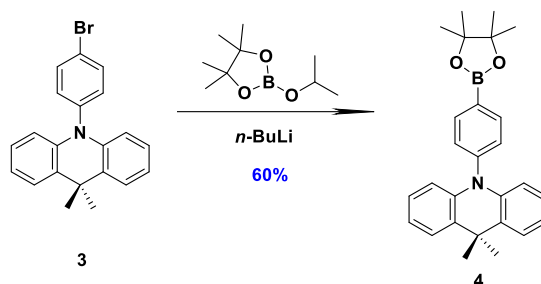


Figure 6.20. ¹³C NMR spectra of **3** in CDCl₃.

Synthesis of 9,9-dimethyl-10-(4-(4,4,5,5-tetramethyl-1,3,2-dioxaborolan-2-yl)phenyl)-9,10-dihydroacridine (4):



To a solution of **3** (5.0 g, 13.8 mmol, 1.0 equiv.) in dry THF (100 mL) was added dropwise *n*-BuLi (2.6 M, 6.0 mL, 16 mmol, 1.15 equiv.) at -78 °C. The mixture was stirred for 1 h at -78 °C. Then, 2-isopropoxy-4,4,5,5-tetramethyl-1,3,2-dioxaborolane (3.1 g, 16.5 mmol, 1.2 equiv.) was added dropwise to the mixture at -78 °C. The reaction mixture was allowed to warm to room temperature and stirred for a further 3 h. The resulting mixture was added into water, and then extracted with chloroform (3 × 25 mL). The combined organic layers were washed with water, dried over anhydrous magnesium sulfate and concentrated under reduced pressure. The crude product was purified by column chromatography on silica gel (DCM: hexane/ =1: 4, v/v) to afford **4** as a white solid (yield =3.40 g).

9,9-dimethyl-10-(4-(4,4,5,5-tetramethyl-1,3,2-dioxaborolan-2-yl)phenyl)-9,10-

dihydroacridine (4): R_f = 0.4 (25% DCM/Hexane). **Yield:** 60%. **Mp** = 169-171 °C. $^1\text{H NMR}$ (400 MHz, DMSO-d_6) δ 8.02 – 7.93 (m, 2H), 7.49 (dd, J = 7.6, 1.7 Hz, 2H), 7.40 – 7.35 (m, 2H), 6.99 – 6.87 (m, 4H), 6.13 (dd, J = 8.1, 1.4 Hz, 2H), 1.61 (s, 6H), 1.35 (s, 12H) ppm. $^{13}\text{C NMR}$ (101 MHz, CDCl_3): δ = 143.99, 140.72, 137.33, 130.66, 129.94, 126.34, 125.23, 120.53, 114.09, 84.13, 77.36, 77.04, 76.72, 35.98, 31.34, 24.96. Analytical data matches that previously reported.⁴⁵⁸

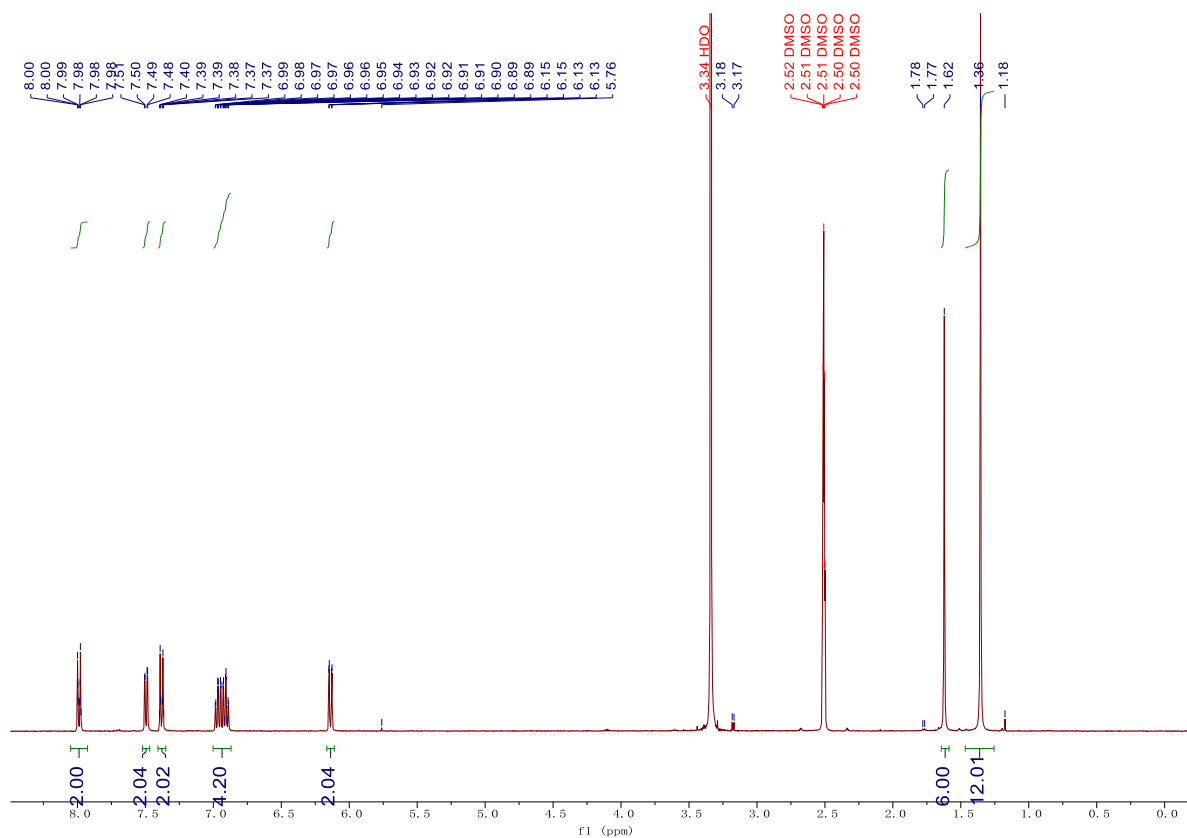


Figure 6.21. ^1H NMR spectra of **4** in DMSO-d_6 .

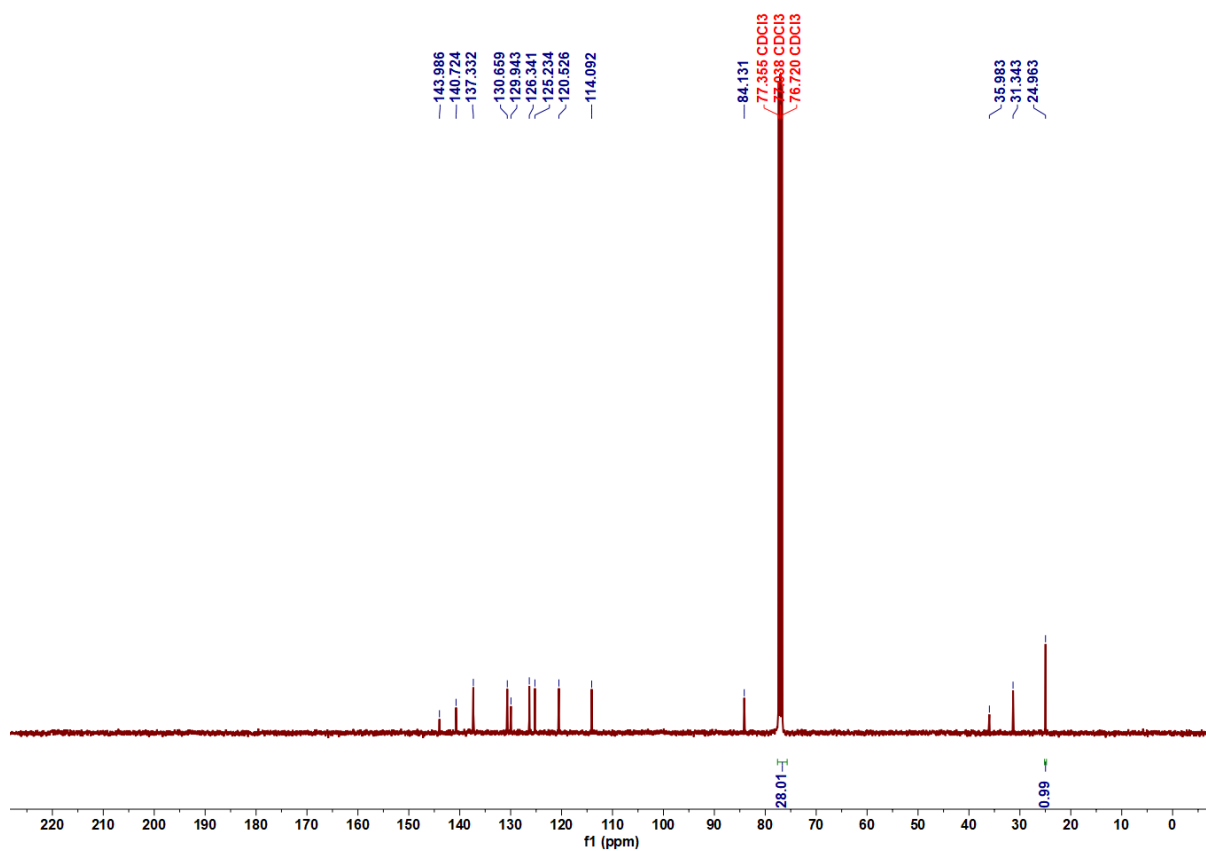
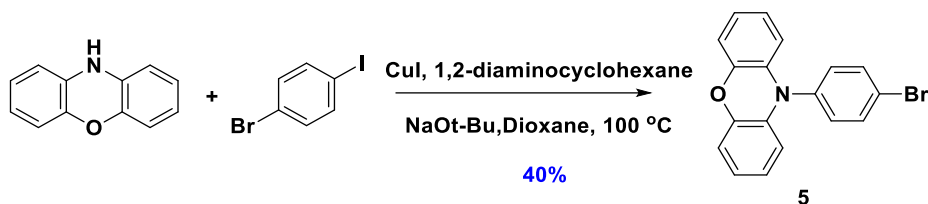


Figure 6.22. ^{13}C NMR spectra of **4** in CDCl_3 .

Synthesis of 10-(4-bromophenyl)-10H-phenoxazine (5):



Compound **5** was synthesized according to the same procedure as described above for the synthesis of **3**, except that phenoxazine (5 g, 27 mmol) was used as the reactant instead of 9,9-dimethylacridan, yielding a white solid (yield = 3.70 g).

10-(4-bromophenyl)-10H-phenoxazine (5): $R_f=0.6$ (10% DCM/Hexane). **Yield:** 40%. **Mp** = 180–183 °C. (Lit. Mp:⁴⁵⁹ 184–185 °C) **¹H NMR (500 MHz, CDCl₃):** δ 7.89–7.82 (m, 2H), 7.43–7.37 (m, 2H), 6.77–6.71 (m, 2H), 6.70–6.63 (m, 4H), 5.91–5.83 (m, 2H) ppm. **¹³C NMR (101 MHz, CDCl₃):** δ = 143.91, 134.45, 133.99, 133.73, 132.76, 123.29, 122.38, 121.62, 115.58, 113.18, 77.36, 77.04, 76.73 ppm. Analytical data matches that previously reported.⁴⁵⁸

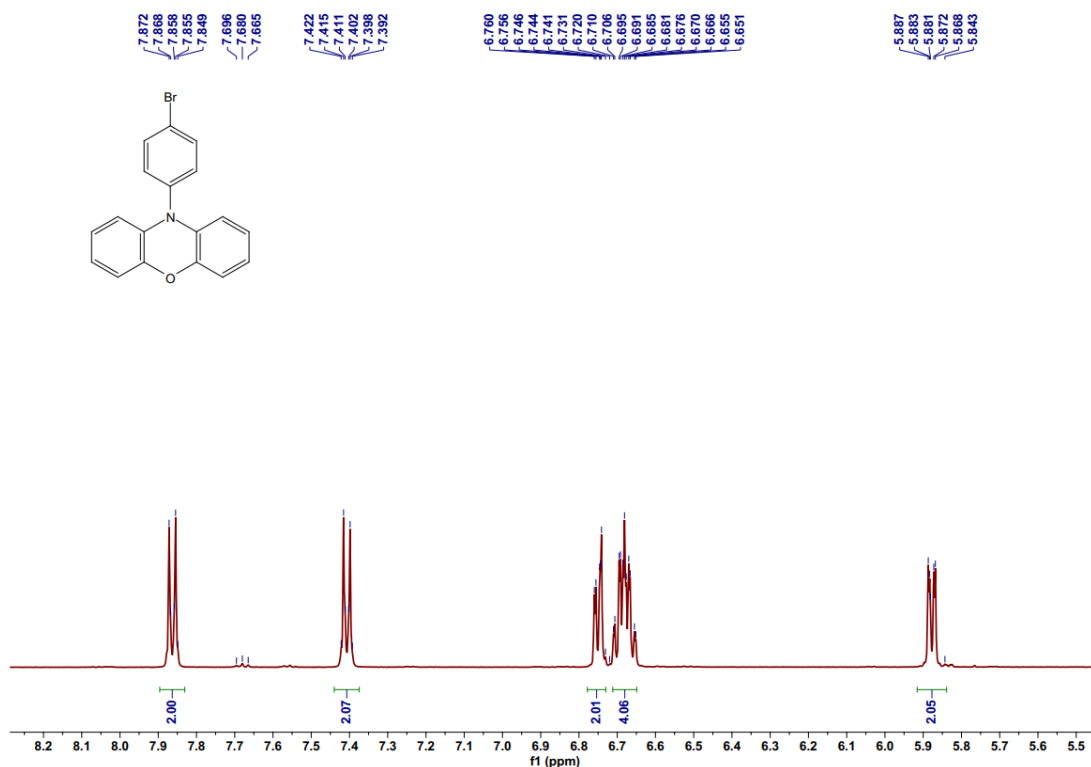


Figure 6.23. ¹H NMR spectra of **5** in CDCl₃.

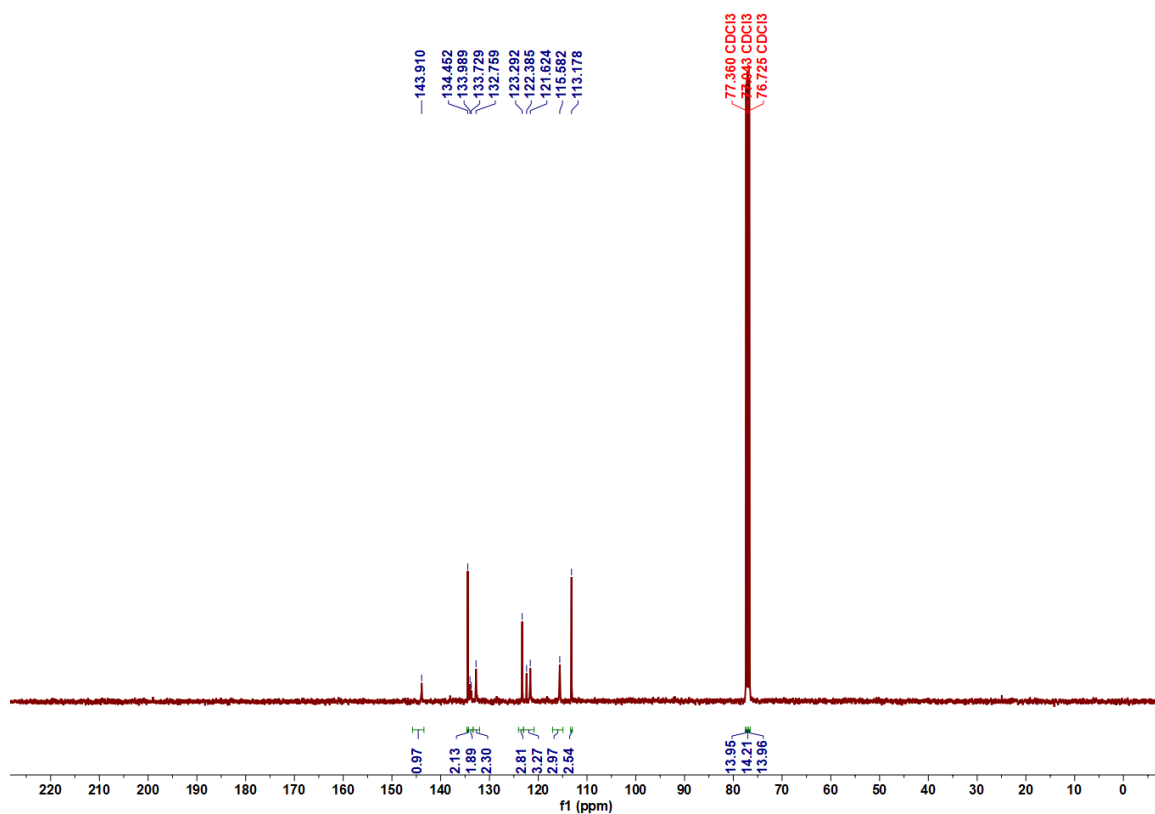
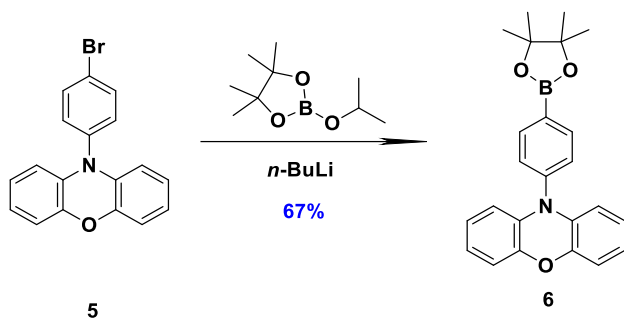


Figure 6.24. ^{13}C NMR spectra of **5** in CDCl_3 .

Synthesis of 10-(4-(4,4,5,5-tetramethyl-1,3,2-dioxaborolan-2-yl)phenyl)-10H-phenoxazine (**6**):



Compound **6** was synthesized according to the same procedure as described above for the synthesis of **4**, except that **5** (3.1 g, 9 mmol) was used as the reactant instead of **3**, yielding a white solid (yield = 2.36 g).

10-(4-(4,4,5,5-tetramethyl-1,3,2-dioxaborolan-2-yl)phenyl)-10H-phenoxazine (6**):** $R_f=0.3$ (20% DCM/Hexane). **Yield:** 67%. **Mp**=120-123 °C. ^1H NMR (400 MHz, CDCl_3): δ 8.06 (d, $J = 7.6$ Hz, 2H), 7.37 (d, $J = 7.9$ Hz, 2H), 6.65 (dd, $J = 43.1, 7.5$ Hz, 6H), 5.93 (s, 2H), 1.29 (s,

12H) ppm. ^{13}C NMR (101 MHz, CDCl_3): δ = 137.50, 123.20, 113.31, 84.15, 83.53, 77.35, 77.04, 76.72, 25.05, 24.93 ppm. Analytical data matches that previously reported.⁴⁵⁸

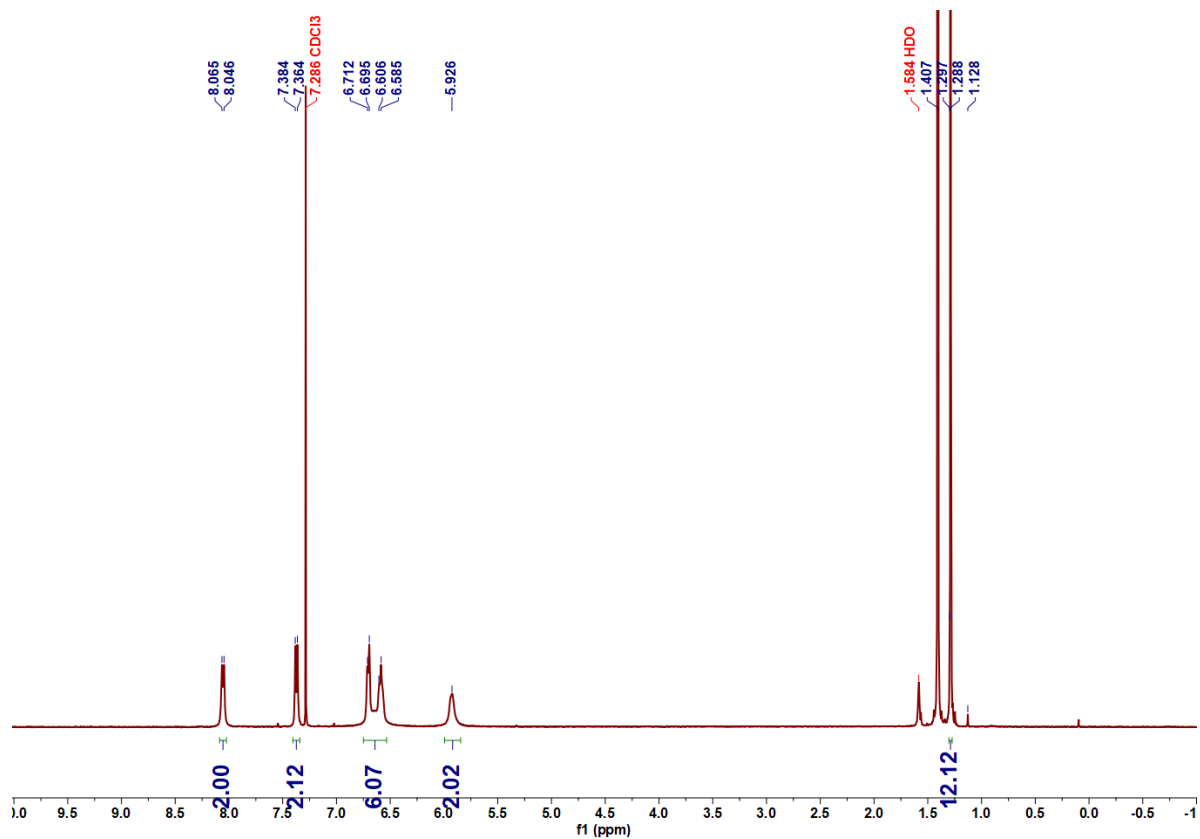


Figure 6.25. ^1H NMR spectra of **6** in CDCl_3 .

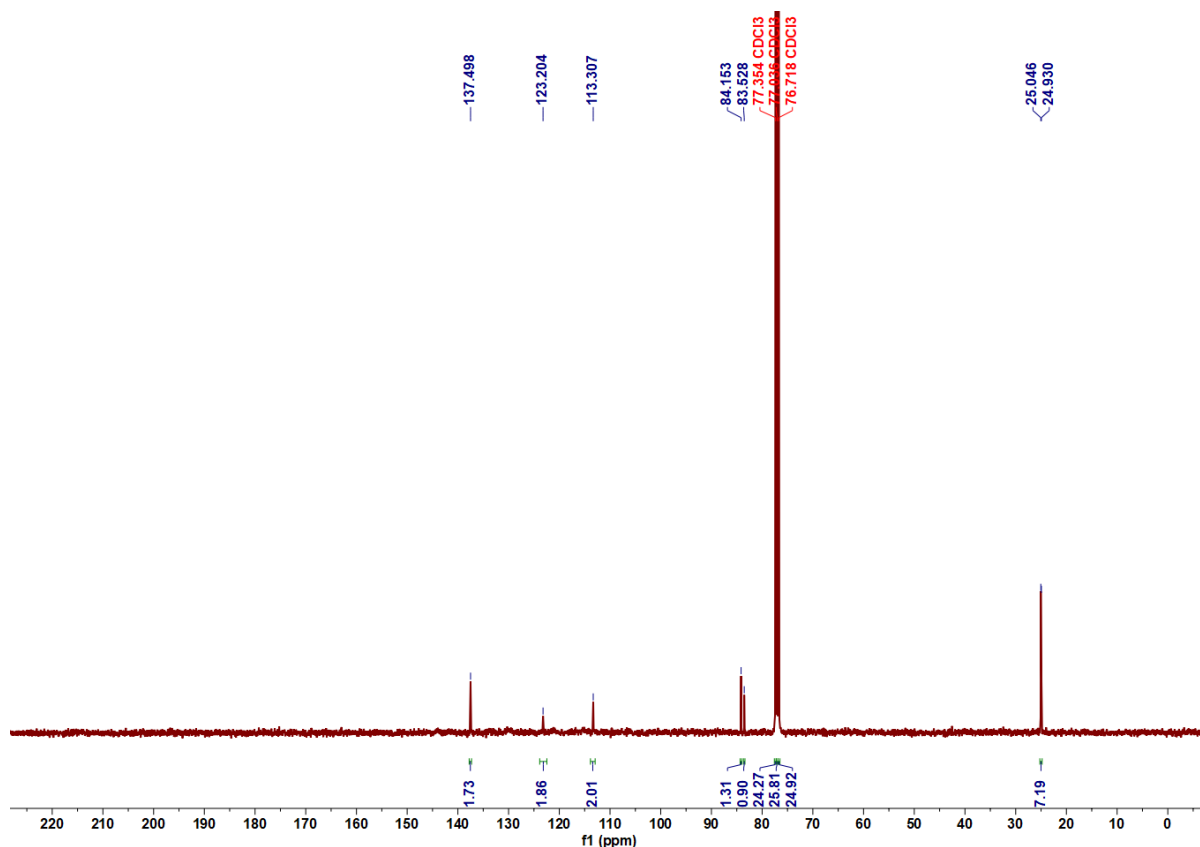
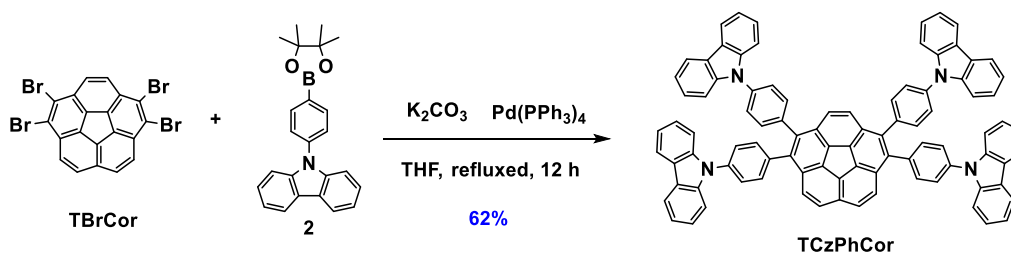


Figure 6.26. ^{13}C NMR spectra of **6** in CDCl_3 .

Synthesis of 9,9',9'',9'''-(dibenzo[ghi,mno]fluoranthene-1,2,5,6-tetrayltetrakis(benzene-4,1-diyl))tetrakis(9H-carbazole) (TCzPhCor):



In a two-necked round bottom flask **TBrCor** (0.6 g, 1.06 mmol, 1.0 equiv.) and compound **2** (2 g, 5.3 mmol, 5.0 equiv.) were dissolved in a mixture of THF (40 mL) and 2 M aqueous solution of potassium carbonate (10.0 mL). The mixture was degassed under nitrogen flow for 15 min, then tetrakis(triphenylphosphine)palladium(0) (185 mg, 0.3 mmol, 0.3 equiv.) was added under nitrogen. The reaction mixture was stirred at 70 °C for 12 h before cooling to room temperature. The reaction mixture was extracted with DCM (3 × 50 mL) and the combined organic layers were dried with anhydrous sodium sulfate and concentrated under reduced

pressure. The crude product was purified by silica gel flash column chromatography using DCM : hexane = 2:8 as eluent to give final compound as light-yellow solid (yield = 0.798 g).

9,9',9'',9'''-(dibenzo[ghi,mno]fluoranthene-1,2,5,6-tetrayltetrakis(benzene-4,1-diyl))tetrakis(9H-carbazole) (TCzPhCor): $R_f = 0.6$ (25% DCM/Hexane). **Yield:** 62%. **Mp** = 264-265 °C. **$^1\text{H NMR}$ (500 MHz, CDCl_3):** δ 8.22 – 8.16 (m, 8H), 8.05 (d, $J = 8.8$ Hz, 2H), 7.98 (s, 2H), 7.94 (d, $J = 8.8$ Hz, 2H), 7.67 – 7.60 (m, 16H), 7.50 – 7.43 (m, 8H), 7.37 – 7.29 (m, 16H) ppm. **$^{13}\text{C NMR}$ (101 MHz, CDCl_3):** δ 140.81, 138.88, 138.51, 137.62, 136.61, 136.57, 135.56, 135.38, 134.49, 133.11, 130.89, 130.49, 130.05, 127.86, 127.44, 127.31, 126.46, 126.19, 123.49, 120.43, 120.11, 109.66, 109.63, 77.39, 77.07, 76.75 ppm. **HR-MS** (Xevo G2-S) $[\text{M}+\text{H}]^+$ **Calculated:** ($\text{C}_{92}\text{H}_{54}\text{N}_4$) 1215.47; **Found:** 1215.439. **Anal. Calcd. for $\text{C}_{92}\text{H}_{54}\text{N}_4$:** C, 90.91%; H, 4.48%; N, 4.61%. **Found:** C, 90.80%; H, 4.38%; N, 4.61%. HPLC analysis: 99.8% pure on HPLC analysis, retention time 10.3 minutes in 100% THF.

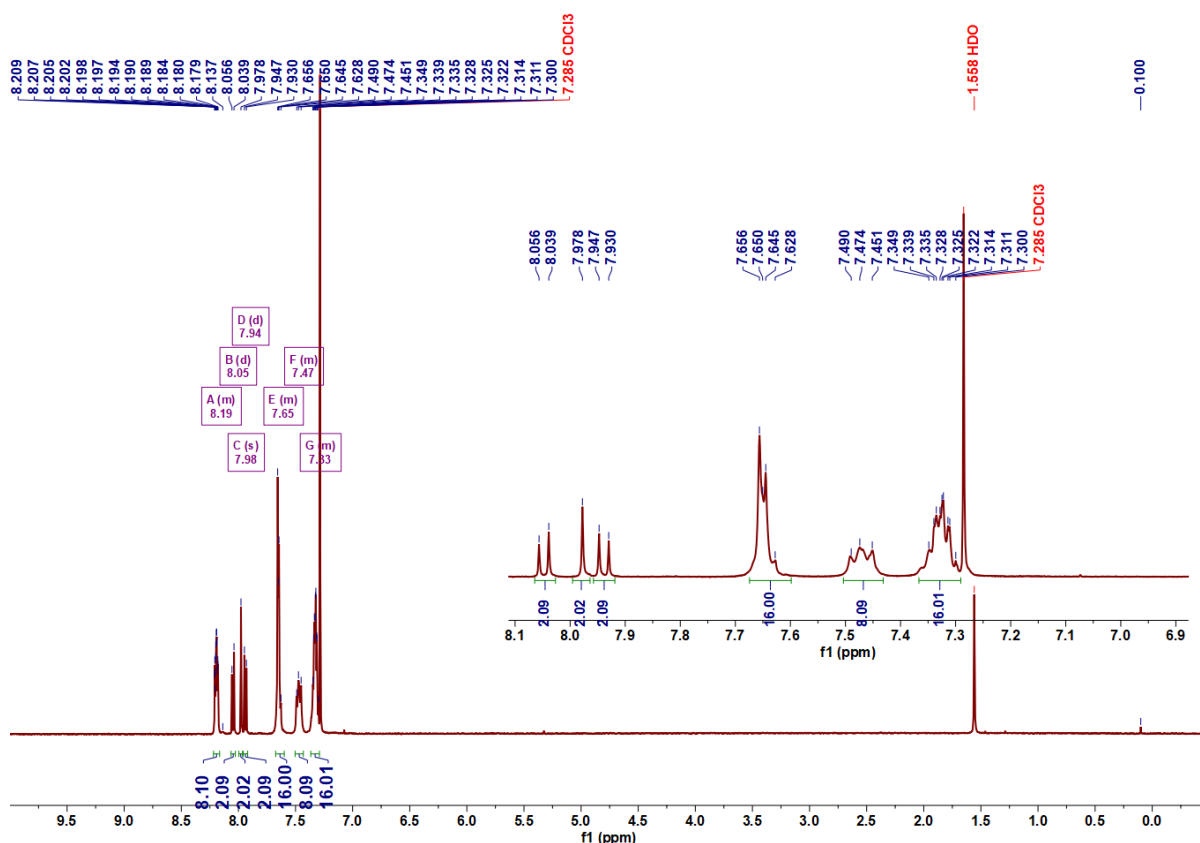


Figure 6.27. $^1\text{H NMR}$ spectra of TCzPhCor in CDCl_3 .

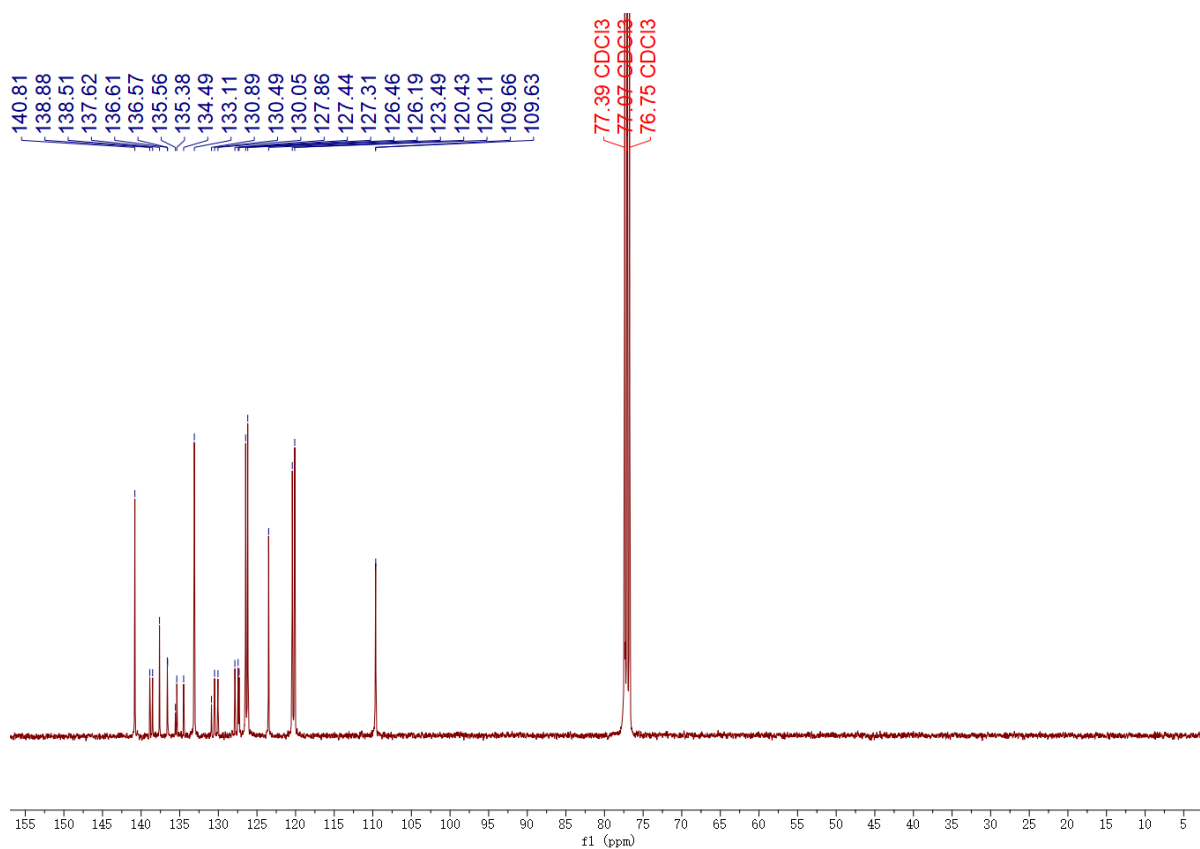


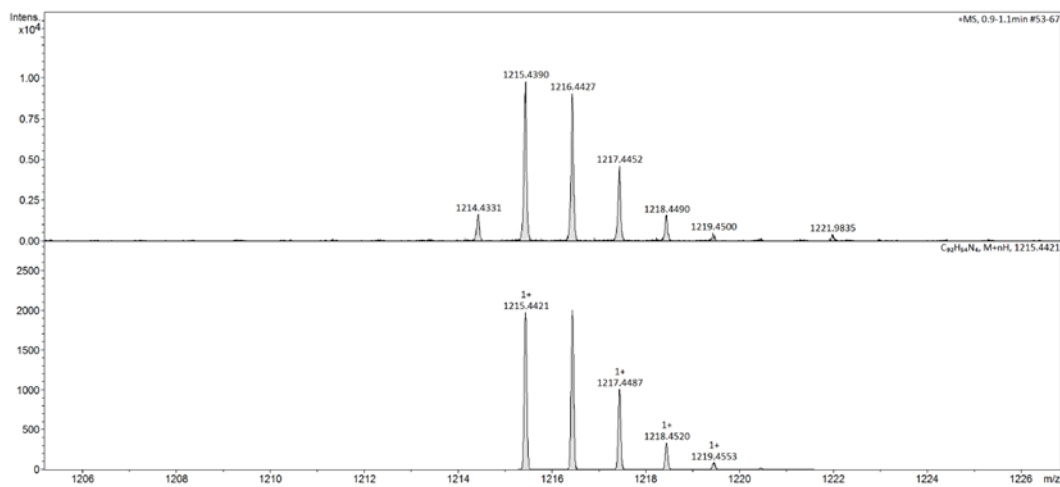
Figure 6.28. ^{13}C NMR spectra of **TCzPhCor** in CDCl_3 .

School of Chemistry Mass Spectrometry Service

SampleID
 Sample Description
 Analysis Name D:\Data\stuartwarriner\chmstw\155-TCzPhCor_f.d
 Method DIP Pos 2 m
 Instrument maXis impact

Submitter

Supervisor
 Acquisition Date 04/01/2021 15:00:23
 Scan Begin 50 m/z
 Scan End 2200 m/z



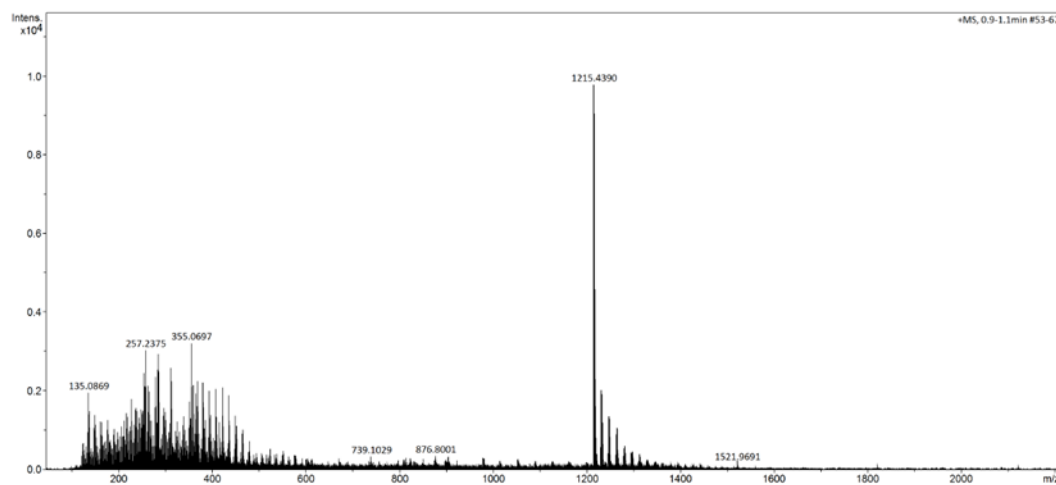
Bruker Compass DataAnalysis 4.3 Analysis Name 155-TCzPhCor_f.d 04/01/2021 15:37:24 1 of 1

School of Chemistry Mass Spectrometry Service

SampleID
 Sample Description
 Analysis Name D:\Data\stuartwarriner\chmstw\155-TCzPhCor_f.d
 Method DIP Pos 2 m
 Instrument maXis impact

Submitter

Supervisor
 Acquisition Date 04/01/2021 15:00:23
 Scan Begin 50 m/z
 Scan End 2200 m/z



Bruker Compass DataAnalysis 4.3 Analysis Name 155-TCzPhCor_f.d 04/01/2021 15:36:49 1 of 1

Figure 6.29. HRMS of TCzPhCor.

Elemental Analysis Service

Please send completed form and samples to:

Stephen Boyer
School of Human Sciences
Science Centre
London Metropolitan University
29 Hornsey Road
London N7 7DD

Telephone: 020 7133 3605
Fax: 020 7133 2577
Email: s.boyer@londonmet.ac.uk

Sample submitted by: Changfeng Si	
Address: EZC group, School of Chemistry, University of St Andrews, North Haugh, St Andrews, Fife, KY16 9ST	
Telephone: 07519611858	Email: cs339@st-andrews.ac.uk
Date Submitted:	

Please submit ca. 5 mg of sample.

Sample Reference No.: I55-Cor4PhCz
Name of Compound: 9,9',9'',9'''-(dibenzo[ghi,mno]fluoranthene-1,2,5,6-tetrayl)tetrakis(benzene-4,1-diyl)tetrakis(9H-carbazole)
Molecular Formula: C ₉₂ H ₅₄ N ₄
Stability: air stable
Hazards: no hazards
Other Remarks:

Element	Expected %	Found (1)	Found (2)
Carbon	90.91	90.76	90.83
Hydrogen	4.48	4.35	4.41
Nitrogen	4.61	4.57	4.65

Authorising Signature:

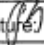
Date Completed: 15/11/14	Signature: 
Comments:	

Figure 6.30. Elemental analysis of TCzPhCor.

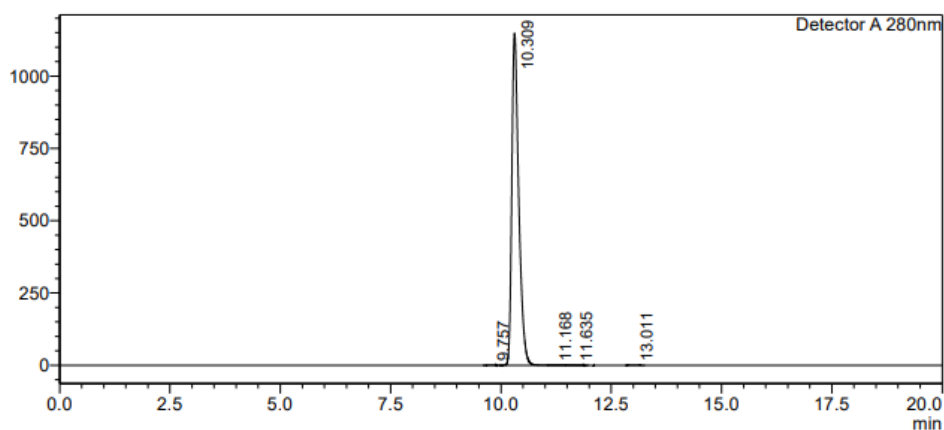
HPLC Trace Report 31 May 2022

<Sample Information>

Sample Name : TCzPhCor
 Sample ID : TdmacPhCor
 Method Filename : 100% THF 20 mins 280nm - DH.lcm
 Batch Filename : 2pDMACBP-2pDMAC-1.lcb
 Vial # : 1-24
 Injection Volume : 10 uL
 Date Acquired : 31/05/2022 21:12:10
 Date Processed : 31/05/2022 21:32:11
 Sample Type : Unknown
 Acquired by : System Administrator
 Processed by : System Administrator

<Chromatogram>

mV



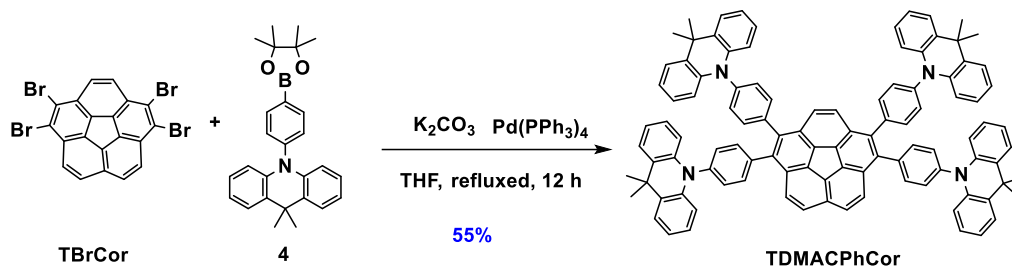
<Peak Table>

Detector A 280nm

Peak#	Ret. Time	Area	Height	Area%	Area/Height	Width at 5% Height
1	9.757	2143	193	0.017	11.096	-
2	10.309	12529545	1145260	99.890	10.940	0.384
3	11.168	4399	447	0.035	9.835	0.315
4	11.635	2855	226	0.023	12.648	0.370
5	13.011	4438	422	0.035	10.525	0.329
Total		12543380	1146548	100.000		

Figure 6.31. HPLC trace of TCzPhCor.

Synthesis of 10,10',10'',10'''-(dibenzo[ghi,mno]fluoranthene-1,2,5,6-tetrayltetrakis(benzene-4,1-diyl))tetrakis(9,9-dimethyl-9,10-dihydroacridine) (TDMACPhCor):



Compound **TDMACPhCor** was synthesized according to the same procedure as described above for the synthesis of **TCzPhCor**, except that **4** (2.2 g, 5.3 mmol) was used as the reactant instead of **2**, yielding a yellow solid (Yield = 0.805 g).

10,10',10'',10'''-(dibenzo[ghi,mno]fluoranthene-1,2,5,6-tetrayltetrakis(benzene-4,1-diyl))-tetrakis-(9,9-dimethyl-9,10-dihydroacridine) (TDMACPhCor): $R_f = 0.6$ (25% DCM/Hexane). **Yield:** 55%. **Mp** = 269-272 °C. $^1\text{H NMR}$ (500 MHz, CDCl_3): $\delta = 8.05$ (d, $J = 8.8$ Hz, 2H), 7.97 (s, 2H), 7.94 (d, $J = 8.8$ Hz, 2H), 7.67 (d, $J = 7.7$ Hz, 8H), 7.47 (ddd, $J = 7.5, 5.4, 1.6$ Hz, 8H), 7.41 (t, $J = 8.2$ Hz, 8H), 6.91 – 6.74 (m, 16H), 6.35 (ddd, $J = 13.4, 8.1, 1.3$ Hz, 8H), 1.73 (d, $J = 4.7$ Hz, 24H) ppm. $^{13}\text{C NMR}$ (101 MHz, CDCl_3): $\delta = 140.87, 140.84, 140.19, 140.17, 138.75, 138.49, 138.47, 135.49, 135.36, 134.52, 134.19, 130.86, 130.30, 130.13, 130.09, 129.94, 127.84, 127.47, 127.27, 126.62, 124.95, 120.65, 114.02, 114.00, 77.38, 77.06, 76.75, 36.05, 30.82, 30.79$ ppm. **HR-MS** (Xevo G2-S) $[\text{M}+\text{H}]^+$ **Calculated:** ($\text{C}_{104}\text{H}_{78}\text{N}_4$) 1382.62; **Found:** 1382.6197. **Anal. Calcd. for $\text{C}_{104}\text{H}_{78}\text{N}_4$:** C, 90.27%; H, 5.68%; N, 4.05%. **Found:** C, 89.98%; H, 5.76%; N, 3.94%. HPLC analysis: 99.2% pure on HPLC analysis, retention time 10.1 minutes in 100% THF.

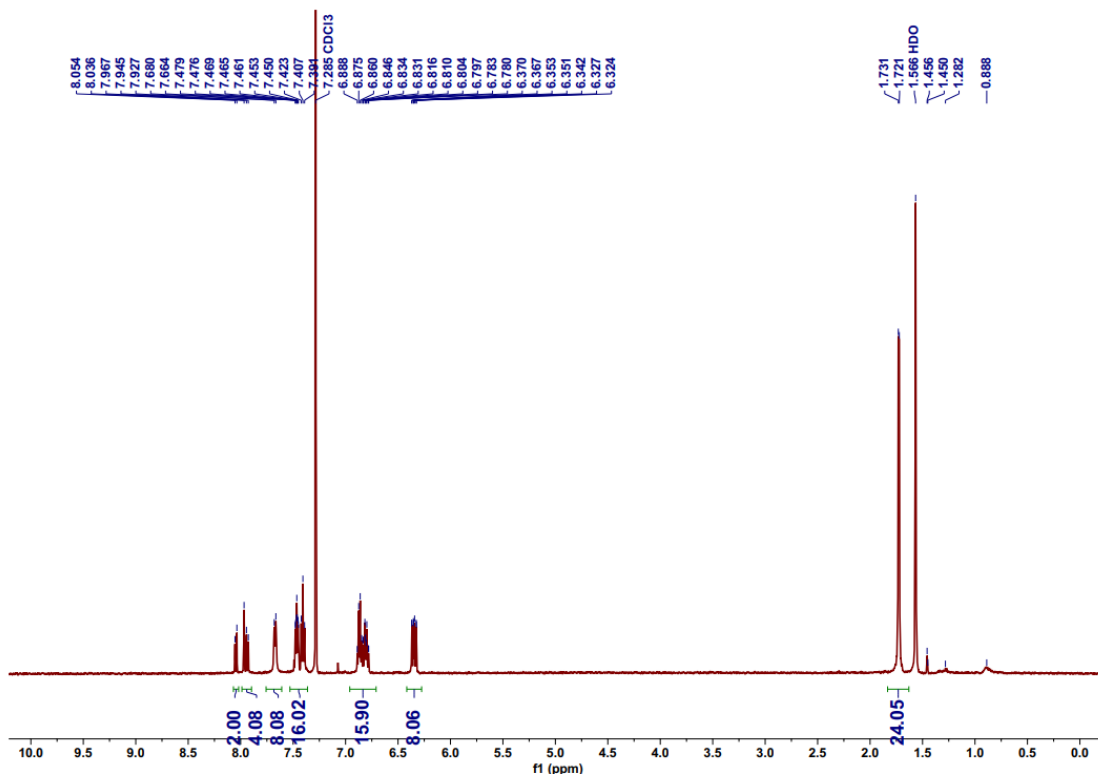


Figure 6.32. ¹H NMR spectra of TDMACPhCor in CDCl₃.

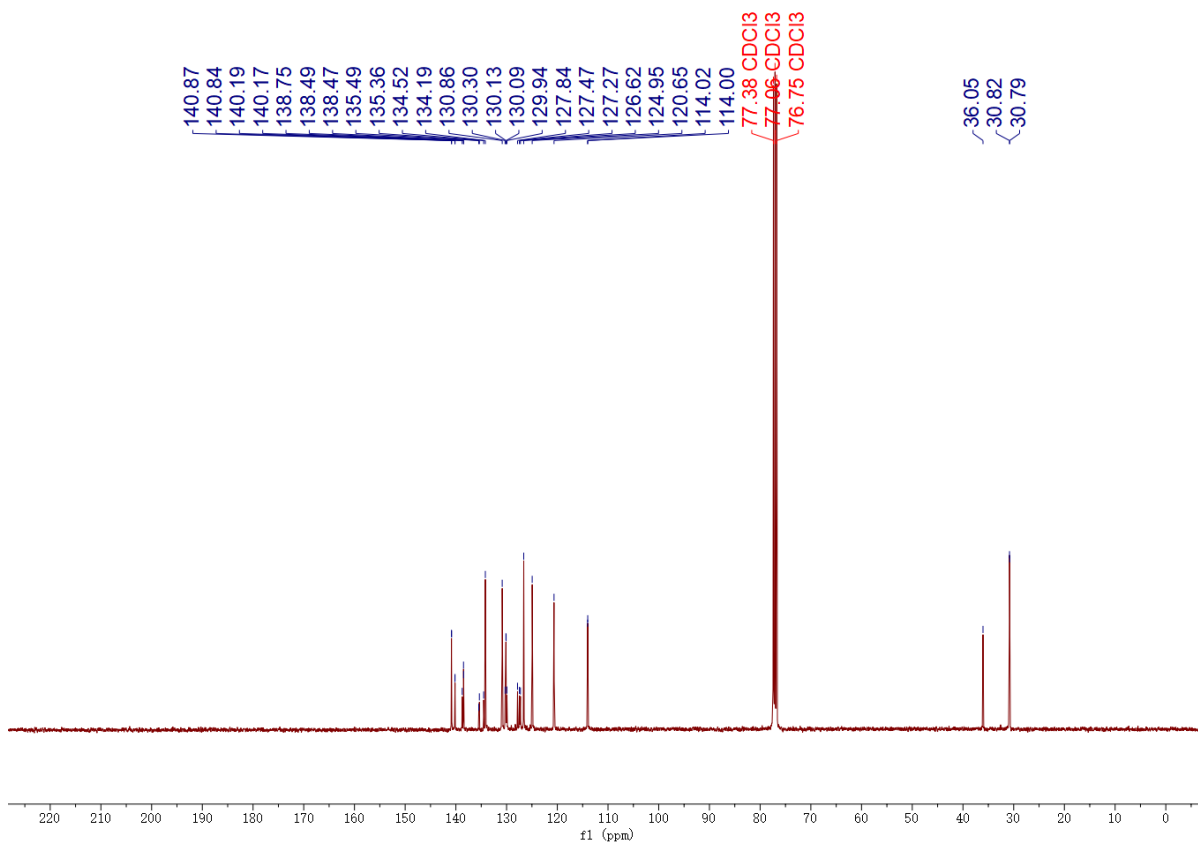
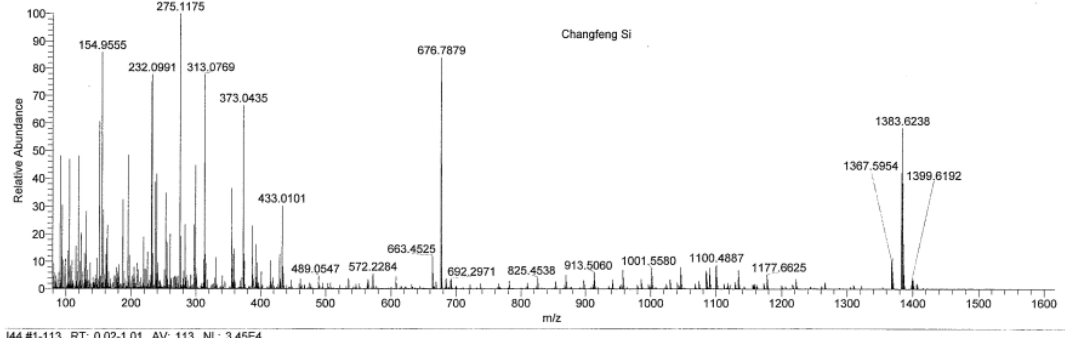


Figure 6.33. ¹³C NMR spectra of TDMACPhCor in CDCl₃.

I44 #1-113 RT: 0.02-1.01 AV: 113 NL: 5.92E4
T: FTMS + p ESI Full ms [80.00-1600.00]



I44 #1-113 RT: 0.02-1.01 AV: 113 NL: 3.45E4
T: FTMS + p ESI Full ms [80.00-1600.00]

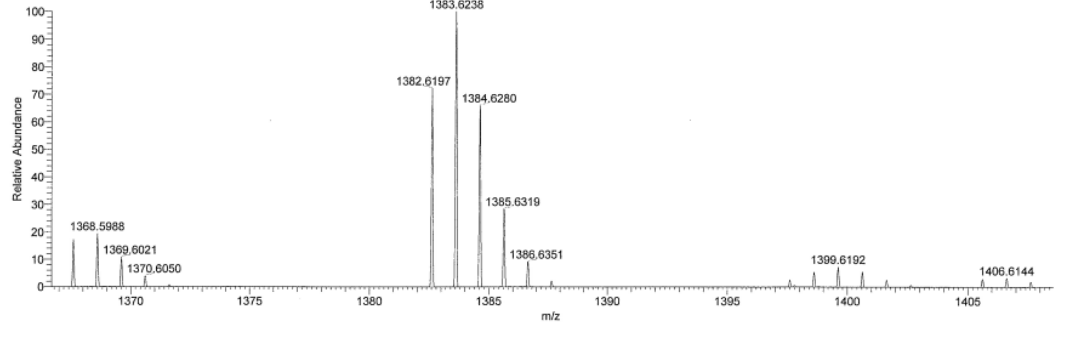


Figure 6.34. HRMS of TDMACPhCor.

Elemental Analysis Service Request Form

Researcher name Changfeng Si

Researcher email cs339@st-andrews.ac.uk

NOTE: Please submit ca. 10 mg of sample

Sample reference number	I44-Cor4PhDMAC
Name of Compound	10,10',10'',10'''-(dibenzo[ghi,mno]-fluoranthene-1,2,5,6-tetrayltetrakis(benzene-4,1-diyl))tetrakis(9,9-dimethyl-9,10-dihydroacridine)
Molecular formula	C104H78N4
Stability	
Hazards	
Other Remarks	

Analysis type:

Single Duplicate Triplicate

Analysis Result:

Element	Expected %	Found (1)	Found (2)	Found (3)
Carbon	90.27	88.66	89.98	
Hydrogen	5.68	5.69	5.82	
Nitrogen	4.05	3.88	3.94	
Oxygen				

Authorising Signature:

Date completed	20.11.20
Signature	J-PC
comments	

Figure 6.35. Elemental analysis of TDMACPhCor.

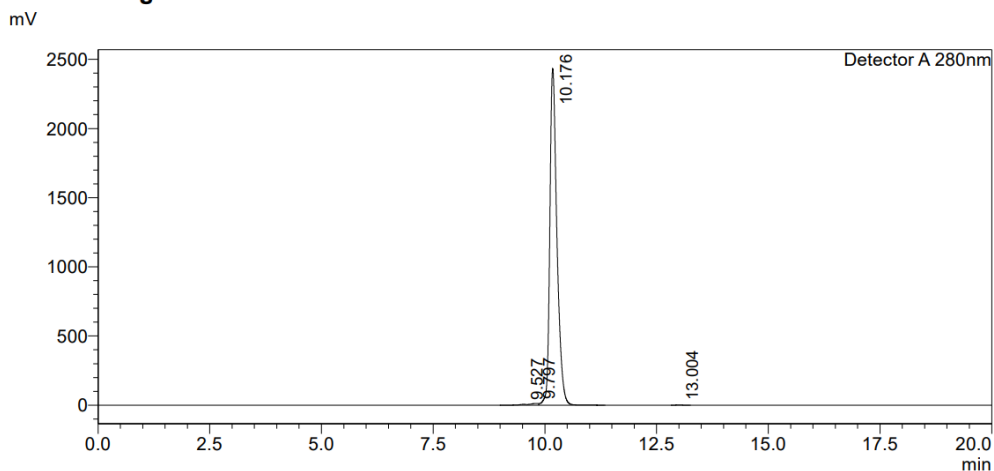
HPLC Trace Report 31 May 2022

<Sample Information>

Sample Name : TdmacPhCor
 Sample ID : TdmacPhCor
 Method Filename : 100% THF 20 mins 280nm - DH.lcm
 Batch Filename : 2pDMACBP-2pDMAC-1.lcb
 Vial # : 1-23
 Injection Volume : 10 uL
 Date Acquired : 31/05/2022 21:32:33
 Date Processed : 31/05/2022 21:52:34

Sample Type : Unknown
 Acquired by : System Administrator
 Processed by : System Administrator

<Chromatogram>



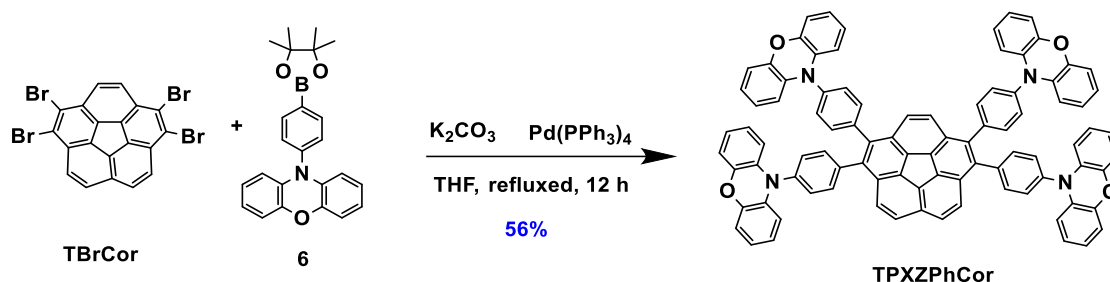
<Peak Table>

Detector A 280nm

Peak#	Ret. Time	Area	Height	Area%	Area/Height	Width at 5% Height
1	9.527	63600	5703	0.234	11.151	--
2	9.797	146176	12367	0.538	11.820	--
3	10.176	26965309	2428477	99.212	11.104	0.392
4	13.004	4412	406	0.016	10.861	0.341
Total		27179496	2446954	100.000		

Figure 6.36. HPLC trace of TDMACPhCor.

Synthesis of 10,10',10'',10'''-(dibenzo[ghi,mno]fluoranthene-1,2,5,6-tetrayltetrakis(benzene-4,1-diyl))tetrakis(10H-phenoxazine) (TPXZPhCor):



Compound **TPXZPhCor** was synthesized according to the same procedure as described above for the synthesis of **TCzPhCor**, except that **6** (2.0 g, 5.3 mmol) was used as the reactant instead of **4**, yielding a yellow solid (Yield = 0.758 g).

10,10',10'',10'''-(dibenzo[ghi,mno]fluoranthene-1,2,5,6-tetrayltetrakis(benzene-4,1-diyl))tetrakis(10H-phenoxazine) (TPXZPhCor): $R_f=0.6$ (25% DCM/Hexane). **Yield:** 56%. **Mp** = 366-368 °C. **¹H NMR (500 MHz, CDCl₃)** δ 8.00 (d, $J = 8.8$ Hz, 2H), 7.83 (d, $J = 10.7$ Hz, 4H), 7.59 (d, $J = 7.7$ Hz, 8H), 7.37 (t, $J = 8.4$ Hz, 8H), 6.71 (dd, $J = 7.7, 6.0$ Hz, 8H), 6.62 (q, $J = 7.2$ Hz, 8H), 6.50 (dt, $J = 14.3, 7.6$ Hz, 8H), 5.91 (dd, $J = 14.6, 7.9$ Hz, 8H).ppm. **¹³C NMR (101 MHz, CDCl₃):** δ 143.86, 138.72, 138.55, 138.21, 138.00, 135.41, 135.30, 134.43, 134.34, 134.18, 130.83, 130.36, 130.18, 129.81, 129.07, 128.26, 127.86, 127.33, 127.15, 125.32, 123.53, 121.41, 115.46, 113.11, 113.07, 77.36, 77.04, 76.73 ppm. **HR-MS (Xevo G2-S) [M+H]⁺ Calculated:** (C₉₂H₅₄N₄O₄) 1278.41; **Found:** 1279.3588. **Anal. Calcd. for C₉₂H₅₄N₄O₄:** C, 86.36%; H, 4.25%; N, 5.00%. **Found:** C, 86.23%; H, 4.25%; N, 4.89%. HPLC analysis: 99.7% pure on HPLC analysis, retention time 10.2 minutes in 100% THF.

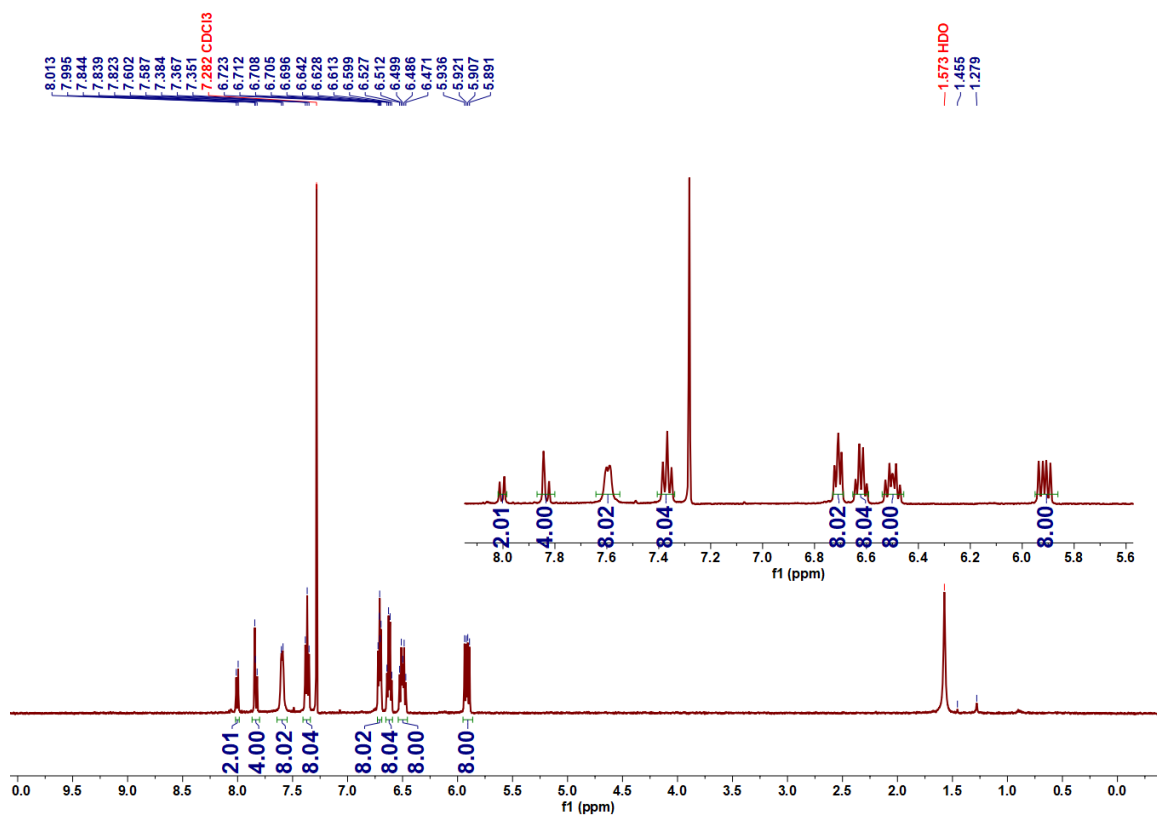


Figure 6.37. ^1H NMR spectra of TPXZPhCor in CDCl_3 .

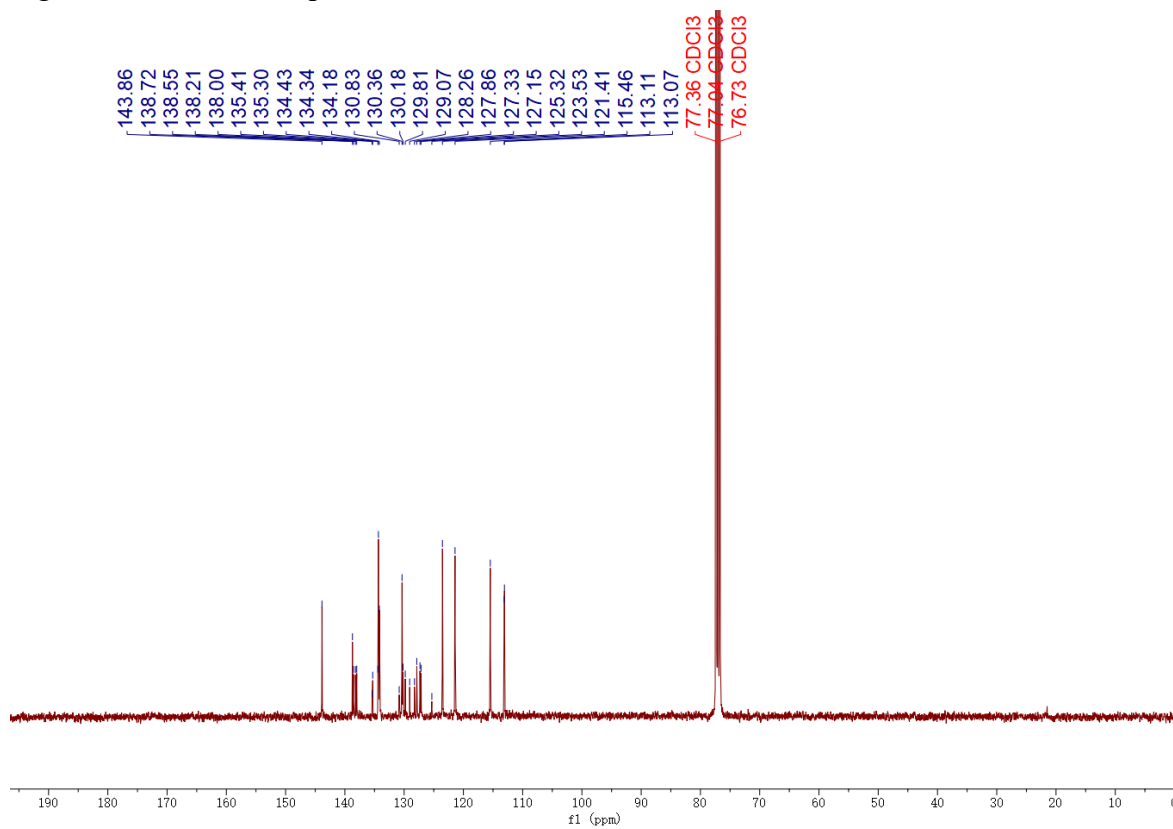


Figure 6.38. ^{13}C NMR spectra of TPXZPhCor in CDCl_3 .



Elemental Analysis Service

Please send completed form and samples to:

Stephen Boyer
 School of Human Sciences
 Science Centre
 London Metropolitan University
 29 Hornsey Road
 London N7 7DD

Telephone: 020 7133 3605
 Fax: 020 7133 2577
 Email: s.boyer@londonmet.ac.uk

Sample submitted by: Changfeng Si	
Address: EZC group, School of Chemistry, University of St Andrews, North Haugh, St Andrews, Fife, KY16 9ST	
Telephone: 07519611858	Email: cs339@st-andrews.ac.uk
Date Submitted:	

Please submit ca. 5 mg of sample.

Sample Reference No.: I54-Cor4PhPXZ
Name of Compound: 10,10',10'',10'''-(dibenzo[ghi,mno]fluoranthene-1,2,5,6-tetrayltetrakis(benzene-4,1-diy))tetrakis(10H-phenoxazine)
Molecular Formula: C92H54N4O4
Stability: air stable
Hazards: no hazards
Other Remarks:

Element	Expected %	Found (1)	Found (2)
Carbon	86.36	86.23	86.18
Hydrogen	4.25	4.22	4.29
Nitrogen	5.00	4.82	4.92

Authorising Signature:

Date Completed: 15/11/19	Signature:
Comments:	

Figure 6.39. Elemental analysis of TPXZPhCor.

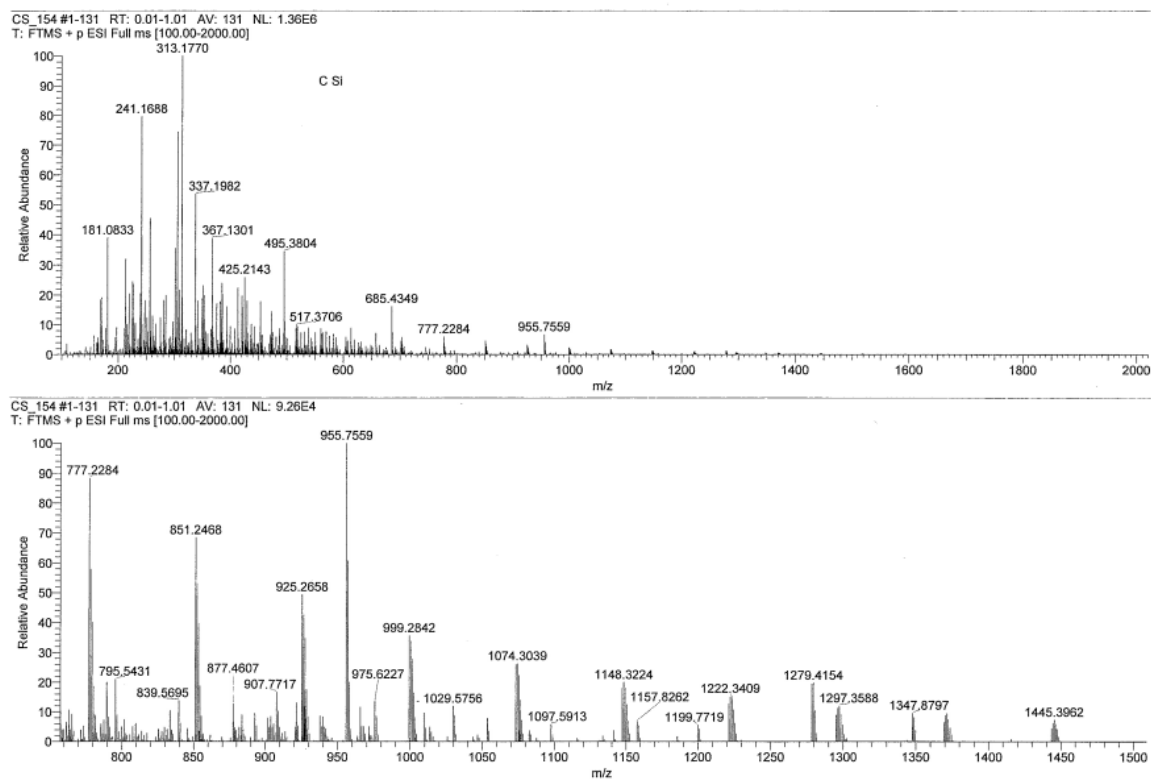


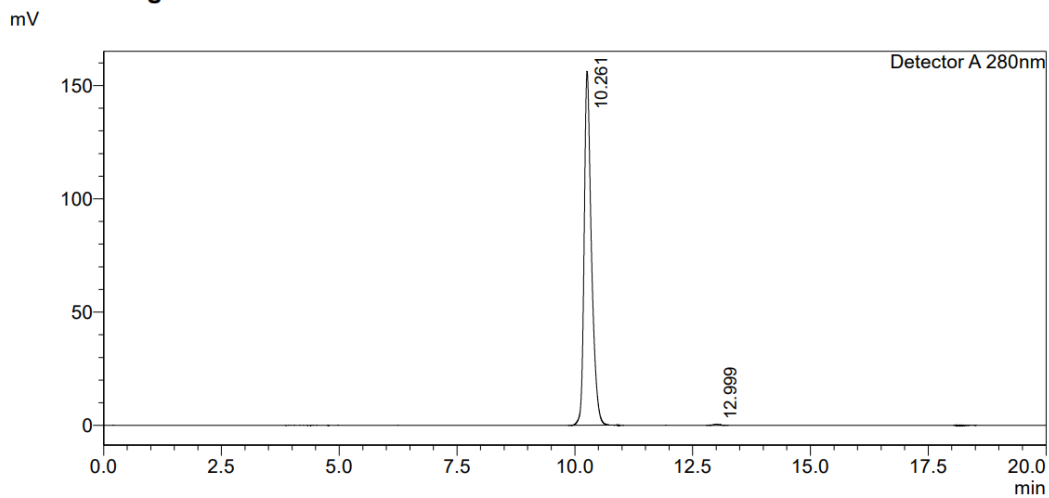
Figure 6.40. HRMS of TPXZPhCor.

HPLC Trace Report 31 May 2022

<Sample Information>

Sample Name : TPXZPhCor
Sample ID : TPXZPhCor
Method Filename : 100% THF 20 mins 280nm - DH.lcm
Batch Filename : 2pDMACBP-2pDMAC-1.lcb
Vial # : 1-25
Injection Volume : 10 uL
Date Acquired : 31/05/2022 20:48:12
Date Processed : 31/05/2022 21:08:14
Sample Type : Unknown
Acquired by : System Administrator
Processed by : System Administrator

<Chromatogram>



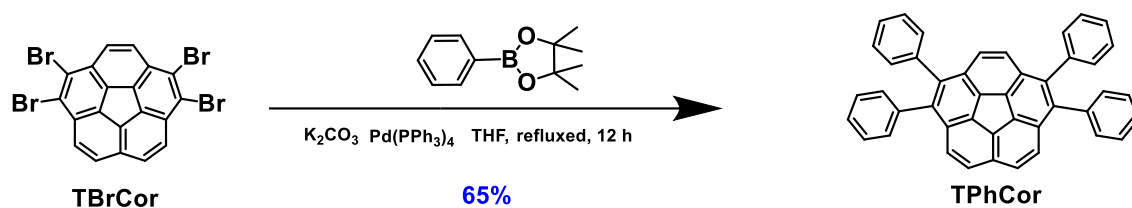
<Peak Table>

Detector A 280nm

Peak#	Ret. Time	Area	Height	Area%	Area/Height	Width at 5% Height
1	10.261	1673608	156147	99.706	10.718	0.386
2	12.999	4934	451	0.294	10.950	0.343
Total		1678542	156597	100.000		

Figure 6.41. HPLC trace of TPXZPhCor.

Synthesis of 1,2,5,6-tetraphenyldibenzo[ghi,mno]fluoranthene (TPhCor):



Compound **TPXZPhCor** was synthesized according to the same procedure as described above for the synthesis of **TCzPhCor**, except that 4,4,5,5-tetramethyl-2-phenyl-1,3,2-dioxaborolane (1.08 g, 5.3 mmol) was used as the reactant instead of **4**, yielding a yellow solid (Yield = 0.380 g).

1,2,5,6-tetraphenyldibenzo[ghi,mno]fluoranthene (TPhCor): $R_f=0.6$ (25% DCM/Hexane). **Yield:** 65%. **Mp** = 220-222 °C. $^1\text{H NMR}$ (400 MHz, $\text{DMSO-}d_6$) δ 7.98 (d, $J = 8.9$ Hz, 2H), 7.53 – 7.47 (m, 4H), 7.37 – 7.24 (m, 20H) ppm. $^{13}\text{C NMR}$ (101 MHz, $\text{DMSO-}d_6$): δ 139.33, 139.00, 138.13, 138.10, 135.06, 134.63, 133.71, 131.57, 130.82, 130.73, 130.19, 128.42, 128.17, 127.62, 127.42, 127.34 ppm. **HR-MS** (Xevo G2-S) $[\text{M}+\text{H}]^+$ **Calculated:** ($\text{C}_{44}\text{H}_{26}$) 554.2035; **Found:** 554.2029.

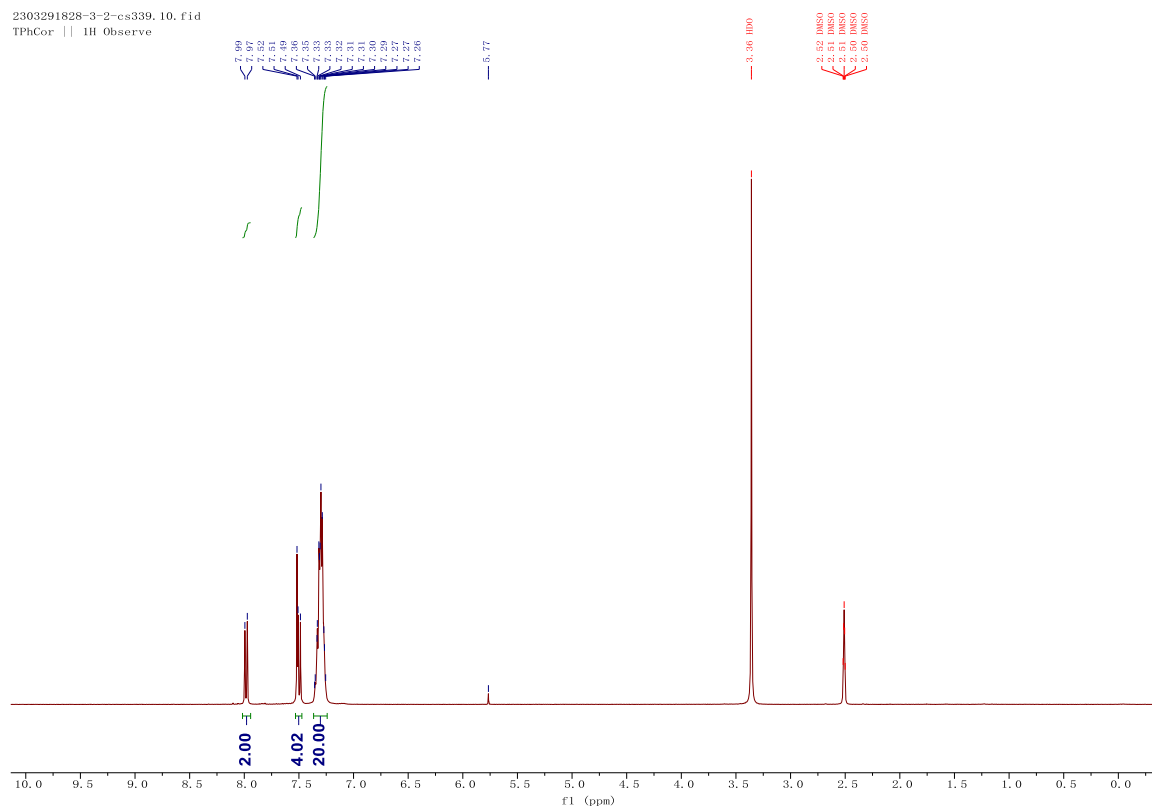


Figure 6.42 $^1\text{H NMR}$ spectra of **TPhCor** in $\text{DMSO-}d_6$.

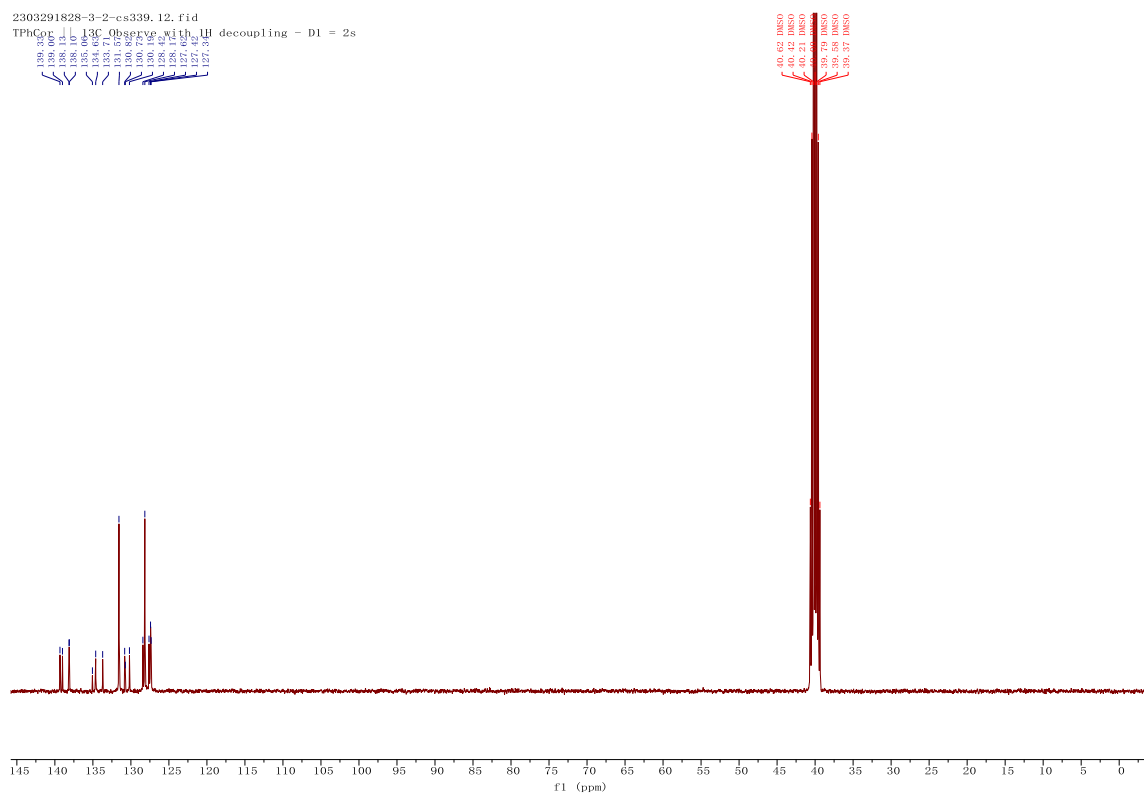


Figure 6.43. ^{13}C NMR spectra of **TPhCor** in $\text{DMSO-}d_6$.

Generic Display Report (all)

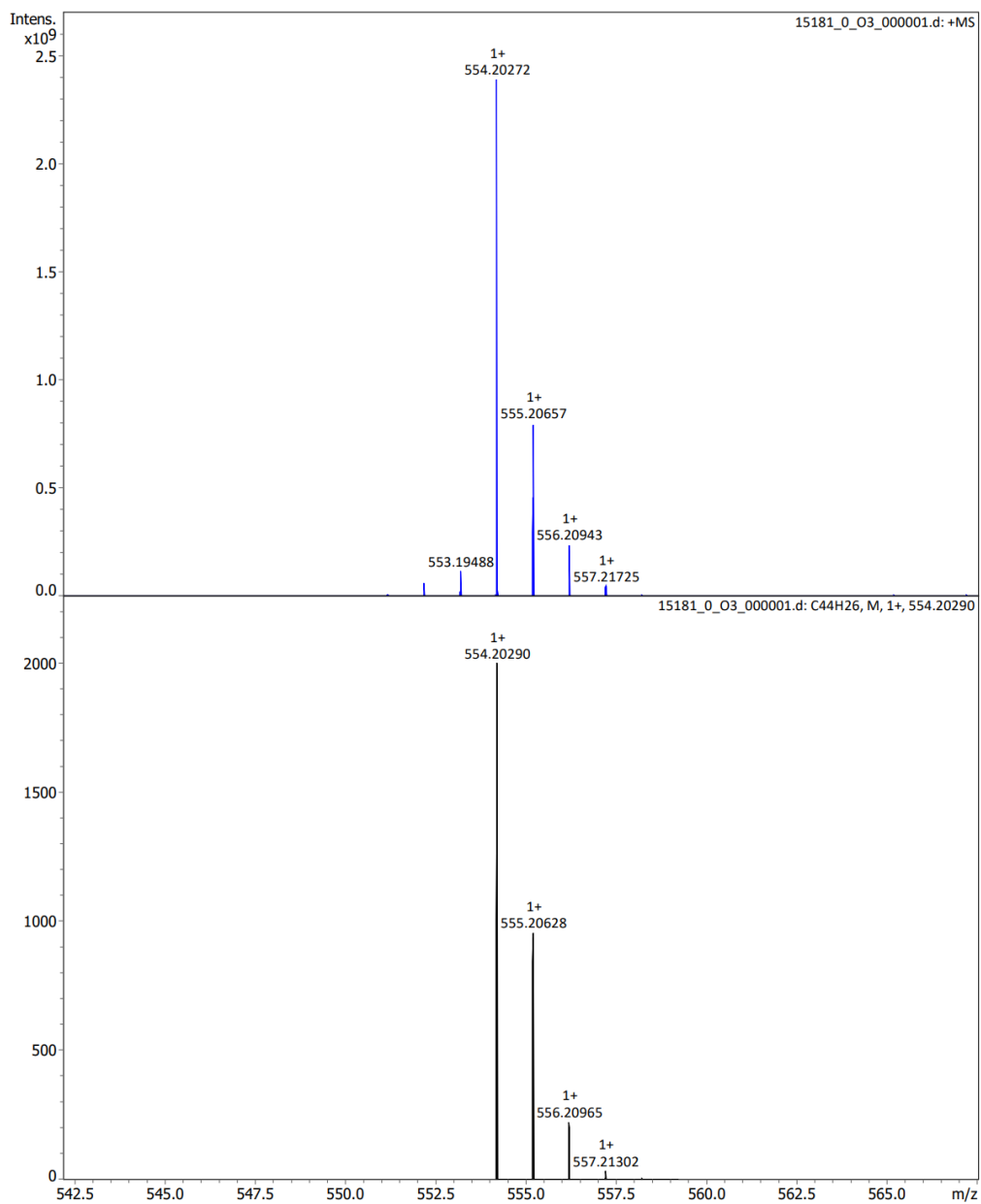
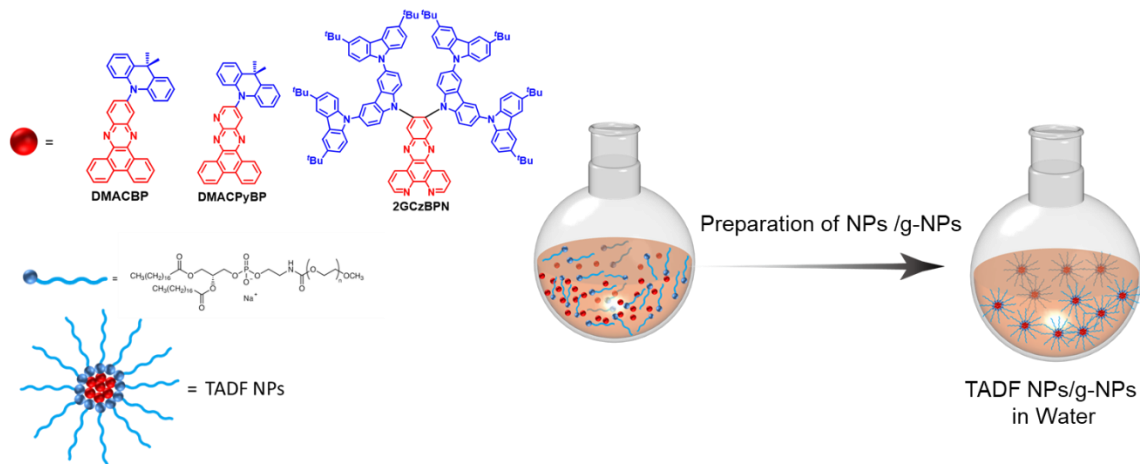


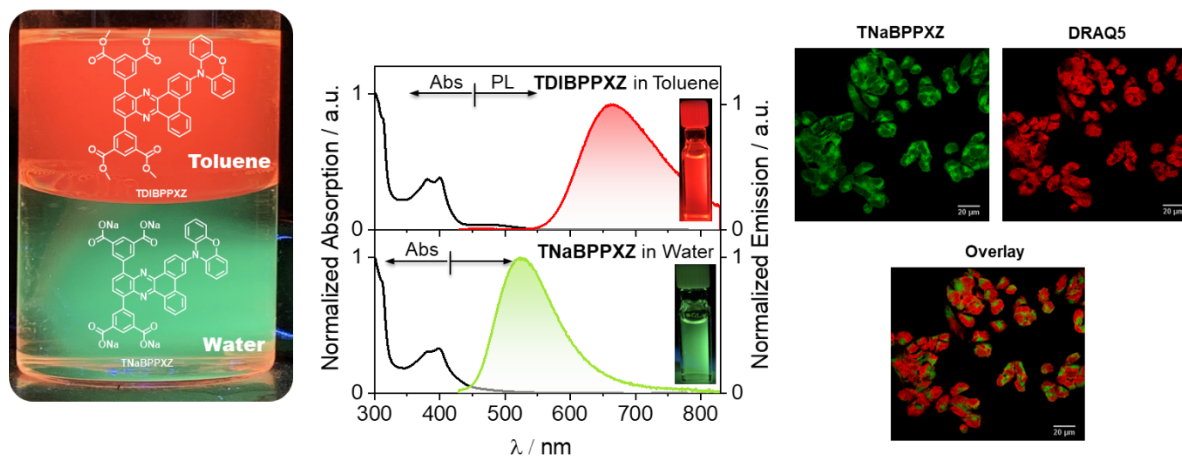
Figure 6.44. HRMS of TPhCor.

Chapter 7: Exploration of Water-soluble D-A TADF Emitters for Bioimaging

Method 1: Water soluble Nanoparticles



Method 2: Water soluble sodium-salt emitters



Collaborators in this Chapter are from

1. Will Primrose and Prof. Zac Hudson, Department of Chemistry, The University of British Columbia, Vancouver, BC, Canada

Will Primrose helped with the glassy NP preparation, SEM characterization and bioimaging experiments.

2. Felicity Noakes and Prof. Jim A Thomas, Department of Chemistry, University of Sheffield, Sheffield S3 7HF, United Kingdom.

Felicity Noakes carried out the bioimaging part based on water-soluble sodium-salt emitters.

I completed all the syntheses, NP preparation and characterization, DFT and TD-DFT calculations, photophysics measurements and I am the principal author of the text.

7.1 Introduction

In the previous **Chapters**, we explored several families of D-A TADF compounds and fully investigated the effect of π -conjugation and electron-withdrawing abilities of the acceptor, donor strength and donor substitution position on the photophysical properties, like emission color, Φ_{PL} , delay lifetime and k_{RISC} . Furthermore, we employed our emitters in OLEDs, ZnCl_2 sensors, and temperature sensors.

In this Chapter, we will explore the use of D-A TADF emitters in bioimaging. In **Chapter 1.6**, we reviewed the development of TADF emitters for bioimaging^{170–172} and we summarized the principal design criteria for TADF luminophores, like a sufficiently long lifetime, good biocompatibility, and tolerance of both atmospheric and intracellular oxygen. To achieve these properties, the design strategies are as follows: 1) TADF emitters capped with BSA/HSA;^{163,168} 2) TADF-based Odots formed by encapsulating TADF emitters in an amphiphilic polymer;^{191,193} 3) Silica-based nanoparticles as hosts for the encapsulation of the TADF emitter;¹⁹⁶ 4) Self-assembled nanoparticles;^{175,199–201} 5) Aggregation-induced delayed fluorescence;²⁰⁴ and 6) water-soluble TADF compounds.^{209,210} Here, we have developed water-soluble TADF luminophores through two strategies: one is making water soluble TADF NP by encapsulating TADF emitters in an amphiphilic polymer, DSPE-PEG2000; another one is trying to design a new water-soluble TADF compounds.

Among these emitters we discussed in the previous Chapters, we picked three emitters, **DMACBP**, **DMACPyBP** (**Chapter 2**) and **2GCzBPN** (**Chapter 5**), due to their red emission, high Φ_{PL} , efficient TADF, and relatively long delayed lifetime and then we fabricated NPs and investigated their photophysical properties. Secondly, we designed a red TADF emitter **TDIBPPXZ**, which is substituted by dimethyl isophthalate units followed by ester hydrolysis. Furthermore, we obtained a water-soluble sodium-salt emitters, **TNaBPPXZ**, which was fully characterized and shows promising potential for use in bioimaging applications.

7.2 Preparation of NPs and its Characterization

7.2.1 Preparation of NPs

The preparation of NPs in aqueous solution was achieved using a well-documented matrix-encapsulation method. DSPE-PEG2000 was selected as the encapsulation matrix due to its good encapsulation performance and high biocompatibility.^{460–462} Figure 7.1 illustrates the step-by-step process involved in preparing NPs. Initially, 1 mg of TADF emitters and 2 mg of DSPE-PEG2000 were dissolved in 1 mL of THF, followed by stirring for 4 hours. Next, the resulting homogeneous solution was diluted by adding a mixture of 2 mL of THF and Milli-Q water, with a water volume fraction of 20%. Following a 2-minute sonication of the diluted solution, it was promptly added to 7 mL Milli-Q water in the bath sonicator. Prior to concentrating the solution to 5 mL using a rotary evaporator, THF was eliminated through nitrogen stripping.¹⁷⁸ The resulting TADF NPs suspension was filtered using a 0.22 μm syringe filter and the solution could be stored at 4 °C without noticeable decomposition.

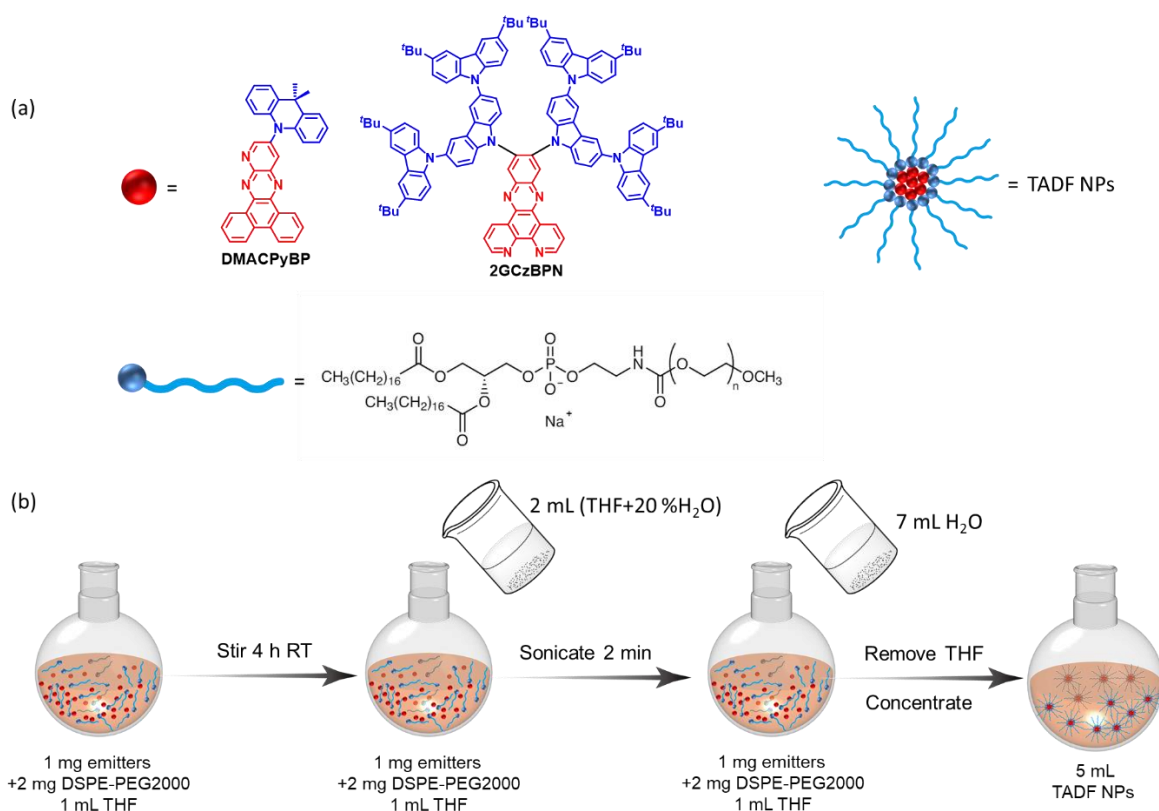


Figure 7.1. The procedure of the preparation of NPs.

7.2.2 Characterization of NPs

Figure 7.2a displays the PL of **DMACPyBP NP** in water, which shows a red-shifted emission at λ_{PL} of 671 nm compared to that of **DMACPyBP** in toluene ($\lambda_{\text{PL}} = 630$ nm, **Chapter 2**). The PL decays with biexponential kinetics, with τ_{p} of 6 ns and τ_{d} of 0.2 μs , respectively (Figure 7.2), which is much shorter than that of **DMACPyBP** in toluene ($\tau_{\text{p}} = 20$ ns, τ_{d} of 3.5 μs). The Φ_{PL} of **DMACPyBP NP** drops to 3% compared to **DMACPyBP** in toluene ($\Phi_{\text{PL}} = 20\%$), which could be result from ACQ in the NPs. Similarly, **2GCzBPN NP** exhibits deep red emission at $\lambda_{\text{PL}} = 663$ nm (Figure 7.2c), different from that in toluene ($\lambda_{\text{PL}} = 624$ nm, **Chapter 5**), a corresponding a decrease in Φ_{PL} of 5% from the parent **2GCzBPN** ($\Phi_{\text{PL}} = 42\%$) in toluene. In the degassed NP water solution, the delayed fluorescence lifetime of **2GCzBPN NPs** is slightly shorter with the value of 1.3 μs than that of parent **2GCzBPN** ($\tau_{\text{d}} = 7.5$ μs) in degassed toluene. These results demonstrate the long lifetime of **2GCzBPN** can be maintained when the NPs were prepared and used as nanoprobe for TRLI.

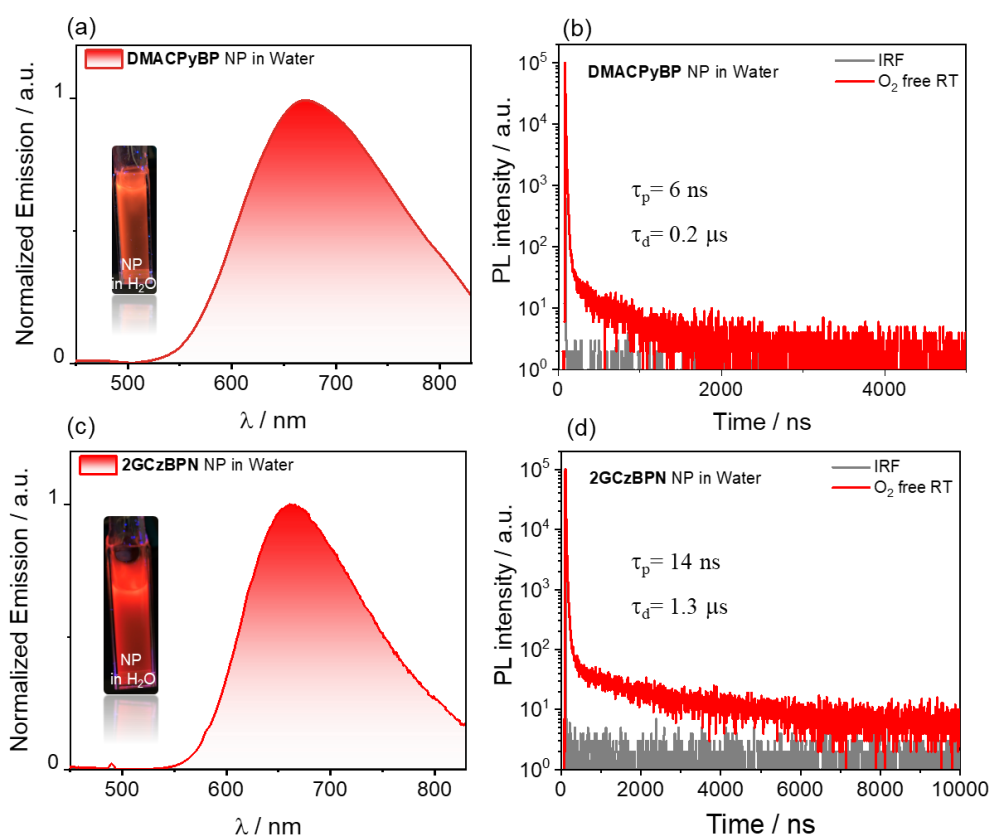


Figure 7.2. (a) The PL of **DMACPYBP NPs** ($\lambda_{\text{exc}} = 360$ nm) and (b) corresponding PL decay ($\lambda_{\text{exc}} = 375$ nm); (c) The PL of **2GCzBPN NPs** ($\lambda_{\text{exc}} = 360$ nm) and (d) corresponding PL decay ($\lambda_{\text{exc}} = 375$ nm).

7.3 Preparation of g-NPs and its Characterization

Adachi and co-workers demonstrated a novel preparation method to obtain glassy nanoparticle (g-NPs) by incorporating the TADF emitter into a glassy host matrix of mCP, along with DSPE-PEG2000, which shows high Φ_{PL} , good dispersibility and high photostability.⁴⁶³ Recently, Hudson and co-workers also explored other g-NPs based on heptazine-type TADF emitters (details discussed in **Chapter 1.6.2**). These g-Odots were then used as biological imaging probes for immortalized human kidney cancer (HEK293) cells, and both for single- and multi-photon excited microscopy coupled with time-gated luminescence measurements.⁴⁶⁴

7.3.1 Preparation of g-NPs

By using a similar method, we also prepared two kinds of g-NPs based on **DMACBP** and **DMACPyBP** (**Chapter 2**). The procedure of the g-NPs is shown in Figure 7.3: Firstly, the stock solutions of mCP, DSPE-PEG2000 and the emitters were prepared at a concentration of 12.0 mmol L⁻¹, 10.5 mmol L⁻¹ and 1.3 mmol L⁻¹, respectively. To the reaction vial, each stock solution was added mCP (875 μL , 4.3 mg): DSPE-PEG2000 (100 μL , 3.0 mg) (weight ratio 1.5:1), along with the emitter in an amount of 5 wt% to mCP (338 μL , 0.22 mg). The solutions were concentrated under a nitrogen stream, yielding a film followed by a one-hour drying under vacuum at 60 °C. A magnetic stir bar was introduced into the vial, along with 20 mL of MilliQ water. The vial was sealed with a Reseal cap and stirred for 30 min and then placed into the microwave reactor. The reaction vial was stirred at 600 rpm and heated at 180 °C for 10 mins in a microwave reactor. After cooling to room temperature, the contents were centrifuged at 1500 rpm for 15 mins, collecting the supernatant. The supernatant was then further centrifuged to pelletize the suspended nanoparticles at 6000 rpm three times. The final pellet was resuspended in MilliQ water (1.0 mL) and stored in fridge.

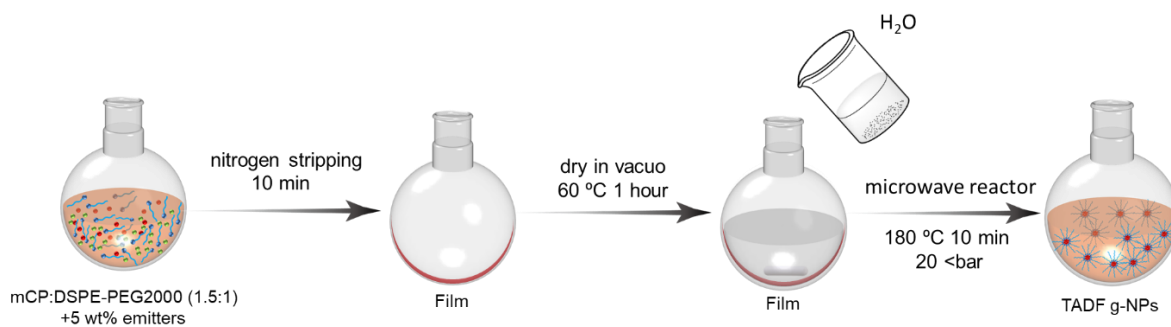


Figure 7.3. The procedure of the preparation of g-NPs.

7.3.2 Characterization of g-NPs

The size of **DMACBP** g-NPs and **DMACPyBP** g-NPs was verified by nanoparticle tracking analysis (NTA). The stock solutions of g-NPs samples were diluted by a factor of 100 with MilliQ water before measurements were taken. The measurements were conducted in scattering mode with a 488 nm laser and in fluorescence mode using a 500 nm long-pass emission filter (NanoSight NS300, Malvern Panalytical, Malvern, UK). Figure 7.4a-b shows that both **DMACBP** g-NPs and **DMACPyBP** g-NPs have similar average diameter of around 200 nm, with reasonable polydispersity (PDI) of 0.19 and 0.18, respectively. The size of the g-NPs confirmed that the emitters are encapsulated by the DSPE-PEG2000. The spherical morphology of the g-NPs was characterized by scanning electron microscopy (SEM) (Hitachi S-2600 Variable Pressure SEM electron microscope) as shown in Figure 7.4c-d. Both **DMACBP** g-NPs and **DMACPyBP** g-NPs were spherical with diameters of less than 1000 nm.

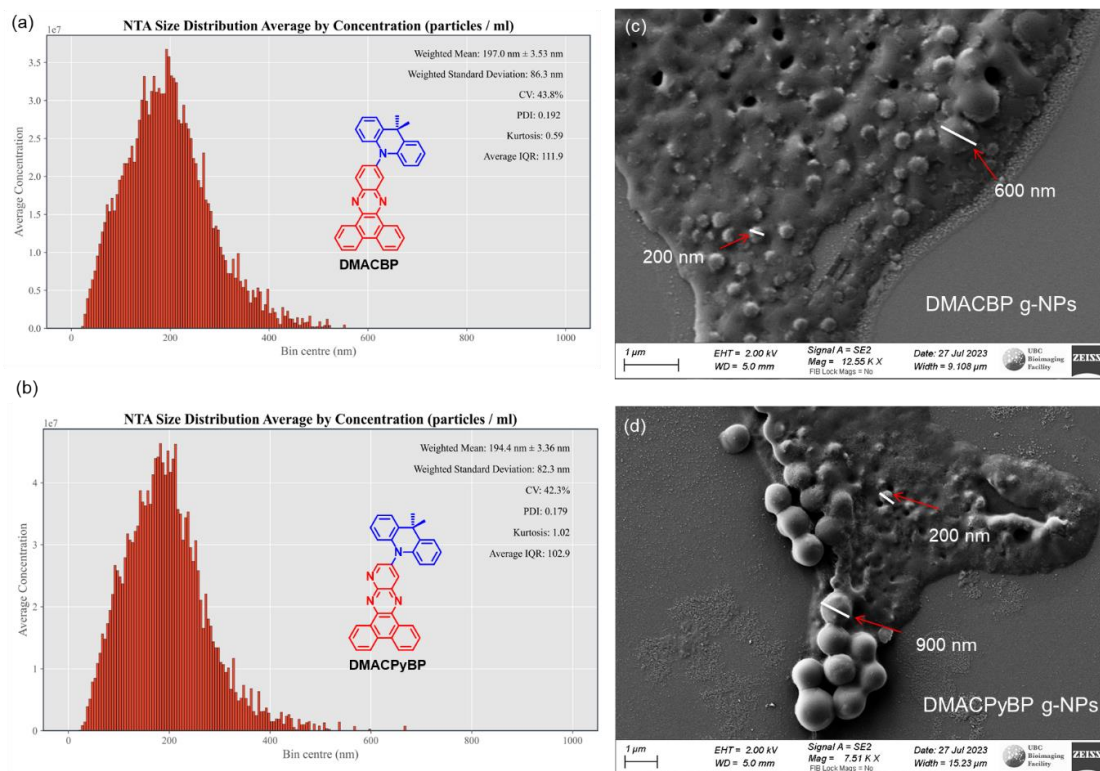


Figure 7.4. NTA distribution for (a) **DMACBP** g-NPs and (b) **DMACPyBP** g-NPs; SEM images of (c) **DMACBP** g-NPs and (d) **DMACPyBP** g-NPs.

The PL and lifetime of **DMACBP** g-NPs and **DMACPyBP** g-NPs in water are shown in Figure 7.5. **DMACBP** g-NPs shows yellow greenish emission at λ_{PL} of 572 nm (Figure 7.5a), similar to that of 5 wt% **DMACBP** in doped CBP film ($\lambda_{PL} = 574$ nm, In Chapter 2, we did all the photophysics in CBP not mCP). Furthermore, **DMACBP** g-NPs also have a similar τ_d of 197.5 μ s (Figure 7.5b), compared to that of 130.3 μ s in the doped film. However, the Φ_{PL} of **DMACBP** g-NPs is only 28%, much lower than that of 70% in 5 wt% doped CBP films. **DMACPyBP** g-NPs have a red shifted emission spectrum ($\lambda_{PL} = 614$ nm) compared to both **DMACBP** g-NPs and the **DMACPyBP** doped film (610 nm in 5 wt% CBP). The **DMACPyBP** g-NPs have a longer τ_d of 26.2 μ s than that of 5.9 μ s for **DMACPyBP** doped film (Figure 7.5d). The Φ_{PL} of **DMACPyBP** g-NP drops to 11% in comparison to the **DMACPyBP** doped CBP film ($\Phi_{PL} = 41\%$), which could be result from ACQ in the NPs. However, the Φ_{PL} of **DMACPyBP** g-NP shows a threefold increase compared to **DMACPyBP** NPs, which has a Φ_{PL} of 3% (without the mCP host matrix). This result confirmed the outstanding performance of these glassy NPs.^{463,464} We also attempted to use these g-NPs as biological imaging agents

in HeLa cells. However, in our initial experiments, the HeLa cells did not successfully phagocytize the g-NPs. Further bioimaging applications will be explored in subsequent studies.

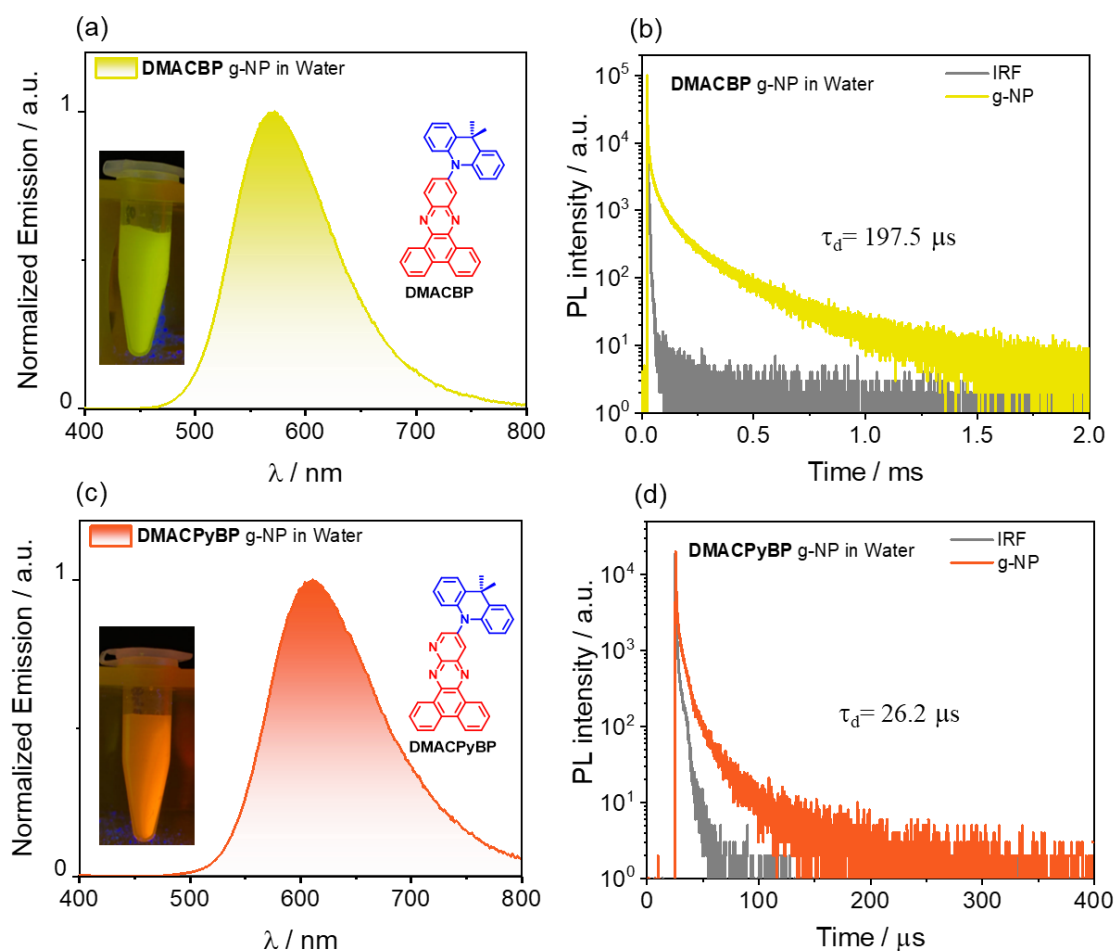
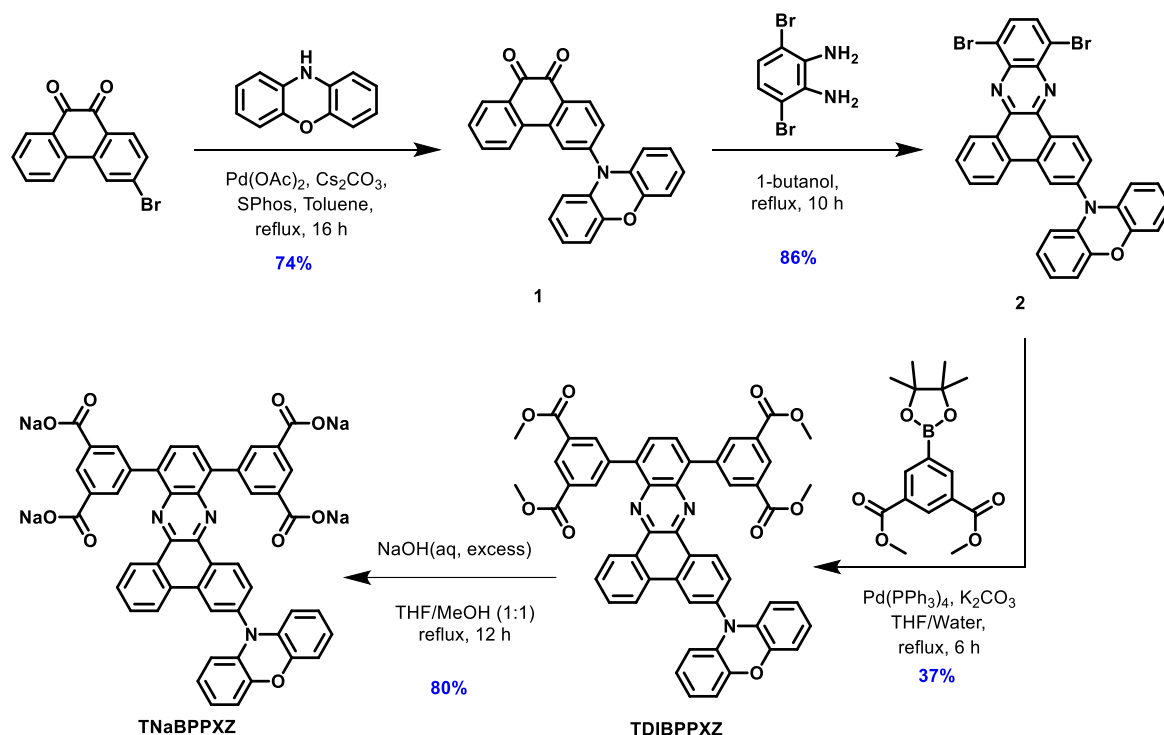


Figure 7.5. (a) The PL of **DMACBP** g-NPs ($\lambda_{\text{exc}} = 360$ nm) and (b) corresponding PL decay ($\lambda_{\text{exc}} = 375$ nm); (c) The PL of **DMACPyBP** g-NPs ($\lambda_{\text{exc}} = 360$ nm) and (d) corresponding PL decay ($\lambda_{\text{exc}} = 375$ nm).

7.4 Synthesis of TNaBPPXZ

The synthetic route for **TNaBPPXZ** is shown in Scheme 7.1. Intermediate **1** was synthesized in 74% yield following a Buchwald-Hartwig coupling between 3-bromophenanthrene-9,10-dione and phenanthrene-9,10-dione in 1-butanol and 10H-phenoxazine. Intermediate **2** was obtained through the cyclization reaction of 3,6-dibromobenzene-1,2-diamine and Intermediate **1** in 1-butanol. The TADF emitter **TDIBPPXZ** was synthesized in yields of 37% following a Suzuki-Miyaura cross-coupling reaction between

intermediate **2** and dimethyl 5-(4,4,5,5-tetramethyl-1,3,2-dioxaborolan-2-yl)isophthalate. The final target compound **TNaBPPXZ** was obtained from the hydrolysis from **TDIBPPXZ** in a yield of 80%. The identity and purity of **TDIBPPXZ** were verified by ^1H NMR and ^{13}C NMR spectroscopy, melting point determination, HRMS, EA, and HPLC.



Scheme 7.1. Synthetic Routes for **TNaBPPXZ**.

7.5 Characterization of **TDIBPPXZ** and **TNaBPPXZ**

We first modelled the ground-state structure of **TDIBPPXZ** in the gas phase using DFT at the PBE0/6-31G(d,p) level of theory.^{265,266} The calculated energy levels of the HOMO and LUMO are shown in Figure 7.6a. The HOMO is localized on the PXZ donor while the LUMO is located on both the BP acceptor and extended over the two phenyl groups substituted at the 10/13 position of BP, leading to a stabilized T_1 compared to the parent BP acceptor (**Chapter 2**). The corresponding LUMO and HOMO values are -2.50 eV and -4.87 eV, respectively, and result in a small $\Delta E_{\text{HOMO-LUMO}}$ of 2.37 eV. The S_1 and T_1 energies are 1.91 eV and 1.86 eV, respectively, which were calculated using TD-DFT within the TDA based on the optimized S_0 . So, the small ΔE_{ST} value (0.05 eV) indicates the potential TADF could be easy to arrive.

The HOMO and LUMO energy levels of **TDIBPPXZ** were obtained using CV and DPV

measurements in the degassed DCM solution (Figure 7.6c). The E_{red} and E_{ox} determined from the DPV peak values are -1.36 V and 0.72 V, respectively. The corresponding LUMO and HOMO levels are -2.98 eV and -5.06 eV, respectively. The LUMO value is similar to that of the BP acceptor (-2.94 eV) discussed in Chapter 2, while the HOMO is much more destabilized compared to DMAC-based emitters (e.g., **DMACBP**: -5.34 eV) due to the use of the stronger PXZ donor here. Figure 7.6d displays the UV-Vis absorption spectra of **TDIBPPXZ** in dilute toluene. The intense bands centered at ~ 390 nm are assigned to locally excited (LE) $\pi-\pi^*$ transitions of the donors and acceptor moiety,^{225,226} while a hypochromic broad band at ~ 490 nm originates from ICT transitions from the PXZ donor to the acceptor moiety.^{143,225} **TDIBPPXZ** exhibits a pure red CT emission with a peak of 666 nm. A strong positive solvatochromism is observed (Figure 7.6e), which is consistent with the CT nature of the emissive excited state. While the emission band at around 490 nm can be associated with a LE state due to absence of spectral shift with increasing solvent polarity.¹⁰² The prompt PL and phosphorescence spectra in 2-MeTHF glass at 77 K were used to extract the S_1 and T_1 energies from their respective onsets (Figure 7.6f, Table). The S_1 energy of **TDIBPPXZ** is 2.32 eV with CT character while the T_1 energy is 2.6 eV, which possess LE character from the structure phosphorescence spectra. The corresponding ΔE_{ST} value is 0.16 eV. PL decays of **TDIBPPXZ** in toluene under degassed conditions were measured using TCSPC/MCS. The ICT emission band decays biexponentially with τ_p of 21.8 ns and τ_d of 90.8 μs (Figure 7.6g), and the then intensity of delayed emission obviously decreased upon the oxygen, demonstrating their high sensitivity of oxygen and typical TADF properties. The fluorescence intensity change observed in Figure 7.6h provides further evidence of the key role played by oxygen in quenching delayed fluorescence, align with the decreasing from Φ_{PL} of 16% in degassed toluene to 8% in aerated toluene. Next, we measured the PL of **TDIBPPXZ** in the 10 wt% PMMA, which shows a deep red emission with $\lambda_{\text{PL}} = 695$ nm (Figure 7.6i, insert). This emission band in decays with biexponential kinetics with τ_p of 18.3 ns, and τ_d of 2.8 μs , respectively, showing the TADF properties.

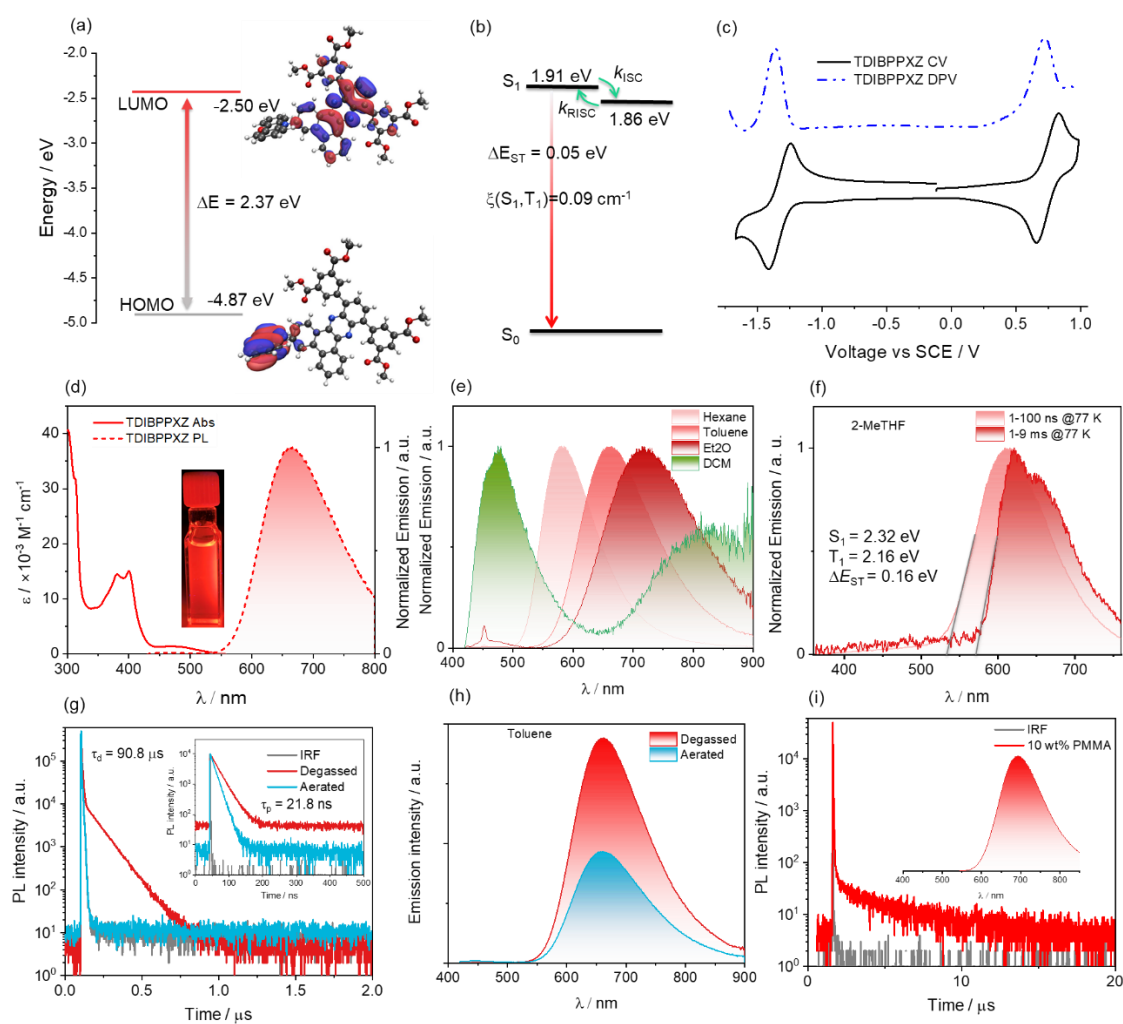


Figure 7.6. (a) Frontier molecular orbitals (isovalue: 0.02) and (b) Vertical excitation energy levels of **TDIBPPXZ** calculated at the optimized S_0 geometry in the gas phase at the PBE0/6-31G(d,p) level; (c) Cyclic and differential pulse voltammograms measured in degassed DCM with 0.1 M [n Bu $_4$ N]PF $_6$ as the supporting electrolyte and Fc/Fc $^+$ as the internal reference (0.46 V vs SCE).²²⁴ (d) UV-vis absorption and SSPL spectra in toluene at room temperature (λ_{exc} = 390 nm). (e) PL solvatochromism study (f) prompt fluorescence (1-100 ns) and phosphorescence spectra (1-10 ms) in 2-MeTHF at 77 K of **TDIBPPXZ** (λ_{exc} = 390 nm); (g) time-resolved PL decay (λ_{exc} = 375 nm) and (h) SS PL spectra in degassed and aerated toluene (λ_{exc} = 390 nm); (i) time-resolved PL decay (λ_{exc} = 375 nm) and PL spectra (insert) in 10 wt% doped in PMMA.

The UV-Vis absorption spectrum of **TDIBPPXZ** in dilute toluene and **TNaBPPXZ** in water are shown in Figure 7.7. Compared to **TDIBPPXZ**, the intensity of CT absorption band

(450~500 nm) decreased dramatically in **TNaBPPXZ** in water, while there is no change for the LE absorption band at ~400 nm. **TNaBPPXZ** exhibited a green emission at $\lambda_{\text{PL}} = 520$ nm in water and a low Φ_{PL} of ~1%. This emission showed a significant blue shift compared to **TDIBPPXZ** ($\lambda_{\text{PL}} = 666$ nm in toluene), which could be from the LE emission of the acceptor. A similar phenomenon was also observed in DMSO, demonstrating that the emission behavior of **TNaBPPXZ** is totally different from **TDIBPPXZ**. The PL decay of **TNaBPPXZ** in both degassed and aerated water overlapped very well with the same τ_{p} of 5.8 ns, much shorter than **TDIBPPXZ** ($\tau_{\text{p}} = 21.8$ ns). Furthermore, there is negligible emission change between degassed and aerated water. It is thus likely that the emission from **TNaBPPXZ** in water is normal fluorescence but given the large amount of non-radiative decay it is not possible to know for certain given the photophysical data available.

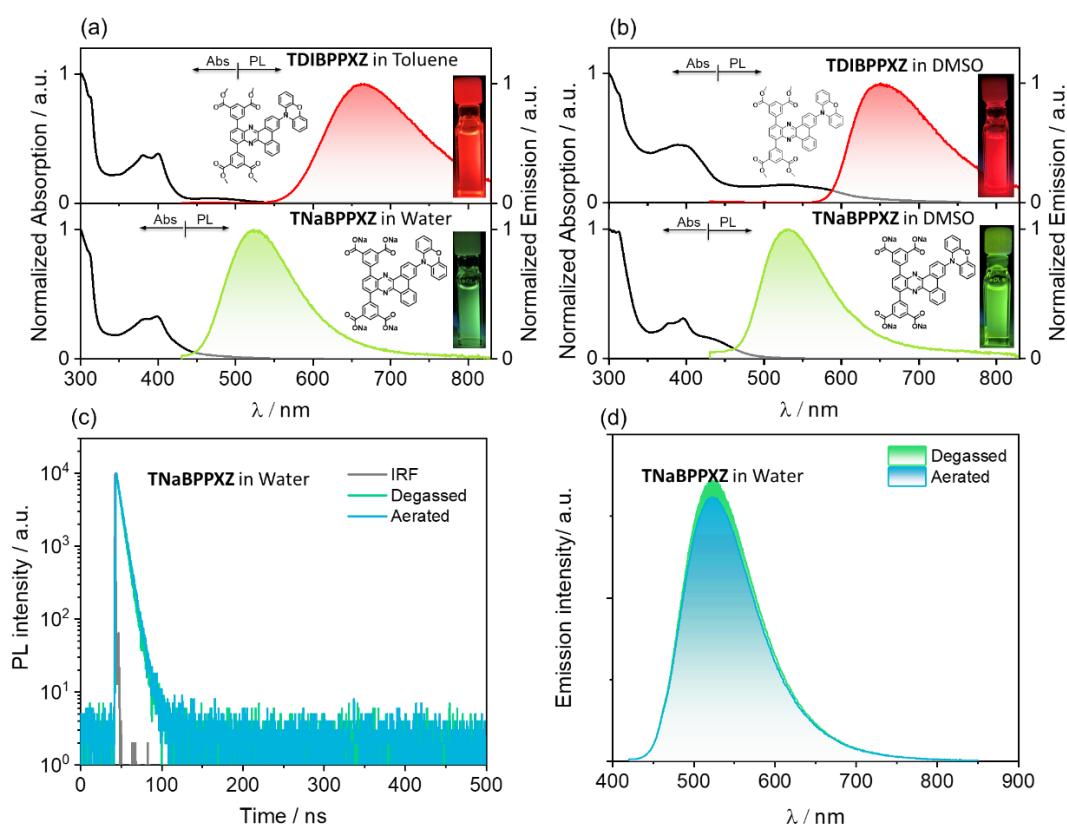


Figure 7.7. UV-vis absorption and SSPL spectra of (a) **TDIBPPXZ** in toluene, **TNaBPPXZ** in water and (b) **TDIBPPXZ**, **TNaBPPXZ** in DMSO at room temperature ($\lambda_{\text{exc}} = 390$ nm); (c) time-resolved PL decay ($\lambda_{\text{exc}} = 375$ nm) and (h) SS PL spectra in degassed and aerated water ($\lambda_{\text{exc}} = 390$ nm).

7.6 Bioimaging Exploration of TNaBPPXZ

7.6.1 Cytotoxicity Studies (MTT Assay)

A2780 (human ovarian carcinoma) cells were seeded in a 48 well plate at a density of 5×10^4 cells per well. Stock solutions of compounds were prepared in PBS (phosphate buffered saline) and then diluted into cell culture medium (RPMI supplemented with 10% fetal bovine serum (FBS), 2 mM L-glutamine, 100 IU mL⁻¹ penicillin and 100 µg mL⁻¹ streptomycin). Compound solutions were sterile filtered through a 0.22 µm filter. Cisplatin was used as a positive control. After 24 hours cells were treated with a range of concentrations (0.1 – 100 µM) of each compound in triplicate. After 48 hours, the media was removed and replaced with MTT (0.5 mg mL⁻¹ in serum free media). After 30 minutes incubation, the MTT solution was removed, and the resulting formazan eluted and dissolved in 130 µL *isopropanol* per well. 100 µL from each well was transferred to a 96 well plate and the absorbance read by spectrophotometer at 595 nm. The average absorbance was determined for each concentration and the cell viability calculated as a percentage of the untreated control well. The IC₅₀ for each compound was determined by interpolation. Under these conditions, TNaBPPXZ display negligible cytotoxicity towards A2780 cells with IC₅₀ values >100 µM (Figure 7.8a).

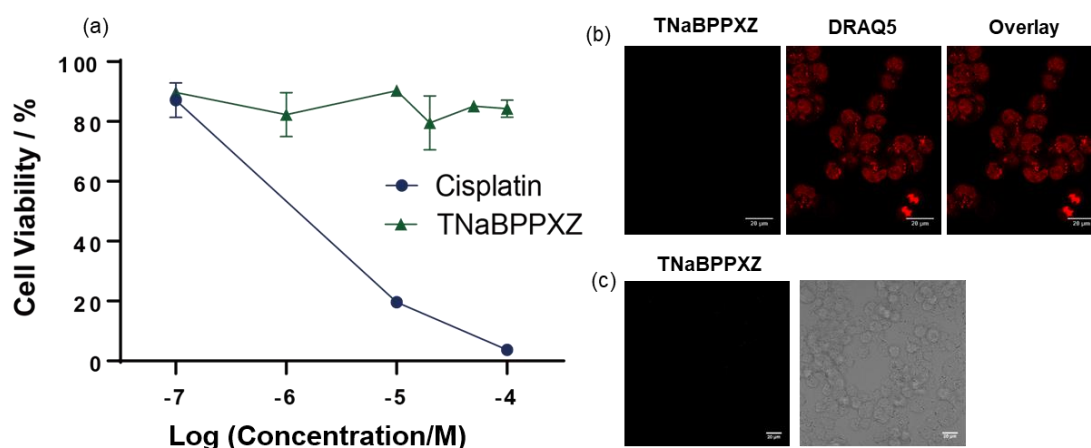


Figure 7.8. (a) Cell viability graph of A2780 cells after treatment with varying concentrations of TNaBPPXZ and Cisplatin. Experiments were carried out in triplicate; (b) Live A2780 cells treated with 500 µM TNaBPPXZ for 1 hr and co-stained with DRAQ5; (c) Live A2780 cells treated with 500 µM TNaBPPXZ for 24 hours.

7.6.2 Live Cell Microscopy

Cells were seeded onto 35 mm imaging μ -dishes at a density of 6×10^4 cells and incubated for 24 hours. Media was removed, cells washed with PBS and the corresponding concentration of either compound added and incubated for either 1 or 24 hours. 1 hour prior to imaging, media was removed, and the cells washed twice with PBS before co-staining some samples with DRAQ5. Cells were washed thrice with PBS before replacing with fresh media. Samples were imaged immediately on an Airyscan confocal laser scanning inverted microscope ZEISS LSM 880. Images were taken with an oil immersion 40 \times objective using 518 F immersion oil. The 405 nm laser was used to excite the compound and luminescent images collected between 500-600 nm. The 633 nm laser was used to excite DRAQ5, and the emission collected above 650 nm. Images were processed with FIJI Image J software. Figure 7.8b and c display that there is no staining in live cells, suggesting that **TNaBPPXZ** can't be taken up by cells.

7.6.3 Fixed Cell Microscopy – Staining After Fixation and Permeabilization

Cells were seeded onto glass cover slips (22 mm \times 22 mm) and incubated for 24 hours. Media was removed, cells washed with PBS and fixed with 4% PFA (paraformaldehyde) for 20 minutes. PFA was removed and any remaining quenched with ammonium chloride solution (50 mM). Cells were either kept in PBS or permeabilised with 0.4% Triton-X100 for 10 minutes. Cells were incubated with compounds in PBS (250 μ M) for 15 minutes at room temperature. Compounds were then removed and DRAQ5 (nucleic acid dye) was added for a further 15 minutes at room temperature. Cells were washed twice with PBS and coverslips mounted glass slides using mounting medium (ProLong Gold Antifade). Slides were imaged on an Airyscan confocal laser scanning inverted microscope ZEISS LSM 880. Images were taken with an oil immersion 40 \times objective using 518 F immersion oil. The 405 nm laser was used to excite the compound and luminescent images collected between 500-600 nm. The 633 nm laser was used to excite DRAQ5, and the emission collected above 650 nm. As shown in Figure 7.9, **TNaBPPXZ** displays cytoplasmic staining when added to fixed permeabilised cells, indicating that it interacts with components in the cytoplasm of dead cells. As mentioned in **Section 7.6.2**, **TNaBPPXZ** does not show any staining in live cells, so this limits that application as a

live/dead cell stain. Live/dead cell stains are used to distinguish between live (viable) and dead (non-viable) cells in a sample. These stains typically have different fluorescent properties when they interact with live or dead cells, allowing for easy differentiation under a fluorescence microscope. In this case, **TNaBPPXZ** shows staining only in fixed permeabilized cells, suggesting that it does not enter or interact with the cytoplasm of viable cells. So, by utilizing **TNaBPPXZ** as a stain, it could potentially be used to distinguish between live and dead cells, allowing researchers to assess cell viability or perform viability assays.

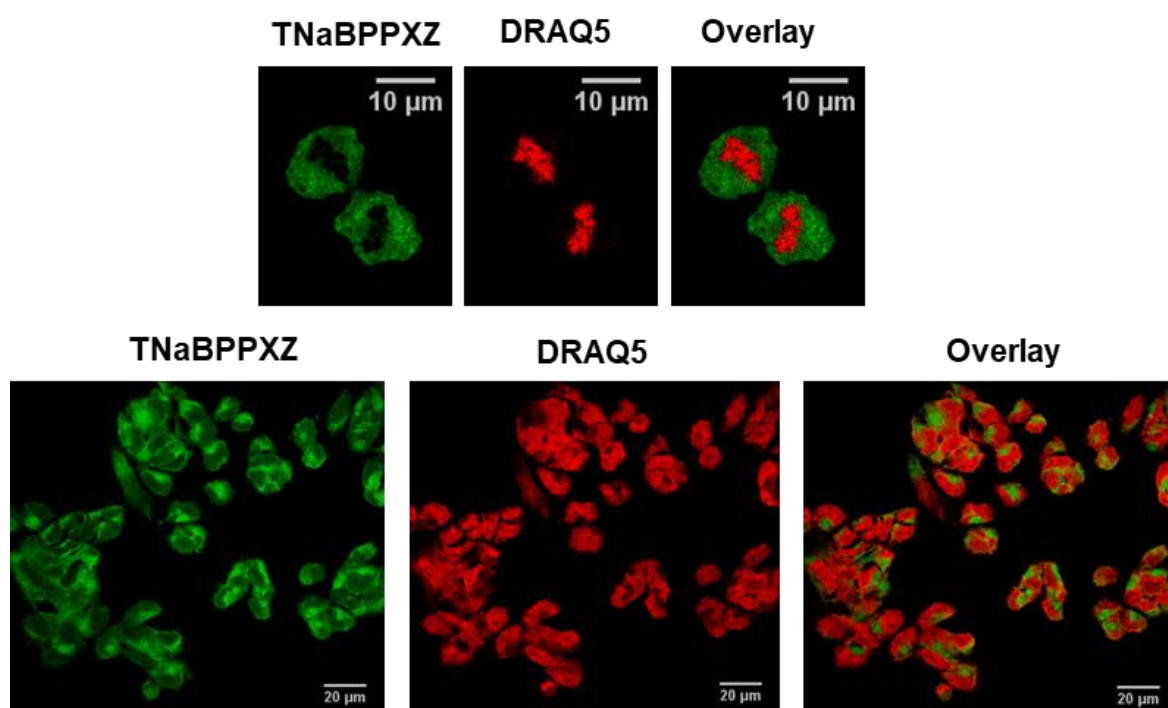


Figure 7.9. Fixed and permeabilised A2780 cells stained with 250 μM **TNaBPPXZ** for 15 mins and co-stained with DRAQ5.

7.7 Conclusions

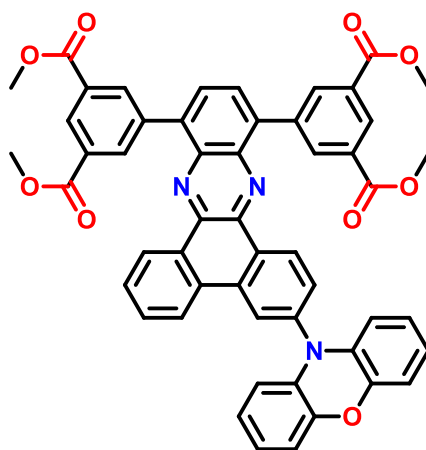
In this Chapter, we employed two methods to make water-soluble TADF emitter for bioimaging. Firstly, we fabricated two kinds of NPs by using amphiphilic and biocompatible polymer, DSPE-PEG2000. Specifically, we encapsulated several red emitters mentioned in previous chapters, **DMACPyBP** (Chapter 2), and **2GCzBPN** (Chapter 5) into DSPE-PEG2000. Both **DMACPyBP** NPs and **2GCzBPN** NPs exhibit red shifted emission compared to **DMACPyBP** and **2GCzBPN** in toluene maintain the delayed fluorescence with a lifetime

of 0.2 μs and 1.3 μs , respectively. Unfortunately, the Φ_{PL} of the NPs decreased significantly, which could be the ACQ. To avoid ACQ, two kinds of g-NPs were synthesized by incorporating the TADF emitter (**DMACBP** and **DMACPyBP**, **Chapter 2**) into a glassy host matrix of mCP. Both **DMACBP** g-NPs and **DMACPyBP** g-NPs exhibit good water solubility, longer lifetime compared to their doped films and **DMACPyBP** g-NPs also shows an enhanced Φ_{PL} compared to that of **DMACPyBP** NPs. Secondly, we made one water soluble sodium-salt emitter, **TNaBPPXZ**, which is hydrolysis from the TADF emitter **TDIBPPXZ**. In the beginning, **TDIBPPXZ** was fully characterized by theoretical and photophysical investigations in solution and solid state, demonstrating its TADF properties. **TNaBPPXZ** shows good water-solubility and green emission in water. Although there is no delayed emission observed in water, it is still shown promising potential application as a live/dead cell stain.

7.8 Experimental Section

All commercially available chemicals and reagent grade solvents were used as received. 3-(10*H*-phenoxazin-10-yl)phenanthrene-9,10-dione (1) and 10-(10,13-dibromodibenzo[*a,c*]phenazin-3-yl)-10*H*-phenoxazine (2) were synthesized according to the literature.¹⁴⁶

Tetramethyl 5,5'-(3-(10*H*-phenoxazin-10-yl)dibenzo[*a,c*]phenazine-10,13-diyl)diisophthalate (TDIBPPXZ):



TDIBPPXZ

In a two-necked round bottom flask compound **2** (0.35 g, 0.56 mmol, 1.0 equiv.) and dimethyl 5-(4,4,5,5-tetramethyl-1,3,2-dioxaborolan-2-yl)isophthalate (0.40 g, 1.24 mmol, 2.2 equiv.) were dissolved in a mixture of THF (40 mL) and 2 M aqueous solution of potassium carbonate (10.0 mL). The mixture was degassed under nitrogen flow for 15 min, then tetrakis(triphenylphosphine)palladium(0) (65 mg, 0.056 mmol, 0.1 equiv.) was added under nitrogen. The reaction mixture was stirred at 80 °C for 6 h before cooling to room temperature. The reaction mixture was extracted with DCM (3 × 50 mL) and the combined organic layers were dried with anhydrous sodium sulfate and concentrated under reduced pressure. The crude product was purified by silica gel flash column chromatography using hexanes:DCM = 1:1 as eluent to give final compound as light-yellow solid (yield = 0.180 g).

Tetramethyl 5,5'-(3-(10*H*-phenoxazin-10-yl)dibenzo[*a,c*]phenazine-10,13-diyl)diisophthalate (TDIBPPXZ): Yield: 37%. *R*_f = 0.4 (50% DCM/Hexane). *Mp* = 314-316 °C. ¹H NMR (500 MHz, Chloroform-*d*) δ 9.41 (d, *J* = 8.4 Hz, 1H), 9.19 (d, *J* = 8.0 Hz, 1H),

9.01 (q, $J = 1.3, 0.8$ Hz, 4H), 8.90 (dt, $J = 16.8, 1.7$ Hz, 2H), 8.58 (s, 1H), 8.50 (d, $J = 8.1$ Hz, 1H), 8.20 (s, 2H), 7.81 (t, $J = 7.5$ Hz, 1H), 7.75 – 7.65 (m, 2H), 6.78 (d, $J = 7.9$ Hz, 2H), 6.71 (s, 2H), 6.61 (t, $J = 7.8$ Hz, 2H), 6.08 (d, $J = 8.0$ Hz, 2H), 4.07 – 4.04 (m, 12H). **^{13}C NMR (126 MHz, CDCl_3)** δ 166.49, 166.45, 143.97, 142.05, 141.32, 139.80, 139.69, 138.79, 138.51, 138.48, 136.51, 136.47, 135.15, 134.15, 131.56, 130.89, 130.58, 130.30, 130.14, 130.07, 129.97, 128.79, 126.77, 125.56, 123.39, 123.29, 121.72, 115.67, 113.38, 77.32, 77.06, 76.81, 52.66, 52.63. **HR-MS $[\text{M}+\text{H}]^+$ Calculated:** ($\text{C}_{52}\text{H}_{35}\text{N}_3\text{O}_9$) 845.2373; **Found:** 845.2363. HPLC analysis: 99.7% pure on HPLC analysis, retention time 10.65 minutes in 100% THF.

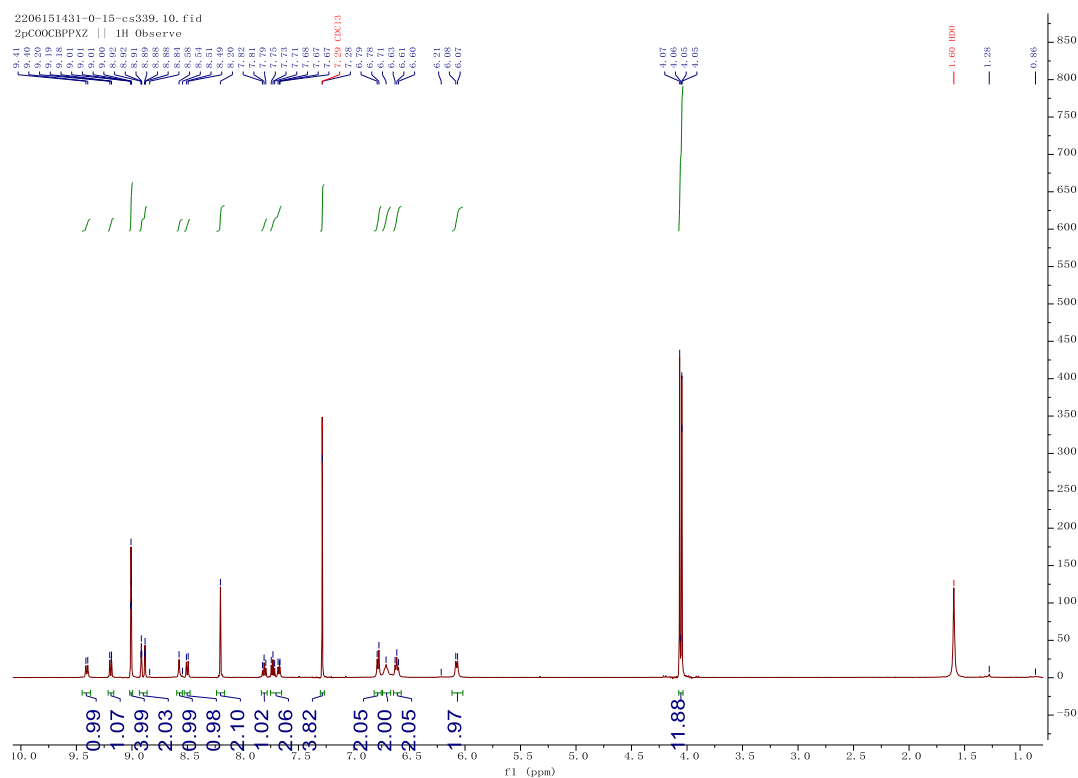


Figure 7.10. ^1H NMR spectra of TDIBPPXZ in CDCl_3 .

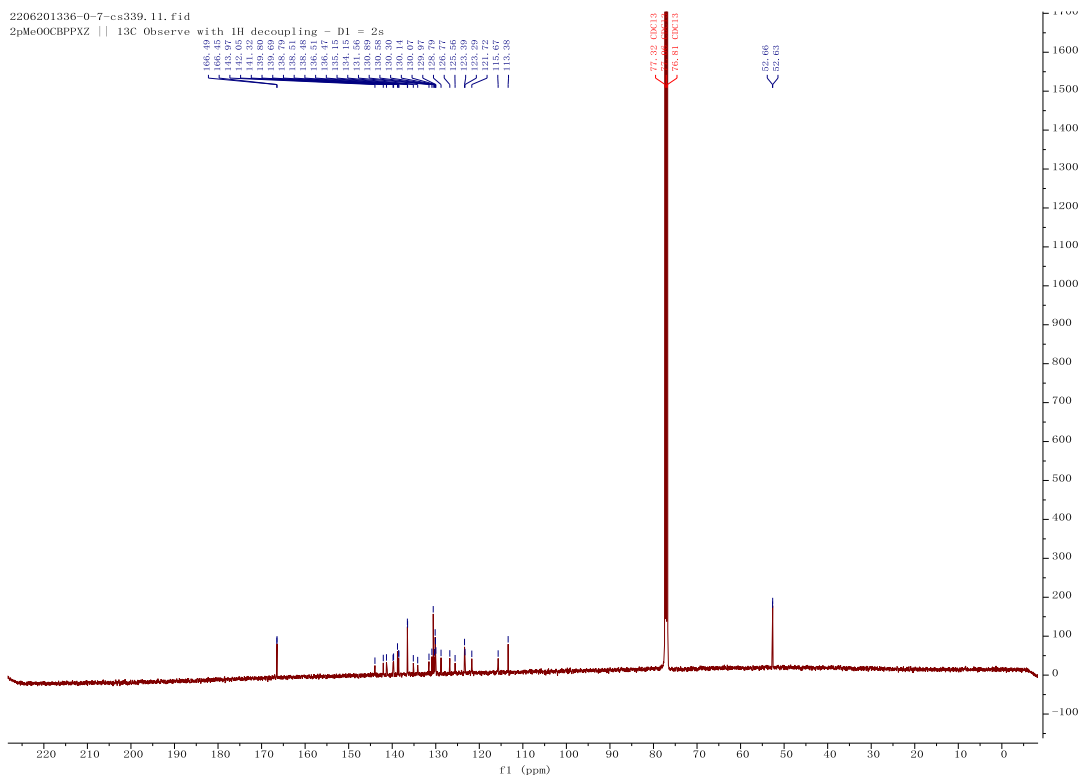


Figure 7.11. ¹³C NMR spectra of TDIBPPXZ in CDCl₃.

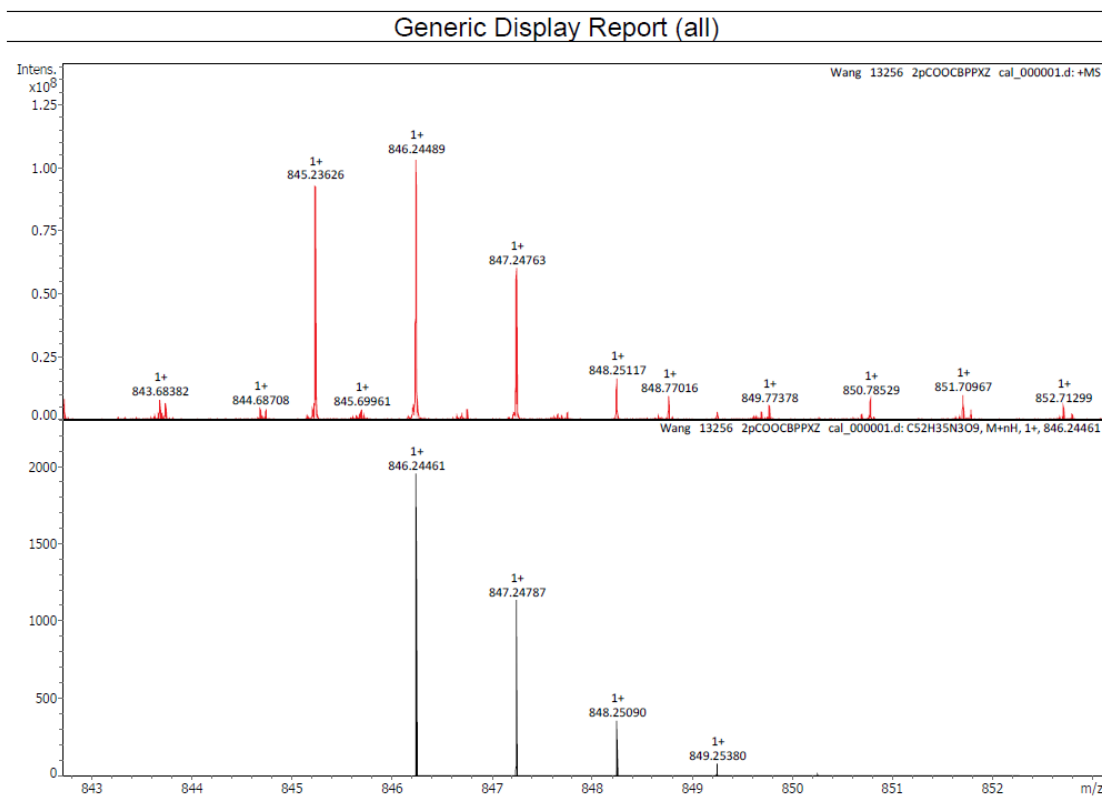


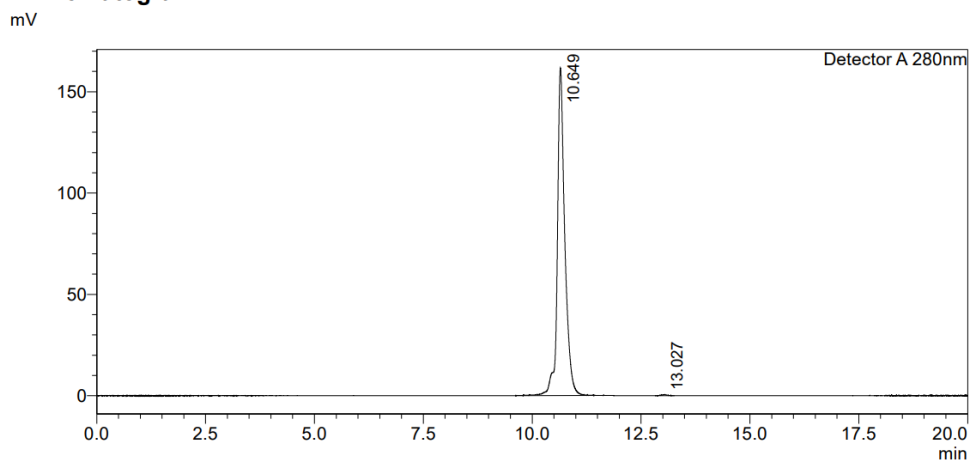
Figure 7.12. HRMS of TDIBPPXZ

HPLC Trace Report 21 Jun 2022

<Sample Information>

Sample Name : 2pMeOOCBPPXZ
Sample ID : 2pMeOOCBPPXZ
Method Filename : 100% THF 20 mins 280nm - new-please use.lcm
Batch Filename : TPAPyBPN-1.lcb
Vial # : 1-12
Injection Volume : 10 uL
Date Acquired : 21/06/2022 19:08:17
Date Processed : 21/06/2022 19:28:19
Sample Type : Unknown
Acquired by : System Administrator
Processed by : System Administrator

<Chromatogram>



<Peak Table>

Peak#	Ret. Time	Area	Height	Area%	Area/Height	Width at 5% Height
1	10.649	1926374	161352	99.756	11.939	0.516
2	13.027	4704	434	0.244	10.845	0.335
Total		1931078	161786	100.000		

Figure 7.13. HPLC trace of TDIBPPXZ.

Chapter 8: Conclusions and Future Outlooks

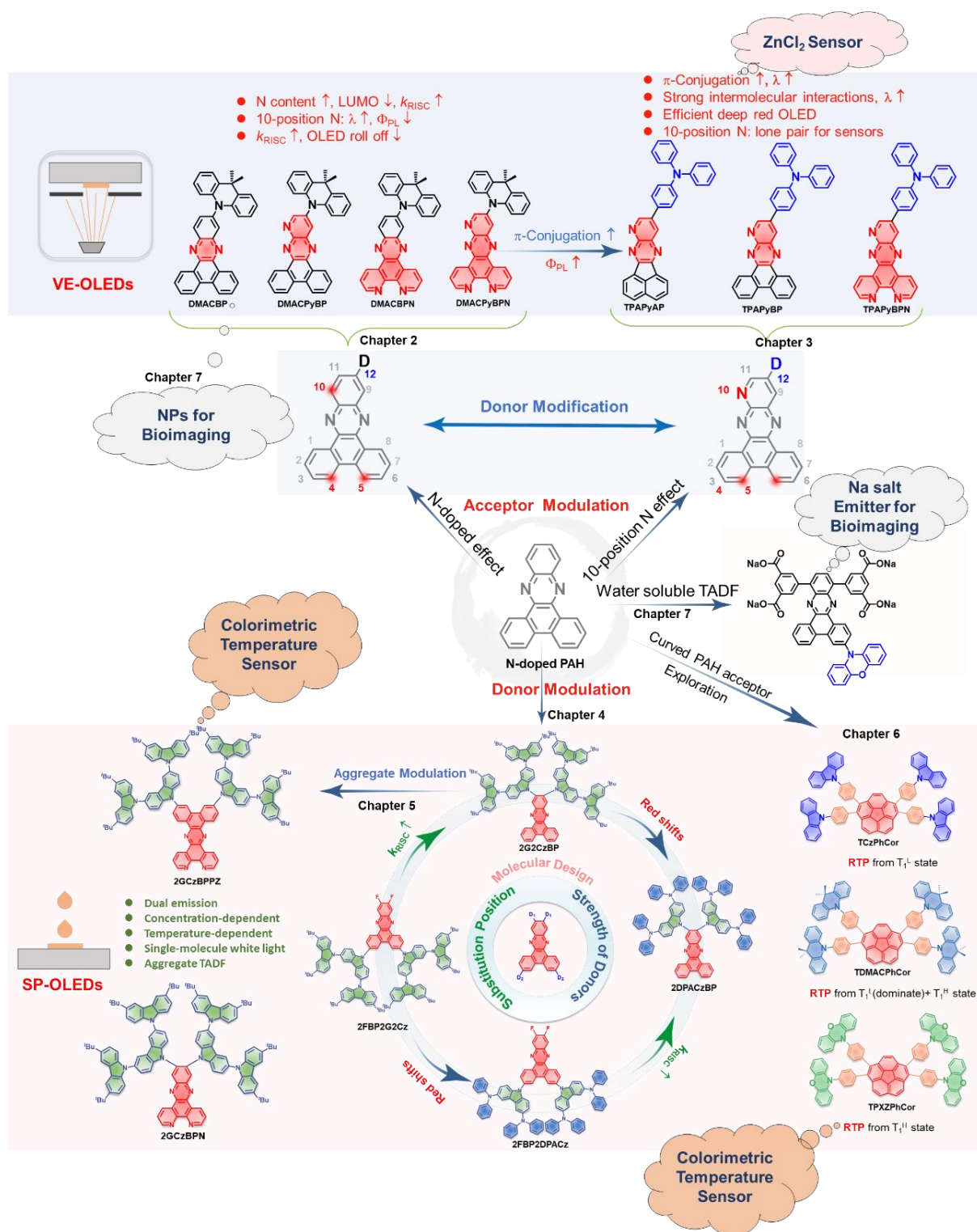


Figure 8.1. The summary of all molecular structures and relationship among chapters in this thesis.

This thesis focused on the D-A type orange-red TADF materials, covering aspects from molecular design and computation to synthesis, photophysics and their applications in OLEDs, sensors and bioimaging. The N-doped polycyclic aromatic hydrocarbon (PAH) acceptor, dibenzo[a,c]phenazine (BP), has been selected as a component in the design of red TADF emitters due to its deep LUMO and high rigidity. In **Chapter 2**, we fully investigated four different DMAC-based orange-to-red TADF emitters whose structures differed by the number of nitrogen atoms contained within BP acceptor core. It was found that increasing the nitrogen atom content in BP of the D-A typed compounds results in a more stabilized LUMO, smaller ΔE_{ST} and faster k_{RISC} . In particular, having a nitrogen at the 10-position of BP notably enhances k_{RISC} , as demonstrated in **DMACPyBP** ($\lambda_{PL} = 601$ nm, $\Phi_{PL} = 47\%$, $k_{RISC} = 19.4 \times 10^4$ s⁻¹) and **DMACPyBPN** ($\lambda_{PL} = 606$ nm, $\Phi_{PL} = 37\%$, $k_{RISC} = 42.6 \times 10^4$ s⁻¹) compared to **DMACBP** ($\lambda_{PL} = 568$ nm, $\Phi_{PL} = 75\%$, $k_{RISC} = 1.0 \times 10^4$ s⁻¹) and **DMACBPN** ($\lambda_{PL} = 586$ nm, $\Phi_{PL} = 71\%$, $k_{RISC} = 2.9 \times 10^4$ s⁻¹), despite the small decrease in Φ_{PL} . Vacuum evaporated (VE) OLEDs with **DMACBPN** showed an EQE_{max} of 19.4% and an electroluminescence maximum of 588 nm. As the N/C ratio increased, the EL spectra of the corresponding devices progressively red-shifted, with the reddest-emitting device ($\lambda_{EL} = 640$ nm) employing **DMACPyBPN**, but its EQE_{max} was only 5.4% due to its low Φ_{PL} . Furthermore, the **DMACPyBP/ DMACPyBPN** (with 10-position N)-based OLEDs showed remarkably low efficiency roll-off of only 8 and 5%, compared to 40 and 25% at 100 cd m⁻² for the devices with **DMACBP/ DMACBPN**, respectively.

Having a nitrogen at the 10-position of BP notably enhances k_{RISC} and leads to a large red-shift of the emission but results in a big decrease in the Φ_{PL} . To address this issue, emitters **TPAPyBP** and **TPAPyBPN** (**Chapter 3**) were designed by using same acceptor as **DMACPyBP** and **DMACPyBPN**, respectively, where the DMAC donor was replaced by a TPA donor in order to increase the overlap between HOMO and LUMO and further increase f and thus Φ_{PL} . As expected, the Φ_{PL} increased in doped film and the emission red-shifted including with increasing polarity of the host due to strong intermolecular interactions. Both **TPAPyBP** and **TPAPyBPN** emit in the red ($\lambda_{PL} = 624$ nm, $\Phi_{PL} = 63\%$) and deep red ($\lambda_{PL} = 675$

nm, $\Phi_{\text{PL}} = 57\%$) in the high-polarity host PPT, respectively. Similarly, the VE-OLEDs with **TPAPyBPN** emitted at 657 nm in PPT and showed an EQE_{max} 12.5%, whose electroluminescence was 61 nm red-shifted in comparison to device fabricated in CBP host ($\lambda_{\text{EL}} = 596$ nm, $\text{EQE}_{\text{max}} = 13.6\%$), without significant loss in efficiency. Due to lone pair of the nitrogen at the 10-position, it can be also act as ligands for metal binding and the change in photophysics can be exploited in metal ion sensing. We found that these compounds exhibited a stark spectral response for the detection of ZnCl_2 . This is due to the formation of zinc chlorido complexes. Of these three emitters, **TPAPyBP** showed the most dramatic fluorescence response toward ZnCl_2 by shifting emission from green (550 nm) to deep red (675 nm), which is the first documented TADF optical sensor for ZnCl_2 . We observed that the lone-pair on N was crucial for the ZnCl_2 sensing. Through molecular structure engineering, this might also be compatible with other Lewis acids and further employed as Lewis acid sensor in future.

Although OLEDs have demonstrated their practical applications in displays and solid-state lighting, most OLEDs are fabricated using vacuum deposition technology that has high operating costs and a complicated multilayered device architecture. An alternative strategy would be to make the OLEDs using lower-cost solution-processing techniques such as spin coating or ink-jet printing, which shows great potential in enabling large-area applications. In **Chapter 4**, we explored four yellow to red solution processable TADF dendrimer emitters (**2GCzBP**, **2DPACzBP**, **2FBP2GCz** and **2FBP2DPACz**) containing the same BP acceptor in **DMACBP**. We systematically investigated the effect of substitution position and strength of donors on the opto-electronic properties. The k_{RISC} of the emitters having donors substituted at the 11- and 12-positions (Figure **8.1**) of the BP acceptor is more than 10-times faster than that of compounds substituted having donors substituted at 3- and 6-position. Compound **2DPACzBP**, containing stronger donors than **2GCzBP**, exhibits a red-shifted emission and smaller DE_{ST} of 0.01 eV. The solution-processed OLED with 10 wt% **2DPACzBP** doped in mCP emitted at 640 nm and showed an EQE_{max} of 7.8%, which was effectively maintained out to a luminance of 1000 cd m^{-2} . Such a device's performance at relevant display luminance is among the highest for red TADF SP-OLEDs. The efficiency of the devices was improved significantly by using 4CzIPN as an assistant dopant in a HF configuration, where the **2DPACzBP** HF device shows an EQE_{max} of 20.0% at λ_{EL} of 605 nm and remains high at 11.8%

at a luminance of 1000 cd m^{-2} , which makes this device one of the highest efficiency orange-to-red HF SP-OLEDs to date. While the performance of OLEDs lags behind that of other vacuum-deposited devices, future enhancements could be achieved through modifications in emitter doping concentration and OLED structural engineering.

Chapter 5 continues the work on TADF dendrimers by discussing a design using a stronger acceptor BPN and larger π -conjugation acceptor BPPZ for **2GCzBPN** and **2GCzBPPZ**, respectively. By modulating the molecular geometry, compound **2GCzBPN** with a strongly twisted geometry exhibits TADF, while **2GCzBPPZ**, possessing a less twisted geometry, shows dual emission with an emission peak at 475 nm associated with the monomer and one at 575 nm linked to aggregates that is TADF. This dual emission is both concentration-dependent and temperature-dependent in solution. This is the first observation of aggregate emission from TADF dendrimers in solution. The control of the contributions from intramolecular and intermolecular charge-transfer states permits a wide color tuning from sky blue through white to yellow light emission. We demonstrate how **2GCzBPPZ** can serve as a temperature sensor and exhibits excellent temperature sensitivity across a very wide temperature range ($-70 \text{ }^{\circ}\text{C}$ to $70 \text{ }^{\circ}\text{C}$) in *n*-hexane, accompanied by a significant spectral response, ranging from yellow to white, and then blue emission, which is the widest detected temperature range and color response reported for an organic luminescent material in solution and also to the best of our knowledge the first small molecule TADF compound used for colorimetric temperature sensing. By embedding **2GCzBPPZ** into paraffin, we demonstrated a spatio-temperature sensor that showed a noticeable emission shift from yellow to green and ultimately to blue as the temperature increased from 20 to 200 $^{\circ}\text{C}$. In an attempt to use a non-polar solid host with a higher melting temperature, we also incorporated **2GCzBPPZ** into CBP or PMMA. However, there was no temperature-dependent emission observed, which implies that in these host it is not possible to change significantly intramolecular distances as a function of temperature. The fact that the optical thermometer phenomenon works in paraffin but not the other hosts may be due to the paraffin having a greater thermal expansion coefficient compared to these other host compounds. Finally, SP-OLEDs using these two dendrimer emitters showed divergent performance, with a three-times higher EQE_{max} of 15.0% for the

device with **2GCzBPPZ** compared to the device with **2GCzBPN** (5.3%). However, at this stage it is unclear why the EQE_{max} for **2GCzBPN** is so low, which will be addressed in the future work.

In the previous Chapters, we investigated several families of D-A type orange-red TADF emitters containing BP derivatives as acceptors, which are planar, highly conjugated N-doped PAH. In **Chapter 6**, we explored a novel family of D-A emitters using a curved PAH without N-doping, corannulene, as the acceptor. Corannulene, known as a buckybowl, is a curved PAH often visualized as the hydrogen-terminated C_{20} cap of C_{60} . To date, all of the reported corannulene-based emitters are fluorescent, emitting from the S_1 state. And there are no examples of luminescent corannulene derivatives that harvest triplet excitons in their emission, like TADF and RTP. Here, we devised three tetra(donor)-acceptor compounds **TCzPhCor**, **TDMACPhCor**, and **TPXZPhCor** employing corannulene as the acceptor and **Cz**, **DMAC**, and **PXZ**, respectively, as peripheral donors. In a bid to develop TADF materials, we hypothesized that the introduction of multiple donors would provide multiple avenues for ISC/RISC via spin-vibronic coupling. However, instead we discovered unusual RTP behavior in these compounds, showing three different types of RTP from different triplet excited states. We found that using mCP as the host, **TCzPhCor** shows RTP from only one LE state. By contrast, dual RTP from T_1^{H} and T_1^{L} , and T_1^{H} -dominated RTP are observed in **TDMACPhCor**, **TPXZPhCor**, respectively. We have explored colorimetric temperature sensing using **TPXZPhCor** and found that it exhibits excellent sensitivity and exhibits a wide range of color changes, from cyan at 298 K to orange at 77 K. To the best of our knowledge, it represents the most promising performance for temperature sensing using phosphorescent afterglow materials. Further, we have also demonstrated the utility of **TPXZPhCor** as the emitter in an afterglow OLED, which shows the highest device performance reported to date for this class of devices, with an EQE_{max} and L_{max} of 3.3% and 5167 cd m^{-2} , respectively. In future work, for the development of TADF emitters based on corannulene, we will implement these design approaches: 1) Corannulene will be directly substituted with stronger donor, bypassing the π -linker; 2) Multiple donors can be incorporated; 3) Electron-withdrawing units will be added to amplify CT characteristics.

In the previous Chapters, we explored several families of D-A TADF compounds and fully investigated the effect of π -conjugation and electron-withdrawing abilities of the acceptor, donor strength and donor substitution position on the photophysical properties, like emission color, Φ_{PL} , delay lifetime and k_{RISC} . Furthermore, we employed our emitters in OLEDs, ZnCl_2 sensors, and temperature sensors. In **Chapter 7**, we explored the use of D-A TADF emitters in bioimaging. Among the emitters discussed in the previous Chapters, we picked three emitters, **DMACBP**, **DMACPyBP** (**Chapter 2**) and **2GCzBPN** (**Chapter 5**) to investigate for biomimaging due to their red emission, high Φ_{PL} , efficient TADF, and relatively long delayed lifetime and then we fabricated NPs and investigated their photophysical properties. We also attempted to use these glassy-NPs (g-NPs) as biological imaging agents in HeLa cells. However, in our initial experiments, the HeLa cells did not successfully phagocytize the g-NPs. Further bioimaging applications will be explored in subsequent studies. Secondly, we designed a red TADF emitter **TDIBPPXZ**, which is substituted by dimethyl isophthalate units followed by ester hydrolysis. Furthermore, we obtained a water-soluble sodium-salt emitters, **TNaBPPXZ**, which shows staining only in fixed permeabilized cells, suggesting that it does not enter or interact with the cytoplasm of viable cells. So, by utilizing **TNaBPPXZ** as a stain, it could potentially be used to distinguish between live and dead cells, allowing researchers to assess cell viability or perform viability assays. These experiments will be conducted in the future.

Chapter 9: Experimental Methods

9.1 General Synthetic Procedures

All commercially available chemicals and reagent grade solvents were used as received. Air-sensitive reactions were performed under a nitrogen atmosphere using Schlenk techniques. Flash column chromatography was carried out using silica gel (Silica-P from Silicycle, 60 Å, 40-63 µm). Analytical thin-layer-chromatography (TLC) was performed with silica plates with aluminum backings (250 µm with F-254 indicator). TLC visualization was accomplished by 254/365 nm UV lamp. HPLC analysis was conducted on a Shimadzu Prominence Modular HPLC system. HPLC traces were performed using an ACE Excel 2 C18 analytical column. ^1H and ^{13}C NMR spectra were recorded on a Bruker Advance spectrometer (400 or 500 MHz for ^1H , 101 or 126 MHz for ^{13}C). The following abbreviations have been used for multiplicity assignments: “s” for singlet, “d” for doublet, “t” for triplet, “dd” for doublet of doublets, “dt” for doublet of triplets, “ddd” for doublet of doublet of doublets, “q” for quintet and “m” for multiplet. CDCl_3 or $\text{DMSO}-d_6$ was used as the solvent of record. ^1H NMR and ^{13}C NMR spectra were referenced to the solvent peak. Melting points were measured using open-ended capillaries on an Electrothermal 1101D Mel-Temp apparatus and are uncorrected. HRMS was performed at the University of Edinburgh. Elemental analyses were performed by the School of Geosciences at the University of Edinburgh.

9.2 Theoretical Calculations

Density functional theoretical (DFT) calculation and time-dependent density functional theoretical (TDDFT) calculations were performed using Gaussian 16 Revision D.01 software in the gas phase.⁴⁶⁵ The ground-state geometries were optimized employing the PBE0²⁶⁵ or M062X⁴⁴⁰ functional with the Pople 6-31G(d,p) basis set, in the gas phase.²⁶⁶ Transitions to excited singlet states and triplet states were calculated using TDDFT within the Tamm-Dancoff approximation (TDA) based on the optimized ground-state geometries.^{222,268} Molecular orbitals were visualized using GaussView 6.0⁴⁶⁶ and Silico 2.1, an in-house built software

package.^{223,467-473} Hole-electron and reduced density gradient (RDG)⁴⁷⁴ analyses were conducted using the Multiwfn program,⁴⁷⁵ and the corresponding molecular orbitals were visualized using VMD program.²²³

9.3 Electrochemistry Measurements

An Electrochemical Analyzer potentiostat model 620E from CH Instruments was used to carry out Cyclic Voltammetry (CV) and differential pulse voltammetry (DPV) analysis. The samples for the measurements were prepared in dichloromethane (DCM) solutions, and then degassed by flushing with DCM-saturated nitrogen gas for five minutes. All measurements were performed using 0.1 M tetra-*n*-butylammonium hexafluorophosphate, [*n*Bu₄N]PF₆, in DCM. The reference electrode for the tests was an Ag/Ag⁺ electrode, with a platinum electrode serving as the working electrode and a platinum wire as the counter electrode. The redox potentials are reported relative to a saturated calomel electrode (SCE) with a ferrocene/ferrocenium (Fc/Fc⁺) redox couple as the internal standard (0.46 V vs SCE).²²⁴ The HOMO and LUMO energies were calculated using the relation $E_{\text{HOMO/LUMO}} = -(E_{\text{ox}}/E_{\text{red}} - E_{\text{Fc/Fc}^+} + 4.8) \text{ eV}$,⁴⁷⁶ where E_{ox} and E_{red} are anodic and cathodic peak potentials obtained from DPV, respectively.

9.4 X-ray Crystallography

X-ray diffraction data for both compounds were collected at either 173 K or 125 K using a Rigaku MM-007HF High Brilliance RA generator/confocal optics with XtaLAB P200 diffractometer [Cu K α radiation ($\lambda = 1.54187 \text{ \AA}$)]. Intensity data were collected using ω steps accumulating area detector images spanning at least a hemisphere of reciprocal space. Data were collected using CrystalClear⁴⁷⁷ and processed (including correction for Lorentz, polarization and absorption) using CrysAlisPro.⁴⁷⁸ The structure was solved by dual space (SHELXT⁴⁷⁹) or direct (SIR2011⁴⁸⁰) methods and refined by full-matrix least-squares against F^2 (SHELXL-2018/3⁴⁸¹). Non-hydrogen atoms were refined anisotropically, and hydrogen atoms were refined using a riding model. All calculations except SQUEEZE were performed using the Olex2⁴⁸² or CrystalStructure⁴⁸³ interface.

9.5 Photophysical Measurements

All samples were prepared in HPLC grade toluene (PhMe), dichloromethane (DCM) or acetonitrile (MeCN) with varying concentrations on the order of 10^{-5} or 10^{-6} M for absorption and emission study. Absorption spectra were recorded at RT using a Shimadzu UV-2600 double beam spectrophotometer. Molar absorptivity determination was verified by linear least-squares fit of values obtained from at least five independent solutions at varying concentrations.

Degassed solutions were prepared via three freeze-pump-thaw cycles prior to emission analysis using an in-house adapted fluorescence cuvette, itself purchased from Starna. Steady-state emission and time-resolved emission spectra were recorded at 298 K using an Edinburgh Instruments F980 fluorimeter or FS5. All the samples for the steady-state measurements were excited using a Xenon lamp, while the samples for the time-resolved measurements were excited at 379 nm using a pico-second laser (PicoQuant, LDH-D-C-375) driven by a laser driver (PDL 800-D) or . The short-time range (200 ns-20 μ s) of PL decays were measured using time-correlated single photon counting (TCSPC) mode. The long-time range (10 ms-4 s) of PL decays were measured using multi-channel scaling (MCS) mode. In MCS mode, the picosecond laser was triggered by a delay generator (Stanford Research Systems, DG645) in the burst mode. The burst mode increased the excitation pulse duration to increase the excitation power to reduce the measurement time.

The singlet-triplet splitting energy, ΔE_{ST} , was estimated by recording the prompt fluorescence and the delayed phosphorescence spectra at 77 K. 77 K glass samples were prepared by transferring toluene solution into NMR tubes and the NMR tubes were cooled down inside a suprasil nitrogen Dewar flask by liquid nitrogen. Prompt fluorescence spectra (1-100 ns) in toluene at 77 K were measured by time-resolve PL spectroscopy using a 5 mW EPL-375 picosecond pulsed laser as the excitation source. Phosphorescence spectra in toluene or 2-MeTHF at 77 K were measured using time-gated PL spectroscopy, where the samples were excited by a 5 W microsecond flash lamp. The energy values of the lowest singlet and triplet states were determined from the onset of fluorescence and phosphorescence spectra at 77 K, respectively. Phosphorescence spectra for all doped films were collected with a 5 W

microsecond flash lamp by the MCS mode using an Edinburgh Instruments FS5.

Photoluminescence quantum yields for solutions were determined using the optically dilute method.^{484,485} The Beer-Lambert law was found to be linear at the concentrations of the solutions. For each sample, linearity between absorption and emission intensity was verified through linear regression analysis and additional measurements were acquired until the Pearson regression factor (R^2) for the linear fit of the data set surpassed 0.9. Individual relative quantum yield values were calculated for each solution and the values reported represent the gradient value. The equation $\Phi_s = \Phi_r(A_r/A_s)(I_s/I_r)(n_s/n_r)^2$ was used to calculate the relative quantum yield of each of the sample, where Φ_r is the absolute quantum yield of the reference, n is the refractive index of the solvent, A is the absorbance at the excitation wavelength, and I is the integrated area under the corrected emission curve. The subscripts s and r refer to the sample and reference, respectively. A solution of quinine sulfate ($\Phi_r = 54.6\%$ in $1\text{ N H}_2\text{SO}_4$)²⁷⁷ was used as the external reference. An integrating sphere Hamamatsu C9920-02 (or SC-30 module on FS5 fluorimeter) was employed for Φ_{PL} measurements for thin film samples. A xenon lamp coupled to a monochromator enabled selective excitation. The output was then fed into the integrating sphere via a fiber, exciting the sample. PL spectra were collected with a multimode fiber and detected with a backthinned CCD. The doped thin films were prepared by spin-coating a chloroform solution of emitter in a host in a different concentration. The quantum yields of the films were measured in air and N_2 atmosphere by purging the integrating sphere with flowing N_2 gas.

9.6 OLED Fabrication and Characterization

The OLED devices were fabricated in a bottom emitting architecture on indium-doped tin oxide (ITO, $12\text{ mm} \times 12\text{ mm} \times 1.1\text{ mm}$, resistivity: $15\ \Omega\ \text{sq}^{-1}$) substrates. A pre-patterned glass substrate coated with ITO were washed sequentially by ultrasonication in acetone, and isopropanol for 20 min and then exposed to oxygen plasma for 10 min to remove all the dust and organics on the ITO surface and to increase the work function of ITO anode for better hole injection from the anode to organic layer.

For solution-processed OLEDs: the hole injection layer, poly(3,4-ethylenedioxythiophene):poly(styrenesulfonate) (PEDOT:PSS; Heraeus; Clevios P VP AI 4083; charge: 9001157883), was spin coated onto the ITO surface under 4000 rpm for 1 min, and baked at 130 °C for 15 min to remove the residual water, then the substrates were transferred into a nitrogen-filled glovebox. The emitting layer (emitter/host in CHCl₃) was spin-coated under 2000 rpm (30 nm), and then annealed at 60 °C in the nitrogen-filled glovebox. The electron transporting layer (2,2',2''-(1,3,5-benzinetriyl)-tris(1-phenyl-1-*H*-benzimidazole), TPBi, 50 nm), the electron injecting layer (lithium fluoride, LiF 1 nm), and the aluminum cathode (100 nm) were successively thermally evaporated in a vacuum chamber under $<1 \times 10^{-6}$ mbar.

For vacuum evaporated OLEDs: organic layers were deposited at a rate of 0.3-0.6 Å/s, which was controlled in situ using the quartz crystal monitors. Doping of the emission layers was achieved through co-evaporation of the emitter and host materials. The electron injection layer, LiF, was deposited at a rate of 0.05 Å/s, while the Al cathode was deposited initially with a rate of 0.5 Å/s to obtain 10 nm thickness and after that the rate of Al cathode was increased to 3 Å/s through the shadow mask defining the top electrode.

After the evaporation, the OLEDs were taken out from the evaporator and encapsulated inside the glovebox. The devices were taken out from the glovebox for current–voltage–luminance characteristics. The luminance-current-voltage characteristics were measured in an ambient environment using a Keithley 2400 source meter combined with a homemade photodiode connected to a Keithley 2000 multimeter for the voltage reading. The external quantum efficiency was calculated assuming Lambertian emission distribution. The electroluminescence spectra were recorded by an Andor DV420-BV CCD spectrometer.

Chapter 10: Appendix

10.1 Characterization Data

Research data underpinning this thesis are available at: <https://doi.org/10.17630/54b79926-d8ae-4019-ad10-d2bbf1777816>.

10.2 Publications Arising from my Work

10.2.1 Published Manuscripts

- [1] **Si, C.**; Hu, Y.; Sun, D.; Wang, K., Zhang, X.; and Zysman-Colman, E. The influence of nitrogen doping of the acceptor in orange–red thermally activated delayed fluorescence emitters and OLEDs. *J. Mater. Chem. C* **2023**, *11*, 12174–12184. <https://doi.org/10.1039/D3TC02352D>
- [2] **Si, C.**; Wang T; Gupta A K; Cordes D; Slawin A M. Z.; Siegel Jay S.; Zysman-Colman, E. “Room-temperature multiple phosphorescence from functionalized corannulenes: temperature sensing and afterglow organic light-emitting diode.” *Angewandte Chemie International Edition* **2023**, e202309718. <https://doi.org/10.1002/anie.202309718>.
- [3] Suresh, S. M.; Zhang, L.; Matulaitis, T.; Hall, D.; **Si, C.**; Ricci, G.; Slawin, A. M. Z.; Warriner, S.; Beljonne, D.; Olivier, Y.; Samuel, I. D.; Zysman-Colman, E. Judicious Heteroatom Doping Produces High Performance Deep Blue/Near UV Multiresonant Thermally Activated Delayed Fluorescence OLEDs. *Adv. Mater.* **2023**. <https://doi.org/10.1002/adma.202300997>.
- [4] Madayanad Suresh, S.; Zhang, L.; Hall, D.; **Si, C.**; Ricci, G.; Matulaitis, T.; Slawin, A. M. Z.; Warriner, S.; Olivier, Y.; Samuel, I. D. W.; Zysman-Colman, E. A Deep-Blue-Emitting Heteroatom-Doped MR-TADF Nonacene for High-Performance Organic Light-Emitting Diodes. *Angew. Chemie* **2023**, *135* (8). <https://doi.org/10.1002/ange.202215522>.
- [5] Yuan, K.; Gupta, A. K.; **Si, C.**; Uzelac, M.; Zysman-Colman, E.; Ingleson, M. J.

- Brominated B 1-Polycyclic Aromatic Hydrocarbons for the Synthesis of Deep-Red to Near-Infrared Delayed Fluorescence Emitters. *Org. Lett.* **2023**, 25 (31), 5880–5884. <https://doi.org/10.1021/acs.orglett.3c02167>.
- [6] Sun, D.; **Si, C.**; Wang, T.; Zysman-Colman, E. 1,3,5-Triazine-Functionalized Thermally Activated Delayed Fluorescence Emitters for Organic Light-Emitting Diodes. *Adv. Photonics Res.* **2022**, 2200203. <https://doi.org/10.1002/adpr.202200203>.
- [7] Hong, G.[†]; **Si, C.**[†] (co-first); Gupta, A. K.; Bizzarri, C.; Nieger, M.; Samuel, I. D. W.; Zysman-Colman, E.; Bräse, S. Fluorinated Dibenzo[a,c]-Phenazine-Based Green to Red Thermally Activated Delayed Fluorescent OLED Emitters. *J. Mater. Chem. C* **2022**, 10 (12), 4757–4766. <https://doi.org/10.1039/D1TC04918F>.
- [8] Li, W.; Li, Z.; **Si, C.**; Wong, M. Y.; Jinnai, K.; Gupta, A. K.; Kabe, R.; Adachi, C.; Huang, W.; Zysman-Colman, E.; Samuel, I. D. W. Organic Long-Persistent Luminescence from a Thermally Activated Delayed Fluorescence Compound. *Adv. Mater.* **2020**, 32 (45), 2003911. <https://doi.org/10.1002/adma.202003911>.
- [9] Yuan, K.; Kahan, R. J.; **Si, C.**; Williams, A.; Kirschner, S.; Uzelac, M.; Zysman-Colman, E.; Ingleson, M. J. The Synthesis of Brominated-Boron-Doped PAHs by Alkyne 1,1-Bromoboration: Mechanistic and Functionalisation Studies. *Chem. Sci.* **2020**, 11 (12), 3258–3267. <https://doi.org/10.1039/c9sc05404a>.
- [10] Sun, D.; Suresh, S. M.; Hall, D.; Zhang, M.; **Si, C.**; Cordes, D. B.; Slawin, A. M. Z.; Olivier, Y.; Zhang, X.; Zysman-Colman, E. The Design of an Extended Multiple Resonance TADF Emitter Based on a Polycyclic Amine/Carbonyl System. *Mater. Chem. Front.* **2020**, 4 (7), 2018–2022. <https://doi.org/10.1039/d0qm00190b>.

10.2.2 Unpublished Manuscripts

- [1] **C Si**, D Sun, and E Zysman-Colman “A sensitive temperature sensor with a large dynamic spectral range based on a dual-emissive thermally activated delayed fluorescence dendrimer material.” (Manuscript in preparation)
- [2] **C Si**, A K Gupta, B Basumatary, D Cordes, A M. Z. Slawin, I. D. W. Samuel and E Zysman-

Colman “Multi-responsive thermally activated delayed fluorescence: ZnCl₂ sensor and efficient green to deep-red OLEDs” (Manuscript in preparation)

[3] **C Si**, D Sun, D B. Cordes, and E Zysman-Colman “Rational molecular design of highly efficient yellow-red dendrimer TADF for solution-processed OLED: A Combined Effect of substitution position and strength of donors” (Manuscript in preparation)

[4] **C Si**, W Primrose, Z Hudson and E Zysman-Colman “Red multiresonant thermally activated delayed fluorescence emitters-based O-dots for Bioimaging Applications” (Manuscript in preparation)

10.3 Conference Contributions

1. Oral presentation at *2nd EPSRC-JSPS Core-to-Core Grant Symposium on Frontiers in Organic Optoelectronics, UK* with the title of *Efficient deep red TADF emitters for OLED and sensing*.

2. Oral presentation at *Postgraduate Symposium 2021, St Andrews* with the title of *Dibenzo[a,c]phenazine based red thermally activated delayed fluorescent OLED emitters*.

References

- 1 B. Valeur and M. N. Berberan-Santos, *Molecular fluorescence: principles and applications*, John Wiley & Sons, 2012.
- 2 S. A. Empedocles, R. Neuhauser, K. Shimizu and M. G. Bawendi, *Adv. Mater.*, 1999, **11**, 1243–1256.
- 3 H. B. Bebb and E. W. Williams, in *Semiconductors and semimetals*, Elsevier, 1972, **8**, 181–320.
- 4 U. Mitschke and P. Bäuerle, *J. Mater. Chem.*, 2000, **10**, 1471–1507.
- 5 H. K. Henisch, *Reports Prog. Phys.*, 1964, **27**, 369.
- 6 O. Shimomura, *Bioluminescence: chemical principles and methods*, World Scientific, 2012.
- 7 C. E. Badr and B. A. Tannous, *Trends Biotechnol.*, 2011, **29**, 624–633.
- 8 C. Dodeigne, L. Thunus and R. Lejeune, *Talanta*, 2000, **51**, 415–439.
- 9 A. K. Campbell, *Chemiluminescence. Principles and applications in biology and medicine*, 1988.
- 10 G. N. Lewis and M. Kasha, *J. Am. Chem. Soc.*, 1944, **66**, 2100–2116.
- 11 C. A. Parker and C. G. Hatchard, *Trans. Faraday Soc.*, 1961, **57**, 1894–1904.
- 12 H. Uoyama, K. Goushi, K. Shizu, H. Nomura and C. Adachi, *Nature*, 2012, **492**, 234–238.
- 13 M. Y. Wong and E. Zysman-Colman, *Adv. Mater.*, 2017, **29**, 1605444.
- 14 Z. Yang, Z. Mao, Z. Xie, Y. Zhang, S. Liu, J. Zhao, J. Xu, Z. Chi and M. P. Aldred, *Chem. Soc. Rev.*, 2017, **46**, 915–1016.
- 15 M. A. Bryden and E. Zysman-Colman, *Chem. Soc. Rev.*, 2021, **50**, 7587–7680.
- 16 D. Sun, C. Si, T. Wang and E. Zysman-Colman, *Adv. Photonics Res.*, 2022, **3**, 2200203.
- 17 Y. Liu, C. Li, Z. Ren, S. Yan and M. R. Bryce, *Nat. Rev. Mater.*, 2018, **3**, 1–20.
- 18 T. N. Singh-Rachford and F. N. Castellano, *Coord. Chem. Rev.*, 2010, **254**, 2560–2573.
- 19 C. Bohne, E. B. Abuin and J. C. Scaiano, *J. Am. Chem. Soc.*, 1990, **112**, 4226–4231.
- 20 W. Becker, *Advanced time-correlated single photon counting techniques*, Springer Science & Business Media, 2005, vol. 81.
- 21 W. Becker, *The bh TCSPC handbook*, Becker & Hickl GmbH, 2021.
- 22 W. Becker, A. Bergmann, G. L. Biscotti and A. Rueck, in *Commercial and Biomedical Applications of Ultrafast Lasers IV*, SPIE, 2004, **5340**, 104–112.
- 23 A. Ghosh and B. Norton, *Sol. Energy Mater. Sol. Cells*, 2017, **163**, 218–223.
- 24 J. Eng and T. J. Penfold, *Chem. Rec.*, 2020, **20**, 831–856.
- 25 G. A. Crosby and J. N. Demas, *J. Phys. Chem.*, 1971, **75**, 991–1024.
- 26 E. M. Kober, J. V Caspar, R. S. Lumpkin and T. J. Meyer, *J. Phys. Chem.*, 1986, **90**, 3722–3734.
- 27 Y. Hong, J. W. Y. Lam and B. Z. Tang, *Chem. Commun.*, 2009, 4332–4353.
- 28 Y. Huang, J. Xing, Q. Gong, L. C. Chen, G. Liu, C. Yao, Z. Wang, H. L. Zhang, Z. Chen and Q. Zhang, *Nat. Commun.*, 2019, **10**, 169.
- 29 H. Wang and G. Liu, *J. Mater. Chem. B*, 2018, **6**, 4029–4042.
- 30 Y. Hong, J. W. Y. Lam and B. Z. Tang, *Chem. Soc. Rev.*, 2011, **40**, 5361–5388.

- 31 D. Ding, K. Li, B. Liu and B. Z. Tang, *Acc. Chem. Res.*, 2013, **46**, 2441–2453.
- 32 X. Peng, F. Song, E. Lu, Y. Wang, W. Zhou, J. Fan and Y. Gao, *J. Am. Chem. Soc.*, 2005, **127**, 4170–4171.
- 33 K. I. Priyadarsini, *J. Photochem. Photobiol. C Photochem. Rev.*, 2009, **10**, 81–95.
- 34 A. Samanta, *J. Phys. Chem. B*, 2006, **110**, 13704–13716.
- 35 C. Reichardt, in *Green Chemistry*, 2005, **7**, 339–351.
- 36 S. Ma, S. Du, G. Pan, S. Dai, B. Xu and W. Tian, *Aggregate*, 2021, **2**, e96.
- 37 J. Mei, N. L. C. Leung, R. T. K. Kwok, J. W. Y. Lam and B. Z. Tang, *Chem. Rev.*, 2015, **115**, 11718–11940.
- 38 J. Xue, Q. Liang, R. Wang, J. Hou, W. Li, Q. Peng, Z. Shuai and J. Qiao, *Adv. Mater.*, 2019, **31**, 1808242.
- 39 M. KASHA, *Radiat. Res.*, 1963, **20**, 55–70.
- 40 R. M. Hochstrasser and M. Kasha, *Photochem. Photobiol.*, 1964, **3**, 317–331.
- 41 N. J. Hestand and F. C. Spano, *Chem. Rev.*, 2018, **118**, 7069–7163.
- 42 J. Luo, Z. Xie, Z. Xie, J. W. Y. Lam, L. Cheng, H. Chen, C. Qiu, H. S. Kwok, X. Zhan, Y. Liu, D. Zhu and B. Z. Tang, *Chem. Commun.*, 2001, **18**, 1740–1741.
- 43 Z. Zhao, H. Zhang, J. W. Y. Lam and B. Z. Tang, *Angew. Chemie Int. Ed.*, 2020, **59**, 9888–9907.
- 44 X. Zhang, T. Lu, C. Zhou, H. Liu, Y. Wen, Y. Shen, B. Li, S. T. Zhang and B. Yang, *CCS Chem.*, 2022, **4**, 625–637.
- 45 C. W. Tang and S. A. Vanslyke, *Appl. Phys. Lett.*, 1987, **51**, 913–915.
- 46 B. Geffroy, P. le Roy and C. Prat, *Polym. Int.*, 2006, **55**, 572–582.
- 47 T. Sekitani, H. Nakajima, H. Maeda, T. Fukushima, T. Aida, K. Hata and T. Someya, *Nat. Mater.*, 2009, **8**, 494–499.
- 48 H. Uoyama, K. Goushi, K. Shizu, H. Nomura and C. Adachi, *Nature*, 2012, **492**, 234–238.
- 49 R. H. Friend, R. W. Gymer, A. B. Holmes, J. H. Burroughes, R. N. Marks, C. Taliani, D. D. C Bradley, D. A. Dos Santos, J. L. BreÃ das, M. Lo È gdlund and W. R. Salaneck, *Nature*, 1999, **397**, 121–128.
- 50 B. Geffroy, P. Le Roy and C. Prat, *Polym. Int.*, 2006, **55**, 572–582.
- 51 Y. Huang, E.-L. Hsiang, M.-Y. Deng and S.-T. Wu, *Light Sci. Appl.*, 2020, **9**, 105.
- 52 G. Hong, X. Gan, C. Leonhardt, Z. Zhang, J. Seibert, J. M. Busch and S. Bräse, *Adv. Mater.*, 2021, **33**, 2005630.
- 53 J. C. Scott, S. Karg and S. A. Carter, *J. Appl. Phys.*, 1997, **82**, 1454–1460.
- 54 A. Köhler and H. Bässler, *Mater. Sci. Eng. R Reports*, 2009, **66**, 71–109.
- 55 T. Hofbeck and H. Yersin, *Inorg. Chem.*, 2010, **49**, 9290–9299.
- 56 R. Pode, *Renew. Sustain. Energy Rev.*, 2020, **133**, 110043.
- 57 B. Kim, T. Kim and H.-J. Suk, *J. Inf. Disp.*, 2023, **24**, 273–281.
- 58 H. Shen, Q. Gao, Y. Zhang, Y. Lin, Q. Lin, Z. Li, L. Chen, Z. Zeng, X. Li, Y. Jia, S. Wang, Z. Du, L. S. Li and Z. Zhang, *Nat. Photonics*, 2019, **13**, 192–197.
- 59 L. H. Smith, J. A. E. Wasey, I. D. W. Samuel and W. L. Barnes, *Adv. Funct. Mater.*, 2005, **15**, 1839–1844.
- 60 A. Salehi, X. Fu, D. Shin and F. So, *Adv. Funct. Mater.*, 2019, **29**, 1808803.
- 61 F. Tenopala-Carmona, O. S. Lee, E. Crovini, A. M. Neferu, C. Murawski, Y. Olivier, E.

- Zysman-Colman and M. C. Gather, *Adv. Mater.*, 2021, **33**, 2100677.
- 62 J. M. Pitarke, V. M. Silkin, E. V Chulkov and P. M. Echenique, *Reports Prog. Phys.*, 2007, **70**, 1–87.
- 63 S. Sudheendran Swayamprabha, D. K. Dubey, Shah Nawaz, R. A. K. Yadav, M. R. Nagar, A. Sharma, F. Tung and J. Jou, *Adv. Sci.*, 2021, **8**, 2002254.
- 64 A. Köhler and H. Bässler, *Mater. Sci. Eng. R Reports*, 2009, **66**, 71–109.
- 65 M. A. Baldo, D. F. O'Brien, Y. You, A. Shoustikov, S. Sibley, M. E. Thompson and S. R. Forrest, *Nature*, 1998, **395**, 151–154.
- 66 C. Adachi, M. A. Baldo, M. E. Thompson and S. R. Forrest, *J. Appl. Phys.*, 2001, **90**, 5048–5051.
- 67 C. Wang, X. Li, Y. Pan, S. Zhang, L. Yao, Q. Bai, W. Li, P. Lu, B. Yang, S. Su and Y. Ma, *ACS Appl. Mater. Interfaces*, 2016, **8**, 3041–3049.
- 68 W. Li, Y. Pan, L. Yao, H. Liu, S. Zhang, C. Wang, F. Shen, P. Lu, B. Yang and Y. Ma, *Adv. Opt. Mater.*, 2014, **2**, 892–901.
- 69 W. Li, Y. Pan, R. Xiao, Q. Peng, S. Zhang, D. Ma, F. Li, F. Shen, Y. Wang, B. Yang and Y. Ma, *Adv. Funct. Mater.*, 2014, **24**, 1609–1614.
- 70 J. Sanz-Rodrigo, G. Ricci, Y. Olivier and J. C. Sancho-García, *J. Phys. Chem. A*, 2021, **125**, 513–522.
- 71 P. De Silva, *J. Phys. Chem. Lett.*, 2019, **10**, 5674–5679.
- 72 N. Aizawa, Y. J. Pu, Y. Harabuchi, A. Nihonyanagi, R. Ibuka, H. Inuzuka, B. Dhara, Y. Koyama, K. ichi Nakayama, S. Maeda, F. Araoka and D. Miyajima, *Nature*, 2022, **609**, 502–506.
- 73 H. S. Kim, J. Y. Lee, S. Shin, W. Jeong, S. H. Lee, S. Kim, J. Lee, M. C. Suh and S. Yoo, *Adv. Funct. Mater.*, 2021, **31**, 2104646.
- 74 Y. Tsuchiya, S. Diesing, F. Bencheikh, Y. Wada, P. L. dos Santos, H. Kaji, E. Zysman-Colman, I. D. W. Samuel and C. Adachi, *J. Phys. Chem. A*, 2021, **125**, 8074–8089.
- 75 K. Schmidt, S. Brovelli, V. Coropceanu, D. Beljonne, J. Cornil, C. Bazzini, T. Caronna, R. Tubino, F. Meinardi, Z. Shuai and J. L. Brédas, *J. Phys. Chem. A*, 2007, **111**, 10490–10499.
- 76 E. Zysman-Colman, *Nat. Photonics*, 2020, **14**, 593–594.
- 77 F. B. Dias, K. N. Bourdakos, V. Jankus, K. C. Moss, K. T. Kamtekar, V. Bhalla, J. Santos, M. R. Bryce and A. P. Monkman, *Adv. Mater.*, 2013, **25**, 3707–3714.
- 78 Q. Zhang, J. Li, K. Shizu, S. Huang, S. Hirata, H. Miyazaki and C. Adachi, *J. Am. Chem. Soc.*, 2012, **134**, 14706–14709.
- 79 M. A. El-Sayed, *J. Chem. Phys.*, 1963, **38**, 2834–2838.
- 80 J. Tatchen, N. Gilka and C. M. Marian, *Phys. Chem. Chem. Phys.*, 2007, **9**, 5209–5221.
- 81 C. A. Parker and C. G. Hatchard, *Trans. Faraday Soc.*, 1963, **59**, 284–295.
- 82 A. Maciejewski, M. Szymanski and R. P. Steer, *J. Phys. Chem.*, 1986, **90**, 6314–6318.
- 83 M. W. Wolf, K. D. Legg, R. E. Brown, L. A. Singer and J. H. Parks, *J. Am. Chem. Soc.*, 1975, **97**, 4490–4497.
- 84 W. L. Parker and G. A. Crosby, *J. Phys. Chem.*, 1989, **93**, 5692–5696.
- 85 A. Endo, M. Ogasawara, A. Takahashi, D. Yokoyama, Y. Kato and C. Adachi, *Adv. Mater.*, 2009, **21**, 4802–4806.
- 86 J. C. Deaton, S. C. Switalski, D. Y. Kondakov, R. H. Young, T. D. Pawlik, D. J. Giesen,

- S. B. Harkins, A. J. M. Miller, S. F. Mickenberg and J. C. Peters, *J. Am. Chem. Soc.*, 2010, **132**, 9499–9508.
- 87 A. Endo, K. Sato, K. Yoshimura, T. Kai, A. Kawada, H. Miyazaki and C. Adachi, *Appl. Phys. Lett.*, 2011, **98**, 2009–2012.
- 88 H. Uoyama, K. Goushi, K. Shizu, H. Nomura and C. Adachi, *Nature*, 2012, **492**, 234–238.
- 89 H. Wang, L. Xie, Q. Peng, L. Meng, Y. Wang, Y. Yi and P. Wang, *Adv. Mater.*, 2014, **26**, 5198–5204.
- 90 T. A. Lin, T. Chatterjee, W. L. Tsai, W. K. Lee, M. J. Wu, M. Jiao, K. C. Pan, C. L. Yi, C. L. Chung, K. T. Wong and C. C. Wu, *Adv. Mater.*, 2016, **28**, 6976–6983.
- 91 Y. Chen, D. Zhang, Y. Zhang, X. Zeng, T. Huang, Z. Liu, G. Li and L. Duan, *Adv. Mater.*, 2021, **33**, 2103293.
- 92 S. Madayanad Suresh, D. Hall, D. Beljonne, Y. Olivier and E. Zysman-Colman, *Adv. Funct. Mater.*, 2020, **30**, 1908677.
- 93 H. J. Kim and T. Yasuda, *Adv. Opt. Mater.*, 2022, **10**, 2201714.
- 94 S. Shao and L. Wang, *Aggregate*, 2020, **1**, 45–56.
- 95 B. Li, Z. Yang, W. Gong, X. Chen, D. W. Bruce, S. Wang, H. Ma, Y. Liu, W. Zhu and Z. Chi, *Adv. Opt. Mater.*, 2021, **9**, 2100180.
- 96 W. Shao, J. Hao, H. Jiang, P. M. Zimmerman and J. Kim, *Adv. Funct. Mater.*, 2022, **32**, 2201256.
- 97 Y.-C. Wei, Z. Zhang, Y.-A. Chen, C.-H. Wu, Z.-Y. Liu, S.-Y. Ho, J.-C. Liu, J.-A. Lin and P.-T. Chou, *Commun. Chem.*, 2019, **2**, 10.
- 98 N. Sharma, E. Spuling, C. M. Mattern, W. Li, O. Fuhr, Y. Tsuchiya, C. Adachi, S. Bräse, I. D. W. Samuel and E. Zysman-Colman, *Chem. Sci.*, 2019, **10**, 6689–6696.
- 99 X. Li, Y. Xie and Z. Li, *Adv. Photonics Res.*, 2021, **2**, 2000136.
- 100 Q. Wei, Z. Ge and B. Voit, *Macromol. Rapid Commun.*, 2019, **40**, 1800570.
- 101 D. Sun, R. Saxena, X. Fan, S. Athanasopoulos, E. Duda, M. Zhang, S. Bagnich, X. Zhang, E. Zysman-Colman and A. Köhler, *Adv. Sci.*, 2022, **9**, 2201470.
- 102 D. Sun, E. Duda, X. Fan, R. Saxena, M. Zhang, S. Bagnich, X. Zhang, A. Köhler and E. Zysman-Colman, *Adv. Mater.*, 2022, **34**, 2110344.
- 103 F. Ni, N. Li, L. Zhan and C. Yang, *Adv. Opt. Mater.*, 2020, **8**, 1–13.
- 104 N. R. Paisley, C. M. Tonge and Z. M. Hudson, *Front. Chem.*, 2020, **8**, 229.
- 105 M. A. Bryden and E. Zysman-Colman, *Chem. Soc. Rev.*, 2021, **50**, 7587–7680.
- 106 Y. Meng, J. Zhang, C. Liu, K. Zheng, L. Xie, S. Bu, B. Han, R. Cao, X. Yin and C. Liu, *Adv. Funct. Mater.*, 2023, **33**, 2210600.
- 107 J. Zhang, F. Fang, B. Liu, J.-H. Tan, W.-C. Chen, Z. Zhu, Y. Yuan, Y. Wan, X. Cui and S. Li, *ACS Appl. Mater. Interfaces*, 2019, **11**, 41051–41061.
- 108 F. Fang, Y. Yuan, Y. Wan, J. Li, Y. Song, W. Chen, D. Zhao, Y. Chi, M. Li and C. Lee, *Small*, 2022, **18**, 2106215.
- 109 S. Li, J. Chen, Y. Wei, J. De, H. Geng, Q. Liao, R. Chen and H. Fu, *Angew. Chemie*, 2022, **134**, e202209211.
- 110 C. Yan, X. Wang and L. Liao, *Adv. Sci.*, 2022, **9**, 2200525.
- 111 R. Englman and J. Jortner, *Mol. Phys.*, 1970, **18**, 145–164.
- 112 J. H. Kim, J. H. Yun and J. Y. Lee, *Adv. Opt. Mater.*, 2018, **6**, 1800255.

- 113 K. Guo, M. Righetto, A. Minotto, A. Zampetti and F. Cacialli, *iScience*, 2021, **24**, 102545.
- 114 D. Sun, C. Si, T. Wang and E. Zysman-Colman, *Adv. Photonics Res.*, 2022, 2200203.
- 115 M. Y. Wong and E. Zysman-Colman, *Adv. Mater.*, 2017, **29**, 1605444.
- 116 Y. Xiao, H. Wang, Z. Xie, M. Shen, R. Huang, Y. Miao, G. Liu, T. Yu and W. Huang, *Chem. Sci.*, 2022, **13**, 8906–8923.
- 117 K. Rayappa Naveen, K. Prabhu CP, R. Braveenth and J. Hyuk Kwon, *Chem. – A Eur. J.*, 2022, **28**, e202103532.
- 118 D. Karthik, Y. H. Jung, H. Lee, S. Hwang, B. Seo, J. Kim, C. W. Han and J. H. Kwon, *Adv. Mater.*, 2021, **33**, 2007724.
- 119 Z. Chen, Z. Wu, F. Ni, C. Zhong, W. Zeng, D. Wei, K. An, D. Ma and C. Yang, *J. Mater. Chem. C*, 2018, **6**, 6543–6548.
- 120 H. Liu, J. Li, W. C. Chen, X. Lv, C. Zhou, C. S. Lee and C. Yang, *J. Phys. Chem. C*, 2020, **124**, 25489–25498.
- 121 C. Li, R. Duan, B. Liang, G. Han, S. Wang, K. Ye, Y. Liu, Y. Yi and Y. Wang, *Angew. Chemie - Int. Ed.*, 2017, **56**, 11525–11529.
- 122 S. Kothavale, K. H. Lee and J. Y. Lee, *ACS Appl. Mater. Interfaces*, 2019, **11**, 17583–17591.
- 123 S. Kothavale, W. J. Chung and J. Y. Lee, *J. Mater. Chem. C*, 2021, **9**, 528–536.
- 124 T. Huang, D. Liu, D. Li, W. Jiang and J. Jiang, *New J. Chem.*, 2019, **43**, 13339–13348.
- 125 J. Liang, C. Li, Y. Cui, Z. Li, J. Wang and Y. Wang, *J. Mater. Chem. C*, 2020, **8**, 1614–1622.
- 126 Y. Yuan, Y. Hu, Y. X. Zhang, J. D. Lin, Y. K. Wang, Z. Q. Jiang, L. S. Liao and S. T. Lee, *Adv. Funct. Mater.*, 2017, **27**, 1–5.
- 127 Q. Zhang, H. Kuwabara, W. J. Potscavage, S. Huang, Y. Hatae, T. Shibata and C. Adachi, *J. Am. Chem. Soc.*, 2014, **136**, 18070–18081.
- 128 S. Wang, X. Yan, Z. Cheng, H. Zhang, Y. Liu and Y. Wang, *Angew. Chemie*, 2015, **127**, 13260–13264.
- 129 D. G. Congrave, B. H. Drummond, P. J. Conaghan, H. Francis, S. T. E. Jones, C. P. Grey, N. C. Greenham, D. Credgington and H. Bronstein, *J. Am. Chem. Soc.*, 2019, **141**, 18390–18394.
- 130 C. Leng, S. You, Y. Si, H. M. Qin, J. Liu, W. Q. Huang and K. Li, *J. Phys. Chem. A*, 2021, **125**, 2905–2912.
- 131 X. Gong, P. Li, Y. H. Huang, C. Y. Wang, C. H. Lu, W. K. Lee, C. Zhong, Z. Chen, W. Ning, C. C. Wu, S. Gong and C. Yang, *Adv. Funct. Mater.*, 2020, **30**, 1908839.
- 132 J. F. Cheng, Z. H. Pan, K. Zhang, Y. Zhao, C. K. Wang, L. Ding, M. K. Fung and J. Fan, *Chem. Eng. J.*, 2022, **430**, 132744.
- 133 X. Gong, C. H. Lu, W. K. Lee, P. Li, Y. H. Huang, Z. Chen, L. Zhan, C. C. Wu, S. Gong and C. Yang, *Chem. Eng. J.*, 2021, **405**, 126663.
- 134 S. Wang, Z. Cheng, X. Song, X. Yan, K. Ye, Y. Liu, G. Yang and Y. Wang, *ACS Appl. Mater. Interfaces*, 2017, **9**, 9892–9901.
- 135 B. Wang, X. Qiao, Z. Yang, Y. Wang, S. Liu, D. Ma and Q. Wang, *Org. Electron.*, 2018, **59**, 32–38.
- 136 B. Wang, H. Yang, Y. Zhang, G. Xie, H. Ran, T. Wang, Q. Fu, Y. Ren, N. Sun, G. Zhao,

- J. Y. Hu and Q. Wang, *J. Mater. Chem. C*, 2019, **7**, 12321–12327.
- 137 R. Furue, K. Matsuo, Y. Ashikari, H. Ooka, N. Amanokura and T. Yasuda, *Adv. Opt. Mater.*, 2018, **6**, 1701147.
- 138 Y. L. Zhang, Q. Ran, Q. Wang, Y. Liu, C. Hänisch, S. Reineke, J. Fan and L. S. Liao, *Adv. Mater.*, 2019, **31**, 1902368.
- 139 S. Kothavale, W. J. Chung and J. Y. Lee, *ACS Appl. Mater. Interfaces*, 2020, **12**, 18730–18738.
- 140 S. Kothavale, W. J. Chung and J. Y. Lee, *J. Mater. Chem. C*, 2020, **8**, 7059–7066.
- 141 F. M. Xie, P. Wu, S. J. Zou, Y. Q. Li, T. Cheng, M. Xie, J. X. Tang and X. Zhao, *Adv. Electron. Mater.*, 2020, **6**, 1900843.
- 142 F. M. Xie, X. Y. Zeng, J. X. Zhou, Z. D. An, W. Wang, Y. Q. Li, X. H. Zhang and J. X. Tang, *J. Mater. Chem. C*, 2020, **8**, 15728–15734.
- 143 C. Zhou, W. C. Chen, H. Liu, X. Cao, N. Li, Y. Zhang, C. S. Lee and C. Yang, *J. Mater. Chem. C*, 2020, **8**, 9639–9645.
- 144 J. X. Chen, W. W. Tao, Y. F. Xiao, K. Wang, M. Zhang, X. C. Fan, W. C. Chen, J. Yu, S. Li, F. X. Geng, X. H. Zhang and C. S. Lee, *ACS Appl. Mater. Interfaces*, 2019, **11**, 29086–29093.
- 145 J. Chen, Y. Xiao, K. Wang, D. Sun, X. Fan, X. Zhang, M. Zhang, Y. Shi, J. Yu, F. Geng, C. Lee and X. Zhang, *Angew. Chemie*, 2021, **133**, 2508–2514.
- 146 J. X. Chen, W. W. Tao, W. C. Chen, Y. F. Xiao, K. Wang, C. Cao, J. Yu, S. Li, F. X. Geng, C. Adachi, C. S. Lee and X. H. Zhang, *Angew. Chemie - Int. Ed.*, 2019, **58**, 14660–14665.
- 147 J. X. Chen, K. Wang, C. J. Zheng, M. Zhang, Y. Z. Shi, S. L. Tao, H. Lin, W. Liu, W. W. Tao, X. M. Ou and X. H. Zhang, *Adv. Sci.*, 2018, **5**, 1800436.
- 148 H. Wang, B. Zhao, P. Ma, Z. Li, X. Wang, C. Zhao, X. Fan, L. Tao, C. Duan, J. Zhang, C. Han, G. Chen and H. Xu, *J. Mater. Chem. C*, 2019, **7**, 7525–7530.
- 149 K. Zhang, X. Zhang, J. Fan, Y. Song, J. Fan, C. K. Wang and L. Lin, *J. Phys. Chem. Lett.*, 2022, 4711–4720.
- 150 J. H. Tan, J. M. Jin, W. C. Chen, C. Cao, R. Wang, Z. L. Zhu, Y. Huo and C. S. Lee, *ACS Appl. Mater. Interfaces*, 2022, **14**, 53120–53128.
- 151 S. Kothavale, W. J. Chung and J. Y. Lee, *J. Mater. Chem. C*, 2022, **10**, 6043–6049.
- 152 F. X. Huang, H. Z. Li, F. M. Xie, X. Y. Zeng, Y. Q. Li, Y. Y. Hu, J. X. Tang and X. Zhao, *Dye. Pigment.*, 2021, **195**, 109731.
- 153 U. Balijapalli, R. Nagata, N. Yamada, H. Nakanotani, M. Tanaka, A. D'Aléo, V. Placide, M. Mamada, Y. Tsuchiya and C. Adachi, *Angew. Chemie - Int. Ed.*, 2021, **60**, 8477–8482.
- 154 T. Yang, B. Liang, Z. Cheng, C. Li, G. Lu and Y. Wang, *J. Phys. Chem. C*, 2019, **123**, 18585–18592.
- 155 T. Yang, Z. Cheng, Z. Li, J. Liang, Y. Xu, C. Li and Y. Wang, *Adv. Funct. Mater.*, 2020, **30**, 2002681.
- 156 Y. Yang, Q. Zhao, W. Feng and F. Li, *Chem. Rev.*, 2013, **113**, 192–270.
- 157 P. Sharma, S. Brown, G. Walter, S. Santra and B. Moudgil, *Adv. Colloid Interface Sci.*, 2006, **123–126**, 471–485.
- 158 O. S. Wolfbeis, *Chem. Soc. Rev.*, 2015, **44**, 4743–4768.

- 159 R. Guan, L. Xie, T. W. Rees, L. Ji and H. Chao, *J. Inorg. Biochem.*, 2020, **204**, 110985.
- 160 X. Zhen, R. Qu, W. Chen, W. Wu and X. Jiang, *Biomater. Sci.*, 2021, **9**, 285–300.
- 161 Q. Zhao, H. Huang and F. Li, *Chem. Soc. Rev.*, 2011, **40**, 2508–2524.
- 162 F. Ni, N. Li, L. Zhan and C. Yang, *Adv. Opt. Mater.*, 2020, **8**, 1902187.
- 163 X. Xiong, F. Song, J. Wang, Y. Zhang, Y. Xue, L. Sun, N. Jiang, P. Gao, L. Tian and X. Peng, *J. Am. Chem. Soc.*, 2014, **136**, 9590–9597.
- 164 Q. Liu, B. Yin, T. Yang, Y. Yang, Z. Shen, P. Yao and F. Li, *J. Am. Chem. Soc.*, 2013, **135**, 5029–5037.
- 165 A. Ogunsipe and T. Nyokong, *Photochem. Photobiol. Sci.*, 2005, **4**, 510–516.
- 166 A. Jahanban-Esfahlan, A. Ostadrahimi, R. Jahanban-Esfahlan, L. Roufegarinejad, M. Tabibiazar and R. Amarowicz, *Int. J. Biol. Macromol.*, 2019, **138**, 602–617.
- 167 Y. Wu, F. Song, W. Luo, Z. Liu, B. Song and X. Peng, *ChemPhotoChem*, 2017, **1**, 79–83.
- 168 S. Gan, J. Zhou, T. A. Smith, H. Su, W. Luo, Y. Hong, Z. Zhao and B. Z. Tang, *Mater. Chem. Front.*, 2017, **1**, 2554–2558.
- 169 F. Ni, Z. Zhu, X. Tong, M. Xie, Q. Zhao, C. Zhong, Y. Zou and C. Yang, *Chem. Sci.*, 2018, **9**, 6150–6155.
- 170 X. Xu, R. Liu and L. Li, *Chem. Commun.*, 2015, **51**, 16733–16749.
- 171 B. Bao, M. Ma, H. Zai, L. Zhang, N. Fu, W. Huang and L. Wang, *Adv. Sci.*, 2015, **2**, 1400009.
- 172 C. Wu and D. T. Chiu, *Angew. Chemie - Int. Ed.*, 2013, **52**, 3086–3109.
- 173 F. Fang, M. Li, J. Zhang and C.-S. Lee, *ACS Mater. Lett.*, 2020, **2**, 531–549.
- 174 D. Horn and J. Rieger, *Angew. Chemie Int. Ed.*, 2001, **40**, 4330–4361.
- 175 K. Petkau, A. Kaeser, I. Fischer, L. Brunsveld and A. P. H. J. Schenning, *J. Am. Chem. Soc.*, 2011, **133**, 17063–17071.
- 176 C. Wu, C. Szymanski, Z. Cain and J. McNeill, *J. Am. Chem. Soc.*, 2007, **129**, 12904–12905.
- 177 L. Feng, C. Zhu, H. Yuan, L. Liu, F. Lv and S. Wang, *Chem. Soc. Rev.*, 2013, **42**, 6620–6633.
- 178 T. Li, D. Yang, L. Zhai, S. Wang, B. Zhao, N. Fu, L. Wang, Y. Tao and W. Huang, *Adv. Sci.*, 2017, **4**, 1600166.
- 179 T. He, C. Ren, Z. Li, S. Xiao, J. Li, X. Lin, C. Ye, J. Zhang, L. Guo, W. Hu and R. Chen, *Appl. Phys. Lett.*, 2018, **112**, 1–5.
- 180 Y. Tsuchiya, K. Ikesue, H. Nakanotani and C. Adachi, *Chem. Commun.*, 2019, **55**, 5215–5218.
- 181 Z. Zhu, D. Tian, P. Gao, K. Wang, Y. Li, X. Shu, J. Zhu and Q. Zhao, *J. Am. Chem. Soc.*, 2018, **140**, 17484–17491.
- 182 Q. Z. Shi, Huifang, Liang Zou Kaiwei Huang, He Wang, Chen Sun, Shan Wang, Huili Ma, Yarong He, Jianpu Wang, Haidong Yu, Wei Yao, Zhongfu An, *ACS Appl. Mater. Interfaces*, 2019, **11**, 18103–18110.
- 183 C. Tang, T. Yang, X. Cao, Y. Tao, F. Wang, C. Zhong, Y. Qian, X. Zhang and W. Huang, *Adv. Opt. Mater.*, 2015, **3**, 786–790.
- 184 S. Chen, H. Wang, Y. Hong and B. Z. Tang, *Mater. Horizons*, 2016, **3**, 283–293.
- 185 W. Zhao, H. Wei, F. Liu and C. Ran, *Photodiagnosis Photodyn. Ther.*, 2020, **30**, 101744.

- 186 Y. F. Xiao, J. X. Chen, S. Li, W. W. Tao, S. Tian, K. Wang, X. Cui, Z. Huang, X. H. Zhang and C. S. Lee, *Chem. Sci.*, 2020, **11**, 888–895.
- 187 C. I. C. Crucho, J. Avó, A. M. Diniz, S. N. Pinto, J. Barbosa, P. O. Smith, M. N. Berberan-Santos, L. O. Pålsson and F. B. Dias, *Front. Chem.*, 2020, **8**, 1–14.
- 188 M. Luo, X. Li, L. Ding, G. Baryshnikov, S. Shen, M. Zhu, L. Zhou, M. Zhang, J. Lu, H. Ågren, X. Wang and L. Zhu, *Angew. Chemie*, 2020, **132**, 17166–17173.
- 189 X. Li, G. Baryshnikov, L. Ding, X. Bao, X. Li, J. Lu, M. Liu, S. Shen, M. Luo, M. Zhang, H. Ågren, X. Wang and L. Zhu, *Angew. Chemie*, 2020, **132**, 7618–7624.
- 190 D. M. Mayder, R. Hojo, W. L. Primrose, C. M. Tonge and Z. M. Hudson, *Adv. Funct. Mater.*, 2022, **32**, 2204087.
- 191 D. M. Mayder, C. J. Christopherson, W. L. Primrose, A. S.-M. Lin and Z. M. Hudson, *J. Mater. Chem. B*, 2022, **10**, 6496–6506.
- 192 N. R. Paisley, S. V. Halldorson, M. V. Tran, R. Gupta, S. Kamal, W. R. Algar and Z. M. Hudson, *Angew. Chemie - Int. Ed.*, 2021, **60**, 18630–18638.
- 193 K. F. Hsu, S. P. Su, H. F. Lu, M. H. Liu, Y. J. Chang, Y. J. Lee, H. K. Chiang, C. P. Hsu, C. W. Lu and Y. H. Chan, *Chem. Sci.*, 2022, **13**, 10074–10081.
- 194 W. Zeng, H. Y. Lai, W. K. Lee, M. Jiao, Y. J. Shiu, C. Zhong, S. Gong, T. Zhou, G. Xie, M. Sarma, K. T. Wong, C. C. Wu and C. Yang, *Adv. Mater.*, 2018, **30**, 1704961.
- 195 F. Ni, Z. Wu, Z. Zhu, T. Chen, K. Wu, C. Zhong, K. An, D. Wei, D. Ma and C. Yang, *J. Mater. Chem. C*, 2017, **5**, 1363–1368.
- 196 C. I. C. Crucho, C. Baleizão and J. P. S. Farinha, *Anal. Chem.*, 2017, **89**, 681–687.
- 197 C. I. C. Crucho, J. Avó, R. Nobuyasu, S. N. Pinto, F. Fernandes, J. C. Lima, M. N. Berberan-Santos and F. B. Dias, *Mater. Sci. Eng. C*, 2020, **109**, 110528.
- 198 L. Mo, X. Xu, Z. Liu, H. Liu, B. Lei, J. Zhuang, Z. Guo, Y. Liu and C. Hu, *Chem. Eng. J.*, 2021, **426**, 130728.
- 199 A. Jana, K. S. P. Devi, T. K. Maiti and N. D. P. Singh, *J. Am. Chem. Soc.*, 2012, **134**, 7656–7659.
- 200 A. Jana, K. T. Nguyen, X. Li, P. Zhu, N. S. Tan, H. Ågren and Y. Zhao, *ACS Nano*, 2014, **8**, 5939–5952.
- 201 E. Genin, Z. Gao, J. A. Varela, J. Daniel, T. Bsaibess, I. Gosse, L. Groc, L. Cognet and M. Blanchard-Desce, *Adv. Mater.*, 2014, **26**, 2258–2261.
- 202 J. Zhang, W. Chen, S. Kalytchuk, K. F. Li, R. Chen, C. Adachi, Z. Chen, A. L. Rogach, G. Zhu, P. K. N. Yu, W. Zhang, K. W. Cheah, X. Zhang and C. S. Lee, *ACS Appl. Mater. Interfaces*, 2016, **8**, 11355–11365.
- 203 R. Wei, L. Zhang, S. Xu, Q. Zhang, Y. Qi and H. Y. Hu, *Chem. Commun.*, 2020, **56**, 2550–2553.
- 204 W. Hu, L. Guo, L. Bai, X. Miao, Y. Ni, Q. Wang, H. Zhao, M. Xie, L. Li, X. Lu, W. Huang and Q. Fan, *Adv. Healthc. Mater.*, 2018, **7**, 1800299.
- 205 S. Qi, S. Kim, V. N. Nguyen, Y. Kim, G. Niu, G. Kim, S. J. Kim, S. Park and J. Yoon, *ACS Appl. Mater. Interfaces*, 2020, **12**, 51293–51301.
- 206 B. Zhao, H. Wang, M. Xie, C. Han, H. Yang, W. Zhao, Q. Zhao and H. Xu, *Adv. Photonics Res.*, 2021, **2**, 2000096.
- 207 S. K. Sarkar, M. Pegu, S. K. Behera, S. K. Narra and P. Thilagar, *Chem. - An Asian J.*, 2019, **14**, 4588–4593.

- 208 F. Ni, Z. Zhu, X. Tong, M. Xie, Q. Zhao, C. Zhong, Y. Zou and C. Yang, *Chem. Sci.*, 2018, **9**, 6150–6155.
- 209 Y. Wu, F. Song, W. Luo, Z. Liu, B. Song and X. Peng, *ChemPhotoChem*, 2017, **1**, 79–83.
- 210 F. Ni, Z. Zhu, X. Tong, W. Zeng, K. An, D. Wei, S. Gong, Q. Zhao, X. Zhou and C. Yang, *Adv. Sci.*, 2019, **6**, 1801729.
- 211 M. Yu, W. Zhao, F. Ni, Q. Zhao and C. Yang, *Adv. Opt. Mater.*, 2022, **10**, 2102437.
- 212 Y. Liu, C. Li, Z. Ren, S. Yan and M. R. Bryce, *Nat. Rev. Mater.*, 2018, **3**, 18020.
- 213 Z. Yang, Z. Mao, Z. Xie, Y. Zhang, S. Liu, J. Zhao, J. Xu, Z. Chi and M. P. Aldred, *Chem. Soc. Rev.*, 2017, **46**, 915–1016.
- 214 S. Sharma and A. K. Pal, *J. Mater. Chem. C*, 2022, **10**, 15681–15707.
- 215 J. S. Wilson, N. Chawdhury, M. R. A. Al-Mandhary, M. Younus, M. S. Khan, P. R. Raithby, A. Köhler and R. H. Friend, *J. Am. Chem. Soc.*, 2001, **123**, 9412–9417.
- 216 J. V. Caspar, E. M. Kober, B. P. Sullivan and T. J. Meyer, *J. Am. Chem. Soc.*, 1982, **104**, 630–632.
- 217 Y. J. Yu, Y. Hu, S. Y. Yang, W. Luo, Y. Yuan, C. C. Peng, J. F. Liu, A. Khan, Z. Q. Jiang and L. S. Liao, *Angew. Chemie - Int. Ed.*, 2020, **59**, 21578–21584.
- 218 S. Wang, X. Yan, Z. Cheng, H. Zhang, Y. Liu and Y. Wang, *Angew. Chemie - Int. Ed.*, 2015, **54**, 13068–13072.
- 219 S. Wang, Z. Cheng, X. Song, X. Yan, K. Ye, Y. Liu, G. Yang and Y. Wang, *ACS Appl. Mater. Interfaces*, 2017, **9**, 9892–9901.
- 220 Y. L. Zhang, Q. Ran, Q. Wang, Y. Liu, C. Hänisch, S. Reineke, J. Fan and L. S. Liao, *Adv. Mater.*, 2019, **31**, 1902368.
- 221 F. M. Xie, H. Z. Li, G. L. Dai, Y. Q. Li, T. Cheng, M. Xie, J. X. Tang and X. Zhao, *ACS Appl. Mater. Interfaces*, 2019, **11**, 26144–26151.
- 222 S. Hirata and M. Head-Gordon, *Chem. Phys. Lett.*, 1999, **314**, 291–299.
- 223 W. Humphrey, A. Dalke and K. Schulten, *J. Mol. Graph.*, 1996, **14**, 33–38.
- 224 N. G. Connelly and W. E. Geiger, *Chem. Rev.*, 1996, **96**, 877–910.
- 225 X. Zeng, J. Zhou, S. Zou, Y. Tang, H. Li, Y. He, Y. Li, W. Wang and J. Tang, *Adv. Opt. Mater.*, 2022, **10**, 2200277.
- 226 U. Balijapalli, Y. T. Lee, B. S. B. Karunathilaka, G. Tumen-Ulzii, M. Auffray, Y. Tsuchiya, H. Nakanotani and C. Adachi, *Angew. Chemie - Int. Ed.*, 2021, **0395**, 19364–19373.
- 227 A. Endo and C. Adachi, *Chem. Phys. Lett.*, 2009, **483**, 224–226.
- 228 C. Adachi, R. C. Kwong, P. Djurovich, V. Adamovich, M. A. Baldo, M. E. Thompson and S. R. Forrest, *Appl. Phys. Lett.*, 2001, **79**, 2082–2084.
- 229 M. Albota, D. Beljonne, J. L. Brédas, J. E. Ehrlich, J. Y. Fu, A. A. Heikal, S. E. Hess, T. Kogej, M. D. Levin, S. R. Marder, D. McCord-Maughon, J. W. Perry, H. Röckel, M. Rumi, G. Subramaniam, W. W. Webb, X. L. Wu and C. Xu, *Science*, 1998, **281**, 1653–1656.
- 230 A. Hirono, H. Sakai, S. Kochi, T. Sato and T. Hasobe, *J. Phys. Chem. B*, 2020, **124**, 9921–9930.
- 231 Y. P. Ma, G. Wang, M. Zhao, Z. F. Shi, Y. Miao, X. P. Cao and H. L. Zhang, *Dye. Pigment.*, 2023, **212**, 111084.

- 232 A. Steinegger, O. S. Wolfbeis and S. M. Borisov, *Chem. Rev.*, 2020, **120**, 12357–12489.
- 233 K. T. V Grattan and T. Sun, *Sensors Actuators A Phys.*, 2000, **82**, 40–61.
- 234 X. Yan, H. Li and X. Su, *TrAC Trends Anal. Chem.*, 2018, **103**, 1–20.
- 235 N. Sabri, S. A. Aljunid, M. S. Salim, R. B. Ahmad and R. Kamaruddin, in *Journal of Physics: Conference Series*, IOP Publishing, 2013, **423**, 12064.
- 236 M. Vendrell, D. Zhai, J. C. Er and Y. T. Chang, *Chem. Rev.*, 2012, **112**, 4391–4420.
- 237 L. Basabe-Desmonts, D. N. Reinhoudt and M. Crego-Calama, *Chem. Soc. Rev.*, 2007, **36**, 993–1017.
- 238 A. P. Demchenko, *Introduction to fluorescence sensing*, Springer Science & Business Media, 2008.
- 239 H. N. Kim, M. H. Lee, H. J. Kim, J. S. Kim and J. Yoon, *Chem. Soc. Rev.*, 2008, **37**, 1465–1472.
- 240 Y. Wang, X. Wang, W. Ma, R. Lu, W. Zhou and H. Gao, *Chemosensors*, 2022, **10**, 399.
- 241 B. Sam, L. George and A. Varghese, *J. Fluoresc.*, 2021, **31**, 1251–1276.
- 242 X. Chen, T. Pradhan, F. Wang, J. S. Kim and J. Yoon, *Chem. Rev.*, 2012, **112**, 1910–1956.
- 243 M. Poddar and R. Misra, *Coord. Chem. Rev.*, 2020, **421**, 213462.
- 244 A. Loudet and K. Burgess, *Chem. Rev.*, 2007, **107**, 4891–4932.
- 245 N. Roy, A. Dutta, P. Mondal, P. C. Paul and T. Sanjoy Singh, *J. Fluoresc.*, 2017, **27**, 1307–1321.
- 246 S. M. Borisov, G. Zenkl and I. Klimant, *ACS Appl. Mater. Interfaces*, 2010, **2**, 366–374.
- 247 Y. You, S. Cho and W. Nam, *Inorg. Chem.*, 2014, **53**, 1804–1815.
- 248 Q. Zhao, F. Li and C. Huang, *Chem. Soc. Rev.*, 2010, **39**, 3007–3030.
- 249 M. Han, Y. Tian, Z. Yuan, L. Zhu and B. Ma, *Angew. Chemie Int. Ed.*, 2014, **53**, 10908–10912.
- 250 M. A. Bryden and E. Zysman-Colman, *Chem. Soc. Rev.*, 2021, **50**, 7587–7680.
- 251 F. Fang, L. Zhu, M. Li, Y. Song, M. Sun, D. Zhao and J. Zhang, *Adv. Sci.*, 2021, **8**, 2102970.
- 252 A. Russegger, L. Eiber, A. Steinegger and S. M. Borisov, *Chemosensors*, 2022, **10**, 91.
- 253 S. Qiu, J. Yu, T. Zhou, K. Zhang, Y. Duan, X. Ban, Q. Zhu, L. Shi and D. Zhang, *Opt. Mater. (Amst.)*, 2021, **119**, 111303.
- 254 C. J. Christopherson, D. M. Mayder, J. Poisson, N. R. Paisley, C. M. Tonge and Z. M. Hudson, *ACS Appl. Mater. Interfaces*, 2020, **12**, 20000–20011.
- 255 J. C. Fister, D. Rank and J. M. Harris, *Anal. Chem.*, 1995, **67**, 4269–4275.
- 256 A. Steinegger, I. Klimant and S. M. Borisov, *Adv. Opt. Mater.*, 2017, **5**, 1700372.
- 257 C. M. Tonge, N. R. Paisley, A. M. Polgar, K. Lix, W. R. Algar and Z. M. Hudson, *ACS Appl. Mater. Interfaces*, 2020, **12**, 6525–6535.
- 258 X. Li, G. Baryshnikov, C. Deng, X. Bao, B. Wu, Y. Zhou, H. Ågren and L. Zhu, *Nat. Commun.*, 2019, **10**, 731.
- 259 H. Yin, Y. Wu, X. Peng and F. Song, *Chem. Commun.*, 2020, **56**, 10549–10551.
- 260 S. M. Wei, K. Feng, C. Li, N. Xie, Y. Wang, X. L. Yang, B. Chen, C. H. Tung and L. Z. Wu, *Matter*, 2020, **2**, 495–506.
- 261 P. P. Das, P. Mohanty, A. K. Barick, P. Mohapatra and B. R. Jali, *Trends Sci.*, 2023, **20**, 5005.

- 262 F. Himo, Z. P. Demko, L. Noodleman and K. B. Sharpless, *J. Am. Chem. Soc.*, 2003, **125**, 9983–9987.
- 263 E. Manandhar, J. H. Broome, J. Myrick, W. Lagrone, P. J. Cragg and K. J. Wallace, *Chem. Commun.*, 2011, **47**, 8796–8798.
- 264 T. Ghosh, B. G. Maiya and A. Samanta, *Dalt. Trans.*, 2006, 795.
- 265 C. Adamo and V. Barone, *J. Chem. Phys.*, 1999, **110**, 6158–6170.
- 266 G. A. Petersson, T. G. Tensfeldt and J. A. Montgomery, *J. Chem. Phys.*, 1991, **94**, 6091–6101.
- 267 *At the S1 geometries, for 2GCzBPPZ, S1=2.16 eV, T1=2.11 eV, totally CT for S1 and T1; for 2GCzBPN, S1=1.50 eV, T1=1.48 eV, totally CT for both., .*
- 268 S. Grimme, *Chem. Phys. Lett.*, 1996, **259**, 128–137.
- 269 Y. Y. Wang, Y. L. Zhang, K. Tong, L. Ding, J. Fan and L. S. Liao, *J. Mater. Chem. C*, 2019, **7**, 15301–15307.
- 270 C. Zhou, S. Xiao, M. Wang, W. Jiang, H. Liu, S. Zhang and B. Yang, *Front. Chem.*, 2019, **7**, 1–10.
- 271 J. L. He, Y. Tang, K. Zhang, Y. Zhao, Y. C. Lin, C. K. Hsu, C. H. Chen, T. L. Chiu, J. H. Lee, C. K. Wang, C. C. Wu and J. Fan, *Mater. Horizons*, 2022, **9**, 772–779.
- 272 I. Danyliv, Y. Danyliv, R. Lytvyn, O. Bezikonnyi, D. Volyniuk, J. Simokaitiene, K. Ivaniuk, U. Tsiko, A. Tomkeviciene, A. Dabulienė, E. Skuodis, P. Stakhira and J. V. Grazulevicius, *Dye. Pigment.*, 2021, **193**, 109493.
- 273 U. Tsiko, O. Bezikonnyi, G. Sych, R. Keruckiene, D. Volyniuk, J. Simokaitiene, I. Danyliv, Y. Danyliv, A. Bucinskas, X. Tan and J. V. Grazulevicius, *J. Adv. Res.*, 2021, **33**, 41–51.
- 274 C. A. DeRosa, J. Samonina-Kosicka, Z. Fan, H. C. Hendargo, D. H. Weitzel, G. M. Palmer and C. L. Fraser, *Macromolecules*, 2015, **48**, 2967–2977.
- 275 A. Steinegger and S. M. Borisov, *ACS Omega*, 2020, **5**, 7729–7737.
- 276 A. K. Mazumdar, G. P. Nanda, N. Yadav, U. Deori, U. Acharyya, B. Sk and P. Rajamalli, *Beilstein J. Org. Chem.*, 2022, **18**, 1177–1187.
- 277 W. H. Melhuish, *J. Phys. Chem.*, 1961, **65**, 229–235.
- 278 P. L. Santos, J. S. Ward, P. Data, A. S. Batsanov, M. R. Bryce, F. B. Dias and A. P. Monkman, *J. Mater. Chem. C*, 2016, **4**, 3815–3824.
- 279 N. Li, F. Ni, X. Lv, Z. Huang, X. Cao and C. Yang, *Adv. Opt. Mater.*, 2022, **10**, 1–27.
- 280 C. F. Madigan and V. Bulović, *Phys. Rev. Lett.*, 2003, **91**, 247403.
- 281 M. Kasha, H. R. Rawls and M. A. El-Bayoumi, *Pure Appl. Chem.*, 1965, **11**, 371–392.
- 282 S. J. Su, T. Chiba, T. Takeda and J. Kido, *Adv. Mater.*, 2008, **20**, 2125–2130.
- 283 H. Y. Yang, H. yuan Zhang, M. Zhang, X. chun Fan, H. Lin, S. L. Tao, C. J. Zheng and X. H. Zhang, *Chem. Eng. J.*, 2022, **448**, 137717.
- 284 S. J. Zou, Y. Shen, F. M. Xie, J. De Chen, Y. Q. Li and J. X. Tang, *Mater. Chem. Front.*, 2020, **4**, 788–820.
- 285 T. Huang, W. Jiang and L. Duan, *J. Mater. Chem. C*, 2018, **6**, 5577–5596.
- 286 N. Thejo Kalyani and S. J. Dhoble, *Renew. Sustain. Energy Rev.*, 2012, **16**, 2696–2723.
- 287 S. Wang, H. Zhang, B. Zhang, Z. Xie and W. Y. Wong, *Mater. Sci. Eng. R Reports*, 2020, **140**, 100547.
- 288 Y. Xie and Z. Li, *J. Polym. Sci. Part A Polym. Chem.*, 2017, **55**, 575–584.

- 289 A. S. Abd-El-Aziz, A. A. Abdelghani, B. D. Wagner and R. Bissessur, *Macromol. Rapid Commun.*, 2019, **40**, 58–61.
- 290 K. Albrecht, K. Matsuoka, K. Fujita and K. Yamamoto, *Angew. Chemie - Int. Ed.*, 2015, **54**, 5677–5682.
- 291 P. L. Burn, S. C. Lo and I. D. W. Samuel, *Adv. Mater.*, 2007, **19**, 1675–1688.
- 292 G. Zhao, D. Liu, P. Wang, X. Huang, H. Chen, Y. Zhang, D. Zhang, W. Jiang, Y. Sun and L. Duan, *Angew. Chemie Int. Ed.*, 2022, **61**, e202212861.
- 293 S. Zeng, C. Xiao, J. Zhou, Q. Dong, Q. Li, J. Lim, H. Ma, J. Y. Lee, W. Zhu and Y. Wang, *Adv. Funct. Mater.*, 2022, **32**, 2113183.
- 294 J. Liu, L. Chen, X. Wang, Q. Yang, L. Zhao, C. Tong, S. Wang, S. Shao and L. Wang, *Macromol. Rapid Commun.*, 2022, **43**, 2200079.
- 295 Y. H. Kim, C. Wolf, H. Cho, S. H. Jeong and T. W. Lee, *Adv. Mater.*, 2016, **28**, 734–741.
- 296 Y. Wada, S. Kubo and H. Kaji, *Adv. Mater.*, 2018, **30**, 1705641.
- 297 X. Li, K. Wang, Y. Z. Shi, M. Zhang, G. Le Dai, W. Liu, C. J. Zheng, X. M. Ou and X. H. Zhang, *J. Mater. Chem. C*, 2018, **6**, 9152–9157.
- 298 Y. Zhang, J. Wu, J. Song, Z. Chen, J. He, X. Wang, H. Liu, S. Chen, J. Qu and W. Y. Wong, *Adv. Electron. Mater.*, 2019, **5**, 1–7.
- 299 W. Zeng, T. Zhou, W. Ning, C. Zhong, J. He, S. Gong, G. Xie and C. Yang, *Adv. Mater.*, 2019, **31**, 1901404.
- 300 S. M. Kerwin, *J. Am. Chem. Soc.*, 2010, **132**, 2466–2467.
- 301 E. Duda, D. Hall, S. Bagnich, C. L. Carpenter-Warren, R. Saxena, M. Y. Wong, D. B. Cordes, A. M. Z. Slawin, D. Beljonne, Y. Olivier, E. Zysman-Colman and A. Köhler, *J. Phys. Chem. B*, 2022, **126**, 552–562.
- 302 G. Hong, C. Si, A. K. Gupta, C. Bizzarri, M. Nieger, I. D. W. Samuel, E. Zysman-Colman and S. Bräse, *J. Mater. Chem. C*, 2022, **10**, 4757–4766.
- 303 Y. Liu, Y. Chen, H. Li, S. Wang, X. Wu, H. Tong and L. Wang, *ACS Appl. Mater. Interfaces*, 2020, **12**, 30652–30658.
- 304 C. Y. Chan, M. Tanaka, Y. T. Lee, Y. W. Wong, H. Nakanotani, T. Hatakeyama and C. Adachi, *Nat. Photonics*, 2021, **15**, 203–207.
- 305 J. W. Sun, J. H. Lee, C. K. Moon, K. H. Kim, H. Shin and J. J. Kim, *Adv. Mater.*, 2014, **26**, 5684–5688.
- 306 S. Wu, A. Kumar Gupta, K. Yoshida, J. Gong, D. Hall, D. B. Cordes, A. M. Z. Slawin, I. D. W. Samuel and E. Zysman-Colman, *Angew. Chemie Int. Ed.*, 2022, **61**, e202213697.
- 307 H. S. Kim, S. R. Park and M. C. Suh, *J. Phys. Chem. C*, 2017, **121**, 13986–13997.
- 308 D. Chen, X. Cai, X. L. Li, Z. He, C. Cai, D. Chen and S. J. Su, *J. Mater. Chem. C*, 2017, **5**, 5223–5231.
- 309 J. Y. Woo, M. Park, S. Jeong, Y. Kim, B. Kim, T. Lee and T. Han, *Adv. Mater.*, 2023, **35**, 2207454.
- 310 N. R. Wallwork, M. Mamada, A. B. Keto, S. K. M. McGregor, A. Shukla, C. Adachi, E. H. Krenske, E. B. Namdas and S. C. Lo, *Macromol. Rapid Commun.*, 2022, **43**, 1–12.
- 311 N. R. Wallwork, M. Mamada, A. Shukla, S. K. M. McGregor, C. Adachi, E. B. Namdas and S.-C. Lo, *J. Mater. Chem. C*, 2022, **10**, 4767–4774.
- 312 A. Shahalizad, A. Malinge, L. Hu, G. Laflamme, L. Haeberlé, D. M. Myers, J. Mao, W.

- G. Skene and S. Kéna-Cohen, *Adv. Funct. Mater.*, 2021, **31**, 2007119.
- 313 K. Sun, Z. Cai, J. Jiang, W. Tian, W. Guo, J. Shao, W. Jiang and Y. Sun, *Dye. Pigment.*, 2020, **173**, 107957.
- 314 D. Jiang, H. Sasabe, H. Arai, K. Nakao, K. Kumada and J. Kido, *Adv. Opt. Mater.*, 2022, **10**, 2102774.
- 315 S. S. Reddy, V. G. Sree, K. Gunasekar, W. Cho, Y.-S. Gal, M. Song, J.-W. Kang and S.-H. Jin, *Adv. Opt. Mater.*, 2016, **4**, 1236–1246.
- 316 A. M. Butterfield, B. Gilomen and J. S. Siegel, *Org. Process Res. Dev.*, 2012, **16**, 664–676.
- 317 S. Kawata, J. Furudate, T. Kimura, H. Minaki, A. Saito, H. Katagiri and Y. J. Pu, *J. Mater. Chem. C*, 2017, **5**, 4909–4914.
- 318 M. K. Etherington, J. Gibson, H. F. Higginbotham, T. J. Penfold and A. P. Monkman, *Nat. Commun.*, 2016, **7**, 13680.
- 319 H. Qian, M. E. Cousins, E. H. Horak, A. Wakefield, M. D. Liptak and I. Aprahamian, *Nat. Chem.*, 2017, **9**, 83–87.
- 320 A. P. Demchenko, V. I. Tomin and P. T. Chou, *Chem. Rev.*, 2017, **117**, 13353–13381.
- 321 Y. Liu, G. Xie, Z. Ren and S. Yan, *ACS Appl. Polym. Mater.*, 2019, **1**, 2204–2212.
- 322 M. Luo, X. Li, L. Ding, G. Baryshnikov, S. Shen, M. Zhu, L. Zhou, M. Zhang, J. Lu, H. Ågren, X. Wang and L. Zhu, *Angew. Chemie*, 2020, **132**, 17166–17173.
- 323 H. Tanaka, K. Shizu, H. Nakanotani and C. Adachi, *J. Phys. Chem. C*, 2014, **118**, 15985–15994.
- 324 X. Cai, Z. Qiao, M. Li, X. Wu, Y. He, X. Jiang, Y. Cao and S. J. Su, *Angew. Chemie - Int. Ed.*, 2019, **58**, 13522–13531.
- 325 Y. Geng, A. D’Aleo, K. Inada, L. Cui, J. U. Kim, H. Nakanotani and C. Adachi, *Angew. Chemie*, 2017, **129**, 16763–16767.
- 326 Z. Xie, Q. Huang, T. Yu, L. Wang, Z. Mao, W. Li, Z. Yang, Y. Zhang, S. Liu, J. Xu, Z. Chi and M. P. Aldred, *Adv. Funct. Mater.*, 2017, **27**, 1703918.
- 327 J. Chen, T. Yu, E. Ubba, Z. Xie, Z. Yang, Y. Zhang, S. Liu, J. Xu, M. P. Aldred and Z. Chi, *Adv. Opt. Mater.*, 2019, **7**, 1801593.
- 328 X. Zhang, T. Lu, C. Zhou, H. Liu, Y. Wen, Y. Shen, B. Li, S. T. Zhang and B. Yang, *CCS Chem.*, 2022, **4**, 625–637.
- 329 X. Chen, Z. He, F. Kausar, G. Chen, Y. Zhang and W. Z. Yuan, *Macromolecules*, 2018, **51**, 9035–9042.
- 330 X. Feng, C. Qi, H. T. Feng, Z. Zhao, H. H. Y. Sung, I. D. Williams, R. T. K. Kwok, J. W. Y. Lam, A. Qin and B. Z. Tang, *Chem. Sci.*, 2018, **9**, 5679–5687.
- 331 Y. Liu, M. Nishiura, Y. Wang and Z. Hou, *J. Am. Chem. Soc.*, 2006, **128**, 5592–5593.
- 332 M. H. Filby, S. J. Dickson, N. Zaccheroni, L. Prodi, S. Bonacchi, M. Montalti, M. J. Paterson, T. D. Humphries, C. Chiorboli and J. W. Steed, *J. Am. Chem. Soc.*, 2008, **130**, 4105–4113.
- 333 Q. Y. Yang and J. M. Lehn, *Angew. Chemie - Int. Ed.*, 2014, **53**, 4572–4577.
- 334 R. Yoshii, A. Hirose, K. Tanaka and Y. Chujo, *J. Am. Chem. Soc.*, 2014, **136**, 18131–18139.
- 335 P. P. Neelakandan and D. Ramaiah, *Angew. Chemie - Int. Ed.*, 2008, **47**, 8407–8411.
- 336 D. Mansell, N. Rattray, L. L. Etchells, C. H. Schwalbe, A. J. Blake, E. V. Bichenkova,

- R. A. Bryce, C. J. Barker, A. Díaz, C. Kremer and S. Freeman, *Chem. Commun.*, 2008, 5161.
- 337 D. Thirion, M. Romain, J. Rault-Berthelot and C. Poriel, *J. Mater. Chem.*, 2012, **22**, 7149–7157.
- 338 P. I. Shih, C. Y. Chuang, C. H. Chien, E. W. G. Diau and C. F. Shu, *Adv. Funct. Mater.*, 2007, **17**, 3141–3146.
- 339 G. Klärner, M. H. Davey, W.-D. Chen, J. C. Scott and R. D. Miller, *Adv. Mater.*, 1998, **10**, 993–997.
- 340 J. Zhang, X. Zhao, H. Shen, J. W. Y. Lam, H. Zhang and B. Z. Tang, *Adv. Photonics*, 2021, **4**, 014001.
- 341 F. C. Spano, *Acc. Chem. Res.*, 2010, **43**, 429–439.
- 342 O. P. Dimitriev, Y. P. Piryatinski and Y. L. Slominskii, *J. Phys. Chem. Lett.*, 2018, **9**, 2138–2143.
- 343 C. Zhao, Z. Ding, Y. Zhang, Z. Ni, S. Li, S. Gong, B. Zou, K. Wang and L. Yu, *Chem. Sci.*, 2023, **14**, 1089–1096.
- 344 T. Qin, B. Liu, K. Zhu, Z. Luo, Y. Huang, C. Pan and L. Wang, *TrAC - Trends Anal. Chem.*, 2018, **102**, 259–271.
- 345 Y. Sun, M. Fu, M. Bian and Q. Zhu, *Biotechnol. Bioeng.*, 2023, **120**, 7–21.
- 346 M. M. A. Mazza and F. M. Raymo, *J. Mater. Chem. C*, 2019, **7**, 5333–5342.
- 347 F. Vetrone, R. Naccache, A. Zamarrón, A. Juarranz de la Fuente, F. Sanz-Rodríguez, L. Martínez Maestro, E. Martín Rodríguez, D. Jaque, J. García Solé and J. A. Capobianco, *ACS Nano*, 2010, **4**, 3254–3258.
- 348 G. Feng, H. Zhang, X. Zhu, J. Zhang and J. Fang, *Biomater. Sci.*, 2022, **10**, 1855–1882.
- 349 M. M. Ogle, A. D. Smith McWilliams, B. Jiang and A. A. Martí, *ChemPhotoChem*, 2020, **4**, 255–270.
- 350 S. A. Pfeiffer and S. Nagl, *Methods Appl. Fluoresc.*, 2015, **3**, 034003.
- 351 V. F. Pais, J. M. Lassaletta, R. Fernández, H. S. El-Sheshtawy, A. Ros and U. Pischel, *Chem. - A Eur. J.*, 2014, **20**, 7638–7645.
- 352 S. Uchiyama and C. Gota, *Rev. Anal. Chem.*, 2017, **36**, 20160021.
- 353 J. Feng, L. Xiong, S. Wang, S. Li, Y. Li and G. Yang, *Adv. Funct. Mater.*, 2013, **23**, 340–345.
- 354 J. Jenkins, S. M. Borisov, D. B. Papkovsky and R. I. Dmitriev, *Anal. Chem.*, 2016, **88**, 10566–10572.
- 355 J. Feng, K. Tian, D. Hu, S. Wang, S. Li, Y. Zeng, Y. Li and G. Yang, *Angew. Chemie - Int. Ed.*, 2011, **50**, 8072–8076.
- 356 A. Ito, S. Ishizaka and N. Kitamura, *Phys. Chem. Chem. Phys.*, 2010, **12**, 6641–6649.
- 357 L. Meng, S. Jiang, M. Song, F. Yan, W. Zhang, B. Xu and W. Tian, *ACS Appl. Mater. Interfaces*, 2020, **12**, 26842–26851.
- 358 C. Baleizão and M. N. Berberan-Santos, *Ann. N. Y. Acad. Sci.*, 2008, **1130**, 224–234.
- 359 A. Steingger, I. Klimant and S. M. Borisov, *Adv. Opt. Mater.*, 2017, **5**, 1700372.
- 360 F. Fang, L. Zhu, M. Li, Y. Song, M. Sun, D. Zhao and J. Zhang, *Adv. Sci.*, 2021, **8**, 2102970.
- 361 V. Augusto, C. Baleizão, M. N. Berberan-Santos and J. P. S. Farinha, *J. Mater. Chem.*, 2010, **20**, 1192–1197.

- 362 C. Baleizão, S. Nagl, S. M. Borisov, M. Schäferling, O. S. Wolfbeis and M. N. Berberan-Santos, *Chem. - A Eur. J.*, 2007, **13**, 3643–3651.
- 363 T. Förster, *Angew. Chemie Int. Ed. English*, 1969, **8**, 333–343.
- 364 Z. Chen, B. Fimmel and F. Würthner, *Org. Biomol. Chem.*, 2012, **10**, 5845–5855.
- 365 D. Simionesie, G. O’Callaghan, J. R. H. Manning, T. Düren, J. A. Preece, R. Evans and Z. J. Zhang, *Polycycl. Aromat. Compd.*, 2023, **43**, 3790–3809.
- 366 J. Yang, M. Fang and Z. Li, *Aggregate*, 2020, **1**, 6–18.
- 367 Q. Peng, L. Yang, Y. Li, Y. Zhang, T. Li, Y. Qin, Y. Song, H. Hou and K. Li, *J. Phys. Chem. C*, 2020, **124**, 22684–22691.
- 368 Y. Hong, J. W. Y. Y. Lam and B. Z. Tang, *Chem. Commun.*, 2009, 4332–4353.
- 369 W. Zeng, T. Zhou, W. Ning, C. Zhong, J. He, S. Gong, G. Xie and C. Yang, *Adv. Mater.*, 2019, **31**, 1901404.
- 370 B. W. E. Lawton R G, *J. Am. Chem. Soc.*, 1971, **93**, 1730–1745.
- 371 J. C. Hanson and C. E. Nordman, *Acta Crystallogr. Sect. B Struct. Crystallogr. Cryst. Chem.*, 1976, **32**, 1147–1153.
- 372 T. J. Seiders, K. K. Baldridge, G. H. Grube and J. S. Siegel, *J. Am. Chem. Soc.*, 2001, **123**, 517–525.
- 373 Y.-T. Wu and J. S. Siegel, *Chem. Rev.*, 2006, **106**, 4843–4867.
- 374 M. Juriček, N. L. Strutt, J. C. Barnes, A. M. Butterfield, E. J. Dale, K. K. Baldridge, J. F. Stoddart and J. S. Siegel, *Nat. Chem.*, 2014, **6**, 222–228.
- 375 X. Li, F. Kang and M. Inagaki, *Small*, 2016, 3206–3223.
- 376 J. J. Huang, H. A. Lin, C. Chen, P. W. Tang and S. C. Luo, *J. Mater. Chem. C*, 2021, **9**, 7919–7927.
- 377 A. Ayalon, M. Rabinovitz, P. -C Cheng and L. T. Scott, *Angew. Chemie Int. Ed. English*, 1992, **31**, 1636–1637.
- 378 E. Nestoros and M. C. Stuparu, *Chem. Commun*, 2018, **54**, 6503–6519.
- 379 J. J. Huang, H. I. Liang, H. A. Lin and S. C. Luo, *ACS Appl. Electron. Mater.*, 2022, **4**, 4996–5007.
- 380 A. Mishra, M. Ulaganathan, E. Edison, P. Borah, A. Mishra, S. Sreejith, S. Madhavi and M. C. Stuparu, *ACS Macro Lett.*, 2017, **6**, 1212–1216.
- 381 M. Gaboardi, F. Pratt, C. Milanese, J. Taylor, J. Siegel and F. Fernandez-Alonso, *Carbon N. Y.*, 2019, **155**, 432–437.
- 382 R. Q. Lu, Y. Q. Zheng, Y. N. Zhou, X. Y. Yan, T. Lei, K. Shi, Y. Zhou, J. Pei, L. Zoppi, K. K. Baldridge, J. S. Siegel and X. Y. Cao, *J. Mater. Chem. A*, 2014, **2**, 20515–20519.
- 383 B. T. Muhammad, V. Barát, T. M. Koh, X. Wu, A. Surendran, N. Yantara, A. Bruno, A. C. Grimsdale, M. C. Stuparu and W. L. Leong, *Chem. Commun.*, 2020, **56**, 11997–12000.
- 384 M. W. An, B. S. Wu, S. Wang, Z. C. Chen, Y. Su, L. L. Deng, S. H. Li, Z. A. Nan, H. R. Tian, X. L. Liu, D. Q. Yun, Q. Zhang, S. Y. Xie and L. S. Zheng, *Cell Reports Phys. Sci.*, 2021, **2**, 100662.
- 385 Z. Xing, M.-W. An, Z.-C. Chen, M. Hu, X. Huang, L.-L. Deng, Q. Zhang, X. Guo, S.-Y. Xie and S. Yang, *J. Am. Chem. Soc.*, 2022, **144**, 13839–13850.
- 386 R. Q. Lu, Y. N. Zhou, X. Y. Yan, K. Shi, Y. Q. Zheng, M. Luo, X. C. Wang, J. Pei, H. Xia, L. Zoppi, K. K. Baldridge, J. S. Siegel and X. Y. Cao, *Chem. Commun.*, 2015, **51**, 1681–1684.

- 387 R. Chen, R. Q. Lu, K. Shi, F. Wu, H. X. Fang, Z. X. Niu, X. Y. Yan, M. Luo, X. C. Wang, C. Y. Yang, X. Y. Wang, B. Xu, H. Xia, J. Pei and X. Y. Cao, *Chem. Commun.*, 2015, **51**, 13768–13771.
- 388 X. Fu, Y. Zhen, Z. Ni, Y. Li, H. Dong, J. S. Siegel and W. Hu, *Angew. Chemie Int. Ed.*, 2020, **59**, 14024–14028.
- 389 S. Sreejith, N. V. Menon, Y. Wang, H. Joshi, S. Liu, K. C. Chong, Y. Kang, H. Sun and M. C. Stuparu, *Mater. Chem. Front.*, 2017, **1**, 831–837.
- 390 R. Q. Lu, S. Wu, L. L. Yang, W. Bin Gao, H. Qu, X. Y. Wang, J. B. Chen, C. Tang, H. Y. Shi and X. Y. Cao, *Angew. Chemie - Int. Ed.*, 2019, **58**, 7600–7605.
- 391 X. Gu, X. Zhang, H. Ma, S. Jia, P. Zhang, Y. Zhao, Q. Liu, J. Wang, X. Zheng, J. W. Y. Lam, D. Ding and B. Z. Tang, *Adv. Mater.*, 2018, **30**, 1801065.
- 392 Y. Wang, H. Jiang, X. Liu, J. Xu, Y. Gao and N. S. Finney, *Chem. Commun.*, 2021, **57**, 5818–5821.
- 393 W. E. Barth and R. G. Lawton, *J. Am. Chem. Soc.*, 1966, **88**, 380–381.
- 394 P. Bachawala, T. Ratterman, N. Kaval and J. Mack, *Tetrahedron*, 2017, **73**, 3831–3837.
- 395 J. Mack, P. Vogel, D. Jones, N. Kaval and A. Sutton, *Org. Biomol. Chem.*, 2007, **5**, 2448–2452.
- 396 S. Nakatsuka, N. Yasuda and T. Hatakeyama, *J. Am. Chem. Soc.*, 2018, **140**, 13562–13565.
- 397 J. Li, A. Terec, W. Yue, H. Joshi, Y. Lu, H. Sun and M. C. Stuparu, *J. Am. Chem. Soc.*, 2017, **139**, 3089–3094.
- 398 A. M. Rice, W. B. Fellows, E. A. Dolgoplova, A. B. Greytak, A. K. Vannucci, M. D. Smith, S. G. Karakalos, J. A. Krause, S. M. Avdoshenko, A. A. Popov and N. B. Shustova, *Angew. Chemie Int. Ed.*, 2017, **56**, 4525–4529.
- 399 C. S. Jones, E. Elliott and J. S. Siegel, *Synlett*, 2004, **1**, 187–191.
- 400 B. Minaev, G. Baryshnikov and H. Agren, *Phys. Chem. Chem. Phys.*, 2014, **16**, 1719–1758.
- 401 C. Ulbricht, B. Beyer, C. Friebe, A. Winter and U. S. Schubert, *Adv. Mater.*, 2009, **21**, 4418–4441.
- 402 Q. Dang, Y. Jiang, J. Wang, J. Wang, Q. Zhang, M. Zhang, S. Luo, Y. Xie, K. Pu, Q. Li and Z. Li, *Adv. Mater.*, 2020, **32**, 2006752.
- 403 S. M. A. Fateminia, Z. Mao, S. Xu, Z. Yang, Z. Chi and B. Liu, *Angew. Chemie Int. Ed.*, 2017, **56**, 12160–12164.
- 404 G. Zhang, G. M. Palmer, M. W. Dewhirst and C. L. Fraser, *Nat. Mater.*, 2009, **8**, 747–751.
- 405 W. Dai, X. Niu, X. Wu, Y. Ren, Y. Zhang, G. Li, H. Su, Y. Lei, J. Xiao, J. Shi, B. Tong, Z. Cai and Y. Dong, *Angew. Chemie Int. Ed.*, 2022, **61**, e202200236.
- 406 X. Wang, H. Shi, H. Ma, W. Ye, L. Song, J. Zan, X. Yao, X. Ou, G. Yang, Z. Zhao, M. Singh, C. Lin, H. Wang, W. Jia, Q. Wang, J. Zhi, C. Dong, X. Jiang, Y. Tang, X. Xie, Y. Yang, J. Wang, Q. Chen, Y. Wang, H. Yang, G. Zhang, Z. An, X. Liu and W. Huang, *Nat. Photonics*, 2021, **15**, 187–192.
- 407 Z. Yu, Y. Wu, L. Xiao, J. Chen, Q. Liao, J. Yao and H. Fu, *J. Am. Chem. Soc.*, 2017, **139**, 6376–6381.
- 408 W. Zhao, Z. He and B. Z. Tang, *Nat. Rev. Mater.*, 2020, **5**, 869–885.

- 409 M. Y. Wong and E. Zysman-Colman, *Adv. Mater.*, 2017, **29**, 1605444.
- 410 Y. Zhou, W. Qin, C. Du, H. Gao, F. Zhu and G. Liang, *Angew. Chemie Int. Ed.*, 2019, **58**, 12102–12106.
- 411 L. Huang, B. Chen, X. Zhang, C. O. Trindle, F. Liao, Y. Wang, H. Miao, Y. Luo and G. Zhang, *Angew. Chemie Int. Ed.*, 2018, **57**, 16046–16050.
- 412 J.-A. Li, Z. Song, Y. Chen, C. Xu, S. Li, Q. Peng, G. Shi, C. Liu, S. Luo, F. Sun, Z. Zhao, Z. Chi, Y. Zhang and B. Xu, *Chem. Eng. J.*, 2021, **418**, 129167.
- 413 Y. Tao, C. Liu, Y. Xiang, Z. Wang, X. Xue, P. Li, H. Li, G. Xie, W. Huang and R. Chen, *J. Am. Chem. Soc.*, 2022, **144**, 6946–6953.
- 414 Y. Wang, J. Yang, M. Fang, Y. Gong, J. Ren, L. Tu, B. Z. Tang and Z. Li, *Adv. Funct. Mater.*, 2021, **31**, 2101719.
- 415 T. Zhang, Y. Wu and X. Ma, *Chem. Eng. J.*, 2021, **412**, 128689.
- 416 W. Ye, H. Ma, H. Shi, H. Wang, A. Lv, L. Bian, M. Zhang, C. Ma, K. Ling, M. Gu, Y. Mao, X. Yao, C. Gao, K. Shen, W. Jia, J. Zhi, S. Cai, Z. Song, J. Li, Y. Zhang, S. Lu, K. Liu, C. Dong, Q. Wang, Y. Zhou, W. Yao, Y. Zhang, H. Zhang, Z. Zhang, X. Hang, Z. An, X. Liu and W. Huang, *Nat. Mater.*, 2021, **20**, 1539–1544.
- 417 X. Liu, L. Yang, X. Li, L. Zhao, S. Wang, Z. Lu, J. Ding and L. Wang, *Angew. Chemie Int. Ed.*, 2021, **60**, 2455–2463.
- 418 J. Wang, J. Liang, Y. Xu, B. Liang, J. Wei, C. Li, X. Mu, K. Ye and Y. Wang, *J. Phys. Chem. Lett.*, 2019, **10**, 5983–5988.
- 419 T. Wang, X. Su, X. Zhang, X. Nie, L. Huang, X. Zhang, X. Sun, Y. Luo and G. Zhang, *Adv. Mater.*, 2019, **31**, 1904273.
- 420 W. Zhao, Z. He and B. Z. Tang, *Nat. Rev. Mater.*, 2020, **5**, 869–885.
- 421 D. Tu, S. Cai, C. Fernandez, H. Ma, X. Wang, H. Wang, C. Ma, H. Yan, C. Lu and Z. An, *Angew. Chemie Int. Ed.*, 2019, **58**, 9129–9133.
- 422 Z. Mao, Z. Yang, C. Xu, Z. Xie, L. Jiang, F. L. Gu, J. Zhao, Y. Zhang, M. P. Aldred and Z. Chi, *Chem. Sci.*, 2019, **10**, 7352–7357.
- 423 S. Tian, H. Ma, X. Wang, A. Lv, H. Shi, Y. Geng, J. Li, F. Liang, Z. Su, Z. An and W. Huang, *Angew. Chemie Int. Ed.*, 2019, **58**, 6645–6649.
- 424 Y. Gong, G. Chen, Q. Peng, W. Z. Yuan, Y. Xie, S. Li, Y. Zhang and B. Z. Tang, *Adv. Mater.*, 2015, **27**, 6195–6201.
- 425 Z. Yang, Z. Mao, X. Zhang, D. Ou, Y. Mu, Y. Zhang, C. Zhao, S. Liu, Z. Chi, J. Xu, Y.-C. Wu, P.-Y. Lu, A. Lien and M. R. Bryce, *Angew. Chemie Int. Ed.*, 2016, **55**, 2181–2185.
- 426 T. Ono, A. Taema, A. Goto and Y. Hisaeda, *Chem. – A Eur. J.*, 2018, **24**, 17487–17496.
- 427 A. Cheng, Y. Jiang, H. Su, B. Zhang, J. Jiang, T. Wang, Y. Luo and G. Zhang, *Angew. Chemie Int. Ed.*, 2022, **61**, e202206366.
- 428 X. Yan, H. Peng, Y. Xiang, J. Wang, L. Yu, Y. Tao, H. Li, W. Huang and R. Chen, *Small*, 2022, **18**, 2104073.
- 429 M. Kasha, *Discuss. Faraday Soc.*, 1950, **9**, 14.
- 430 Z. He, W. Zhao, J. W. Y. Lam, Q. Peng, H. Ma, G. Liang, Z. Shuai and B. Z. Tang, *Nat. Commun.*, 2017, **8**, 1–7.
- 431 Y. Wu, H. Xiao, B. Chen, R. G. Weiss, Y. Chen, C. Tung and L. Wu, *Angew. Chemie Int. Ed.*, 2020, **59**, 10173–10178.

- 432 F. Li, S. Guo, Y. Qin, Y. Shi, M. Han, Z. An, S. Liu, Q. Zhao and W. Huang, *Adv. Opt. Mater.*, 2019, **7**, 1900511.
- 433 L. Gu, H. Shi, L. Bian, M. Gu, K. Ling, X. Wang, H. Ma, S. Cai, W. Ning, L. Fu, H. Wang, S. Wang, Y. Gao, W. Yao, F. Huo, Y. Tao, Z. An, X. Liu and W. Huang, *Nat. Photonics*, 2019, **13**, 406–411.
- 434 T. Wang, Z. Hu, X. Nie, L. Huang, M. Hui, X. Sun and G. Zhang, *Nat. Commun.*, 2021, **12**, 1364.
- 435 T. Wang, J. De, S. Wu, A. K. Gupta and E. Zysman-Colman, *Angew. Chemie Int. Ed.*, 2022, **61**, e202206681.
- 436 Y. Liu, X. Xiao, Z. Huang, D. Yang, D. Ma, J. Liu, B. Lei, Z. Bin and J. You, *Angew. Chemie Int. Ed.*, 2022, **61**, e202210210.
- 437 I. V. Kuvychko, S. N. Spisak, Y.-S. Chen, A. A. Popov, M. A. Petrukhina, S. H. Strauss and O. V. Boltalina, *Angew. Chemie Int. Ed.*, 2012, **51**, 4939–4942.
- 438 C. Dubceac, A. S. Filatov, A. V. Zabula and M. A. Petrukhina, *Cryst. Growth Des.*, 2015, **15**, 778–785.
- 439 B. Topolinski, B. M. Schmidt, S. Schwagerus, M. Kathan and D. Lentz, *Eur. J. Inorg. Chem.*, 2014, **2014**, 5391–5405.
- 440 Y. Zhao and D. G. Truhlar, *Theor. Chem. Acc.*, 2008, **120**, 215–241.
- 441 G. Rouillé, C. Jäger, M. Steglich, F. Huisken, T. Henning, G. Theumer, I. Bauer and H. J. Knölker, *ChemPhysChem*, 2008, **9**, 2085–2091.
- 442 P. L. Dos Santos, J. S. Ward, A. S. Batsanov, M. R. Bryce and A. P. Monkman, *J. Phys. Chem. C*, 2017, **121**, 16462–16469.
- 443 S. Izumi, H. F. Higginbotham, A. Nyga, P. Stachelek, N. Tohnai, P. de Silva, P. Data, Y. Takeda and S. Minakata, *J. Am. Chem. Soc.*, 2020, **142**, 1482–1491.
- 444 Y. Xu, C. Wang, X. Zhou, J. Zhou, X. Guo, X. Liang, D. Hu, F. Li, D. Ma and Y. Ma, *J. Phys. Chem. Lett.*, 2019, **10**, 6878–6884.
- 445 W. Li, D. Liu, F. Shen, D. Ma, Z. Wang, T. Feng, Y. Xu, B. Yang and Y. Ma, *Adv. Funct. Mater.*, 2012, **22**, 2797–2803.
- 446 W. R. Ware, *J. Phys. Chem.*, 1962, **66**, 455–458.
- 447 D. Zhang, M. Cai, Z. Bin, Y. Zhang, D. Zhang and L. Duan, *Chem. Sci.*, 2016, **7**, 3355–3363.
- 448 Y. Wang, J. Yang, M. Fang, Y. Yu, B. Zou, L. Wang, Y. Tian, J. Cheng, B. Z. Tang and Z. Li, *Matter*, 2020, **3**, 449–463.
- 449 C. Chen, Z. Chi, K. C. Chong, A. S. Batsanov, Z. Yang, Z. Mao, Z. Yang and B. Liu, *Nat. Mater.*, 2021, **20**, 175–180.
- 450 D. Lee, O. Bolton, B. C. Kim, J. H. Youk, S. Takayama and J. Kim, *J. Am. Chem. Soc.*, 2013, **135**, 6325–6329.
- 451 W. Qin, J. Ma, Y. Zhou, Q. Hu, Y. Zhou and G. Liang, *Chem. Eng. J.*, 2020, **400**, 125934.
- 452 J. X. Wang, L. Y. Peng, Z. F. Liu, X. Zhu, L. Y. Niu, G. Cui and Q. Z. Yang, *J. Phys. Chem. Lett.*, 2022, **13**, 1985–1990.
- 453 R. Kabe, N. Notsuka, K. Yoshida and C. Adachi, *Adv. Mater.*, 2016, **28**, 655–660.
- 454 S. Tan, K. Jinnai, R. Kabe and C. Adachi, *Adv. Mater.*, 2021, **33**, 2008844.
- 455 G. Xie, J. Wang, X. Xue, H. Li, N. Guo, H. Li, D. Wang, M. Li, W. Huang, R. Chen and Y. Tao, *Appl. Phys. Rev.*, 2022, **9**, 031410.

- 456 H. Lv, R. Ma, X. Zhang, M. Li, Y. Wang, S. Wang and G. Xing, *Tetrahedron*, 2016, **72**, 5495–5501.
- 457 N. Venkatramaiah, G. Dinesh Kumar, Y. Chandrasekaran, R. Ganduri and S. Patil, *ACS Appl. Mater. Interfaces*, 2018, **10**, 3838–3847.
- 458 I. S. Park, S. Y. Lee, C. Adachi and T. Yasuda, *Adv. Funct. Mater.*, 2016, **26**, 1813–1821.
- 459 N. Liu, B. Wang, W. Chen, C. Liu, X. Wang and Y. Hu, *RSC Adv.*, 2014, **4**, 51133–51139.
- 460 J. Qian and B. Z. Tang, *Chem*, 2017, **3**, 56–91.
- 461 S. Lee, C. S. Park and H. Yoon, *Int. J. Mol. Sci.*, 2022, **23**, 4949.
- 462 W. Chen and F. Song, *Chinese Chem. Lett.*, 2019, **30**, 1717–1730.
- 463 Y. Tsuchiya, K. Ikesue, H. Nakanotani and C. Adachi, *Chem. Commun.*, 2019, **55**, 5215–5218.
- 464 D. M. Mayder, R. Hojo, W. L. Primrose, C. M. Tonge and Z. M. Hudson, *Adv. Funct. Mater.*, 2022, **32**, 2204087.
- 465 D. F. MJ Frisch, GW Trucks, HB Schlegel, GE Scuseria, MA Robb, JR Cheeseman, G Scalmani, V Barone, GA Petersson, HJRA Nakatsuji, X Li, M Caricato, AV Marenich, J Bloino, BG Janesko, R Gomperts, B Mennucci, HP Hratchian, JV Ortiz, AF Izmaylov, JL Sonnenberg, D W, *Gaussian 16 rev. C.01*, 2016, 2016.
- 466 J. M. Dennington, R., Keith, T. A., Millam, *Semichem Inc. Shawnee Mission KS.*, 2019, 2019.
- 467 N. M. O’Boyle and G. R. Hutchison, *Chem. Cent. J.*, 2008, **2**, 1–10.
- 468 N. M. O’Boyle, M. Banck, C. A. James, C. Morley, T. Vandermeersch and G. R. Hutchison, *J. Cheminform.*, 2011, **3**, 33.
- 469 A. Allouche, *J. Comput. Chem.*, 2012, **32**, 174–182.
- 470 J. D. Hunter, *Comput. Sci. Eng.*, 2007, **9**, 90–95.
- 471 J. Schirmer, *Phys. Rev. A*, 1982, **26**, 2395–2416.
- 472 X. Gao, S. Bai, D. Fazzi, T. Niehaus, M. Barbatti and W. Thiel, *J. Chem. Theory Comput.*, 2017, **13**, 515–524.
- 473 A. B. Trofimov and J. Schirmer, *J. Phys. B At. Mol. Opt. Phys.*, 1995, **28**, 2299–2324.
- 474 E. R. Johnson, S. Keinan, P. Mori-Sánchez, J. Contreras-García, A. J. Cohen and W. Yang, *J. Am. Chem. Soc.*, 2010, **132**, 6498–6506.
- 475 T. Lu and F. Chen, *J. Comput. Chem.*, 2012, **33**, 580–592.
- 476 J. Pommerehne, H. Vestweber, W. Guss, R. F. Mahrt, H. Bässler, M. Porsch and J. Daub, *Adv. Mater.*, 1995, **7**, 551–554.
- 477 CrystalClear-SM Expert v2.1. Rigaku Americas, Woodlands, Texas, USA, Rigaku Corp. Tokyo, Japan,.
- 478 CrysAlisPro, *CrysAlisPro v1.171.39.8d. Rigaku Oxford Diffraction, Rigaku Corp. Oxford, U.K.*
- 479 G. M. Sheldrick, *Acta Crystallogr. Sect. A Found. Adv.*, 2015, **71**, 3–8.
- 480 M. C. Burla, R. Caliendo, M. Camalli, B. Carrozzini, G. L. Casciarano, C. Giacovazzo, M. Mallamo, A. Mazzone, G. Polidori and R. Spagna, *J. Appl. Crystallogr.*, 2012, **45**, 357–361.
- 481 G. M. Sheldrick, *Acta Crystallogr. Sect. C Struct. Chem.*, 2015, **71**, 3–8.

- 482 O. V Dolomanov, L. J. Bourhis, R. J. Gildea, J. A. K. Howard and H. Puschmann, *J. Appl. Crystallogr.*, 2009, **42**, 339–341.
- 483 CrystalStructure v4.3.0.Rigaku Americas, The Woodlands, Texas, USA, and Rigaku Corporation, Tokyo, Japan, 2018.
- 484 J. N. Demas and G. A. Crosby, *J. Phys. Chem.*, 1971, **75**, 991–1024.
- 485 S. Fery-Forgues and D. Lavabre, *J. Chem. Educ.*, 1999, **76**, 1260–1264.